frontiers | Research Topics

Advances and applications of predictive toxicology in knowledge discovery, risk assessment, and drug development

Edited by
Huaqiang Zhai, Yong-Long Han and Jiayu Liao

Coordinated by
Nan Zhang

Published in
Frontiers in Pharmacology

ISSN 1664-8714
ISBN 978-2-8325-7015-9
DOI 10.3389/978-2-8325-7015-9

Generative AI statement
Any alternative text (Alt text) provided alongside figures in the articles in this ebook has been generated by Frontiers with the support of artificial intelligence and reasonable efforts have been made to ensure accuracy, including review by the authors wherever possible. If you identify any issues, please contact us.

About Frontiers

Frontiers is more than just an open access publisher of scholarly articles: it is a pioneering approach to the world of academia, radically improving the way scholarly research is managed. The grand vision of Frontiers is a world where all people have an equal opportunity to seek, share and generate knowledge. Frontiers provides immediate and permanent online open access to all its publications, but this alone is not enough to realize our grand goals.

Frontiers journal series

The Frontiers journal series is a multi-tier and interdisciplinary set of open-access, online journals, promising a paradigm shift from the current review, selection and dissemination processes in academic publishing. All Frontiers journals are driven by researchers for researchers; therefore, they constitute a service to the scholarly community. At the same time, the *Frontiers journal series* operates on a revolutionary invention, the tiered publishing system, initially addressing specific communities of scholars, and gradually climbing up to broader public understanding, thus serving the interests of the lay society, too.

Dedication to quality

Each Frontiers article is a landmark of the highest quality, thanks to genuinely collaborative interactions between authors and review editors, who include some of the world's best academicians. Research must be certified by peers before entering a stream of knowledge that may eventually reach the public - and shape society; therefore, Frontiers only applies the most rigorous and unbiased reviews. Frontiers revolutionizes research publishing by freely delivering the most outstanding research, evaluated with no bias from both the academic and social point of view. By applying the most advanced information technologies, Frontiers is catapulting scholarly publishing into a new generation.

What are Frontiers Research Topics?

Frontiers Research Topics are very popular trademarks of the *Frontiers journals series*: they are collections of at least ten articles, all centered on a particular subject. With their unique mix of varied contributions from Original Research to Review Articles, Frontiers Research Topics unify the most influential researchers, the latest key findings and historical advances in a hot research area.

Find out more on how to host your own Frontiers Research Topic or contribute to one as an author by contacting the Frontiers editorial office: frontiersin.org/about/contact

Advances and applications of predictive toxicology in knowledge discovery, risk assessment, and drug development

Topic editors
Huaqiang Zhai — Beijing University of Chinese Medicine, China
Yong-Long Han — Shanghai Jiao Tong University, China
Jiayu Liao — University of California, Riverside, United States

Topic coordinator
Nan Zhang — Beijing University of Chinese Medicine, China

Citation
Zhai, H., Han, Y.-L., Liao, J., Zhang, N., eds. (2025). *Advances and applications of predictive toxicology in knowledge discovery, risk assessment, and drug development*. Lausanne: Frontiers Media SA. doi: 10.3389/978-2-8325-7015-9

Table of contents

frontiers | Frontiers in Pharmacology

TYPE Editorial
PUBLISHED 20 October 2025
DOI 10.3389/fphar.2025.1721364

OPEN ACCESS

EDITED AND REVIEWED BY
Ursula Gundert-Remy,
Charité University Medicine Berlin, Germany

*CORRESPONDENCE
Huaqiang Zhai,
jz711@qq.com
Yonglong Han,
yonglongh@126.com
Jiayu Liao,
jiayu.liao@ucr.edu

RECEIVED 09 October 2025
ACCEPTED 13 October 2025
PUBLISHED 20 October 2025

CITATION
Zhang F, Li F, Tan J, Zhang N, Han Y, Liao J and Zhai H (2025) Editorial: Advances and applications of predictive toxicology in knowledge discovery, risk assessment, and drug development.
Front. Pharmacol. 16:1721364.
doi: 10.3389/fphar.2025.1721364

Editorial: Advances and applications of predictive toxicology in knowledge discovery, risk assessment, and drug development

Fengxian Zhang[1], Feiyu Li[1], Jiaqi Tan[1], Nan Zhang[1], Yonglong Han[2]*, Jiayu Liao[3]* and Huaqiang Zhai[1]*

[1]Standardization Research Center of Traditional Chinese Medicine Dispensing, School of Chinese Materia Medica, Beijing University of Chinese Medicine, Beijing, China, [2]Shanghai Sixth People's Hospital Affiliated to Shanghai Jiao Tong University School of Medicine, Shanghai, China, [3]Department of Bioengineering, College of Engineering, Bourns College of Engineering, University of California at Riverside, Riverside, CA, United States

KEYWORDS

predictive toxicology, mechanistic studies, drug toxicity, risk assessment, new drug development

Editorial on the Research Topic
Advances and applications of predictive toxicology in knowledge discovery, risk assessment, and drug development

1 Introduction

In the 20th century, toxicology made slow progress due to overreliance on animal-based assays, incompatible with 3R ethical guidelines while dealing with species-specific inaccuracies, excessive resource use, and sluggish workflows that delayed progress. Moreover, traditional *in vivo* animal tests often contained uncertainties, making it challenging to reliably project chemical toxicities in humans. These two problems—compounded by growing public opposition to animal experimentation—prompted innovation: the 1980s witnessed the rise of *in vitro* systems and computational toxicology, laying the foundation for predictive toxicology.

Driven by converging advances in AI, molecular biology, and data science, this field differs from conventional models of acute and chronic toxicity testing. It uses computational and AI-driven data mining to identify patterns, exploiting existing toxicological datasets to map structure-toxicity relationships, construct predictive models, and forecast potential toxicities of novel compounds.

This Research Topic features 12 contributions aimed at enabling efficient drug toxicity prediction and evaluation through deeper mechanistic understanding and high-throughput risk management—revealing predictive toxicology's transformative potential in clarifying toxicity mechanisms, refining risk assessment, and accelerating safe therapeutic innovation. By integrating computational tools, AI, and *in vitro* techniques, these studies focus on

developing knowledgebases including toxic ingredients, dose-time-toxicity correlations, structure-toxicity links, and clinical toxicity profiles. Such efforts provide comprehensive data foundations for risk forecasting of drug candidates and deliver systematic, quantitative model evaluations for clinical toxicity risk prediction.

2 Predictive modelling and mechanism exploration

Many studies have indicated advancements in applying computational frameworks, AI, and interdisciplinary technologies to drug toxicity prediction and assessment. Through approaches like AI modeling, multi-omics analysis, and integration of mechanistic information, research outcomes in predicting drug-induced toxicities, interpreting their mechanisms, and conducting risk evaluations emphasize the critical role of these tools. They enhance the accuracy of toxicity forecasts, deliver mechanistic insights, and optimize drug safety assessments. For example, Zhao et al. developed an artificial neural network (ANN) model to predict linezolid-induced thrombocytopenia, achieving 96.32% accuracy, which significantly exceeded traditional logistic regression. This highlights of ANN capacity to handle complex nonlinear relationships in toxicity data. Similarly, Roberts et al. combined *in silico* epitope mapping with *in vitro* HLA-binding assays to assess the immunogenicity risks of salmon calcitonin impurities, demonstrating how multi-algorithm approaches enhance prediction robustness. These studies prove AI as a key of next-generation toxicity screening.

Qu et al. further advanced genotoxicity assessment by quantifying γ-H2AX via mass spectrometry in HepG2 cells, a biomarker for DNA double-strand breaks. Their platform detected dose-dependent genotoxicity across 34 chemotherapy agents, with anthracyclines (e.g., doxorubicin) showing the strongest signals, which aligns with clinical cardiotoxicity profiles. These methodologies provide high-resolution mechanistic insights and prioritize compounds for further evaluation.

Rodríguez-Belenguer et al. proposed a novel methodology that integrats mechanistic information (molecular initiating events, MIEs, based on Adverse Outcome Pathways, AOPs) and toxicokinetic (TK) data. By combining multiple QSAR models describing simpler biological phenomena (low-level models, LLMs) and quantitative *in vitro*-to-*in vivo* extrapolation (QIVIVE) models, the sensitivity is enhanced, making it suitable for application to other complex toxicological endpoints (Rodríguez-Belenguer et al., 2024).

Organ toxicity mechanisms were dissected using multi-omics and pathway analysis. Tang et al. revealed that entrectinib induces neuronal apoptosis by suppressing THBS1 and inhibiting the PI3K-AKT/TGF-β pathways, offering therapeutic targets for neurotoxicity mitigation. In hepatotoxicity, Gao et al. linked *Psoralea corylifolia* extract to FXR/PPARα dysregulation in zebrafish, causing bile acid accumulation and lipid metabolism disruption. These findings emphasize the value of pathway-centric models in identifying intervention points. Cardiovascular safety was addressed by Morris et al., who modeled hemodynamic regulation in rats and dogs, incorporating 50 secondary pharmacology targets. Their framework simulated circadian rhythms and drug-induced perturbations (e.g., dopamine's effects on sympathetic activity), providing a template for species-specific toxicity extrapolations.

The Research Topic of delayed immune-related adverse events (irAEs) was explored by Yang et al., who analyzed FAERS data to characterize irAEs occurring >1 year post-ICI initiation. Gastrointestinal and endocrine disorders (ROR_{025} = 10.50) emerged as high-risk late toxicities, urging long-term patient surveillance. This complements the work of Roberts et al. on immunogenicity, highlighting the need for predictive models of delayed T-cell responses.

3 Data-driven risk assessment and validation

Large-scale pharmacovigilance studies have illuminated clinical toxicity patterns. Wu et al. mined the FDA Adverse Event Reporting System (FAERS) to profile KRAS G12C inhibitors (sotorasib/adagrasib), associating sotorasib with hepatobiliary disorders and adagrasib with renal injuries. Similarly, Li et al. identified rosuvastatin-fenofibrate combination risks (e.g., gastrointestinal bleeding) using disproportionality analysis, advocating vigilant clinical monitoring.

Huang et al. leveraged the NHANES data to link osteoporosis to 34 medication ingredients (e.g., levothyroxine and omeprazole), revealing underrecognized drug-induced bone loss. These real-world analyses bridge preclinical predictions and clinical outcomes, thereby refining risk stratification. Zhang et al. established a "toxic component-traditional Chinese medicine-adverse reaction" database targeting traditional Chinese medicines containing toxic components (such as Aconitum alkaloids, mineral medicines, and Arisaema family herbs), identifying four major clinical risk factors: drug-related factors (containing cold and cool medicinal properties/allergenic components), medication-related factors (overdose/treatment duration), individual factors (allergic constitution/special populations), and regulatory factors (incomplete instructions). Gastrointestinal damage (50.8%), skin and appendage damage (33.6%), and allergic reactions (11.0%) were the most prominent adverse events, providing direct evidence for clinical risk stratification of toxic traditional Chinese medicines (Zhang et al., 2024).

Innovative *in vitro* and cross-species platforms have enhanced toxicity prediction. Ma et al. conducted a 90-day rat study of *Lithocarpus litseifolius* extract, establishing a no-observed-adverse-effect level (NOAEL) of 2,000 mg/kg/day and validating its safety for traditional medicine applications. Sung et al. introduced MDTR (Multi-Dimensional Transcriptomic Ruler), a knowledge-guided tool for quantifying liver toxicity via KEGG pathways in transcriptomic data. MDTR outperformed conventional metrics in detecting dose-dependent hepatotoxicity, as seen in LINCS database compounds.

These studies discover clinical toxicity patterns and identify potential risks through large-scale database analyses, while also enhancing toxicity prediction capabilities via innovative *in vitro* experiments and cross-species platforms. Collectively, such efforts provide solid support for drug safety assessment and clinical risk management.

4 New drug development

Developing new pharmaceuticals is a complex, costly task, often stopped by late-stage problems resulting from unanticipated toxic effects. Predictive toxicology addresses this challenge by identifying potential risks early in development process—ultimately reducing expenses and improving patient safety during the drug development. It achieves this by combining chemical analyses, molecular biological frameworks, mathematical algorithms, and computational models to explore links between environmental xenobiotic exposure and chemical-induced adverse outcomes. This integration provides supportive strategies for risk assessment across pharmaceuticals, chemicals and related products.

By combining computational modeling, AI, and high-throughput *in vitro* screening, researchers improve their ability to predict and reduce drug-related risks. This Research Topic compiles various studies that highlight these advanced technologies in toxicological research, offering valuable insights into the mechanisms underlying drug toxicity and facilitating the creation of safer therapeutic compounds.

5 Conclusion

The research featured in this Research Topic has collectively driven progress in predictive toxicology by demonstrating how novel computational and lab-based methodologies can improve our understanding and management of drug-induced toxicity. Distinguished by mechanistic, human-focused models that link chemical structures to biological outcomes, rather than relying on observational endpoints, predictive toxicology has transformed risk assessment for chemicals, pharmaceuticals, and consumer products, becoming a key element in the development and application of modern toxicology.

Consequently, it is essential that we stress raising awareness of predictive toxicology and strictly evaluating associated risks, as these aspects are the foundation for turning scientific advances into practical safety frameworks. Especially, incorporating long-term and acute toxicity evaluations into predictive toxicological processes improves the reliability of toxicity forecasts, ensuring a more complete understanding of potential risks in different exposure situations. These advancements, combined with a greater emphasis on risk awareness, promote the development of safer pharmaceuticals and chemicals while reducing dependence on animal testing, aligning with both ethical imperatives and scientific progress.

However, fully realizing the potential of predictive toxicology requires continued research to address current challenges, including data quality, model interpretability, and regulatory acceptance. Through continued innovation, strengthened partnerships between academia, industry, and regulatory bodies, and a strong focus on risk assessment and awareness, predictive toxicology is expected to play an even more important role in safeguarding human health and environmental safety.

Author contributions

FZ: Writing – original draft, Writing – review and editing. FL: Writing – review and editing. JT: Writing – review and editing. NZ: Writing – review and editing. YH: Writing – review and editing. JL: Writing – review and editing. HZ: Writing – review and editing.

Funding

The author(s) declare that no financial support was received for the research and/or publication of this article.

Conflict of interest

The authors declare that the research was conducted in the absence of any commercial or financial relationships that could be construed as a potential conflict of interest.

Generative AI statement

The author(s) declare that no Generative AI was used in the creation of this manuscript.

Any alternative text (alt text) provided alongside figures in this article has been generated by Frontiers with the support of artificial intelligence and reasonable efforts have been made to ensure accuracy, including review by the authors wherever possible. If you identify any issues, please contact us.

Publisher's note

References

Rodríguez-Belenguer, P., Mangas-Sanjuan, V., Soria-Olivas, E., and Pastor, M. (2024). Integrating mechanistic and toxicokinetic information in predictive models of cholestasis. *J. Chem. Inf. Model.* 64, 2775–2788. doi:10.1021/acs.jcim.3c00945

Zhang, N., Zhong, C., Liu, G., Li, S., Lin, L., Wei, N., et al. (2024). 'Risk-benefit' assessment for comprehensive safety evaluation of Chinese patent medicines containing four common toxic ingredients: an analysis of clinical risk factors. *Front. Pharmacol.* 15, 1324509. doi:10.3389/fphar.2024.1324509

frontiers | Frontiers in Pharmacology

TYPE Original Research
PUBLISHED 21 February 2024
DOI 10.3389/fphar.2024.1308655

OPEN ACCESS

EDITED BY
Yong-Long Han,
Shanghai Jiao Tong University, China

REVIEWED BY
Qiyu Wang,
Jiangxi Academy of Sciences, China
Zigang Cao,
Jinggangshan University, China
Jin Hongtao,
Chinese Academy of Medical Sciences and Peking Union Medical College, China

*CORRESPONDENCE
Shi-Xia Huo,
huoshixia1983@163.com
Yun Zhang,
xiaohan_0818@163.com
Zhi-Jian Li,
lizhijian0220@sina.com

†These authors share first authorship

RECEIVED 06 October 2023
ACCEPTED 31 January 2024
PUBLISHED 21 February 2024

CITATION
Gao S-Y, Zhao J-C, Xia Q, Sun C, Aili M, Talifu A, Huo S-X, Zhang Y and Li Z-J (2024), Evaluation of the hepatotoxicity of *Psoralea corylifolia* L. based on a zebrafish model.
Front. Pharmacol. 15:1308655.
doi: 10.3389/fphar.2024.1308655

Evaluation of the hepatotoxicity of *Psoralea corylifolia* L. based on a zebrafish model

Shu-Yan Gao[1,2†], Jing-Cheng Zhao[3†], Qing Xia[4], Chen Sun[4], Maimaiti Aili[1,2], Ainiwaer Talifu[1,2], Shi-Xia Huo[1,2*], Yun Zhang[4*] and Zhi-Jian Li[1,2*]

[1]Uyghur Medical Hospital of Xinjiang Uyghur Autonomous Region, Ürümqi, China, [2]Xinjiang Key Laboratory of Evidence-Based and Translation, Hospital Preparation of Traditional Chinese Medicine, Ürümqi, China, [3]College of Pharmacy, Xinjiang Medical University, Ürümqi, China, [4]Biology Institute, Qilu University of Technology (Shandong Academy of Sciences), Jinan, China

Objective: *Psoralea corylifolia* L. (FP) has received increasing attention due to its potential hepatotoxicity.

Methods: In this study, zebrafish were treated with different concentrations of an aqueous extract of FP (AEFP; 40, 50, or 60 μg/mL), and the hepatotoxic effects of tonicity were determined by the mortality rate, liver morphology, fluorescence area and intensity of the liver, biochemical indices, and pathological tissue staining. The mRNA expression of target genes in the bile acid metabolic signaling pathway and lipid metabolic pathway was detected by qPCR, and the mechanism of toxicity was initially investigated. AEFP (50 μg/mL) was administered in combination with FXR or a peroxisome proliferator-activated receptor α (PPARα) agonist/inhibitor to further define the target of toxicity.

Results: Experiments on toxic effects showed that, compared with no treatment, AEFP administration resulted in liver atrophy, a smaller fluorescence area in the liver, and a lower fluorescence intensity ($p < 0.05$); alanine transaminase (ALT), aspartate transaminase (AST), and γ-GT levels were significantly elevated in zebrafish ($p < 0.01$), and TBA, TBIL, total cholesterol (TC), TG, low-density lipoprotein cholesterol (LDL-C), and high-density lipoprotein cholesterol (HDL-C) levels were elevated to different degrees ($p < 0.05$); and increased lipid droplets in the liver appeared as fatty deposits. Molecular biological validation revealed that AEFP inhibited the expression of the FXR gene, causing an increase in the expression of the downstream genes SHP, CYP7A1, CYP8B1, BSEP, MRP2, NTCP, peroxisome proliferator-activated receptor γ (PPARγ), ME-1, SCD-1, lipoprotein lipase (LPL), CPT-1, and CPT-2 and a decrease in the expression of PPARα ($p < 0.05$).

Conclusion: This study demonstrated that tonic acid extracts are hepatotoxic to zebrafish through the inhibition of FXR and PPARα expression, thereby causing bile acid and lipid metabolism disorders.

KEYWORDS

***Psoralea corylifolia* L., hepatotoxicity, zebrafish, cholestony, lipid metabolism**

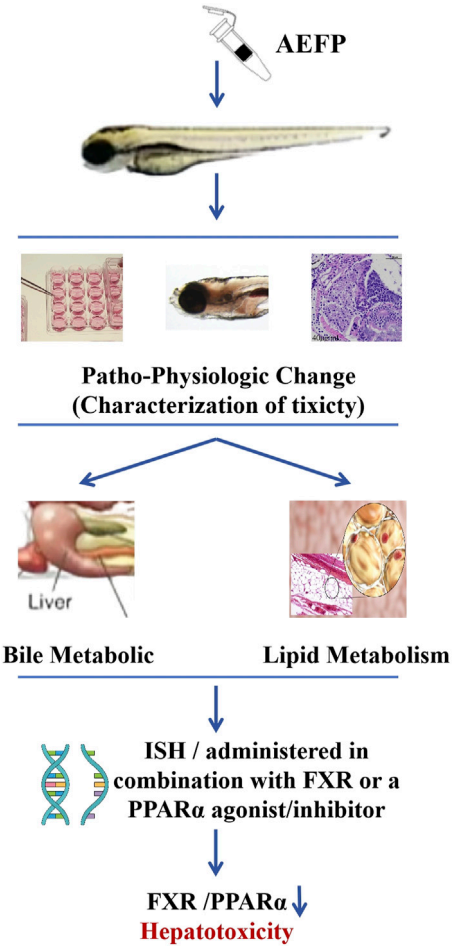

GRAPHICAL ABSTRACT

Introduction

Psoralea corylifolia L. (FP), an important traditional herbal medicine, has a long history of clinical application and has been widely used in many countries. The whole plant has important medicinal value and is used to treat various diseases, such as leucoderma, menstrual disorders, uterine bleeding, and endometriosis (Chen et al., 2023; Alam et al., 2018). FP (*Psoralea corylifolia* L.) and its formulations are also widely used in China for the treatment of bone and skin diseases (Makwana et al., 2020; Li T et al., 2022). More than 200 compounds, mainly coumarins, flavonoids, and terpenoids, have been isolated and identified from psoriasis (Gao et al., 2021; Wu et al., 2020). These major components have biological activities, such as antitumor, anti-inflammatory, antioxidant, and osteogenic effects (Li N et al., 2022; Cariola et al., 2023; Zhang et al., 2016). In recent years, a number of adverse reactions have been associated with psoralens, such as hepatotoxicity, phototoxic dermatitis, and allergy, with hepatic injury being the most common (Shi et al., 2022; Wang et al., 2019). Tian et al. (2017) analyzed 84 cases of adverse reactions due to the use of psoralens from 1978 to 2016. A total of 48 patients had liver injury, which accounted for 57.14% of all cases (Tian et al., 2017). Other clinical studies have shown that PF has a high risk of hepatotoxicity (Li et al., 2019; Rong et al., 2020; Liu et al., 2019). These clinical studies suggest that PF-induced liver injury is mainly hepatocellular injury and cholestasis. The risk of liver injury may increase with an overdose, the use of raw products, or improper dosing.

In the past, PF-induced liver injury has been extensively studied in animal models, such as mice and rats. Wang J et al. (2012) evaluated the effect of FP ethanol extracts (1.875, 1.25, and 0.625 g/kg/day) administered for 28 consecutive days on the liver of Wistar rats, and the results showed that hepatic cholestasis was the main cause of hepatic injury caused by PF. Duan et al. (2020) gavaged male Wistar rats with an FP aqueous extract (2.1 g/kg/day) for 28 consecutive days and found that altered bile acid metabolism and energy metabolism were strongly correlated with hepatic injury via quantitative proteomics and metabolomics analyses. However, some studies have shown that coadministration of PF (0.22 g/kg/day) with Epimedii Folium (EF) for 6 days induces the low-dose lipopolysaccharide-mediated recruitment of hepatic T lymphocytes in rats, possibly leading to specific liver injury. Alanine transaminase (ALT) and aspartate transaminase (AST) levels are significantly elevated, multiple cytokines are overexpressed, and a strong inflammatory response is activated (Gao et al., 2020). The dose and type of liver injury caused by PF, whether inherent or specific,

10.3389/fphar.2024.1308655

TABLE 1 The primers used for Real-time quantitative PCR.

Function	Gene		NCBI
Internal reference	β-actin-F	5′-AGAGCTATGAGCTGCCTGACG-3′	NC_007112.7
	β-actin-R	5′-CCGCAAGATTCCATACCCA-3′	
Lipid metabolism	PPARγ-F	5′-CACTCGCTGGACATCAAGCC-3′	NC_000005.10
	PPARγ-R	5′-TCCTGTAGCTGTACATGTGCGT-3′	
	PPARαa-F	5′-CGGGCTTCAGGTTTCCACTA-3′	NC_007136.7
	PPARαa-R	5′-ACGAATAGCGTTGTGGGACA-3′	
	SCD1-F	5′-AACACCAGCCAATCGGAGAG-3′	NC_007123.7
	SCD1-R	5′-TGCTCTAAACACGTGGACCC-3′	
	ME1-F	5′-ATGTTACACGCAACCCCCAT-3′	NC_007127.7
	ME1-R	5′-ACCCGCAAAACTTGCACATC-3′	
	ACS-F	5′-CTTCAGACGCAACTTCCCCT-3′	NC_007205.1
	ACS-R	5′-CCCTGTGGAAATCCTGCTGT-3′	
	LPL-F	5′-GCTCTCACGAGCGCTCTATT-3′	NC_007133.7
	LPL-R	5′-TCCTGCGTGTGCGAATTTTG-3′	
	ACS-F	5′-CTTCAGACGCAACTTCCCCT-3′	NC_014408.1
	ACS-R	5′-CCCTGTGGAAATCCTGCTGT-3′	
	CPT1-F	5′-TGCAGGGGAGATGTAGACCA-3′	NC_000085.7
	CPT1-R	5′-TGACAGTCCACTTCATCGGC-3′	
	CPT2-F	5′-AACTTCGAGCACTCTTGGGG-3′	NC_000001.11
	CPT2-R	5′-GATGAGTCTACGGACGCAGG-3′	
	PGAR-F	5′-CGAGATGACACCCGAAGGAG-3′	NC_000083.7
	PGAR-R	5′-CCGAGCCAGAACTCACCATT-3′	
Bile acid metabolism	FXR-F	5′-GAATGACCACAAGTTCACC-3′	NC_000003.12
	FXR-R	5′-AAGAAGGGAAGTCCAATACC-3′	
	SHP-F	5′-CGACTGTCCGCTCACTCTG-3′	NC_007121.7
	SHP-R	5′-CCTCCTGCAGTCCTGCTATC-3′	
	CYP7A1-F	5′-TTGCGCATGCTTTTGAACGA-3′	NC_000008.11
	CYP7A1-R	5′-TCAAAGGTTCGCCTCACCTC-3′	
	CYP27A1-F	5′-AACGCATGCTGCATCCAAAG-3′	NC_000002.12
	CYP27A1-R	5′-CGCGTCTCGAAGAGAATGGA-3′	
	CYP8B1-F	5′-CAGACGAACCGGAGAACCTC-3′	NC_000003.12
	CYP8B1-R	5′-CCTCCGAGCTGCACTGTAAA-3′	
	MRP2-F	5′-GGTTCAGGAGGACATGTGGG-3′	NC_054685.1
	MRP2-R	5′-ACCCTCAGCATCTACGGTCT-3′	
	BSEP-F	5′-GCAGGACTCATGGCTCTGTT-3′	NC_007122.7
	BSEP-R	5′-CCCCATTGTTGGGCAGAGAT-3′	
	NTCP-F	5′-ATTGTCGAGGCGCTGATCTT-3′	NC_000002.12
	NTCP-R	5′-TGGGGCTCATTCGTCACTTC-3′	

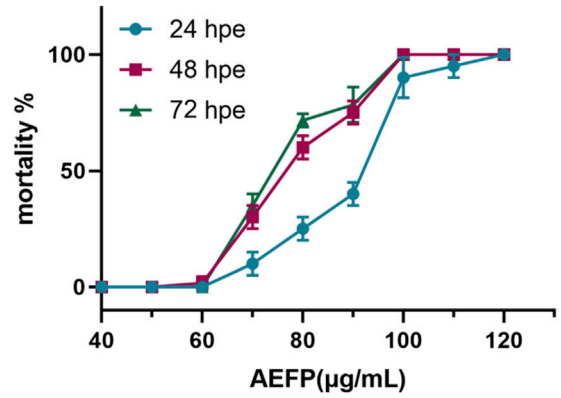

FIGURE 1
Mortality rate of zebrafish at different concentrations (%).

are controversial. Disturbances in bile acid metabolism and transport, oxidative stress, mitochondrial damage, inhibition of hepatocyte regeneration and repair, and inflammatory responses have been the focus of related research (Hou et al., 2020; Wang X et al., 2012; Men et al., 2022). Elucidating the complex mechanism of action of PF is highly challenging because of the problems associated with PF-induced hepatotoxicity. The systematic and efficient study of the process of PF-induced liver injury will help reduce the risk of drug use.

Zebrafish, a new model organism, shares more than 87% homology with humans and is widely used in drug research (Goessling and Sadler, 2015; Cox and Goessling, 2015). Zebrafish have the advantages of small size, easy feeding, high spawning rate, high survival rate, and low reproduction cost, etc. These characteristics can meet the requirements of large sample sizes of experimental animals for toxic drug screening and compensate for the influence of traditional animal models on experimental results due to large individual differences (Rosa et al., 2022; Hernández-Silva et al., 2023). Specific parts of the transgenic zebrafish were stained with fluorescent labels. By observing the location and level of fluorescent markers in specific organs, the target organs affected by drug toxicity can be quickly determined. The safety of 12 kinds of Chinese medicines in Zhuanggu Guanjie pills was rapidly evaluated using a zebrafish model (Chai et al., 2022). Several traditional Chinese medicines (such as *Dipsacus asperata*), which are considered safe, can also cause obvious toxic reactions in zebrafish, but no reports exist on the toxicity of *D. asperata* in traditional animal models. It has been proven that zebrafish are more sensitive to drug toxicity (Cassar et al., 2020). The zebrafish model has the advantages of real-time use, high efficiency, and simplicity in evaluating potential drug toxicity and rapid screening of toxic drugs; it can form a good communication bridge with traditional *in vivo* and *in vitro* models and can be used for preliminary screening of drugs in the early stage of research and development, evaluation of potential toxic components of drugs, and determination of main target organs.

In this study, zebrafish were used to explore the characteristics and mechanism of FP hepatotoxicity. This study provides reliable theoretical support for the use of FP in traditional Chinese medicine and the development and application of preparations.

Materials and methods

Plant materials and preparation of FP extracts

FP was purchased from Xinjiang Xinqikang Pharmaceutical Co., Ltd. and authenticated by researcher Shi-xia Huo (Xinjiang Institute of Traditional Uyghur Medicine). Voucher specimens (No. 20190507) were deposited at the Xinjiang Institute of Traditional Uyghur Medicine, China. A measure of 1,000 g of FP was accurately weighed and extracted thrice with 10 volumes of pure water for 1 h (h) by reflux. After filtration, the three aqueous extracts were combined, concentrated, and dried, and a dry powder with a concentration of 7.74 g/g (equivalent to the crude drug) was obtained. The aqueous extract of FP (AEFP) was stored at 2°C–8°C. The main constituents were quantified by HPLC, and AEFP was found to contain psoralen (3.06 mg/g), isopsoralen (2.20 mg/g), and psoralen phenol (14.65 mg/g).

Chemicals

The FXR agonist obeticholic acid (FXR-A, C10777289, HPLC ≥ 98%) and the peroxisome proliferator-activated receptor α (PPARα) agonist fenofibrate (PPARα-A, C13541890, HPLC ≥ 99%) were purchased from Shanghai Macklin Biochemical Technology Co., Ltd. The FXR inhibitor (Z) guggulsterone (FXR-I, J05j12R136632, HPLC ≥ 98%) and the PPARα inhibitor MK-886 (PPARα-I, C10O11L126310, HPLC ≥ 99%) were purchased from Shanghai Yuanye Biotechnology Co., Ltd. ALT (C009-2-1), AST (C010-2-1), TBA (E003-2-1), TBIL (C019-1-1), γ-GT (C17-2-1), total cholesterol (TC) (A111-1-1), TG (A110-1-1), low-density lipoprotein cholesterol (LDL-C) (A113-1-1), and high-density lipoprotein cholesterol (HDL-C) (A112-1-1) reagent test kits were purchased from Nanjing Jiancheng Bioengineering Institute Co., Ltd.

Zebrafish maintenance

Zebrafish were reared under standard conditions (14 h of light and 10 h of darkness) in a temperature-controlled (28°C) system. In this study, the transgenic zebrafish Tg (*lfabp:EGFP*) strain was used to label hepatocytes with green fluorescent protein. The zebrafish strains were obtained from the Key Laboratory for Drug Screening Technology of Shandong Academy of Sciences. To obtain the transgenic juvenile fish, healthy and sexually mature female and male fish of the transgenic line lfabp–EGFP were placed in a screened mating box. The barrier was removed at 8:30 a.m. The following morning, zebrafish embryos were obtained from 11:00 to 12:00 a.m. The embryos were washed three times and disinfected with 0.1% methylene blue. The embryos were transferred into zebrafish embryo culture water and cultured at 28°C with 14 h of light control. All the experiments were carried out in compliance with the ethical guidelines and under the supervision of the Ethics Committee of the Biology Institute, Shandong Academy of Sciences.

10.3389/fphar.2024.1308655

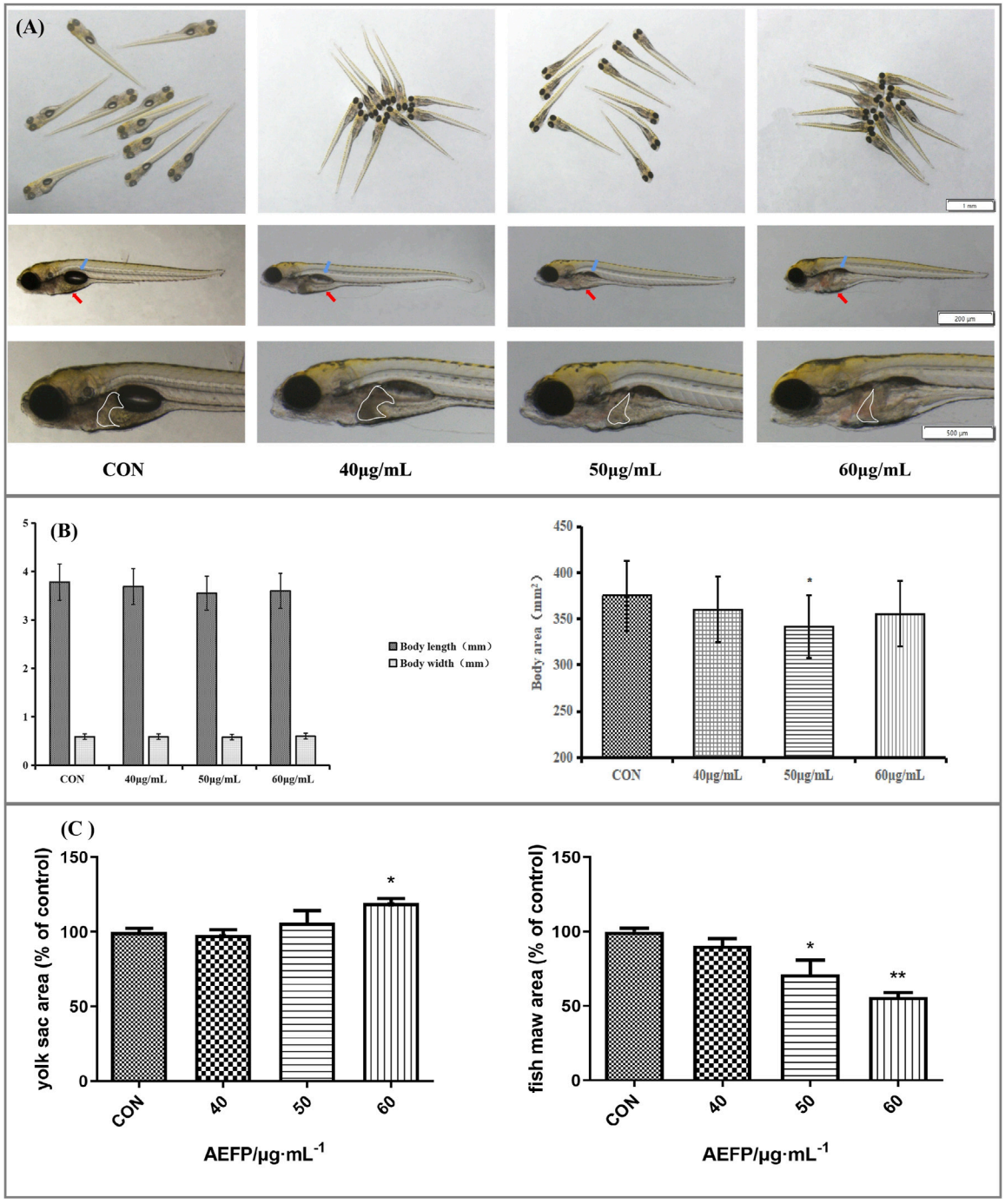

FIGURE 2
(A) Effects of AEFP on swim bladder size, yolk sac absorption, and liver phenotypic changes of zebrafish (blue arrow: swim bladder and red arrow: yolk sac). **(B)** Effects of AEFP on the body length and area growth of zebrafish. **(C)** Effects of AEFP on the yolk sac and fish maw area ($\bar{x}\pm s$, $n = 6$); * $p < 0.05$ vs. the CON group.

Drug treatment

Zebrafish larvae were collected 72 h post-fertilization (hpf). Healthy zebrafish were selected under a microscope and transferred to 6-well plates, with 20 zebrafish in each well. According to the preliminary results, the blank control group (zebrafish culture water), AEFP (40, 50, 60, 70, 80, 90, 100, 110, and 120 μg/mL), FXR-I (1.5 μmol·L^{-1}), FXR-I (1.5 μmol·L^{-1} + AEFP 50 μg/mL), FXR-A (5.5 μmol·L^{-1}), FXR-A (5.5 μmol·L^{-1} + AEFP 50 μg/mL), PPARα-I (0.5 μmol·L^{-1}), PPARα-I (0.5 μmol·L^{-1} + AEFP 50 μg/mL), PPARα-A (6 μmol·L^{-1}), and PPARα-A (6 μmol·L^{-1} + AEFP 50 μg/mL) were used, and 200 μM 1-phenyl 2-thiourea (PTU) was added to each group to inhibit melanin production. The mixture was subsequently incubated in a light incubator at a constant

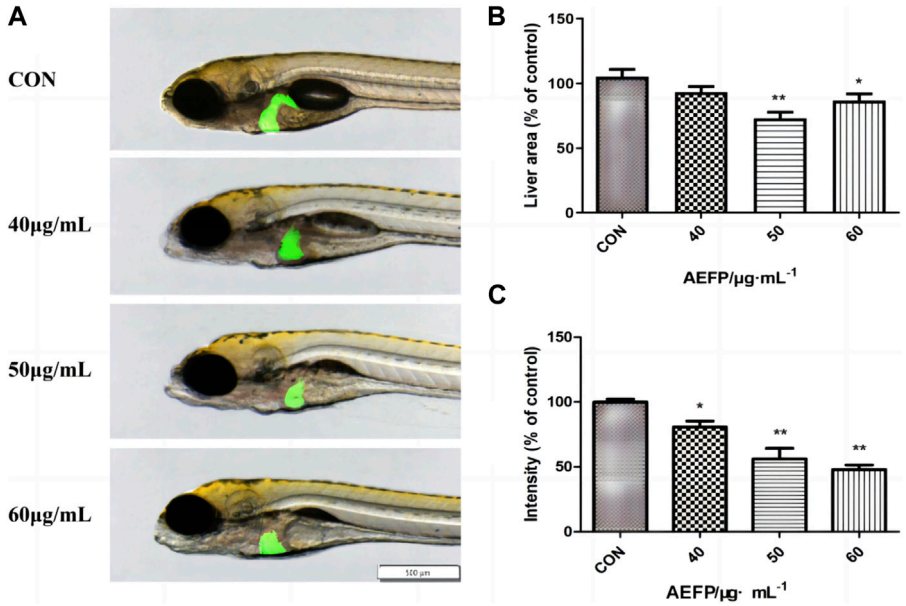

FIGURE 3
(A) Effects of AEFP on liver morphology of Zebrafish; Effects of AEFP on the **(B)** liver fluorescence intensity and **(C)** liver fluorescenc area of zebrafish ($\bar{x}\pm$s, n = 6); *p < 0. 05, and **p < 0.01 vs. the CON group.

temperature of 28.0°C ± 0.5°C for 3 days, after which the solution was changed every day. Three parallel replicates were performed. The development of larvae was observed using an FSX100 Bio Imaging Navigator instrument (Olympus).

Effect of AEFP on mortality and malformation in zebrafish

The deaths of the zebrafish in each group at 24, 48, and 72 h post-exposure (hpe) were recorded (whether the zebrafish survived was judged by the heartbeat).

Liver fluorescence area and intensity

Seventy-two hpf zebrafish were anesthetized with tetracaine, and the zebrafish were photographed by fixing their side position (eyes overlapping). The fluorescence area and intensity of the zebrafish liver were observed using an inverted fluorescence microscope. The parameters for fluorescence observation were as follows: excitation wavelength, 490 nm, and emission wavelength, 516 nm (Olympus SZX16, Tokyo, Japan). Image-Pro Plus 5.1 Chinese software was used to measure the area and intensity of liver fluorescence, and GraphPad Prism 6 software was used to construct a histogram for visual comparison.

Determination of transaminase activity in the zebrafish liver

Seventy-two hours after administration, the zebrafish in the control group and administration group were collected in 1.5-mL EP centrifuge tubes. After 3 rounds of cleaning with 9% normal saline, the cleaning solution was transferred to a preweighed 1.5-mL centrifuge tube after observing that there was no residue. The residual water in the centrifuge tube was removed as much as possible and weighed, and precooled 4-C normal saline was added at a mass ratio of 1:9 (w/w). Juvenile fish (approximately 50 fish) were prepared as 10% tissue homogenates with 180 μL of 4°C normal saline using an ultrasonic crusher. The mixture was centrifuged at 4°C and 3,500 r/min for 10 min, after which the supernatant was collected for later use.

The homogenate was collected to measure the protein concentration of each group by the BCA method, and the enzyme activity and content were subsequently measured according to the instructions of the ALT, AST, TBA, TBIL, γ-GT, TC, TG, LDL-C, and HDL-C kits. The activity of AST and ALT in tissue (U/g prot) = the activity of AST/ALT in the homogenate (U/L) obtained by standard curve ÷ the protein concentration of the homogenate to be measured (g prot/L); TBA, TBIL, γ-GT, TC, TG, LDL-C, and HDL-C content = A (absorbance) to determine ÷ a standard × standard concentration (μmol/L), and the experiment was repeated three times.

Oil Red O staining

Twenty larvae were randomly selected from each group and fixed in paraformaldehyde at 4°C overnight. On the second day, the larvae were washed with phosphate-buffered saline (PBS) twice and then soaked in PBS containing 25%, 50%, 75%, and 100% propylene glycol for dehydration and infiltration. Then, the sections were dyed with 0.5% Oil Red O solution at room temperature for 4 h. After staining, the cells were gradually rehydrated with PBS and propylene glycol until the larvae were in 100% PBS. Finally, the larvae were fixed on methylcellulose slides.

10.3389/fphar.2024.1308655

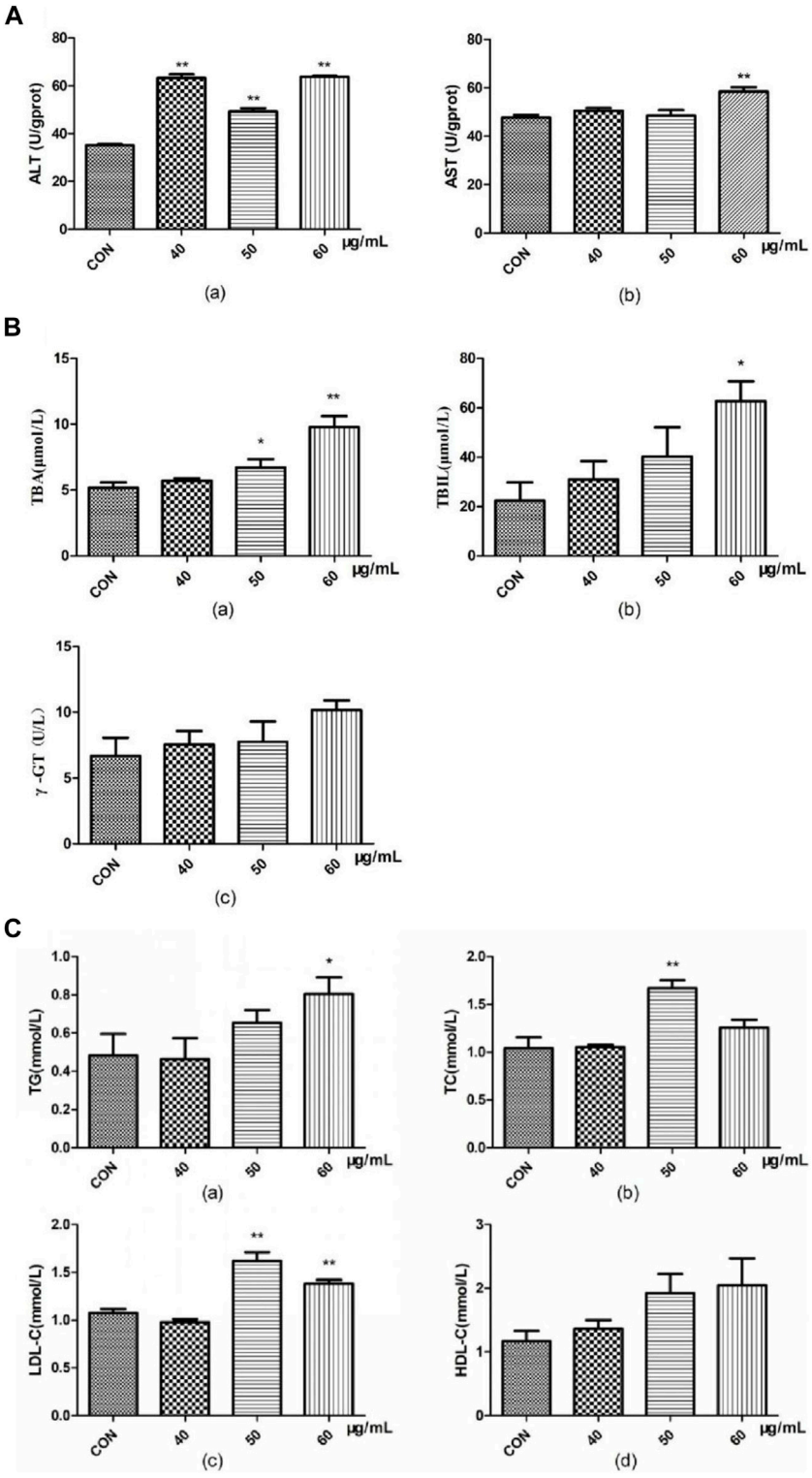

FIGURE 4
Effects of AEFP on **(A)** liver transaminase, **(B)** bile acid metabolism, and **(C)** lipid metabolism of zebrafish ($\bar{x} \pm s$, $n = 6$); $^{**}p < 0.01$ vs. the CON group.

Histopathological examination of the zebrafish liver

Ten zebrafish were randomly selected from each group, fixed with 4% paraformaldehyde, dehydrated with an ethanol gradient, and soaked in xylene. Then, the zebrafish were embedded in paraffin, sliced, stained with hematoxylin–eosin (HE), and sealed. The tissue sections were observed and imaged under a microscope (Olympus FSX100, Tokyo, Japan).

10.3389/fphar.2024.1308655

FIGURE 5
Effects of AEFP on lipid deposition in zebrafish. ***$p < 0.001$ vs. the CON group.

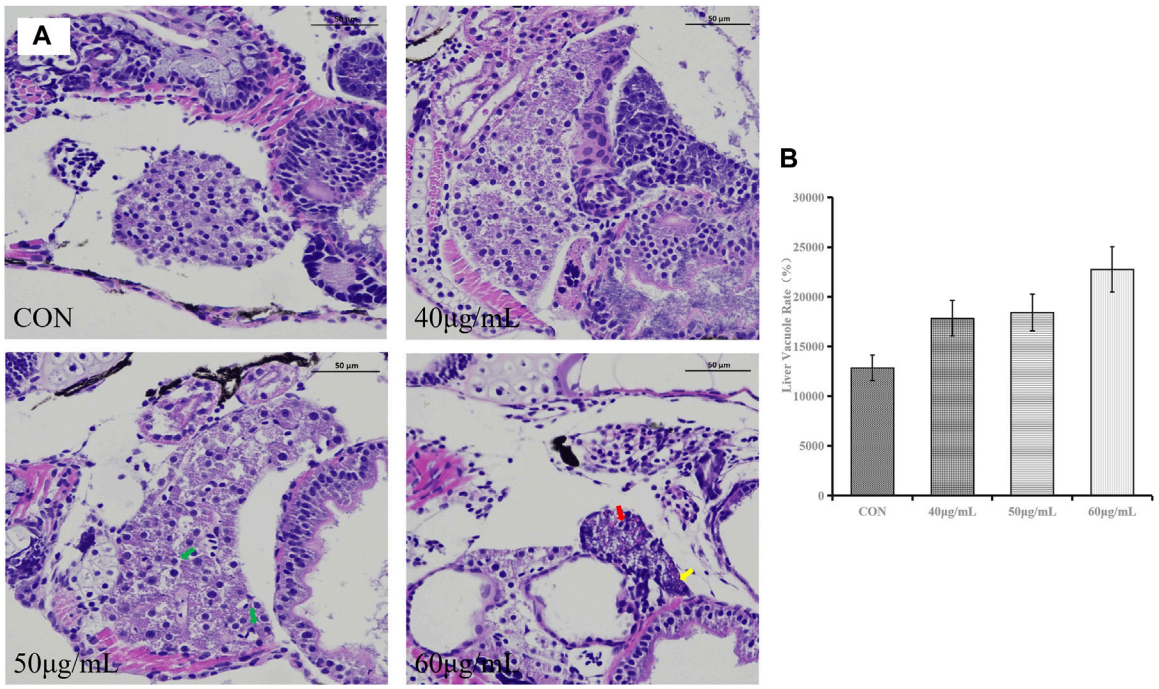

FIGURE 6
(A) Typical histopathological section photographs of zebrafish liver specimens for HE analysis (magnification ×200 and ×100); green arrow: hepatocyte vacuolation, yellow arrow: nuclear pyknosis, and red arrow: steatosis. **(B)** Effects of AEFP on the liver vacuole rate in zebrafish ($\bar{x}\pm s$, $n = 6$), vs. the CON group.

In situ hybridization

Partial coding sequences of the zebrafish FXR and PPARα genes were amplified via PCR using first-strand cDNA templates derived from 6 days post-fertilization (dpf) zebrafish juveniles. The forward primer 5′-TCAAATGCCGTTGGGTGGTA-3′ and reverse primer 5′-TA ATACGACTCACTATAGGGTGCAAGGCTGTGAAACAA CAG-3′ were used to amplify the partial PPARα cDNA. The forward primer 5′-TCAGCTTGACGTCTTTTCCCA-3′ and reverse primer 5′-TAATACGACTCACTATAGGGCACAAGTGAGCGC GTTGTA G-3′ were used to amplify the partial FXR cDNA. PCR products were purified and used as templates for *in vitro* transcription reactions using T7 RNA polymerase (DIGRNALABELINGKIT (SP6/T7) to generate digoxigenin-labeled FXR or PPARα antisense riboprobes. In all the experiments, normal translating ribose was used as a negative control. *In situ* hybridization was performed.

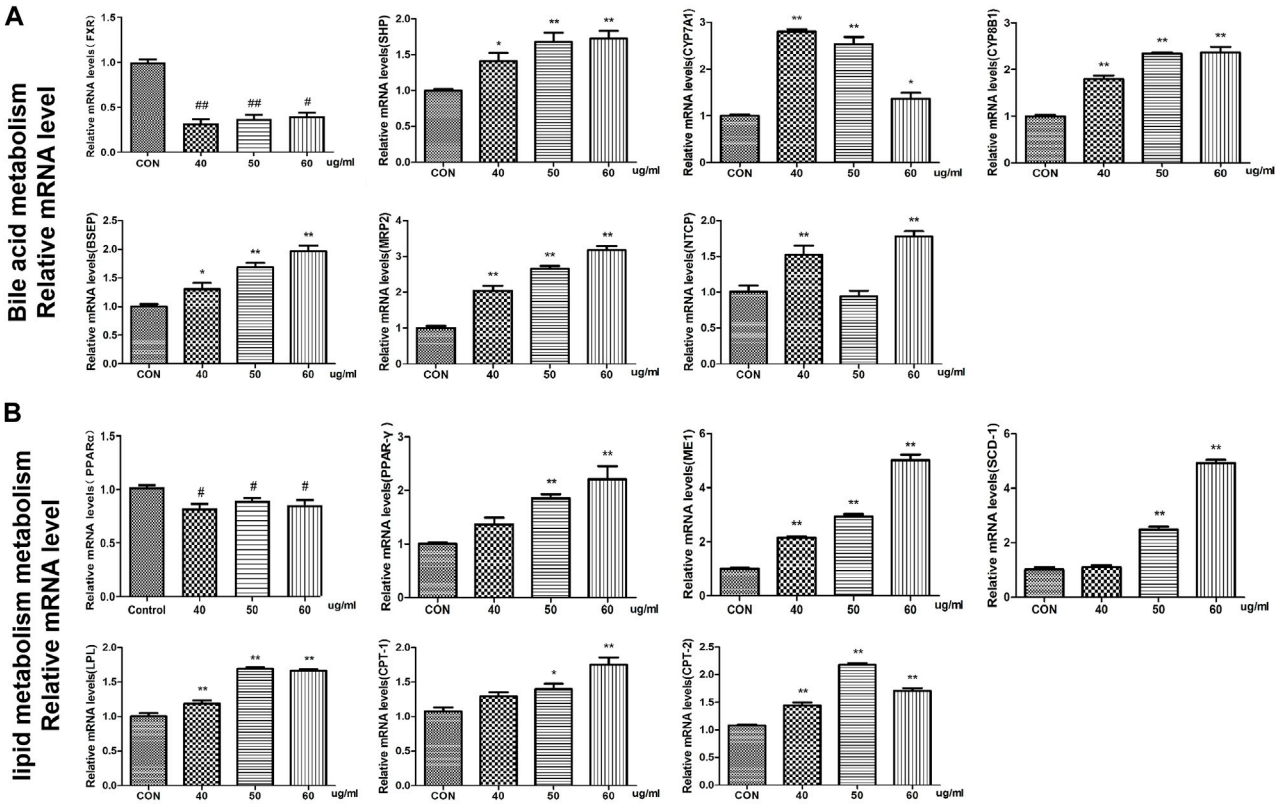

FIGURE 7
Effects of WEFP on the expression of liver injury-related genes in zebrafish **(A)**. Gene expression of the bile acid metabolism pathway. **(B)** Influence of key genes in the fat metabolism pathway;*p < 0. 05 and **p < 0. 01 vs. the CON group.

Analysis of gene expression by RTq-PCR

Fifty zebrafish from each group were homogenized using an ultrasonic pulverizer and added to a 1.5-mL EP tube without enzyme sterilization, after which the RNA was extracted according to the instructions of the SPARK easy IMO proved tissue/cell RNA extraction kit, which was used directly in subsequent experiments.

For RTq-PCR, 2 μL of the synthesized cDNA template was removed, and 10 μL of SYBR qPCR Super Mix Plus was added to a 0.2-mL PCR tube. Then, 1 × 1 μL upstream primer and 1 × 1 μL downstream primer were mixed, and 20 μL of RNase-free water was added. The solution was gently mixed and centrifuged to prepare a 20-μL PCR system with β-actin as the internal reference. The samples were predenatured at 95°C for 60 s, denatured at 95°C for 30 s, annealed at 60°C for 30 s, and annealed at 72°C for 30 s. After 40 cycles, fluorescence quantitative analysis was carried out using PCR software, and CT was obtained. The results of the relative expression of the target gene mRNA were calculated by the 2^{-Ct} method, and the expression multiplier of the target gene in the administration group was calculated by the 2^{-Ct} method. Gene-specific primers for real-time fluorescence quantitative PCR were synthesized by Xi 'an Qingke Biotechnology Co., Ltd., and the primer sequences are shown in Table 1.

Statistical analysis

The experimental data were analyzed using SPSS 25.0 software, and the results are expressed as ± S. A t-test was used to compare the differences between two groups, and ANOVA was used to compare the differences between multiple groups. GraphPad Prism 6 software was used to construct a graph.

Results

Effect of AEFP on the mortality of zebrafish

Using SPSS 21.0, LC_1 = 55.50 μg/mL, LC_{10} = 63.93 μg/mL, and LC_{50} = 76.04 μg/mL were calculated, as shown in Figure 1. The final concentrations used for drug administration were confirmed to be 40, 50, and 60 μg/mL, as shown in Figure 1.

Effects of AEFP on zebrafish morphology

The morphological changes in the juvenile zebrafish induced by different concentrations of drugs were observed under a fluorescence microscope. The bladders of the zebrafish in the blank control group had a normal shape and clear edges. After

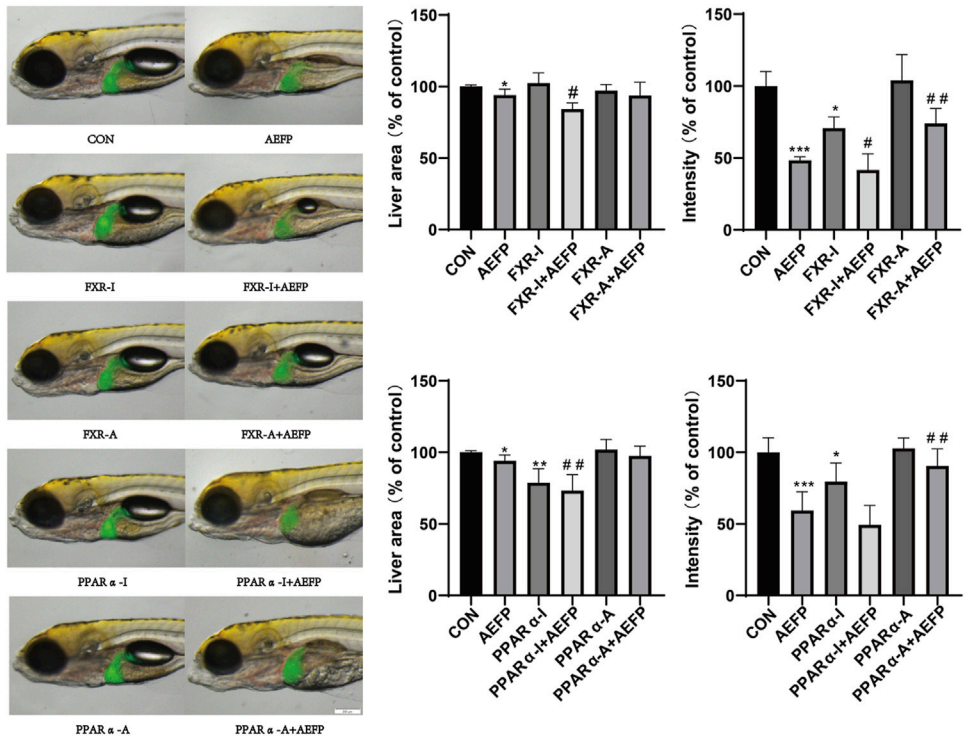

FIGURE 8
Effects of AEFP combined with FXR and PPARα agonists and inhibitors on the liver fluorescence intensity and area of zebrafish. The concentration of AEFP is 50 μg/mL, FXR-I is 1.5 μM, FXR-A is 5.5 μM, PPARα-I is 0.5 μM, and PPARα-A is 6 μM. *$p < 0.05$ and ***$p < 0.001$ vs. the CON group; $^{\#}p < 0.05$ and $^{\#\#}p < 0.01$ vs. the AEFP group.

40 μg/mL, 50 μg/mL, and 60 μg/mL AEFP were administered, the swim bladder obviously decreased or even disappeared. The yolk sac absorption of the blank juvenile fish was normal, and the yolk sac absorption of the zebrafish in each administration group was delayed to different degrees, especially in the group administered 60 μg/mL AEFP, as shown in Figures 2A, C. As the concentration of the AEFP administered increased, the body length of the zebrafish had a tendency to decrease, but no significant difference was observed. Moreover, some inhibition of the body area was observed, which was most obvious at 50 μg/mL ($p < 0.05$), as shown in Figure 2B.

Phenotypic changes in the liver

Changes in the liver morphology and area of zebrafish after administration were observed under a fluorescence microscope. The livers of the juvenile fish in the blank control group were transparent and normal in shape. The livers of the juvenile fish after treatment with different concentrations of AEFP in a medicated bath showed varying degrees of damage. Compared with that of the blank control group, the liver color of zebrafish treated with 40 μg/mL was gray, and the boundary was unclear. The liver area of the group administered 50 μg/mL AEFP decreased significantly. In the group administered 50 μg/mL AEFP, at 72 hpe, the liver of juvenile zebrafish was obviously atrophied and degenerated, and the liver area was reduced, as shown in Figure 3A.

Compared with those in the blank control group, the fluorescence area and intensity in juvenile zebrafish liver tissue were altered at 72 hpe. In the 50-μg/mL group, the liver obviously atrophied and degenerated, and the fluorescence area decreased. With increasing drug bath concentration, the decrease in liver fluorescence intensity became more obvious and dose-dependent, as shown in Figures 3B, C.

Effect of AEFP on the biochemical indices of zebrafish

Compared with that in the blank group, ALT activity in the zebrafish in the AEFP group was significantly greater at 72 hpe ($p < 0.01$). At 72 hpe, 60 μg/mL AEFP significantly increased AST activity in zebrafish ($p < 0.01$) (Figure 4A).

Compared with those in the blank group, the TBA content in the groups administered 50 μg/mL and 60 μg/mL AEFP significantly increased at 72 hpe ($p < 0.05$ and $p < 0.01$, respectively). At 72 hpe, treatment with 60 μg/mL AEFP significantly increased the TBIL concentration in the zebrafish ($p < 0.05$) (Figure 4B).

Compared with those in the blank group, the doses of 50 and 60 μg/mL AEFP significantly increased the TC content in zebrafish at 72 hpe ($p < 0.05$). At 72 hpe, a dose of 50 μg/mL AEFP significantly increased the TC content in the zebrafish ($p < 0.05$). Concentrations of 50 μg/mL and 60 μg/mL

10.3389/fphar.2024.1308655

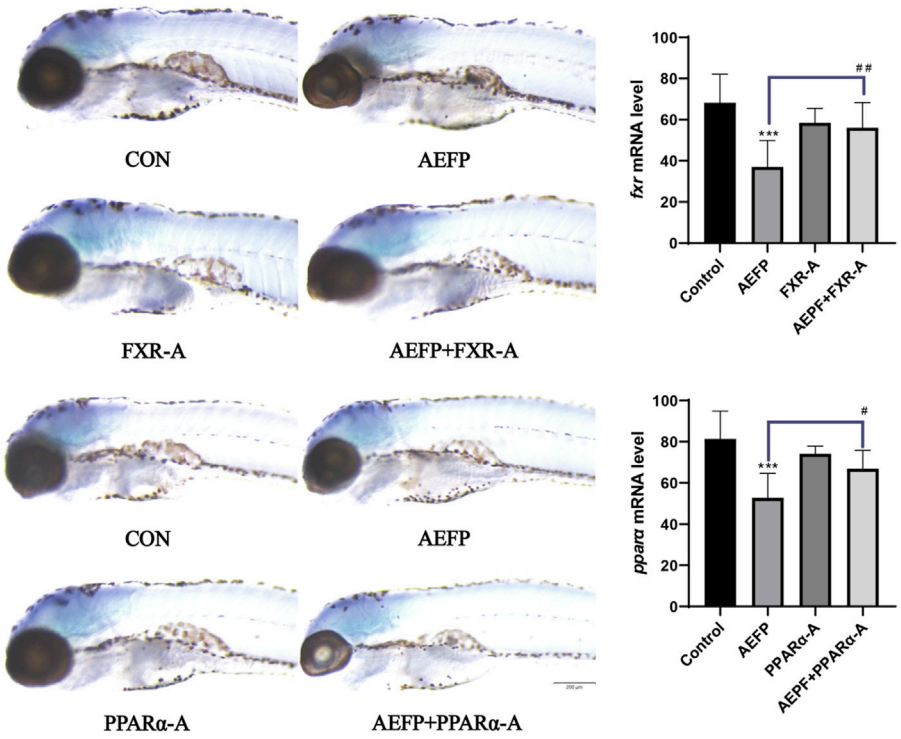

FIGURE 9
Effect of combined administration on the results of *in situ* hybridization. The concentration of AEFP is 50 μg/mL, FXR-I is 1.5 μM, FXR-A is 5.5 μM, PPARα-I is 0.5 μM, and PPARα-A is 6 μM. ***$p < 0.001$ vs. the CON group; $^{\#}p < 0.05$ and $^{\#\#}p < 0.01$ vs. the AEFP group.

significantly increased the LDL-C concentration ($p < 0.05$) (Figure 4C).

Observation of lipid deposition in zebrafish liver tissue

Oil Red O staining was used to study the accumulation of fat in the zebrafish liver. As shown in Figure 9, compared with that in the blank control group, the liver Oil Red O staining in the 40-μg/mL, 50-μg/mL, and 60-μg/mL AEFP dosage groups was deepened to different degrees after 72 hpe was administered, and the color gradually deepened with increasing dosage ($p < 0.001$). This finding indicates that AEFP can lead to fat deposition in zebrafish liver tissue, as shown in Figure 5.

Histopathological observation of liver tissue

In the control group, the liver structure was normal, with clear cell margins and close contact. In the group treated with 40 μg/mL AEFP, no obvious histological change was observed except for the loose connection of local hepatocytes. Compared with those in the control group, some hepatocytes in the group treated with 50 μg/mL AEFP were vacuolated. In the group treated with 60 μg/mL AEFP, the morphology of the hepatocytes was irregular, the volume decreased, and fatty degeneration of the hepatocytes occurred, as shown in Figure 6A. The results given in Figure 6B show that AEFP induced an increase in the rate of vacuolation in the zebrafish liver, but no significant trend was observed.

Effect of AEFP on the mRNA expression in zebrafish

At the mRNA level, we found that the expression of the FXR and CYP27A1 genes was inhibited in the bile acid metabolism signaling pathway in the AEFP-treated group, whereas the expression levels of SHP, CYP7A1, CYP8B1, BSEP, MRP2, and NTCP were significantly increased at 72 hpe after the administration of AEFP (aqueous extract of FP) ($p < 0.01$). WEFP also had a regulatory effect on key genes involved in lipid metabolism, i.e., PPARα, peroxisome proliferator-activated receptor γ (PPARγ), ME-1, SCD-1, lipoprotein lipase (LPL), CPT-1, CPT-2, and PGAR. The regulatory effect and the expression levels of PPARα, PPARγ, ME-1, SCD-1, LPL, CPT-1, CPT-2, and PGAR were significantly greater than those in the blank control group at 72 hpe after drug administration ($p < 0.01$), as shown in Figure 7.

Effects of the combination of AEFP with FXR and PPARα agonists and inhibitors on the liver

Compared with that in the control group, the liver area in the AEFP-alone group was significantly lower ($p < 0.05$), and the liver fluorescence intensity was significantly lower ($p < 0.001$); moreover,

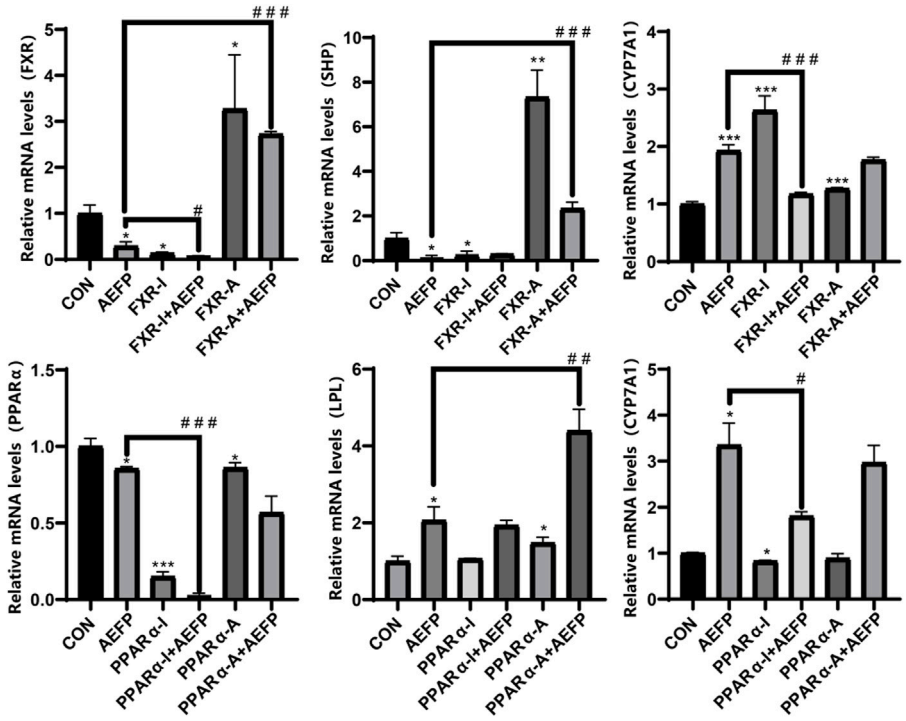

FIGURE 10
Effect of combined administration on the results of mRNA. The concentration of AEFP is 50 μg/mL, FXR-I is 1.5 μM, FXR-A is 5.5 μM, PPARα-I is 0.5 μM, and PPARα-A is 6 μM. *$p < 0.05$, **$p < 0.01$, and ***$p < 0.001$ vs. the CON group; $^{\#}p < 0.05$, $^{\#\#}p < 0.01$, and $^{\#\#\#}3\ p < 0.001$ vs. the AEFP group.

the liver fluorescence intensity in the FXR inhibitor-alone group was significantly lower ($p < 0.05$, $p < 0.001$). The liver area in the PPARα inhibitor group was significantly reduced ($p < 0.01$), and the fluorescence intensity in the liver was significantly decreased ($p < 0.05$). Compared with that in the AEFP group, the liver area in the FXR-A and AEFP groups was significantly lower ($p < 0.05$), and the liver fluorescence intensity was significantly lower ($p < 0.05$). In the FXR stimulation group, the liver area in the zebrafish coadministered with the PPARα inhibitor and AEFP increased significantly ($p < 0.05$), and the liver fluorescence intensity increased significantly ($p < 0.01$). In the group coadministered with the PAPRα inhibitor and AEFP, the liver area decreased significantly ($p < 0.01$), and the liver fluorescence intensity tended to weaken. In the group administered with the PPARα agonist and AEFP together, the liver area increased, and the liver fluorescence intensity increased significantly ($p < 0.01$) (Figure 8).

Effects of FXR and PPARα agonist inhibitors on the expression of FXR and PPARα in the livers of zebrafish

Compared with those in the control group, the staining depth of FXR and PPARα in the liver in the AEFP group was decreased, the FXR staining depth in the liver in the FXR agonist group was increased, and the depth of PPARα staining in the liver in the PPARα agonist group was increased. Compared with that in the AEFP-alone group, the depth of liver FXR staining in the FXR agonist and AEFP coadministration group was greater; moreover, the depth of liver PPARα staining in the PAPRα agonist and AEFP coadministration group was greater, as shown in Figure 9.

Effects of AEFP combined with FXR and PPARα agonists and inhibitors on the mRNA expression of key genes involved in bile acid metabolism and lipid metabolism pathways

The mRNA levels of FXR, SHP, and PPARα in the AEFP group were significantly lower ($p < 0.05$) than those in the control group, while the mRNA levels of CYP7A1 and LPL were significantly greater ($p < 0.05$). In the FXR inhibitor group, the mRNA levels of FXR and SHP were significantly lower ($p < 0.05$), while the mRNA level of CYP7A1 was significantly greater ($p < 0.001$). In the FXR agonist group, the mRNA levels of FXR and SHP were significantly increased ($p < 0.05$), while the mRNA level of CYP7A1 was significantly decreased ($p < 0.001$). In the PPARα inhibitor group, the mRNA level of PPARα was significantly decreased ($p < 0.001$), and the mRNA level of CYP7A1 was significantly decreased ($p < 0.05$). The mRNA levels of PPARα and LPL were significantly lower in the PPARα agonist group ($p < 0.01$).

Compared with those in the AEFP group, the mRNA levels of FXR were significantly downregulated ($p < 0.05$), and the mRNA level of CYP7A1 was significantly downregulated ($p < 0.001$) in the coadministration group of the FXR inhibitor and AEFP. The mRNA levels of FXR and SHP in the coadministration group of the FXR agonist and AEFP were significantly upregulated ($p < 0.001$); the

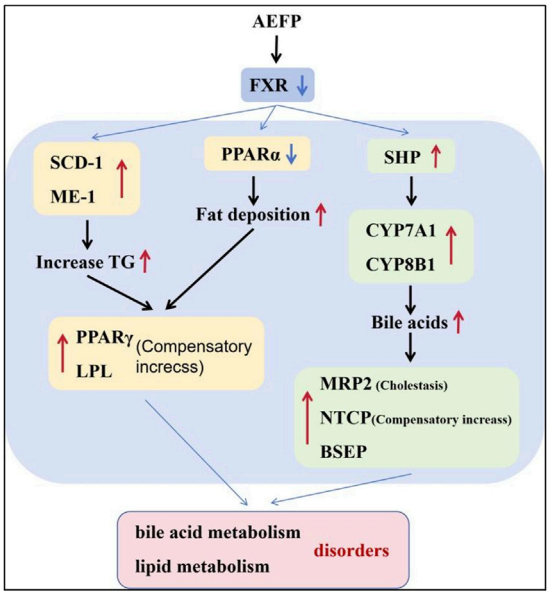

FIGURE 11
Effects of AEFP on the pathways in zebrafish.

mRNA levels of PPARα in the coadministration group of the PAPRα inhibitor and AEFP were significantly decreased ($p < 0.001$), and the mRNA level of CYP7A1 was significantly downregulated ($p < 0.05$); and the mRNA level of LPL in the coadministration group of the PAPRα agonist and AEFP was significantly upregulated ($p < 0.01$), as shown in Figure 10.

Discussion

The use of zebrafish is an important tool for high-throughput screening of drug hepatotoxicity. Although the liver structure of zebrafish is different from that of mammals, the basic physiological processes, genetic mutations, and pathogenic responses of zebrafish to environmental damage are highly similar (Bala et al., 2020; Bambino et al., 2019). In this study, transgenic lfabp:EGFP zebrafish were used as experimental models. After being exposed to different concentrations of AEFP for 72 hpe, the liver was damaged to different degrees, as indicated by a gray color, blurred edges, and a reduced area compared with those in the blank group. With increasing drug concentration, the color of the liver gradually deepened. Moreover, the fluorescence area and intensity in the liver decreased to different degrees. Further observation showed that, compared with that in the blank group, the delay in yolk sac absorption was most obvious when 60 μg/mL AEFP was administered. Approximately 70% of the yolk sac of zebrafish is composed of neutral lipids, which provide nutrients during early embryonic development (Katoch and Patial, 2021; Zhang et al., 2019; Jiang et al., 2022). When the liver is damaged, the metabolic rate of the yolk sac slows, hindering lipid metabolism in the yolk sac and thus causing an absorption delay in the yolk sac. Yolk sac absorption can also be used as an indirect indicator of liver function (Bambino et al., 2019).

The liver biomarkers ALT and AST are important indices for evaluating liver function and mainly exist in the cytoplasm of hepatocytes. Damage to hepatocytes leads to an increase in cell membrane permeability, the release of ALT and AST into the body, and an increase in transaminase levels (Lala et al., 2023; Zhang et al., 2023). After AEFP treatment, the levels of ALT and AST in the zebrafish increased significantly, indicating that AEFP has a certain toxic effect on zebrafish hepatocytes. Moreover, after AEFP administration, the total bile acid, total bilirubin, total cholesterol, triglyceride, LDL-C, and HDL-C levels in zebrafish increased, suggesting that AEFP can cause cholestasis and lipid metabolism disorders. In addition, the liver phenotype, Oil Red O staining, and pathology results showed that the fluorescence intensity of the liver decreased obviously after administration at 72 hpe, and lipid deposition was observed in the liver. The hepatotoxic effect of AEFP on zebrafish was confirmed, and it was hypothesized that the mechanism of hepatotoxicity of AEFP might be related to hepatocellular injury, cholestasis, and lipid metabolism disorders.

Therefore, the study of pathways associated with hepatic bile acid and lipid metabolism is an important direction for elucidating the mechanisms of AEFP hepatotoxicity. Altered expression of genes related to cholesterol biosynthesis and bile acid metabolism was revealed by mRNA analysis of zebrafish liver samples. Bile formation is an essential function of the liver, and bile acids (BAs), which are evolutionarily conserved molecules synthesized from cholesterol in the liver, are critical for the regulation of bile metabolism and lipid metabolism (Chiang and Ferrell, 2018). The lipoid X receptor (FXR) was the first receptor demonstrated to be activated by endogenous bile acids, and FXR plays a crucial role in the regulation of bile acid homeostasis. FXR inhibits the expression of genes related to bile acid synthesis (CYP7A1 and CYP8B1) and, thus, reduces the bile acid concentration in hepatocytes (Appelman et al., 2021; Lee et al., 2021). In addition, FXR activation limits bile acid accumulation in hepatocytes by inhibiting the expression of the bile acid membrane transporter protein NTCP and induces bile acid efflux from the liver by upregulating the expression of the bile acid efflux pump BSEP. The FXR/SHP pathway controls the homeostasis of cholesterol and bile acids in enterohepatic circulation, and FXR inhibits SHP transcription when bile acid levels are elevated (Yu et al., 2021). The results showed that AEFP inhibited the expression of FXR in the liver and that feedback induced the expression of the SHP, CYP7A1, and CYP8B1 genes, thus increasing the synthesis of bile acids; moreover, it induced the upregulation of NTCP expression, causing the accumulation of bile acids in hepatocytes. The increase in the expression of the BSEP and MRP2 genes may be a compensatory response caused by cholestasis. Hepatic transporters play a crucial role in the (ATP-dependent) efflux of BAs and substrates into somatic circulation. MRP2, a member of the multidrug resistance-associated gene family, is expressed in the basolateral membranes of hepatocytes and undergoes adaptive upregulation in response to bile deposition injury or BA feeding (Wang et al., 2023). Additionally, FXR is an important regulator of lipid metabolism. Studies have shown that the bile acid-induced FXR/SHP pathway reduces TG levels by inhibiting adipogenic sterol regulatory element-binding

protein 1 (SREBP-1c), leading to the repression of genes involved in adipogenesis, including desaturase 1 (SCD) and ME-1 (Ding et al., 2021). Another study showed that FXR could prevent hepatic TG accumulation by inducing PPARα activity and stimulating fatty acid β-oxidation in human hepatocellular carcinoma cells (Guan et al., 2022).

Moreover, PPARα efficiently induces the expression of numerous genes involved in a variety of lipid metabolic pathways, including microsomal, peroxisomal, and mitochondrial fatty acid oxidation; fatty acid doping and activation; fatty acid elongation and desaturation; triglyceride synthesis and catabolism; lipoprotein metabolism; glucose metabolism; bile acid metabolism; and a wide range of other metabolic pathways and genes (Samuel and Shulman, 2018; Kersten and Stienstra, 2017). Thus, PPARα deficiency or suppressed expression can cause a reduction in the transcript levels of a series of proteins and enzymes related to fatty acid metabolism in the liver, leading to reduced fatty acid oxidation, impaired lipoprotein anabolism, and intracellular fat deposition in the liver (Attema et al., 2022; Zeng et al., 2022; Yu et al., 2015). PPARγ and LPL are both genes that promote lipolysis. Activation of PPARγ reduces fatty acid delivery to the liver and muscle and decreases fat synthesis. Moreover, PPARγ induces the expression of LPL in adipocytes, which promotes lipid metabolism and reduces blood lipid levels, thereby increasing plasma HDL, LDL, and TG levels. The enzyme LPL is one of the key factors in the process of adipogenic differentiation [Nakamura et al., 2014; Lim et al., 2021].

Moreover, we confirmed that when FXR and PPARα agonists were coadministered with AEFP, the original decreases in fluorescence intensity and area indices in the livers of the zebrafish caused by AEFP were reversed. In contrast, the administration of FXR and PPARα inhibitors reduced the fluorescence intensity and area. The decrease intensified. After testing the relevant mRNA levels (SHP, CYP7A1, and LPL), it was found that AEFP may cause hepatotoxicity by downregulating the expression of the FXR and PPARα genes and affecting downstream pathways. ISH further confirmed that the regulation of the FXR and PPARα genes by AEFP is concentrated in the liver.

AEFP can cause liver injury in juvenile zebrafish via liver inflammation and lipid metabolism disorders, which leads to fat deposition by activating the inflammasomes and inhibiting the expression of key target genes of the PPAR signaling pathway. FXR expression was inhibited, which caused cholestasis and further aggravated the occurrence of liver injury. The AEFP pathway in zebrafish is shown in Figure 11.

Data availability statement

The datasets presented in this study can be found in online repositories. The names of the repository/repositories and accession number(s) can be found in the article/Supplementary Material.

Ethics statement

Ethical approval was not required for the study involving humans in accordance with the local legislation and institutional requirements. Written informed consent to participate in this study was not required from the participants or the participants' legal guardians/next of kin in accordance with the national legislation and the institutional requirements. The animal studies were approved by the Qilu University of Technology (Shandong Academy of Sciences). The studies were conducted in accordance with the local legislation and institutional requirements. Written informed consent was obtained from the owners for the participation of their animals in this study.

Author contributions

S-YG: data curation, methodology, writing–original draft. J-CZ: data curation, formal analysis, project administration, writing–original draft. QX: conceptualization, project administration, writing–review and editing. CS: resources, supervision, writing–review and editing. MA: methodology, supervision, writing–review and editing. AT: methodology, resources, supervision, writing–review and editing. S-XH: resources, supervision, writing–review and editing. YZ: formal analysis, methodology, project administration, supervision, writing–review and editing. Z-JL: methodology, resources, supervision, writing–review and editing.

Funding

The author(s) declare financial support was received for the research, authorship, and/or publication of this article. This study was supported by the National Natural Science Foundation of China (82060782), the Xinjiang Uygur Autonomous Region Youth Science Fund Project (2022D01B191), Tianshan Talents Project of the Xinjiang Uygur Autonomous Region (2022TSYCCX0021 and 2022TSYCLJ009), Young Qhuang Scholars Program, Open Project Foundation of Xinjiang Key Laboratory (2021D04017), and Xinjiang High-level Talents Introduction Tian-chi Plan.

Conflict of interest

The authors declare that the research was conducted in the absence of any commercial or financial relationships that could be construed as a potential conflict of interest.

Publisher's note

References

Alam, F., Khan, G. N., and Asad, MHHB (2018). Psoralea corylifolia L: ethnobotanical, biological, and chemical aspects: a review. *Phytother. Res.* 32 (4), 597–615. Epub 2017 Dec 15. PMID: 29243333; PMCID: PMC7167735. doi:10.1002/ptr.6006

Appelman, M. D., van der Veen, S. W., and van Mil, S. W. C. (2021). Post-translational modifications of FXR; implications for cholestasis and obesity-related disorders. *Front. Endocrinol. (Lausanne)* 12, 729828. PMID: 34646233; PMCID: PMC8503269. doi:10.3389/fendo.2021.729828

Attema, B., Janssen, A. W. F., Rijkers, D., van Schothorst, E. M., Hooiveld, GJEJ, and Kersten, S. (2022). Exposure to low-dose perfluorooctanoic acid promotes hepatic steatosis and disrupts the hepatic transcriptome in mice. *Mol. Metab.* 66, 101602. Epub 2022 Sep 14. PMID: 36115532; PMCID: PMC9526138. doi:10.1016/j.molmet.2022.101602

Bala, A., Mondal, C., and KantiHaldar, P. (2020). Zebra fish in toxicology research: streptavidin conjugated peroxidase assay in the development phase of zebrafish embryos to study liver toxicities. *Curr. Drug Discov. Technol.* 17 (5), 735–739. PMID: 31368875. doi:10.2174/1570163816666190801120016

Bambino, K., Morrison, J., and Chu, J. (2019). Hepatotoxicity in zebrafish larvae. *Methods Mol. Biol.* 1965, 129–138. PMID: 31069672. doi:10.1007/978-1-4939-9182-2_9

Cariola, A., El Chami, M., Granatieri, J., and Valgimigli, L. (2023). Anti-tyrosinase and antioxidant activity of meroterpene bakuchiol from Psoralea corylifolia (L.). *Food Chem.* 405, 134953. Epub 2022 Nov 17. PMID: 36423556. doi:10.1016/j.foodchem.2022.134953

Cassar, S., Adatto, I., Freeman, J. L., Gamse, J. T., Iturria, I., Lawrence, C., et al. (2020). Use of zebrafish in drug discovery toxicology. *Chem. Res. Toxicol.* 33 (1), 95–118. Epub 2019 Nov 16. PMID: 31625720; PMCID: PMC7162671. doi:10.1021/acs.chemrestox.9b00335

Chai, Y. Y., Xu, Y. X., Xia, Z. Y., Li, A. Q., Huang, X., Zhang, L. Y., et al. (2022). Influence of Zhuanggu guanjie pill on seven cytochrome P450 enzymes based on probe cocktail and pharmacokinetics approaches. *Curr. Drug Metab.* 23, 1054–1066. Epub ahead of print. PMID: 36503399. doi:10.2174/1389200224666221209154002

Chen, L., Chen, S., Sun, P., Liu, X., Zhan, Z., and Wang, J. (2023). Psoralea corylifolia L. a comprehensive review of its botany, traditional uses, phytochemistry, pharmacology, toxicology, quality control and pharmacokinetics. *Chin. Med.* 18 (1), 4. PMID: 36627680; PMCID: PMC9830135. doi:10.1186/s13020-022-00704-6

Chiang, J. Y. L., and Ferrell, J. M. (2018). Bile acid metabolism in liver pathobiology. *Gene Expr.* 18 (2), 71–87. Epub 2018 Jan 11. PMID: 29325602; PMCID: PMC5954621. doi:10.3727/105221618X15156018385515

Cox, A. G., and Goessling, W. (2015). The lure of zebrafish in liver research: regulation of hepatic growth in development and regeneration. *Curr. Opin. Genet. Dev.* 32, 153–161. Epub 2015 Apr 6. PMID: 25863341; PMCID: PMC4780866. doi:10.1016/j.gde.2015.03.002

Ding, L., Yang, Q., Zhang, E., Wang, Y., Sun, S., Yang, Y., et al. (2021). Notoginsenoside Ft1 acts as a TGR5 agonist but FXR antagonist to alleviate high fat diet-induced obesity and insulin resistance in mice. *Acta Pharm. Sin. B* 11 (6), 1541–1554. Epub 2021 Mar 30. PMID: 34221867; PMCID: PMC8245856. doi:10.1016/j.apsb.2021.03.038

Duan, J., Dong, W., Xie, L., Fan, S., Xu, Y., and Li, Y. (2020). Integrative proteomics-metabolomics strategy reveals the mechanism of hepatotoxicity induced by Fructus Psoraleae. *J. Proteomics* 221, 103767. Epub 2020 Mar 31. PMID: 32240813. doi:10.1016/j.jprot.2020.103767

Gao, H. T., Lang, G. Z., Zang, Y. D., Ma, J., Yang, J. Z., Ye, F., et al. (2021). Bioactive monoterpene phenol dimers from the fruits of Psoralea corylifolia L. *Bioorg Chem.* 112, 104924. Epub 2021 Apr 20. PMID: 33933806. doi:10.1016/j.bioorg.2021.104924

Gao, Y., Wang, Z., Tang, J., Liu, X., Shi, W., Qin, N., et al. (2020). New incompatible pair of TCM: Epimedii Folium combined with Psoraleae Fructus induces idiosyncratic hepatotoxicity under immunological stress conditions. *Front. Med.* 14 (1), 68–80. Epub 2019 Mar 28. PMID: 30924023. doi:10.1007/s11684-019-0690-z

Goessling, W., and Sadler, K. C. (2015). Zebrafish: an important tool for liver disease research. *Gastroenterology* 149 (6), 1361–1377. Epub 2015 Aug 28. PMID: 26319012; PMCID: PMC4762709. doi:10.1053/j.gastro.2015.08.034

Guan, B., Tong, J., Hao, H., Yang, Z., Chen, K., Xu, H., et al. (2022). Bile acid coordinates microbiota homeostasis and systemic immunometabolism in cardiometabolic diseases. *Acta Pharm. Sin. B* 12 (5), 2129–2149. Epub 2021 Dec 22. PMID: 35646540; PMCID: PMC9136572. doi:10.1016/j.apsb.2021.12.011

Hernández-Silva, D., Alcaraz-Pérez, F., Pérez-Sánchez, H., and Cayuela, M. L. (2023). Virtual screening and zebrafish models in tandem, for drug discovery and development. *Expert Opin. Drug Discov.* 18 (8), 903–915. Epub 2022 Nov 30. PMID: 36383405. doi:10.1080/17460441.2022.2147503

Hou, X. D., Song, L. L., Cao, Y. F., Wang, Y. N., Zhou, Q., Fang, S. Q., et al. (2020). Pancreatic lipase inhibitory constituents from Fructus Psoraleae. *Chin. J. Nat. Med.* 18 (5), 369–378. PMID: 32451094. doi:10.1016/S1875-5364(20)30043-1

Jiang, H. Y., Gao, H. Y., Li, J., Zhou, T. Y., Wang, S. T., Yang, J. B., et al. (2022). Integrated spatially resolved metabolomics and network toxicology to investigate the hepatotoxicity mechanisms of component D of Polygonum multiflorum Thunb. *J. Ethnopharmacol.* 298, 115630. Epub 2022 Aug 17. PMID: 35987407. doi:10.1016/j.jep.2022.115630

Katoch, S., and Patial, V. (2021). Zebrafish: an emerging model system to study liver diseases and related drug discovery. *J. Appl. Toxicol.* 41 (1), 33–51. Epub 2020 Jul 12. PMID: 32656821. doi:10.1002/jat.4031

Kersten, S., and Stienstra, R. (2017). The role and regulation of the peroxisome proliferator activated receptor alpha in human liver. *Biochimie* 136, 75–84. Epub 2017 Jan 8. PMID: 28077274. doi:10.1016/j.biochi.2016.12.019

Lala, V., Zubair, M., and Minter, D. A. (2023). *Liver function tests*. Treasure Island (FL): StatPearls Publishing.

Lee, Y., Kim, B. R., Kang, G. H., Lee, G. J., Park, Y. J., Kim, H., et al. (2021). The effects of PPAR agonists on atherosclerosis and nonalcoholic fatty liver disease in ApoE-/-FXR-/- mice. *Endocrinol. Metab. Seoul.* 36 (6), 1243–1253. Epub 2021 Dec 28. PMID: 34986301; PMCID: PMC8743579. doi:10.3803/EnM.2021.1100

Li, A., Gao, M., Zhao, N., Li, P., Zhu, J., and Li, W. (2019). Acute liver failure associated with Fructus Psoraleae: a case report and literature review. *BMC Complement. Altern. Med.* 19 (1), 84. PMID: 30975110; PMCID: PMC6458792. doi:10.1186/s12906-019-2493-9

Li, N., Liu, T., Zhu, S., Yang, Y., Wang, Z., Zhao, Z., et al. (2022). Corylin from Psoralea fructus (Psoralea corylifolia L.) protects against UV-induced skin aging by activating Nrf2 defense mechanisms. *Phytother. Res.* 36 (8), 3276–3294. Epub 2022 Jul 12. PMID: 35821646. doi:10.1002/ptr.7501

Li, T., Gao, S., Han, W., Gao, Z., Wei, Y., Wu, G., et al. (2022). Potential effects and mechanisms of Chinese herbal medicine in the treatment of psoriasis. *J. Ethnopharmacol.* 294, 115275. Epub 2022 Apr 26. PMID: 35487447. doi:10.1016/j.jep.2022.115275

Lim, S. H., Lee, H. S., Han, H. K., and Choi, C. I. (2021). Saikosaponin A and D inhibit adipogenesis via the AMPK and MAPK signaling pathways in 3T3-L1 adipocytes. *Int. J. Mol. Sci.* 22 (21), 11409. PMID: 34768840; PMCID: PMC8583978. doi:10.3390/ijms222111409

Liu, Y. L., Ge, F. L., Zhu, J. X., Jing, J., Wang, J. B., Zhang, Y. M., et al. (2019). Re-evaluation of liver injury associated with Buguzhi Preparations based on passive monitoring data and hospital cases. *Zhongguo Zhong Yao Za Zhi* 44 (19), 4272–4276. PMID: 31872709. doi:10.19540/j.cnki.cjcmm.20190508.501

Makwana, S., Mehere, N., Bedarkar, P., Biswajyoti, P., and Harisha, C. R. (2020). Comparative pharmacognosy and phytochemical evaluation of leaf, root and stem of Psoralea corylifolia Linn. (Bakuchi). *Ayu* 41 (4), 235–241. Epub 2022 Jun 3. PMID: 35813361; PMCID: PMC9261993. doi:10.4103/ayu.ayu_79_21

Men, W. J., Meng, Z. J., Wang, Q., Chen, M. Y., Zhai, Y. X., Shi, H., et al. (2022). The changes of hepatic bile acid synthesis and transport and bile acids profiles in isopsoralen-induced liver injury C57BL/6J mice. *Pharm. Biol.* 60 (1), 1701–1709. PMID: 36066106; PMCID: PMC9467544. doi:10.1080/13880209.2022.2116057

Nakamura, M. T., Yudell, B. E., and Loor, J. J. (2014). Regulation of energy metabolism by long-chain fatty acids. *Prog. Lipid Res.* 53, 124–144. Epub 2013 Dec 18. PMID: 24362249. doi:10.1016/j.plipres.2013.12.001

Rong, J., Xie, Z., Chen, E., Ma, S., Zhang, S., Zhao, Y., et al. (2020). Fructus psoraleae-induced severe liver injury and treatment with two artificial liver support systems: a case series study. *Ther. Apher. Dial.* 24 (3), 324–332. Epub 2019 Oct 25. PMID: 31577858. doi:10.1111/1744-9987.13438

Rosa, J. G. S., Lima, C., and Lopes-Ferreira, M. (2022). Zebrafish larvae behavior models as a tool for drug screenings and pre-clinical trials: a review. *Int. J. Mol. Sci.* 23 (12), 6647. PMID: 35743088; PMCID: PMC9223633. doi:10.3390/ijms23126647

Samuel, V. T., and Shulman, G. I. (2018). Nonalcoholic fatty liver disease as a nexus of metabolic and hepatic diseases. *Cell Metab.* 27 (1), 22–41. Epub 2017 Aug 31. PMID: 28867301; PMCID: PMC5762395. doi:10.1016/j.cmet.2017.08.002

Shi, Z., Gao, J., Pan, J., Zhang, Z., Zhang, G., Wang, Y., et al. (2022). A systematic review on the safety of Psoraleae Fructus: potential risks, toxic characteristics, underlying mechanisms and detoxification methods. *Chin. J. Nat. Med.* 20 (11), 805–813. PMID: 36427915. doi:10.1016/S1875-5364(22)60234-6

Tian, W. Y., Lan, S., Zhang, L., Sun, L., Huang, J. K., Yang, X. H., et al. (2017). Safety evaluation and risk control measures of Psoralea corylifolia. *Zhongguo Zhong Yao Za Zhi* 42 (21), 4059–4066. PMID: 29271140. doi:10.19540/j.cnki.cjcmm.20170919.011

Wang, J., Jiang, Z., Ji, J., Li, Y., Chen, M., Wang, Y., et al. (2012). Evaluation of hepatotoxicity and cholestasis in rats treated with EtOH extract of Fructus Psoraleae. *J. Ethnopharmacol.* 144 (1), 73–81. Epub 2012 Aug 30. PMID: 22954498. doi:10.1016/j.jep.2012.08.028

Wang, S., Feng, R., Wang, S. S., Liu, H., Shao, C., Li, Y., et al. (2023). FOXA2 prevents hyperbilirubinaemia in acute liver failure by maintaining apical MRP2 expression. *Gut* 72 (3), 549–559. Epub 2022 Apr 20. PMID: 35444014. doi:10.1136/gutjnl-2022-326987

Wang, X., Lou, Y. J., Wang, M. X., Shi, Y. W., Xu, H. X., and Kong, L. D. (2012). Furocoumarins affect hepatic cytochrome P450 and renal organic ion transporters in mice. *Toxicol. Lett.* 209 (1), 67–77. doi:10.1016/j.toxlet.2011.11.030

Wang, Y., Zhang, H., Jiang, J. M., Zheng, D., Tan, H. S., Tang, L. M., et al. (2019). Multiorgan toxicity induced by EtOH extract of fructus psoraleae in wistar rats. *Phytomedicine* 58, 152874. Epub 2019 Feb 25. PMID: 30889421. doi:10.1016/j.phymed.2019.152874

Wu, X., Gao, X., Liu, X., Zhang, S., Yang, H., Zhu, X., et al. (2020). Quality control of Psoralea corylifolia L. Based on high-speed countercurrent chromatographic fingerprinting. *Molecules* 25 (2), 279. PMID: 31936676; PMCID: PMC7024294. doi:10.3390/molecules25020279

Yu, L., Lu, H., Yang, X., Li, R., Shi, J., Yu, Y., et al. (2021). Diosgenin alleviates hypercholesterolemia via SRB1/CES-1/CYP7A1/FXR pathway in high-fat diet-fed rats. *Toxicol. Appl. Pharmacol.* 412, 115388. doi:10.1016/j.taap.2020.115388

Yu, X. H., Zheng, X. L., and Tang, C. K. (2015). Peroxisome proliferator-activated receptor α in lipid metabolism and atherosclerosis. *Adv. Clin. Chem.* 71, 171–203. Epub 2015 Jul 23. PMID: 26411415. doi:10.1016/bs.acc.2015.06.005

Zeng, W., Yin, X., Jiang, Y., Jin, L., and Liang, W. (2022). PPARα at the crossroad of metabolic-immune regulation in cancer. *FEBS J.* 289 (24), 7726–7739. Epub 2021 Sep 19. PMID: 34480827. doi:10.1111/febs.16181

Zhang, C. J., Meyer, S. R., O'Meara, M. J., Huang, S., Capeling, M. M., Ferrer-Torres, D., et al. (2023). A human liver organoid screening platform for DILI risk prediction. *J. Hepatol.* 78 (5), 998–1006. Epub 2023 Feb 3. PMID: 36738840. doi:10.1016/j.jhep.2023.01.019

Zhang, X., Zhao, W., Wang, Y., Lu, J., and Chen, X. (2016). The chemical constituents and bioactivities of Psoralea corylifolia linn. a review. *Am. J. Chin. Med.* 44 (1), 35–60. PMID: 26916913. doi:10.1142/S0192415X16500038

Zhang, Y., Cen, J., Jia, Z., Hsiao, C. D., Xia, Q., Wang, X., et al. (2019). Hepatotoxicity induced by isoniazid-lipopolysaccharide through endoplasmic reticulum stress, autophagy, and apoptosis pathways in zebrafish. *Antimicrob. Agents Chemother.* 63 (5), 016399–e1718. doi:10.1128/AAC.01639-18

frontiers | Frontiers in Pharmacology

TYPE Original Research
PUBLISHED 21 February 2024
DOI 10.3389/fphar.2024.1292828

OPEN ACCESS

EDITED BY
Huaqiang Zhai,
Beijing University of Chinese Medicine, China

REVIEWED BY
Lifan Zhang,
West China Hospital, Sichuan University, China
Xin Huang,
Shandong Provincial Qianfoshan Hospital, China

*CORRESPONDENCE
Jingwen Wang,
wangjingwen8021@163.com
Yi Ding,
dingyi.007@163.com

RECEIVED 12 September 2023
ACCEPTED 29 January 2024
PUBLISHED 21 February 2024

CITATION
Zhao X, Peng Q, Hu D, Li W, Ji Q, Dong Q, Huang L, Piao M, Ding Y and Wang J (2024), Prediction of risk factors for linezolid-induced thrombocytopenia based on neural network model.
Front. Pharmacol. 15:1292828.
doi: 10.3389/fphar.2024.1292828

Prediction of risk factors for linezolid-induced thrombocytopenia based on neural network model

Xian Zhao[1], Qin Peng[2], Dongmei Hu[1], Weiwei Li[1], Qing Ji[1], Qianqian Dong[1], Luguang Huang[3], Miyang Piao[1], Yi Ding[1]* and Jingwen Wang[1]*

[1]Department of Pharmacy, First Affiliated Hospital of Air Force Medical University, Xi'an, Shaanxi, China, [2]Department of Hepatobiliary Surgery, First Affiliated Hospital of Air Force Medical University, Xi'an, Shaanxi, China, [3]Department of Information, First Affiliated Hospital of Air Force Medical University, Xi'an, Shaanxi, China

Background: Based on real-world medical data, the artificial neural network model was used to predict the risk factors of linezolid-induced thrombocytopenia to provide a reference for better clinical use of this drug and achieve the timely prevention of adverse reactions.

Methods: The artificial neural network algorithm was used to construct the prediction model of the risk factors of linezolid-induced thrombocytopenia and further evaluate the effectiveness of the artificial neural network model compared with the traditional Logistic regression model.

Results: A total of 1,837 patients receiving linezolid treatment in a hospital in Xi 'an, Shaanxi Province from 1 January 2011 to 1 January 2021 were recruited. According to the exclusion criteria, 1,273 cases that did not meet the requirements of the study were excluded. A total of 564 valid cases were included in the study, with 89 (15.78%) having thrombocytopenia. The prediction accuracy of the artificial neural network model was 96.32%, and the AUROC was 0.944, which was significantly higher than that of the Logistic regression model, which was 86.14%, and the AUROC was 0.796. In the artificial neural network model, urea, platelet baseline value and serum albumin were among the top three important risk factors.

Conclusion: The predictive performance of the artificial neural network model is better than that of the traditional Logistic regression model, and it can well predict the risk factors of linezolid-induced thrombocytopenia.

KEYWORDS

ANN, logistic regression, linezolid, thrombocytopenia, risk factor, ADR

1 Introduction

Linezolid is a widely used oxazolidinone that penetrates cerebrospinal fluid and bone tissue and exhibits good antibacterial effects against Gram-positive bacteria, especially methicillin-resistant *Staphylococcus aureus* (MRSA) and other resistant Gram-positive bacteria (Dryden, 2011; Cazavet et al., 2020). However, during the clinical application of all drugs, a serious problem cannot be avoided, namely, adverse reactions (Edwards and

Aronson, 2000; Coleman and Pontefract, 2016). Thrombocytopenia is one of the major adverse reactions of linezolid, and existing studies have shown (Bernstein et al., 2003; Hanai et al., 2016a) that the mechanism of linezolid-induced thrombocytopenia, mainly including immune-mediation, myelosuppression, inhibitory release and oxidative stress. Although this adverse drug reaction is treatable, it may cause the discontinuation of linezolid therapy and have an impact on its clinical use. Studies have shown (M et al., 2022; Cossu et al., 2014; An and Wang, 2013) that reversible myelosuppression, such as thrombocytopenia and anemia, often occurs after 4–6 weeks of continuous linezolid treatment, with an incidence of 7.4%–31.3%.

In recent years, the improvement and enhancement of computer computing power and the innovation and improvement of algorithms have greatly promoted the use of machine learning. In addition, many researchers have applied machine learning to various subdivisions, such as survival prediction of gastric cancer patients (Yazdani Charati et al., 2018), risk prediction of fetal congenital heart disease (Li et al., 2017), early outcome prediction and risk classification of cardiac arrest patients in out-of-hospital intensive care (Johnsson et al., 2020), and conducted more intensified studies. Among many machine learning algorithms, Artificial Neural Network (ANN), also called Multilayer Perceptron (MLP), is one of the important algorithms of machine learning. ANN is a typical supervised learning algorithm, the creation of which is inspired by the human brain and nervous system (Pergialiotis et al., 2018). Compared with the traditional logistic regression model, ANN can be used to find the approximate mapping between the input and output patterns of patient data and realize non-intuitive and complex nonlinear separation between various types of patients.

In the present study, we reported the risk factors of linezolid-induced thrombocytopenia in a single-center retrospective study combined with several literature (Cazavet et al., 2020; M et al., 2022; Cossu et al., 2014; Niwa et al., 2009; Ikuta et al., 2011; Takahashi et al., 2011; Chen et al., 2012; Nukui et al., 2013; Ishida et al., 2013; Natsumoto et al., 2014; Ni et al., 2014; Zhang et al., 2014; Jie, 2016; Tajima et al., 2016; Choi et al., 2019; Kaya Kılıç et al., 2019; Kim et al., 2019; Qin et al., 2022). Based on real-world medical data, an artificial neural network model was used to predict the risk factors and prediction accuracy of linezolid-induced thrombocytopenia, and compared with the traditional logistic regression model, so as to further evaluate the effectiveness of the neural network model and provide a reference for better clinical use of this drug for timely prevention of the adverse drug reactions.

2 Materials and methods

2.1 Inclusion criteria

This single-center retrospective observational study was conducted in a hospital in Xi'an, Shaanxi Province. In the present study, diagnosis and treatment data were collected from the HIS system of this hospital, and the inclusion criteria for patients were having received linezolid between 1 January 2011 and 1 January 2021. The collected clinic data were stored in a Microsoft Excel file. In order to protect the privacy of patients,

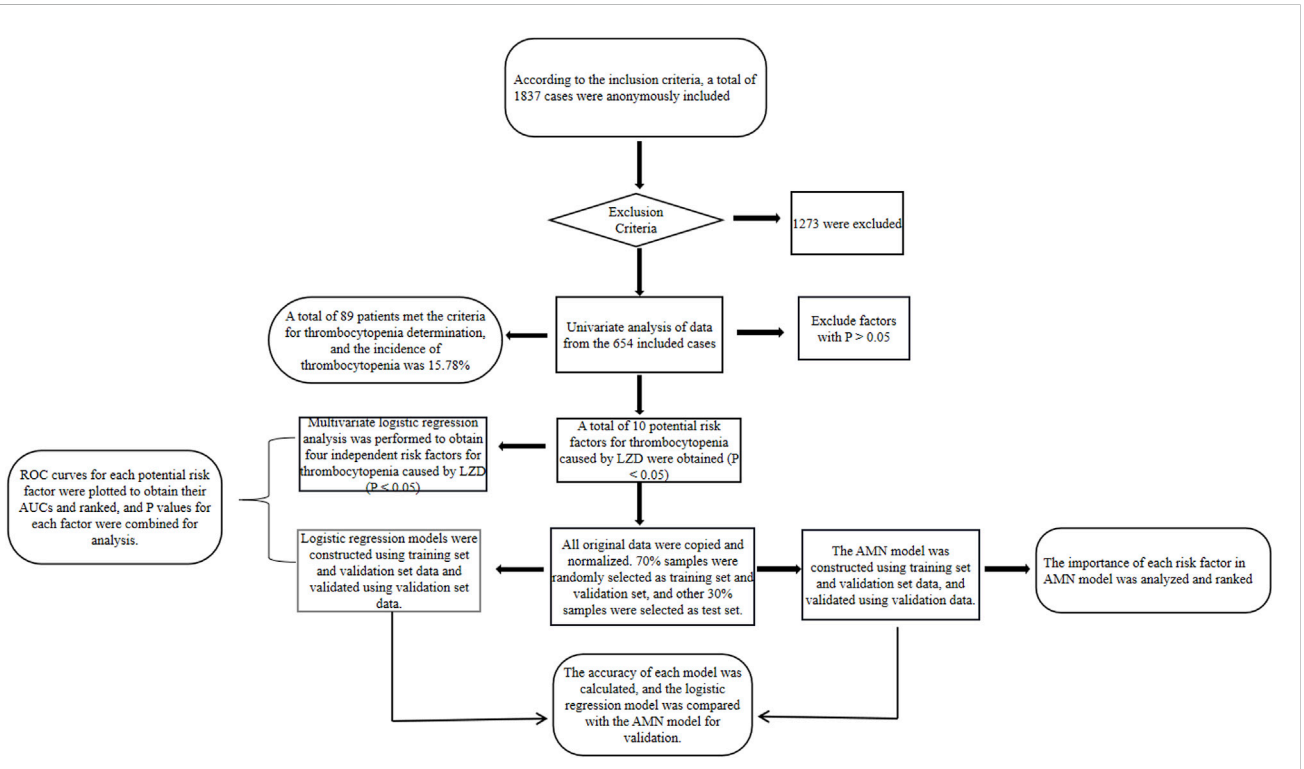

FIGURE 1
Flowchart of studies predicting risk factors for linezolid-induced thrombocytopenia.

the collected data were anonymous, the names and/or numbers of patients were not identified, and there was no adverse effect on patients. Since this was a retrospective study, informed consent was not required for the collection of patient care data in the present study. The study protocol was reviewed and approved by the Ethics Committee of this hospital and the study was conducted according to the World Medical Association Declaration of Helsinki (THE WORLD MEDICAL ASSOCIATION and INC, 2013).

2.2 Exclusion criteria

The last platelet count value before linezolid use was defined as the baseline platelet value. Exclusion criteria for patients were (Hirano et al., 2014): 1) Patients with blood system diseases (such as myelosuppression, hemophilia, etc.), immune system abnormalities (such as systemic lupus erythematosus, organ transplantation, etc.), hepatoblastoma, severe acute pancreatitis; 2) chemotherapy, hemodialysis, or combined use of antiplatelet drugs (such as clopidogrel, etc.) during treatment; 3) baseline platelet values <100 × 10⁹/L or >400 × 10⁹/L; 4) the total number of platelet count test points was less than 3; 5) no baseline platelet values; 6) non-standard linezolid treatment programs.

2.3 Criteria for determining thrombocytopenia

Taking the nadir of platelet count within 15 times after linezolid use as the basis for judging whether thrombocytopenia occurs, if it was lower than the normal value of platelet count (i.e., less than 100 × 10⁹/L) and at the same time lower than 75% of the baseline value of platelets, the patient was defined as having developed thrombocytopenia (Niwa et al., 2009).

2.4 Data collection

Taking into account the risk factors for linezolid-induced thrombocytopenia reported in the literature (Cazavet et al., 2020; M et al., 2022; Cossu et al., 2014; Niwa et al., 2009; Ikuta et al., 2011; Takahashi et al., 2011; Chen et al., 2012; Nukui et al., 2013; Ishida et al., 2013; Natsumoto et al., 2014; Ni et al., 2014; Zhang et al., 2014; Jie, 2016; Tajima et al., 2016; Choi et al., 2019; Kaya Kılıç et al., 2019; Kim et al., 2019; Qin et al., 2022), various data in clinical diagnosis and treatment of the included study subjects were recorded and assessed, including gender, age, height, weight, BMI, route of linezolid administration, total days of administration, baseline platelet values, dynamic changes in platelet count values during treatment, TP, ALB, TBIL, DBIL, urea, history of hypertension, history of diabetes, history of malignant tumors, and combined use of unfractionated heparin. Alanine aminotransferase (ALT) and aspartate aminotransferase (AST) were selected for liver enzyme parameters, and creatinine clearance (Ccr) was used to reflect the renal function. Creatinine clearance was calculated using the Cockcroft-Gault equation (Cockcroft and Gault, 1976).

2.5 Data analysis

Both univariate and multivariate analyses were performed using SPSS 22.0. The analysis was performed in two steps. First, univariate analysis was carried out. Categorical variables in the chart were identified as (1), expressed as n (%), with the assumption verified using the $\chi 2$ test; continuous variables were not identified, expressed as " ± s," with the assumption verified adjusted *t*-test. All tests were two-sided and differences were considered statistically significant at $p < 0.05$ (Takahashi et al., 2011; Hirano et al., 2014; Zhang et al., 2014). The potential risk factors for linezolid-induced thrombocytopenia were identified (factors with $p < 0.05$).

Multivariate analysis was then performed to obtain the odds ratio (OR), 95% confidence interval (95% CI), and *p*-value of each potential risk factor to determine the independent risk factors for linezolid-induced thrombocytopenia (factors with $p < 0.05$).

2.6 Data processing

In order to increase the rate of gradient descent, the data were normalized so that the processed data met the standard normal distribution; 70% of the samples were randomly selected as the training set along with the validation set for constructing the model, and the remaining 30% were used as the test set for validating the accuracy of the model. The study flow chart is shown in Figure 1.

3 Results

3.1 Case statistics

A total of 1,837 patients who had received linezolid treatment from 1 January 2011 to 1 January 2021 were collected, 1,273 patients who did not meet the requirements of the present study were excluded according to the exclusion criteria, and a total of 564 valid cases were finally included in the present study, including 357 males (63.30%) and 207 females (36.70%), with an average age of 50.26 ± 20.87 years, an age span of 1–100 years, average total days of medication of 6.90 ± 7.87 days, and a time span of use of 1–76 days. Of the 564 cases included, 89 were positive for meeting the criteria for thrombocytopenia in 2.2, which means that the incidence of linezolid-induced thrombocytopenia in the present study was 15.78%.

In addition, we also statistically analyzed the discharging department of the cases in the present study (Supplementary Table S1), with Geriatrics, Gastroenterology, and Urology department among the top three departments in the incidence of linezolid-induced thrombocytopenia, 40%, 35.71%, and 20.00%, respectively; of the 564 cases, 480 cases were from general departments, 84 cases were from intensive care units, and the incidence of thrombocytopenia in intensive care units was 35.71%, which was significantly higher than that in general departments (12.29%); in the intensive care units of each department, the incidence of thrombocytopenia in cardiovascular surgical care units was the highest, 63.64%.

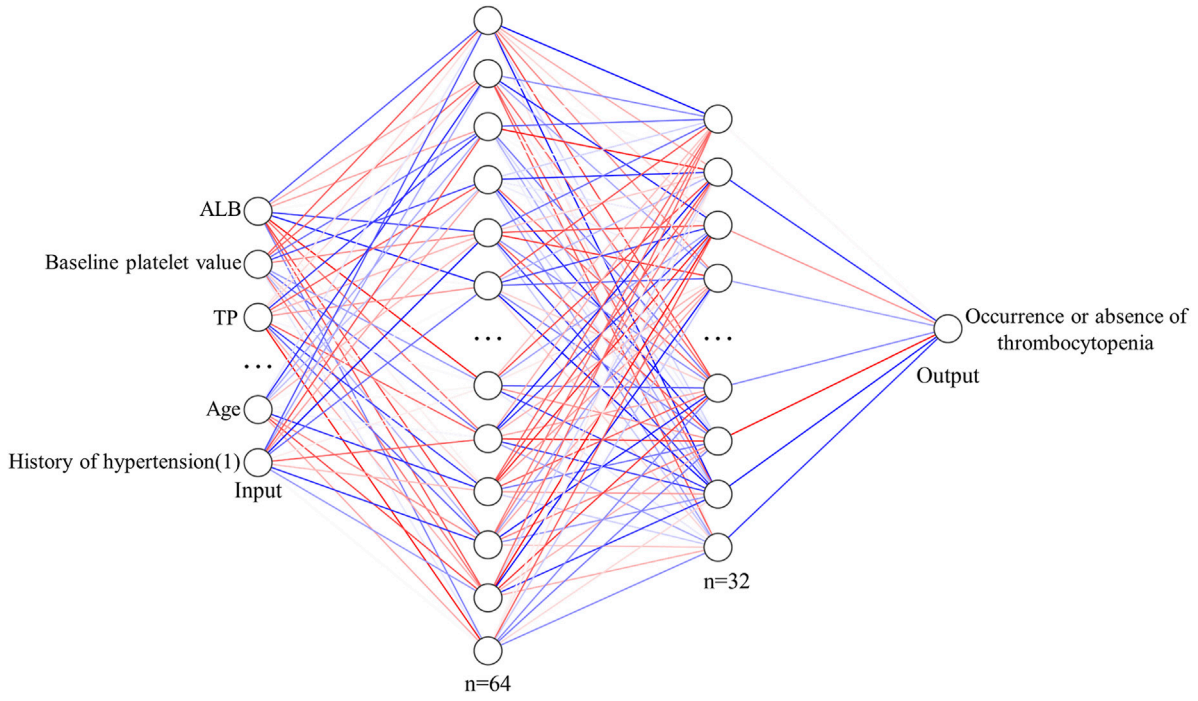

FIGURE 2
Structural diagram of ANN model for predicting the risk of thrombocytopenia caused by linezolid.

3.2 Univariate analysis

The results of univariate analysis (Supplementary Table S2) showed that there were significant differences in age, history of hypertension, history of malignancy, baseline platelet values, TP, ALB, AST, DBIL, urea, and CCr between patients who developed thrombocytopenia and those who did not ($p < 0.05$).

3.3 Multivariate analysis

The OR, 95% CI and p-value of each factor were calculated by multivariate analysis using the factors with $p < 0.05$ in univariate analysis as independent variables and the occurrence or absence of thrombocytopenia as dependent variables. As shown in Supplementary Table S3, urea, baseline platelet value, age, and TP were independent risk factors for linezolid-induced thrombocytopenia in multivariate analysis ($p < 0.05$).

3.4 Construction of logistic regression model

On the basis of taking the factors with $p < 0.05$ in the univariate analysis as independent variables and the occurrence or absence of thrombocytopenia as dependent variables, after the steps of constructing the logistic regression model, logistic regression model and equation were obtained, and the logistic regression equation was as follows:

$$\begin{aligned}\text{Logit}(P) = {} & 0.42936452\,\text{XUrea} - 0.72150774\,\text{XPLT} \\ & + 0.36437262\,\text{XHTN} + 0.42472864\,\text{XAge} \\ & - 0.11102075\,\text{XCcr} + 0.1818322\,\text{XDBIL} \\ & - 0.06335601\,\text{XALB} + 0.13845654\,\text{XAST} \\ & + 0.20871324\,\text{XMT} - 0.28616011\,\text{XTP} - 2.19748157\end{aligned}$$

Where: XUrea, XPLT, XHTN, XAge, XCcr, XDBIL, XALB, XAST, XMT, and XTP denote Urea, platelet baseline value, history of hypertension, age, Ccr, DBIL, ALB, AST, history of malignancy, and TP, respectively.

3.5 Construction of ANN model

The ANN model is implemented on the PyTorch1.10 deep learning framework with Python3.8. Factors with $p < 0.05$ in univariate analysis were used as independent variables, and the occurrence or absence of thrombocytopenia was the dependent variable. As shown in Figure 2, ANN consists of two fully connected hidden layers connected sequentially, and the numbers of neurons in these layers are 64 and 32, respectively. The activation function of the hidden layer is ReLU and batch normalization is applied for the features output from the hidden layer. The Binary Cross Entropy is used as a loss function for training.

The data were preprocessed before being entered into the ANN. In detail, continuous factors were normalized by the max and min values of this factor. Discrete variables were coded by one-hot.

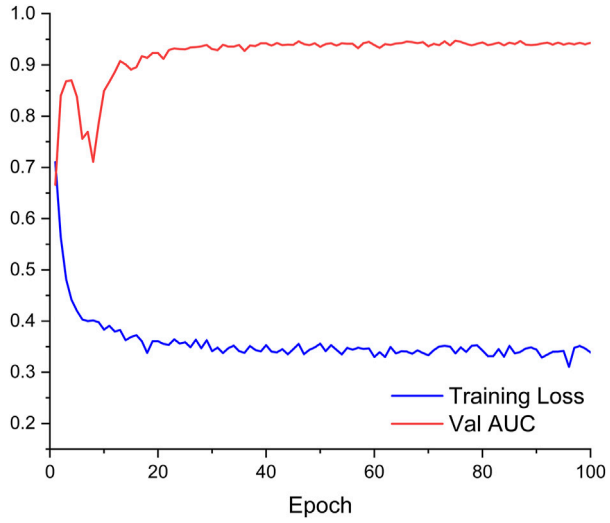

FIGURE 3
Training loss and AUC on validation dataset of ANN model during training process.

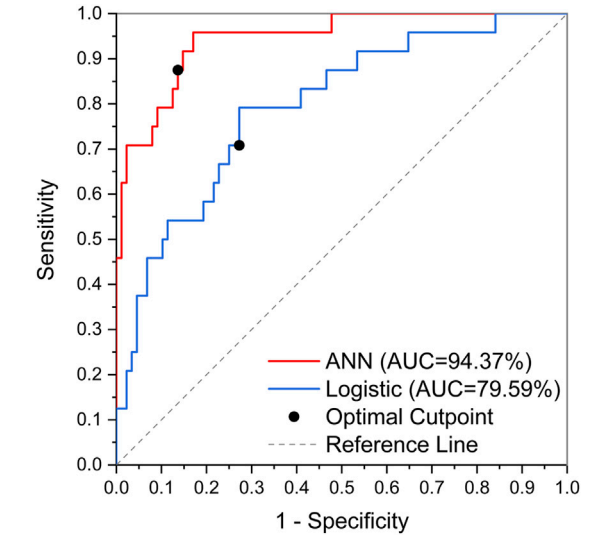

FIGURE 4
The ROC curves and AUCs of ANN and Logistic models on test dataset.

3.6 Validation of logistic regression model compared to ANN model

The obtained logistic regression model was subjected to the Hosmer-Lemeshow test, and the results are shown in Supplementary Table S4, resulting in a $\chi 2$ value of 12.493 and a p-value of 0.131 > 0.05, indicating that the logistic regression model constructed in the present study fitted well. Predictive validation of the logistic regression model with the test set yielded a prediction accuracy of 86.14%, with an AUC of 0.796. According to the prediction results of the logistic regression model, the sensitivity and specificity of each potential risk factor were calculated, and their

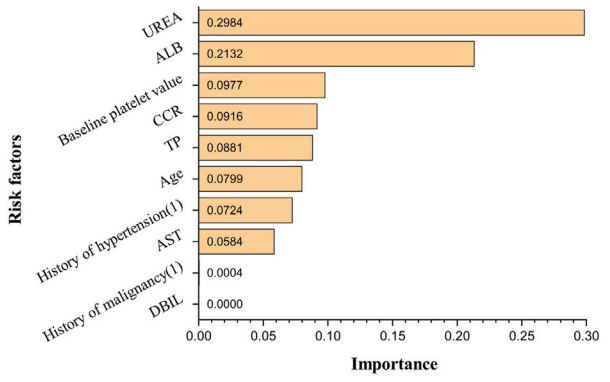

FIGURE 5
The importance and ranking diagram of potential risk factors in ANN model.

AUC and ranking were obtained. The results are shown in Supplementary Table S5. In the present study, the factors with AUC >0.65 were considered to be well correlated, and then by combining again the p values of each potential risk factor in the multifactorial analysis, it can be concluded that urea, baseline platelet values, and age are significant risk factors for linezolid-induced thrombocytopenia as predicted by the logistic regression model.

The obtained ANN model was validated for prediction using the test set with an accuracy of 96.32%, with an AUC of 0.944, indicating that the ANN model constructed in the present study has good predictive ability. Figure 3 shows the ROC curves and AUCs of ANN and Logistic models on the test dataset. We used SMOTE to augment the training data to alleviate overfitting and data imbalance. We set up batch-normal and drop-out layers after each layer of the ANN, which effectively avoids overfitting. As shown in Figure 4, we have plotted the loss and validation AUC curves of the ANN model during the training process. As can be seen from the curves, both the loss and the AUC on the validation set gradually remain stable with training, and there is no significant overfitting. This demonstrates the generalizability of the ANN we used. Figure 5 shows the importance and ranking of each potential risk factor obtained from the ANN model analysis, and urea, baseline platelet value, and ALB are among the top three important risk factors for ANN model prediction of linezolid-induced thrombocytopenia.

4. Discussion

Of the 564 cases included in the study, 89 developed thrombocytopenia, and the incidence of linezolid-induced thrombocytopenia was 15.78%; univariate analysis showed that age, history of hypertension, history of malignancy, baseline platelet value, TP, ALB, AST, DBIL, urea, and Ccr were potential risk factors for linezolid-induced thrombocytopenia ($p < 0.05$); in multivariate analysis, urea, baseline platelet value, age, and TP were independent risk factors for linezolid-induced thrombocytopenia ($p < 0.05$). According to the logistic regression model and in

combination with the AUC of each potential risk factor and *p*-value in multivariate analysis, it is concluded that urea, baseline platelet value, and age were possible risk factors for linezolid-induced thrombocytopenia predicted by the logistic regression model. The importance of each potential risk factor obtained by ANN model analysis showed that urea, baseline platelet value, and ALB were among the top three possible risk factors for linezolid-induced thrombocytopenia predicted by the ANN model. Multiple studies have demonstrated a positive association between renal insufficiency and elevated concentrations of Linezolid, thereby increasing the risk of thrombocytopenia. Specifically, the risk of thrombocytopenia is found to be significantly elevated by 2-fold, 8-fold, and 9-fold in patients with mild, moderate, and severe renal insufficiency, respectively (Hanai et al., 2016b; Crass et al., 2019). Notably, Matsumoto K et al. (Matsumoto, 2012) have reported a negative correlation between Linezolid clearance and blood urea nitrogen levels. Similarly, Lin YH et al. (Lin et al., 2006) have observed a higher frequency of elevated blood urea nitrogen in patients with impaired renal function at the initiation of treatment, aligning with the findings of the present study. Urea, as the end product of protein metabolism, is subject to various influencing factors including intake, disease, and renal excretion capacity. In the current study, the thrombocytopenia group exhibited a higher mean age and a greater proportion of comorbidities such as hypertension, diabetes, and malignant tumors compared to the non-thrombocytopenia group. These factors may contribute to the observed elevation in blood urea nitrogen levels, suggesting that it may serve as a more reliable indicator of heightened catabolic state, increased renal burden, and an augmented risk of acute kidney injury. However, further investigations are warranted to validate these findings. It has been reported that patients with thrombocytopenia have significantly lower baseline platelet counts than those without thrombocytopenia, and patients with low baseline platelet counts should be closely monitored (Choi et al., 2019; Qin et al., 2022). Studies have shown that patients receiving human serum albumin therapy during Linezolid treatment have a low incidence of thrombocytopenia, and there is a significant negative correlation between serum albumin concentration and Linezolid-induced thrombocytopenia (Zhang et al., 2023). Chen et al. (Chen et al., 2012)found a high correlation between serum albumin concentration ≤33.5 g/L and thrombocytopenia, which is consistent with the results of our study with the mean albumin concentration of 33.48 g/L in the thrombocytopenia group. The decrease in albumin can reduce the protein binding rate of Linezolid in plasma and alter its distribution, leading to increased drug exposure and the occurrence of thrombocytopenia (Cattaneo et al., 2023). The findings need to be validated by further research as well. The results showed that the prediction accuracy of the logistic regression model was 86.14%, while that of the ANN model was 96.32%, which was much higher than that of the logistic regression model. Therefore, it can be concluded that the artificial neural network model constructed in the present study can be well predictive of the risk factors and their occurrence of linezolid-induced thrombocytopenia. In addition, in the actual clinical environment, there is always a complex nonlinear mixture of predictor variables. Most studies on linezolid-induced thrombocytopenia are mainly analyzed by retrospective analysis of small samples or traditional linear multivariate statistics, which can't perform the analysis of large samples and complex relationships between multiple factors. Hence the combination of ANN with traditional statistical analysis (such as logistic regression analysis and log-likelihood analysis) could be a more effective solution to the problem of analyzing complex, multifactorial data in real-world data.

Although a risk prediction model for adverse drug reactions was successfully constructed using ANNs, ANNs also have some limitations compared with logistic regression analysis. First, ANNs have certain "Black Box" properties, that is, ANNs cannot explain why the constructed model can be obtained, nor can they give specific model equations. Therefore, the ANN model can only show the importance of each independent variable and rank them, but can not calculate their sensitivity and specificity, so their ROC curve and Youden index cannot be obtained to determine the cutoff value of each independent variable. This disadvantage will hinder its wider clinical use. Second, the ANN model requires high data diversity, and if the amount of data is too small, or the data source is not wide enough, the performance statistics (prediction accuracy, sensitivity, specificity, etc.) may become unstable and unreliable, meaning that false negative or false positive errors will have a greater impact on the analysis results, and will greatly affect the prediction accuracy of the ANN model. Third, ANNs have the risk of overtraining and the possibility of overfitting models, which may provide overconfidence predictions. Finally, in terms of clinical application, ANN requires the use of certain statistical analysis software or the possession of a programming language basis, so it is difficult to widely use the ANN model in clinical practice at present. However, Pergialiotis V et al. (Pergialiotis et al., 2018) believe that these problems can be solved by including more patients (in addition to the need for special statistical analysis software), that is, establishing a larger database, which is necessary to construct a more accurate and safe ANN model.

The present study also has some limitations. First, the study was a single-center study and there may have been bias in patient selection, which would reduce the likelihood of extrapolating the results to other populations, necessitating multi-center, bigger sample sizes in future research. Second, the number of samples remains small relative to possible risk factors, and there are more missing values for some variables (patient height, weight). The study drew on Johnsson J's method (Johnsson et al., 2020) and replaced them with the mean of continuous variables. Third, only ROC curves of each potential risk factor were plotted in the logistic regression model, while Youden index was not further obtained to determine the cutoff value of each potential risk factor. Fourth, although heparin use may lower platelet counts during actual clinical treatment, the univariate analysis in this study did not reveal a significant difference in the impact of combining heparin use on the outcomes. This could be due to the study experiencing a small sample size, and more research is required to determine the impact of combining heparin use on platelets. In addition, for some other risk factors, including trough concentrations of linezolid, $PaCO_2$, APACHE II, etc., the corresponding data could not be extracted due to conditional limitations, so their association with thrombocytopenia could not be assessed.

To the best of our knowledge, this is the first study to use the ANN model to predict risk factors for linezolid-induced thrombocytopenia from real-world medical data. In the present study, the ANN model built based on 10 indicators such as age,

history of hypertension, history of malignant tumor, baseline platelet value, TP, ALB, AST, DBIL, Urea and Ccr could effectively predict the risk of linezolid-induced platelet reduction, with an accuracy of 96.32%, which was significantly higher than that of Logistic regression model. ANN model shows good performance in predicting adverse drug reactions, which can help clinicians and clinical pharmacists to predict adverse drug reactions more accurately, choose more appropriate drug treatment plans, and guide patients to individual drug use.

Data availability statement

The raw data supporting the conclusion of this article will be made available by the authors, without undue reservation.

Ethics statement

The studies involving humans were approved by Ethics Committee of Xijing Hospital. The studies were conducted in accordance with the local legislation and institutional requirements. Written informed consent for participation was not required from the participants or the participants' legal guardians/next of kin in accordance with the national legislation and institutional requirements.

Author contributions

XZ: Writing–original draft, Writing–review and editing. QP: Writing–original draft, Writing–review and editing. DH: Writing–original draft, Writing–review and editing. WL: Writing–original draft, Writing–review and editing. QJ: Writing–original draft, Writing–review and editing. QD: Writing–original draft, Writing–review and editing. LH: Writing–original draft, Writing–review and editing. MP: Writing–original draft, Writing–review and editing. YD: Writing–original draft, Writing–review and editing. JW: Writing–original draft, Writing–review and editing.

Funding

The author(s) declare financial support was received for the research, authorship, and/or publication of this article. This research was financially supported by the National Natural Science Foundation of China (Nos. 72074218).

Conflict of interest

The authors declare that the research was conducted in the absence of any commercial or financial relationships that could be construed as a potential conflict of interest.

Publisher's note

Supplementary material

The Supplementary Material for this article can be found online at: https://www.frontiersin.org/articles/10.3389/fphar.2024.1292828/full#supplementary-material

References

An, R. F., and Wang, L. L. (2013). Linezolid-induced thrombocytopenia. *Chin. J. New Drugs* 22 (12), 1469–1472.

Bernstein, W. B., Trotta, R. F., Rector, J. T., Tjaden, J. A., and Barile, A. J. (2003). Mechanisms for linezolid-induced anemia and thrombocytopenia. *Ann. Pharmacother.* 37 (4), 517–520. doi:10.1345/aph.1C361

Cattaneo, D., Marriott, D. J., and Gervasoni, C. (2023). Hematological toxicities associated with linezolid therapy in adults: key findings and clinical considerations. *Expert Rev. Clin. Pharmacol.* 16 (3), 219–230. doi:10.1080/17512433.2023.2181160

Cazavet, J., Bounes, F. V., Ruiz, S., Seguin, T., Crognier, L., Rouget, A., et al. (2020). Risk factor analysis for linezolid-associated thrombocytopenia in critically ill patients. *Eur. J. Clin. Microbiol. Infect. Dis.* 39 (3), 527–538. doi:10.1007/s10096-019-03754-1

Chen, C., Guo, D. H., Cao, X., Cai, Y., Xu, Y., Zhu, M., et al. (2012). Risk factors for thrombocytopenia in adult Chinese patients receiving linezolid therapy. *Curr. Ther. Res. Clin. Exp.* 73 (6), 195–206. doi:10.1016/j.curtheres.2012.07.002

Choi, G. W., Lee, J. Y., Chang, M. J., Kim, Y. K., Cho, Y., Yu, Y. M., et al. (2019). Risk factors for linezolid-induced thrombocytopenia in patients without haemato-oncologic diseases. *Basic Clin. Pharmacol. Toxicol.* 124 (2), 228–234. doi:10.1111/bcpt.13123

Cockcroft, D. W., and Gault, M. H. (1976). Prediction of creatinine clearance from serum creatinine. *Nephron* 16 (1), 31–41. doi:10.1159/000180580

Coleman, J. J., and Pontefract, S. K. (2016). Adverse drug reactions. *Clin. Med. (Lond)* 16 (5), 481–485. doi:10.7861/clinmedicine.16-5-481

Cossu, A. P., Musu, M., Mura, P., De Giudici, L. M., and Finco, G. (2014). Linezolid-induced thrombocytopenia in impaired renal function: is it time for a dose adjustment? A case report and review of literature. *Eur. J. Clin. Pharmacol.* 70 (1), 23–28. doi:10.1007/s00228-013-1585-6

Crass, R. L., Cojutti, P. G., Pai, M. P., and Pea, F. (2019). Reappraisal of linezolid dosing in renal impairment to improve safety. *Antimicrob. Agents Chemother.* 63 (8), e00605-19. doi:10.1128/AAC.00605-19

Dryden, M. S. (2011). Linezolid pharmacokinetics and pharmacodynamics in clinical treatment. *J. Antimicrob. Chemother.* 66 (4), iv7–iv15. doi:10.1093/jac/dkr072

Edwards, I. R., and Aronson, J. K. (2000). Adverse drug reactions: definitions, diagnosis, and management. *Lancet* 356 (9237), 1255–1259. doi:10.1016/S0140-6736(00)02799-9

Hanai, Y., Matsuo, K., Ogawa, M., Higashi, A., Kimura, I., Hirayama, S., et al. (2016a). A retrospective study of the risk factors for linezolid-induced thrombocytopenia and anemia. *J. Infect. Chemother.* 22 (7), 536–542. doi:10.1016/j.jiac.2016.05.003

Hanai, Y., Matsuo, K., Ogawa, M., Higashi, A., Kimura, I., Hirayama, S., et al. (2016b). A retrospective study of the risk factors for linezolid-induced thrombocytopenia and anemia. *J. Infect. Chemother.* 22 (8), 536–542. doi:10.1016/j.jiac.2016.05.003

Hirano, R., Sakamoto, Y., Tachibana, N., and Ohnishi, M. (2014). Retrospective analysis of the risk factors for linezolid-induced thrombocytopenia in adult Japanese patients. *Int. J. Clin. Pharm.* 36 (4), 795–799. doi:10.1007/s11096-014-9961-6

Ikuta, S., Tanimura, K., Yasui, C., Aihara, T., Yoshie, H., Iida, H., et al. (2011). Chronic liver disease increases the risk of linezolid-related thrombocytopenia in methicillin-resistant Staphylococcus aureus-infected patients after digestive surgery. *J. Infect. Chemother.* 17 (3), 388–391. doi:10.1007/s10156-010-0188-8

Ishida, S., Maeda, K., Nishio, C., and Nakai, Y. (2013). Risk factors of linezolid associated thrombocytopenia. *Jpn. J. Chemother.* 61 (1), 1–4.

Jie, F. (2016). A retrospective study on linezolid-induced hematological adverse reactions in Chinese population. *Chest* 149 (4), A95. doi:10.1016/j.chest.2016.02.100

Johnsson, J., Björnsson, O., Andersson, P., Jakobsson, A., Cronberg, T., Lilja, G., et al. (2020). Artificial neural networks improve early outcome prediction and risk classification in out-of-hospital cardiac arrest patients admitted to intensive care. *Crit. Care* 24 (1), 474. doi:10.1186/s13054-020-03103-1

Kaya Kılıç, E., Bulut, C., Sönmezer, M., Ozel, Ö., Ataman Hatipoğlu, Ç., Tuncer Ertem, G., et al. (2019). Risk factors for linezolid-associated thrombocytopenia and negative effect of carbapenem combination. *J. Infect. Dev. Ctries.* 13 (10), 886–891. doi:10.3855/jidc.10859

Kim, H. S., Lee, E., Cho, Y. J., and Rhie, S. J. (2019). Linezolid-induced thrombocytopenia increases mortality risk in intensive care unit patients, a 10 year retrospective study. *J. Clin. Pharm. Ther.* 44 (1), 84–90. doi:10.1111/jcpt.12762

Li, H., Luo, M., Zheng, J., Zeng, R., and Feng, N. (2017). An artificial neural network prediction model of congenital heart disease based on risk factors: a hospital-based case-control study. *Med. Baltim.* 96 (6), e6090. doi:10.1097/MD.0000000000006090

Lin, Y. H., Wu, V. C., Tsai, I. J., Ho, Y. L., Hwang, J. J., Tsau, Y. K., et al. (2006). High frequency of linezolid-associated thrombocytopenia among patients with renal insufficiency. *Int. J. Antimicrob. Agents* 28 (4), 345–351. doi:10.1016/j.ijantimicag.2006.04.017

Maray, I., Rodríguez-Ferreras, A., Álvarez-Asteinza, C., Alaguero-Calero, M., Valledor, P., and Fernández, J. (2022). Linezolid induced thrombocytopenia in critically ill patients: risk factors and development of a machine learning-based prediction model. *J. Infect. Chemother.* 28 (9), 1249–1254. doi:10.1016/j.jiac.2022.05.004

Matsumoto, K. (2012). The development of appropriate dosage of anti-bacterial and anti-fungal agents based on pharmacokinetics and pharmacodynamics. *Yakugaku Zasshi* 132 (10), 1171–1177. doi:10.1248/yakushi.12-00214

Natsumoto, B., Yokota, K., Omata, F., and Furukawa, K. (2014). Risk factors for linezolid-associated thrombocytopenia in adult patients. *Infection* 42 (6), 1007–1012. doi:10.1007/s15010-014-0674-5

Niwa, T., Suzuki, A., Sakakibara, S., Kasahara, S., Yasuda, M., Fukao, A., et al. (2009). Retrospective cohort chart review study of factors associated with the development of thrombocytopenia in adult Japanese patients who received intravenous linezolid therapy. *Clin. Ther.* 31 (10), 2126–2133. doi:10.1016/j.clinthera.2009.10.017

Niwa, T., Watanabe, T., Suzuki, A., Ohmori, T., Tsuchiya, M., Suzuki, T., et al. (2014). Reduction of linezolid-associated thrombocytopenia by the dose adjustment based on the risk factors such as basal platelet count and body weight. *Diagn Microbiol. Infect. Dis.* 79 (1), 93–97. doi:10.1016/j.diagmicrobio.2014.01.012

Nukui, Y., Hatakeyama, S., Okamoto, K., Yamamoto, T., Hisaka, A., Suzuki, H., et al. (2013). High plasma linezolid concentration and impaired renal function affect development of linezolid-induced thrombocytopenia. *J. Antimicrob. Chemother.* 68 (9), 2128–2133. doi:10.1093/jac/dkt133

Pergialiotis, V., Pouliakis, A., Parthenis, C., Damaskou, V., Chrelias, C., Papantoniou, N., et al. (2018). The utility of artificial neural networks and classification and regression trees for the prediction of endometrial cancer in postmenopausal women. *Public Health* 164, 1–6. doi:10.1016/j.puhe.2018.07.012

Qin, Y., Chen, Z., Gao, S., Shen, Y., and Ye, Y. (2022). Development and validation of a risk prediction model for linezolid-induced thrombocytopenia in elderly patients. *Eur. J. Hosp. Pharm.* 2022, 003258. doi:10.1136/ejhpharm-2022-003258

Tajima, M., Kato, Y., Matsumoto, J., Hirosawa, I., Suzuki, M., Takashio, Y., et al. (2016). Linezolid-induced thrombocytopenia is caused by suppression of platelet production via phosphorylation of myosin light chain 2. *Biol. Pharm. Bull.* 39 (11), 1846–1851. doi:10.1248/bpb.b16-00427

Takahashi, Y., Takesue, Y., Nakajima, K., Ichiki, K., Tsuchida, T., Tatsumi, S., et al. (2011). Risk factors associated with the development of thrombocytopenia in patients who received linezolid therapy. *J. Infect. Chemother.* 17 (3), 382–387. doi:10.1007/s10156-010-0182-1

THE WORLD MEDICAL ASSOCIATION, INC (2013). *Declaration of Helsinki. Ethical principles for medical research involving human subjects*. THE WORLD MEDICAL ASSOCIATION, INC.

Yazdani Charati, J., Janbabaei, G., Alipour, N., Mohammadi, S., Ghorbani Gholiabad, S., and Fendereski, A. (2018). Survival prediction of gastric cancer patients by Artificial Neural Network model. *Gastroenterol. Hepatol. Bed Bench* 11 (2), 110–117.

Zhang, D., Xu, Y., Wang, X., Hou, L., Xing, M., Xu, S., et al. (2023). Risk factors for thrombocytopenia in patients receiving linezolid therapy: a systematic review and meta-analysis. *Eur. J. Clin. Pharmacol.* 79 (10), 1303–1314. doi:10.1007/s00228-023-03542-z

Zhang, Z., Liang, Z., Li, H., Chen, L., and She, D. (2014). Comparative evaluation of thrombocytopenia in adult patients receiving linezolid or glycopeptides in a respiratory intensive care unit. *Exp. Ther. Med.* 7 (2), 501–507. doi:10.3892/etm.2013.1437

frontiers | Frontiers in Pharmacology

TYPE Original Research
PUBLISHED 19 June 2024
DOI 10.3389/fphar.2024.1356753

OPEN ACCESS

EDITED BY
Yong-Long Han,
Shanghai Jiao Tong University, China

REVIEWED BY
Masato Ooka,
National Institutes of Health (NIH), United States
Qiyu Wang,
Jiangxi Academy of Sciences, China

*CORRESPONDENCE
Hua Xu,
huarxu@163.com
Jianwei Xie,
xiejw@bmi.ac.cn

RECEIVED 16 December 2023
ACCEPTED 03 June 2024
PUBLISHED 19 June 2024

CITATION
Qu M, Chen J, Xu B, Shi Q, Zhao S, Wang Z, Li Z, Ma B, Xu H, Ye Q and Xie J (2024), Assessing genotoxic effects of chemotherapy agents by a robust *in vitro* assay based on mass spectrometric quantification of γ-H2AX in HepG2 cells.
Front. Pharmacol. 15:1356753.
doi: 10.3389/fphar.2024.1356753

Assessing genotoxic effects of chemotherapy agents by a robust *in vitro* assay based on mass spectrometric quantification of γ-H2AX in HepG2 cells

Minmin Qu[1,2], Jia Chen[2], Bin Xu[2], Qinyun Shi[2], Shujing Zhao[2], Zhaoxia Wang[2], Zhi Li[2], Bo Ma[2], Hua Xu[2]*, Qinong Ye[1] and Jianwei Xie[2]*

[1]Department of Medical Molecular Biology, Beijing Institute of Biotechnology, Beijing, China, [2]Beijing Institute of Pharmacology and Toxicology, Beijing, China

Chemotherapy has already proven widely effective in treating cancer. Chemotherapeutic agents usually include DNA damaging agents and non-DNA damaging agents. Assessing genotoxic effect is significant during chemotherapy drug development, since the ability to attack DNA is the major concern for DNA damaging agents which relates to the therapeutic effect, meanwhile genotoxicity should also be evaluated for chemotherapy agents' safety especially for non-DNA damaging agents. However, currently applicability of *in vitro* genotoxicity assays is hampered by the fact that genotoxicity results have comparatively high false positive rates. γ-H2AX has been shown to be a bifunctional biomarker reflecting both DNA damage response and repair. Previously, we developed an *in vitro* genotoxicity assay based on γ-H2AX quantification using mass spectrometry. Here, we employed the assay to quantitatively assess the genotoxic effects of 34 classic chemotherapy agents in HepG2 cells. Results demonstrated that the evaluation of cellular γ-H2AX could be an effective approach to screen and distinguish types of action of different classes of chemotherapy agents. In addition, two crucial indexes of DNA repair kinetic curve, i.e., *k* (speed of γ-H2AX descending) and t_{50} (time required for γ-H2AX to drop to half of the maximum value) estimated by our developed online tools were employed to further evaluate nine representative chemotherapy agents, which showed a close association with therapeutic index or carcinogenic level. The present study demonstrated that mass spectrometric quantification of γ-H2AX may be an appropriate tool to preliminarily evaluate genotoxic effects of chemotherapy agents.

KEYWORDS

chemotherapy agents, genotoxicity, γ-H2AX, DNA damage repair, HepG2 cells

Introduction

Cancer remains one of the most dreaded diseases over the last few decades (Roy and Saikia, 2016). The incidence of cancer is extremely high, which seriously affects human health (Torre et al., 2016). At the beginning of the 20th century, Paul Ehrlich coined the word "chemotherapy," which means to use the drugs to kill pathogenic microorganisms to treat infectious diseases (DeVita and Chu, 2008). At present, chemotherapy is very effective in cancer treatment and plays an important role in current treatment methods (Knezevic and Clarke, 2020). Broadly, chemotherapy agents presently used have been classified as: alkylating agents, antimetabolites, antitumor antibiotics, antitumor plant products, antitumor hormones and various miscellaneous agents (Masood et al., 2016; Bukowski et al., 2020). Although this classification is the one now in general usage, it is a relatively simple classification mainly based on the source, biological action, chemical reaction and other characteristics of drugs. In fact, a common trait of chemotherapy drugs is that they cause changes at the cellular level by interfering with the complex intermediate metabolism of cells or affecting cell division at the metaphase (Masood et al., 2016).

Alkylating agents, also known as bio-alkylating agents, form compounds with reactive electrophilic groups that can covalently bind to biological macromolecules within cells, thereby changing their structures and possibly destroying their functions (Fu et al., 2012). Among them, nitrogen mustard-derived DNA alkylating agents were the first antitumor drugs to achieve outstanding efficacy and remain key drugs against a variety of cancers to date (Singh et al., 2018). Although alkylating agents pose a significant threat to human health due to various toxic effects, some toxic alkylating agents are still used as chemotherapeutic agents in cancer patients (Sauter and Gillingham, 2020). Consequently, while with cancer-inducing potency, alkylating agents are still used to kill cancer cells given their DNA-damaging characteristics (Fu et al., 2012; Sauter and Gillingham, 2020). Meanwhile, the double-edged sword of their therapeutic and cytotoxic potential has received attention.

It is well known that the structural integrity of DNA is particularly important for cells to maintain normal cellular function and proliferation (Cheung-Ong et al., 2013). During the S phase of the cell cycle, the initiation of replication is inhibited when DNA is damaged, slowing DNA replication and possibly causing DNA double-strand breaks (DSBs), one of the most toxic forms of DNA damages (Waterman et al., 2020). Cell death can occur when DNA damage is too severe to be repaired (Chatterjee and Walker, 2017). So far, chemotherapy for cancer has a history of about 80 years and the idea of developing various types of antitumor drugs comes from using DNA as the target of antitumor drugs (DeVita and Chu, 2008; Sauter and Gillingham, 2020), such as antimetabolites, antitumor antibiotics and antitumor plant products. Just like alkylating agents, these agents have double-edged properties, i.e., they quickly target and hurt dividing cells, but also nonspecifically affect normal cells (DeVita and Chu, 2008).

Overall evaluation of the double-edged characteristics of DNA-damaging agents is essential for balancing the chemo-efficacy and toxicity, especially genotoxicity, unfortunately which is often obscure and still a challenge mainly due to the lack of a robust *in vitro* analysis method (Cheung-Ong et al., 2013; Motoyama et al., 2018). On the other side, there are also some chemotherapy agents, which cure cancer through other mechanisms such as cytotoxicity, hormonal mimicry or epigenetic effects (Masood et al., 2016). Given that information on genotoxicity is indispensable for evaluating the therapeutic effect and side effect of DNA damaging agents, genotoxicity data are required for chemotherapy agents.

Genotoxicity assessment is an important cutting-edge safety tool during the development of pharmaceutics, and genotoxicity assays can draw conclusions about the genotoxicity and potential carcinogenicity of chemotherapeutics (Choudhuri et al., 2021; Luan and Honma, 2022). Positive results in standard genotoxicity assays such as the Ames test, mouse lymphoma assay (MLA), and *in vitro* micronucleus (MN) assay or chromosome aberration (CA) assay are of great significance during drug development (Kirkland et al., 2005). The performance of the three most commonly used assays has been evaluated in terms of their sensitivity, specificity, and positive and negative predictivity using data from 700 rodent carcinogens and non-carcinogens (Kirkland et al., 2005). The three-test battery of mammalian cell-based assays exhibits high sensitivity but a propensity towards misleading positive results (poor specificity). The phosphorylation of histone H2AX on serine (Ser) 139 (designated as γ-H2AX), a robust biomarker of DNA damage, has emerged as a reliable tool to evaluate genotoxic effects for a long time (Kopp et al., 2019; Rahmanian et al., 2021). After the occurrence of DSBs, γ-H2AX is amplified, which reflects global genotoxic damage that could derive from diverse forms of DNA damage such as DNA adducts, DNA crosslinking, or transposition (Rahmanian et al., 2021). γ-H2AX, which is an acknowledged attractive bifunctional biomarker, is thought to be primarily related to DNA damage, but changes in γ-H2AX content also play a role in DNA repair (Qu et al., 2021).

Conventionally, γ-H2AX was extensively measured by immunology-based methods including Western blotting, immunofluorescence staining and flow cytometry (Kopp et al., 2019). Although immunoassays provide good sensitivity, their specificity is limited due to poor batch-to-batch reproducibility as well as some cross-reactivity derived from antibodies, and accurate quantification is still challenging. Previously, we developed an *in vitro* genotoxicity assay based on γ-H2AX quantification using mass spectrometry (MS). This assay has been used to assess the genotoxicity of different chemicals and demonstrates high specificity and sensitivity (Qu et al., 2020). In addition, the assay has the advantage of dynamically monitoring specific processes of DNA damage and repair caused by genotoxic chemicals. Recently, we further validate the feasibility of using this MS-based γ-H2AX *in vitro* assay to assess the potential carcinogenicity of genotoxic compounds based on a large set of compounds from the European Centre for the Validation of Alternative Methods (ECVAM) list (Qu et al., 2021), and quantitatively determined the DNA damage repair characteristics of aristolochic acids (Qu et al., 2022).

In this article, we firstly quantified γ-H2AX induced by 34 classical chemotherapy agents including DNA damaging agents and non-DNA damaging agents in HepG2 cells, based on MS. The preliminary results obtained suggest that the detection of γ-H2AX against different classes of chemotherapy agents could be an effective approach to obtain information related to the DNA-damaging efficacy of chemotherapy agents. We then proved that

TABLE 1 *In vitro* genotoxicity of 34 chemotherapy agents tested by γ-H2AX MS assay.

Name of agents	CAS number	Required metabolic activation	*In vitro* assays	γ-H2AX $_{MEC/MS}$
Alkylating agent				
Nimustine	55661-38-6	–	+	↑(0.01)
Carmustine	154-93-8	–	+	↑(0.01)
Cyclophosphamide	6055-19-2	+	+	↑(1000)
Ifosfamide	3778-73-2	+	+	↑(1000)
Antimetabolites				
5-fluorouracil	51-21-8	–	+	↑(10)
Deoxyfluridine	436349	–	+	↑(10)
Tegafur	17902-23-7	–	+	↑(10)
Carmofur	6122-45-5	–	+	↑(1)
6-mercaptopurine	50-44-2	+	+	↑(10)
Thioguanine	154-42-7	+	+	↑(10)
Hydroxyurea	127-07-1	–	+	↑(1000)
Antitumor antibiotics				
Daunorubicin	20830-81-3	–	+	↑(0.01)
Doxorubicin	25316-40-9	–	+	↑(0.01)
Pirarubicin	72496-41-4	–	+	↑(0.01)
Epirubicin hydrochloride	56390-09-1	–	+	—
Antitumor plant products				
Irinotecan	97,682-44-5	–	+	↑(0.1)
Topotecan	119413-54-6	–	+	↑(0.1)
Exatecan	171335-80-1	–	+	↑(0.01)
Etoposide	33419-42-0	–	+	↑(1)
Teniposide	29767-20-2	–	+	↑(1)
Vinorelbine	71486-22-1	–	E	—
Paclitaxel	33069-62-4	–	E	—
Vincristine	57-22-7	–	E	—
Antitumor hormones				
Tamoxifen	10540-29-1	+	–	—
Aminoglutethimide	125-84-8	–	–	—
Anastrozole	120511-73-1	–	–	—
Letrozole	112809-51-5	–	–	—
Formestane	566-48-3	–	–	—
Exemestane	107868-30-4	–	–	—
Miscellaneous agents				
Cisplatin	15663-27-1	–	+	↑(10)
Carboplatin	41575-94-4	–	+	↑(100)
Oxaliplatin	61825-94-3	–	+	↑(100)

(Continued on following page)

TABLE 1 (*Continued*) *In vitro* genotoxicity of 34 chemotherapy agents tested by γ-H2AX MS assay.

Name of agents	CAS number	Required metabolic activation	*In vitro* assays	γ-H2AX $_{MEC/MS}$
Dacarbazine	891986	+	+	↑(100)
Mitoxantrone	65271-80-9	–	+	↑(1)

Notes: *In vitro* assays refer to the results of genotoxicity of compounds through the combination of *in vitro* mouse lymphoma, chromosomal aberration, and micronucleus tests. + tested as "positive"; – tested as "negative"; E tested as "equivocal". Micromolar concentrations measured in the last column refer to the MEC measured by our MS method. The arrows illustrate an obvious increase in the value of γ-H2AX.

DSBs repair kinetics of nine tested chemotherapy agents according to γ-H2AX time-effect curves have a close association with therapeutic index and carcinogenic level, which may guide the evaluation and clinical application of chemotherapy agents.

Materials and methods

Materials and reagents

Thirty-four chemotherapy agents were obtained from Yuanye Bio-Technology Co., Ltd. (Shanghai, China) and their purity exceeded 98%. The identities of the 34 chemotherapy agents are shown in Table 1. All the agents were chosen from major categories (classes) based on their chemical structures and the way they act on cancer cells, representing a broad range of chemotherapy activities. Based on the concentration used in the *in vitro* genotoxicity tests reported in the literature, the maximum concentration of agents used in this study is 1 mM (Kirkland et al., 2016).

Peptide P1, ATQASQEY and peptide P2, ATQA*p*SQEY, representing the sequences of tryptic products of H2AX and γ-H2AX at its 135–142 site, and isotope-labelled peptides with $^{13}C3$ and ^{15}N-labelled amino terminal alanine, i.e., [$^{13}C3$, ^{15}N] ATQASQEY and [$^{13}C3$, ^{15}N]ATQA*p*SQEY were synthesized by Sangon Biotech Co., Ltd. (Shanghai, China). Sequencing-grade trypsin was obtained from Promega Biotech Co., Ltd. (Beijing, China). HPLC-grade acetonitrile was provided by J&K Scientific Ltd. (Beijing, China). Formic acid (FA) was purchased from Sigma-Aldrich Inc. (St. Louis, United States). Other compounds or reagents were obtained from Sinopharm Compound Reagents Co., Ltd. (Beijing, China). All reagents were of analytical reagent grade or higher.

Dulbecco's modified Eagle's medium (DMEM) and fetal bovine serum (FBS) were purchased from Life Technologies (Paisley, United Kingdom). A kit for performing a cell proliferation assay was obtained from Promega Biotech Co., Ltd. (Beijing, China). C18 disks were purchased from Empore, 3 M (Shanghai, China).

Ultrapure water (18.2 MΩ cm) was prepared using a Milli-Q A10 purification system from Millipore Co. (Watford, United Kingdom). Before use, all solutions were sterilized by a high-pressure sterilizer (Zhongya Co., Shanghai, China). Unless noted, stock solutions of all compounds were prepared in 100% dimethyl sulfoxide (DMSO, Sigma, St. Louis, United States).

Cell culture and treatment

Human hepatoblastoma cells (HepG2) were cultivated in DMEM medium under standard conditions (37°C in a 5% CO_2 atmosphere). The culturing medium was added with 10% FBS, 100 U/mL penicillin and 100 μg/mL streptomycin.

In accordance to our previous study, cells were exposed to the chemotherapeutic agent by adding a proper volume of chemotherapeutic agent stock solution to the fresh medium without serum. Controls were treated with DMSO (0.1%) in medium. Independent biological experiments with three technical replicates were conducted.

The cells were then treated with different chemotherapy agents in serum-free medium. For a dose-effect relationship experiment, cells were exposed to each agent at either of three concentrations with a 10-fold increase for 24 h. For the time-effect relationship experiment of nine tested chemotherapy agents, cells were exposed to selected chemotherapy agents at 0.5, 1, 2, 4, 8, 12, and 24 h, with the concentration of 100 μM. Independent biological experiments with three technical replicates were performed.

Assessment of cytotoxicity

The assessment of cytotoxicity was assessed using the 3-(4,5-dimethylthiazol-2-yl)-5-(3-carboxymethoxyphenyl)-2-(4-sulfophenyl)-2H-tetrazolium (MTS) assay according to the manufacturer's instructions (Promega), with minor modifications, after 24 h of exposure to compounds. Briefly, after exposure, a freshly prepared mixture of MTS solution was added to each well of a multiwell plate and incubated for an additional 3 h. Afterwards, cell viability was measured using a spectrofluorimeter (Synergy MX, BioTek, Winooski, United States) at 490 nm. Three independent experiments were performed for each time in six replicates, with each replicate represented by one well. The relative cytotoxicity was obtained by the ratio of the surviving cells in the treatment groups to that of control (solvent) group.

γ-H2AX MS quantitation

The quantification of γ-H2AX was carried out according to the previous report (Qu et al., 2021). In short, the cell clumps were collected after a certain period of cell culture and histones were obtained by acid extraction. After nuclear isolation, histone extraction, trypsin digestion in the solution, and desalting, the peptide sample from the carboxy terminus of H2AX was analyzed. LC–MS/MS analysis was conducted using a QTRAP 5500 (AB Sciex, Framingham, United States) with an ACQUITY UPLC system (Waters Co., Manchester, United Kingdom). Chromatographic separation was carried out with an ACQUITY UPLC BEH C18 column (100 mm × 2.1 mm, 1.7 μm). The column temperature was maintained at 40°C. A 10 μL sample aliquot was injected for analysis. Mobile phases A and B were 0.1% FA in

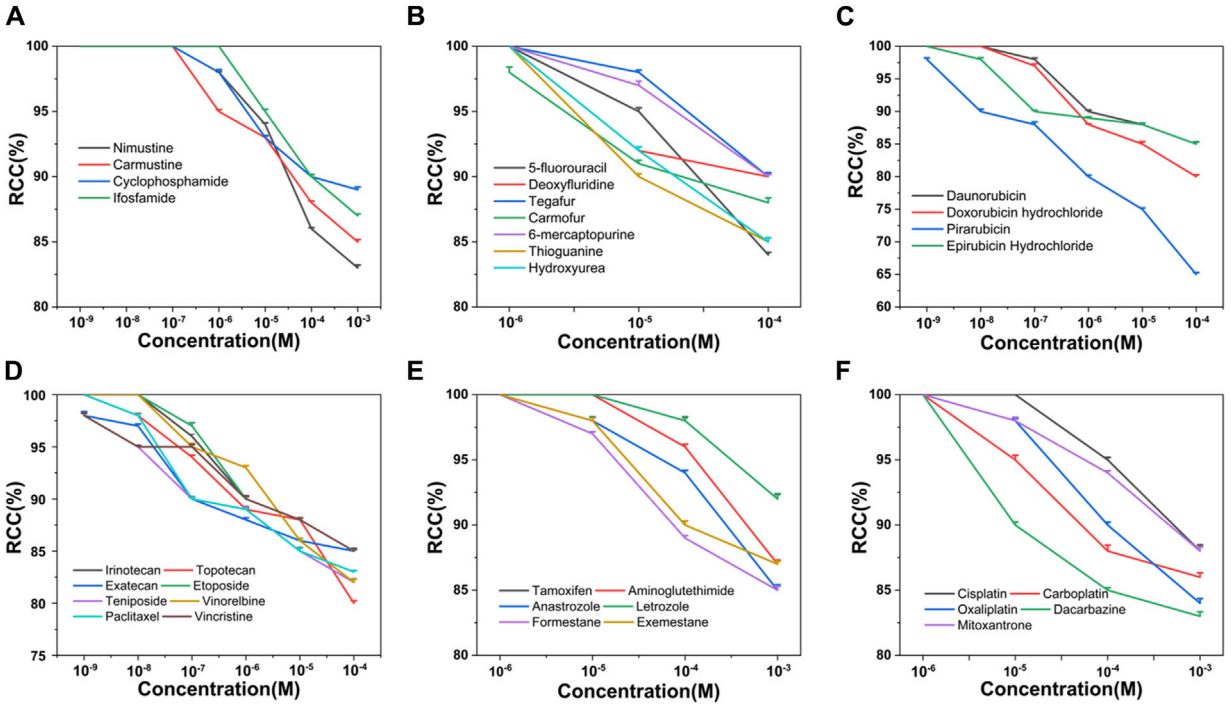

FIGURE 1
Cytotoxicity of 34 chemotherapy agents in HepG2 cells, including alkylating agents **(A)**, antimetabolites **(B)**, antitumor antibiotics **(C)**, antitumor plant products **(D)**, antitumor hormones **(E)** and various miscellaneous agents **(F)**. The value of RCC indicates the cytotoxicity. Each value was expressed in the form of mean ± SD ($n \geq 3$).

distilled H_2O and acetonitrile, respectively. The elution gradient was initiated with 1% B and linearly increased to 30% B in 8 min at a flow rate of 0.25 mL/min. The eluent composition was maintained for 2 min, after which the system returned to 1% B and was re-equilibrated for 2 min. The eluates in the first 1 min were switched to waste to prevent contaminating the ion source. The electrospray ionization source was operated in positive mode using nitrogen as the nebulizing gas. All experiments were performed independently in at least triplicate.

Statistical analysis

All data were expressed in the form of means ± standard deviation (SD). The IBM-SPSS Statistics Ver.21.0 software (IBM Corp., Armonk, NY, United States) was used for statistical analysis. Differences among treatments were evaluated by using one-way analysis of variance (ANOVA). Independent biological experiments with three technical replicates were performed. $^{*}p \leq 0.05$ was considered statistically significant, and $^{**}p \leq 0.01$ was considered highly significant.

Results and disscussion

Cytotoxicity evaluation of 34 chemotherapy agents in HepG2 cell line

Based on the criteria of positive genotoxicity (Qu et al., 2021), a compound that resulted in a 1.5-fold increase in the value of γ-H2AX and produced a level of cytotoxicity below 50% relative to the control group, is considered to be genotoxic. To this end, we firstly examined the cytotoxicity of 34 chemotherapy agents, all of which were already well classified in terms of diverse characteristics. These tested chemotherapy agents were serially diluted for exposure to check the effects on cell viability. Relative cell count (RCC; % control) results were obtained by the MTS assay. As shown in Figure 1, the values of RCC for all chemotherapy agents were higher than 50% in HepG2 cells within our chosen exposure concentration range.

γ-H2AX tested results for alkylating agents

Nitrogen mustard ushered in a new era in cancer chemotherapy in 1942 (Chabner and Roberts, 2005). At the molecular level, nitrogen mustard produces an intermediate called an "aziridiniumion" that is highly reactive against DNA in both tumor and normal cells, leading to serious side effects and therapeutic implications (Singh et al., 2018). This class of valuable alkylating agents can bind covalently to DNA in an essentially irreversible manner, resulting in major changes in DNA structure and function (Misiak et al., 2016). To improve efficacy and enhance specificity for tumor cells, various nitrogen mustard derivatives have been developed (DeVita and Chu, 2008), including DNA alkylators nimustine, carmustine, cyclophosphamide, and ifosfamide, all of which are widely used in clinical treatment. We tested the four alkylating agents in HepG2 cells for γ-H2AX biomarker. Table 1 and Figure 2A showed the results.

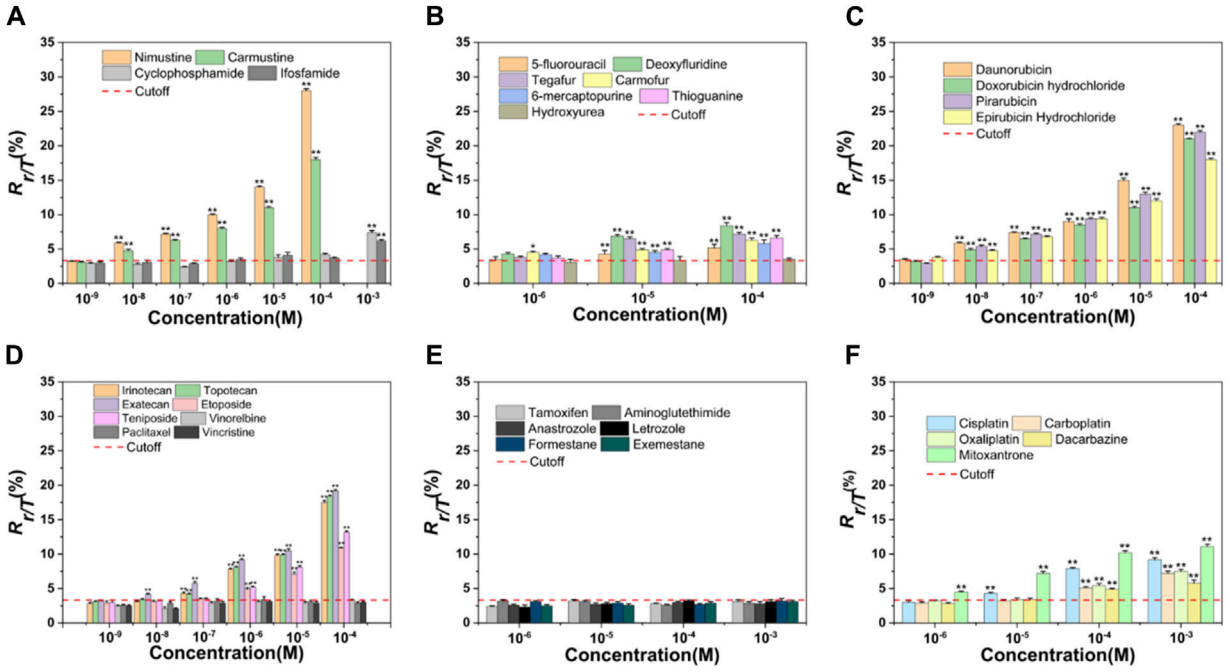

FIGURE 2
Dose-effect relationships of γ-H2AX after HepG2 cells were exposed to 34 chemotherapy agents for 24 h, including alkylating agents **(A)**, antimetabolites **(B)**, antitumor antibiotics **(C)**, antitumor plant products **(D)**, antitumor hormones **(E)** and various miscellaneous agents **(F)**. The horizontal axis represents different concentrations and the vertical axis represents the proportion of the number of phosphorylated peptides to the total number of peptides ($R_{\gamma\text{-H2AX/Total H2AX}}$, briefly, $R_{\gamma/T}$) in a cell. The differences between chemotherapy agents treated groups and negative control are obvious ($n \geq 3$, mean ± SD; $^{*}p \leq 0.05$, $^{**}p \leq 0.01$). Red dashed line represents the solvent control value of HepG2 cells.

As chloroethylnitrosoureas derivatives, nimustine and carmustine are typical chloroethylating agents which can be used in tumor chemotherapy, especially brain tumors due to the capacity to get over the blood-brain barrier (Nikolova et al., 2012; Nikolova et al., 2017). These two reagents can combine with guanine N1 on one DNA strand and cytosine N3 on the other strand to form inter-strand crosslinks and prevent DNA replication (Drabløs et al., 2004; Yamada et al., 2019). However, carmustine was reported to be six to eight times less cytotoxic than nimustine in cell lines (Büch and Zeller, 2002). In our result, nimustine and carmustine induced significant phosphorylation of H2AX at Ser 139 with a minimum effective concentration (MEC) of 0.01 μM. Nimustine-induced γ-H2AX amount was always greater than that induced by carmustine at the same molar concentration, which was consistent with the report from Nikolova et al. (2017), where authors indicated that nimustine had a higher potency for inducing deoxyribonucleic acid inter-strand crosslinks than carmustine. Our result indicated that the genotoxicity of nimustine and carmustine can be preliminarily obtained by comparing the γ-H2AX values, even if their MEC values were same, which may be an effective approach to obtain related information on efficacy of alkylating agents.

During the development of nitrogen mustard derivatives, developing alkylating agents which exhibit genotoxic ability after enzymatic degradation is a route to pursue selectivity (World Health Organization, 1962). Both cyclophosphamide and ifosfamide are examples of this, and the two agents are highly stable and need to be activated by liver microsomal enzymes metabolism. After the two agents are distributed throughout the body, they spontaneously degrade at the tumor site to form their own cytotoxic substances, namely, phosphoramide mustard and ifophosphamide mustard (Mulder et al., 2015). These cytotoxic species will alkylate DNA, forming inter-strand crosslinks which ultimately inhibit DNA synthesis (Fresneau et al., 2017). As observed in Figure 2A, the highest concentration of cyclophosphamide and ifosfamide tested (1 mM) was genotoxic. The results for cyclophosphamide and ifosfamide, which share a genotoxic mode of action related to a specific biotransformation process, indicated a good sensitivity for γ-H2AX MS analysis (Wu et al., 2017). Although ifosfamide and cyclophosphamide are closely related (Fresneau et al., 2017), structural changes in ifosfamide result in a reduction in liver activation, which in turn reduces efficacy. In our result, the value of γ-H2AX induced by ifosfamide was lower than that of cyclophosphamide under the same exposure concentration of 1 mM.

γ-H2AX tested results for antimetabolites

Antimetabolites are a class of antineoplastic agents that disrupt DNA replication. Most antimetabolites belong to the category of chain-terminating nucleoside analogs which interfere with subsequent steps of DNA biosynthesis through competitive inhibition (Masood et al., 2016). Among them, pyrimidine analogs and purine analogs are widely used. During the S phase of the cell cycle, purine and pyrimidine analogs are able to incorporate into DNA and prevent nucleotide addition, leading to DNA replication failure (Lansiaux, 2011).

Seven agents with antimetabolite mechanism of action were tested: 5-fluorouracil (5-FU), deoxyfluridine, tegafur, carmofur, 6-mercaptopurine (6-MP), thioguanine (TG), and hydroxyurea (Table 1). Since the action mechanism of these agents were mainly metabolite-related (Masood et al., 2016), antimetabolites would not cause large change in the value of γ-H2AX within the selected concentration range, as shown in Figure 2B. Of these, carmofur with MEC of 1 μM was the only antimetabolite which induced an increase of γ-H2AX in a dose-dependent manner at the three tested concentrations, with no apparent cytotoxicity. 5-FU, deoxyfluridine, tegafur, 6-MP, and TG had a MEC of 10 μM. As previously mentioned, hydroxyurea suppresses pyrimidine biosynthesis by inhibiting the enzyme ribonucleotide reductase thus exhibiting a MEC of 1 mM in γ-H2AX MS assay (Qu et al., 2020).

5-FU is a naturally occurring analogue of pyrimidine uracil and is metabolized in the same way as uracil. Due to the fact that most antimetabolites have poor selectivity and are toxic to normal tissues that proliferate rapidly, such as bone marrow, gastrointestinal mucosa and skin (Ciaffaglione et al., 2021), many derivatives of 5-FU, including deoxyfluridine, tegafur and carmofur, have been devised to improve the topical delivery and reduce the side effects. As shown in Figure 2B, at equimolar concentration, the values of γ-H2AX induced by 5-FU were always the lowest, in support of that, the therapeutic indexes of three derivative agents are higher than that of 5-FU (Hashimoto et al., 2020).

6-MP and TG belong to purine nucleoside analogues. Studies have shown that both agents undergo broad metabolism prior to incorporation into DNA to induce cytotoxicity (Elgemeie, 2003; Coulthard and Hogarth, 2005). As observed in Figures 1B, 2B, the cytotoxicity and genotoxicity of TG were stronger than that of 6-MP in HepG2 cell line at equimolar concentration. Since TG can be directly converted to thioguanine nucleotides, avoiding a few enzymatic checkpoints in 6-MP metabolism, TG exhibits higher toxicity (Lennard et al., 1993). Additionally, Adamson et al. has demonstrated that TG has higher cytotoxicity than 6-MP in diverse cell lines (Adamson et al., 1994).

γ-H2AX tested results for antitumor antibiotics

Clinically, anthracyclines are a class of natural antibiotics among the most effective antineoplastic drugs, acting against nearly all cancer types (Martins-Teixeira and Carvalho, 2020). Anthracyclines share planar aromatic rings that can enter and form stacking relations between near DNAs to stabilize, harden, prolong and relax the DNA double helix (Bauer and Vinograd, 1970; Canals et al., 2005; Martins-Teixeira and Carvalho, 2020). Anthracyclines exert the anticancer action via intercalation into the double helix of DNA, binding to topoisomerase II, and generation of reactive oxygen species (Meredith and Dass, 2016; Martins-Teixeira and Carvalho, 2020). Four anthracyclines (daunorubicin, doxorubicin, pirarubicin, epirubicin hydrochloride) with an antitumor antibiotic effect were tested. These selected four antitumor antibiotics had the same MEC (0.01 μM) in the cell line used. For all these four agents, we found that they induced γ-H2AX/H2AX$_{total}$ ($R_{\gamma/T}$) value was as high as 25% at the higher concentration, which might explain that anthracyclines are the most potent anti-cancer chemotherapeutics (Weiss, 1992; Martins-Teixeira and Carvalho, 2020).

Both doxorubicin and pirarubicin belong to second-generation antibiotics. Because pirarubicin was more efficient for entering cells (Miller and Salewski, 1994), the γ-H2AX level caused by pirarubicin showed a slight tendency to be higher than that of doxorubicin. According to the literature, second-generation analogues like doxorubicin and pirarubicin exhibit improvements in their therapeutic indexes compared with the first-generation antibiotic daunorubicin (Minotti et al., 2004). Here, the γ-H2AX level they induced was not as high as daunorubicin. This may be due to the broad antitumor spectrum of second-generation antibiotics.

Epirubicin hydrochloride, an isomer of doxorubicin (Minotti et al., 2004), is as effective as doxorubicin. As observed in Figure 2C, these two agents induced almost the same level of γ-H2AX at equimolar concentration.

γ-H2AX tested results for antitumor plant products

The effect of a set of eight antitumor plant products (Table 1) on γ-H2AX in the HepG2 cell line were evaluated. Table 1 and Figure 2D showed the results. Irinotecan and topotecan had MECs of 0.1 μM, exatecan had a MEC of 0.01 μM, etoposide and teniposide had a MEC of 1 μM. Our previous work showed that aneugens induced γ-H2AX less than 1.5-fold compared to controls in HepG2 cells, identified as a negative test result (Qu et al., 2020). Consistent with our previous report, here three agents with an aneugen genotoxicity, vinorelbine, paclitaxel and vincristine, were detected as with no variations of γ-H2AX in HepG2 cells.

It is well known that camptothecin plays a crucial role in clinical cancer therapy, and many pharmaceutical researchers are working on developing its derivatives (Soepenberg et al., 2003). As derivatives of camptothecin, topotecan and exatecan have been approved by the FDA and used in clinical practice (Zhu et al., 2018). With no doubt, the anticancer activities of camptothecin derivatives emerge from their potent and specific inhibition of the ubiquitous DNA-manipulating enzymes, DNA topoisomerases. DNA topoisomerases are inherent enzymes existing in all nucleated cells with two major topoisomerase forms: the type I enzyme which catalyses the change of topological isomerism of DNA replication by forming a short single strand cleavage and type II enzyme which changes the topological state of DNA by causing the break of the transient double stranded enzyme bridge (Wang, 1996). These enzymes are related to the adjustment of DNA topology and are required for the maintenance of the completeness of DNA structure during DNA metabolism (Champoux, 2001).

In our result, the MEC for exatecan causing H2AX significant phosphorylation was lower than that for irinotecan and topotecan, thus, the genotoxicity of exatecan seems to be stronger. It is reported that exatecan is a totally synthetic analogue that does not require enzymatic activation like some of the other prodrugs such as irinotecan (Soepenberg et al., 2003). Here, exatecan was also evidenced to be a more potent inhibitor of topoisomerase I than irinotecan and topotecan.

As semisynthetic derivatives of podophyllotoxin, etoposide and teniposide are growingly used in cancer treatment. Etoposide is one

of the topoisomerase II poisons, which stabilizes topoisomerase II on DNA, leading to a toxic DNA-topoisomerase II covalent complex. Teniposide mainly block DNA synthesis by inhibiting the action of DNA topoisomerase II (Holthuis, 1988). Our results indicated that γ-H2AX induced by teniposide always showed a slightly higher trend than that of etoposide at different concentration administration groups, which is in line with the report of Clark et al., that teniposide was more effective in generating the DNA damage and cytotoxicity (Clark and Slevin, 1987). In addition, *in vitro* studies have demonstrated that the topoisomerase I inhibitors were more mutagenic relative to topoisomerase II inhibitors (Soepenberg et al., 2003). As observed in Figure 2D, the value of γ-H2AX caused by topoisomerase I inhibitors was always higher than that of topoisomerase II-inhibitors at equimolar concentration.

Contrary to the above five topoisomerase inhibitors, three microtubule inhibitors did not increase the phosphorylation value of H2AX in cells. During the metaphase of the cell cycle, microtubule inhibitors function by disturbing cell division, which does not affect DNA synthesis (Yamada and Gorbsky, 2006). These changes may result in aneuploidy in daughter cells and cell cycle dysregulation etc., instead of real DNA damage (Aardema et al., 1998). Numerous studies have described the effects of microtubule inhibitors on H2AX phosphorylation. In our previous study, microtubule inhibitors did not cause H2AX phosphorylation in HepG2 and HeLa cells (Qu et al., 2020). Nonetheless, based on an in-cell Western technique, researchers (Khoury et al., 2013) found that microtubule inhibitors led to changes of γ-H2AX level in HepG2 cells, which may be a false positive result because the concentrations used in their experiment were higher than in ours. Although the result needs to be verified by performing the MS of γ-H2AX in a larger number of microtubule inhibitors, our results support that the γ-H2AX quantitation by MS analysis may be more specific in genotoxicity assessment.

γ-H2AX tested results for antitumor hormones

Oral hormonal agents have been used to treat cancer for many years (Masood et al., 2016). In our work, we chose six antitumor hormones (tamoxifen, aminoglutethimide, anastrozole, letrozole, formestane and exemestane) and monitored the γ-H2AX levels in HepG2 cells. As shown in Figure 2E, none of the selected antitumor hormones exhibited genotoxicity in the HepG2 cell line, even when the tested concentration of agents was 1 mM.

Many breast cancers require estrogen to maintain growth, and they regress without these hormones (Gompel, 2019). As a widely used endocrine agent, tamoxifen has been the first-line treatment for postmenopausal metastatic breast cancer. Tamoxifen is a selective estrogen receptor (ER) regulator which competes with estradiol for the ER and forms a stable complex with it, thereby inhibiting the growth and development of cancer cells (Jordan and Dowse, 1976). Recently, agents acting differently from tamoxifen by inhibiting aromatase and converting androgens into estrogens have been developed (Gradishar, 2004). These reagents can be essentially divided into two classes: type I steroids, which compete at the substrate-binding site, and type II nonsteroids, which interfere with the aromatase (Kharb et al., 2020).

Formestane and exemestane belong to type I steroids, whereas aminoglutethimide, anastrozole and letrozole are type II nonsteroids. Obviously, these agents act primarily on non-DNA targets and they do not damage DNA (Masood et al., 2016). γ-H2AX is a typical marker closely associated with DNA damage, which promotes related repair proteins to the damage sites in the course of DNA damage repair (Rahmanian et al., 2021). Hence, it's not difficult to understand why these antitumor hormones do not induce a significant γ-H2AX induction.

γ-H2AX tested results for miscellaneous agents

Agents that do not belong to the above mentioned types or whose mechanisms of action without full clarification are classified as miscellaneous agents. In our work, we selected five miscellaneous agents. As shown in Figure 2F, the MECs of cisplatin and mitoxantrone were 10 and 1 μM, and those of carboplatin, oxaliplatin and dacarbazine were 100 μM.

The development of platinum-based agents is of great significance to the research of antitumor drugs. Studies have shown that cisplatin could induce DNA damage, hinder the generation of DNA, mRNA and protein, prevent DNA replication, and ultimately result in the occurrence of apoptosis or necrosis (Rosenberg et al., 1965; Ghosh, 2019). Unfortunately, cisplatin has not shown its greatest potential in clinical use due to side effects and resistance. For this reason, drugs including carboplatin and oxaliplatin have been developed that act in a similar way of cisplatin but with different pharmacological properties and synergistic effect on different tumors (Monneret, 2011). Compared to cisplatin, carboplatin requires a higher dosage for efficacy and oxaliplatin creates fewer crosslinks per base (Dilruba and Kalayda, 2016).

The main mode of action of platinum-based analogues is to induce DNA damage. On the other hand, because of the genotoxicity, such drugs will in turn lead to tumor formation (Monneret, 2011; Dilruba and Kalayda, 2016). We observed that the value of γ-H2AX induced by cisplatin was the highest among the selected three platinum agents. This may be attributed to the fact that the side effects of platinum chemotherapy drugs are reduced with the development of platinum drugs from generation to generation, namely, carboplatin and oxaliplatin have decreased side effects (Dilruba and Kalayda, 2016).

Dacarbazine is an antitumor drug independent of cell cycle, which could exert an alkylation effect or interfere with purine biosynthesis (Al-Badr and Alodhaib, 2016). The therapeutic efficacy of dacarbazine is low due to the consequence of rapid removal of DNA lesions by repair systems (Koprowska and Czyż, 2011). Since it needs to be metabolized and activated in the liver to become an active metabolite, dacarbazine would not induce significant phosphorylation of H2AX until the concentration reaches 100 μM.

Mitoxantrone is a synthetic anthraquinone and a recognized antitumor drug. It embeds into DNA to inhibit topoisomerase II enzyme, thus preventing the connection of DNA strands and delaying the progress of cell cycle. Although mitoxantrone has been identified as a DNA topoisomerase II poison in mammalian cells, studies have determined that the drug interacts with a wider range of biological macromolecules in covalent and non-covalent

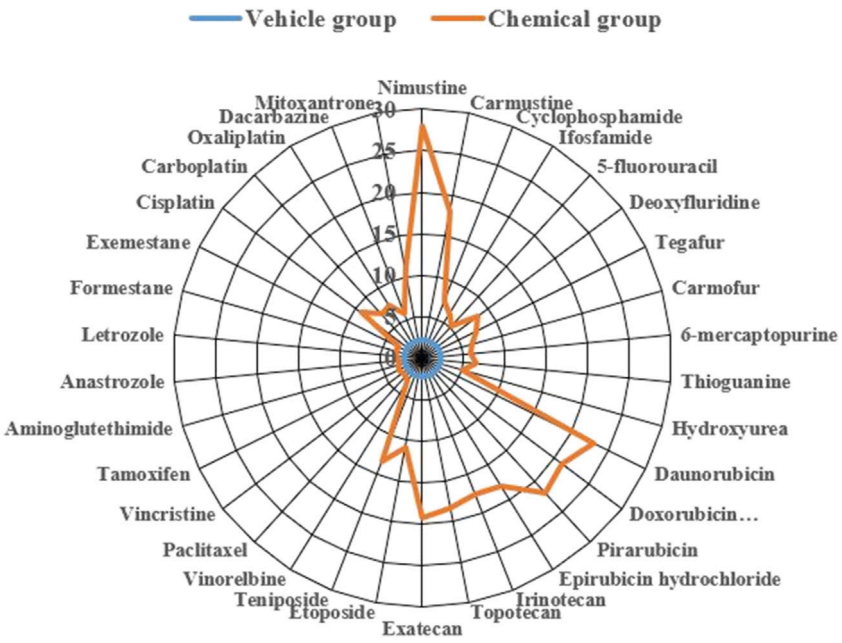

FIGURE 3
Radar plot of data for 34 chemotherapy agents with different mode of actions on γ-H2AX in HepG2 cells. Orange line represents the chemical group and blue line represents the solvent control group.

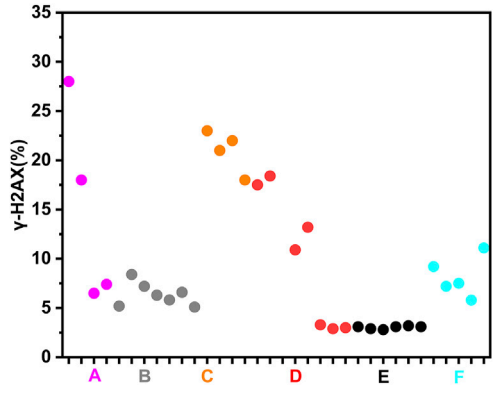

FIGURE 4
Scatterplot of data for chemotherapy agents on γ-H2AX in HepG2 cells. "A" refers to alkylating agents; "B" refers to antimetabolites; "C" refers to antitumor antibiotics; "D" refers to antitumor plant products; "E" refers to antitumor hormones; "F" refers to miscellaneous agents.

ways (Scott and Figgitt, 2004). The MEC of mitoxantrone was 1 μM, which may be due to its extensive toxicity other than just as a topoisomerase II poison.

Dynamic profiles of γ-H2AX in HepG2 cell line treated with nine representative chemotherapy agents

To more clearly demonstrate effects of chemotherapy agents on γ-H2AX, the values of γ-H2AX in HepG2 cell line caused by 34 chemotherapy agents were shown in Supplementary Table S1. The data were further plotted as radar chart and scatterplot. As observed in Figures 3, 4, values of $R_{\gamma/T}$ induced by different classes of chemotherapy agents were varying. Agents with diverse classification have obviously different values of γ-H2AX. Additionally, agents function mainly on non-DNA targets, like antitumor hormones and aneugens in antitumor plant products, could be explicitly distinguished from DNA-targeted agents by the radar chart and scatterplot.

In addition, we aimed to further obtain the specific profiles related to DNA damage repair induced by chemotherapy agents. To this end, we selected nine representative chemotherapy agents which induce relatively large γ-H2AX value in their respective categories, and thus investigated time effect relationship of these nine agents within 24 h. As shown in Figure 5, we found that the shapes of time effect curves for the nine representative chemotherapy agents were similar. A sharp drop was observed after 0.5 h of treatment and followed by a slow drop after 2 h. The level of γ-H2AX in a cell for the nine agents slowly decreased to the lowest value at the time of 8 h. After that, the proportion of γ-H2AX increased from 8 to 24 h.

Recently, studies have demonstrated that chemical genotoxicity has a close association with the DNA repair capacity after the exposure (Lee et al., 2019). To investigate the DNA repair ability, the data of γ-H2AX time effect after cells exposure to chemicals have been used to simulate DNA repair kinetics, and a network server (http://ccb1.bmi.ac.cn:81/shiny-server/sample-apps/prediction) was correspondingly developed to calculate two crucial indexes reflecting DNA damage and repair, that is, k (speed of γ-H2AX descending) and t_{50} (time required for γ-H2AX to drop to half of the maximum value) (Qu et al., 2021). Here, we estimated k and t_{50} after exposure to nine representative chemotherapy agents based on the 0.5–8 h γ-

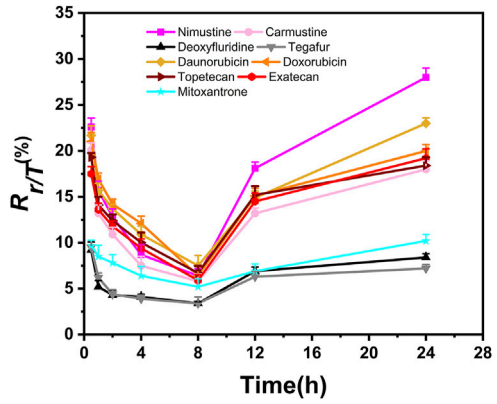

FIGURE 5
Time-dependent curves of γ-H2AX after HepG2 cells exposed to nine selected chemotherapy agents at the concentration of 100 μM. Seven time points were checked within 24 h, including 0.5, 1, 2, 4, 8, 12 and 24 h ($n \geq 3$, mean ± SD).

TABLE 2 *k* and t_{50} values of the selected nine chemotherapy agents.

Name of chemicals	*k*	t_{50} (h)	Class
Nimustine	0.160	2.465	Alkylating agents
Carmustine	0.169	2.298	
Deoxyfluridine	4.157	1.201	Antimetabolites
Tegafur	3.015	1.442	
Daunorubicin	0.139	3.344	Antitumor antibiotics
Doxorubicin	0.088	4.269	
Topotecan	0.132	3.545	Antitumor plant products
Exatecan	0.114	3.925	
Mitoxantrone	0.111	7.999	Miscellaneous agents

H2AX time-dependent kinetics (Figure 5) and then obtained these parameters to describe each agent DSB repair capacity using the functions *optim and optimize* in R language.

As shown in Table 2, we found *k* and t_{50} values were close among the selected chemotherapy drugs, except for two antimetabolites and mitoxantrone. Typically, due to the low therapeutic index, antimetabolites are used at higher clinical doses than other chemotherapy agents (Lansiaux., 2011). For example, the clinical doses of deoxyfluridine and tegafur are around 15–20 mg/kg. The relatively large *k* and relatively small t_{50} values of two antimetabolites reflect repair of DNA damage induced by antimetabolites was comparatively easier than that induced by other chemotherapy agents. Moreover, the values of γ-H2AX induced by deoxyfluridine (8.4) and tegafur (7.2) were both low at 100 μM of exposure concentration. In short, the values of *k*, t_{50} and γ-H2AX for antimetabolites indicated that antimetabolites cause weak DNA damage, that is, low genotoxicity, which may also be in part consistent with their low therapeutic indexes (Lansiaux, 2011; Masood et al., 2016). As for mitoxantrone, it induces DNA damage via a broader range of biological mechanism of action (Scott and Figgitt, 2004). Therefore, the *k* of mitoxantrone was smaller and the t_{50} of mitoxantrone was longer. In addition, similar to our previously reported work, *k* and t_{50} values varied with the carcinogenic grades of agents. Daunorubicin and doxorubicin belong to the 2B and 2A groups of the IARC classification, respectively. As shown in Table 2, the *k* of daunorubicin was greater than that of doxorubicin, and the t_{50} of daunorubicin was smaller, which support DNA damage related repair induced by doxorubicin was comparatively harder than that induced by daunorubicin.

Conclusion

In summary, the γ-H2AX MS technique in HepG2 cell line seems to be a proper way to evaluate genotoxicity caused by chemotherapy agents, enabling preliminary classification of the agents and providing preprimary reference data for therapeutic effect assessment and safety evaluation. The quantification of γ-H2AX is extremely easy, gives highly specific and repeatable results, and provides a guided evaluation of chemotherapy agents, which is a potential *in vitro* assay that may eventually reduce the number of animals required for genotoxicity assessment experiments of chemotherapy agents. Future work is needed to be expanded to complementary cell lines with different metabolic activities to further confirm the feasibility of this method in assessing genotoxic effects of chemotherapy agents which may give extra important information about metabolic activation involved in genotoxicity induction.

Data availability statement

The raw data supporting the conclusions of this article will be made available by the authors, without undue reservation.

Ethics statement

Ethical approval was not required for the studies on humans in accordance with the local legislation and institutional requirements because only commercially available established cell lines were used. Ethical approval was not required for the studies on animals in accordance with the local legislation and institutional requirements because only commercially available established cell lines were used.

Author contributions

MQ: Writing–original draft, Validation, Methodology. JC: Writing–original draft, Methodology. BX: Writing–review and editing, Methodology. QS: Writing–original draft. SZ: Writing–original draft. ZW: Writing–original draft. ZL: Writing–original draft. BM: Writing–original draft. HX: Writing–review and editing, Funding acquisition, Conceptualization. QY: Writing–review and editing. JX: Writing–review and editing, Project administration.

Funding

The author(s) declare financial support was received for the research, authorship, and/or publication of this article. This work was supported by the National Natural Science Foundation of China (No. 21974151) and the National Key Research and Development Program (No. 2018YFC1602600).

Conflict of interest

The authors declare that the research was conducted in the absence of any commercial or financial relationships that could be construed as a potential conflict of interest.

Publisher's note

All claims expressed in this article are solely those of the authors and do not necessarily represent those of their affiliated organizations, or those of the publisher, the editors and the reviewers. Any product that may be evaluated in this article, or claim that may be made by its manufacturer, is not guaranteed or endorsed by the publisher.

Supplementary material

The Supplementary Material for this article can be found online at: https://www.frontiersin.org/articles/10.3389/fphar.2024.1356753/full#supplementary-material

References

Aardema, M. J., Albertini, S., Arni, P., Henderson, L. M., Kirsch-Volders, M., Mackay, J. M., et al. (1998). Aneuploidy: a report of an ecetoc task force. *Mutat. Res.* 410, 3–79. doi:10.1016/s1383-5742(97)00029-x

Adamson, P. C., Poplack, D. G., and Balis, F. M. (1994). The cytotoxicity of thioguanine vs mercaptopurine in acute lymphoblastic leukemia. *Leuk. Res.* 18, 805–810. doi:10.1016/0145-2126(94)90159-7

Al-Badr, A. A., and Alodhaib, M. M. (2016). Dacarbazine. *Excip. Relat. Methodol.* 41, 323–377. doi:10.1016/bs.podrm.2015.12.002

Bauer, W., and Vinograd, J. (1970). The interaction of closed circular DNA with intercalative dyes. 3. Dependence of the buoyant density upon superhelix density and base composition. *J. Mol. Biol.* 54, 281–298. doi:10.1016/0022-2836(70)90430-4

Büch, T. R., and Zeller, W. J. (2002). Comparative cytotoxicity of carmustine (BCNU), nimustine (ACNU) and elmustine (HeCNU) after depletion of O6-alkylguanine-DNA alkyltransferase (O6-AGT). *Anticancer Res.* 22, 697–701.

Bukowski, K., Kciuk, M., and Kontek, R. (2020). Mechanisms of multidrug resistance in cancer chemotherapy. *Int. J. Mol. Sci.* 21, 3233. doi:10.3390/ijms21093233

Canals, A., Purciolas, M., Aymamí, J., and Coll, M. (2005). The anticancer agent ellipticine unwinds DNA by intercalative binding in an orientation parallel to base pairs. *Acta Crystallogr. D. Biol. Crystallogr.* 61, 1009–1012. doi:10.1107/S0907444905015404

Chabner, B. A., and Roberts, T. G. (2005). Timeline: chemotherapy and the war on cancer. *Nat. Rev. Cancer* 5, 65–72. doi:10.1038/nrc1529

Champoux, J. J. (2001). DNA topoisomerases: structure, function, and mechanism. *Annu. Rev. Biochem.* 70, 369–413. doi:10.1146/annurev.biochem.70.1.369

Chatterjee, N., and Walker, G. C. (2017). Mechanisms of DNA damage, repair and mutagenesis. *Environ. Mol. Mutagen* 58, 235–263. doi:10.1002/em.22087

Cheung-Ong, K., Giaever, G., and Nislow, C. (2013). DNA-damaging agents in cancer chemotherapy: serendipity and chemical biology. *Chem. Biol.* 20, 648–659. doi:10.1016/j.chembiol.2013.04.007

Choudhuri, S., Kaur, T., Jain, S., Sharma, C., and Asthana, S. (2021). A review on genotoxicity in connection to infertility and cancer. *Chem. Biol. Interact.* 345, 109531. doi:10.1016/j.cbi.2021.109531

Ciaffaglione, V., Modica, M. N., Pittalà, V., Romeo, G., Salerno, L., and Intagliata, S. (2021). Mutual prodrugs of 5-fluorouracil: from a classic chemotherapeutic agent to novel potential anticancer drugs. *ChemMedChem* 16, 3496–3512. doi:10.1002/cmdc.202100473

Clark, P. I., and Slevin, M. L. (1987). The clinical pharmacology of etoposide and teniposide. *Clin. Pharmacokinet.* 12, 223–252. doi:10.2165/00003088-198712040-00001

Coulthard, S., and Hogarth, L. (2005). The thiopurines: an update. *Invest. New Drugs* 23, 523–532. doi:10.1007/s10637-005-4020-8

DeVita, V. T., and Chu, E. (2008). A history of cancer chemotherapy. *Cancer Res.* 68, 8643–8653. doi:10.1158/0008-5472.CAN-07-6611

Dilruba, S., and Kalayda, G. V. (2016). Platinum-based drugs: past, present and future. *Cancer Chemother. Pharmacol.* 77, 1103–1124. doi:10.1007/s00280-016-2976-z

Drabløs, F., Feyzi, E., Aas, P. A., Vaagbø, C. B., Kavli, B., Bratlieet, M. S., et al. (2004). Alkylation damage in DNA and RNA—repair mechanisms and medical significance. *DNA Repair (Amst)* 3, 1389–1407. doi:10.1016/j.dnarep.2004.05.004

Elgemeie, G. H. (2003). Thioguanine, mercaptopurine: their analogs and nucleosides as antimetabolites. *Curr. Pharm. Des.* 9, 2627–2642. doi:10.2174/1381612033453677

Fresneau, B., Hackshaw, A., Hawkins, D. S., Paulussen, M., Anderson, J. R., Judson, I., et al. (2017). Investigating the heterogeneity of alkylating agents' efficacy and toxicity between sexes: a systematic review and meta-analysis of randomized trials comparing cyclophosphamide and ifosfamide (MAIAGE study). *Pediatr. Blood Cancer* 64, 8. doi:10.1002/pbc.26457

Fu, D., Calvo, J. A., and Samson, L. D. (2012). Balancing repair and tolerance of DNA damage caused by alkylating agents. *Nat. Rev. Cancer* 12, 104–120. doi:10.1038/nrc3185

Ghosh, S. (2019). Cisplatin: the first metal based anticancer drug. *Bioorg Chem.* 88, 102925. doi:10.1016/j.bioorg.2019.102925

Gompel, A. (2019). Hormone and breast cancer. *Presse Med.* 48, 1085–1091. doi:10.1016/j.lpm.2019.09.021

Gradishar, W. J. (2004). Tamoxifen—what next? *Oncologist* 9, 378–384. doi:10.1634/theoncologist.9-4-378

Hashimoto, Y., Yoshida, Y., Yamada, T., Aisu, N., Yoshimatsu, G., Yoshimura, F., et al. (2020). Current status of therapeutic drug monitoring of 5-fluorouracil prodrugs. *Anticancer Res.* 40, 4655–4661. doi:10.21873/anticanres.14464

Holthuis, J. J. (1988). Etoposide and teniposide. bioanalysis, metabolism and clinical pharmacokinetics. *Pharm. Weekbl. Sci.* 10, 101–116. doi:10.1007/BF01959294

Jordan, V. C., and Dowse, L. J. (1976). Tamoxifen as an anti-tumour agent: effect on oestrogen binding. *J. Endocrinol.* 68, 297–303. doi:10.1677/joe.0.0680297

Kharb, R., Haider, K., Neha, K., and Yar, M. S. (2020). Aromatase inhibitors: role in postmenopausal breast cancer. *Arch. Pharm. Weinh.* 353, e2000081. doi:10.1002/ardp.202000081

Khoury, L., Zalko, D., and Audebert, M. (2013). Validation of high-throughput genotoxicity assay screening using γ-H2AX in-cell western assay on HepG2 cells. *Environ. Mol. Mutagen* 54, 737–746. doi:10.1002/em.21817

Kirkland, D., Aardema, M., Henderson, L., and Müller, L. (2005). Evaluation of the ability of a battery of three *in vitro* genotoxicity tests to discriminate rodent carcinogens and non-carcinogens I. sensitivity, specificity and relative predictivity. *Mutat. Res.* 584, 1–256. doi:10.1016/j.mrgentox.2005.02.004

Kirkland, D., Kasper, P., Martus, H. J., Müller, L., van Benthem, J., Madia, F., et al. (2016). Updated recommended lists of genotoxic and non-genotoxic chemicals for assessment of the performance of new or improved genotoxicity tests. *Mutat. Res. Genet. Toxicol. Environ. Mutagen* 795, 7–30. doi:10.1016/j.mrgentox.2015.10.006

Knezevic, C. E., and Clarke, W. (2020). Cancer chemotherapy: the case for therapeutic drug monitoring. *Ther. Drug Monit.* 42, 6–19. doi:10.1097/FTD.0000000000000701

Kopp, B., Khoury, L., and Audebert, M. (2019). Validation of the γH2AX biomarker for genotoxicity assessment: a review. *Arch. Toxicol.* 93, 2103–2114. doi:10.1007/s00204-019-02511-9

Koprowska, K., and Czyż, M. (2011). Dacarbazine, a chemotherapeutic against metastatic melanoma and a reference drug for new treatment modalities. *Postep Hig. Med. Dosw* 65, 734–751. doi:10.5604/17322693.966832

Lansiaux, A. (2011). Antimetabolites. *Bull. Cancer* 98, 1263–1274. doi:10.1684/bdc.2011.1476

Lee, Y., Wang, Q., Shuryak, I., Brenner, D. J., and Turner, H. C. (2019). Development of a high-throughput γ-H2AX assay based on imaging flow cytometry. *Radiat. Oncol.* 14, 150. doi:10.1186/s13014-019-1344-7

Lennard, L., Davies, H. A., and Lilleyman, J. S. (1993). Is 6-thioguanine more appropriate than 6-mercaptopurine for children with acute lymphoblastic leukaemia? *Br. J. Cancer* 68, 186–190. doi:10.1038/bjc.1993.311

Luan, Y., and Honma, M. (2022). Genotoxicity testing and recent advances. *GIAD* 3 (1), 1–21. doi:10.1007/s42764-021-00058-7

Martins-Teixeira, M. B., and Carvalho, I. (2020). Antitumour anthracyclines: progress and perspectives. *ChemMedChem* 15, 933–948. doi:10.1002/cmdc.202000131

Masood, I., Kiani, M. H., Ahmad, M., Masood, M. I., and Sadaquat, H. (2016). Major contributions towards finding a cure for cancer through chemotherapy: a historical review. *Tumorl* 102, 6–17. doi:10.5301/tj.5000387

Meredith, A. M., and Dass, C. R. (2016). Increasing role of the cancer chemotherapeutic doxorubicin in cellular metabolism. *J. Pharm. Pharmacol.* 68, 729–741. doi:10.1111/jphp.12539

Miller, A. A., and Salewski, E. (1994). Prospects for pirarubicin. *Med. Pediatr. Oncol.* 22, 261–268. doi:10.1002/mpo.2950220410

Minotti, G., Menna, P., Salvatorelli, E., Cairo, G., and Gianni, L. (2004). Anthracyclines: molecular advances and pharmacologic developments in antitumor activity and cardiotoxicity. *Pharmacol. Rev.* 56, 185–229. doi:10.1124/pr.56.2.6

Misiak, M., Mantegazza, F., and Beretta, G. L. (2016). Methods for elucidation of DNA-anticancer drug interactions and their applications in the development of new drugs. *Curr. Pharm. Des.* 22, 6596–6611. doi:10.2174/1381612822666160831114622

Monneret, C. (2011). Platinum anticancer drugs. from serendipity to rational design. *Ann. Pharm. Fr.* 69, 286–295. doi:10.1016/j.pharma.2011.10.001

Motoyama, S., Takeiri, A., Tanaka, K., Harada, A., Matsuzaki, K., Taketo, J., et al. (2018). Advantages of evaluating γ-H2AX induction in non-clinical drug development. *Genes Environ.* 40, 10–17. doi:10.1186/s41021-018-0098-z

Mulder, R. L., Paulides, M., Langer, T., Kremer, L. C. M., and van Dalen, E. C. (2015). Cyclophosphamide versus ifosfamide for paediatric and young adult bone and soft tissue sarcoma patients. *Cochrane Database Syst. Rev.* 9, CD006300. doi:10.1002/14651858.CD006300.pub4

Nikolova, T., Hennekes, F., Bhatti, A., and Kaina, B. (2012). Chloroethylnitrosourea-induced cell death and genotoxicity: cell cycle dependence and the role of DNA double-strand breaks. HR and NHEJ. *Cell Cycle* 11, 2606–2619. doi:10.4161/cc.20862

Nikolova, T., Roos, W. P., Krämer, O. H., Strik, H. M., and Kaina, B. (2017). Chloroethylating nitrosoureas in cancer therapy: DNA damage, repair and cell death signaling. *Biochim. Biophys. Acta Rev. Cancer* 1868, 29–39. doi:10.1016/j.bbcan.2017.01.004

Qu, M., Xu, H., Chen, J., Xu, B., Li, Z., Ma, B., et al. (2022). Differential comparison of genotoxic effects of aristolochic acid I and II in human cells by the mass spectroscopic quantification of γ-H2AX. *Toxicol Vitro* 81, 105349. doi:10.1016/j.tiv.2022.105349

Qu, M., Xu, H., Chen, J., Zhang, Y., Xu, B., Guo, L., et al. (2020). Distinct orchestration and dynamic processes on γ-H2AX and p-H3 for two major types of genotoxic chemicals revealed by mass spectrometry analysis. *Chem. Res. Toxicol.* 33, 2108–2119. doi:10.1021/acs.chemrestox.0c00104

Qu, M., Xu, H., Li, W., Chen, J., Zhang, Y., Xu, B., et al. (2021). Dynamically monitoring cellular γ-H2AX reveals the potential of carcinogenicity evaluation for genotoxic compounds. *Arch. Toxicol.* 95, 3559–3573. doi:10.1007/s00204-021-03156-3

Rahmanian, N., Shokrzadeh, M., and Eskandani, M. (2021). Recent advances in γH2AX biomarker-based genotoxicity assays: a marker of DNA damage and repair. *DNA Repair (Amst)* 108, 103243. doi:10.1016/j.dnarep.2021.103243

Rosenberg, B., Vancamp, L., and Krigas, T. (1965). Inhibition of cell division in escherichia coli by electrolysis products from a platinum electrode. *Nature* 205, 698–699. doi:10.1038/205698a0

Roy, P. S., and Saikia, B. J. (2016). Cancer and cure: a critical analysis. *Indian J. Cancer* 53, 441–442. doi:10.4103/0019-509X.200658

Sauter, B., and Gillingham, D. (2020). DNA damaging agents in chemical biology and cancer. *Chim. (Aarau)* 74, 693–698. doi:10.2533/chimia.2020.693

Scott, L. J., and Figgitt, D. P. (2004). Mitoxantrone: a review of its use in multiple sclerosis. *CNS Drugs* 18, 379–396. doi:10.2165/00023210-200418060-00010

Singh, R. K., Kumar, S., Prasad, D. N., and Bhardwaj, T. R. (2018). Therapeutic journery of nitrogen mustard as alkylating anticancer agents: historic to future perspectives. *Eur. J. Med. Chem.* 10, 401–433. doi:10.1016/j.ejmech.2018.04.001

Soepenberg, O., Sparreboom, A., and Verweij, J. (2003). Clinical studies of camptothecin and derivatives. *Alkaloids Chem. Biol.* 60, 1–50. doi:10.1016/s0099-9598(03)60001-5

Torre, L. A., Siegel, R. L., Ward, E. M., and Jemal, A. (2016). Global cancer incidence and mortality rates and trends—an update. *Cancer Epidem Biomar* 25, 16–27. doi:10.1158/1055-9965.EPI-15-0578

Wang, J. C. (1996). DNA topoisomerases. *Annu. Rev. Biochem.* 65, 635–692. doi:10.1146/annurev.bi.65.070196.003223

Waterman, D. P., Haber, J. E., and Smolka, M. B. (2020). Checkpoint responses to DNA double-strand breaks. *Annu. Rev. Biochem.* 89, 103–133. doi:10.1146/annurev-biochem-011520-104722

Weiss, R. B. (1992). The anthracyclines: will we ever find a better doxorubicin? *Semin. Oncol.* 19, 670–686.

World Health Organization (1962). *Technical report series. Chemotherapy of cancer*. Geneva: WHO.

Wu, Y. F., Chitranshi, P., Loukotková, L., da Costa, G. G., Beland, F. A., Zhang, J., et al. (2017). Cytochrome P450-mediated metabolism of triclosan attenuates its cytotoxicity in hepatic cells. *Arch. Toxicol.* 91, 2405–2423. doi:10.1007/s00204-016-1893-6

Yamada, H. Y., and Gorbsky, G. J. (2006). Spindle checkpoint function and cellular sensitivity to antimitotic drugs. *Mol. Cancer Ther.* 5, 2963–2969. doi:10.1158/1535-7163.MCT-06-0319

Yamada, Y., Watanabe, S., Okamoto, K., Arimoto, S., Takahashi, E., Negishi, K., et al. (2019). Chloroethylating anticancer drug-induced mutagenesis and its repair in *Escherichia coli*. *Genes Environ.* 41, 11. doi:10.1186/s41021-019-0123-x

Zhu, Q., Yu, X., Shen, Q., Zhang, Q., Su, M., Zhou, Y., et al. (2018). A series of camptothecin prodrugs exhibit HDAC inhibition activity. *Bioorg Med. Chem.* 26, 4706–4715. doi:10.1016/j.bmc.2018.08.008

frontiers | Frontiers in Pharmacology

TYPE Original Research
PUBLISHED 20 June 2024
DOI 10.3389/fphar.2024.1385550

OPEN ACCESS

EDITED BY
Yong-Long Han,
Shanghai Jiao Tong University, China

REVIEWED BY
Robin Joshi,
University of Pennsylvania, United States
Xiaolong Ji,
Zhengzhou University of Light Industry, China

*CORRESPONDENCE
Yujia Wei,
361491282@qq.com
Guangqiu Qin,
qinguangqiu@hotmail.com

RECEIVED 13 February 2024
ACCEPTED 24 May 2024
PUBLISHED 20 June 2024

CITATION
Ma J, Wei Y, Sun J, Tan F, Liu P and Qin G (2024), Toxicological safety assessment of a water extract of *Lithocarpus litseifolius* by a 90-day repeated oral toxicity study in rats. *Front. Pharmacol.* 15:1385550. doi: 10.3389/fphar.2024.1385550

Toxicological safety assessment of a water extract of *Lithocarpus litseifolius* by a 90-day repeated oral toxicity study in rats

Jinfeng Ma, Yujia Wei*, Jingfeng Sun, Fang Tan, Penghe Liu and Guangqiu Qin*

Department of Preventive Medicine, Guangxi University of Chinese Medicine, Nanning, China

Lithocarpus litseifolius although known as "Sweet Tea" (ST), has been traditionally accepted as a daily beverage and used as a folk medicine in southern China with little understanding of its potential toxicity. This study evaluated the safety of a water extract of ST by a subchronic toxicity study in Sprague-Dawley rats. A total of 80 rats were randomized divided into 4 groups with 10 males and 10 females in each group, treated with 2000, 1,000, 500 and 0 mg/kg body weight of ST extract by gavage for 90 days, respectively. The results of the study showed that ST extract did not induce treatment-related changes in the body and organ weight, food intake, blood hematology and serum biochemistry, urine indices, and histopathology in rats. The NOAEL of ST extract was observed to be 2000 mg/kg/day for rats of both sexes. These results indicated that ST extract was of low toxicity in the experimental conditions of the current study and had the potential for application in food-related products.

KEYWORDS

***Lithocarpus litseifolius*, Sweet Tea, subchronic toxicity, safety assessment, oral exposure**

1 Introduction

Lithocarpus litseifolius (Hance) Chun, an evergreen tree belongs to the family Fagaceae, has about 40 alternative names, with the most commonly used being "Sweet Tea" (ST). This name first appeared in the Song Dynasty's "Annals of Qingshuiyan in Anxi" (Chen, 1996). Wild ST grows primarily in the southern region of the Yangtze River in China, including Jiangxi, Guangxi and Hunan provinces. Traditionally, tender leaves and roots of ST are used to brew tea or stew soup for consumption. The use of tender leaves of ST as tea can be traced back to 423 AD (Chongqing Beibei District Chronicle Compilation Committee, 1989). For centuries, its roots, stems, and leaves have been widely used as a traditional herb in southern China to treat hypertension, obesity and hyperlipidemia (Wu et al., 2019).

Chemical analysis revealed that leaves of ST are rich of flavonoids (including phloridzin and trilobatin) and polyphenolic compounds (Li et al., 2014). The results of modern biomedical studies have shown that the chemical components of ST have multiple biological activities. For example, the extract of ST was observed to have broad-spectrum antibacterial activity toward Gram-positive bacteria and fungi (Wang et al., 2020). Different fractions from ST leaves, including total extract, petroleum ether fraction, n-butyl-alcohol fraction, water fraction, phlorizin, phloretin and 2′-O-acetylph loridzin could significantly promote the glucose consumption of insulin-resistant HepG2 cells and improve the insulin resistance of HepG2 cells (Pan et al., 2015). Tea extract mainly composed of ST was observed to reduce

uric acid in mice with hyperuricemia nephropathy, possibly through the inhibition of uric acid reabsorption (Chen et al., 2024). Trilobatin, phlorizin, isoquercitrin and other components of ST could improve ulcerative colitis in model mice, mainly through the regulation of PI3K-AKT and TNF signaling pathways that are related to inflammation, immunity, anti-oxidation, and the intestinal barrier (Liu, 2023). Historical use and emerging preclinical and clinical evidence suggest that there is potential for the extract of ST to be used in teas or as a dietary supplement, and it has been applied in health food-related products (Ji et al., 2020; Huang, 2021; Chen et al., 2023).

Although the biological effects of ST and its extract have been widely recognized and confirmed by modern biomedical research, there is still relatively little understanding of its potential toxicity. There are no records of dietary taboos or toxicity of ST in traditional Chinese medicine works and literature throughout history (Lin et al., 2023). A previous study reported that 25-weeks repeated oral administration of ST extract at dose of 2.0 g/kg led to reversible damage to the liver function of Wistar rats (Zeng et al., 2010). Another study reported that three phlorizin derivatives and four dihydrochalcones isolated from the leaves of ST were shown to be non-cytotoxic when tested against A549, HeLa, HepG2, and MCF-7 cell lines (Wei et al., 2020). The objective of the present study was to evaluate the subchronic toxicity of a water-extract of ST in rats to provide necessary information for safety assessment of ST in food-related products.

2 Materials and methods

2.1 Preparation and standardization of plant extract

The fresh leaves of ST were collected from Bama Yao Autonomous County, Guangxi province, China in the summer of 2018. Leaves were dried in a 60°C oven, powdered and ultrasonically extracted twice with distilled water (1:10, w:v) at 60°C for 1 h each time. The aqueous extract was mixed, filtered, concentrated using a rotary evaporator (Heidolph Advantage ML/G3, Germany), and freeze-dried to obtain a powdered extract (1 g of powder is equivalent to 31.8 g of dried leaves). The phloridzin content of the extract was determined to be 84.3 mg/g using high performance liquid chromatography, following the method reported (Chen et al., 2017). The extract was stored at −20 °C and diluted with distilled water before being used.

2.2 Experimental animals

Three-week-old specific pathogen-free Sprague-Dawley (SD) rats were purchased from the Medical Experimental Animal Center of Guangdong Province (Guangzhou, China). Animals were housed in an environment with a 12 h light/dark cycle, a temperature of 23°C ± 1°C and a relative humidity of 60% ± 5%. Animals were housed in polycarbonate cages with unrestricted access to standard diets and distilled water. They were acclimated for 3 days before the experiments. The protocol of this study was reviewed and approved by the Animal Experimentation Ethics Committee of Guangxi University of Chinese Medicine.

2.3 Animal grouping and exposure

A 90-day subchronic oral toxicity study was conducted following a standard protocol established by the National Health Commission of China (National Health Commission of China, 2015; Qin et al., 2020). A total of 80 healthy male and female SD rats were randomly assigned to 3 treatment groups and 1 control group, with 10 males and 10 females in each group. Animals in the treatment groups were administered 2000, 1,000, and 500 mg/kg body weight of ST extract (dissolved in distilled water) by gavage once per day in the morning for 90 days, respectively. In contrast, those in the control group were given 10 mL/kg of distilled water daily by gavage. Doses were determined based on our preliminary, unpublished acute toxicity study on this ST extract, which concluded with a NOAEL of >5,000 mg/kg body weight in Kunming mice. Animals of different sexes were housed separately in polycarbonate cages, with a maximum of three animals per cage. Conventional diets and water were freely available to all animals during the experiment.

2.4 Clinical observation

Clinical signs and behavioral symptoms were recorded daily, including hair condition, skin appearance, eyes health, mucous membranes status, secretions, excretions, respiratory system function, nervous system responses and behavioral manifestations. Individual body weight was recorded weekly. Food consumption was recorded twice a week throughout the study. Feed efficiency was calculated as follows: Feed efficiency (%) = body weight gain (g)/food intake (g) × 100% (Qin et al., 2020).

2.5 Ophthalmological examination

The ophthalmological examination was conducted during the acclimation period and repeated on the final day of the exposure. The cornea, lens, bulbar conjunctiva, and iris were observed using an ophthalmoscope.

2.6 Hematological and serum biochemical analyses

After 90 days of exposure, rats were fasted overnight. Blood samples were collected from the arteria abdominalis under pentobarbital anesthesia. Hematological examination of blood was conducted using a Sysmex XT-1800 automated hematological analyzer (Sysmex, Kobe, Japan). The hematological indexes examined included the following: white blood cell count, red blood cell count, hemoglobin concentration, hematocrit, platelet count, mean platelet volume, mean corpuscular volume, mean corpuscular hemoglobin, mean corpuscular hemoglobin concentration, number and percentage of neutrophils, number and percentage of lymphocytes, number and percentage of monocytes, number and percentage of eosinophils, number and percentage of basophils.

Serum from rats was collected by centrifuging approximately 4 mL of whole blood at 2,500 × rpm for 10 min. The activity of aspartate transaminase and alanine transaminase in serum was

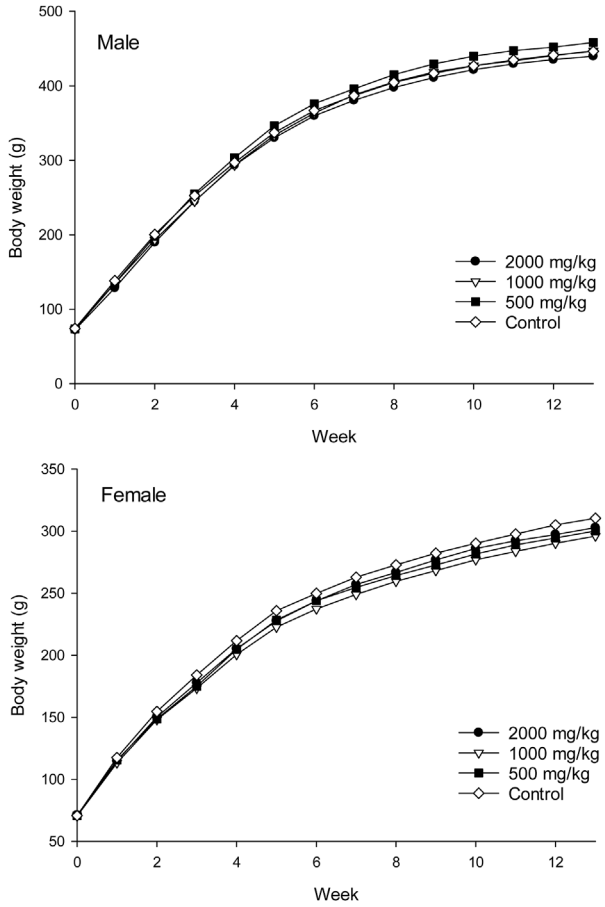

FIGURE 1
Average body weights of rats treated with ST extract for 90 days (represent by mean, n = 10).

analyzed using commercial kits (Beijing Wantai BioPharm, Beijing, China). Biochemical indexes of serum, including blood urea nitrogen, creatinine, total cholesterol, triglycerides, total protein, albumin, and glucose, were analyzed using an Olympus AU400 analyzer (Olympus, Tokyo, Japan).

2.7 Urinalysis

Urine samples were collected from the bladders of rats after blood collection using syringes. Urine indicators, including specific gravity, pH, white blood cells, ketone bodies, nitrite, urobilinogen, bilirubin, protein, glucose, occult blood, creatinine, calcium, and microalbumin, were analyzed using a Urit-500B urine chemistry analyzer (Urit, Guilin, China).

2.8 Necropsy

After being sacrificed by exsanguination from the abdominal aorta, a visual pathological examination was conducted on all rats. The weights of the liver, spleen, kidneys, testes, ovaries, brain, heart, thymus, adrenal glands, epididymis and uterus were measured. Relative organ weight was determined as organ weight divided by body weight and then multiplied by 100%.

2.9 Histopathological examination

Samples of organs and tissues were preserved for histopathological examination, including the brain, thyroid gland, liver, spleen, pancrea, heart, kidneys, adrenal gland, stomach, mesenteric lymph nodes, small intestine, jejunum, ileum, prostate, bladder, testes, and ovaries. Samples were fixed in 4% neutral buffered formaldehyde, embedded in paraffin, and stained with Giemsa. Pathological sections of organs and tissues were examined under a Leica DM 6000B optical microscope (Wetzler, Germany). The number of animals with histopathological lesions was recorded. The types of histopathological lesions were recorded, and the degree of each lesion was scored into four levels: normal (0), mild (1), moderate (2), and severe (3).

2.10 Statistical analysis

The data were analyzed using SPSS v16.0 (SPSS Inc., Chicago, United States). The homogeneity of variances in the data was assessed using Bartlett's test. The data from the treatment groups were compared to those of the control group using one-way ANOVA followed by Dunnett's test. A p-value of ≤ 0.05 was considered statistically significant.

3 Results

3.1 Clinical and ophthalmological examination

During the 90-day toxicity study, no mortality occurred, and there were no treatment-related clinical changes or abnormal behavior observed. No alterations were observed on ophthalmologic examinations before and on Day 90 of the treatment.

3.2 Body and organ weights

Body weights and weight gains of the treated groups were comparable to those of the control group for both sexes ($p > 0.05$, Figure 1; Table 1). No significant difference was observed in the total food intake and average feed efficiency of rats between the treated and control groups of both sexes ($p > 0.05$, Table 1). The absolute weights and relative weights of major organs in the treated groups of rats were similar to those of the control group for both sexes ($p > 0.05$, Tables 2, 3).

3.3 Blood hematology and serum biochemistry

For blood hematology, in male rats at a dose of 2000 mg/kg, the hemoglobin (HGB) level was significantly higher than in the

10.3389/fphar.2024.1385550

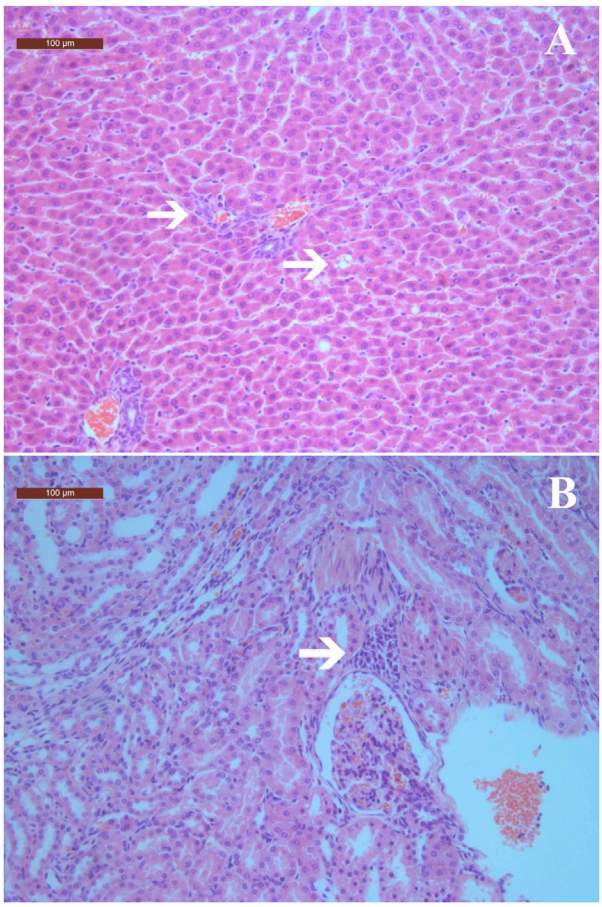

FIGURE 2
Histopathological changes in liver and kidneys of rats treated with ST extract for 90 days (×100). **(A)** Inflammatory cell infiltration in portal tract areas and fatty degeneration of hepatocytes; **(B)** Cells infiltration in renal interstitium. Arrows indicate histopathological changes. The scale bars are 100 μm.

control group ($p < 0.05$, Table 4). The red blood cell (RBC) levels increased significantly in female rats treated with 500 mg/kg ST extract compared to those in the control group. Platelet (PLT) and white blood cell (WBC) count, as well as their ratios, were not affected by the extract treatment.

Coagulation indexes, including fibrinogen (FIB), thrombin time (TT), prothrombin time (PT) and activated partial thromboplastin time (APTT) were not affected by the extract treatment and were similar in all groups (Table 5).

For serum biochemical indexes, in male rats at 2000 mg/kg, the albumin (ALB) level was slightly but significantly higher than that of the control ($p < 0.05$, Table 6). In female animals, the blood urea nitrogen (BUN) level at 1,000 mg/kg decreased significantly; the chlorine level at 2000 mg/kg was significantly higher than that of the control, while the natrium level at 1,000 mg/kg was significantly lower than that of the control ($p < 0.05$, Table 6).

3.4 Urinalysis

For urinalysis, the urine color and clarity, specific gravity, and pH of the treatment groups were comparable to those of the control group ($p > 0.05$, Table 7). Several elevated values of white blood cells (WBC), protein (PRO), blood (BLD), creatinine (Cr), calcium (Ca), and microalbumin (MA) were observed in all groups (Table 7).

3.5 Histopathological examinations

In the visual pathological examination, no apparent symptoms of pathological lesions were observed in rats from the treatment and control groups. Therefore, histopathological examinations were conducted only in the highest dose (2000 mg/kg) group and the control group. In the histopathological examinations, mild histopathological changes, including inflammatory cell infiltration and fatty degeneration of hepatocytes, as well as cell infiltration in the renal cortex of kidneys were observed in both the treatment and control groups (Figure 2 and Table 8). Scoring of histopathological lesions showed no statistical difference between the treatment and control groups for both sexes ($p > 0.05$, data not shown).

TABLE 1 Body weight gain, food intake and food utilization rate of rats treated with ST extract for 90 days.

Sex	Dose (mg/kg)	Total body weight gain (g)			Total food intake (g)			Average feed efficiency (%)		
Male	2,000	367.4	±	26.0	2,463.7	±	60.5	14.9	±	1.1
	1,000	374.0	±	24.4	2,432.4	±	116.7	15.4	±	0.8
	500	384.8	±	28.5	2,532.9	±	116.8	15.2	±	0.7
	Control	372.4	±	29.2	2,447.6	±	93.9	15.2	±	0.8
Female	2,000	231.8	±	13.0	2,112.0	±	143.7	11.0	±	0.7
	1,000	225.7	±	13.5	2054.4	±	157.3	11.0	±	0.9
	500	229.6	±	18.9	2044.1	±	150.3	11.3	±	0.9
	Control	239.7	±	15.5	2,131.3	±	182.2	11.3	±	0.6

Note: values represent mean ± standard deviation of 10 rats. Feed efficiency (%) = (total body weight gain/total food intake) ×100%. Values of the treatment groups did not differ statistically from the control according to one-way ANOVA, at $p < 0.05$.

TABLE 2 Absolute organ weights of rats treated with ST extract for 90 days.

Dose (mg/kg)	Liver			Kidneys			Spleen			Testes/ovaries			Brain			Heart			Thymus			Adrenal			Epididymis/uterus		
Male																											
2,000	10.11	±	0.57	2.88	±	0.25	0.70	±	0.04	3.11	±	0.15	1.596	±	0.104	1.249	±	0.134	0.407	±	0.081	0.064	±	0.007	1.125	±	0.146
1,000	10.45	±	0.60	2.83	±	0.22	0.73	±	0.08	3.11	±	0.20	1.747	±	0.201	1.207	±	0.145	0.456	±	0.102	0.066	±	0.003	1.094	±	0.138
500	10.64	±	0.77	2.98	±	0.22	0.75	±	0.07	3.14	±	0.34	1.670	±	0.183	1.289	±	0.139	0.414	±	0.068	0.068	±	0.010	1.026	±	0.160
Control	10.27	±	0.78	2.86	±	0.25	0.75	±	0.08	3.02	±	0.22	1.669	±	0.160	1.291	±	0.088	0.431	±	0.111	0.065	±	0.009	1.071	±	0.153
Female																											
2,000	7.56	±	0.36	1.99	±	0.11	0.60	±	0.10	0.158	±	0.016	1.905	±	0.183	0.963	±	0.069	0.447	±	0.018	0.078	±	0.009	0.603	±	0.073
1,000	7.40	±	0.47	1.91	±	0.15	0.58	±	0.08	0.148	±	0.012	1.880	±	0.203	1.014	±	0.116	0.448	±	0.024	0.068	±	0.011	0.613	±	0.063
500	7.46	±	0.58	1.91	±	0.14	0.57	±	0.10	0.153	±	0.016	1.860	±	0.162	1.036	±	0.108	0.448	±	0.034	0.069	±	0.008	0.590	±	0.076
Control	7.78	±	0.40	1.97	±	0.14	0.62	±	0.07	0.158	±	0.011	1.953	±	0.198	1.070	±	0.089	0.458	±	0.025	0.071	±	0.008	0.634	±	0.060

Note: values represent mean ± standard deviation of 10 rats. Values of the treatment groups did not differ statistically from the control according to one-way ANOVA, at $p < 0.05$.

TABLE 3 Relative organ weights of rats treated with ST extract for 90 days.

Dose (mg/kg)	Liver			Kidneys			Spleen			Testes/ovaries			Brain			Heart			Thymus			Adrenal			Epididymis/uterus		
Male																											
2,000	2.399	±	0.078	0.683	±	0.035	0.167	±	0.009	0.738	±	0.029	0.380	±	0.031	0.296	±	0.027	0.096	±	0.017	0.015	±	0.001	0.267	±	0.037
1,000	2.441	±	0.035	0.661	±	0.040	0.169	±	0.013	0.726	±	0.032	0.401	±	0.036	0.281	±	0.026	0.106	±	0.019	0.015	±	0.002	0.256	±	0.039
500	2.420	±	0.061	0.679	±	0.038	0.170	±	0.010	0.712	±	0.038	0.380	±	0.031	0.294	±	0.032	0.095	±	0.016	0.015	±	0.002	0.234	±	0.040
Control	2.401	±	0.054	0.669	±	0.039	0.175	±	0.010	0.707	±	0.028	0.390	±	0.034	0.303	±	0.021	0.101	±	0.024	0.015	±	0.002	0.250	±	0.034
Female																											
2,000	2.603	±	0.032	0.684	±	0.017	0.205	±	0.034	0.055	±	0.005	0.655	±	0.047	0.332	±	0.029	0.154	±	0.005	0.027	±	0.002	0.208	±	0.025
1,000	2.604	±	0.032	0.674	±	0.030	0.206	±	0.029	0.052	±	0.003	0.662	±	0.054	0.357	±	0.036	0.158	±	0.004	0.024	±	0.003	0.216	±	0.025
500	2.592	±	0.030	0.664	±	0.039	0.197	±	0.032	0.053	±	0.004	0.647	±	0.040	0.361	±	0.032	0.156	±	0.004	0.024	±	0.003	0.204	±	0.019
Control	2.616	±	0.019	0.662	±	0.028	0.208	±	0.026	0.053	±	0.004	0.656	±	0.050	0.360	±	0.033	0.154	±	0.004	0.024	±	0.002	0.214	±	0.022

Note: values represent mean ± standard deviation of 10 rats. Relative organ weight (%) = (absolute organ weight/fasting body weight) ×100%. Values of the treatment groups did not differ statistically from the control according to one-way ANOVA, at $p < 0.05$.

10.3389/fphar.2024.1385550

TABLE 4 Hematological indexes of rats treated with ST extract for 90 days.

Sex	Dose (mg/kg)	HGB (g/L)			RBC (10^{12}/L)			PLT (10^9/L)		
Male	2,000	160.8	±	10.9*	7.71	±	0.95	904.9	±	105.7
	1,000	147.9	±	9.4	7.89	±	0.63	871.5	±	151.7
	500	152.4	±	12.5	7.60	±	0.79	809.2	±	137.1
	Control	147.4	±	7.2	7.94	±	1.07	859.3	±	165.9
Female	2,000	144.6	±	8.4	7.72	±	0.45	832.6	±	147.1
	1,000	146.5	±	15.4	8.10	±	0.61	881.3	±	122.6
	500	154.0	±	11.1	8.38	±	0.80*	848.1	±	139.5
	Control	146.7	±	10.1	7.48	±	0.67	880.1	±	96.8

Sex	Dose (mg/kg)	WBC (10^9/L)			LYM (%)			NEUT (%)			MONO (%)			EO (%)			BASO (%)		
Male	2,000	7.61	±	0.74	80.9	±	3.7	12.4	±	3.5	5.67	±	0.79	0.87	±	0.41	0.21	±	0.14
	1,000	7.39	±	0.71	81.0	±	3.1	12.3	±	3.7	5.65	±	0.89	0.83	±	0.52	0.24	±	0.07
	500	7.66	±	0.99	79.0	±	2.3	14.3	±	2.0	5.73	±	0.99	0.83	±	0.19	0.25	±	0.08
	Control	6.94	±	0.86	82.2	±	4.0	11.4	±	3.8	5.64	±	0.59	0.69	±	0.29	0.15	±	0.10
Female	2,000	7.16	±	0.66	81.6	±	4.5	11.9	±	4.6	5.34	±	1.15	0.97	±	0.33	0.18	±	0.12
	1,000	7.16	±	0.98	80.0	±	2.9	13.8	±	2.7	5.33	±	0.96	0.74	±	0.30	0.21	±	0.06
	500	7.50	±	0.52	82.6	±	3.9	11.0	±	4.2	5.55	±	0.75	0.65	±	0.38	0.20	±	0.08
	Control	7.05	±	1.19	80.2	±	3.1	12.8	±	3.6	5.86	±	0.83	0.93	±	0.35	0.23	±	0.07

Note: values represent mean ± standard deviation of 10 rats. HGB, hemoglobin concentration; RBC, red blood cell count; PLT, platelet count; WBC, white blood cell count; LYM, percent of lymphocytes; NEUT, percent of neutrophils; MONO, percent of monocytes; EO, percent of eosinophils; BASO, percent of basophils. *$p < 0.05$ compared with the control.

TABLE 5 Coagulation indexes of rats treated with ST extract for 90 days.

Sex	Dose (mg/kg)	FIB (g/L)			TT (s)			PT (s)			APTT (s)		
Male	2,000	2.47	±	0.24	58.1	±	5.6	11.0	±	0.8	16.0	±	0.7
	1,000	2.38	±	0.18	58.3	±	5.3	11.2	±	0.8	16.2	±	0.8
	500	2.57	±	0.27	58.7	±	3.7	11.2	±	0.9	16.0	±	0.6
	Control	2.50	±	0.23	59.9	±	4.9	10.9	±	0.7	16.0	±	0.8
Female	2,000	2.08	±	0.14	55.7	±	3.8	9.1	±	0.2	16.0	±	0.5
	1,000	1.95	±	0.13	55.5	±	3.3	9.3	±	0.2	15.8	±	0.5
	500	2.03	±	0.14	55.0	±	4.1	9.4	±	0.2	16.2	±	0.5
	Control	2.03	±	0.13	55.3	±	4.4	9.2	±	0.3	15.8	±	0.5

Note: values represent mean ± standard deviation of 10 rats. FIB, fibrinogen; TT, thrombin time; PT, prothrombin time; APTT, activated partial thromboplastin time. Values of the treatment groups did not differ statistically from the control according to one-way ANOVA, at $p < 0.05$.

4 Discussion

The extract of ST leaves has been shown to have various biological effects, including hypoglycemic (Liu et al., 2020; Li et al., 2022), hypolipidemic, antioxidant, and antimicrobial effects (Wu et al., 2019; Wang et al., 2020; Fu, 2023), and was developed to health food and traditional Chinese medicine (Liu, 2017; Wu et al., 2019; Huang, 2021). In 2017, ST leaf was listed as a new food ingredient by the National Health Commission of China (National Health Commission of China, 2017). The recommended method of using ST dry leaves is brewing with a suggested dosage of up to 10 g/day based on dry product. Until now, published preclinical safety assessments on ST and its extract are still rare, and the understanding of the potential toxicity of ST is still limited. A long-term toxicity study reported that blood glucose level in Wistar rats were significantly decreased after treated with 2.0, 1.0, and 0.5 g/kg water-extract of ST leaves for 13 and 25 weeks. The AST and ALT activities were significantly increased in rats treated with 2.0 g/kg ST extract for 25 weeks but reduced to a level comparable to the control group 2 weeks after discontinuing administration.

TABLE 6 Serum biochemical indexes of rats treated ST with extract for 90 days.

Sex	Dose (mg/kg)	AST (U/L)			ALT (U/L)			BUN (mmol/L)			CR (μmol/L)			TC (mmol/L)			TG (mmol/L)			TP (g/L)		
Male	2,000	113.8	±	9.4	49.80	±	4.26	6.26	±	0.62	49.44	±	3.98	1.93	±	0.20	1.02	±	0.13	72.32	±	5.60
	1,000	113.4	±	7.9	50.67	±	7.35	5.99	±	0.42	45.85	±	5.61	1.88	±	0.17	1.07	±	0.20	69.59	±	4.75
	500	116.5	±	8.5	52.66	±	7.55	6.05	±	0.42	47.53	±	4.75	1.96	±	0.07	0.96	±	0.19	72.09	±	7.12
	Control	111.5	±	8.9	49.12	±	8.66	6.20	±	0.61	47.62	±	4.27	2.00	±	0.21	1.02	±	0.24	72.55	±	5.37
Female	2,000	115.1	±	6.1	47.73	±	7.97	5.71	±	0.49	48.24	±	2.88	1.91	±	0.23	1.00	±	0.15	73.55	±	4.17
	1,000	119.4	±	6.8	51.20	±	8.28	5.70	±	0.45*	46.39	±	3.80	1.95	±	0.12	0.95	±	0.23	75.64	±	5.21
	500	117.4	±	10.3	48.34	±	6.69	6.09	±	0.45	46.67	±	5.33	1.88	±	0.29	0.96	±	0.26	71.33	±	4.63
	Control	113.1	±	10.5	47.66	±	6.91	6.26	±	0.61	47.06	±	6.58	1.96	±	0.25	0.93	±	0.21	73.17	±	5.27
Sex	Dose (mg/kg)	ALB (g/L)			GLU (mmol/L)			GGT (U/L)			ALP (U/L)			Cl (mmol/L)			K (mmol/L)			Na (mmol/L)		
Male	2,000	36.27	±	2.04*	5.49	±	0.35	0.47	±	0.19	159.0	±	16.1	91.3	±	3.7	7.46	±	0.34	158.1	±	1.6
	1,000	34.41	±	1.20	5.67	±	0.31	0.44	±	0.20	160.3	±	12.2	90.0	±	3.5	7.33	±	0.35	159.8	±	3.4
	500	35.47	±	1.61	5.53	±	0.34	0.52	±	0.18	157.3	±	14.0	93.0	±	2.3	7.43	±	0.35	159.8	±	3.3
	Control	33.66	±	3.05	5.42	±	0.48	0.58	±	0.16	168.1	±	11.7	92.0	±	3.3	7.29	±	0.35	159.6	±	3.1
Female	2,000	35.47	±	1.52	5.46	±	0.40	0.52	±	0.17	145.2	±	13.1	90.8	±	1.4*	7.07	±	0.23	154.7	±	2.2
	1,000	34.65	±	2.18	5.30	±	0.42	0.43	±	0.13	144.6	±	14.5	89.9	±	1.6	7.25	±	0.28	152.9	±	1.6*
	500	35.03	±	2.25	5.29	±	0.34	0.48	±	0.15	148.9	±	18.1	89.5	±	1.7	7.09	±	0.20	156.3	±	2.4
	Control	35.10	±	1.87	5.33	±	0.33	0.48	±	0.19	146.1	±	14.0	88.9	±	1.7	7.11	±	0.29	155.7	±	2.0

Note: values represent mean ± standard deviation of 10 rats. AST, aspartate transaminase; ALT, alanine transaminase; BUN, blood urea nitrogen; CR, creatinine; TC, total cholesterol; TG, triglyceride; TP, total protein; ALB, albumin; GLU, glucose; GGT, glutamyltransferase; ALP, alkaline phosphatase; Cl, chlorine; K, potassium; Na, natrium. *$p < 0.05$ compared with the control.

10.3389/fphar.2024.1385550

10.3389/fphar.2024.1385550

TABLE 7 Urinalysis of rats treated with ST extract for 90 days.

Sex	Dose (mg/kg)	Number of abnormal color/clarity	SG		pH		Number of positive										
							WBC	KET	NIT	URO	BIL	PRO	GLU	BLD	Cr	Ca	MA
Male	2,000	0	1.024	± 0.004	7.4	± 0.8	1	0	0	0	0	2	0	1	0	1	2
	1,000	0	1.020	± 0.006	7.3	± 0.9	0	0	0	0	0	3	0	2	0	1	1
	500	0	1.023	± 0.005	7.2	± 0.7	1	0	0	0	0	2	0	2	0	2	2
	Control	0	1.025	± 0.006	7.4	± 0.7	1	0	0	0	0	2	0	1	1	2	2
Female	2,000	0	1.022	± 0.007	7.3	± 0.7	1	0	0	0	0	2	0	2	0	2	1
	1,000	0	1.020	± 0.006	7.2	± 0.6	0	0	0	0	0	1	0	1	0	2	2
	500	0	1.016	± 0.006	7.0	± 0.5	0	0	0	0	0	1	0	3	1	1	1
	Control	0	1.020	± 0.006	7.1	± 0.7	1	0	0	0	0	2	0	2	0	1	1

Note: values represent mean ± standard deviation of 10 rats. SG, specific gravity; WBC, white blood cell; KET, ketone body; NIT, nitrite; URO, urobilinogen; BIL, bilirubin; PRO, protein; GLU, glucose; BLD, occult blood; Cr, creatinine; Ca, Calcium; MA, micro albumin. Values of the treatment groups did not differ statistically from the control according to one-way ANOVA, at $p < 0.05$.

Hepatic cell edema was observed in rats treated with 2.0 g/kg ST extract for 25 weeks but cells edema was not observed 2 weeks after discontinuing administration. These results indicate that long-term treatment with ST extract could lead to reversible damage to the liver function of rats (Zeng et al., 2010). Other studies have reported little or no cytotoxicity of ST extract (Wang et al., 2020; Lin et al., 2023). The current study evaluated the toxicological potential of ST extract in a 90-day repeated dose subchronic oral toxicity study in Sprague-Dawley rats.

During the 90-day treatment period, no treatment-related general clinical observations were recorded. The body weights and food intake of rats in all treatment groups were comparable to those of the control group, indicating that the ST extract did not have a significant effect on the weight or appetite of rats during the experiment.

Several statistically significant fluctuations in blood hematological and serum biochemical indexes were observed in the subchronic toxicity study. However, the levels of these measurements remained within historical ranges in our laboratory and were consistent with reported values for SD rats. Therefore, these changes were not deemed treatment-related or of toxicological concern. A previous toxicity study reported decreased blood glucose levels in Wistar rats after being treated with ST extract for 13 and 25 weeks (Zeng et al., 2010); this effect was not observed in the 90-day toxicity study described in this paper. Possible explanations for this discrepancy include the use of different strains and varying methods for extracting ST leaves. Previous studies have reported that various extraction methods yield extracts with different components (Liu HY. et al., 2021; Liu Y. et al., 2021).

For urinalysis, a few positive values, including WBC, PRO, BLD, Cr, Ca, and MA, were recorded in rats from both the treatment and control groups. The absolute and relative weights of the kidneys were comparable across all groups. In the meantime, mild cell infiltration in the renal cortex observed in the kidneys of the treatment groups was similar to that of the control. These results indicate that the ST extract had minimal nephrotoxicity in rats.

In the gross examination, no apparent pathological lesions were observed in rats from all groups, and no specific tissues or organs were identified. In the histopathological examinations, inflammatory cell infiltration was observed in portal tract areas, along with fatty degeneration of hepatocytes in rats treated with 2000 mg/kg of ST extract. These changes were considered to be spontaneous lesions, as the occurrences of these minor histopathological changes were relatively low (≤30%) and comparable to those of the control group, and no treatment-related abnormalities in liver function indices were observed. Other than liver and kidney, no histopathological lesions were observed, which is consistent with a previous study that reported treatment with ST extract up to 2 g/kg for 25 weeks did not induce treatment-related histopathological changes in rats (Zeng et al., 2010).

5 Conclusion

In conclusion, the results of the 90-days subchronic oral toxicity study support the safety for the repeated oral consumption of the water extract of "Sweet Tea," *L. litseifolius*. The no-observed-adverse-effect level of ST extract was considered to be 2,000 mg/kg/day for both male and female SD rats.

TABLE 8 Histopathology examination of rats treated with ST extract for 90 days.

Organs	Histopathological changes	Male		Female	
		2000 mg/kg	Control	2000 mg/kg	Control
Liver	Inflammatory cell infiltration in portal duct areas	3	2	2	1
	Mild fatty degeneration of hepatocytes	1	2	1	2
Kidneys	Cell infiltration in renal cortex	2	2	2	1

Note: values represent numbers of rats with histopathological changes in 10 rats of each group.

Data availability statement

The data presented in the study are deposited in the Figshare repository, accession: https://doi.org/10.6084/m9.figshare.25965574.

Ethics statement

The animal study was approved by the Animal Experimentation Ethics Committee of Guangxi University of Chinese Medicine. The study was conducted in accordance with the local legislation and institutional requirements.

Author contributions

JM: Writing–original draft, Formal Analysis, Data curation. YW: Writing–original draft, Resources, Project administration, Funding acquisition. JS: Writing–original draft, Methodology, Investigation, Data curation. FT: Writing–original draft, Methodology, Investigation, Data curation. PL: Writing–original draft, Methodology, Investigation, Data curation. GQ: Writing–review and editing, Writing–original draft, Supervision, Funding acquisition.

Funding

The author(s) declare that financial support was received for the research, authorship, and/or publication of this article. This work was supported by Guangxi University of Chinese Medicine (Grant No. 2022A009), and the Guangxi Administration of Traditional Chinese Medicine (Grant No. 20210174).

Conflict of interest

The authors declare that the research was conducted in the absence of any commercial or financial relationships that could be construed as a potential conflict of interest.

Publisher's note

All claims expressed in this article are solely those of the authors and do not necessarily represent those of their affiliated organizations, or those of the publisher, the editors and the reviewers. Any product that may be evaluated in this article, or claim that may be made by its manufacturer, is not guaranteed or endorsed by the publisher.

References

Chen, J. (1996) *Annals of qingshuiyan in Anxi*. Yangzhou City, China: Jiangsu Guangling Ancient Book Engraving Society, 290–291.

Chen, J., Deng, L., Gao, M., and Fang, W. (2023). A study on the technology of *Lithocarpus Litseifolius Lactobacilus* beverage. *Mod. Food* 17, 120–125. doi:10.16736/j.cnki.cn41-1434/ts.2023.17.029

Chen, Y., Yin, L. Z., Zhao, L., Shu, G., Lin, J. C., Fu, H. L., et al. (2017). Optimization of the ultrasound-assisted extraction of antioxidant phloridzin from *Lithocarpus polystachyus* Rehd. using response surface methodology. *J. Sep. Sci.* 40, 4329–4337. doi:10.1002/jssc.201700686

Chen, Y., Zeng, Y., Du, X., Mu, Z., Liao, C., and Zhang, C. (2024). Effects of compound active tea of *Lithocarpus litseifolius* on uric acid and renal function in mice with hyperuricemia nephropathy. *Chin. J. Comp. Med.* 34, 60–68. doi:10.3969/j.issn.1671-7856.2024.01.007

Chongqing Beibei District Chronicle Compilation Committee (1989) *Chongqing Beibei District Chronicle*. Scientific and Technical Documentation Press.

Fu, M. (2023) *Extraction optimization, structural characterization, and biological functions of polysaccharides from the leaves of* Lithocarpus litseifolius. Master thesis. Chengdu, China: Sichuan Agricultural University.

Huang, Y. (2021) *Preparation of* Lithocarpus olystachyrus *Rehd compound antidiabetic tablets process and quality evaluation research*. Master thesis. Nanchang, China: Jiangxi University of Chinese Medicine.

Ji, X., Hou, C., Gao, Y., Xue, Y., Yan, Y., and Guo, X. (2020). Metagenomic analysis of gut microbiota modulatory effects of jujube (*Ziziphus jujuba* Mill.) polysaccharides in a colorectal cancer mouse model. *Food and Funct.* 11, 163–173. doi:10.1039/c9fo02171j

Li, W., Wu, W., Wan, M., Li, T., Chen, S., and Yao, Y. (2022). Research progress on hypoglycemic effects of *Lithocarpus litseifolius*. *Mod. Food Sci. Technol.* 38, 292–297. 281. doi:10.13982/j.mfst.1673-9078.2022.4.0684

Li, X., Zhao, Y., Hou, S., Huang, S., Yang, W., Lai, X., et al. (2014). Identification of the bioactive components of orally administered *Lithocarpus polystachyus* Rehd and their metabolites in rats by liquid chromatography coupled to LTQ Orbitrap mass spectrometry. *J. Chromatogr. B, Anal. Technol. Biomed. Life Sci.* 962, 37–43. doi:10.1016/j.jchromb.2014.05.016

Lin, X., Wang, Q., Qin, X., Huang, S., Yan, H., Zou, S., et al. (2023). Herbalogical study on sweet tea *Lithocarpus litseifolius* (Hance) Chun. *J. Fujian Agric. For. Univ. Nat. Sci. Ed.* 52, 785–792. doi:10.13323/j.cnki.j.fafu(nat.sci.).2023.06.009

Liu, D. (2023) *The anti-ulcerative colitis activity and potential mechanism of action of sweet tea (*Lithocarpus litseifolius *[Hance] Chun)*. Master thesis. Chengdu, China: Chengdu University.

Liu, H. Y., Liu, Y., Mai, Y. H., Guo, H., He, X. Q., Xia, Y., et al. (2021a). Phenolic Content, main flavonoids, and antioxidant capacity of instant sweet tea (*Lithocarpus litseifolius* [Hance] Chun) prepared with different raw materials and drying methods. *Foods* 10, 1930. doi:10.3390/foods10081930

Liu, W. (2017) *Study on Yinduo instant health tea*. Master thesis. Changsha, China: Hunan Agricultural University.

Liu, W., Huang, W., Li, C., Liu, A., Wang, T., and Tang, T. (2020). Active components and hypoglycemic activities of the whole fermentation tea of *Lithocarpus litseifolius*. *Food Ferment. Industries* 46, 53–60. doi:10.13995/j.cnki.11-1802/ts.024248

Liu, Y., Liu, H., Xia, Y., Guo, H., He, X.-Q., Li, L., et al. (2021b). Screening and process optimization of ultrasound-assisted extraction of main antioxidants from sweet tea (*Lithocarpus litseifolius* [Hance] Chun). *Food Biosci.* 43, 101277. doi:10.1016/j.fbio.2021.101277

National Health Commission of China (2015) *National food safety standard: 90 day oral toxicity test (GB15193.13-2015)*.

National Health Commission of China (2017) *Announcement on 10 new food ingredients including Shea Butter Oil*. Announcement No. 7 of 2017).

Pan, H. M., He, C. N., Jiang, B. P., Wan, W. T., and Xu, L. J. (2015). Effect of different fractions and 5 main compounds from *Lithocarpus litseifolius* on improving HepG2 cells insulin resistance. *Cent. South Pharm.* 13, 570–574. doi:10.7539/j.issn.1672-2981.2015.06.003

Qin, H., Zhang, J., Yang, H., Yao, S., He, L., Liang, H., et al. (2020). Safety assessment of water-extract sericin from silkworm (*Bombyx mori*) cocoons using different model approaches. *BioMed Res. Int.* 2020, 9689386. doi:10.1155/2020/9689386

Wang, M., Liu, X., Zhang, Z., Yu, J., Liu, J., and Wu, Y. (2020). Phytochemicals and bioactive analysis of different sweet tea (*Lithocarpus litseifolius* [Hance] Chun) varieties. *J. Food Biochem.* 45, e13183. doi:10.1111/jfbc.13183

Wei, W. W., Wu, P., You, X. Y., Xue, J. H., and Wei, X. Y. (2020). Dihydrochalcones from the leaves of *Lithocarpus litseifolius*. *J. Asian Nat. Prod. Res.* 23, 819–824. doi:10.1080/10286020.2020.1786067

Wu, X., Li, S., Zeng, J., and Wang, Y. (2019) *The research for industrial key technologies of medicinal and edible homologous plant: using the example of* Lithocarpus litseifolius *(Hance) Chun*. Beijing: Science Press.

Zeng, X. B., Wei, B. W., Li, M., Qin, L., and Deng, Y. Y. (2010). Studies on long-term toxicity of the extract of *Lithocarpus litseifolius* in rats. *Guangxi Med. J.* 32, 1326–1329. doi:10.3969/j.issn.0253-4304.2010.11.005

frontiers | Frontiers in Pharmacology

TYPE Original Research
PUBLISHED 09 August 2024
DOI 10.3389/fphar.2024.1363139

OPEN ACCESS

EDITED BY
Yong-Long Han,
Shanghai Jiao Tong University, China

REVIEWED BY
Eddie A. James,
Benaroya Research Institute, United States
Laszlo Otvos,
Olpe LLC, United States

*CORRESPONDENCE
Anne S. De Groot,
annied@epivax.com

RECEIVED 29 December 2023
ACCEPTED 10 May 2024
PUBLISHED 09 August 2024

CITATION
Roberts BJ, Mattei AE, Howard KE, Weaver JL, Liu H, Lelias S, Martin WD, Verthelyi D, Pang E, Edwards KJ and De Groot AS (2024), Assessing the immunogenicity risk of salmon calcitonin peptide impurities using *in silico* and *in vitro* methods.
Front. Pharmacol. 15:1363139.
doi: 10.3389/fphar.2024.1363139

Assessing the immunogenicity risk of salmon calcitonin peptide impurities using *in silico* and *in vitro* methods

Brian J. Roberts[1], Aimee E. Mattei[1], Kristina E. Howard[2], James L. Weaver[2], Hao Liu[3], Sandra Lelias[1], William D. Martin[1], Daniela Verthelyi[4], Eric Pang[3], Katie J. Edwards[5] and Anne S. De Groot[1]*

[1]EpiVax Inc., Providence, RI, United States, [2]Division of Applied Regulatory Sciences, Office of Clinical Pharmacology, Office of Translational Sciences, Center for Drug Evaluation and Research, U.S. Food and Drug Administration, Silver Spring, MD, United States, [3]Division of Therapeutic Performance I, Office of Research and Standards, Office of Generic Drugs, Center for Drug Evaluation and Research, U.S. Food and Drug Administration, Silver Spring, MD, United States, [4]Division of Biotechnology Review and Research III, Office of Biotechnology Products, Office of Pharmaceutical Quality, Center for Drug Evaluation and Research, U.S. Food and Drug Administration, Silver Spring, MD, United States, [5]CUBRC, Inc., Buffalo, NY, United States

Advances in synthetic peptide synthesis have enabled rapid and cost-effective peptide drug manufacturing. For this reason, peptide drugs that were first produced using recombinant DNA (rDNA) technology are now being produced using solid- and liquid-phase peptide synthesis. While peptide synthesis has some advantages over rDNA expression methods, new peptide-related impurities that differ from the active pharmaceutical ingredient (API) may be generated during synthesis. These impurity byproducts of the original peptide sequence feature amino acid insertions, deletions, and side-chain modifications that may alter the immunogenicity risk profile of the drug product. Impurities resulting from synthesis have become the special focus of regulatory review and approval for human use, as outlined in the FDA's Center for Drug Evaluation and Research guidance document, "ANDAs for Certain Highly Purified Synthetic Peptide Drug Products That Refer to Listed Drugs of rDNA Origin," published in 2021. This case study illustrates how *in silico* and *in vitro* methods can be applied to assess the immunogenicity risk of impurities that may be present in synthetic generic versions of the salmon calcitonin (SCT) drug product. Sponsors of generic drug abbreviated new drug applications (ANDAs) should consider careful control of these impurities (for example, keeping the concentration of the immunogenic impurities below the cut-off recommended by FDA regulators). Twenty example SCT impurities were analyzed using *in silico* tools and assessed as having slightly more or less immunogenic risk potential relative to the SCT API peptide. Class II human leukocyte antigen (HLA)-binding assays provided independent confirmation that a 9-mer sequence present in the C-terminus of SCT binds promiscuously to multiple HLA DR alleles, while T-cell assays confirmed the expected T-cell responses to SCT and selected impurities. *In silico* analysis combined with *in vitro* assays that directly compare the API to each

individual impurity peptide may be a useful approach for assessing the potential immunogenic risk posed by peptide impurities that are present in generic drug products.

KEYWORDS

salmon calcitonin, peptide drug, impurity, immunogenicity, computational immunology, T-cell epitope, HLA binding, T-cell assay

Introduction

The US generic drug market was valued at 62 billion USD in 2023 and expected to increase in the future, as more generics are approved (IQVIA Institute of Human Data Science, 2027). Due to advances in synthetic peptide synthesis that allow for more rapid and cost-effective manufacturing, combined with improved analytical techniques, peptide drugs that were once manufactured by recombinant DNA technology can now be produced using solid- and liquid-phase synthesis. However, a byproduct of peptide synthesis is the generation of new peptide-related impurities. Additionally, degradation product impurities may result from factors such as formulation, storage conditions, and container closure, leading to impurities independent of the manufacturing process. The resulting impurities may have an impact on the safety and efficacy of the final drug product. In addition, contaminants, such as extractables and leachables, may also be present in the final drug formulation and may have an impact on new product degradants. This paper discusses peptide-related impurities that could be presented in the context of the human leukocyte antigen (HLA) or alter the binding of the active pharmaceutical ingredient (API) to the histocompatibility complex (MHC) and lead to a *de novo* T-cell response that could impact the immunogenicity (and safety) of the final product.

Peptide-related impurities include modifications to the API peptide that are introduced during the synthesis process due to 1) failures in peptide synthesis: amino acid insertions and duplications, amino acid deletions, and racemization; 2) contaminated raw materials leading to the incorporation of unnatural amino acids and insertion of β-amino acids; and 3) incomplete removal of protecting groups that can result in unintentional side-chain modifications. Additionally, peptide-related impurities can result from post-synthesis degradation, leading to aggregation and side-chain modifications such as oxidation and deamidation of susceptible amino acid residues. Peptide-related impurity modifications can also result in the introduction of new T-cell epitopes, not present in the API, which may induce an unwanted immune response to the impurity, causing an anti-drug immune response to occur and impacting both the safety and efficacy of the drug product.

The presence of impurities in synthetically prepared generic peptide products referencing recombinant glucagon, liraglutide, nesiritide, teriparatide, and teduglutide is addressed in the United States Food and Drug Administration (FDA) document, "*ANDAs for Certain Highly Purified Synthetic Drug Products That Refer to Listed Drugs of rDNA Origin*" (Center for Biologics Evaluation and Research CDER, 2021). Abbreviated new drug application (ANDA) refers to an approval pathway for drugs that eliminates the need to repeat clinical trials for a generic drug that is shown to be the same as an approved drug. This guidance recommends that generic drug applicants aiming to obtain ANDA approval for their generic peptides identify and describe all peptide impurities present at a concentration greater than 0.10% of the API in the final drug product and determine if these impurities are different from those found in the reference listed drug (RLD). Furthermore, ANDA applicants are recommended to assess whether any peptide impurities that are different from those in the RLD, or present at a higher concentration than found in the RLD, could increase the risk of immunogenicity of the proposed generic drug compared to that of the RLD.

Although the immunogenicity of new peptide drug products is typically assessed clinically by measuring anti-drug antibodies (ADAs) in the patient population, the immunogenicity risk potential or immunogenicity risk profile of generic peptide drugs can be informed by existing information about the RLD. Hence, under the ANDA filing pathway, a thorough characterization of the product and its impurities, including any novel HLA ligands (and potential T-cell epitopes) that may be present within the sequence of the peptide-related impurities, is recommended. Most generic peptide drug impurities can be evaluated for immunogenicity risk using *in silico* tools, and their immunogenic risk potential can also be independently assessed in parallel in *in vitro* studies (Jawa et al., 2020). A detailed description of methods that apply to all peptides is provided by De Groot et al. (2023).

In vivo, peptide drugs undergo endocytosis by antigen-presenting cells (APCs), such as dendritic cells (DCs), and are cleaved into smaller peptide fragments that are presented to helper T cells on class II HLA molecules expressed on the surface of the APC. Upon recognition of the peptide–HLA complex by the T-cell receptor, the T cells will become activated and provide the necessary stimulus for B cells to mature and produce antibodies. This is the mechanism by which peptide impurities containing new T-cell epitopes may drive unwanted immune responses. In the absence of T-helper epitopes, helper T cells fail to activate antigen-specific B-cell maturation, reducing antibody class switching and the formation of ADAs (Duke and Mitra-Kaushik, 2019; Jawa et al., 2020).

In this case study, we describe an exercise to assess the immunogenicity risk of generic peptide impurities that were identified in salmon calcitonin (SCT). SCT is a peptide drug currently under development for the generic market by several manufacturers. Salmon calcitonin is a 32-amino acid peptide drug approved in the United States for the treatment of postmenopausal osteoporosis, Paget's disease, and hypercalcemia. Salmon calcitonin shares only 50% amino acid sequence homology with human calcitonin (Figure 1), and despite its therapeutic benefits, in clinical trials, 40%–70% of patients treated with SCT develop ADAs within 4 months of treatment. While not all of these

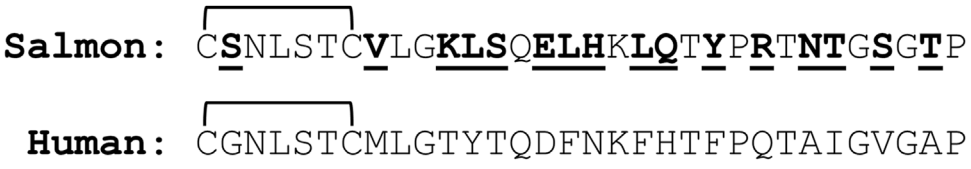

FIGURE 1
Comparison of the salmon (SCT) and human calcitonin sequences. Amino acids in SCT that are bold and underlined differ between the two forms of the peptide. The bracket connecting cysteines 1 and 7 indicates the disulfide bond that forms a ring structure in the N-terminus of the peptide (Kozono et al., 1992).

patients develop neutralizing anti-SCT antibodies (NADAs), more than 60% of those who develop ADAs do, causing them to become resistant to SCT therapy, ultimately requiring alternative forms of treatment (LEVY et al., 1988; Grauer et al., 1995).

Despite the risk of immunogenicity, SCT is preferred for therapeutic use over human calcitonin due to its 50-fold greater potency *in vivo*. Increased potency is attributed to the ability of the peptide to adopt an α-helical structure and bind to the human calcitonin receptor with a greater, and nearly irreversible, affinity relative to the human homolog (Epand et al., 1983; Lee et al., 2011; Andreassen et al., 2014).

The API in the salmon calcitonin RLD, Miacalcin®, is produced using recombinant DNA (rDNA) technology, while most generic SCT products are produced by synthetic peptide synthesis. Due to the differences in the manufacturing processes, the impurity profile of synthetically produced peptide drugs could differ from those in the RLD; thus, an assessment of the impurities that are present in the synthetic drug product is usually required for approval of the generic drug product.

While salmon calcitonin is known to induce ADA production *in vivo*, less is known about the T-cell response to the peptide. In a previous study, Tangri et al. (2005) identified a region located within the center of SCT, GKLSQELHKLQTYPRT, that contains a T-cell epitope shown to bind to HLA DRB1*0101 and *0401. It is important to note that this epitope resides within a region of SCT that differs from human calcitonin by 10 of the 16 amino acids. This 9-mer frame (frame 16 in Figure 2) is contained near regions previously identified as T- and B-cell epitopes by Tangri and Kozono, respectively (Kozono et al., 1992; Tangri et al., 2005), although the two types of epitopes do not overlap with the N-terminal region.

To assess the utility of *in silico* and *in vitro* immunogenicity risk screening tools for the evaluation of peptide drug impurities, the FDA Center for Drug Evaluation and Research (CDER) provided EpiVax with a list of 20 peptide-related salmon calcitonin impurities identified as byproducts of synthetic salmon calcitonin synthesis or degradation under FDA contract HHSF223018186C. The immunogenicity risk was assessed utilizing three independent (orthogonal) methods: *in silico* analysis, class II HLA binding assays, and naïve T-cell assays (De Groot et al., 2023). The *in silico* analysis indicated that immune responses to SCT are likely to be related to the presence of a 9-mer binding frame, which is not conserved with any human protein and contains a promiscuous HLA DR-binding T-cell epitope. This 9-mer frame overlaps with the epitopes previously identified by Kozono et al. (1992) and Tangri et al. (2005). The selected SCT impurities were compared to the API, and an *in silico* assessment was performed to identify new (putative) T-cell epitopes in the impurity sequences.

In vitro HLA-binding and T-cell assays were used to determine whether any of the 20 impurities had the potential to be immunogenic. One key finding reported here is that, consistent with the high incidence of ADAs in the patients treated with SCT, the API peptide elicited naïve T-cell responses from multiple donors, *in vitro*, on its own. Also consistent with the *in silico* analysis, the number of donor peripheral blood mononuclear cell (PBMC) samples responding to the peptide impurities was increased, when compared to donor PBMC sample responses to the SCT API peptide, in the naïve CD4 T-cell assays.

Taken together, the results indicate that the *in vitro* class II HLA binding and T-cell assays that were performed using the API peptide and selected impurities were generally aligned with the *in silico* risk assessments of the same sequences, suggesting that this approach of combining *in silico* and *in vitro* evaluation methods is useful for evaluating the immunogenicity risk of peptide impurities, as recommended in the FDA guidance document, "*ANDAs for Certain Highly Purified Synthetic Drug Products That Refer to Listed Drugs of rDNA Origin*."

Material and methods

Bioinformatics analysis screening of salmon calcitonin and impurities

A wide range of tools have been developed and applied to therapeutic proteins and peptides for identifying T-cell epitopes. Here, we describe the application of tools developed by EpiVax; however, alternative *in silico* tools can be used to achieve similar results (Supplementary Table S1). First, the SCT API and impurities were evaluated for immunogenic potential using the EpiMatrix T-cell epitope-mapping and JanusMatrix human homology algorithms (De Groot et al., 2003; Moise et al., 2013). In some instances, impurity sequences contained unnatural or otherwise modified amino acid residues. The HLA-binding properties of peptides containing chemically modified or unnatural amino acids could not be directly estimated by the EpiMatrix system. In those instances, a three-step approach was applied to identify potential natural amino acid substitutions, enabling existing *in silico* tools to assess potential HLA binding. The three-step approach to the *in silico* analysis of sequences containing unnatural amino acids is described in detail in a recent publication (Mattei et al., 2022).

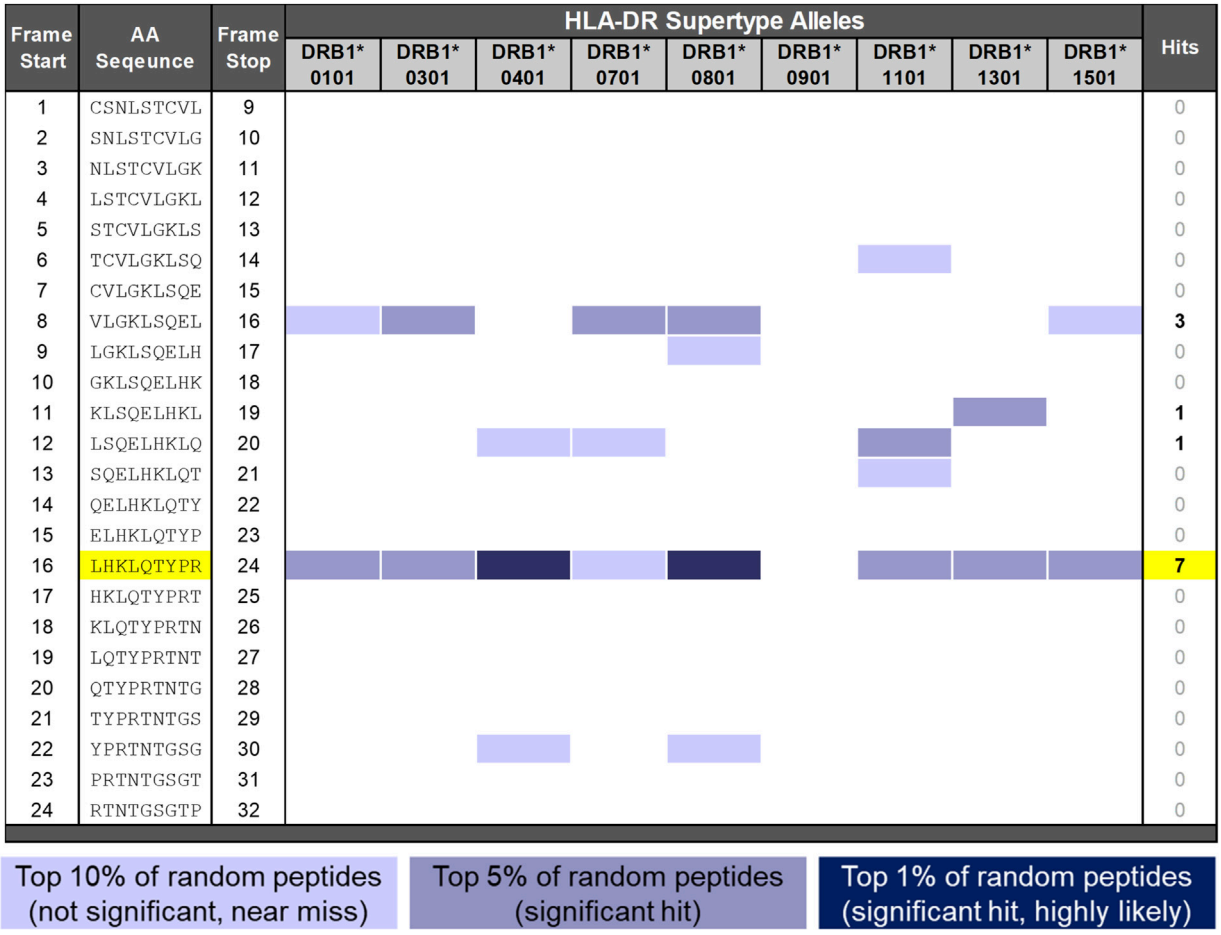

FIGURE 2
EpiMatrix analysis of SCT. The potential of a 9-mer frame to bind to a given human leukocyte antigen (HLA) allele is indicated by a Z-score (scores omitted for simplicity); the strength of the score is indicated by the blue shading. All scores in the top 5% of the normal distribution are considered "hits" (medium- and dark-blue shading). Scores in the top 10% are considered elevated but not significant (light blue shading). Frames containing four or more alleles scoring in the top 5% and above are referred to as EpiBars and are highlighted in yellow. These frames have an increased likelihood of binding to a range of HLA alleles. The 9-mer epitope bar highlighted in yellow is a putative promiscuous epitope.

Using EpiMatrix to search for T-cell epitopes, the SCT API and 20 impurity sequences were parsed into overlapping 9-mer frames, where each frame was evaluated for potential binding to a panel of 9 HLA DR supertype alleles (HLA-DRB1*0101, *0301, *0401, *0701, *0801, *0901, *1101, *1301, and *1501) for binding likelihood. Taken together, these nine supertype alleles, along with their respective family members, cover greater than 95% of HLA types present in most human population groups (Southwood et al., 1998; Mattei et al., 2024). The method used to identify and calculate the HLA DR coverage described above is described in detail in Drug Discovery Today by De Groot et al. (2023). HLA DR is selected for the *in silico* analysis of adaptive T-cell response as it has consistently been the most prevalent HLA allele associated with the immunogenicity of biologic products (Hyun et al., 2021; Ramarathinam and Purcell, 2021). Summing across the collective 9-mer frames by HLA DR allele assessments, an EpiMatrix Peptide Immunogenicity Score can be obtained. This score is a measure of the predicted T-cell epitope content contained within the peptide (Moise et al., 2015). While the overall score provides a measurement of the global immunogenic potential, it is also important to assess the peptides for regional immunogenic potentials, specifically for the presence of promiscuous T-cell epitopes. Regional analysis using the HLA DR supertypes in EpiMatrix sometimes reveals an Epitope Bar (EpiBar) feature, which refers to a single 9-mer frame likely to bind at least four different HLA DR supertype alleles. In general, it is expected that these promiscuous class II HLA ligands are the most likely regions of a given peptide or protein to induce $CD4^+$ T-cell response.

Next, to identify specific homologies with human proteome T-cell epitopes that may reduce immunogenic potentials, an algorithm called JanusMatrix was used to analyze the impurity sequence epitopes. For any of the putative T-cell epitopes identified in the API and its impurities, the JanusMatrix algorithm identified cross-conserved T-cell epitopes with the same HLA restriction, which are present in the human proteome (thus immunologically related to but not necessarily identical to the input peptide). T-cell epitopes, which are extensively conserved with other peptides in common human proteins, as defined using JanusMatrix, are more likely to be tolerated and may even be tolerogenic in healthy human subjects (Moise et al., 2013; De

Groot et al., 2021; 2023). The immunoinformatics tools used in the evaluation of generic drug peptides and their impurities are discussed by De Groot et al. (2023).

Once the *in silico* identification of putative HLA ligands and their conservation within the human proteome were assessed, the next step of the analysis is to compare the API sequence to the impurities to quantify the number of putative new T-cell epitopes present in the impurity sequences, but not the API sequence. In some cases, the modified amino acid sequences of product impurities may include amino acid patterns that are capable of binding to HLA molecules where the unmodified amino acid sequence may not bind. In other cases, modifications may alter the TCR-facing contours of HLA ligands already present in the amino acid sequence of the unmodified product. These modifications often affect serial frames in the sequence. In these instances, all of the newly created epitopes, whether sequential HLA-binding epitopes or sequential T-cell receptor (TCR)-facing epitopes, are considered to be "new epitopes" that can contribute to the potential immunogenicity of the impurity. Modification of the epitope sequence can also "twist" the peptide configuration in the MHC-binding groove, leading to changes in the TCR-facing residues that may impact immunogenicity as well (Singh et al., 2020).

Selecting salmon calcitonin and impurity peptides for *in vitro* assays

The 20 impurity peptides used in these studies were selected from a survey of SCT impurities that were identified in commercially available nasal salmon calcitonin products and provided by the Office of Generic Drugs (OGD, within the CDER, at the FDA). A detailed list of the 20 impurities is provided in Supplementary Table S2. Of the 20 impurities evaluated *in silico*, a smaller subset was selected for evaluation in independent *in vitro* assays. Each of the impurities contained a single modification relative to the salmon calcitonin baseline sequence.

Peptides for HLA-binding assays

SCT impurities that featured modifications to putative HLA-binding residues were selected for *in vitro* HLA DRB1-binding assays. This method was used to assess the impact of the modification on the HLA binding affinity, relative to the baseline. Since most class II HLA-binding peptides range in length from 12 to 25 amino acids, and longer peptides may interfere with HLA binding, shorter versions of the impurity peptides were designed, featuring the HLA-binding region centered in the middle of the synthesized peptide.

Peptides for *in vitro* immunogenicity protocol naïve T-cell assays

SCT impurities featuring TCR-facing residue modifications and alterations in the overall number of T-cell epitopes as compared to the API were tested using T-cell assays. This method was used to assess the impact of the modification on T-cell responses, relative to baseline. Full-length peptides (both API and impurities) were evaluated in the T-cell assays.

Impurity peptides were synthesized by 21st Century Biochemicals (Marlborough, MA). Their molecular weight was verified by mass spectrometry, and all peptides were determined to have a purity of higher than 95% by high-performance liquid chromatography (HPLC). The synthetic salmon calcitonin API peptide was provided by the Office of Generic Drugs. Miacalcin® was purchased from Pharmaceutical Buyers Inc. (New Hyde Park, NY).

Class II HLA binding assays

The class II HLA binding assays performed for these studies measure the binding affinity of a target peptide to HLA DRB1*0101, *0301, *0401, *0701, *0901, *1101, *1301, and *1501 in a standardized competition assay. This assay was originally described by Steere et al. (2006) and adapted by EpiVax. Previous publications have described the assay in detail (McMurry et al., 2007; Ardito et al., 2011). Briefly, unlabeled test peptides are incubated overnight to equilibrium with a soluble HLA DR molecule (Benaroya Research Institute, Seattle, Washington) and a biotinylated, allele-specific competitor peptide. The binding reaction is then neutralized, and peptide–HLA complexes are transferred to a 96-well plate coated with the pan-HLA DR antibody, clone L243 (BioLegend), and incubated overnight. The following day, Europium-labeled streptavidin (PerkinElmer, Waltham, MA) is added to identify the peptide–HLA complexes. An indirect measure of binding is determined by time-resolved fluorescence. Each peptide–HLA binding reaction is evaluated in triplicate over a range of seven concentrations. The percent inhibition values at seven distinct concentrations are used to calculate the IC_{50} value, defined as the concentration at which the test peptide inhibits 50% of the labeled competitor peptide.

Peptides that bind to the HLA at an IC_{50} value of 100 nM or less are considered very high-affinity binders. Peptides that bind at IC_{50} values ranging from 100 nM to 1,000 nM are considered high-affinity binders. Peptides that bind at IC_{50} values ranging from 1,000 nM to 10,000 nM are considered moderate-affinity binders. Peptides that bind at IC_{50} values ranging from 10,000 nM to 100,000 nM are considered low-affinity binders, and those with IC_{50} values ranging from 100,000 nM to 1,000,000 nM are considered negligible-affinity binders. Peptides that bind at IC_{50} values greater than 1,000,000 nM and those that do not exhibit dose-dependent inhibition of the competitor peptide are considered non-binders. We note that these concentrations are specific for the *in vitro* HLA-binding assay and are used to compare the relative binding affinities of the impurity sequences to the API and independent from the peptide concentrations described for the *in vitro* T-cell assays described below. A more detailed description of this assay, as used for generic peptide studies, and references to other comparable approaches is provided in Drug Discovery Today by De Groot et al. (2023).

Human peripheral blood mononuclear cells

To improve the sensitivity of the T-cell assays, fresh (not frozen) blood samples were obtained from human blood donors for the T-cell assays (internal observations). Specifically, PBMCs were isolated from leukocyte reduction filters obtained from the

Rhode Island Blood Center (RIBC) in Providence, RI. To confirm the sufficient breadth of HLA coverage in the donor cohort, high-resolution (4-digit) class II HLA haplotyping of donors was performed at the Transplant Immunology Laboratory at Hartford Hospital in Hartford, CT, using the sequence-specific oligonucleotide method (SSP-PCR). Five supertype alleles were expressed by the donor PBMCs used in the assays reported here (HLA DRB1*0301, *0401, *0701, *1101, *1301, and *1501). The HLA identified for the cohort of subjects used in this study is representative of 81.81% of the HLA alleles expressed by the global population. Forty percent of the donors were female and 60% of the donors were male, and their ages ranged from 17 to 83 years. Donor cohort demographic information and HLA types for each donor are provided in Supplementary Figure S1.

In vitro immunogenicity protocol

To measure the naïve T-cell response to salmon calcitonin and impurity peptides, cells were plated at a density of 2.5×10^5 cells per well in 96-well U-bottom cell plates in RPMI 1640 cell culture medium supplemented with IL-2 (10 ng/mL) and IL-7 (20 ng/mL) (Gibco). The cells were incubated with Miacalcin®, or a synthetic salmon calcitonin peptide, or individual peptide impurities, at a concentration of 20 µg/mL for 14 days at 37°C/5% CO_2, with medium exchanges that include cytokine support (IL-2 and IL-7) on days 4, 7, and 11. A concentration of 20 µg/mL (5.8 µM) was the dose selected for the SCT API and the four selected impurities, following a dose-ranging study performed with Miacalcin® to determine the maximum dose at which a T-cell response could be observed with no observed toxicity to the cells. The dose-ranging study was performed following the same protocol as described above.

The following control antigens were used in the T-cell assays for each of the PBMC samples: positive controls, keyhole limpet hemocyanin (KLH; Thermo Fisher), and the antigenic peptide pool CEFT (ImmunoSpot). In addition, human serum albumin (HSA; Sigma-Aldrich) was used as a negative control antigen, and phytohemagglutinin (PHA; Thermo Fisher), a T-cell mitogen, was used to confirm T-cell functionality. Donors for which a positive response to KLH, CEFT, and PHA and a negative response to HSA were observed were included in the final data compilation; donors that did not respond as expected to the control antigens were excluded. Responses were considered positive if (1) the number of spots was at least twice the background (stimulation index [SI] ≥ 2); (2) there were greater than 50 spot-forming cells (SFCs) per 1.0×10^6 PBMCs; and (3) responses were statistically different from the media (Student's *t*-test). Each of the test articles (SCT API, RLD, or impurity peptide) and each of the positive and negative controls were evaluated in nine replicate wells containing donor PBMCs.

FluoroSpot assay

Following the 14-day incubation, cells in the nine replicate wells were collected, pooled by the treatment condition, and re-plated in triplicate on a precoated anti-human IFNγ FluoroSpot plate (Mabtech) at a concentration of 1.0×10^5 cells per well in the presence of an appropriate test article or control reagent in supplemented RPMI 1640 culture medium. The FluoroSpot plates were incubated for 48 h at 37°C/5% CO_2. After 48 h, FluoroSpot plates were developed according to the manufacturer's directions. Spots were counted on an iSpot Spectrum FluoroSpot reading system (AID, Strassberg, Germany) using software 7.0, build 14790. Fluorophore-specific spot parameters were defined using the spot size, spot intensity, and spot gradient. A spot separation algorithm was applied for optimal spot detection. Analysis and counting of spots were performed by unbiased experts at ZellNet Consulting, Inc. (Fort Lee, NJ).

The IFNγ cytokine was selected as the biomarker for this assay. This cytokine supports the proliferation of early activated T cells and can induce Bcl-6 expression to drive follicular T-helper cell differentiation (Sweet et al., 2012). Bcl-6 is the signature transcription factor of follicular T-helper cells that are pivotal to promoting B-cell differentiation into high-affinity antibody-producing plasma cells and memory B cells. IFNγ also supports antigen presentation to CD4 T cells by increasing the quantity of peptide–HLA class II complexes on the surface of antigen-presenting cells through upregulated production of the HLA complex itself, the invariant chain, lysosomal proteases implicated in the peptide production for MHC loading (cathepsins B, H, and L), DMA and DMB (which remove CLIP from the class II HLA–peptide-binding cleft to make it available for peptide loading), and class II transactivator, a key transcription factor for the regulation of expression of genes involved in the class II HLA complex (Figueiredo et al., 1989; Chang and Flavell, 1995; Laha et al., 1995).

Results

In silico results

In silico analysis of the salmon calcitonin API sequence

SCT features an N-terminal 7-amino acid ring structure held in place by a disulfide bond between the cysteine in position 1 and the cysteine in position 7. As noted previously, HLA molecules bind to linear peptides. Before potential T-cell epitopes can bind to HLA molecules, secondary and tertiary peptide structures must be degraded. In this case, the disulfide bond between positions 1 and 7 may be reduced by gamma-interferon-inducible lysosomal thiol (GILT) reductase in the endocytic compartment (Hastings, 2013). For the purposes of *in silico* analysis, the disulfide bond was ignored, and the fully linearized sequence was analyzed. However, we note that the presence of disulfide bonds has been shown to impact human T-cell recognition (Mannering et al., 2005). Furthermore, the C-terminus of the SCT peptide is amidated in the drug product. This feature is not expected to impact the interaction between the peptide side chains of the SCT molecule and the binding pockets of any HLA molecule. Therefore, this feature was not considered in the *in silico* analysis.

A detailed *in silico* analysis of the salmon calcitonin API sequence as performed by EpiMatrix is shown in Figure 2 (see

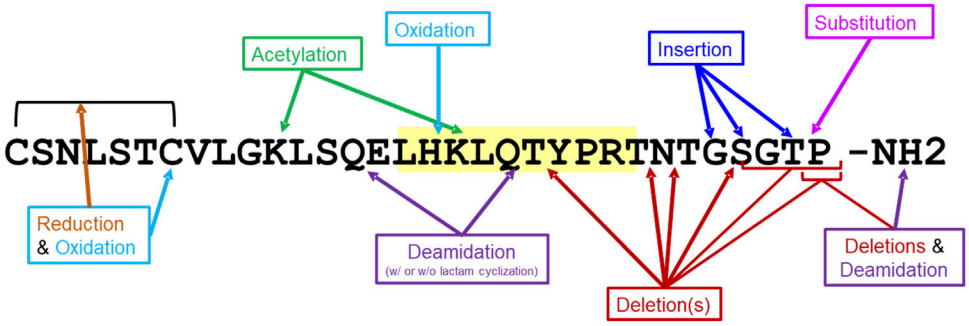

FIGURE 3
Impurity modifications on salmon calcitonin sequence. Twenty salmon calcitonin impurity peptides were analyzed for immunogenic potential *in silico*. The modifications to the salmon calcitonin active pharmaceutical ingredient (API) sequence are shown. The frame 16 promiscuous T-cell epitope is highlighted in yellow.

the figure legend for details on the interpretation of the assessment). As shown in the figure, the salmon calcitonin API sequence contains 12 predicted HLA DR ligands defined by EpiMatrix, which is slightly more than would be expected in a random peptide sequence of equivalent length. Seven of the 12 EpiMatrix-defined ligands are found within a single 9-mer frame of the SCT sequence located in frame 16. This feature indicates that the frame may serve as a promiscuous T-cell epitope and is likely to be immunogenic, especially as it contains relatively high-scoring HLA ligands, as defined using EpiMatrix. When considered in isolation, the frame 16 EpiBar has an EpiMatrix score of 14.26, which further indicates a high potential for immunogenicity, similar to other immunogenic T-cell epitope sequences. Additional EpiMatrix-defined ligands that may also be immunogenic are located in frames 8, 11, and 12—these sequences may be true ligands, but their effects may be HLA-restricted.

The JanusMatrix algorithm was then applied to the putative T-cell epitopes to estimate the cross-conservation of the epitopes with similar HLA-binding epitopes found in the human proteome. The salmon calcitonin API peptide has a low Human Homology Score (0.92), indicating that the putative epitopes found within the sequence are relatively unique to salmon calcitonin when compared to the human proteome.

To summarize the *in silico* results for the SCT API peptide, it contains slightly more epitopes than would be expected in a randomly generated peptide sequence of similar length, as identified using EpiMatrix. Considering its foreign origin, low JanusMatrix Human Homology Score, and the presence of multiple putative HLA ligands, the potential of the SCT API to drive a T-cell-dependent immune response was found to be slightly above average. Furthermore, the promiscuous T-cell epitope in frame 16 and the EpiMatrix-defined HLA ligands present in frames 8, 11, and 12 were considered likely to be contributing factors to the development of the anti-SCT immune response.

In silico analysis of SCT impurities

The 20 salmon calcitonin impurity sequences (Supplementary Table S2) were analyzed for T-cell-dependent immunogenic potential using EpiMatrix and JanusMatrix, as was described above for the SCT API. These 20 sequences include impurities that result from amino acid deletions and insertions, oxidation, acetylation, deamidation, and substitution (Figure 3). In addition to EpiMatrix and JanusMatrix analyses, these 20 peptide-related impurity sequences were also analyzed for new T-cell epitope content compared to the SCT API sequence.

The EpiMatrix immunogenicity scores of the submitted impurity sequences fall within the upper neutral range on the peptide immunogenicity scale, but above the score for most human proteins (including the human proteome and secretome), indicating potential for immunogenicity. The impurity scores were not significantly different from the EpiMatrix score of the SCT API across the 20 peptide-related impurities. In addition, a JanusMatrix analysis of the impurity sequences demonstrated scores ranging from 0.13 to 1.44. Like the parent API sequence, these lower JanusMatrix scores suggest limited potential for homology-induced tolerance. Relative to the SCT API, some of the impurity modifications create new epitopes. It was hypothesized that these new epitopes would be the most likely drivers of any potential impurity-induced immune responses.

The results of the *in silico* analysis of the SCT API and 20 related impurities are shown in an immunogenicity quadrant plot (Figure 4). This figure shows that peptides and their impurities can be classified into one of four quadrants defined as putative T-cell epitope-dense or epitope-sparse, more common in human proteins and less common in human proteins. Immunogenic (vaccine epitope) and tolerogenic (Treg epitope) peptides are included as examples or "control" peptides in the relevant quadrants.

Salmon calcitonin and its impurities fall into the "Epitope Sparse, Less Common in Human Proteins" quadrant. Peptides in this quadrant still carry some risk of immunogenicity, particularly peptides containing foreign T-cell epitopes like salmon calcitonin and most of the analyzed impurity sequences. The overall score of the promiscuous T-cell epitope in the peptide (see SCT EpiBar, in Figure 4) is much higher and more foreign than that of most generic peptides. Thus, much of the observed immunogenicity to SCT is attributed to foreign epitopes within the API sequence.

Class II HLA binding studies

To determine the impact of modifications to HLA-facing amino acid residues on HLA binding, 3 of the 20 identified

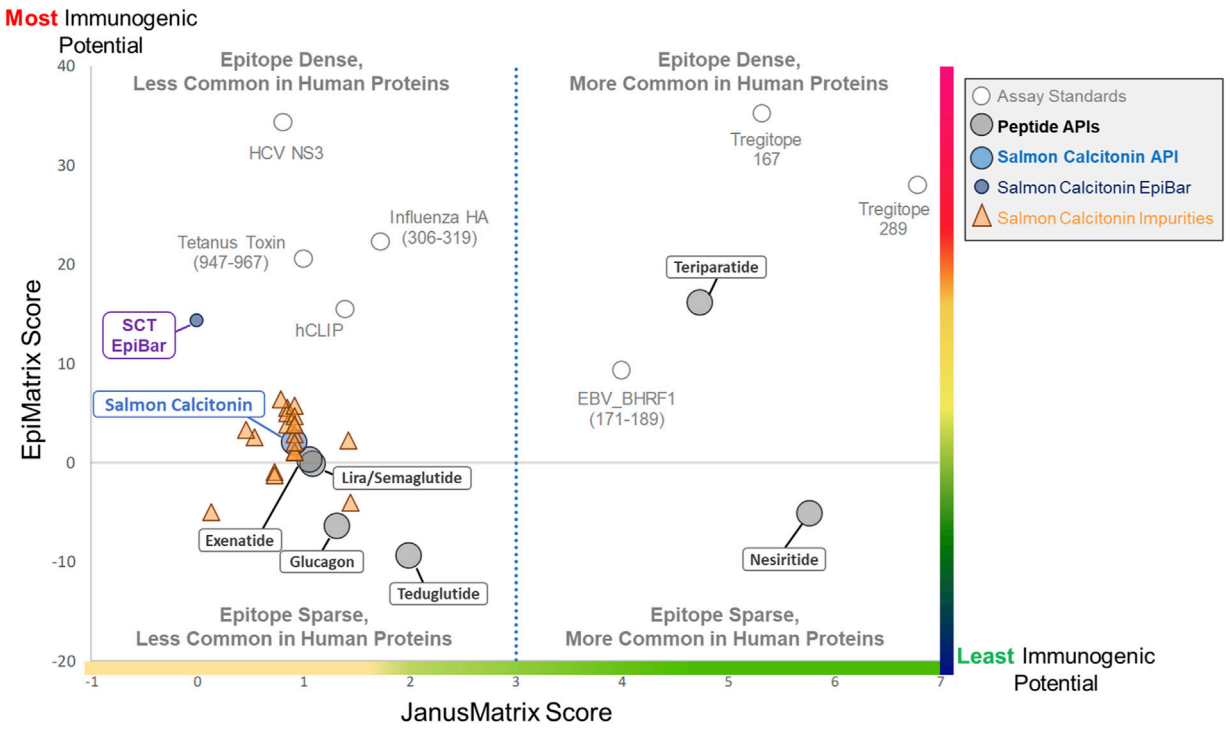

FIGURE 4
Immunogenicity quadrant plot. Immunogenicity quadrant analysis categorizes peptides and impurities by their immunogenicity risk. EpiMatrix (EMX) and JanusMatrix (JMX) human homology scores are plotted for each peptide and impurity. The graph is divided into four quadrants based on epitope content and human cross-conservation. Peptides and impurities that fall into the epitope-dense, less common in the human proteins quadrant are likely to induce an immune response, while peptides and impurities that fall into the epitope-sparse, more common in human proteins quadrant are considered a lower risk for inducing an immune response. Full-length salmon calcitonin scores above the expectation for a random peptide sequence (gray line), along with the full-length SCT impurities, falls into the epitope-sparse, less common in human proteins quadrant, which still carries some risk of immunogenicity. When assessed in isolation, the salmon calcitonin EpiBar falls into the epitope-dense, less common in human proteins quadrant. The EpiMatrix and JanusMatrix scores of several "benchmark" peptides are included to aid in the interpretation of relative risk.

impurities, LYS-AC11 (acetylation of lysine 11), DES-THR21 (deletion of threonine 21), and DES-ASN26 (deletion of asparagine 26), were selected for *in vitro* validation in the class II HLA-binding assay (Table 1). These three impurities were selected based on the *in silico* analysis for modifications to HLA-facing residues of the predicted epitopes. For the *in vitro* HLA-binding assays, the salmon calcitonin API was divided into N- and C-terminal peptides, which permitted a more accurate evaluation of the impact of the impurity modifications on HLA binding relative to the corresponding region of the API peptide as longer peptides tend to take on secondary structures *in vitro*, which may interfere with accurate binding assessments. These shorter versions of the API and impurity peptides were evaluated for their ability to bind to a panel of eight class II HLA DRB1 supertype alleles (Southwood et al., 1998), namely, HLA DRB1*0101, *0301, *0401, *0701, *0901, *1101, *1301, and *1501.

These two API and three SCT impurity peptides (LYS-AC11_SCT, DES-THR21_SCT, and DES-ASN26_SCT) were evaluated for binding in HLA-binding assays (Table 1). As previously mentioned, these impurities had been selected for binding assays because of observed modifications to HLA-facing residues, suggesting that they may bind differently from the API, impacting the T-cell response. The N-terminal API peptide serves as the HLA-binding control for the LYS-AC11_SCT impurity, whereas the C-terminal API peptide provides the baseline HLA-binding control for impurities DES-THR21_SCT and DES-ASN26_SCT. The results of the HLA-binding assays for the SCT C- and N- terminal peptides were generally aligned with the results of the *in silico* analysis of salmon calcitonin. For example, the N-terminus of SCT, which shares the greatest sequence homology with human calcitonin and contains limited T-cell epitope content compared to the C-terminus, did not bind to HLA DR with high affinity, which is consistent with the *in silico* analysis result. As expected, the N-terminal peptide STSVLGKLSQELHKLQTY bound to supertype allele HLA DRB1*1101 with negligible affinity (IC_{50} = 104,638 nM) and to alleles HLA DR*0101 (IC_{50} = 11,134 nM) and *1501 (IC_{50} = 95,929 nM) with weak affinity (Figure 5). These results indicate that the N-terminus of SCT is not expected to contribute to the immunogenicity of SCT due to minimal T-cell epitope content and its weak binding profile in these assays.

In contrast, the C-terminal salmon calcitonin API peptide, SQELHKLQTYPRTNT, containing the majority of the putative foreign T-cell epitopes, bound five of the eight HLA alleles evaluated in these assays. These results align with the *in silico* identification of a C-terminal EpiBar and with the results published by Kozono et al. (1992) and Tangri et al. (2005). The C-terminal peptide bound with moderate affinity to DRB1*0101 (IC_{50} = 3,348), *1301 (IC_{50} = 8,742), and *1501 (IC_{50} = 2,291) and to

TABLE 1 Sequence of salmon calcitonin and selected impurities evaluated in the class II human leukocyte antigen (HLA)-binding assay.

Peptide name	HLA-binding assay peptide sequence	EMX hits	EMX score	JMX score
API: salmon calcitonin	*N-term:* STSVLGKLSQELHKLQTY	12	1.99	0.92
	C-term: SQELHKLQTYPRTNT			
IMP: LYS-AC11_SCT	STSVLG (Ac – K)LSQELHKL	13	5.55	0.85
IMP: DES-THR21_SCT	SQELHKLQ–YPRTNTGSGT	9	−4.06	1.44
IMP: DES-ASN26_SCT	HKLQTYPRT–TGSGT	14	6.38	0.79

Short peptides compatible with the HLA-binding assay were designed to center the predicted epitope content for the API and three impurities. Note that in peptides synthesized for the HLA-binding assays, the cysteine in position 7 was replaced with serine (shown in blue) with no predicted impact on binding relative to the native peptide. This substitution was made to prevent the formation of aggregates due to disulfide bond formation between cysteines in the peptides. EpiMatrix (EMX) hits are the number of predicted HLA ligands in the full-length sequence. The EpiMatrix (EMX) score indicates the score for the full-length sequence. JanusMatrix (JMX) homology scores indicate the average depth of epitope cross-conservation with the human proteome. For a foreign peptide, JMX scores above 2.00 are considered to have an elevated potential for homology-induced tolerance. Residues in red indicate differences in the impurity sequence as compared to the API; for the deletion impurities (DES) a red (-) represents the deleted amino acid.

DRB1*0301 with weak affinity (IC_{50} = 66,416). It bound with negligible affinity to DRB1*1101 (IC_{50} = 161,114) (Figure 5).

Results of impurity peptide binding studies

LYS-AC11_SCT

LYS-AC11_SCT is an N-terminal SCT impurity, where the lysine in position 11 is acetylated relative to the baseline sequence. The sequence of this impurity peptide is STSVLG (Ac-K)LSQELHKL. The *in silico* analysis was aligned with the following results: LYS-AC11_SCT bound with weak affinity to the DRB1*0101 allele (IC_{50} = 12,306 nM) and to the DRB1*1501 allele (IC_{50} = 12,774 nM). Compared to the N-terminal API peptide, binding was nearly equivalent for DRB1*0101. LYS-AC11_SCT showed increased affinity for the DRB1*1501 allele. Similar to the API control peptide, LYS-AC11_SCT is a non-binder to DRB1*0301, *0401, *0701, *0901, and *1301. Relative to the SCT API peptide, a loss of binding to DRB1*1101 was observed for LYS-AC11_SCT. Consistent with our expectations based on the *in silico* analysis, LYS-AC11_SCT exhibited an increase in binding affinity to the DRB1*1501 allele, and no change in binding was observed for DRB1*0101 and *0901. In contrast to what we expected from the *in silico* analysis, no change in binding affinity was observed for alleles HLA DRB1*0301, *0401, *0701, *1101, and *1301.

DES-THR21_SCT

DES-THR21_SCT is a C-terminal SCT impurity, where the threonine in position 21 is deleted relative to the baseline sequence. The sequence of this impurity peptide is SQELHKLQ–YPRTNTGSGT. *In silico* analysis was aligned with *in vitro* observations: EpiMatrix analysis indicated that the SQELHKLQ–YPRTNTGSGT would no longer bind to the DRB1*0301, *0401, and *1301 alleles *in vitro*. Consistent with the *in silico* assessment results, DES-THR21_SCT did not bind to any of these three alleles. Further in alignment with the *in silico* analysis, DES–THR21_SCT bound to both DRB1*0101 (IC_{50} = 14,771 nM) and *1501 (IC_{50} = 178,709 nM) with reduced affinity as compared to the C-terminal API peptide. Consistent with the *in silico* analysis results, DES-THR21 showed decreased affinity to HLA DRB1*1301, and no change in binding was observed for alleles DRB1*0101, *0301, *0401, *0901, and *1501. Contrary to the *in silico* analysis, no change in binding affinity was observed for HLA DRB1*0701, and a decrease in binding affinity was observed for HLA DRB1*1101.

DES-ASN26_SCT

DES-ASN26_SCT is a C-terminal SCT impurity, where the asparagine in position 26 is deleted relative to the baseline sequence. The sequence of this impurity peptide is HKLQTYPRT–TGSGT. This amino acid deletion is located outside of the frame 16 EpiBar, in a region of the peptide where minimal epitope content was identified *in silico*. Relative to the SCT C-terminal API peptide, the DES-ASN26_SCT impurity was expected to show a loss of binding to DRB1*0401 but to gain affinity to DRB1*1301. This impurity peptide bound with negligible affinity to DRB1*1101 (IC_{50} = 308,378 nM) and with moderate affinity to DRB1*1501 (IC_{50} = 9,789 nM). Consistent with the *in silico* assessment, no binding was observed based on the *in silico* analysis, no binding was observed for alleles HLA DRB1*0101, *0301, *0401, and *0901, and binding affinity was decreased for DRB1*1101. In contrast to our assumptions based on the *in silico* analysis, there was no change in binding affinity to HLA DRB1*0701 and *1501.

Evaluation of salmon calcitonin and impurities in *in vitro* naive T-cell assays

To evaluate the impact of peptide impurities present within the generic SCT product on its overall immunogenic potential, two separate approaches were employed. In the first study, the SCT API and several individual peptide impurities were evaluated at equivalent concentrations in *in vitro* T-cell assays to determine their individual immunogenic risk potential (n = 16 donors). In the second study, the RLD product, Miacalcin®, was spiked with individual impurities equal to the observed abundances identified in the generic SCT product, and the combination was tested in T-cell assays. The drug product assay was designed to estimate the ability of the impurities to increase the immunogenic potential relative to the drug product alone (n = 20 donors).

10.3389/fphar.2024.1363139

A

B

	Peptide	DRB1*0101	DRB1*0301	DRB1*0401	DRB1*0701	DRB1*0901	DRB1*1101	DRB1*1301	DRB1*1501
N-terminus	API SCT(5-22)	11,134	Non-Binder	Non-Binder	Non-Binder	Non-Binder	104,638	Non-Binder	95,929
	LYS-AC11_SCT(5-19)	12,306	Non-Binder	Non-Binder	Non-Binder	Non-Binder	Non-Binder ↓	Non-Binder	12,774 ↑
C-terminus	API SCT(13-27)	3,348	66,416	Non-Binder	Non-Binder	Non-Binder	161,114	8,724	2,291
	DES-THR21_SCT(13-27)	14,771 ↓	Non-Binder ↓	Non-Binder	Non-Binder	Non-Binder	Non-Binder ↓	Non-Binder ↓	187,709 ↓
	DES-ASN26_SCT(17-31)	Non-Binder ↓	Non-Binder ↓	Non-Binder	Non-Binder	Non-Binder	308,378 ↓	Non-Binder ↓	9,798 ↓

FIGURE 5
Results of the class II HLA-binding assay. **(A)** Results of a typical assay shown for the C-terminal API SCT (13–27) peptide. The orange bar on each graph denotes the maximum fluorescence value (no inhibition). **(B)** Summary of the binding results for the three impurities listed in Table 1. Top half of the table: results for the N-terminal SCT API peptide and its impurity. Bottom half of the table: the C-terminal peptide and its two impurities. Green-shaded box: binding results align with *in silico* analysis results; no change in binding was expected or observed. ↓Blue arrows: binding is decreased, consistent with *in silico* assessment results. ↑Red arrows: binding is increased, consistent with *in silico* assessment results. Gray-shaded box: Binding diverges from *in silico* assessment.

Four SCT impurities were selected for validation using T-cell assays based on changes to TCR-facing residues as these were expected to modify the immunogenic potential of each peptide relative to the API *in vitro*: LYS-AC18 (acetylation of lysine 18), Q20E_SCT (glutamine in position 20 is deamidated to form glutamic acid), ENDO-GLY28 (insertion of glycine at position

TABLE 2 Peptides evaluated using T-cell assays.

Peptide name	HLA-binding assay peptide sequence	EMX hits	EMX score	JMX score	Relative abundance (% of API)
API: salmon calcitonin	CSNLSTCVLGKLSQELHKLQTYPRTNTGSGTP	12	1.99	0.92	n/a
IMP: LYS-AC18_SCT	CSNLSTCVLGKLSQELH(Ac – K)LQTYPRTNTGSGTP	13	3.33	0.46	0.24%
IMP: Q20E_SCT	CSNLSTCVLGKLSQELHKLETYPRTNTGSGTP	11	−0.92	0.73	0.36%
IMP: ENDO-GLY28_SCT	CSNLSTCVLGKLSQELHKLQTYPRTNTGGSGTP	12	1.06	0.92	2.62%
IMP: ENDO-THR31_SCT	CSNLSTCVLGKLSQELHKLQTYPRTNTGSGTTP	12	1.06	0.92	3.30%

Peptides were selected based on changes to the TCR-facing residues of the predicted epitopes. The observed relative abundance of the impurities was provided as the percentage of the API by the FDA. Amino acid modifications to the impurity peptides are in red. Full-length peptides synthesized for the IVIP T-cell assays contain a disulfide bond between the cysteines in positions 1 and 7, forming the N-terminal ring structure present in the native salmon calcitonin peptide. API, active pharmaceutical ingredient; IMP, abbreviate impurity. EpiMatrix (EMX) hits are the number of predicted HLA ligands in the full-length sequence. JanusMatrix (JMX) homology scores indicate the average depth of epitope cross-conservation with the human proteome. JMX scores above 2.00 are elevated for foreign-derived sequences and indicate potential for homology-induced tolerance. Residues in red indicate differences in the impurity sequence as compared to the API.

28), and ENDO-THR31_SCT (insertion of threonine at position 31). Peptide sequences, EpiMatrix scores, and JanusMatrix scores are listed in Table 2.

Of the blood donors selected for this cohort, 40% were women, and 60% were men. The ages of donor cohort members ranged from 17 to 83 years. The following class II HLA supertype alleles were expressed by the donor PBMCs used in these assays: HLA DRB1*0301, *0401, *0701, *1101, *1301, and *1501 (see Supplementary Figure S1 for detailed HLA information about each donor). No differences in the naïve T-cell response rate were related to the age or sex of the donor in this dataset (data not shown).

For the initial set of assays, the peptides were each evaluated at a concentration of 20.0 μg/mL in 16 individual donor PBMC samples. As shown in Figure 6A, the salmon calcitonin API peptide elicited a response in 44% (7 of 16) of the donors. This high overall response is consistent with the clinical observations and the *in silico* analysis results.

Interestingly, of the 10 that showed no response to the API, 7 responded to 1 or more impurities. Indeed, compared to the salmon calcitonin API at an equivalent concentration (20 μg/mL) *in vitro*, LYS18_SCT (5.8 μM) and Q20E_SCT (5.8 μM) generated a response in 56% (9 of 16) of donors, ENDO-GLY28_SCT (5.7 μM) in 63% (10 of 16) of donors, and ENDO_THR31_SCT (5.7 μM) in 69% (11 of 16) of donors (Figure 6A) (see Supplementary Table S3 for peptide-specific responses by donors). A substantial difference between the number of responding PBMC donors to the API and the four impurities was not observed; however, this may be due to the limited sample size. Differences in PBMC donor responses between the API and the impurities shown in Figure 6A were more striking when the results were normalized to the results for the salmon calcitonin API peptide (Supplementary Figure S2A). These results indicate that both the SCT API and selected impurities evoke immune responses from a high proportion of PBMC donors when tested *in vitro*. These results suggest that individually, the API and impurities have the potential to cause anti-drug immunity, although not necessarily in the same subjects.

Of note, the evaluation of a number of SFCs by each of the PBMC donor responses showed that although LYS-AC18 and Q20E elicited a higher number of IFNg-secreting cells in some donors, the differences in the intensity of the response between the API and individual impurities were not significant (Figure 6B). Two non-parametric tests, the Mann–Whitney and Wilcoxon matched-paired signed rank tests, were used to measure statistical differences in the SFC response between the API and the four impurities. For both tests, no statistical significance was observed for all comparisons.

Overall, these results suggest that several of the evaluated impurities have the potential to enhance the immunogenicity of the drug product when evaluated at the same concentration as the API. However, the observed difference in the number of donor samples that responded to the API and to the individual impurities was not sizable, and the difference in the intensity of response (SFCs) did not reach statistical significance (Mann–Whitney and Wilcoxon matched-paired rank tests).

Taking into consideration that the impurities, although immunogenic, would be present at a lower concentration than the API in an SCT preparation, we next sought to determine whether the impurities could enhance the immunogenic potential of SCT in the presence of the drug product. For these experiments, a second set of T-cell assays was performed in which the reference drug product, Miacalcin®, was "spiked" with the individual impurities at the concentrations at which they were observed in a generic SCT product provided by the FDA (Table 2). As shown in Figure 7A, three out of four impurities increased the overall incidence of response among PBMC donors when added to Miacalcin® at their observed abundances when compared to Miacalcin® alone. Differences in PBMC donor responses between the API and the impurities shown in Figure 7A were easier to observe when normalized to the results for the salmon calcitonin API peptide (Supplementary Figure S2B) for each of the donor PBMC results.

Of note, the overall percentage of donors responding to the Miacalcin® drug product was much lower than that observed in the assays performed with the API peptide. This may have been due to the impact of the product formulation buffer on immune responses *in vitro* (Thacker et al., 2022). Despite the disparity between the results for the API and the formulated drug product (discussed in Supplementary Material: Impact of formulation on *in vitro* T-cell assays), these studies provide support for the hypothesis that product-related impurities can potentially increase the immunogenicity risk of generic drug products and suggest that

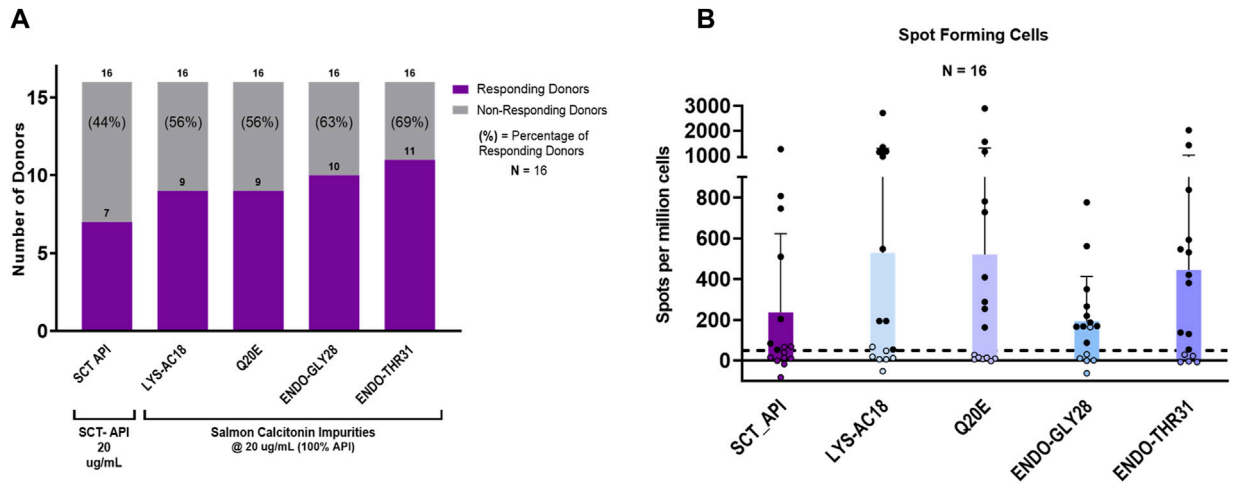

FIGURE 6
IVIP immunogenic potential. **(A)** Comparison of the number of donor PBMCs responding to the salmon calcitonin (API) *versus* each impurity. Donor PBMC positivity includes three criteria: (1) INFg spot-forming cells (SFCs) > 50, (2) stimulation index (SI) > 2, and (3) a statistical difference between medium and peptide stimulation as determined by Student's *t*-test ($p < 0.05$). The *left panel* shows the number (purple bar) and percentage of responders (%) to each of the test peptides. All peptides were evaluated at 20 μg/mL, and the total number of donors evaluated was 16. **(B)** The *right panel* shows the comparison of individual donor responses by the number of IFNg SFCs for the SCT API and peptide impurities. Note that the mean response for impurity Endo-GLY28 is lower than the mean response for the SCT API and other impurities, but 10 donor PBMC samples met the positivity criteria described. Filled circles indicate responsive donors that met the positivity criteria described above. The dashed line indicates the SFC positivity threshold at 50 SFCs.

the use of orthogonal methods to assess their binding to the MHC and their ability to induce novel T-cell responses may be useful in understanding the immunogenicity risk they pose.

Of the two PBMC donors that responded to Miacalcin®, only one responded to the Miacalcin® spiked with the impurity peptides; specifically, this PBMC donor responded to the RLD product spiked with Q20E_SCT, ENDO-GLY28_SCT, or ENDO-THR31_SCT. Spot counts for Miacalcin® spiked with impurity Q20E_SCT or ENDO-GLY28_SCT were higher than those for Miacalcin® alone for this donor. Additionally, donors that responded to Miacalcin® plus Q20E_SCT or ENDO-GLY28_SCT exhibited higher spot counts to the spiked product than the responses to Miacalcin® alone, indicating a more robust response to the impurities (Supplementary Table S4).

In summary, SCT is an interesting peptide, given its significant immunogenic potential linked to the presence of multiple non-human HLA ligands. The above data suggest that impurities introduced during the manufacturing of the peptide could elicit responses from donors that do not respond to SCT, underscoring the need to identify and control these peptides to reduce the potential risk.

Discussion

This study describes the application of *in silico* and *in vitro* methods to evaluate the immunogenicity risk potential of synthetic peptide impurities that could be present in generic versions of Miacalcin®. For this initial evaluation of orthogonal methods that could be used to assess immunogenicity risk, the SCT API and three synthesis-related impurity peptides identified in the synthetic SCT API were assessed for the presence of new HLA ligands (putative T-cell epitopes) in HLA-binding assays, and four impurities were compared to the API in independent T-cell assays.

Each generic product is likely to have different inherent immunogenic risk potential levels depending on the sequence of the peptide itself. In this case study, most of the putative T-cell epitopes identified in SCT (API sequence) and its impurities were unlike any similar ligand or epitope in the human genome. Regardless of the generic peptide drug, homologies between epitopes in the API and the human genome may influence the potential of the API peptide to induce immune responses, and therefore, homology between HLA-binding peptides in the API and the human proteome should be evaluated.

Consistent with its clinical history, the *in silico* analysis of SCT revealed that SCT contains multiple features that indicated a high potential for immunogenicity. These features include 1) a promiscuous 9-mer binding frame epitope bar, or "EpiBar," located within the C-terminus of the peptide, and 2) minimal homology between the HLA ligands identified in the SCT API sequence and the human proteome. Due to high HLA binding potential and the non-self-nature of the region, this region of the peptide is likely responsible for the immunogenicity associated with salmon calcitonin, *in vivo*. This *in silico* analysis also confirmed published findings of a C-terminal immunogenic region (Kozono et al., 1992; Tangri et al., 2005). The results presented here further show that *in silico* analysis may be useful for identifying epitopes within peptide drugs that have the potential for eliciting unwanted immune responses and that the *in silico* analysis data may be useful when designing peptides comparing these regions to the corresponding regions of impurities.

We next compared the *in silico* and *in vitro* binding of SCT and selected impurities. Following *in silico* analysis, three impurities that showed changes to HLA-binding residues (positions 1, 4, 6, and 9 of

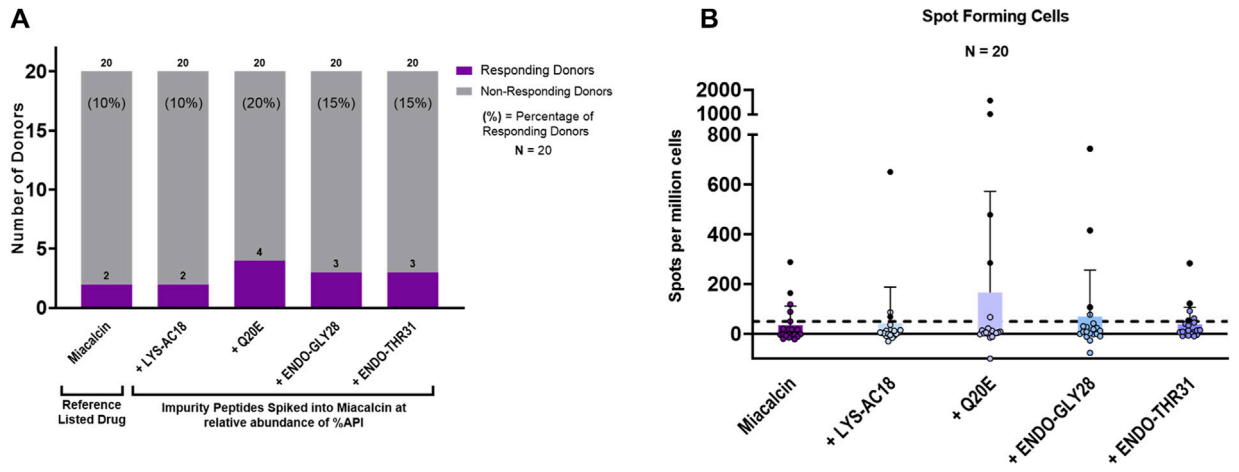

FIGURE 7
IVIP spiked impurities. **(A)** Comparison of the Miacalcin® drug product to the Miacalcin spiked with individual impurities at their observed concentrations relative to the API. Donor PBMC positivity includes three criteria: (1) INFg SFCs > 50, (2) SI > 2, and (3) a statistical difference between medium and peptide stimulation as determined by Student's *t*-test ($p < 0.05$). The *left panel* shows the number (purple bar) and percentage of responders (%) to each of the test peptides. The total number of donors tested was 20. Miacalcin was evaluated at 20 μg/mL. The LYS-AC18_SCT impurity was added at 0.24%, Q20E_SCT at 0.36%, ENDO-GLY28 at 2.62%, and ENDO-THR31_SCT at 3.30% of SCT in Miacalcin. **(B)** *Right panel* shows the comparison of individual donor responses by the number of IFNg SFCs for Miacalcin and Miacalcin spiked with peptide impurities. Black-filled circles indicate responsive donors that met the positivity criteria described above. The dashed line indicates the SFC positivity threshold at 50 SFCs.

a predicted binding frame), and could, therefore, impact HLA binding, were selected for class II HLA-binding assays. The *in silico* assessment results generally aligned with the results of class II HLA DRB1 *in vitro* binding assays. These assays demonstrated that the C-terminal region containing the promiscuous T-cell epitope, and impurities containing this same feature, bound to multiple class II HLA DRB1 alleles. The N-terminus of SCT and the impurity that included an amino acid side-chain modification in this region exhibited reduced HLA binding relative to the C-terminus. A review of published HLA-binding assays in the Immune Epitope Database (IEDB) (Tangri et al., 2005) (using overlapping 15-mer peptides) showed that the sequences in frames 8 (VLGKLSQEL) and 16 (LHKLQTYPRT) were reported to bind to several HLA DRB1 alleles with low to high affinity, confirming the results of both the *in silico* assessment and the HLA-binding assays reported here.

Some HLA-specific binding results for the impurities were not aligned with those of the *in silico* analysis. Differences between *in silico* and *in vitro* HLA-binding results are not unexpected for the N-terminal region impurity as the impurity featured unnatural or modified amino acids (Lys-Ac) for which accurate *in silico* models were not yet available. Because the *in silico* and *in vitro* results were not 100% aligned, this case study underscores the advantages of combining *in silico* analysis with *in vitro* testing to better assess the immunogenicity risk. This is especially true when unnatural amino acids or post-translational modifications are present in generic peptide impurities. The combination of two orthogonal methods is likely to provide a more accurate picture of overall immunogenicity risk. Additional research is warranted to elucidate the impact of post-translational modifications on immunogenicity risk.

The study also examined the relative risk of SCT and additional selected impurities using an *in vitro* naïve donor T-cell assay to determine their overall immunogenic risk potential. Two different strategies were employed: (1) T-cell responses to the individual peptide impurities were compared to the responses to a synthetic SCT peptide and (2) donor PBMC responses to the SCT RLD drug product (Miacalcin®) were compared to the RLD that had been spiked with the impurities.

Consistent with the results of the *in silico* analysis, the API was observed to be immunogenic, inducing immune responses in a large proportion of donor PBMC samples, *in vitro*. Importantly, the selected SCT variants induced immune responses from donors that did not respond to SCT when evaluated at an equivalent concentration.

Of note, the proportion of donor PBMC samples responding to impurities spiked into RLD Miacalcin® was lower, but this could be due to the diminished immune response to SCT that was observed when using the Miacalcin® drug product when compared to the API peptide. The presence of excipients in the drug product formulation may have impacted the health of the cells in culture (see Supplementary Materials for a discussion of the SCT formulation and its impact on immune response). This information is provided as a caution to future practitioners of the *in vitro* method of immunogenicity risk assessment. The use of the drug product formulation in *in vitro* assays may lead to inaccurate immunogenicity risk assessment due to poor cellular viability. It has been suggested that harmful excipients can be removed from the drug product by dialysis prior to their inclusion in *in vitro* studies. For the purpose of evaluating the immunogenicity of generic drug products, however, we believe that it is important to evaluate the intact product as it would be administered to the patient. Excipients

within the formulation buffer that could be removed through dialysis may promote a separate innate immune response that could impact the overall adaptive immune response (Thacker et al., 2022).

The presence of pro-inflammatory cytokines and chemokines released by activated T cells targeting new epitopes can spread, inducing local and usually transitory autoimmune responses related to co-expressed "self" epitopes (Dalum et al., 1997; Powell and Black, 2001; Disis et al., 2004; Hintermann et al., 2011). In contrast, peptide epitopes that are identical in both the unmodified product and the amino acid sequences of product impurities (common epitopes) may engage and activate cognate T cells but are unlikely to induce new immune responses targeting the API. In summary, these *in vitro* assays provide an approximate indicator of the potential for an immune response under clinical conditions. In our study, the overall number of donor PBMC samples responding to the impurity peptides was increased, although the differences in responses between the API and the impurities did not reach statistical significance. This is likely to be due to the size of the cohort. Currently, the FDA recommends using at least 30 donors to achieve broad HLA coverage with multiple donors per allele. While broad HLA coverage can be achieved by including 30 donors for the *in vitro* T-cell assays, additional donors may aid in the interpretation of data for high-risk, low-frequency HLA alleles.

As demonstrated in this case study, when performing *in vitro* T-cell assays, the number of PBMC donors should be large enough 1) to provide power to the analysis and 2) to obtain sufficient breadth of global HLA coverage. Assays performed for regulatory submissions would ideally include at least two, if not three, donors per HLA type, and greater than 80% of the HLA alleles in the United States population should be represented. Currently, adequate HLA coverage can be attained by obtaining PBMCs from at least 30 blood donors. However, for peptide drugs that have low overall immunogenicity (as assessed by *in silico* analysis), it may be necessary to increase the number of donors further to confirm the low immunogenicity of the impurities in assays that are intended to confirm a negative response (ImmunXperts, Denies S. et al., manuscript in process).

Our study shows that the use of the three orthogonal approaches discussed here, together with an assessment of innate immune response-modulating impurities (Mattei et al., 2022), can provide information regarding the potential increase in risk immunogenicity due to impurities in the product. However, neither *in silico* nor *in vitro* assays recapitulate the complex interactions between the generic drug, generic drug impurities, and immune system components that occur *in vivo*. For example, the studies performed did not address HLAs other than HLA DRB1. Other HLAs may contribute to immune responses, although in retrospective and prospective studies, HLA DRB1 is most often associated with unwanted immune responses to biologics (Hyun et al., 2021; Ramarathinam and Purcell, 2021). In addition, the impact of unnatural amino acids on the accuracy of *in silico* and *in vitro* studies may be over or underestimated. Further research is necessary to improve the accuracy of the predictions.

The use of primary cells, such as PBMCs isolated from whole blood from human donors, can present its own set of challenges, including donor-to-donor variability in the observed T-cell responses *in vitro*. Such variability can be attributed to a host of factors including genetic differences at the individual donor level and the health of the individual at the time of donation, which is often self-reported. When performing a comprehensive immunogenicity risk assessment, however, it is important to consider the risk to the population as a whole rather than on an individual basis. Variability in the results of a risk assessment is expected when using primary cells; however, it is important to remember that the emphasis of the immunogenic risk is not on the individual donor but on the collective cohort. This approach of evaluating a broad range of individual donors provides an insight into the risk posed to the population.

Finally, regardless of how many different donor PBMC samples are included in *in vitro* assays, the complexity of the human HLA system precludes an accurate representation of the diverse immune responses that may occur in a human population. Furthermore, it is important not to overestimate the ability of *in vitro* assays to accurately replicate clinical conditions. For example, generic drug products may be administered repeatedly during treatment. Repeated dosing may further increase immunogenicity or, in contrast, could contribute to tolerance (depending on the nature of the immune response). Further investigation into the impact of repeated dosing on immunogenicity in clinical settings is warranted.

Conclusion

This case study shows that the *in silico* analysis of the API and any new impurities provides a good starting point for evaluating the immunogenicity risk potential of a generic peptide. An initial *in silico* assessment of the immunogenic risk potential posed by peptide impurities may enable manufacturers to adjust their processes to remove the highest-risk impurities prior to initiating *in vitro* studies. Once the final impurities are identified, *in silico* assessments of potential HLA binding can then be validated with HLA-binding assays and/or T-cell assays. The selection of the type of assay to be performed and the need to query specific HLA types may depend on the findings in the initial *in silico* analysis. Immunogenicity risk assessment accuracy is improved by the use of orthogonal techniques to better assess the relative risk contributed by the impurities in the ANDA product.

Data availability statement

The original contributions presented in the study are included in the article/Supplementary Material; further inquiries can be directed to the corresponding author.

Ethics statement

Ethical approval was not required for the studies on humans in accordance with the local legislation and institutional requirements because only de-indentified whole blood samples were obtained from Rhode Island Blood Center (Providence, RI) in accordance with FDA regulations and US Federal Policy for the Protection of Human Subjects (45 CFR 46).

Author contributions

BR: conceptualization, formal analysis, methodology, writing–original draft, writing–review and editing, data curation, investigation, and visualization. AM: conceptualization, formal analysis, investigation, methodology, writing–original draft, writing–review and editing, data curation, software, validation, and visualization. KH: writing–review and editing. JW: writing–review and editing. HL: writing–review and editing. SL: data curation, validation, visualization, and writing–review and editing. WM: conceptualization, data curation, formal analysis, investigation, methodology, software, and writing–review and editing. DV: writing–review and editing. EP: project administration and writing–review and editing. KE: project administration and writing–review and editing. ADG: conceptualization, formal analysis, methodology, supervision, writing–original draft, and writing–review and editing.

Funding

The author(s) declare financial support was received for the research, authorship, and/or publication of this article. The research described in this report was performed by EpiVax in collaboration with CUBRC and the FDA contributors listed in the acknowledgment below. The work for this project was supported by an FDA contract HHSF223018186C.

Acknowledgments

The authors acknowledge the contributions from the EpiVax laboratory members: Frances Terry, Bethany McGonnigal, Christopher Talbot, Olivia Orsini, Hannah Tremblay, and Ellie Deju Calixto. The authors also thank Christine Boyle and Mitchell McAllister for their careful review and critique of this manuscript and Seth Thacker for his active scientific discussions that led to improvements to the analysis. In addition, we acknowledge the data management and curation efforts of Holly Clifford and Stephanie Elkins at EpiVax, and thank KE of CUBRC for her excellence in project management of the underlying research program.

Conflict of interest

ADG and WM are senior officers and majority shareholders of EpiVax, a privately held immunoinformatics and vaccine design company. BR, AM, and SL are current employees. All of these authors acknowledge that there is a potential conflict of interest related to their employment status and/or ownership relationship with EpiVax and attest that the work contained in this research report is free of any bias that might be associated with the commercial goals of the company. The findings and conclusion in this article have not been formally disseminated by the Food and Drug Administration and should not be construed to represent any Agency determination or policy.

The remaining authors declare that the research was conducted in the absence of any commercial or financial relationships that could be construed as a potential conflict of interest.

Publisher's note

Supplementary material

The Supplementary Material for this article can be found online at: https://www.frontiersin.org/articles/10.3389/fphar.2024.1363139/full#supplementary-material

References

Andreassen, K. V., Hjuler, S. T., Furness, S. G., Sexton, P. M., Christopoulos, A., Nosjean, O., et al. (2014). Prolonged calcitonin receptor signaling by salmon, but not human calcitonin, reveals ligand bias. *PLoS One* 9, e92042. doi:10.1371/journal.pone.0092042

Ardito, M., Fueyo, J., Tassone, R., Terry, F., DaSilva, K., Zhang, S., et al. (2011). An integrated genomic and immunoinformatic approach to *H. pylori* vaccine design. *Immunome Res.* 7. doi:10.4172/1745-7580.1000049

Center for Biologics Evaluation and Research (CDER) (2021). ANDAs for Certain highly purified synthetic peptide drug products that refer to listed drugs of rDNA origin - may 2021. *U. S. Food Drug Adm.* Avaliable at: https://www.regulations.gov/document/FDA-2017-D-5767-0029 (Accessed July 22, 2024).

Chang, C. H., and Flavell, R. A. (1995). Class II transactivator regulates the expression of multiple genes involved in antigen presentation. *J. Exp. Med.* 181, 765–767. doi:10.1084/jem.181.2.765

Dalum, I., Jensen, M. R., Gregorius, K., Thomasen, C. M., Elsner, H. I., and Mouritsen, S. (1997). Induction of cross-reactive antibodies against a self protein by immunization with a modified self protein containing a foreign T helper epitope. *Mol. Immunol.* 34, 1113–1120. doi:10.1016/S0161-5890(97)00147-8

De Groot, A. S., Jesdale, B., Martin, W., Saint Aubin, C., Sbai, H., Bosma, A., et al. (2003). Mapping cross-clade HIV-1 vaccine epitopes using a bioinformatics approach. *Vaccine* 21, 4486–4504. doi:10.1016/s0264-410x(03)00390-6

De Groot, A. S., Roberts, B. J., Mattei, A., Lelias, S., Boyle, C., and Martin, W. D. (2023). Immunogenicity risk assessment of synthetic peptide drugs and their impurities. *Drug Discov. Today* 28, 103714. doi:10.1016/j.drudis.2023.103714

De Groot, A. S., Rosenberg, A. S., Miah, S. M. S., Skowron, G., Roberts, B. J., Lélias, S., et al. (2021). Identification of a potent regulatory T cell epitope in factor V that modulates CD4+ and CD8+ memory T cell responses. *Clin. Immunol.* 224, 108661. doi:10.1016/j.clim.2020.108661

Disis, M. L., Goodell, V., Schiffman, K., and Knutson, K. L. (2004). Humoral epitope-spreading following immunization with a HER-2/neu peptide based vaccine in cancer patients. *J. Clin. Immunol.* 24, 571–578. doi:10.1023/B:JOCI.0000040928.67495.52

Duke, B. R., and Mitra-Kaushik, S. (2019). Current *in vitro* assays for prediction of T cell mediated immunogenicity of biotherapeutics and manufacturing impurities. *J. Pharm. Innov.* 15, 202–218. doi:10.1007/s12247-019-09412-5

Epand, R. M., Epand, R. F., Orlowski, R. C., Schlueter, R. J., Boni, L. T., and Hui, S. W. (1983). Amphipathic helix and its relationship to the interaction of calcitonin with phospholipids. *Biochemistry* 22, 5074–5084. doi:10.1021/bi00291a005

Figueiredo, F., Koerner, T. J., and Adams, D. O. (1989). Molecular mechanisms regulating the expression of class II histocompatibility molecules on macrophages. Effects of inductive and suppressive signals on gene transcription. *J. Immunol.* 143, 3781–3786. doi:10.4049/jimmunol.143.11.3781

Grauer, A., Ziegler, R., and Raue, F. (1995). Clinical significance of antibodies against calcitonin. *Exp. Clin. Endocrinol. Diabetes* 103, 345–351. doi:10.1055/s-0029-1211376

Hastings, K. T. (2013). GILT: shaping the MHC class II-restricted peptidome and CD4(+) T cell-mediated immunity. *Front. Immunol.* 4, 429. doi:10.3389/fimmu.2013.00429

Hintermann, E., Holdener, M., Bayer, M., Loges, S., Pfeilschifter, J. M., Granier, C., et al. (2011). Epitope spreading of the anti-CYP2D6 antibody response in patients with autoimmune hepatitis and in the CYP2D6 mouse model. *J. Autoimmun.* 37, 242–253. doi:10.1016/j.jaut.2011.06.005

Hyun, Y.-S., Jo, H.-A., Lee, Y.-H., Kim, S.-M., Baek, I.-C., Sohn, H.-J., et al. (2021). Comprehensive analysis of CD4+ T cell responses to CMV pp65 antigen restricted by single HLA-DR, -dq, and -DP allotype within an individual. *Front. Immunol.* 11, 602014. doi:10.3389/fimmu.2020.602014

IQVIA Institute of Human Data Science (2027). The use of medicines in the U.S. 2023 - usage and spending trends and outlook to 2027. Available at: https://www.iqvia.com/-/media/iqvia/pdfs/institute-reports/the-use-of-medicines-in-the-us-2023/the-use-of-medicines-in-the-us-2023.pdf.

Jawa, V., Terry, F., Gokemeijer, J., Mitra-Kaushik, S., Roberts, B. J., Tourdot, S., et al. (2020). T-cell dependent immunogenicity of protein therapeutics pre-clinical assessment and mitigation-updated consensus and review 2020. *Front. Immunol.* 11, 1301. doi:10.3389/fimmu.2020.01301

Kozono, T., Hirata, M., Endo, K., Satoh, K., Takanashi, H., Miyauchi, T., et al. (1992). A chimeric analog of human and salmon calcitonin eliminates antigenicity and reduces gastrointestinal disturbances. *Endocrinology* 131, 2885–2890. doi:10.1210/endo.131.6.1280207

Laha, T. T., Hawley, M., Rock, K. L., and Goldberg, A. L. (1995). Gamma-interferon causes a selective induction of the lysosomal proteases, cathepsins B and L, in macrophages. *FEBS Lett.* 363, 85–89. doi:10.1016/0014-5793(95)00287-J

Lee, S. L., Yu, L. X., Cai, B., Johnsons, G. R., Rosenberg, A. S., Cherney, B. W., et al. (2011). Scientific considerations for generic synthetic salmon calcitonin nasal spray products. *AAPS J.* 13, 14–19. doi:10.1208/s12248-010-9242-9

Levy, F., Muff, R., Dotti-Sigrist, S., Dambacher, M. A., and Fischer, J. A. (1988). Formation of neutralizing antibodies during intranasal synthetic salmon calcitonin treatment of Paget's disease. *J. Clin. Endocrinol. Metab.* 67, 541–545. doi:10.1210/jcem-67-3-541

Mannering, S. I., Harrison, L. C., Williamson, N. A., Morris, J. S., Thearle, D. J., Jensen, K. P., et al. (2005). The insulin A-chain epitope recognized by human T cells is posttranslationally modified. *J. Exp. Med.* 202, 1191–1197. doi:10.1084/jem.20051251

Mattei, A. E., Gutierrez, A. H., Martin, W. D., Terry, F. E., Roberts, B. J., Rosenberg, A. S., et al. (2022). *In silico* immunogenicity assessment for sequences containing unnatural amino acids: a method using existing *in silico* algorithm infrastructure and a vision for future enhancements. *Front. Drug Discov.* 2, 952326. doi:10.3389/fddsv.2022.952326

Mattei, A. E., Gutierrez, A. H., Seshadri, S., Tivin, J., Ardito, M., Rosenberg, A. S., et al. (2024). *In silico* methods for immunogenicity risk assessment and human homology screening for therapeutic antibodies. *MAbs* 16, 2333729. doi:10.1080/19420862.2024.2333729

McMurry, J. A., Gregory, S. H., Moise, L., Rivera, D., Buus, S., and De Groot, A. S. (2007). Diversity of Francisella tularensis Schu4 antigens recognized by T lymphocytes after natural infections in humans: identification of candidate epitopes for inclusion in a rationally designed tularemia vaccine. *Vaccine* 25, 3179–3191. doi:10.1016/j.vaccine.2007.01.039

Moise, L., Gutierrez, A., Kibria, F., Martin, R., Tassone, R., Liu, R., et al. (2015). iVAX: an integrated toolkit for the selection and optimization of antigens and the design of epitope-driven vaccines. *Hum. Vaccin. Immunother.* 11, 2312–2321. doi:10.1080/21645515.2015.1061159

Moise, L., Gutierrez, A. H., Bailey-Kellogg, C., Terry, F., Leng, Q., Abdel Hady, K. M., et al. (2013). The two-faced T cell epitope: examining the host-microbe interface with JanusMatrix. *Hum. Vaccin. Immunother.* 9, 1577–1586. doi:10.4161/hv.24615

Powell, A. M., and Black, M. M. (2001). Epitope spreading: protection from pathogens, but propagation of autoimmunity? *Clin. Exp. Dermatol.* 26, 427–433. doi:10.1046/j.1365-2230.2001.00852.x

Ramarathinam, S. H., and Purcell, A. W. (2021). Proteomics special issue: precision immunology and oncology. *Proteomics* 21, e2000159. doi:10.1002/pmic.202000159

Singh, N. K., Abualrous, E. T., Ayres, C. M., Noé, F., Gowthaman, R., Pierce, B. G., et al. (2020). Geometrical characterization of T cell receptor binding modes reveals class-specific binding to maximize access to antigen. *Proteins Struct. Funct. Bioinforma.* 88, 503–513. doi:10.1002/prot.25829

Southwood, S., Sidney, J., Kondo, A., del Guercio, M.-F., Appella, E., Hoffman, S., et al. (1998). Several common HLA-DR types share largely overlapping peptide binding repertoires. *J. Immunol.* 160, 3363 LP–3373. doi:10.4049/jimmunol.160.7.3363

Steere, A. C., Klitz, W., Drouin, E. E., Falk, B. A., Kwok, W. W., Nepom, G. T., et al. (2006). Antibiotic-refractory Lyme arthritis is associated with HLA-DR molecules that bind a Borrelia burgdorferi peptide. *J. Exp. Med.* 203, 961–971. doi:10.1084/jem.20052471

Sweet, R. A., Lee, S. K., and Vinuesa, C. G. (2012). Developing connections amongst key cytokines and dysregulated germinal centers in autoimmunity. *Curr. Opin. Immunol.* 24, 658–664. doi:10.1016/j.coi.2012.10.003

Tangri, S., Mothé, B. R., Eisenbraun, J., Sidney, J., Southwood, S., Briggs, K., et al. (2005). Rationally engineered therapeutic proteins with reduced immunogenicity. *J. Immunol.* 174, 3187 LP–3196. doi:10.4049/jimmunol.174.6.3187

Thacker, S. G., Her, C., Kelley-Baker, L., Ireland, D. D. C., Manangeeswaran, M., Pang, E. S., et al. (2022). Detection of innate immune response modulating impurities (IIRMI) in therapeutic peptides and proteins: impact of excipients. *Front. Immunol.* 13, 970499. doi:10.3389/fimmu.2022.970499

Glossary

ADA	anti-drug antibody
ANDA	abbreviated new drug application: drug application to the U.S. Food and Drug Administration to manufacture and market a generic drug in the U.S. The application is termed "abbreviated" since it does not require preclinical (animal) and clinical trials (human) to show safety efficacy but requires the applicant to demonstrate bio-equivalence to the reference listed drug (RLD)
API	active pharmaceutical ingredient: this is the active ingredient in a drug product
APC	antigen presenting cell: a type of immune cell (e.g. dendritic cell, macrophage and B cell) that binds peptide antigens via major histocompatibility complex (MHC) proteins on its surface and presents them to T cells
Contaminant	This include extractables and leachables and other potential impurities derived from the manufacturing process. These impurities are not related to peptide
DP	drug product: The finished dosage form of a drug that includes the active pharmaceutical ingredient and the inactive ingredients
Formulation	The process of the chemical and API components into the final drug product
HLA	human leukocyte antigen: also referred to as MHC, major histocompatibility complex, a group of highly polymorphic proteins that display peptide antigens to T cells
IVIP	*in vitro* immunogenicity protocol: an *in vitro* assay that is sufficiently prolonged to measure the expansion and activation of naïve T cells (details in methods section)
Peptide-related impurity	a molecular variant of the peptide drug resulting from synthetic peptide synthesis or storage (e.g., deletions, insertions, truncated, degraded and/or aggregate product)
rDNA	recombinant DNA
RLD	reference listed drug: this is the originator product for which a generic counterpart is made
SCT	salmon calcitonin.

frontiers | Frontiers in Pharmacology

TYPE Original Research
PUBLISHED 28 August 2024
DOI 10.3389/fphar.2024.1418469

OPEN ACCESS

EDITED BY
Yong-Long Han,
Shanghai Jiao Tong University, China

REVIEWED BY
Fengmei Pi,
Genscript, United States
Carina Bethlehem,
Medical Center Leeuwarden, Netherlands

*CORRESPONDENCE
Tao Qin,
qint6@mail.sysu.edu.cn
Jinxiu Yu,
josse_yu@foxmail.com

†These authors have contributed equally to this work

RECEIVED 16 April 2024
ACCEPTED 14 August 2024
PUBLISHED 28 August 2024

CITATION
Wu L, Xu M, Li X, Aierken D, Yu J and Qin T (2024) A real-world pharmacovigilance study of KRAS G12C mutation inhibitors based on the food and drug administration adverse event reporting system.
Front. Pharmacol. 15:1418469.
doi: 10.3389/fphar.2024.1418469

A real-world pharmacovigilance study of KRAS G12C mutation inhibitors based on the food and drug administration adverse event reporting system

Lisha Wu[1,2†], Maosheng Xu[2†], Xueqin Li[2], Dilinuer Aierken[2], Jinxiu Yu[3*] and Tao Qin[1,2*]

[1]Department of Oncology, Sun Yat-sen Memorial Hospital, Sun Yat-sen University, Guangzhou, Guangdong, China, [2]Department of Oncology, Shenshan Medical Center, Sun Yat-sen Memorial Hospital, Sun Yat-sen University, Shanwei, Guangdong, China, [3]Department of Neurosurgery, Huashan Hospital, Fudan University, Shanghai, China

Introduction: Sotorasib and adagrasib have been widely used for the non-small cell lung cancer (NSCLC) patients harboring Kirsten rat sarcoma viral oncogene homolog (KRAS) G12C mutation. It's necessary to assess their safety profiles in the real-world population.

Methods: A retrospective pharmacovigilance was conducted to examine adverse events (AEs) associated with sotorasib and adagrasib therapies using the US Food and Drug Administration (FDA) Adverse Event Reporting System (FAERS). Disproportionality analysis was performed employing Venn analysis and four data-mining algorithms, including the reporting odds ratio (ROR), the proportional reporting ratio (PRR), the Bayesian confidence propagation neural network (BCPNN), and the multi-item gamma Poisson shrinker (MGPS).

Results: The most commonly reported system organ classes (SOCs) for both adagrasib and sororasib were general, gastrointestinal, and investigations disorders. Notably, sotorasib exhibited significant signals for neoplasms and hepatobiliary disorders in four algorithms. Specifically, AEs related to neoplasms were predominantly associated with lung malignancies, all of which were consistent with the therapeutic indications of KRAS G12C mutation inhibitor. A total of 19 common AEs were identified in sotorasib and adagrasib, spanning gastrointestinal, general, hepatobiliary, investigations, metabolism, musculoskeletal, neoplasms, and respiratory disorders. 4 severe AEs (SAEs) were identified in sotorasib, with 3 SAEs displaying significant signals in four algorithms, including drug-induced liver injury, pancreatitis, and hepatic failure. In adagrasib, only 2 SAEs were detected, with renal failure showing significant signals in four algorithms.

Conclusion: This study offers a comprehensive evaluation of the major safety signals associated with sotorasib and adagrasib, providing valuable information for clinicians regarding drug selection and safety considerations, thereby facilitating the design of future prospective safety studies.

KEYWORDS

adverse events, FAERS, disproportionality analysis, pharmacovigilance, sotorasib, adagrasib

1 Introduction

The Kirsten rat sarcoma viral oncogene homolog (KRAS) encodes a membrane-bound guanosine triphosphatase (GTPase), which serves as a pivotal regulator in signal transduction cascades (Simanshu et al., 2017). GTPases, acting as molecular switches, catalyze the hydrolysis of GTP to GDP and regulate downstream activities by transitioning between a GTP-bound activated state and a GDP-bound inactive state (Vetter and Wittinghofer, 2001; Bos et al., 2007). KRAS mutations reduce the rate of GTP hydrolysis, leading to sustained activation of mutant proteins. This results in the continuous transmission of signals to downstream proteins, directing several different pathways in an uncontrolled manner, and showing a significant impact on tumorigenesis (Mustachio et al., 2021). The major KRAS mutations, including G12C, G12D, and G12V, are crucial drivers in the development of multiple tumor types (Liu et al., 2022). Particularly, the G12C stands out as the one of most common mutations in non-small cell lung cancer (NSCLC) patients, accounting for approximately 14% of non-squamous NSCLC (Lee et al., 2022a).

Sotorasib (AMG-510), a covalent inhibitor specific to KRAS G12C mutation, breaking the shackle that KRAS mutated patients have no target medicine for more than 30 years (Huang et al., 2021). The multicenter, single-arm, open-label Phase I/II trial (CodeBreak 100) demonstrated promising effects of sotorasib on locally advanced or metastatic KRAS G12C-mutated NSCLC patients previously received standard treatments. The results showed an objective response rate (ORR) of 37.1%, a median duration of response (DOR) of 11.1 months, a median progression-free survival (PFS) of 6.8 months, and a median overall survival (OS) of 12.5 months (Skoulidis et al., 2021). Sotorasib received FDA approval for the treatment of NSCLC patients with KRAS G12C mutations since May 2021, and was the world's first targeted drug for KRAS mutations (Nakajima et al., 2022). Adagrasib (MRTX849), the second potent inhibitor of the KRAS G12C mutation, was also approved by the FDA in December 2022 for the treatment of KRAS G12C mutated locally advanced or metastatic NSCLC. The efficacy of adagrasib was observed in the Phase I/II KRYSTAL-1 trial, with an ORR of 42.9%, a median PFS of 6.5 months, and a median OS of 12.6 months (Jänne et al., 2022).

It is essential to investigate the safety profiles of KRAS G12C mutation inhibitors given their widespread application in NSCLC patients. However, due to limited follow-up time, selected populations, and lack of statistical power, clinical trials may not capture all aspects of sotorasib or adagrasib related adverse reactions in the real world. In particular, the Food and Drug Administration Adverse Event Reporting System (FAERS) serves as the largest publicly accessible pharmacovigilance databases for detection the adverse drug reactions (ADRs) of recently marketed drugs (FDA, 2018; Giunchi et al., 2023). Through its spontaneous reporting mechanism, FAERS is more efficient to identify AEs and provide accurate information among large population compared to clinical trials (Kumar, 2019). In this study, we conduct a real-world pharmacovigilance study to assess the AEs via FAERS data mining, for the purpose of providing comprehensive reference and theoretical guidance for the sotorasib and adagrasib safety in the clinical practice.

2 Method

2.1 Data source and data mining

We performed the retrospective study based on the FDA Adverse Event Reporting System (FAERS). The keywords (Sotorasib, Lumakras, AMG-510) were used for data mining. Data covering the period from April 2021 to December 2023 were cleaned and analyzed via SAS9.4 software. Similarly, the keywords (Adagrasib, Krazati, MRTX849) were used for AE cases related to adagrasib treatment, covering September 2022 to December 2023. Data were cleaned by de-duplication and excluding missing values according to the method recommended by the FDA. CaseID represented the patient's identification, FDA_DT indicated the date of FDA report acceptance, and PRIMARYID denoted the unique report ID. A patient might submit multiple reports to the FDA at different time points. Reports with the same CASEID were sorted by CASEID, FDA_DT, and PRIMARYID. The report with the highest FDA_DT value among those with the same CASEID was retained. For reports with the same CASEID and FDA_DT, the one with the highest PRIMARYID value was retained. The de-duplicated data had unique CaseID and PRIMARYID values, ensuring accurate analysis (Khaleel et al., 2022). AE names in the FAERS database were described using the preferred terms (PT) from the Medical Dictionary for Regulatory Activities (MedDRA), which was updated each year (MedDRA, 2024). The updated system organ class (SOC) and preferred terms (PT) were obtained from the latest version of MedDRA for subsequent analysis. AEs related to "product issues", "injury, poisoning and procedural complications", "social circumstances" and "surgical and medical procedures" were not shown in the study for which were not drug related AEs (Fang et al., 2023).

2.2 Statistical analysis

This pharmacovigilance study conducted disproportionality analysis, which involved assessing the frequency of AEs associated with a specific drug compared to all other

TABLE 1 Four main algorithms used to calculate the safety signals of sotorasib and adagrasib.

Algorithms	Equation	Criteria
ROR	$ROR = \frac{a/c}{b/d} = \frac{ad}{bc}$	Lower limit of 95% CI > 1, N ≥ 3
	$95\%CI = e^{\ln(ROR) \pm 1.96\sqrt{(\frac{1}{a}+\frac{1}{b}+\frac{1}{c}+\frac{1}{d})}}$	
PRR	$PRR = \frac{a/(a+b)}{c/(c+d)}$	PRR ≥2, $\chi^2 \geq 4$, N ≥ 3
	$\chi^2 = \frac{(ad-bc)^2(a+b+c+d)}{(a+b)(a+c)(c+d)(b+d)}$	
IC	$IC = \log_2 \frac{a(a+b+c+d)}{(a+b)(a+c)}$	IC025 > 0
	$95\%CI = E(IC) \pm 2V(IC)0.5$	
MGPS	$EBGM = \frac{a(a+b+c+d)}{(a+c)(a+b)}$	EBGM05 > 2
	$95\%CI = e^{\ln(EGBM) \pm 1.96(\sqrt{\frac{1}{a}+\frac{1}{b}+\frac{1}{c}+\frac{1}{d}})}$	

ROR, reporting odds ratio; PRR, proportional reporting ratio; IC, bayesian confidence propagation neural networks of information component; EBGM, empirical Bayes geometric mean; a, number of reports containing both the target drug and target adverse drug reaction; b, number of reports containing other adverse drug reaction of the target drug; c, number of reports containing the target adverse drug reaction of other drugs; d, number of reports containing other drugs and other adverse drug reactions; CI, confidence interval; N, number of reports; χ2, chi-squared; IC025, the lower limit of 95% CI, of the IC; E (IC), the IC, expectations; V(IC), the variance of IC; EBGM05, the lower limit of 95% CI, of EBGM.

pharmaceutical agents (FDA, 2005). Disproportionality analysis was a critical analytical tool in pharmacovigilance research for identifying drug-related safety signals. In order to identify statistical associations between sotorasib and all AEs, the four major algorithms were used for data-mining (Zhang et al., 2023): the reporting odds ratio (ROR), the proportional reporting ratio (PRR), the Bayesian confidence propagation neural networks of information component (IC), and the empirical Bayes geometric mean (EBGM). The criteria for these four algorithms were shown in Table 1. Particularly, ROR was the key indicator for evaluating safety signals. We performed Venn analysis to differentiate common AEs from drug-specific ones. Microsoft EXCEL 365 and GraphPad Prism 8 software were employed for the major parts of statistical analysis.

3 Results

3.1 Population characteristics of sotorasib and adagrasib

Between April 2021 and December 2023, a total of 2028 cases, including 3588 AE reports following sotorasib administration, were obtained from the FAERS database. From September 2022 to December 2023, there were 338 cases, including 895 AE reports, involving adagrasib treatment. Table 2 presented the patient characteristics and AE reports for sotorasib and adagrasib. The proportions of female and male patients were nearly equal (35.75% vs. 34.17% and 28.99% vs. 25.15%, respectively). Patients aged 45 years and older constituted the majority of AE reports for sotorasib (42.85%). However, the age distribution of adagrasib was unclear due to over 90% missing data. From 2021 to 2023, the proportion of all AE reports showed an upward trend. The reporters of AEs for sotorasib and adagrasib were primarily physicians (55.23% vs. 24.26%), pharmacists (25.15% vs. 26.04%), and consumers (16.52% vs. 49.70%). The top three regions reporting adverse reactions were North America (37.73% vs. 83.14%), Europe (35.36% vs. 11.24%), and Asia (16.81% vs. 2.66%). The most frequent adverse reaction outcome for sotorasib was classified as "other serious" (52.61%), followed by "life-threatening or death" (24.56%) and "hospitalization" (18.49%). For adagrasib, the most common adverse outcomes were "life-threatening or death" (42.9%), "hospitalization" (41.12%), and "other serious" (16.27%). The analysis of time-to-onset revealed that most AEs occurred within the first 60 days of starting the drugs, whereas the missing data for time-to-onset exceeded 70%.

3.2 SOC spectrum of sotorasib and adagrasib

Disproportionality analysis was conducted at the SOC level to identify safety signals for AEs associated with both drugs, as illustrated in Figure 1. The top five reported SOCs for sotorasib were general disorders (24.3%), neoplasms (15.66%), gastrointestinal disorders (13.1%), investigations (8.75%), and hepatobiliary disorders (7.44%). Similarly, the most frequently reported SOCs for adagrasib included general disorders (25.47%), gastrointestinal disorders (17.88%), nervous system disorders (7.6%), investigations (7.6%), and metabolism and nutrition disorders (4.8%). Both sotorasib and adagrasib exhibited safety signals in general, gastrointestinal, investigations and metabolism disorders (lower limit of ROR 95% CI > 1 and N ≥ 3). Particularly, sotorasib exhibited significant signals for neoplasms and hepatobiliary disorders in four algorithms (ROR, PRR, IC and EBGM).

3.3 PT spectrum of sotorasib and adagrasib

There were total 68 PTs across 13 SOCs exhibited safety signals corresponding to sotorasib-induced AEs upon the calculations of four algorithms. The PTs (report cases exceeding 15) were described in Supplementary Table S1. In our study, the most prevalent PTs associated with neoplasms were non-small cell lung cancer (304), non-small cell lung cancer metastatic (56), and lung neoplasm malignant (39). The top three reported PTs corresponding to hepatobiliary disorder were hepatotoxicity (55), hepatic function

TABLE 2 Clinical characteristics of reports associated with sotorasib and adagrasib [n (%)].

	Sotorasib	Adagrasib
Sex		
Female	725 (35.75)	98 (28.99)
Male	693 (34.17)	85 (25.15)
Not Specified	610 (30.08)	155 (45.86)
Age		
<18	0 (0.00)	0 (0.00)
≥18, <45	16 (0.79)	1 (0.30)
≥45, <65	329 (16.22)	13 (3.85)
65≤	540 (26.63)	13 (3.85)
Not Specified	1,143 (56.36)	311 (92.01)
Year		
2021	146 (7.20)	/
2022	617 (30.42)	5 (1.48)
2023	1,265 (62.38)	333 (98.52)
Reporter		
Consumer	335 (16.52)	168 (49.70)
Not Specified	63 (3.11)	/
Pharmacist	510 (25.15)	88 (26.04)
Physician	1,120 (55.23)	82 (24.26)
Region		
North America	765 (37.72)	281 (83.14)
Europe	717 (35.36)	38 (11.24)
Asia	341 (16.81)	9 (2.66)
Oceania	36 (1.78)	1 (0.30)
South America	9 (0.44)	/
Not Specified	160 (7.89)	9 (2.66)
Outcome		
Life-Threatening/Death	498 (24.56)	5 (42.9)
Hospitalization	375 (18.49)	139 (41.12)
Disability	10 (0.49)	4 (1.18)
Required Intervention	2 (0.10)	0 (0.00)
Other serious	1,067 (52.61)	55 (16.27)
Time onset		
0-30d	174 (8.58)	112 (33.14)
31-60d	103 (5.08)	26 (7.69)
61-90d	63 (3.11)	8 (2.37)
91-120d	30 (1.48)	16 (4.73)
121-150d	17 (0.84)	4 (1.18)
151-180d	18 (0.89)	2 (0.59)
181-360d	40 (1.97)	5 (1.48)
>360d	21 (1.04)	0 (0.00)
missing value	1,562 (77.02)	165 (48.82)

(Continued in next column)

TABLE 2 (*Continued*) Clinical characteristics of reports associated with sotorasib and adagrasib [n (%)].

abnormal (44), and hepatic cytolysis (28). Similarly, the most reported PTs in investigation were aspartate aminotransferase increased (43), alanine aminotransferase increased (43), and liver function test increased (34). In term of gastrointestinal disorder, diarrhoea (196) and colitis (16) were notable. As for respiratory disorder, pulmonary embolism (19) and pneumonitis (17) represented the most common seen PTs. Regarding to general disorders, the top three reported PTs were disease progression (281), death (203), and adverse event (26).

Subsequent analysis indicated that adagrasib-related 22 PTs across 11 SOCs showed safety signals in four algorithms. The PTs (report cases exceeding 4) were described in Supplementary Table S2. The most prevalent PTs associated with general disorder were death (126), asthenia (25). The top three reported PTs related to gastrointestinal disorder were nausea (42), diarrhoea (41) and vomiting (30). Regarding to respiratory disorder, the most reported PTs were dyspnoea (16). Decreased appetite (15) and dehydration (11) exhibited signals in metabolism disorder. Dizziness (13) and seizure (9) were seen in nervous system disorders. The most reported PTs in investigation were weight decreased (9), blood creatinine increased (7), and electrocardiogram QT prolonged (6). Besides, renal failure (7) in renal and urinary disorders, hypotension (7) in vascular disorders, sepsis (6) in infections also showed signals, respectively.

3.4 Common AEs of sotorasib and adagrasib

Using Venn analysis, 19 common AEs with safety signals were identified in sotorasib and adagrasib across four algorithms. These AEs span multiple categories: gastrointestinal disorders (diarrhea, nausea, and vomiting); general disorders (death, general physical health deterioration, peripheral edema, and edema); hepatobiliary disorders (hepatotoxicity); investigations (increased aspartate aminotransferase, increased alanine aminotransferase, increased hepatic enzyme, increased gamma-glutamyltransferase, and increased blood creatinine); metabolism disorders (decreased appetite and dehydration); musculoskeletal disorders (myalgia); neoplasms (neoplasm progression); and respiratory disorders (pneumonitis and pleural effusion), as shown in Table 3.

3.5 Disproportionality analysis of SAEs

Total 4 SAEs were identified in FAERS database related to sotorasib treatment, shown in Table 4, with 3 SAEs exhibiting

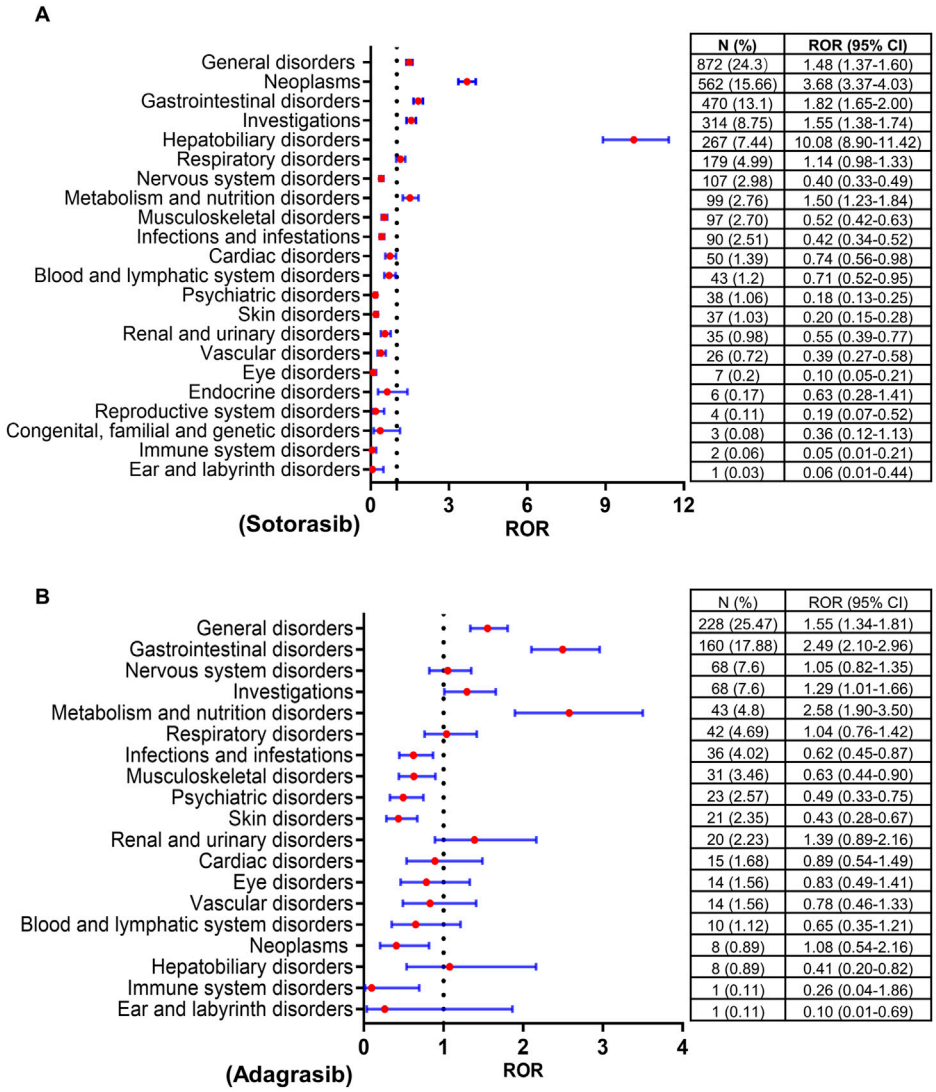

FIGURE 1
Forrest plots of the SOCs of sotorasib **(A)** and adagrasib **(B)**. SOC, system organ classification; ROR, reporting odds ratio; N, number of reports; CI, confidence interval..

significant signals in the four algorithms and reported number larger than three. These 3 SAEs associated with sotorasib treatment were drug-induced liver injury [ROR (95% CI) = 5.92 (3.36–10.44), n = 12], pancreatitis [ROR (95% CI) = 5.10 (2.74–9.50), n = 10] and hepatic failure [ROR (95% CI) = 7.61 (3.95–14.64), n = 9]. There were only 2 SAEs detected in adagrasib, and renal failure [ROR (95% CI) = 5.18 (2.46–10.91), n = 7] exhibited significant signals in four algorithms, shown in Table 5.

4 Discussion

KRAS mutation is a pivotal driver gene of NSCLC. Its complex spatial structure has historically rendered KRAS mutation the most challenging target for drug development (Huang et al., 2021). Sotorasib and adagrasib have emerged as promising agents for precision-targeted therapy in KRAS-mutant NSCLC, with several clinical trials underway for drugs targeting KRAS G12C mutation (Skoulidis et al., 2021; Jänne et al., 2022; Hong et al., 2020; de Langen et al., 2023). Our study represents the inaugural long-term pharmacovigilance investigation utilizing real-world data to assess the safety profiles of sotorasib and adagrasib. Our study provides a comprehensive overview of the major safety signals associated with KRAS G12C mutantation inhibitors, offering valuable insights for clinicians in drug selection and safety considerations, paving the way for future prospective safety studies.

Based on clinical research data and retrospective analysis, hepatotoxicity is a significant adverse reaction associated with KRAS G12C mutation inhibitors treatment. In the CodeBreak200 study, sotorasib-induced liver adverse reactions manifested as elevated levels of alanine aminotransferase (ALT) (10% for any grade, 8% for grade 3 or higher) and aspartate

TABLE 3 Common AEs between sotorasib and adagrasib.

SOC	PT	Sotorasib		Adagrasib	
		N	ROR	N	ROR
Gastrointestinal disorders	Diarrhoea	196	5.54	41	4.49
	Nausea	69	1.75	42	4.24
	Vomiting	33	1.47	30	5.36
General disorders	Death	203	4.32	126	12.05
	General physical health deterioration	14	2.10	7	4.12
	Oedema peripheral	9	2.09	6	5.47
	Oedema	8	3.33	3	4.62
Hepatobiliary disorders	Hepatotoxicity	55	39.18	3	9.02
Investigations	AST increased	43	20.52	5	8.87
	ALT increased	43	17.11	4	5.96
	Hepatic enzyme increased	34	8.67	4	3.94
	GGT increased	16	20.49	4	20.53
	Blood creatinine increased	7	2.14	7	8.50
Metabolism disorders	Decreased appetite	35	2.66	15	4.43
	Dehydration	14	2.38	11	7.35
Musculoskeletal disorders	Myalgia	18	2.37	5	2.43
Neoplasms	Neoplasm progression	11	3.57	6	7.52
Respiratory disorders	Pneumonitis	17	10.32	5	11.83
	Pleural effusion	15	5.45	3	4.47

AE, adverse event; SOC, system organ classification; PT, preferred terms; N, number of reports; ROR, reporting odds ratio; AST, aspartate aminotransferase; ALT, alanine aminotransferase; GGT, gamma-glutamyltransferase.

TABLE 4 SAEs cases for sotorasib exhibited safety signals in four algorithms.

SAE	N	ROR (95% CI)	PRR (x2)	IC (IC025)	EGBM (EGBM05)
Drug-induced liver injury	12	5.92 (3.36–10.44)	5.90 (48.83)	2.56 (1.30)	5.90 (3.34)
Pancreatitis	10	5.10 (2.74–9.50)	5.09 (32.86)	2.35 (1.02)	5.09 (2.73)
Hepatic failure	9	7.61 (3.95–14.64)	7.59 (51.42)	2.92 (1.28)	7.58 (3.84)
Acute hepatic failure	3	4.19 (1.35–13.01)	4.19 (7.27)	2.07 (−0.22)	4.18 (1.35)

SAE, severe adverse event; N, number of reports; ROR, reporting odds ratio; PRR, proportional reporting ratio; IC, bayesian confidence propagation neural networks of information component; EBGM, empirical Bayes geometric mean; CI, confidence interval; N, number of reports; χ2, chi-squared; IC025, the lower limit of 95% CI, of the IC; EBGM05, the lower limit of 95% CI, of EBGM.

TABLE 5 SAEs cases for adagrasib exhibited safety signals in four algorithms.

SAE	N	ROR (95% CI)	PRR (χ2)	IC (IC025)	EBGM (EBGM05)
Renal failure	7	5.18 (2.46–10.91)	5.15 (23.43)	2.36 (0.74)	5.15 (2.45)
Acute kidney injury	7	2.95 (1.40–6.20)	2.93 (8.94)	1.55 (0.21)	2.93 (1.39)

SAE, severe adverse event; N, number of reports; ROR, reporting odds ratio; PRR, proportional reporting ratio; IC, bayesian confidence propagation neural networks of information component; EBGM, empirical Bayes geometric mean; CI, confidence interval; N, number of reports; χ2, chi-squared; IC025, the lower limit of 95% CI, of the IC; EBGM05, the lower limit of 95% CI, of EBGM.

aminotransferase (AST) (10% for any grade, 5% for grade 3 or higher) (de Langen et al., 2023). In the KRYSTAL-1 study, the increased levels of ALT (28.4% for any grade, 5.2% for grade 3 or higher) and AST (26.7% for any grade, 5.2% for grade 3 or higher) also represented the one of the most common AEs (Jänne et al., 2022). These findings align with results obtained from our analysis of real-world data. The precise underlying mechanism of KRAS G12C mutation inhibitors induced liver injury is currently unclear. Post hoc analysis of CodeBreaK200 revealed a higher incidence of severe liver adverse events in patients treated with sotorasib 1–2.6 months after receiving treatment with immune checkpoint inhibitors. Studies revealed the correlation between prior use of programmed death-1 (PD-1)/programmed death-ligand 1 (PD-L1) and severe hepatotoxicity associated with sotorasib. The short intervals, history of previous immune-related hepatitis, and high plasma concentrations of anti-PD-1 were identified as key factors (Ernst et al., 2024; Chour et al., 2023). Preclinical investigation suggested that sotorasib might induce an inflammatory tumor microenvironment, increasing infiltration of $CD8^+$ T cells (Canon et al., 2019), which could be a contributing factor to the occurrence of immune-related hepatotoxicity following combination or sequential use of sotorasib with immune checkpoint inhibitors. The use of corticosteroids agents should be considered in addition to discontinuing treatment in cases of severe hepatotoxicity (Garassino et al., 2023). Additionally, reports suggest the feasibility and safety of sequential adagrasib treatment in patients who encountered grade 3 sotorasib-related hepatotoxicity and discontinued sotorasib (Luo et al., 2024). Adagrasib's distinct off-target effects and pharmacokinetic profiles compared to sotorasib supported this transition (Ou et al., 2022; Wang et al., 2023).

Another significant adverse reaction of sotorasib and adagrasib is gastrointestinal disturbance. In our study, the most common symptoms of treatment-induced gastrointestinal disturbance were diarrhea, nausea, and vomiting. These findings were consistent with the CodeBreak100 clinical study, where the rates of diarrhea, nausea, and vomiting were 29.5%, 20.9%, and 17.8%, respectively (Hong et al., 2020). Similarly, the Codebreak200 study reported diarrhea, nausea, and vomiting at rates of 34%, 24%, and 5%, respectively (de Langen et al., 2023). The rates were much higher in the KRYSTAL-1 study, where diarrhea, nausea, and vomiting represented 70.7%, 69.8% and 56.9%, respectively (Jänne et al., 2022). The precise mechanism of KRAS G12C mutation inhibitor-related gastrointestinal toxicity is still unknown. A multicenter retrospective study examining the clinical characteristics of advanced non-small cell lung cancer patients with KRAS G12C mutation found an association between sotorasib toxicity and recent exposure to immune checkpoint inhibitors, which could also explain the occurrence of sotorasib-induced enteritis (Thummalapalli et al., 2023).

Our study findings indicated that another primary adverse reaction associated with KRAS G12C mutation inhibitors were respiratory system related. Specifically, AEs related to tumors associated with sotorasib were predominantly linked to lung malignancies, including non-small cell lung cancer (NSCLC), NSCLC metastatic, malignant lung neoplasms, and lung adenocarcinomas, all of which align with the therapeutic indications of sotorasib. Our results revealed that pneumonitis and pleural effusion were the common AEs in respiratory disorders. Fatal events of respiratory system were rare. In the Codebreak200, only one case (<1%) in the sotorasib cohort reported fatal interstitial lung disease. One case in the KRYSTAL-1 reported fatal pulmonary hemorrhage. Beyond the established correlation between exposure to anti-PD-(L)1 therapy and KRAS G12C mutation inhibitor related-toxicity, parallels may also exist with severe adverse events observed with tyrosine kinase inhibitors (Shah, 2016). Given the role of KRAS as a downstream factor in the receptor tyrosine kinases (RTKs) pathway, which contributes to the activation of receptor pathways such as epidermal growth factor receptor (EGFR) and human epidermal growth factor receptor-2 (Her-2) (Heppner and Eck, 2021; Zenonos and Kyprianou, 2013), and considering the involvement of these membrane surface receptors in the growth and repair of airway epithelial cells as well as lung injury repair, it is plausible to infer an association between KRAS inhibitors and interstitial pneumonia. Notably, the predominant demographic among individuals with KRAS-mutant NSCLC comprises males with a history of smoking (Wang et al., 2021; Lee et al., 2022b), of which recognized as high-risk factor for interstitial pneumonia (Dawod et al., 2020; Choi et al., 2018).

There are several limitations to our study. Firstly, the number of adverse reactions to specific drugs may be influenced by factors such as drug dosage, reporting populations, and the nature of adverse reactions, which could impede the accurate reflection of all adverse reactions caused by sotorasib and adagrasib in our study. Secondly, the FAERS database may not capture complete information, resulting in numerous clinical data gaps including patient status, comorbidities, and treatment indications, thereby compromising result accuracy and introducing bias. Thirdly, the lack of comprehensive data from all individuals makes it impossible to determine the incidence of adverse reactions. Fourthly, disproportionality analysis can only evaluate signal strength, thus incapable of quantifying risk or establishing causality. Lastly, our study suffers from a limited number of reports on sotorasib and adagrasib, necessitating additional reports or larger-scale clinical studies for further validation.

5 Conclusion

In conclusion, we conducted the disproportionality analysis of KRAS G12C mutation inhibitors induced AEs according to the FAERS database. Data were collected between April 2021 and December 2023. The three most frequently reported SOCs of adagrasib and sororasib were general, gastrointestinal, and investigations disorders. Sotorasib showed significant signals for neoplasms and hepatobiliary disorders in four algorithms. Specifically, AEs related to tumors are predominantly linked to lung malignancies, all of which align with the therapeutic indications of sotorasib. There were 19 common AEs detected in sotorasib and adagrasib. Total 4 SAEs identified in sotorasib and 2 SAEs were detected in adagrasib, respectively. This comprehensive post-marketing safety surveillance significantly enhances the understanding of safety profiles of KRAS G12C mutation inhibitors, thereby offering valuable insights for studies and clinical practice in the future.

Data availability statement

The data is openly available in the FDA Adverse Event Reporting System Public Dashboard at: https://fis.fda.gov/extensions/FPD-QDE-FAERS/FPD-QDE-FAERS.html. Further inquiries can be directed to the corresponding author.

Author contributions

LW: Data curation, Formal Analysis, Funding acquisition, Investigation, Methodology, Resources, Software, Writing–original draft, Writing–review and editing. MX: Data curation, Formal Analysis, Investigation, Methodology, Software, Writing–original draft. XL: Data curation, Writing–original draft. DA: Data curation, Writing–original draft. JY: Supervision, Validation, Visualization, Writing–review and editing. TQ: Conceptualization, Supervision, Validation, Visualization, Writing–review and editing.

Funding

The author(s) declare that financial support was received for the research, authorship, and/or publication of this article. This work was supported by the Basic Research and Application of Guangzhou Science and Technology Planning Project (2023A04J2100), Beijing Xisike Clinical Oncology Research Foundation (Y-HR2020QN-0686).

Conflict of interest

The authors declare that the research was conducted in the absence of any commercial or financial relationships that could be construed as a potential conflict of interest.

Publisher's note

All claims expressed in this article are solely those of the authors and do not necessarily represent those of their affiliated organizations, or those of the publisher, the editors and the reviewers. Any product that may be evaluated in this article, or claim that may be made by its manufacturer, is not guaranteed or endorsed by the publisher.

Supplementary material

The Supplementary Material for this article can be found online at: https://www.frontiersin.org/articles/10.3389/fphar.2024.1418469/full#supplementary-material

References

Bos, J. L., Rehmann, H., and Wittinghofer, A. (2007). GEFs and GAPs: critical elements in the control of small G proteins. *Cell* 129 (5), 865–877. doi:10.1016/j.cell.2007.05.018

Canon, J., Rex, K., Saiki, A. Y., Mohr, C., Cooke, K., Bagal, D., et al. (2019). The clinical KRAS(G12C) inhibitor AMG 510 drives anti-tumour immunity. *Nature* 575 (7781), 217–223. doi:10.1038/s41586-019-1694-1

Choi, W. I., Dauti, S., Kim, H. J., Park, S. H., Park, J. S., and Lee, C. W. (2018). Risk factors for interstitial lung disease: a 9-year Nationwide population-based study. *BMC Pulm. Med.* 18 (1), 96. doi:10.1186/s12890-018-0660-2

Chour, A., Denis, J., Mascaux, C., Zysman, M., Bigay-Game, L., Swalduz, A., et al. (2023). Brief report: severe sotorasib-related hepatotoxicity and non-liver adverse events associated with sequential anti-programmed cell death (Ligand)1 and sotorasib therapy in KRAS(G12C)-Mutant lung cancer. *J. Thorac. Oncol.* 18 (10), 1408–1415. doi:10.1016/j.jtho.2023.05.013

Dawod, Y. T., Cook, N. E., Graham, W. B., Madhani-Lovely, F., and Thao, C. (2020). Smoking-associated interstitial lung disease: update and review. *Expert Rev. Respir. Med.* 14 (8), 825–834. doi:10.1080/17476348.2020.1766971

de Langen, A. J., Johnson, M. L., Mazieres, J., Dingemans, A. C., Mountzios, G., Pless, M., et al. (2023). Sotorasib versus docetaxel for previously treated non-small-cell lung cancer with KRAS(G12C) mutation: a randomised, open-label, phase 3 trial. *Lancet* 401 (10378), 733–746. doi:10.1016/S0140-6736(23)00221-0

Ernst, S. M., Hofman, M. M., van der Horst, T. E., Paats, M. S., Heijboer, F., Aerts, J., et al. (2024). Hepatotoxicity in patients with non-small cell lung cancer treated with sotorasib after prior immunotherapy: a comprehensive clinical and pharmacokinetic analysis. *EBioMedicine* 102, 105074. doi:10.1016/j.ebiom.2024.105074

Fang, Z., Xu, Z., Zhu, W., Yu, M., and Ji, C. (2023). A real-world disproportionality analysis of apalutamide: data mining of the FDA adverse event reporting system. *Front. Pharmacol.* 14, 1101861. doi:10.3389/fphar.2023.1101861

FDA (2005). Good pharmacovigilance practices and pharmacoepidemiologic assessment. Available at: https://www.fda.gov/regulatory-information/search-fda-guidance-documents/good-pharmacovigilance-practices-and-pharmacoepidemiologic-assessment (Accessed April 14, 2024).

FDA (2018). Questions and answers on FDA's adverse event reporting system (FAERS). Available at: https://www.fda.gov/drugs/surveillance/questions-and-answers-fdas-adverse-event-reporting-system-faers (Accessed April 14, 2024).

Garassino, M. C., Theelen, W. S. M. E., Jotte, R., Laskin, J., de Marinis, F., Aguado, C., et al. (2023). LBA65 KRYSTAL-7: efficacy and safety of adagrasib with pembrolizumab in patients with treatment-naïve, advanced non-small cell lung cancer (NSCLC) harboring a KRASG12C mutation. *Ann. Oncol.* 34, S1309–S1310. doi:10.1016/j.annonc.2023.10.066

Giunchi, V., Fusaroli, M., Hauben, M., Raschi, E., and Poluzzi, E. (2023). Challenges and opportunities in accessing and analysing FAERS data: a call towards a collaborative approach. *Drug. Saf.* 46 (10), 921–926. doi:10.1007/s40264-023-01345-w

Heppner, D. E., and Eck, M. J. (2021). A structural perspective on targeting the RTK/Ras/MAP kinase pathway in cancer. *Sci.* 30 (8), 1535–1553. doi:10.1002/pro.4125

Hong, D. S., Fakih, M. G., Strickler, J. H., Desai, J., Durm, G. A., Shapiro, G. I., et al. (2020). KRAS(G12C) inhibition with sotorasib in advanced solid tumors. *N. Engl. J. Med.* 383 (13), 1207–1217. doi:10.1056/NEJMoa1917239

Huang, L., Guo, Z., Wang, F., and Fu, L. (2021). KRAS mutation: from undruggable to druggable in cancer. *Signal Transduct. Target. Ther.* 6 (1), 386. doi:10.1038/s41392-021-00780-4

Jänne, P. A., Riely, G. J., Gadgeel, S. M., Heist, R. S., Ou, S. I., Pacheco, J. M., et al. (2022). Adagrasib in non-small-cell lung cancer harboring a *G12C* mutation. *N. Engl. J. Med.* 387 (2), 120–131. doi:10.1056/NEJMoa2204619

Khaleel, M. A., Khan, A. H., Ghadzi, S., Adnan, A. S., and Abdallah, Q. M. (2022). A standardized dataset of a spontaneous adverse event reporting system. *Healthcare* 10 (3), 420. doi:10.3390/healthcare10030420

Kumar, A. (2019). The newly available FAERS public dashboard: implications for health care professionals. *Hosp. Pharm.* 54 (2), 75–77. doi:10.1177/0018578718795271

Lee, J., Tan, A. C., Zhou, S., Yoon, S., Liu, S., Masuda, K., et al. (2022). Clinical characteristics and outcomes in advanced KRAS-mutated NSCLC: a multicenter collaboration in Asia (ATORG-005). *JTO Clin. Res. Rep.* 3 (1), 100261. doi:10.1016/j.jtocrr.2021.100261

Lee, J. K., Sivakumar, S., Schrock, A. B., Madison, R., Fabrizio, D., Gjoerup, O., et al. (2022). Comprehensive pan-cancer genomic landscape of KRAS altered cancers and real-world outcomes in solid tumors. *NPJ Precis. Oncol.* 6 (1), 91. doi:10.1038/s41698-022-00334-z

Liu, J., Kang, R., and Tang, D. (2022). The KRAS-G12C inhibitor: activity and resistance. *Cancer Gene Ther.* 29 (7), 875–878. doi:10.1038/s41417-021-00383-9

Luo, J., Florez, N., Donnelly, A., Lou, Y., Lu, K., Ma, P. C., et al. (2024). Adagrasib treatment after sotorasib-related hepatotoxicity in patients with KRAS(G12C)-Mutated non-small cell lung cancer: a case series and literature review. *JCO Precis. Oncol.* 8, e2300644. doi:10.1200/PO.23.00644

MedDRA (2024). English. Available at: https://www.meddra.org/how-to-use/support-documentation/english (Accessed April 14, 2024).

Mustachio, L. M., Chelariu-Raicu, A., Szekvolgyi, L., and Roszik, J. (2021). Targeting KRAS in cancer: promising therapeutic strategies. *Cancers* 13 (6), 1204. doi:10.3390/cancers13061204

Nakajima, E. C., Drezner, N., Li, X., Mishra-Kalyani, P. S., Liu, Y., Zhao, H., et al. (2022). FDA approval summary: sotorasib for KRAS G12C-mutated metastatic NSCLC. *Clin. Cancer Res.* 28 (8), 1482–1486. doi:10.1158/1078-0432.CCR-21-3074

Ou, S. I., Jänne, P. A., Leal, T. A., Rybkin, I. I., Sabari, J. K., Barve, M. A., et al. (2022). First-in-Human phase I/IB dose-finding study of adagrasib (MRTX849) in patients with advanced *KRAS*^{G12C} solid tumors (KRYSTAL-1). *J. Clin. Oncol.* 40 (23), 2530–2538. doi:10.1200/JCO.21.02752

Shah, R. R. (2016). Tyrosine kinase inhibitor-induced interstitial lung disease: clinical features, diagnostic challenges, and therapeutic dilemmas. *Drug. Saf.* 39 (11), 1073–1091. doi:10.1007/s40264-016-0450-9

Simanshu, D. K., Nissley, D. V., and Mccormick, F. (2017). RAS proteins and their regulators in human disease. *Cell* 170 (1), 17–33. doi:10.1016/j.cell.2017.06.009

Skoulidis, F., Li, B. T., Dy, G. K., Price, T. J., Falchook, G. S., Wolf, J., et al. (2021). Sotorasib for lung cancers with KRAS p.G12C mutation. *N. Engl. J. Med.* 384 (25), 2371–2381. doi:10.1056/NEJMoa2103695

Thummalapalli, R., Bernstein, E., Herzberg, B., Li, B. T., Iqbal, A., Preeshagul, I., et al. (2023). Clinical and genomic features of response and toxicity to sotorasib in a real-world cohort of patients with advanced KRAS G12C-mutant non-small cell lung cancer. *JCO Precis. Oncol.* 7, e2300030. doi:10.1200/PO.23.00030

Vetter, I. R., and Wittinghofer, A. (2001). The guanine nucleotide-binding switch in three dimensions. *Science* 294 (5545), 1299–1304. doi:10.1126/science.1062023

Wang, X., Ricciuti, B., Nguyen, T., Li, X., Rabin, M. S., Awad, M. M., et al. (2021). Association between smoking history and tumor mutation burden in advanced non-small cell lung cancer. *Cancer Res.* 81 (9), 2566–2573. doi:10.1158/0008-5472.CAN-20-3991

Wang, Y., Zhong, B., Xu, C., Zhan, D., Zhao, S., Wu, H., et al. (2023). Global profiling of AMG510 modified proteins identified tumor suppressor KEAP1 as an off-target. *iScience* 26 (2), 106080. doi:10.1016/j.isci.2023.106080

Zenonos, K., and Kyprianou, K. (2013). RAS signaling pathways, mutations and their role in colorectal cancer. *World J. Gastrointest. Oncol.* 5 (5), 97–101. doi:10.4251/wjgo.v5.i5.97

Zhang, Y., Ran, L., Liang, Y., Zhang, Y., and An, Z. (2023). Safety analysis of pemigatinib leveraging the US Food and Drug administration adverse event reporting system. *Front. Pharmacol.* 14, 1194545. doi:10.3389/fphar.2023.1194545

frontiers | Frontiers in Pharmacology

TYPE Original Research
PUBLISHED 29 October 2024
DOI 10.3389/fphar.2024.1402462

OPEN ACCESS

EDITED BY
Yong-Long Han,
Shanghai Jiao Tong University, China

REVIEWED BY
Sangseon Lee,
Seoul National University, Republic of Korea
Hitesh Mistry,
The University of Manchester, United Kingdom
Will Redfern,
Certara UK Limited, United Kingdom
Ismael Hernández Avalos,
National Autonomous University of Mexico, Mexico

*CORRESPONDENCE
Giovanni Y. Di Veroli,
ydiveroli@gmail.com

RECEIVED 17 March 2024
ACCEPTED 28 August 2024
PUBLISHED 29 October 2024

CITATION
Morris CJ, Rolf MG, Starnes L, Villar IC, Pointon A, Kimko H and Di Veroli GY (2024) Modelling hemodynamics regulation in rats and dogs to facilitate drugs safety risk assessment. *Front. Pharmacol.* 15:1402462. doi: 10.3389/fphar.2024.1402462

Modelling hemodynamics regulation in rats and dogs to facilitate drugs safety risk assessment

Christopher J. Morris[1], Michael G. Rolf[2], Linda Starnes[2], Inmaculada C. Villar[3], Amy Pointon[3], Holly Kimko[1] and Giovanni Y. Di Veroli[1]*

[1]Clinical Pharmacology and Quantitative Pharmacology, Clinical Pharmacology and Safety Science, R&D, AstraZeneca, Cambridge, United Kingdom, [2]Safety Sciences, Clinical Pharmacology and Safety Science, R&D, AstraZeneca, Gothenburg, Sweden, [3]Safety Sciences, Clinical Pharmacology and Safety Science, R&D, AstraZeneca, Cambridge, United Kingdom

Pharmaceutical companies routinely screen compounds for hemodynamics related safety risk. *In vitro* secondary pharmacology is initially used to prioritize compounds while *in vivo* studies are later used to quantify and translate risk to humans. This strategy has shown limitations but could be improved via the incorporation of molecular findings in the animal-based toxicological risk assessment. The aim of this study is to develop a mathematical model for rat and dog species that can integrate secondary pharmacology modulation and therefore facilitate the overall pre-clinical safety translation assessment. Following an extensive literature review, we built two separate models recapitulating known regulation processes in dogs and rats. We describe the resulting models and show that they can reproduce a variety of interventions in both species. We also show that the models can incorporate the mechanisms of action of a pre-defined list of 50 pharmacological mechanisms whose modulation predict results consistent with known pharmacology. In conclusion, a mechanistic model of hemodynamics regulations in rat and dog species has been developed to support mechanism-based safety translation in drug discovery and development.

KEYWORDS

hemodynamic drug safety, clinical translation, quantitative systems toxicology, rat, dog, secondary pharmacology, telemetry, cardiovascular safety

Abbreviations: ACE, Angiotensin converting enzyme; AZ, AstraZeneca; AIC, Akaike information criterion; BIC, Bayes information criterion; CI, Confidence interval; CR, Circadian rhythm; dPdt, Maximum rate of left ventricular pressure increase; HE, Handling effects; HR, Heart rate; IC50, concentration inhibiting 50% of the control response; LTCC, long (L) type calcium channel; MAP, Mean arterial pressure; NO, Nitric oxide; PK, Pharmacokinetics; PRA, Plasma renin activity; RAAS, Renin-angiotensin-aldosterone system; SV, Stroke volume; TPR, Total peripheral resistance.

Introduction

Cardiotoxic effects are a common safety concern and a cause of drug failure (Kelleni and Abdelbasset, 2018; Bhatt et al., 2019). However, translation of preclinical hemodynamics findings remains a challenge. For example, a large review of 83 compounds in the Pfizer historical pipeline showed that 23% of heart rate (HR) and 26% of blood pressure changes in the rat went in the opposite direction to those in large animals (Bhatt et al., 2019). When assessing translation from large animal to human (Phase 1 clinical trial), false positive and negative were found in 21% and 22% of cases, respectively. Notably, the assessment only considered the presence of any signal, ignoring the magnitude or direction of these changes (which can be opposite in rodent vs. large animals). In another study of 113 compounds looking at phase 2 outcomes, it was shown that dogs are not a sensitive predictor of clinical changes in diastolic blood pressure (sensitivity 20%) and heart rate (sensitivity 29%) (Ewart et al., 2014). For cardiovascular related safety, extensive Guidance documents have been developed (and recently updated) for QTc and repolarisation abnormality-related arrhythmias (ICH E14/S7B Implementation working group, 2022; ICH Expert Working Group, 2005). In contrast, hemodynamics endpoints have received much less attention (Bhatt et al., 2019). Nonetheless, there is increasing focus on hemodynamics and recognition that this is an important area of drug safety (FDA, 2022).

The lack of consistent translatability can be attributed at least partially to a failure in identifying mechanisms which could translate from preclinical species to humans. *In vitro* assays are commonly used to screen compounds for hemodynamics safety. Secondary pharmacology screens allow identification of individual drug targets associated with hemodynamic regulation and annotated responses, however they are not integrated to provide an overall assessment of hemodynamic change. Preclinical *in vivo* studies, in contrast, provide overall hemodynamics readouts but provide little insight into mechanistic causes (Litwin et al., 2011; Bonizzoni et al., 1995). Both types of studies are extensively used to assess cardiovascular safety but our current development approach is rather linear, with *in vitro* methods being initially used to prioritize compounds at earlier stages while *in vivo* models are applied later to evaluate potential changes in pre-clinical species. Translation to humans is, however, mostly empirical and often based on the most sensitive species with pre-clinical findings (Bhatt et al., 2019).

A number of mathematical modelling approaches can improve the translational assessment. The Snelder model, notably, connects total peripheral resistance (TPR), HR and stroke volume (SV) interactions with mean arterial pressure (MAP) (Snelder et al., 2014; Snelder et al., 2013). This model consists of a set of three ordinary differential equations in a linked turnover model with negative feedback terms inhibiting increase of HR, SV, and TPR depending on MAP. More recently, the TransQST consortium has made a number of adaptations to this approach, which has also been shown to be applicable to dogs (Venkatasubramanian et al., 2020). Another expansion of the Snelder model for the hemodynamic responses incorporated contractility and better represented the cardiac pressure-volume loop (Fu et al., 2022). The Snelder model could be used to suggest if a drug impacts blood pressure through HR, TPR or SV: it is often used to translate findings in the most sensitive species to human by leveraging predicted clinical pharmacokinetics (Venkatasubramanian et al., 2020; Fu et al., 2022).

A variety of more biology orientated research explored the mathematical modelling of cardiovascular physiology by integrating multi-scale data from individual processes to whole-system function. The virtual physiological rat project from University of Michigan Medical Schools focuses on systems biology modelling of cardiovascular diseases and has involved development of detailed multi-scale models for different components of the cardiovascular system (Virtual Physiological Rat Project, 2023). For important processes such as baroreceptor function, multiple mathematical models have been developed, many of them including details of the arterial wall biomechanics or the stretch of baroreceptors (Mahdi et al., 2013; Bugenhagen et al., 2010; Beard et al., 2013), among others. These models proposed detailed representation at very short time scales (<1 s), typically in response to a step change in the mean arterial pressure. Ion currents, involved in depolarizing neuron membranes, have also been modelled (Schild et al., 1994). Vasoconstriction in response to sympathetic nerve activity has also been the subject of a detailed model that separately considers the mechanisms of action potential generation, its transmission along the axon, as well as release of noradrenaline and contraction of smooth muscle cells (Briant et al., 2015).

At the kidney level, a highly detailed systems physiology model was developed that includes its effects on hemodynamics (Guyton et al., 1972). The Guyton model consists of 354 blocks, each of which represents a factor of circulatory function with one or more mathematical equations and has been the subject of many updates (Uttamsingh et al., 1985; Coleman and Hall, 1992; Karaasalan et al., 2005), including a simplified version (Guyton, 1990). A summary table of the key differences between various versions is included as Table 1 in Karaasalan et al. (2005).

A semi-mechanistic pharmacokinetic/pharmacodynamic (PKPD) model has also been developed for the renin-angiotensin-aldosterone system specifically for the purpose of studying Aliskiren, an active renin inhibitor, in humans (Hong et al., 2008). Additionally, a model has been developed for the control mechanisms of renal physiology relating to maintaining sodium and water homeostasis (Hallow and Gebremichael, 2017). Other modelling efforts have focussed on the effects of salt on hypertension to allow the study of kidney-independent causes (Averina et al., 2012).

While aforementioned significant progress has been made in hemodynamic modeling, we recognized the need to integrate these models for a more comprehensive approach in drug development workflows. More specifically, we designed our model such that:

- Physiological processes are explicitly incorporated, which can be decomposed and parametrized individually by leveraging *in vitro*, *in vivo* and *ex-vivo* research in pre-clinical species.
- Main secondary pharmacology targets affecting hemodynamic function are incorporated.
- Dog and rat species are represented through a common model structure but with different parametrizations.
- Model complexity is minimized whilst applicability to the drug development process workflow is maximized.
- Simulations are readily interpreted in terms of explicit mechanistic hypotheses rooted in screened secondary pharmacology.

10.3389/fphar.2024.1402462

TABLE 1 Variable used to represent each block with its symbol and unit.

Block	Variable	Symbol	Units
Baroreceptors	Firing rate of baroreceptor afferent nerves	n	Hz
Dopamine	Concentration of dopamine	D	M
Kidney renin-angiotensin-aldosterone pathway	Plasma renin activity measured as the rate of synthesis of angiotensin I per unit volume	PRA	$ng\,AngI/mL/min$
Sympathetic nerves	Firing rate of sympathetic efferent nerves	n_s	Hz
Long-type calcium channels	Peak amplitude of current	$LTCC$	pA/pF
Parasympathetic nerves	Firing rate of parasympathetic efferent nerves	n_p	Hz
Nitric oxide	Concentration of nitric oxide in the plasma	NO	M
Endothelin	Concentration of endothelin in the plasma	E	M
Stroke volume	Difference in diastolic and systolic volumes of the left ventricle	SV	mL
Contractility	Maximum rate of increase of left ventricular pressure	$dPdt$	$mmHg/s$
Heart rate	Number of heart beats per minute	HR	bpm
Total peripheral resistance	Pressure difference required to generate volumetric flow rate	TPR	$mmHg\,min/L$
Mean arterial pressure	Time-averaged blood pressure	MAP	$mmHg$

Rat and dog species are indeed commonly used preclinically to study drug-induced hemodynamic effects. Increasing the mechanistic understanding of responses in these species (often of different nature, magnitude or even directionality) would contribute to informed decision-making during drug discovery and development. Here, our dog and rat mathematical models are described, and preliminary simulations of basic interventions are explored. Results showed that once assembled, both model versions can simulate appropriate trends in a number of situations. We also show that modulating the mechanism of action for a pre-defined list of 50 secondary pharmacology targets resulted in predictions which aligned with reported observations. These secondary pharmacology targets are regularly screened internally at AstraZeneca for hemodynamic safety risk, based on evidence suggesting that their disruption can lead to significant hemodynamic changes (see Supplementary Table S39 for more details).

Two main parts can be found in the results. We first briefly review current knowledge of hemodynamic regulation as well as critical molecular mechanisms involved in these pathways. We then present the resulting model structure and its assembly. The assembled model is then investigated through *in silico* experiments that provide its response to secondary pharmacology modulations.

Methods

Model structure

The model was designed around main physiological processes connecting HR, MAP and contractility. The various physiological processes are reviewed and described in the first part of the Results section. The model was pragmatically decomposed into a reasonable number of components in which a pre-determined list of 50 secondary pharmacology targets could be readily integrated. The interactions of each of these components (e.g., influence of baroreceptor firing rate on cardiovascular sympathetic firing rate) were modelled independently using publicly available data from experiments where other interaction influences were minimized. Each pathway was modelled as a single variable (Table 1). The interactions of these pathways lead to modulation of five physiological variables which can be measured *in vivo* (Figure 1, yellow). Three of these variables can be readily measured, namely contractility of the left ventricle (measured as the maximum rate of increase of left ventricular pressure, dPdt), HR and MAP. Additionally, two important intermediate mechanical variables (which are not easily or routinely measured) were also added to facilitate the model construction (SV and TPR). We attempted to reduce complexity to a strict minimum, resulting in 13 model variables and 24 interactions. Whilst baroreceptors are not directly modulated by any of the secondary pharmacology targets, they were included to drive circadian rhythm at baroreceptor level. The structure of the model is the same for dogs and rats species except for direct influence of dopamine on kidney renin (RAAS) which was only included in the dog model (interaction 5): Direct influence of dopamine on RAAS was not modelled in the rat model because direct effect of dopamine on renin synthesis was only observed in the rat *in vitro* or *in vivo* when the cyclooxygenase 2 pathway was inhibited by increased sodium intake but not otherwise (Armando et al., 2011).

Time effects

With the exception of baroreceptor resetting and renin effects, interactions in the processes considered here occur at a much shorter timescale than in in vivo preclinical studies (Bonizzoni et al., 1995; Litwin et al., 2011) where changes are typically averaged and observed over hours. The model was therefore based on algebraic equations for all processes except for MAP-

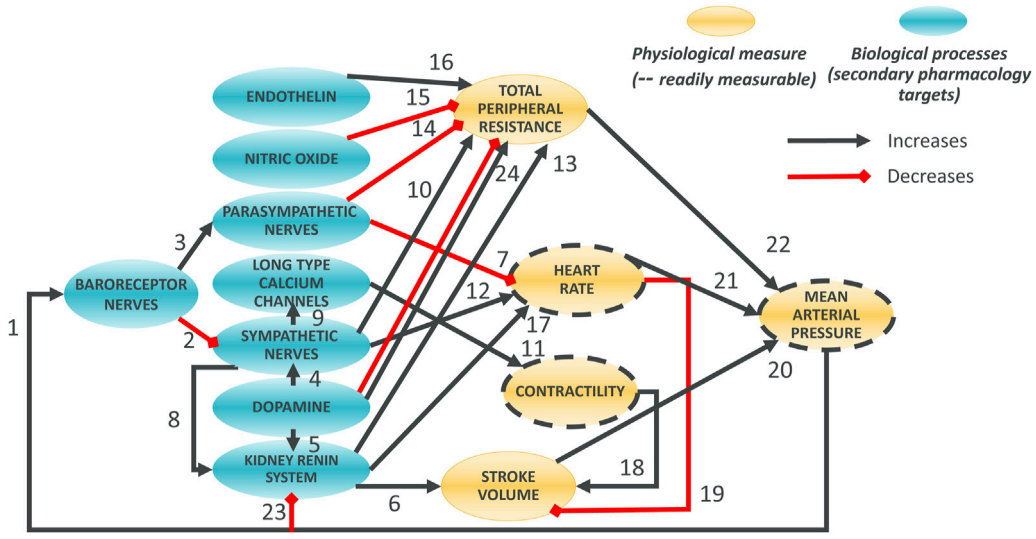

FIGURE 1
Overall Hemodynamics model. There are 8 blue ellipses corresponding to molecular pathways which contribute to overall heart beating and blood circulation. Drug disruption of hemodynamics at the molecular level can be incorporated as modulation of these variables. Three main *in vivo* readouts are shown in gold (with broken line contours) as well as two intermediate physiological variables (not routinely measured; no contour). Black arrows indicate positive effects on the downstream variables whilst red interactions indicate negative effects. Note that, for dopamine to total peripheral resistance is initially decreased then increased when increasing dopamine concentration.

baroreceptor, renin-SV, renin-HR and renin-TPR effects where time delays were introduced. These were introduced via a first order differential equation where the variable X of interest had an effective time-dependent representation (Xeff) which relaxes toward a target value (Xtar) with a time scale τ according to Equation 1:

$$\frac{dX_{eff}}{dt} = \frac{\left(X_{tar} - X_{eff}\right)}{\tau} \quad (1)$$

Taher et al. (1988) modelled baroreceptor firing in response to a step change in pressure in rats and used a time constant of 1,000 s. In dog, the time constant for baroreceptor resetting is 4 min based on the time taken for complete resetting (Coleridge et al., 1981) and after five half-lives the value will have reached 97% of its final value (Hallare and Gerriets, 2023).

The time delay in renin effect on HR, SV, and TPR was assumed to be the same for these three variables and was estimated to be 10 h for the rat based on the observation that it took 2–3 days after increased sodium intake for the Cardiac Output (CO) and TPR to reach their peak change in a previous model of renin effects (Averina et al., 2012). This is also consistent with the time to peak decrease in MAP after renal denervation (Li et al., 2016). In dogs, the renin time constant was also estimated to be 10 h based on peak effects in CO and TPR occurring 2–4 days and arterial pressure reaching a plateau approximately 4–5 days after increased sodium intake (Coleman and Guyton, 1969).

Circadian rhythm was introduced as a sinusoidal modulator (Equation 2) similar to what has been done previously (Snelder et al., 2014; Snelder et al., 2013). The circadian rhythm was incorporated into the baroreceptor nerves and into plasma renin activity (PRA), which is driven by release from the kidneys. Several authors showed that circadian rhythm in cardiovascular activity is indeed mostly driven by these systems (Makino et al., 1997; Ohashi et al., 2017; Lecarpentier et al., 2020; Hilfenhaus, 1976). It has been hypothesized that a circadian rhythm in glomerular permeability might be the reason for this circadian regulation associated with PRA (Ohashi et al., 2017). Circadian rhythm was therefore incorporated as a modulating coefficient, CR, modelled using Equation 2:

$$CR = 1 + Amp \times cos\left(\frac{2\pi\left(t - Phase\right)}{24}\right) \quad (2)$$

where *CR* is a dimensionless modulation variable representing the temporal effect of circadian rhythm, *t* is the time, *Amp* is the magnitude of the variation throughout the day, and *Phase* is a parameter allowing to adjust for the phase.

Block interaction modelling

To the extent possible, block interactions were individually modelled using literature data. Two sets of parameters were derived, one for the rat and one for the dog species. The choice of model equations for each block interaction was primarily driven by the data and the use of simple equations to describe them. The Akaike Information Criterion (AIC) was used to select between competing equations to describe the processes. Where possible, the same model equation was used for the same interaction in both species, unless differences in data trends favoured different equations (again based on the AIC). In some instances, block interactions could not be modelled in isolation due to lack of relevant experimental set-ups and data. In this case they were modelled together with others as discussed below. The data used for parameterising the block interactions is summarized in Table 2

TABLE 2 Data used for modelling the block interactions in rats and dogs.

Interaction	Rat data source	Dog data source
1 MAP to Baroreceptor	*Ex vivo* preparation of aorta pressure varied (Andresen and Yang, 1989)	*In vivo* infusion of inactive fluids to raise pressure (Coleridge et al., 1987; Coleridge et al., 1981)
2 Baroreceptor to Sympathetic	*In vivo* phenylephrine for vasoconstriction to increase pressure. Interaction 1 used to estimate baroreceptor at pressures measured (Miki et al., 2003)	*In vivo* phenylephrine for vasoconstriction to increase pressure. Interaction 1 used to estimate baroreceptor at pressures measured (Minisi et al., 1989)
3 Baroreceptor to Parasympathetic	*In vivo* constriction of aorta to increase pressure. Interaction 1 used to estimate baroreceptor at pressures measured (Rentero et al., 2002)	*In vivo* vasoconstrictors phenylephrine and angiotensin II to increase pressure. Interaction 1 used to estimate baroreceptor at pressures measured (Lumbers et al., 1979)
4 Dopamine to Sympathetic	*In vivo* inhibition of dopamine synthesis, dopamine and norepinephrine measured in sympathetic stellate ganglia. Norepinephrine then related to sympathetic frequency from another study (Brokaw and Hansen, 1987; Lambert et al., 2002)	*In vivo* effects of dopamine infusion on left ventricular contractility used to infer effect on sympathetic frequency (Lundberg et al., 2005)
5 Dopamine to PRA	N/A	*In vivo* PRA after infusion of dopamine (Mizoguchi et al., 1983)
6 PRA to SV	*In vivo* angiotensin II infusion effect on fluid homeostasis extracellular and blood, blood volume on stroke volume (Müller et al., 1995; Fitzsimmons and Simons, 1969; Fernandez et al., 1965; Migita et al., 1997)	*In vivo* renal artery stenosis effects on PRA and stroke volume (Anderson et al., 2007)
7,12 Parasympathetic, Sympathetic to HR	*In vivo* intravenous injections of phenylephrine and nitroprusside to vary pressure. Previous calibrations for baroreceptor, sympathetic and parasympathetic frequencies were used to get frequencies from pressure (Head and McCarty, 1987)	*In vivo* disruption of autonomic feedback and stimulation of sympathetic or parasympathetic nerves (Levy and Blattberg, 1976; Mace and Levy, 1983). Infusion of vasoactive intestinal polypeptide to alter parasympathetic frequency (Roossien et al., 1997)
8,23 Sympathetic, MAP to PRA	*In vivo* response of intact or sympathectomised rats PRA to alterations in MAP (Bertolino et al., 1994)	*In vivo* response of PRA to constriction of the renal artery (Kirchheim et al., 1989). Response of PRA to alpha-adrenoceptor vasocsonstriction (Ehmke et al., 1989)
9 Sympathetic to LTCC	*In vitro* response of calcium flux to norepinephrine (Christ et al., 2009) and *in vivo* increase in contractility by sympathetic stimulation or norepinephrine infusion (Onuki et al., 1999)	*In vivo* response of sympathetic frequency, calcium flux, and contractility to sympathetic activator isoproterenol (Szentandrássy et al., 2012; Furnival et al., 1971)
10 Sympathetic to TPR	*In vivo* regional vascular resistances in response to sympathetic stimulation (Berecek et al., 1987)	*In vivo* constriction of femoral artery in response to sympathetic stimulation (Gerová and Gero, 1969)
11 LTCC to Contractility	*In vitro* response of calcium flux to norepinephrine (Christ et al., 2009) and *in vivo* increase in contractility by sympathetic stimulation or norepinephrine infusion (Onuki et al., 1999)	*In vivo* response of sympathetic frequency, calcium flux, and contractility to sympathetic activator isoproterenol (Szentandrássy et al., 2012; Furnival et al., 1971)
13 PRA to TPR	*In vivo* effect of angiotensin on vascular resistance and relationship of angiotensin to PRA (Stegbauer et al., 2003; Müller et al., 1995)	*In vivo* angiotensin effect on mesenteric vascular resistance and relationship between angiotensin and PRA (Britton et al., 1980; Kitagawa et al., 2000)
14 Parasympathetic to TPR	*In vivo* mesenteric resistance in response to baroreceptor stimulation with sympathetic nerves suppressed (Salgado et al., 2007)	*In vivo* gastric vasodilation in response to vagal stimulation (Ito et al., 1988)
15 NO to TPR	*In vitro* L-NAME release of nitric oxide and vasodilation (Liu et al., 2019)	*In vivo* nitric oxide mediated coronary vasoconstriction (Canty and Schwartz, 1994; Neishi et al., 2005)
16 Endothelin to TPR	*In vivo* cerebrovascular vasoconstriction in response to endothelin (Durgan et al., 2015)	*In vivo* coronary vasoconstriction in response to endothelin (Clozel and Clozel, 1989)
17 PRA to HR	*In vivo* beta adrenoceptor stimulation by isoprenaline caused increased PRA, HR, and MAP (Blanc et al., 2000). Autonomic effects were estimated using other interaction calibrations and subtracted from the data	*In vivo* effects of angiotensin, sodium intake, beta blockade, renal denervation, or carotid occlusion on PRA and HR (Fitzgerald et al., 1997; Anderson et al., 1986; Gross et al., 1981)
18,19 Contractility, HR to SV	*In vivo* effect of water immersion or dobutamine on heart rate, stroke volume, and contractility (Gaustad et al., 2020; Buttrick et al., 1988)	*In vivo* response of HR, SV, and contractility to infusion of dopamine, norepinephrine, or beta blockers (Lundberg et al., 2005; Liang and Hood, 1974)
24 Dopamine to TPR	*In vivo* infusion of dopamine effect on vasoconstriction (Drieman et al., 1994) and *ex vivo* bathing of kidney in dopamine causing vasoconstriction (Augustin et al., 1977)	*In vivo* dopamine infusion effects on vascular resistance (Black and Rolett, 1966)

and main equations are provided below. Additional details, including each block parametrization, are given in the Supplementary Material section "Interaction parameterisations" and Supplementary Tables S1-S35.

Animal weight can differ significantly and there is potentially significant heterogeneity in dog species. Different breeds are used in published studies (mongrels were commonly used) but we did not consider potential weight effects due to lack of information. When available, animal weights were noted for future reference (Supplementary Table S36).

Individual models were parametrized in MATLAB® (2020b) with the inbuilt function "fitnlm." Additive, multiplicative or a combination of both error models were used depending on the data. Confidence intervals (CI) were derived using the inbuilt Matlab® function "nlparci," 95% prediction interval using the inbuilt function "predict."

Model assembly

The assembled model consists of 2 ordinary differential and 10 algebraic equations: The differential equations model the time delay of baroreceptor resetting and the delay in renin effects as explained above. There are 43 and 41 parameters in the rat and dog model, respectively, as well as two parameters to define the magnitude and phase of circadian rhythm. Model equations are briefly described below, while full parametrization for each block and its equations can be found in the Supplementary Material section "Interactions parameterisation." Note that for all models, the parameters values differ between rat and dog species even when the same equations are used.

Baroreceptor, cardiovascular sympathetic, and cardiac parasympathetic model equations

In both rats and dogs, autonomic nerves firing (baroreceptor, cardiovascular sympathetic, and cardiac parasympathetic) is modelled using sigmoidal equations (McDowall and Dampney, 2006; Brown et al., 1976; Seagard et al., 1990; Miki et al., 2003; Kanbar et al., 2007; Taneyama et al., 1990; Accorsi-Mendonça and Machado, 2013). The parameter values for each model are, however, different for the two species. The baroreceptor firing rate is described using Equation 3:

$$n = \frac{a_{Bar}}{1 + exp\left(-b_{Bar}\left(MAP - c_{Bar}\right)\right)} \tag{3}$$

where a_{Bar} is the maximum firing rate, b_{Bar} is a slope parameter, c_{Bar} is the MAP for 50% increase in firing rate.

For firing rate of sympathetic efferent nerves, an additional contribution due to dopamine is added. This second component is modelled differently in the two species. For rats we have Equation 4:

$$n_s = \frac{a_{Symp}}{1 + exp\left(b_{Symp}\left(n - c_{Symp}\right)\right)} + \frac{a_{Symp,Dop}}{1 + exp\left(-b_{Symp,Dop}\left(\left(Dop - c_{Symp,Dop}\right)\right)\right)} \tag{4}$$

where a_{Symp} is the maximum firing rate, b_{Symp} is a slope parameter, c_{Symp} is the baroreceptor frequency for 50% decrease of the maximum firing rate, $a_{Symp,Dop}$ is the maximum change in sympathetic frequency due to changes in dopamine concentration, $b_{Symp,Dop}$ is a slope parameter, $c_{Symp,Dop}$ is the dopamine concentration for 50% effect of dopamine on sympathetic firing rate.

For dog species, we have Equation 5:

$$n_s = \frac{a_{Symp}}{1 + exp\left(b_{Symp}\left(n - c_{Symp}\right)\right)} + a_{Symp,Dop}Dop \tag{5}$$

where a_{Symp} is the maximum firing rate, b_{Symp} is a slope parameter, c_{Symp} is the baroreceptor frequency for 50% decrease in firing rate, $a_{Symp,Dop}$ is the gradient of Dop effect on n_s.

For firing rate of parasympathetic efferent nerves, we have Equation 6:

$$n_p = \frac{a_{Para}}{1 + exp\left(-b_{Para}\left(n - c_{Para}\right)\right)} \tag{6}$$

where a_{Para} is the maximum parasympathetic firing rate, b_{Para} is a slope parameter, c_{Para} is the baroreceptor frequency for 50% increase in firing rate.

Renin synthesis model equations

Renin synthesis is modelled via a decrease in PRA with increasing MAP and a shift in the pressure for renin synthesis based on the sympathetic frequency such that there is higher PRA at the same MAP when sympathetic nerves are more active (Kirchheim et al., 1985). It should be noted that dopamine affects renin synthesis and release in dogs but not in rats. The model equations differ for the two species. For rats we have Equation 7:

$$PRA = a_R\, exp\left(-b_R\left(MAP - c_R n_s\right)\right) \tag{7}$$

where a_R is the magnitude of PRA from MAP, b_R is a shape parameter, c_R is the magnitude of the shift in PRA response to MAP depending on n_s.

For dogs we have Equation 8:

$$PRA = a_R \Big/ \left(1 + exp\left(-b_R\left(MAP - c_R n_s\right)\right)\right) + a_{R,Dop}Dop^{b_{R,Dop}} \tag{8}$$

where a_R is the maximum PRA from MAP, b_R is a shape parameter, c_R is the magnitude of the shift in PRA response to MAP depending on n_s, $a_{R,Dop}$ is the magnitude of dopamine effect on PRA, $b_{R,Dop}$ is the shape of dopamine effect on PRA.

Sympathetic, and parasympathetic effects on the heart rate model equations

In the rat, a simple linear model accounting for both sympathetic and parasympathetic nerves as well as PRA with no interaction (Equation 9) was used:

$$HR = HR_{Basal} + b_{HR}n_s + c_{HR}n_p + a_{HR,R}PRA_{eff} \tag{9}$$

where HR_{Basal} is the basal HR without any effect from n_s, n_p, or PRA_{eff}; b_{HR} is the gradient of n_s effect on HR; c_{HR} is the

gradient of n_p effect on HR; $a_{HR,R}$ is the gradient of PRA_{eff} effect on HR.

In the dog, the effects of sympathetic and parasympathetic nerves on HR were modelled simultaneously based on published data in dogs suggesting interaction between their effects (i.e., effect of sympathetic stimulation on HR depends on frequency of parasympathetic nerves (Levy and Zieske, 1969; Sunagawa et al., 1998; Kobayashi et al., 2012). The heart rate was modelled as the product of a sigmoidal increase with sympathetic frequency and a sigmoidal decrease with parasympathetic frequency. Renin effects were added via a logarithmic term, resulting in Equation 10:

$$HR = HR_{Basal} + \frac{a_{HR}}{\left(1 + exp\left(-b_{HR}\left(n_s - c_{HR}\right)\right)\right)} \left(1 - \frac{1}{\left(1 + exp\left(-d_{HR}\left(n_p - e_{HR}\right)\right)\right)}\right) + a_{HR,R}\, log\left(PRA_{eff} + 1\right) \tag{10}$$

where a_{HR} is the maximum increase in HR from a baseline value without any sympathetic or parasympathetic effect; b_{HR} is the shape of n_s effect on HR; c_{HR} is the sympathetic frequency for 50% effect on HR; d_{HR} is the shape of parasympathetic frequency on HR; e_{HR} is the n_p for 50% effect on HR; $a_{HR,R}$ is the magnitude of PRA_{eff} effect on HR.

Sympathetic effects on the long type calcium channel (LTCC) flux model equations

LTCC was modelled sigmoidally in the rat (Equation 11):

$$LTCC = \frac{a_{LTCC}}{1 + exp\left(-b_{LTCC}\left(n_s - c_{LTCC}\right)\right)} \tag{11}$$

where a_{LTCC} is the maximum $LTCC$, b_{LTCC} is a slope parameter, c_{LTCC} is the n_s for 50% increase in $LTCC$.

LTCC was modelled logarithmically in the dog (Equation 12):

$$LTCC = a_{LTCC}\, log\left(n_s\right) + b_{LTCC} \tag{12}$$

where a_{LTCC} is the magnitude of n_s effect on $LTCC$, b_{LTCC} is a constant.

Contractility due to LTCC model equations

Contractility was modelled linearly in the rat (Equation 13):

$$dPdt = a_{Cont} LTCC + b_{Cont} \tag{13}$$

where a_{Cont} is the gradient of the effect of $LTCC$ on $dPdt$, b_{Cont} is a constant.

Contractility was modelled sigmoidally in the dog (Equation 14):

$$dPdt = \frac{a_{Cont}}{1 + exp\left(-b_{Cont}\left(LTCC - c_{Cont}\right)\right)} + d_{Cont} \tag{14}$$

where a_{Cont} is the maximum increase in $dPdt$ due to $LTCC$, b_{Cont} is a slope parameter, c_{Cont} is the $LTCC$ for 50% increase in $dPdt$, d_{Cont} is the minimum $dPdt$.

SV changes due contractility, HR and PRA model equations

In the rat Equation 15 was used:

$$SV = SV_{Basal} + b_{SV} dPdt - c_{SV} HR + a_{SV,R} PRA_{eff} \tag{15}$$

where SV_{Basal} is the basal SV without any effect from $dPdt$, HR, or PRA_{eff}, b_{SV} is the gradient of $dPdt$ effect on SV, c_{SV} is the gradient of HR effect on SV, $a_{SV,R}$ is the gradient of PRA_{eff} effect on SV.

In the dog Equation 16 was used:

$$SV = SV_{Basal} + a_{SV}\left(1 - \frac{HR}{HR + b_{SV}}\right)\frac{dPdt}{dPdt + c_{SV}} + a_{SV,R} PRA_{eff} \tag{16}$$

where a_{SV} is the maximum SV from HR and $dPdt$, b_{SV} is the HR for 50% decrease in its contribution, c_{SV} is the $dPdt$ for 50% increase in its contribution, $a_{SV,R}$ is the gradient of PRA_{eff} effect on SV. $dPdt$ is a variable corresponding to the maximum rate of left ventricular pressure increase averaged over multiple heart beats.

TPR changes due to sympathetic, parasympathetic, endothelin, nitric oxide (NO), renin and dopamine model equations

In the rat, TPR was modelled using Equation 17:

$$TPR = TPR_{Basal} + \frac{a_{TPR}}{1 + exp\left(-b_{TPR}\left(n_s - c_{TPR}\right)\right)} - d_{TPR} n_p + \frac{a_{TPR,R}}{1 + exp\left(-b_{TPR,R}\left(PRA_{eff} - c_{TPR,R}\right)\right)} + a_{TPR,E}\, exp\left(b_{TPR,E}\left(Endo\right)\right) - \frac{a_{TPR,NO}}{1 + exp\left(b_{TPR,NO}\left(\left(NO\right) - c_{TPR,NO}\right)\right)} + a_{TPR,Dop}\left(-\left(Dop\right)\right)^{b_{TPR,Dop}} \tag{17}$$

where TPR_{Basal} is a baseline TPR without any effect of n_s, n_p, PRA_{eff}, $Endo$, NO, or Dop; a_{TPR} is the maximum increase in TPR from n_s, b_{TPR} is a slope parameter, c_{TPR} is n_s for 50% increase in TPR due to n_s, d_{TPR} is the gradient of TPR decrease due to n_p, PRA_{eff} is the maximum TPR increase due to PRA_{eff}, $b_{TPR,R}$ is a slope parameter, $c_{TPR,R}$ is PRA_{eff} for 50% increase in TPR, $a_{TPR,E}$ is the magnitude of $Endo$ effect on TPR, $b_{TPR,E}$ is the shape of $Endo$ effect on TPR, $a_{TPR,NO}$ is the maximum decrease in TPR due to NO, $b_{TPR,NO}$ is a shape parameter, $a_{TPR,Dop}$ is the magnitude of Dop effect on TPR, $b_{TPR,Dop}$ is the exponent for the magnitude of Dop effect on TPR.

In the dog, TPR was modelled using Equation 18:

$$TPR = TPR_{Basal} + a_{TPR}\, log\left(n_s\right) + b_{TPR}\left(n_p + 1\right)^{c_{TPR}} - a_{NO}\, log\left(NO\right) + a_{TPR,E}\, exp\left(b_{TPR,E} Endo\right) + a_{TPR,R}\, log\left(PRA_{eff} + 1\right) + a_{TPR,Dop} Dop \tag{18}$$

where TPR_{Basal} is a baseline TPR without any effect of n_s, n_p, PRA_{eff}, $Endo$, NO, or Dop; a_{TPR} is the magnitude of n_s effect on TPR, b_{TPR} is the magnitude of n_p effect on TPR, c_{TPR} is the shape of

n_p effect on TPR, a_{NO} is the magnitude of NO effect on TPR, $a_{TPR,E}$ is the magnitude of *Endo* effect on TPR, $b_{TPR,E}$ is the shape of *Endo* effect on TPR, $a_{TPR,R}$ is the shape of PRA_{eff} effect on TPR, $a_{TPR,Dop}$ is the gradient of Dop effect on TPR.

Mean arterial pressure (MAP) model equations

CO is an instantaneous calculation calculated beat-to-beat and represents the blood volume pumped through the heart every minute, calculated directly from the product of HR and SV, giving Equation 19:

$$CO = HR \times SV \tag{19}$$

MAP is then given by the product of CO and TPR, giving Equation 20:

$$MAP = CO \times TPR \tag{20}$$

It should be noted that MAP is calculated as a time-average in practice and could therefore include a proportionality term representing averaging error (Sanders et al., 2011). In the absence of relevant data this coefficient was implicitly assumed to be unity in the above equation.

In silico experiments

In our *in silico* experiments we quantitatively or qualitatively compared overall model simulations in a number of scenarios. For these simulations we use the assembled parametrized block interactions without further fitting to the intact animal data except for several basal values. Namely, when simulating daily changes due to the baroreceptor circadian rhythm, its parameters (amplitude and phase) were first calibrated to match differences across laboratories and individual animals using a non-linear mixed effect approach (Monolix® 2023R1). The amplitude and phase term of the renin circadian rhythm were fixed relative to the amplitude and phase of the baroreceptor, hence effectively reducing the number of circadian parameters to two. The basal values of MAP, SV and TPR were also allowed to vary to account for differences between laboratories and individuals. All other parameters in the assembled hemodynamics model (Figure 1) were kept without variability and were not reparametrized. Whilst the circadian rhythm is expected to cause variations in NO, endothelin and dopamine, it was assumed that these variations were negligible in agreement with the literature (Makino et al., 1997; Gerghel et al., 2004).

For the endothelin *in silico* experiment, no rat or dog PK model could be found in the literature so a two-compartment, target-mediated drug disposition, human PK model (Volz et al., 2017) was scaled allometrically. The allometric exponents were unity for volume of distribution and 0.75 for degradation rate [based on metabolic scaling (West and Brown, 2005)]. The plasma concentration of endothelin was estimated at the two bolus amounts and two infusion rates. These concentrations were then used to predict the maximum change in MAP following bolus or infusion.

For the dopamine *in silico* experiments, a two-compartment human PK model (MacGregor et al., 2000) was also allometrically scaled as for endothelin. To model distribution of dopamine from blood to the ganglions in rats, which affects sympathetic nerve firing, an additional term ($Kp_{\_BloodToNerve}$) was introduced (see Dopamine to Sympathetic interaction in the Supplementary Material) resulting in Equation 21:

$$\Delta nS^R_{Dop} = \frac{a^R_{D,s}}{1 + exp\left(-b^R_{D,s}\left(Dop_{ganglions} - c^R_{D,s}\right)\right)} \tag{21}$$

In dogs, the model is driven by concentrations in plasma (as no information was available about ganglion levels, unlike rats) and the effect on sympathetic firing rates was modelled using Equation 22:

$$\Delta nS^D_{Dop} = a^D_{D,s} Dop_{plasma} \tag{22}$$

In all simulations, daily variations in the readouts were averaged out except for simulations in untreated animals (for which longitudinal data was available). Unless their effect was being investigated, endothelin, NO, and dopamine concentrations were fixed to their baseline values. In nerve stimulation simulations, additional firing was added to the relevant block (e.g., baroreceptor, sympathetic or parasympathetic nerves).

Results

Main mechanisms of hemodynamic regulation

Overall regulation

We performed a literature review in order to define the elements in our mathematical models. This review is at the root of designing our model as a network involving 13 blocks and 23 or 24 interactions in rat and dog species respectively (Figure 1). The complexity of hemodynamic regulation and its related molecular events can be easily appreciated via a vast literature. Overall, blood pressure is regulated by multiple interacting molecular pathways, the two main feedback mechanisms being the autonomic nervous system (predominantly short-term regulation) and the kidney renin-angiotensin-aldosterone system (predominantly long-term regulation) (Shahoud et al., 2022; Boyes et al., 2022; Florea and Cohn, 2014; Kiowski et al., 1992; Navar and Rosivall, 1984). Autonomic nerves are split into sympathetic, parasympathetic, and enteric nerves. Sympathetic and parasympathetic nerves have opposing effects on hemodynamics whilst enteric nerves have little role in hemodynamic regulation (Waxenbaum et al., 2023; Bankenahally and Krovvidi, 2016; McCorry, 2007). The renin system is activated by multiple stimuli including blood pressure, sympathetic nerves, and plasma sodium concentration (Fountain et al., 2023; Ames et al., 2019; Kurtz, 2012). Additional pathways include regulation via dopamine (Armando et al., 2011; Zeng and Jose, 2011; Goldberg, 1984) and vasoactive substances such as NO (Ahmad et al., 2018; Bryan, 2022; Stauss and Persson, 2000; Dominiczak and Bohr, 1995) or endothelin (Schiffrin, 1995; Deehan et al., 2008; Kostov, 2021; Kohan, 2008).

Baroreceptors are stretch sensors located in the aortic arch and carotid sinus which increase their own firing rate in response to

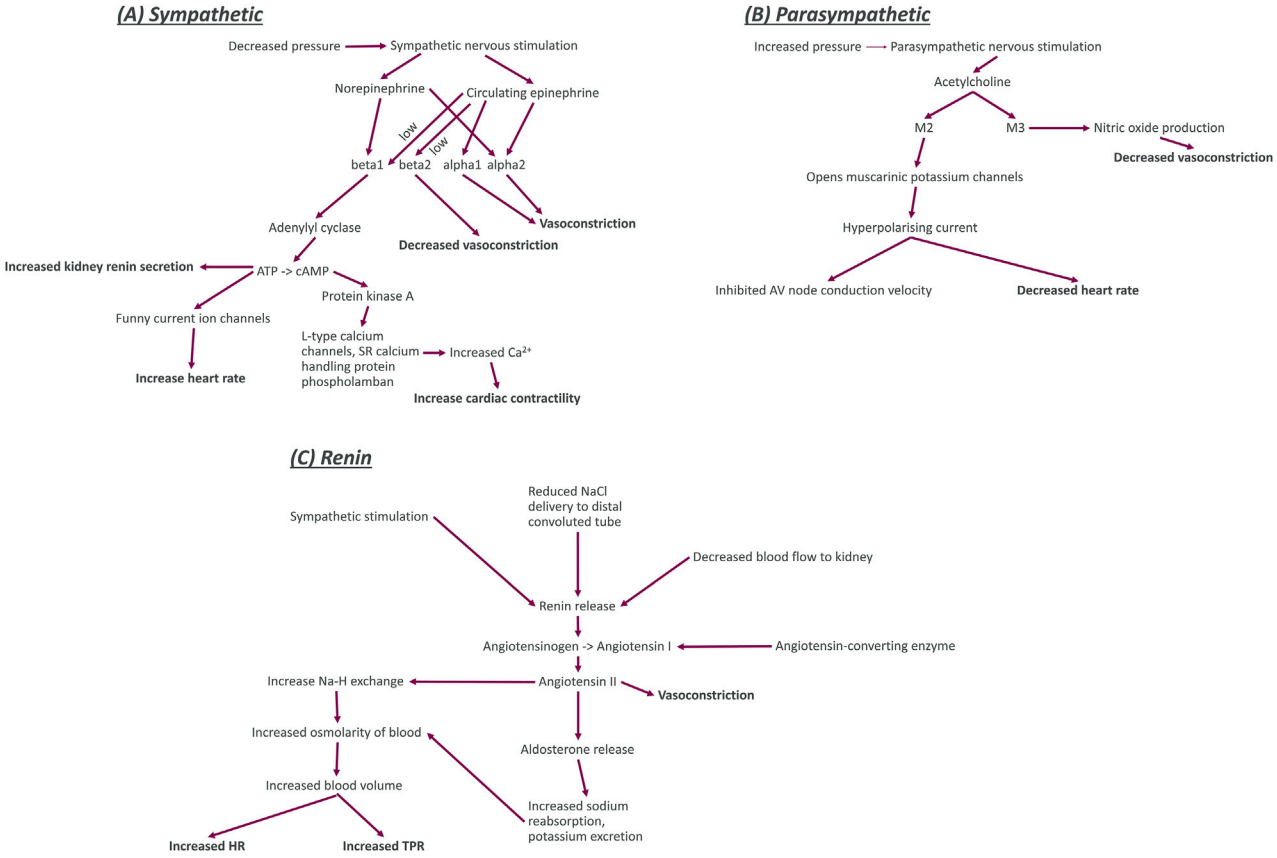

FIGURE 2
Diagrams of the key functional components (including nerve activity, neurotransmitters, enzymes, ion channels, and receptors) for sympathetic nerves, parasympathetic nerves, and the kidney renin system. Bold entries in this diagram indicate the effect of the nerves on other blocks in our model. Sympathetic system **(A)**: The sympathetic nerves are activated by decreased blood pressure and trigger the release of the neurotransmitter and hormone norepinephrine and the hormone epinephrine. Norepinephrine binds to the G-protein coupled beta1 and alpha2 adrenoceptors. When norepinephrine binds to beta1 adrenoceptors, it causes increased activation of the enzyme adenylyl cyclase which increases the conversion of adenosine triphosphate (ATP) to cyclic adenosine monophosphate. This increased production of adenylyl cyclase causes an increase in release of renin from juxtaglomerular cells of the kidney, an increase in the sodium and potassium flux into cardiomyocytes, and an increase in activity of protein kinase **(A)**. The increased activity of protein kinase A activity causes an increase in the calcium concentration within cardiomyocytes by increasing influx through long-type calcium channels and release from sarcoplasmic reticulum (SR) intracellular store. Increased calcium concentration within cardiomyocytes causes an increase in the contractility of the heart. Norepinephrine binding to alpha2 adrenoceptors causes an increase in vasoconstriction. Circulating epinephrine binds to beta adrenoceptors (beta1 and beta2) with low affinity (signified by the word low next to the arrows in the diagram). Epinephrine binding to beta1 and alpha2 adrenoceptors has the same effect as norepinephrine binding. Epinephrine binding to alpha1 adrenoceptors also causes vasoconstriction but binding to beta2 adrenoceptors decreases vasoconstriction. Parasympathetic system **(B)**: The parasympathetic nerves are activated by increased blood pressure and release the neurotransmitter acetylcholine. Acetylcholine then binds to G-protein coupled M2 and M3 muscarinic receptors. M2 opens the muscarinic potassium channels on cardiomyocytes, causing an outflow of potassium ions from the cells for a hyperpolarising current that decreased the heart rate and inhibits electrophysiological coupling of the atria and ventricles via the atrioventricular (AV) node. Renin system **(C)**: Increased sympathetic nervous activity, decreased sodium delivery to the distal convoluted tubule of the kidney (plasma sodium), and decreased blood flow to the kidney all cause an increase in the release of renin. An increase in renin causes greater conversion of angiotensinogen to the inactive peptide angiotensin **(I)**. This process also requires angiotensin converting enzyme to be present. Angiotensin I is then converted to angiotensin II, a powerful vasoconstrictor that also regulates blood volume. Through two pathways that both cause increased osmolarity of blood. The first of these pathways is through an increase in sodium reabsorption by Na-H exchange in the proximal convoluted tubule (decreasing plasma sodium). The second pathway is through increasing aldosterone levels. Aldosterone then increases sodium reabsorption and potassium excretion by apical cells through Na-K ATPase activation.

increased pressure (Wallbach and Koziolek, 2018; Lopez et al., 2022; Min et al., 2019). Higher baroreceptor activity stimulates cardiac parasympathetic nerves and inhibits cardiovascular sympathetic nerves to regulate blood pressure (Sleight, 1991; Lopez et al., 2022; Pratt et al., 2016). Sympathetic nerves are responsible for the "fight-or-flight" response, increasing HR, ventricular contractility, TPR, and PRA (Pratt et al., 2016; Scott-Solomon et al., 2021; LeBouef et al., 2023; Gordon et al., 1967; Gordan et al., 2015). In the "fight-or-flight" response, blood flow to skeletal muscles is increased at the expense of most visceral organs in preparation for more muscle use in fighting or fleeing (McCarty, 2016), thus significantly altering the hemodynamics. HR and contractility both cause an increase in overall blood flow for oxygenation of skeletal muscles whilst the restricted blood flow to visceral organs causes the increased overall TPR (Chu et al., 2024; Curtis and O'Keefe, 2002). Parasympathetic nerves are responsible for "rest and digest," acting to decrease HR and TPR (Pratt et al., 2016; LeBouef et al., 2023; Gordan et al., 2015). Baroreceptors

additionally exhibit resetting with a "set point" firing rate, which is the rate they fire at if the MAP is held constant long enough (Kunze, 1985; Dampney, 2017; Koike et al., 2006; Krieger, 1970; Krieger, 1988; Salgado and Krieger, 1978; Champney et al., 1985). The main neurotransmitter for the afferent and parasympathetic efferent nerves is acetylcholine whilst the neurotransmitter in sympathetic efferent nerves is norepinephrine (aka noradrenaline), which is also a precursor to epinephrine (aka adrenaline) (McCorry, 2007; Burnstock, 1981; Herring, 2015). Renal sympathetic nerves stimulate the release of renin from juxtaglomerular cells of the kidney (the primary location of renin synthesis) via the beta-adrenoceptor-cAMP pathway (Alhayek and Preuss, 2023; Aldehni et al., 2011; Torretti, 1982; Gordon et al., 1967).

Dopamine has multiple effects on different points in hemodynamic regulation, primarily acting via direct impact on the sympathetic nervous system and TPR (Sonne et al., 2023; Missale et al., 1998; Ines et al., 2011; Beaulieu and Gainetdinov, 2011). These effects also have different concentration dependencies–e.g., vascular dilation occurs at low doses (0.5-2ug/kg/min in humans). Dopamine acts through five different receptors classified into two classes (Beaulieu and Gainetdinov, 2011; Sonne et al., 2023; Missale et al., 1998) and is also a precursor to the sympathetic neurotransmitter norepinephrine/noradrenaline (Menniti and Diliberto Jr, 1989; Nakatsuka and Andrews, 2017; Bylund, 2003). A key difference between rats and dogs is that dopamine affects the release of renin in the dog *in vivo* but in the rat this only happens when cyclooxygenase 2 activity is decreased by an increased sodium diet (Armando et al., 2011).

The kidney renin-angiotensin-aldosterone pathway acts over a period of days and primarily affects hemodynamics through regulation of the blood volume and TPR (Fountain et al., 2023; Ames et al., 2019; Navar, 2014; Laragh and Sealey, 2011). In addition to its role in fluid homeostasis, the renin pathway is key for maintenance of salt levels (Fountain et al., 2023; Bernal et al., 2023). Multiple feedback routes can affect the stimulation of the renin pathway in addition to sympathetic stimulation (Figure 2). For instance, reduced salt delivery to the distal convoluted tube of the kidney can be due to variations in salt intake, differential distribution to the blood or decreased blood flow to the kidney (caused by increased resistance of the arteries) (Graudal et al., 2021; Drenjančević-Perić et al., 2011; Laragh and Sealey, 2011; Karlberg, 1983). Decreased blood flow to the kidney is also known to stimulate renin release via stretch sensors (Fountain et al., 2023). Blood volume is regulated by renin through increased thirst, decreased urine output, and increased fluid re-uptake (Fountain et al., 2023; Thornton, 2010; Lote, 2006). Additionally, renin targets angiotensinogen to synthesise angiotensin I, an inactive substance that is the precursor to angiotensin II, with conversion dependent on the angiotensin converting enzyme (ACE) (Fountain et al., 2023; Bernardi et al., 2016) as depicted in Figure 2. Angiotensin II increases sodium retention through increased uptake by sodium-hydrogen exchangers in the thick ascending limb of the loop of Henle in the kidney (Dixit et al., 2004; Xiao et al., 2015). Angiotensin II also stimulates the release of aldosterone from the adrenal cortex to also increase sodium retention (Dixit et al., 2004; Ames et al., 2019). This sodium increase causes greater osmolality and a shift in fluid volume for a higher blood volume (Sharma and Sharma, 2022; Cowley and Roman, 1989).

Cardiac effects

Sympathetic firing induces norepinephrine release which primarily affects HR and contractility through binding to beta1 adrenoceptors (Lorton and Bellinger, 2015; Rengo, 2014) (Figure 2). When beta1 receptors are activated, they upregulate adenylyl cyclase which increases conversion of ATP to cAMP (Velmurugan et al., 2019; Brodde, 1993; Guimaraes and Moura, 2001). Increased cAMP has dual effects, increasing both HR through the funny current (DiFrancesco, 2010; DiFrancesco and Tortora, 1991; Giannetti et al., 2021); myocardial contractility though protein kinase A; and long-type calcium channels, increasing the calcium flux into the cardiomyocytes (Boularan and Gales, 2015; Zaccolo, 2009; Wright et al., 2018; Mika et al., 2013; Tomek and Zaccolo, 2023). It is worth noting that as with beta2 adrenoceptors, epinephrine can bind to beta1 adrenoceptors with low affinity.

Parasympathetic nerves decrease HR through binding of acetylcholine to M2 muscarinic receptors opens muscarinic potassium channels to cause a hyperpolarising current, opposing the depolarisation recovery and delaying the trigger of subsequent action potentials (Sundaram et al., 1989; Tomankova et al., 2015; Kudlak and Tadi, 2023).

Vascular effects

Sympathetic nerves stimulate TPR through vasoconstriction mediated by epinephrine synthesis and binding to alpha1 and alpha2 adrenoceptors (Taylor and Cassagnol, 2023; Ruffolo and Hieble, 1994; Ruffolo et al., 1994; Motiejunaite et al., 2021) (Figure 2). Epinephrine also binds to beta2 adrenoceptors with low affinity, and this acts to cause vasodilation (Dalal and Grujic, 2023; Alhayek and Preuss, 2023; Motiejunaite et al., 2021). Norepinephrine released by sympathetic stimulation also has a role in vasoconstriction through binding to alpha adrenoceptors (Bolli et al., 1984; Reid, 1986; Smith and Maani, 2023).

Whilst there is no evidence for parasympathetic innervation in arterioles, stimulation of parasympathetic nerves has been shown to decrease TPR (Ohke et al., 2020; Ishii et al., 2014; Boysen et al., 2009; Toda and Okamura, 2015; Tindle and Tadi, 2024). It is known that shear stress causes release of acetylcholine from arteriolar endothelial cells, which causes local vasodilation (Wilson et al., 2016). There is, however, also evidence for an endothelium-independent M3 vasodilation shown in rat mesenteric arteries (Tangsucharit et al., 2016), which may be involved in parasympathetic effect on TPR (Figure 2). The impact of parasympathetic stimulation on vascular tone is not as significant as sympathetic stimulation (Gibbins, 2013).

NO is widely recognised as a vasodilator and can be synthesised by three isoforms of the enzyme NO synthase: endothelial NO synthase, neuronal NO synthase, and inducible NO synthase (Förstermann and Sessa, 2012; Andrew and Mayer, 1999; Bredt, 1999). The main synthesis of NO for blood pressure regulation is by endothelial NO synthase in response to shear stress and myogenically increases the diameter of blood vessels, decreasing the resistance to flow (Förstermann and Münzel, 2006; Rees et al., 1989; Bredt, 1999).

Endothelin-1 is a powerful vasoconstrictor that acts through two types of receptors: ETA and ETB. As a vasoconstrictor, endothelin causes the opposite effect to NO, decreasing blood vessel diameter

(Schiffrin, 1995; Dhaun et al., 2008; Maguire and Davenport, 2015; Nishiyama et al., 2017).

In addition to the blood volume effects above, Angiotensin II, released through the renin-angiotenin-aldosterone pathway, also has vasoconstrictive effects, increasing TPR (Stegbauer et al., 2003; di Salvo et al., 1973) (Figure 2). Additionally, there is mounting evidence of an intra-renal renin system as well as a whole-body system (Nishiyama and Kobori, 2018; Chappell, 2012).

Circadian rhythm

Circadian rhythm is a natural oscillation of a variety of processes that repeats roughly every 24 h in correlation to light and dark stimulations (Makino et al., 1997; Rodríguez-Colón et al., 2010). Light detected by the eyes causes activation of the retinohypothalamic tract, which then transmits information about the light state to the suprachiasmatic nucleus in the hypothalamus (Miyamoto and Sancar, 1998; Hannibal, 2002). The signal from the suprachiasmatic nucleus then combines with baroreceptor feedback in the nucleus tractus solitarius to modulate the activity of sympathetic and parasympathetic neurons controlling hemodynamics (Lecarpentier et al., 2020; Makino et al., 1997). A key difference between circadian rhythms of the rat and dog is that the rat is nocturnal (Andreatta and Allen, 2021; Challet, 2007). In nocturnal animals, MAP and HR are increased during active periods, reflecting the higher metabolic demand (Biaggioni, 1992; Gumarova et al., 2021). Additionally, circadian rhythm in the release of renin has been attributed to the central nervous system (Modlinger et al., 1976; Ohashi et al., 2017).

Summary of hemodynamic regulation mechanisms

Considering the aforementioned physiological processes we designed the overall model as a network involving 13 blocks and 23 or 24 interactions in rat and dog species respectively (Figure 1). The main processes in the model can be summarized as follows. At the top, baroreceptor nerves upregulate and downregulate parasympathetic and sympathetic nerves firing, respectively (Figure 1). Parasympathetic firing then downregulates TPR and HR. In contrast, Sympathetic nerves firing, which also affects TPR and HR, also affects contractility (with an intermediate role for the LTCC explicitly described) as well as the kidney renin system. The effect of dopamine has also been included with a role on sympathetic nerves and kidney renin system modulation, as well as a direct, biphasic modulation of TPR. Downstream, the HR and contractility feed into the SV. The SV together with TPR and HR then control the MAP. MAP then feeds back into baroreceptor nerves firing but also into the kidney renin system. The kidney renin system can also directly affect TPR, HR and SV. On top of these elements, the effects of endothelin and NO on TPR were also added to enable additional modelling of additional sites of action for potential secondary pharmacology findings.

The resulting system was modelled as 10 algebraic and 2 ordinary differential equations. The equations were then parametrized for dog and rat species based on a wealth of literature-based data. Table 2 provide a summary of the data used to build each relationship. Overall, all interactions were well captured (Supplementary Figure S1 for the rats and Supplementary Figure S2 for the dogs). The resulting main equations where not necessarily the same in both species (see methods). The organisation and parametrization of all the processes involved in hemodynamics regulation were then combined to a circadian rhythm clock which resulted in the final models (see methods or full details in the Supplementary Material Section "Interaction parameterisations)."

Exploring the model behaviour via *in silico* experiments

Assembling our model in a bottom-up way ensured underlying mechanisms of interest captured to a pre-defined level of granularity. However, this method can easily lead to an overall model which does not produce integrated effects aligned with clinical observations. Therefore, we explored seven cases (diurnal changes and 6 different interventions) to inspect the models' behaviour and face-value. These simulations also enabled defining typical values for some baseline observations such as HR or SV.

Circadian rhythm

In this first set of simulations, we explored if simple diurnal changes in MAP, HR, SV, and TPR could be captured with the models. For the rat species, we combined several telemetry vehicle datasets. One study measured MAP and HR (Teerlink and Clozel, 1993). A second study measured MAP, HR, SV, and TPR (Oosting et al., 1997). A third study measured dPdt (Zheng-rong et al., 1999) and a fourth one measured PRA (Hilfenhaus, 1976). Internal vehicle data including measurements of MAP and HR were also added to enrich the datasets. No studies could be found that simultaneously recorded diurnal variations in PRA and hemodynamics measures.

The model was able to simultaneously capture observed diurnal variations in MAP, HR, dPdt, and PRA (Figure 3). However, across individual animals and labs the amplitude and phase of diurnal changes as well as basal levels of HR and MAP varied. In order to simultaneously capture all the observations we used a non-linear mixed effect approach which allowed variations across animals and labs (according to an underlying distribution around a typical value) in the amplitude and phase as well as basal levels of HR, SV and TPR. Simulations capture the observed data, with typical population values for basal HR, SV and TPR being well estimated and inter-individual variability (random effects) reasonably small; see Supplementary Table S37.

For the dog species we also combined several telemetry studies. In the first study, MAP and HR were measured (Miyazaki et al., 2002). A second study also reported MAP and HR whilst additionally reporting SV (Ashkar, 1979) and a third study reported PRA (Corea et al., 1996). Vehicle data from studies run by AZ were also used to complement MAP, HR and dPdt data. As in rats, the simulations captured diurnal variations for these readouts. Additionally, SV was also available for dog from an experiment of Ashkar (1979). While the SV data is quite noisy, the model is able to reproduce it in a plausible way. It should also be noted that the dPdt data during the first hours show local deviations which can be attributed to experimental handling (Hernández-Avalos et al., 2021; Desborough, 2000; Höglund et al., 2016). The maximum PRA was also underestimated which can be attributed to the few individuals included in the study and potential differences in the animals (we do

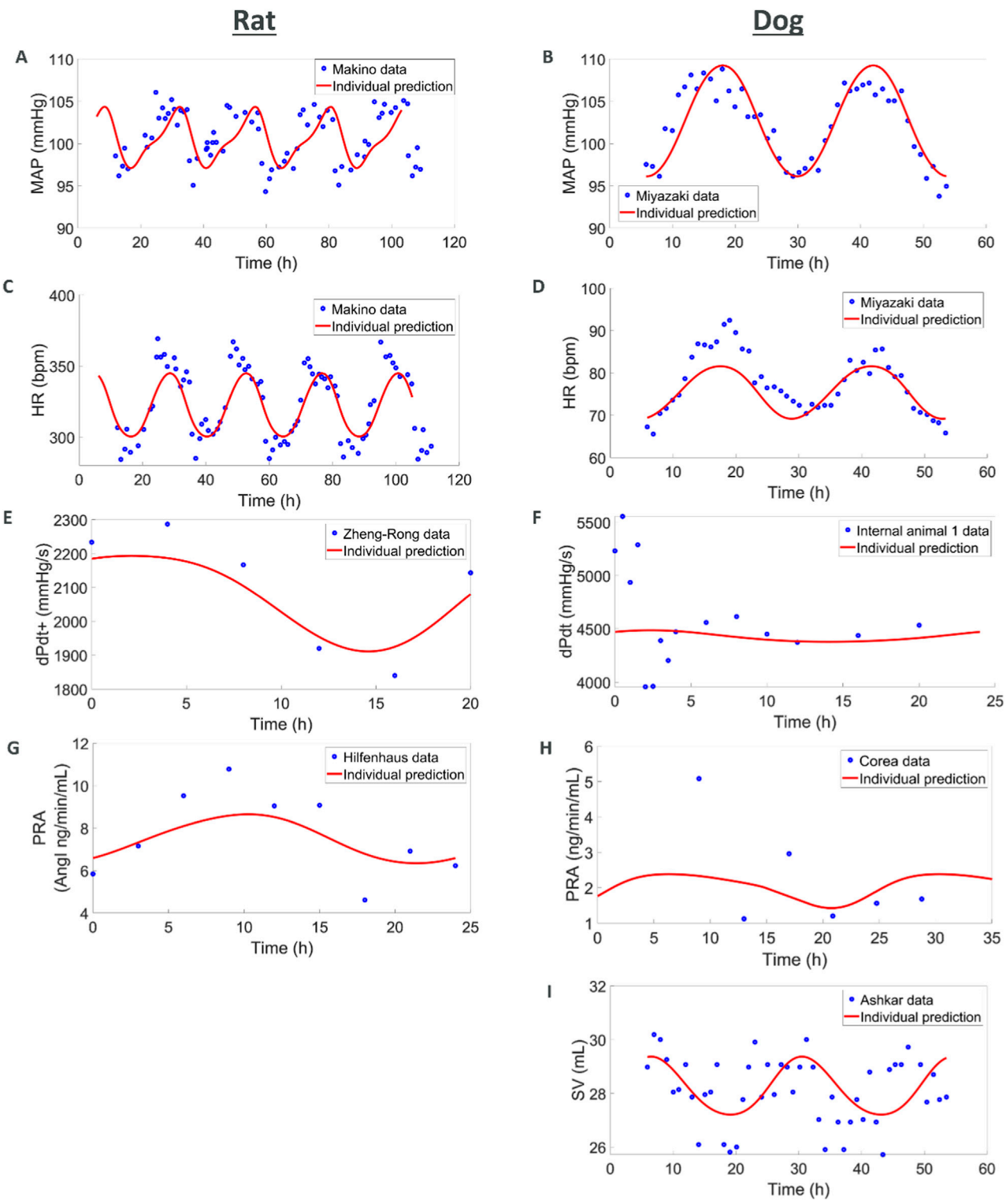

FIGURE 3
Combining multiple literature datasets with vehicle data from AstraZeneca studies show how **(A,C,E, G)** the rat model capture circadian rhythm variations in MAP, HR, contractility, and renin and how **(B, D, F, H, I)** the dog model captures MAP, HR, contractility, renin, and SV. When available, additional animals were also used for MAP, HR and dPdt (see Supplementary Figure S3).

not have any other hemodynamic measures for the same individuals or laboratory as the PRA values). Also, variations in basal levels across individuals were greater in dogs, potentially due to greater excitability of dogs (compared to rats, compounded by diurnal differences), greater variability in breeds and weights across experiments. Like in rats, these simulations capture the observed

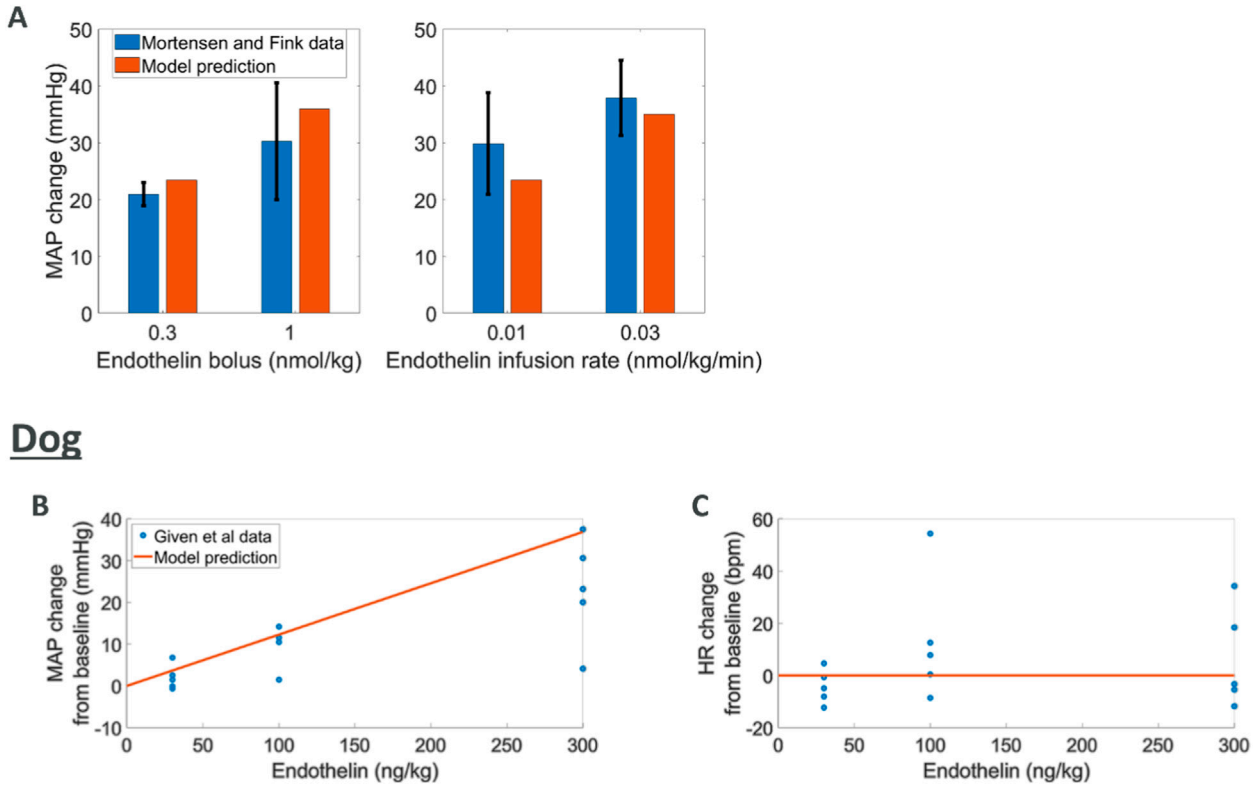

FIGURE 4
Comparing model predictions of hemodynamic changes for various intravenous doses of endothelin to literature data **(A)** rat MAP data (Mortensen and Fink, 1990) **(B, C)** dog MAP and HR data (Given et al., 1989)

diurnal changes and provide typical reference basal values (Supplementary Table S38).

Endothelin effects

Endothelin is known to cause an increase in MAP through vasoconstriction (Schiffrin, 1995; Deehan et al., 2008; Kostov, 2021; Kohan, 2008). The data used for comparison to rat simulations was derived from experiments where endothelin was given intravenously as a bolus or infusion with peak changes in MAP reported (Mortensen and Fink, 1990). We simulated endothelin infusion or bolus in the rat model which led to increases in MAP comparable to those reported (Figure 4). For the dog species, peak changes in both MAP and HR were reported from five dogs after an intravenous bolus of endothelin (Given et al., 1989). Model predictions of MAP and HR response to endothelin showed an increase in MAP which agreed with observations although at the upper end. Changes in observed HR may indicate a slight increase which is not captured by the model.

Dopamine effects

Intravenous dopamine has multiple effects at different points of hemodynamics regulation, overall causing increased MAP but little change in HR in both rats (Perez-Olea et al., 1981; Drieman et al., 1994; Bacq et al., 1990) and dogs (Lundberg et al., 2005). Additionally, contractility and CO have been reported to increase in dogs (Lundberg et al., 2005).

We found different trend in terms of MAP response across the three rats studies considered where different doses and rates of infusions were used (Figure 5). A potential explanation for these differences is the different anaesthetics used in these studies which could significantly impact the response to dopamine. Here the model can capture an average trend across these responses. The tendency to capture average behaviours could be rooted in the heterogeneous source of literature data used to model each one of the blocks in the overall rat model. Dog experiments in (Lundberg et al., 2005) displayed higher variability and simulations capture responses in terms of MAP, HR, dPdt and CO within this experimental variability (Supplementary Figure S4, S5).

Baroreceptor stimulation

Stimulation of baroreceptor nerves is known to decrease MAP by decreasing HR, dPdt, and TPR (Kougias et al., 2010; Armstrong et al., 2023; McCorry, 2007; Bankenahally and Krovvidi, 2016). To our knowledge no quantitative data describing the effects of baroreceptor stimulation in intact animals is available. Rat and dog model simulations were found to agree with the reported decreases (see Supplementary Material Section "Additional *in silico* results)."

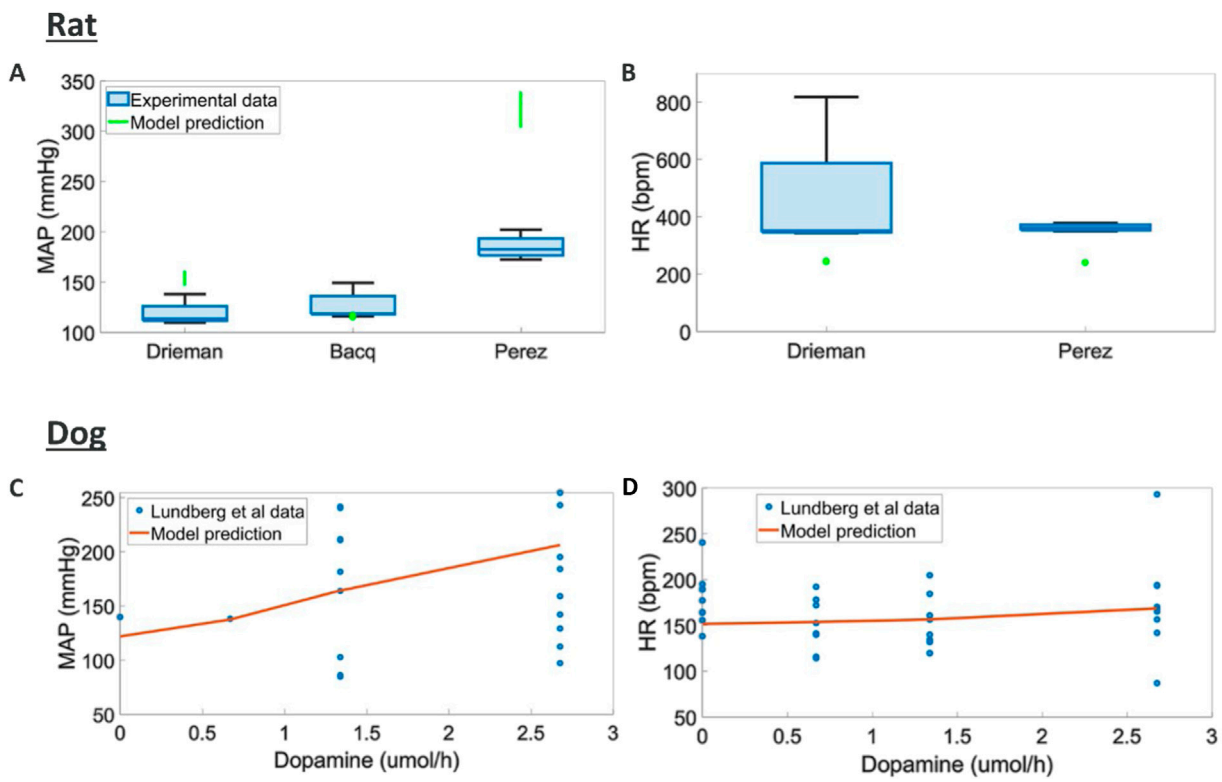

FIGURE 5
Comparison of model predictions to literature hemodynamic data **(A, B)** MAP and HR responses to different doses and intravenous durations of dopamine in rats (MAP and HR were reported at the end of infusion) (Drieman et al., 1994; Bacq et al., 1990; Perez-Olea et al., 1981) **(C, D)** MAP, and HR responses to various intravenous durations of dopamine in dogs (Lundberg et al., 2005)

Sympathetic stimulation

Generally speaking, sympathetic stimulation increases HR, TPR, and dPdt (Bankenahally and Krovvidi, 2016; McCorry, 2007). Stimulation of the renal sympathetic nerve has also been shown to increase PRA (Alhayek and Preuss, 2023; Aldehni et al., 2011; Torretti, 1982; Gordon et al., 1967). Simulations of sympathetic nerves showed overall increased HR, TPR, and dPdt in rats as per reported outcomes (Supplementary Material Section "Additional *in silico* results)." Increase in MAP also led to an overall decrease in PRA in this species (Supplementary Material Section "Additional *in silico* results)." In dogs, simulations of sympathetic nerves also showed overall increased HR, TPR, and dPdt but here the effect of renal sympathetic nerve on PRA is predicted to dominate, resulting in PRA to increase overall (which is opposite to the simulation results in rats, see Supplementary Material Section "Additional *in silico* results)." We could not find experimental evidence for the difference in trend for PRA changes with increased sympathetic stimulation between dogs and rats.

Parasympathetic stimulation

In contrast to the sympathetic nerves, the parasympathetic nerves are reported to decrease MAP through decreased HR and TPR (Khurana et al., 2005; Sundaram et al., 1989). In the absence of quantitative data, we again verified our simulations qualitative agreement with these observations. Rat model predictions showed agreement except for change in TPR which was predicted to increase upon parasympathetic stimulation. While the predictions of TPR appear to diverge from the observed outcomes, it should be noted that the pharmacological intervention in (Khurana et al., 2005) may have precluded feedback responses through the sympathetic system which are accounted for in our model. In dogs, MAP, HR and TPR changes all conformed to the outcomes reported in the literature (Khurana et al., 2005; Sundaram et al., 1989).

Nitric oxide (NO) changes

NO causes vasodilation and a reduction in MAP (Förstermann and Münzel, 2006; Rees et al., 1989; Bredt, 1999). Inhibitors of NO synthase (e.g., L-NAME) and donors (pre-cursors) of NO are commonly used for therapeutic purposes and the hemodynamics effects of these compounds have been reported (although the concentration of NO is not usually reported). Simulations in both rats and dogs indicated significant increase in TPR and MAP with decreased NO (Supplementary Material Section "Varying nitric oxide concentration)." This agrees with observations where the NO synthase inhibitor L-NAME was given in rats (Hu et al., 1997) and showed increased TPR and MAP. The same study also showed a reflex decrease (due to feedback) in HR in rats which was also predicted by both species models. Increase in NO led to predict decrease in TPR and MAP (Supplementary Material Section "Varying nitric oxide concentration") which is also aligned with reports where the NO donors sodium nitroprusside, 3-morpholino sydnonimine, and GEA3162 (an oxatriazole derivative) were administered (Nurminen and Vapaatalo, 1996).

10.3389/fphar.2024.1402462

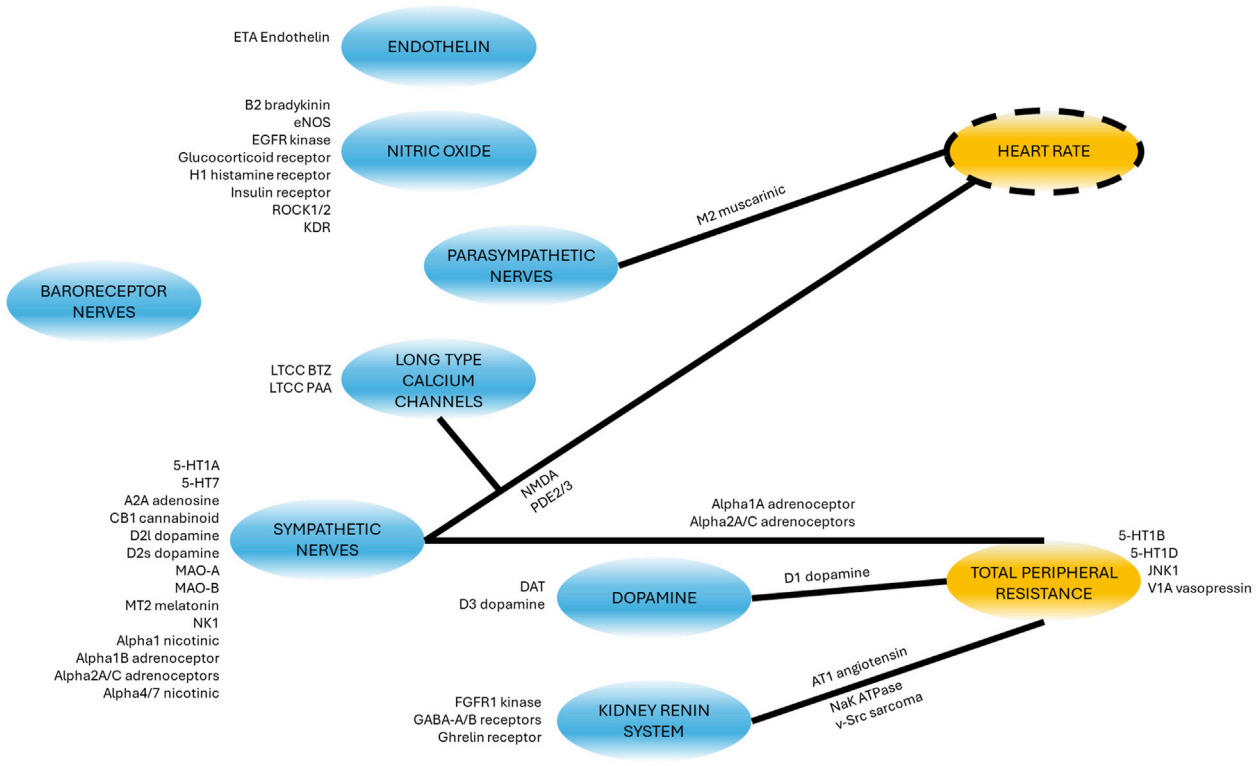

FIGURE 6
Schematic showing where the secondary pharmacology targets of interest affect the model. Targets next to blocks affect the molecular pathway or physiological phenomena whilst targets next to lines modulate the effect of the block (blue) on the other variable (yellow). For a detailed description of the targets full name and function, see Supplementary Table S39.

Qualitative modulation due to secondary pharmacology

A list of 50 secondary pharmacology targets known to be modulated by drugs and to have significant roles in hemodynamics regulation was derived (Supplementary Table S39). These secondary pharmacology targets are regularly screened internally at AstraZeneca for hemodynamic toxicity risk assessment. The model design reflects this pre-defined list by explicitly describing some blocks (e.g., the role of endothelin or NO) in order to enable the integration of this secondary pharmacology. Figure 6 shows the physiological processes which can be affected by disrupting these secondary pharmacology targets. It can be seen that some blocks can be affected by the disruption of many of the targets included in our list (e.g., sympathetic nerves) while others may be related to one target. Direct effects of targets on hemodynamic pathways was implemented in the same way for rats and dogs with the exception of D3 dopamine receptor on RAAS (as modelled via PRA), as explained in the section "Model structure."

We researched the literature in order to derive a list of qualitative outcomes to benchmark the model when antagonising or agonising these targets. We then investigated if simulations were able to reproduce the observed trends by exploring modulation of the affected pathways (reduction or increase for antagonism or agonism respectively). For each target, for each type of modulation (agonism or antagonism) and for each of the two species, we then classified the predicted changes into strong (observations changes greater than 5% in the right direction) and minor (observations changes lower than 5% but still in the right direction).

Figure 7 shows that for each one of the available readouts (HR, dPdt and MAP), simulations predicted potential strong changes in many cases. It should be noted, however, that for some of the readouts (e.g., dPdt) very little information was available and therefore our outcome knowledge is not uniformly distributed across the target of interests. While other simulations only predicted minor changes in the readouts, no outcome was predicted in the wrong direction. Overall, these results provide confidence that the model can capture, mechanistically, a wide panel of secondary pharmacology disruption effects on hemodynamics.

Discussion

In this paper we aimed to develop models for dog and rat species which are routinely used in pre-clinical studies. In the proposed models the various physiological mechanisms involved in the regulation of mean arterial blood pressure (MAP) and heart rate (HR) are decomposed into 13 model variables representing biological pathways, clinical readouts, and their interactions. On one hand, the final choice of this model diagram reflects our understanding of the current literature and a search for a parsimonious model that captures the variety of responses seen in hemodynamics changes, hence the inclusion of essential components such as the autonomic and kidney renin systems. On the other hand, the complexity of the animal

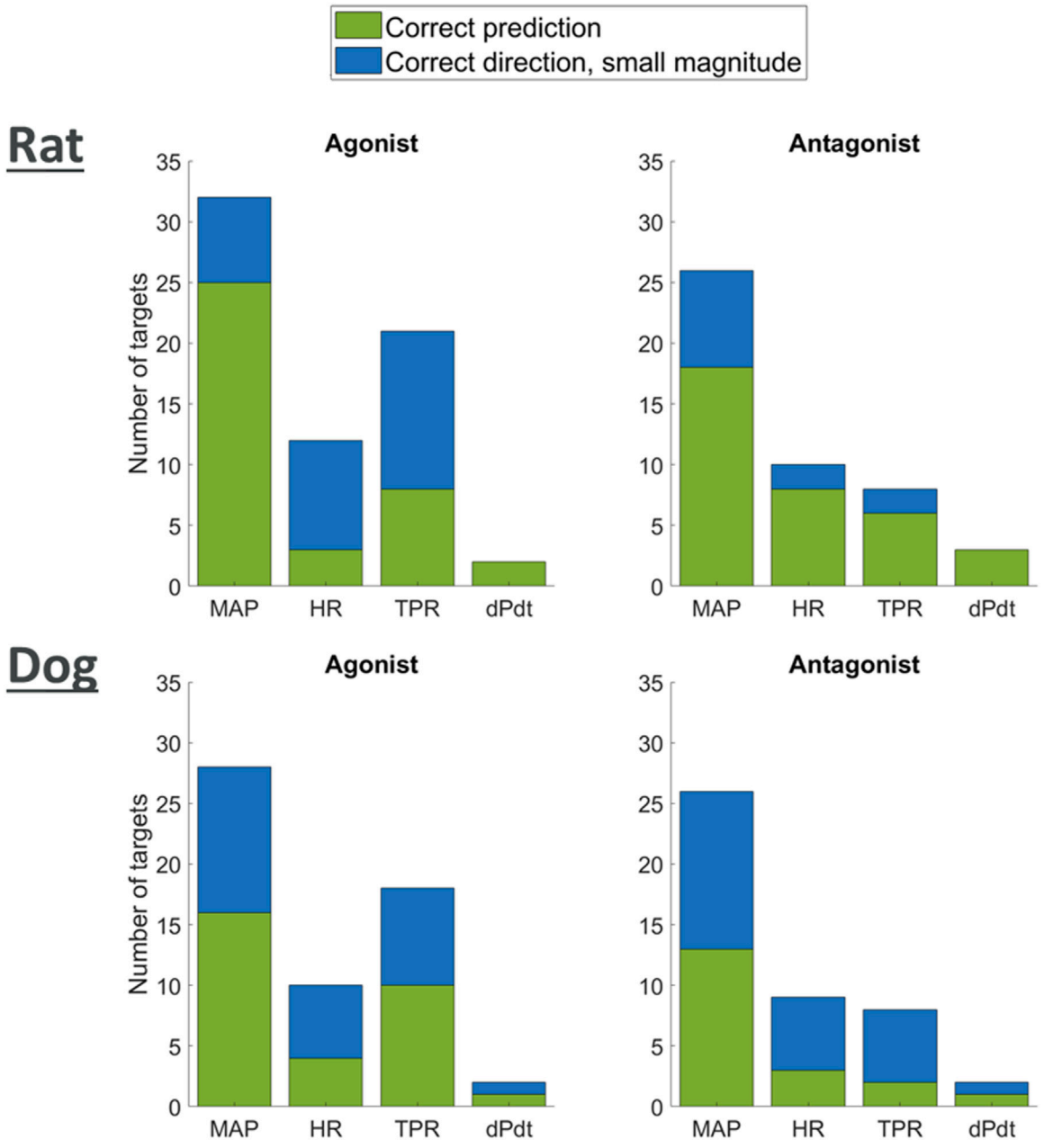

FIGURE 7
Plot showing agreement of model predictions with literature knowledge on the effects of agonism or antagonism of single targets on MAP, HR, TPR, and dPdt.

physiology precludes the inclusion of every single process at the cellular, tissue or systemic level. Many processes have been implicitly integrated in the model: For instance the complex Renin system, whose cascade of events leading to Stroke Volume (SV) and HR modulations (Guyton et al., 1972; Karaasalan et al., 2005), was simply modelled as Plasma Renin Activity (PRA) and its relationship with those readouts.

Several biological quantities and processes (e.g., the effects of dopamine or through LTCC) have been explicitly included to enable studying their disruption. This aligns with our aim to predict the effects of 50 secondary pharmacology targets which was pre-selected (Supplementary Table S39). We regularly screen these targets, which have important role in hemodynamics regulation and are also commonly affected by drug candidate molecules. Our need to enable linking all of this secondary pharmacology necessitated the inclusion of additional pathways and variables. By doing this, we could create a direct connection between each target and the specific part of the model it disrupts (Figure 6).

We developed two versions of the models, mainly based on alternative parametrizations for dog and rat. Once we derived the overall model diagram, each one of its components have been individually modelled based on literature involving *in vitro*, *in vivo* and *ex vivo* experiments in these species. Several notable assumptions had to be made in order to achieve a parsimonious, tractable model. The

representation of pathways has indeed often been encapsulated into a single variable. In the nerves, the action of neurotransmitters and ion fluxes across the cell membrane was simply modelled as changes in firing frequency. Renin-related effects on hemodynamics involve multiple intermediate steps including altering the blood volume through triggering thirst and altering urine output, but this has been combined into single interactions of plasma renin activity on HR, SV and TPR. Plasma sodium concentration is an important factor in renin effects on heart rate but has been neglected because sodium concentration is not expected to vary significantly during telemetry studies performed as part of a preclinical safety assessment. In the future it would be useful to incorporate the effect of changes in sodium concentration to allow simulation of patients with sodium retention and hypertension.

Whilst it is likely that other variables could also be included for representing pathway variables, a minimum number of variables best thought to represent the pathways were chosen to limit the complexity of the model and data requirements. For instance, for nerve experiments, stimulation frequencies were chosen as a natural variable to modulate nerves response and hemodynamic changes. In modelling these nerves response, we could for instance have added the amplitude of spikes voltage or the synapses neurotransmitters concentration which would have introduced additional variables and required additional data. A higher level of granularity could also have involved for instance the modelling of ion fluxes causing changes in the membrane voltage and so on. We did not believe that this increased level of description and modelling was required for the scope delineated here and therefore simply modelled the overall relationship via stimulation frequencies. A similar approach was taken for all other block interactions.

Additionally, we were not able to always find the same type of data for the two species. For instance, the relationship between changes in MAP and baroreceptors firing was modelled in rats using experiments where pressure was varied in an *ex vivo* preparation of the aortic arch to stimulate the baroreceptors. For the dog species, data from experiments where carotid sinus baroreceptors (Coleridge et al., 1987) or aortic arch baroreceptors (Coleridge et al., 1981) were stimulated *in vivo* were used. In some cases, some of the interactions between components could not be isolated and therefore a few pathways had to be modelled concomitantly (e.g., for HR and contractility effects on SV). Overall, we believe however that the results presented here capture hemodynamics regulation in dogs and rats to an appropriate level of complexity. The two models reflect up-to-date data and knowledge and were designed with a moderate level of granularity. Improvements can be done on a need basis by further elaborating on some of the pathways (while ensuring the overall model behaviour remains consistent with known results).

An additional hemodynamic measure that was not included in the model since it is not routinely measured in preclinical telemetry studies is heart rate variability. Heart rate variability is the fluctuation in the time intervals between adjacent heartbeats (Shaffer and Ginsberg, 2017). It is a metric that can be used to assess autonomic activity (Ghezzi et al., 2024; von Borell et al., 2007; Stauss, 2003), particularly control of heart rate (Švorc et al., 2023; Mangin et al., 1998; Ketabchi et al., 2024; Zajączkowski et al., 2018). Heart rate variability, however, differs significantly across studies and reference values for rats are not available (Švorc et al., 2023). For more discussion on the relevance of heart rate variability please see the Supplementary Material Section "Heart Rate Variability." While modelling heart variability has not been done here, it could however constitute an important future step.

Other model extensions could include the effects of anaesthesia (which can have various effects on hemodynamics), or the effects of acute or chronic pain, metabolic diseases (for example diabetes or Cushing's), stress, neoplasms, sepsis and kidney dysfunctions. These were not included since focus was on preclinical healthy animal telemetry studies routinely used in drug development. Nonetheless, we believe that the modelling approaches presented here would be amenable to investigating such situations and could provide an important advancement in the understanding of how different patients may respond to novel medicines.

Modelling all relationships for both rat and dog species in our network diagram resulted in two virtual animal models. Once assembled, these models were used to simulate daily changes and several pharmacological or nerve stimulation interventions, demonstrating that the assembled model predictions agree with quantitative and qualitative observations reported in these settings. While most predictions well aligned with reported outcomes, some discrepancies were noted which should be considered within the context of differences in terms of animals, labs and experimental protocols used in these reference experiments (especially potential effects of anaesthetics, known to have hemodynamic effects). A number of approaches could be taken in the future to address this, such as the inclusion of additional datasets to better assess the needs for further modelling.

We also explored the effects of modulating the likely sites of action in our model for our list of 50 secondary pharmacology targets. In all cases simulations predicted the right direction in terms of changes for MAP, HR and contractility (dPdt). In most of these cases the model was able to induce substantial changes, while in other cases only minor changes were predicted as is. However, this is unlikely to be problematic for two reasons. First, most of the benchmarks were qualitative, and therefore while the directionality of the changes was reported, the true extent of these changes remained unknown. Secondly, the fact that the model can predict the right direction in changes but possibly not in magnitude is something that can likely be addressed via global model calibration using appropriate reference pharmacological datasets. This is indeed the approach that could be taken in order to derive a Quantitative Systems Toxicology (QST) platform based on this work that would support drug discovery and development. This platform could then be deployed as a user-friendly tool (for example an R Shiny or MATLAB Compiled application).

We have focussed on rats and dogs as two of the most common preclinical species for *in vivo* drug development studies. Understanding root causes of hemodynamic changes in these two pre-clinical species increase confidence in predicting translation to human. An obvious expansion could involve a human model which can be used for translation purposes once mechanisms are elucidated in pre-clinical species.

One of the main aims for the use of this mechanistic model is to enable better combined interpretation of pre-clinical secondary pharmacology and *in vivo* data, ultimately improving the establishment of toxicity hypotheses and translation risk. The incorporation of multiple targets and molecular pathways increase the chances of detecting the mechanisms related to observed *in vivo* changes, while it could also explain interaction between target effects. Indeed, some effects might not be individually significant but might, together, cause complex changes in hemodynamics. Such an approach

would complement the use of more phenomenological models such as Snelder for rat (Snelder et al., 2014; Snelder et al., 2013) or Fu for dog (Fu et al., 2022), particularly when elucidating underlying mechanisms and translation.

Conclusion

In this publication we have reviewed the literature and developed mechanistic mathematical models of hemodynamics regulation in rat and dog species. The models integrate many regulatory pathways and their interactions giving rise to hemodynamics changes. They have similar structure but different parametrization (one set per species) and can incorporate the site of actions of at least 50 known secondary pharmacology targets. It was demonstrated that the model can reproduce various interventions in intact animals in a series of *in silico* experiments. A number of additional steps could be taken in the future including global model calibration using large datasets and the development of a human version which could also include disease characteristics.

Data availability statement

The original contributions presented in the study are included in the article/Supplementary Material, further inquiries can be directed to the corresponding author.

Author contributions

CM: Data curation, Formal Analysis, Investigation, Methodology, Writing–original draft. MR: Conceptualization, Writing–review and editing. LS: Writing–review and editing. IV: Writing–review and editing. AP: Conceptualization, Writing-review and editing. HK: Conceptualization, Writing-review and editing. GD: Conceptualization, Funding acquisition, Investigation, Methodology, Project administration, Resources, Supervision, Validation, Visualization, Writing–original draft.

Funding

The author(s) declare that no financial support was received for the research, authorship, and/or publication of this article.

Conflict of interest

Author(s) CM, KH, GD, MR, LS, CV, and AP were employed by the AstraZeneca.

Publisher's note

All claims expressed in this article are solely those of the authors and do not necessarily represent those of their affiliated organizations, or those of the publisher, the editors and the reviewers. Any product that may be evaluated in this article, or claim that may be made by its manufacturer, is not guaranteed or endorsed by the publisher.

Supplementary material

The Supplementary Material for this article can be found online at: https://www.frontiersin.org/articles/10.3389/fphar.2024.1402462/full#supplementary-material

References

Accorsi-Mendonça, M. B., and Machado, B. H. (2013). Synaptic transmission of baro- and chemoreceptors afferents in the NTS second order neurons. *Aut. Neurosci.* 175, 3–8. doi:10.1016/j.autneu.2012.12.002

Ahmad, A., Dempsey, S. K., Daneva, Z., Azam, M., Li, N., Li, P.-L., et al. (2018). Role of nitric oxide in the cardiovascular and renal systems. *Int. J. Mol. Sci.* 19, 2605. doi:10.3390/ijms19092605

Aldehni, F., Tang, T., Madsen, K., Plattner, M., Schreiber, A., Friis, U. G., et al. (2011). Stimulation of renin secretion by catecholamines is dependent on adenylyl cyclases 5 and 6. *Hypertension* 57, 460–468. doi:10.1161/HYPERTENSIONAHA.110.167130

Alhayek, S., and Preuss, C. V. (2023). "Beta 1 receptors," in *StatPearls* (Treasure Island (FL): StatPearls Publishing). Updated 2023 Aug 14.

Ames, M. K., Atkins, C. E., and Pitt, B. (2019). The renin-angiotensin-aldosterone system and its suppression. *J. Veterinary Intern. Med.* 33, 363–382. doi:10.1111/jvim.15454

Anderson, D. E., Gomez-Sanchez, C., and Dietz, J. R. (1986). Suppression of plasma renin and aldosterone in stress-salt hypertension in dogs. *Am. J. Physiology* 251, R181–R186. doi:10.1152/ajpregu.1986.251.1.R181

Anderson, W. P., Shweta, A., Evans, R. G., Edgley, A. J., and Gao, Y. (2007). Total peripheral resistance responsiveness during the development of secondary renal hypertension in dogs. *J. Hypertens.* 25, 649–662. doi:10.1097/HJH.0b013e3280112cf6

Andreatta, G., and Allen, C. N. (2021). Circadian rhythm: how neurons adjust to diurnality. *eLife* 10, e74704. doi:10.7554/eLife.74704

Andresen, M. C., and Yang, M. (1989). Interaction among unitary spike trains: implications for whole nerve measurements. *Am. J. Physiology - Regul. Integr. Comp. Physiology* 256, R997–R1004. doi:10.1152/ajpregu.1989.256.4.R997

Andrew, P. J., and Mayer, B. (1999). Enzymatic function of nitric oxide synthases. *Cardiovasc. Res.* 43, 521–531. doi:10.1016/s0008-6363(99)00115-7

Armando, I., Van Anthony, M. V., and Jose, P. A. (2011). Dopamine and renal function and blood pressure regulation. *Compr. Physiol.* 1, 1075–1117. doi:10.1002/cphy.c100032

Armstrong, M., Kerndt, C. C., and Moore, R. A. (2023). "Physiology, baroreceptors," in *StatPearls* (Treasure Island (FL): StatPearls Publishing). Updated 2023 Mar 6.

Ashkar, E. (1979). Twenty-four-hour pattern of circulation by radiotelemetry in the unrestrained dog. *Am. J. Physiology - Regul. Integr. Comp. Physiology* 5, R231–R236. doi:10.1152/ajpregu.1979.236.3.R231

Augustin, H. J., Baumgarten, H. G., Huland, H., and Leichtweiβ, H.-P. (1977). The vasoconstrictive effect of dopamine in the isolated, perfused rat kidney afer catecholamine depletion. *Res. Exp. Med.* 170, 1–15. doi:10.1007/BF01852114

Averina, V. A., Othmer, H. G., Fink, G. D., and Osborn, J. W. (2012). A new conceptual paradigm for the haemodynamics of salt-sensitive hypertension: a mathematical modelling approach. *J. Physiology* 590, 5975–5992. doi:10.1113/jphysiol.2012.228619

Bacq, Y., Roulot, D., Braillon, A., and Lebrec, D. (1990). Hemodynamic effects of dopamine in conscious rats with secondary biliary cirrhosis. *J. Hepatology* 11, 257–262. doi:10.1016/0168-8278(90)90122-8

Bankenahally, R., and Krovvidi, H. (2016). Autonomic nervous system: anatomy, physiology, and relevance in anaesthesia and critical care medicine. *BJA Educ.* 16, 381–387. doi:10.1093/bjaed/mkw011

Beard, D. A., Pettersen, K. H., Carlson, B. E., Omholt, S. W., and Bugenhagen, S. M. (2013). A computational analysis of the long-term regulation of arterial pressure. *F1000 Res.* 2, 208. doi:10.12688/f1000research.2-208.v2

Beaulieu, J.-M., and Gainetdinov, R. R. (2011). The physiology, signaling, and pharmacology of dopamine receptors. *Pharmacol. Rev.* 63, 182–217. doi:10.1124/pr.110.002642

Berecek, K. H., Kirk, K. A., Nagahama, S., and Oparil, S. (1987). Sympathetic function in spontaneously hypertensive rats after chronic administration of captopril. *Am. J. Physiology* 252, H796–H806. doi:10.1152/ajpheart.1987.252.4.H796

Bernal, A., Zafra, M. A., Simón, M. J., and Mahía, J. (2023). Sodium homeostasis: a balance necessary for life. *Nutrients* 15, 395. doi:10.3390/nu15020395

Bernardi, S., Michelli, A., Zuolo, G., Candido, R., and Fabris, B. (2016). Update on RAAS modulation for the treatment of diabetic cardiovascular disease. *J. Diabetes Res.* 2016, 8917578. doi:10.1155/2016/8917578

Bertolino, S., Julien, C., Medeiros, I. A., Vincent, M., and Barrès, C. (1994). Pressure-dependent renin release and arterial pressure maintenance in conscious rats. *Am. J. Physiology* 266, R1032–R1037. doi:10.1152/ajpregu.1994.266.3.R1032

Bhatt, S., Northcott, C., Wisialowski, T., Li, D., and Steidl-Nichols, J. (2019). Preclinical to clinical translation of hemodynamic effects in cardiovascular safety pharmacology studies. *Toxicol. Sci.* 169, 272–279. doi:10.1093/toxsci/kfz035

Biaggioni, I. (1992). Contrasting excitatory and inhibitory effects of adenosine in blood pressure regulation. *Hypertension* 20, 457–465. doi:10.1161/01.hyp.20.4.457

Black, W. L., and Rolett, E. L. (1966). Dopamine-induced alterations in left ventricular performance. *Circulation Res.* 19, 71–79. doi:10.1161/01.res.19.1.71

Blanc, J., Lambert, G., and Elghozi, J.-L. (2000). Endogenous renin and related short-term blood pressure variability in the conscious rat. *Eur. J. Pharmacol.* 394, 311–320. doi:10.1016/s0014-2999(00)00070-4

Bolli, P., Erne, O., Ji, B. H., Block, L. H., Kiowski, W., and Bühler, F. R. (1984). Adrenaline induces vasoconstriction through post-junctional alpha 2 adrenoceptors and this response is enhanced in patients with essential hypertension. *J. Hypertens.* 2, S115–S118.

Bonizzoni, E., Milani, S., Ongini, E., Casati, C., and Monopoli, A. (1995). Modeling hemodynamic profiles by telemetry in the rat: a study with A1 and A2a adenosine agonists. *Hypertension* 25, 564–569. doi:10.1161/01.hyp.25.4.564

Boularan, C., and Gales, C. (2015). Cardiac cAMP: production, hydrolysis, modulation and detection. *Front. Pharmacol.* 6, 203. doi:10.3389/fphar.2015.00203

Boyes, N. G., Marciniuk, D. D., Haddad, H., and Tomczak, C. R. (2022). Autonomic cardiovascular reflex control of hemodynamics during exercise in heart failure with reduced ejection fraction and the effects of exercise training. *Rev. Cardiovasc. Med.* 23, 72. doi:10.31083/j.rcm2302072

Boysen, N. C., Dragon, D. N., and Talman, W. T. (2009). Parasympathetic tonic dilatory influences on cerebral vessels. *Aut. Neurosci. Basic Clin.* 147, 101–104. doi:10.1016/j.autneu.2009.01.009

Bredt, D. S. (1999). Endogenous nitric oxide synthesis: biological functions and pathophysiology. *Free Radic. Res.* 31, 577–596. doi:10.1080/10715769900301161

Briant, L. J. B., Paton, J. F. R., Pickering, A. E., and Champneys, A. R. (2015). Modelling the vascular response to sympathetic postganglionic nerve activity. *J. Theor. Biol.* 371, 102–116. doi:10.1016/j.jtbi.2015.01.037

Britton, S. L., Sexton, J. M., Fiksen-Olsen, M. J., Werness, P. G., and Romero, J. C. (1980). A comparison of angiotensin II and angiotensin III as vasoconstrictors in the mesenteric circulation of dogs. *Circulation Res.* 46, 146–151. doi:10.1161/01.res.46.1.146

Brodde, O.-E. (1993). Beta-adrenoceptors in cardiac disease. *Pharmacol. and Ther.* 60, 405–430. doi:10.1016/0163-7258(93)90030-h

Brokaw, J. J., and Hansen, J. T. (1987). Evidence that dopamine regulates norepinephrine synthesis in the rat superior cervical ganglion during hypoxic stress. *J. Aut. Nerv. Syst.* 18, 185–193. doi:10.1016/0165-1838(87)90117-2

Brown, A. M., Saum, W. R., and Tuley, F. H. (1976). A comparison of aortic baroreceptor discharge in normotensive and spontaneously hypertensive rats. *Circulation Res.* 39, 488–496. doi:10.1161/01.res.39.4.488

Bryan, N. S. (2022). Nitric oxide deficiency is a primary driver of hypertension. *Biochem. Pharmacol.* 206, 115325. doi:10.1016/j.bcp.2022.115325

Bugenhagen, S. M., Cowley, A. W., and Beard, D. A. (2010). Identifying physiological origins of baroreflex dysfunction in salt-sensitive hypertension in the Dahl SS rat. *Physiol. Genomics* 42, 23–41. doi:10.1152/physiolgenomics.00027.2010

Burnstock, G. (1981). Review lecture. Neurotransmitters and trophic factors in the autonomic nervous system. *J. Physiology* 313, 1–35. doi:10.1113/jphysiol.1981.sp013648

Buttrick, P., Malhotra, A., Factor, S., Geenen, D., and Scheuer, J. (1988). Effects of chronic dobutamine administration on hearts of normal and hypertensive rats. *Circulation Res.* 63, 173–181. doi:10.1161/01.res.63.1.173

Bylund, D. B. (2003). "Norepinephrine," in *Encyclopedia of the neurological sciences*. Editors M. J. Aminoff and R. B. Daroff (Academic Press).

Canty, J. M., and Schwartz, J. S. (1994). Nitric oxide mediates flow-dependent epicardial coronary vasodilation to changes in pulse frequency but not mean flow in conscious dogs. *Circulation* 89, 375–384. doi:10.1161/01.cir.89.1.375

Challet, E. (2007). Minireview: entrainment of the suprachiasmatic clockwork in diurnal and nocturnal mammals. *Endocrinology* 148, 5648–5655. doi:10.1210/en.2007-0804

Champney, T. H., Steger, R. W., Christie, D. S., and Reiter, R. J. (1985). Alterations in components of the pineal melatonin synthetic pathway by acute insulin stress in the rat and Syrian hamster. *Brain Res.* 338, 25–32. doi:10.1016/0006-8993(85)90244-6

Chappell, M. C. (2012). Nonclassical renin-angiotensin system and renal function. *Compr. Physiol.* 2, 2733–2752. doi:10.1002/cphy.c120002

Christ, T., Galindo-Tovar, A., Thoms, M., Ravens, U., and Kaumann, A. J. (2009). Inotropy and L-type Ca^{2+} current, activated by β_1-and β_2-adrenoceptors, are differently controlled by phosphodiesterases 3 and 4 in rat heart. *Br. J. Pharmacol.* 156, 62–83. doi:10.1111/j.1476-5381.2008.00015.x

Chu, B., Marwaha, K., Sanvictores, T., Awosika, A. O., and Ayers, D. (2024). "Physiology, stress reaction," in *StatPearls* (Treasure Island (FL): StatPearls Publishing).

Clozel, J.-P., and Clozel, M. (1989). Effects of endothelin on the coronary vascular bed in open-chest dogs. *Circulation Res.* 65, 1193–1200. doi:10.1161/01.res.65.5.1193

Coleman, T. G., and Guyton, A. C. (1969). Hypertension caused by salt loading in the dog: III. Cinset transients of cardiac output and other circulatory variables. *Circulation Res.* 25, 153–160. doi:10.1161/01.res.25.2.153

Coleman, T. G., and Hall, J. E. (1992). "A mathematical model of renal hemodynamics and excretory function," in *Structuring biological systems: a computer modeling approach*. Editor S. S. Iyenar (Florida, USA: CRC Press).

Coleridge, H. M., Coleridge, J. C., and Schultz, H. D. (1987). Characteristics of C fibre baroreceptors in the carotid sinus of dogs. *J. Physiology* 394, 291–313. doi:10.1113/jphysiol.1987.sp016871

Coleridge, H. M., Coleridge, J. C. G., Kaufman, M. P., and Dangel, A. (1981). Operational sensitivity and acute resetting of aortic baroreceptors in dogs. *Circulation Res.* 48, 676–684. doi:10.1161/01.res.48.5.676

Corea, M., Seeliger, E., Boemke, W., and Reinhardt, H. E. (1996). Diurnal pattern of sodium excretion in dogs with and without chronically reduced renal perfusion pressure. *Kidney Blood Press. Res.* 19, 16–23. doi:10.1159/000174041

Cowley, A. W., and Roman, R. J. (1989). Control of blood and extracellular volume. *Bailliere's Clin. Endocrinol. Metabolism* 3, 331–369. doi:10.1016/s0950-351x(89)80007-2

Curtis, B. M., and O'Keefe, J. H. (2002). Autonomic tone as a cardiovascular risk factor: the dangers of chronic fight or flight. *Mayo Clin. Proc.* 77, 45–54. doi:10.4065/77.1.45

Dalal, R., and Grujic, D. (2023). "Epinephrine," in *StatPearls* (Treasure Island (FL): StatPearls Publishing). Updated 2023 May 1.

Dampney, R. A. L. (2017). Resetting of the baroreflex control of sympathetic vasomotor activity during natural behaviors: description and conceptual model of central mechanisms. *Front. Neurosci.* 11, 461. doi:10.3389/fnins.2017.00461

Deehan, N., Goddard, T., Kohan, D. E., Pollock, D. M., Schiffrin, E. L., and Webb, D. J. (2008). Role of endothelin-1 in clinical hypertension: 20 years on. *Hypertension* 52, 452–459. doi:10.1161/HYPERTENSIONAHA.108.117366

Desborough, J. P. (2000). The stress response to trauma and surgery. *Br. J. Anaesth.* 85, 109–117. doi:10.1093/bja/85.1.109

Dhaun, N., Goddard, J., Kohan, D. E., Pollock, D. M., Schiffrin, E. L., and Webb, D. J. (2008). Role of endothelin-1 in clinical hypertension: 20 years on. *Hypertension* 52, 452–459. doi:10.1161/HYPERTENSIONAHA.108.117366

Difrancesco, D. (2010). The role of the funny current in pacemaker activity. *Circulation Res.* 106, 434–446. doi:10.1161/CIRCRESAHA.109.208041

Difrancesco, D., and Tortora, P. (1991). Direct activation of cardiac pacemaker channels by intracellular cyclic AMP. *Nature* 351, 145–147. doi:10.1038/351145a0

Di Salvo, J., Britton, S., Galvas, P., and Sanders, T. W. (1973). Effects of angiotensin I and antiotensin II on canine hepatic vascular resistance. *Circulation Res.* 32, 85–92. doi:10.1161/01.res.32.1.85

Dixit, M. P., Xu, L., Xu, H., Bai, L., Collins, J. F., and Ghishan, F. K. (2004). Effect of angiotensin-II on renal Na+/H+ exchanger-NHE3 and NHE2. *Biochimica Biophysica Acta (BBA)* 1664, 38–44. doi:10.1016/j.bbamem.2004.03.011

Dominiczak, A. F., and Bohr, D. F. (1995). Nitric oxide and its putative role in hypertension. *Hypertension* 25, 1202–1211. doi:10.1161/01.hyp.25.6.1202

Drenjančević-Perić, I., Jelaković, B., Lombard, J. H., Kunert, M. P., Kibel, A., and Gros, M. (2011). High-salt diet and hypertension: focus on the renin-angiotensin system. *Kidney Blood Press. Res.* 34, 1–11. doi:10.1159/000320387

Drieman, J. C., Van Kan, F. J. P. M., Thijssen, H. H. W., Van Essen, H., Smits, J. F. M., and Struijker Boudier, H. A. J. (1994). Regional haemodynamic effects of dopamine and its prodrugs L-dopa and gludopa in the rat and in the glycerol-treated rat as a model for acute renal failure. *Br. J. Pharmacol.* 111, 1117–1122. doi:10.1111/j.1476-5381.1994.tb14860.x

Durgan, D. J., Crossland, R. F., Loloyd, E. E., Phllips, S. C., and Bryan, R. M. (2015). Increased cerebrovascular sensitivity to endothelin-1 in a rat model of obstructive sleep apnea: a role for endothelin receptor B. *J. Cereb. Blood Flow Metabolism* 35, 402–411. doi:10.1038/jcbfm.2014.214

Ehmke, H., Persson, P., Hackenthal, E., and Kirchheim, H. (1989). Resetting of pressure-dependent renin release by intrarenal alpha1-adrenoceptors in concsious dogs. *Pflügers Arch.* 413, 261–266. doi:10.1007/BF00583539

Ewart, L., Aylott, M., Deurinck, M., Engwall, M., Gallacher, D. J., Geys, H., et al. (2014). The concordance between nonclinical and phase I clinical cardiovascular assessment from a cross-company data sharing initiative. *Toxicol. Sci.* 142, 427–435. doi:10.1093/toxsci/kfu198

FDA (2022). *Assessment of pressor effects of drugs: draft guidance for industry*.

Fernandez, L. A., Rettori, O., and Mejía, R. H. (1965). Correlation between body fluid volumes and body weight in the rat. *Am. J. Physiology* 210, 877–879. doi:10.1152/ajplegacy.1966.210.4.877

Fitzgerald, S. M., Stevenson, K. M., Evans, R. G., and Anderson, W. P. (1997). Low dose angiotensin II infusions into the renal artery induce chronic hypertension in conscious dogs. *Blood Press.* 6, 52–61. doi:10.3109/08037059709086446

Fitzsimmons, J. T., and Simons, B. J. (1969). The effect on drinking in the rat of intravenous infusion of angiotensin, given alone or in combination with other stimuli of thirst. *J. Physiology* 203, 45–57. doi:10.1113/jphysiol.1969.sp008848

Florea, V. G., and Cohn, J. N. (2014). The autonomic nervous system and heart failure. *Circulation Res.* 114, 1815–1826. doi:10.1161/CIRCRESAHA.114.302589

Förstermann, U., and Münzel, T. (2006). Endothelial nitric oxide synthase in vascular disease: from marvel to menace. *Circulation* 113, 1708–1714. doi:10.1161/CIRCULATIONAHA.105.602532

Förstermann, U., and Sessa, W. C. (2012). Nitric oxide synthases: regulation and function. *Eur. Heart J.* 33, 829–837. doi:10.1093/eurheartj/ehr304

Fountain, J. H., Kaur, J., and Lappin, S. L. (2023). "Physiology, renin angiotensin system," in *StatPearls* (Treasure Island (FL): StatPearls Publishing). Updated 2023 Mar 12.

Furnival, C. M., Linden, R. J., and Snow, H. M. (1971). The inotropic and chronotropic effects of catecholamines on the dog heart. *J. Physiology* 214, 15–28. doi:10.1113/jphysiol.1971.sp009416

Fu, Y., Taghvafard, H., Said, M. M., Rossman, E. I., Collins, T. A., Billiald-Desquand, S., et al. (2022). A novel cardiovascular systems model to quantify drugs effects on the inter-relationship between contractility and other hemodynamic variables. *CPT Pharmacometrics and Syst. Pharmacol.* 11, 640–652. doi:10.1002/psp4.12774

Gaustad, S. E., Kondratiev, T. V., Eftedal, I., and Tveita, T. (2020). Continuous hemodynamic monitoring in an intact rat model of simulated diving. *Front. Physiology* 10, 1597. doi:10.3389/fphys.2019.01597

Gerghel, D., Hosking, L., and Orgül, S. (2004). Autonomic nervous system, circadian rhythms, and primary open-angle glaucoma. *Surv. Ophthalmol.* 49, 491–508. doi:10.1016/j.survophthal.2004.06.003

Gerová, M., and Gero, J. (1969). Range of the sympathetic control of the dog femoral artery. *Circulation Res.* 24, 349–359. doi:10.1161/01.res.24.3.349

Ghezzi, M. D., Ceriani, M. C., Domínguez-Oliva, A., Lendez, P. A., Olmos-Hernández, A., Casas-Alvarado, A., et al. (2024). Use of infrared thermography and heart rate variability to evaluate autonomic activity in domestic animals. *Animals* 14, 1366. doi:10.3390/ani14091366

Giannetti, F., Benzoni, P., Campostrini, G., Milanesi, R., Bucchi, A., Baruscotti, M., et al. (2021). A detailed characterization of the hyperpolarization-activated "funny" current (I_f) in human-induced pluripotent stem cell (iPSC)-derived cardiomyocytes with pacemaker activity. *Pflügers Arch.* 473, 1009–1021. doi:10.1007/s00424-021-02571-w

Gibbins, I. (2013). Functional organization of autonomic neural pathways. *Organogenesis* 9, 169–175. doi:10.4161/org.25126

Given, M. B., Lowe, R. F., Lippton, H., Hyman, A. L., Sander, G. E., and Giles, T. D. (1989). Hemodynamic actions of endothelin in conscious and anesthetized dogs. *Peptides* 10, 41–44. doi:10.1016/0196-9781(89)90073-9

Goldberg, L. I. (1984). Dopamine receptors and hypertension: physiologic and pharmacologic implications. *Am. J. Med.* 77, 37–44. doi:10.1016/s0002-9343(84)80036-4

Gordan, R., Gwathmey, J. K., and Xie, L.-H. (2015). Autonomic and endocrine control of cardiovascular function. *World J. Cardiol.* 7, 204–214. doi:10.4330/wjc.v7.i4.204

Gordon, R. D., Küchel, O., Liddle, G. W., and Island, D. P. (1967). Role of the sympathetic nervous system in regulating renin and aldosterone production in man. *J. Clin. Investigation* 46, 599–605. doi:10.1172/JCI105561

Graudal, N., Hubeck-Graudal, T., and Jurgens, G. (2021). Influence of sodium intake and change in sodium intake on plasma-renin in man. *eClinicalMedicine* 33, 100750. doi:10.1016/j.eclinm.2021.100750

Gross, R., Hackenberg, H.-M., Hackenthal, E., and Kirchheim, H. (1981). Interaction between perfusion pressure and sympathetic nerves in renin release by carotid baroreflex in conscious dogs. *J. Physiology* 313, 237–250. doi:10.1113/jphysiol.1981.sp013661

Guimaraes, S., and Moura, D. (2001). Vascular adrenoceptors: an update. *Pharmacol. Rev.* 53, 319–356.

Gumarova, L., Farah, Z., Tyutenova, A., Gumarova, Z., Sackett-Lundeen, L., Kazlausky, T., et al. (2021). Comparative analysis of circadian rhythms of hemodynamics and physical activity. *Biol. Rhythm Res.* 53, 1321–1333. doi:10.1080/09291016.2021.1922827

Guyton, A. C. (1990). Long-term arterial-pressure control - an analysis from animal-experiments and computer and graphic models. *Am. J. Physiology* 259, R865–R877. doi:10.1152/ajpregu.1990.259.5.R865

Guyton, A. C., Granger, H. J., and Coleman, T. G. (1972). Circulation: overall regulation. *Annu. Rev. Physiology* 34, 13–46. doi:10.1146/annurev.ph.34.030172.000305

Hallare, J., and Gerriets, V. (2023). *Half life*. Treasure Island (FL): StatPearls. Updated 2023 Jun 20.

Hallow, K. M., and Gebremichael, Y. (2017). A quantitative systems physiology model of renal function and blood pressure regulation: model description. *CPT Pharmacometrics and Syst. Pharmacol.* 6, 383–392. doi:10.1002/psp4.12178

Hannibal, J. (2002). Neurotransmitters of the retino-hypothalamic tract. *Cell. Tissue Res.* 309, 73–88. doi:10.1007/s00441-002-0574-3

Head, G. A., and Mccarty, R. (1987). Vagal and sympathetic components of the heart rate range and gain of the baroreceptor-heart rate reflex in conscious rats. *J. Aut. Nerv. Syst.* 21, 203–213. doi:10.1016/0165-1838(87)90023-3

Hernández-Avalos, I., Flores-Gasca, E., Mota-Rojas, D., Casas-Alvarado, A., Miranda-Cortés, A. E., and Domínguez-Oliva, A. (2021). Neurobiology of anesthetic-surgical stress and induced behavioral changes in dogs and cats: a review. *Veterinary World* 14, 393–404. doi:10.14202/vetworld.2021.393-404

Herring, N. (2015). Autonomic control of the heart: going beyond the classical neurotransmitters. *Exp. Physiol.* 100, 354–358. doi:10.1113/expphysiol.2014.080184

Hilfenhaus, M. (1976). Circadian rhythm of the renin-angiotensin-aldosterone system in the rat. *Archives Toxicol.* 36, 305–316. doi:10.1007/BF00340536

Höglund, O. V., Lövebrant, J., Olsson, U., and Höglund, K. (2016). Blood pressure and heart rate during ovariohysterectomy in pyometra and control dogs: a preliminary investigation. *Acta Veterinaria Scand.* 58, 80. doi:10.1186/s13028-016-0263-y

Hong, Y., Dingemanse, J., and Mager, D. E. (2008). Pharmacokinetic/pharmacodynamic modeling of renin biomarkers in subjects treated with the renin inhibitor Aliskiren. *Clin. Pharmacol. Ther.* 84, 136–143. doi:10.1038/sj.clpt.6100495

Hu, C.-T., Chang, K.-C., Wu, C.-Y., and Chen, H. I. (1997). Acute effects of nitric oxide blockade with L-NAME on arterial haemodynamics in the rat. *Br. J. Pharmacol.* 122, 1237–1243. doi:10.1038/sj.bjp.0701496

ICH E14/S7B IMPLEMENTATION WORKING GROUP (2022). *Clinical and nonclinical evaluation of QT/QTc interval prolongation and proarrhythmic potential: questions and Answers*.

ICH EXPERT WORKING GROUP (2005). *The non-clinical evaluation of the potential for delayed ventricular repolarization (QT interval prolongation) by human pharmaceuticals S7B*.

Ines, A., Van Anthony, M. V., and Pedro, A. J. (2011). Dopamine and renal function and blood pressure regulation. *Compr. Physiol.* 1, 1075–1117. doi:10.1002/cphy.c100032

Ishii, H., Sato, T., and Izumi, H. (2014). Parasympathetic reflex vasodilation in the cerebral hemodynamics of rats. *J. Comp. Physiology B - Biochem. Syst. Environ. Physiology* 184, 385–399. doi:10.1007/s00360-014-0807-2

Ito, S., Ohga, A., and Ohta, T. (1988). Gastric vasodilatation and vasoactive intestinal peptide output in response to vagal stimulation in the dog. *J. Physiology* 404, 669–682. doi:10.1113/jphysiol.1988.sp017312

Kanbar, R., Oréa, V., Barrès, C., and Kulien, C. (2007). Baroreflex control of renal sympathetic nerve activity during air-jet stress in rats. *Am. J. Physiology - Regul. Integr. Comp. Physiology* 292, R362–R367. doi:10.1152/ajpregu.00413.2006

Karaasalan, F., Denzhan, Y., Kayserilioglu, A., and Gulcur, H. O. (2005). Long-term mathematical model involving renal sympathetic nerve activity, arterial pressure, and sodium excretion. *Ann. Biomed. Eng.* 33, 1607–1630. doi:10.1007/s10439-005-5976-4

Karlberg, B. E. (1983). Adrenergic regulation of renin release and effects on angiotensin and aldosterone. *Acta Medica Scand. Suppl.* 672, 33–40. doi:10.1111/j.0954-6820.1983.tb01611.x

Kelleni, M. T., and Abdelbasset, M. (2018). "Drug induced cardiotoxicity: mechanism, prevention and management," in *Cardiotoxicity*. Editor T. Wenyong 14 November 2018. doi:10.5772/intechopen.79611

Ketabchi, F., Khoram, M., and Dehghanian, A. (2024). Evaluation of electrocardiogram parameters and heart rate variability during blood pressure elevation by phenylephrine in cirrhotic rats. *Cardiovasc. Toxicol.* 24, 321–334. doi:10.1007/s12012-024-09839-4

Khurana, S., Yamada, M., Wess, J., Kennedy, R. H., and Raufman, J.-P. (2005). Deoxycholyltaurine-induced vasodilation of rodent aorta is nitric oxide- and muscarinic M(3) receptor-dependent. *Eur. J. Pharmacol.* 517, 103–110. doi:10.1016/j.ejphar.2005.05.037

Kiowski, W., Linder, L., Kleinboesem, C., Van Brummel, P., and Brühler, F. R. (1992). Blood pressure control by the renin-angiotensin system in normotensive subjects: assessment by angiotensin converting enzyme and renin inhibition. *Circulation* 85, 1–8. doi:10.1161/01.cir.85.1.1

Kirchheim, H., Ehmke, H., and Persson, P. (1989). Sympathetic modulation of renal hemodynamics, renin release and sodium excretion. *Klin. Wochenschr.* 67, 858–864. doi:10.1007/BF01717340

Kirchheim, H., Finke, R., Hackenthal, E., Löwe, W., and Persson, P. (1985). Baroreflex sympathetic activation increases threshold pressure for the pressure-dependent renin release in conscious dogs. *Pflügers Arch.* 405, 127–135. doi:10.1007/BF00584533

Kitagawa, H., Kitoh, K., Inoue, H., Ohba, Y., Suzuki, F., and Sasaki, Y. (2000). Plasma renin activities, angiotensin II concentrations, atrial natriuretic peptide concentrations and cardiopulmonary function values in dogs with severe heartworm disease. *J. Veterinary Med. Sci.* 62, 453–455. doi:10.1292/jvms.62.453

Kobayashi, M., Sakurai, S., Takaseya, T., Shiose, A., Kim, H.-I., Fukjiki, M., et al. (2012). Effects of percutaneous stimulation of both sympathetic and parasympathetic cardiac autonomic nerves on cardiac function in dogs. *Innov. (Phila)* 7, 282–289. doi:10.1097/IMI.0b013e31826f14ff

Kohan, D. E. (2008). Endothelin-1 and hypertension: from bench to bedside. *Curr. Hypertens. Rep.* 10, 65–69. doi:10.1007/s11906-008-0013-2

Koike, M. K., Moreira, E. D., Da Silva, G. J. J., Consolim-Colombo, F. M., Ida, F., Irigoyen, F., et al. (2006). Resetting of aortic baroreceptors in response to hypotension does not alter gain sensitivity. *Clin. Exp. Pharmacol. Physiology* 33, 679–684. doi:10.1111/j.1440-1681.2006.04431.x

Kostov, K. (2021). The causal relationship between endothelin-1 and hypertension: focusing on endothelial dysfunction, arterial stiffness, vascular remodeling, and blood pressure regulation. *Life* 11, 986. doi:10.3390/life11090986

Kougias, P., Weakley, S. M., Yao, Q., Lin, P. H., and Chen, C. (2010). Arterial baroreceptors in the management of systemic hypertension. *Med. Sci. Monit.* 16, RA1–RA8.

Krieger, E. M. (1970). Time course of baroreceptor resetting in acute hypertension. *Am. J. Physiology* 218, 486–490. doi:10.1152/ajplegacy.1970.218.2.486

Krieger, E. M. (1988). Mechanisms of complete baroreceptor resetting in hypertension. *Drugs* 35, 98–103. doi:10.2165/00003495-198800356-00014

Kudlak, M., and Tadi, P. (2023). "Physiology, muscarinic receptor," in *StatPearls* (Treasure Island (FL): StatPearls Publishing). Updated 2023 Aug 8.

Kunze, D. L. (1985). Role of baroreceptor resetting in cardiovascular regulation: acute resetting. *Fed. Proc.* 44, 2408–2411.

Kurtz, A. (2012). Control of renin synthesis and secretion. *Am. J. Hypertens.* 25, 839–847. doi:10.1038/ajh.2011.246

Lambert, E., Du, X.-J., Percy, E., and Lambert, G. (2002). Cardiac response to norepinephrine and sympathetic nerve stimulation following experimental subarachnoid hemorrhage. *J. Neurological Sci.* 198, 43–50. doi:10.1016/s0022-510x(02)00073-4

Laragh, J. H., and Sealey, J. E. (2011). The plasma renin test reveals the contribution of body sodium-volume content (V) and renin-angiotensin (R) vasoconstriction to long-term blood pressure. *Am. J. Hypertens.* 24, 1164–1180. doi:10.1038/ajh.2011.171

Lebouef, T., Yaker, Z., and Whited, L. (2023). "Physiology, autonomic nervous system," in *StatPearls* (Treasure Island (FL): StatPearls Publishing). Updated 2023 May 1.

Lecarpentier, Y., Schussler, O., Hébert, J.-L., and Vallée, A. (2020). Molecular mechanisms underlying the circadian rhythm of blood pressure in normotensive subjects. *Curr. Hypertens. Rep.* 22, 50. doi:10.1007/s11906-020-01063-z

Levy, M. N., and Blattberg, B. (1976). The effect of the pattern of cardiac sympathetic activity on myocardial contractile force and norepinephrine overflow in the dog heart. *Circulation Res.* 39, 341–348. doi:10.1161/01.res.39.3.341

Levy, M. N., and Zieske, H. (1969). Autonomic control of cardiac pacemaker activity and atrioventricular transmission. *J. Appl. Physiology* 27, 465–470. doi:10.1152/jappl.1969.27.4.465

Li, J.-D., Cheng, A.-Y., Huo, Y.-L., Fan, J., Zhang, Y.-P., Fang, Z.-Q., et al. (2016). Bilateral renal denervation ameliorates isoproterenol-induced heart failure through downregulation of the brain renin-angiotensin system and inflammation in rat. *Oxidative Med. Cell. Longev.* 2016, 3562634. doi:10.1155/2016/3562634

Liang, C.-S., and Hood, W. B. (1974). The myocardial depressant effect of beta-receptor blocking agents: comparative study of dl-propranolol, d-propranolol, and practolol in awake dogs with and without myocardial infarction. *Circulation Res.* 35, 272–280. doi:10.1161/01.res.35.2.272

Litwin, D. C., Lengel, D. J., Kamendi, H. W., and Bialecki, R. A. (2011). An integrative pharmacological approach to radio telemetry and blood sampling in pharmaceutical drug discovery and safety assessment. *Biomed. Eng. OnLine* 10, 5. doi:10.1186/1475-925X-10-5

Liu, T., Zhang, M., Mukosera, G. T., Borchardt, D., Li, Q., Tipple, T. E., et al. (2019). L-NAME releases nitric oxide and potentiates subsequent nitroglycerin-mediated vasodilation. *Redox Biol.* 26, 101238. doi:10.1016/j.redox.2019.101238

Lopez, M. U., Mitchell, J. R., Sheldon, R. S., and Tyberg, J. V. (2022). Effector mechanisms in the baroreceptor control of blood pressure. *Adv. Physiology Educ.* 46, 282–285. doi:10.1152/advan.00160.2021

Lorton, D., and Bellinger, D. L. (2015). Molecular mechanisms underlying β-adrenergic receptor-mediated cross-talk between sympathetic neurons and immune cells. *Int. J. Mol. Sci.* 16, 5635–5665. doi:10.3390/ijms16035635

Lote, C. (2006). The renin-angiotensin system and regulation of fluid volume. *Surg. Oxf.* 24, 154–159. doi:10.1383/surg.2006.24.5.154

Lumbers, E. R., Mccloskey, D. I., and Potter, E. K. (1979). Inhibition by angiotensin II of baroreceptor-evoked activity in cardiac vagal efferent nerves in the dog. *J. Physiology* 294, 69–80. doi:10.1113/jphysiol.1979.sp012915

Lundberg, J. F., Martner, J., Raner, C., Winsö, O., and Biber, B. (2005). Dopamine or norepinephrine infusion during thoracic epidural anesthesia? Differences in hemodynamic effects and plasma catecholamine levels. *Acta Anaesthesiol. Scand.* 49, 962–968. doi:10.1111/j.1399-6576.2005.00732.x

Mace, S. E., and Levy, M. N. (1983). Neural control of heart rate: a comparison between puppies and adult animals. *Pediatr. Res.* 17, 491–495. doi:10.1203/00006450-198306000-00014

Macgregor, D. A., Smith, T. E., Prielipp, R. C., Butterworth, J. F., James, R. L., and Scuderi, P. E. (2000). Pharmacokinetics of dopamine in healthy male subjects. *Anesthesiology* 92, 338–346. doi:10.1097/00000542-200002000-00013

Maguire, J. J., and Davenport, A. P. (2015). Endothelin receptors and their antagonists. *Seminars Nephrol.* 35, 125–136. doi:10.1016/j.semnephrol.2015.02.002

Mahdi, A., Sturdy, J., Ottesen, J. T., and Olufsen, M. S. (2013). Modeling the afferent dynamics of the baroreflex control system. *PLOS Comput. Biol.* 9, e1003384. doi:10.1371/journal.pcbi.1003384

Makino, M., Hayashi, H., Takezawa, H., Hirai, M., Saoto, H., and Ebihara, S. (1997). Circadian rhythms of cardiovascular functions are modulated by the baroreflex and the autonomic nervous system in the rat. *Circulation* 96, 1667–1674. doi:10.1161/01.cir.96.5.1667

Mangin, L., Swynghedauw, B., Benis, A., Thibault, N., Lerebours, G., and Carré, F. (1998). Relationships between heart rate and heart rate variability: study in conscious rats. *J. Cardiovasc. Pharmacol.* 32, 601–607. doi:10.1097/00005344-199810000-00012

Mccarty, R. (2016). "Chapter 4 - the fight-or-flight response: a cornerstone of stress research," in *Stress: concepts, cognition, emotion, and behavior*. Editor G. Fink (Elsevier).

Mccorry, L. K. (2007). Physiology of the autonomic nervous system. *Am. J. Pharm. Educ.* 71, 78. doi:10.5688/aj710478

Mcdowall, L. M., and Dampney, R. A. L. (2006). Calculation of threshold and saturation points of sigmoidal baroreflex function curves. *Am. J. Physiology - Heart Circulatory Physiology* 291, H2003–H2007. doi:10.1152/ajpheart.00219.2006

Menniti, F. S., and Diliberto, E. J. (1989). Newly synthesized dopamine as the precursor for norepinephrine synthesis in bovine adrenomedullary chromaffin cells. *J. Neurochem.* 53, 890–897. doi:10.1111/j.1471-4159.1989.tb11788.x

Migita, R., Gonzales, A., Gonzales, M. L., Vandegriff, K. D., and Winslow, R. M. (1997). Blood volume and cardiac index in rats after exchange transfusion with hemoglobin-based oxygen carriers. *J. Appl. Physiology* 82, 1995–2002. doi:10.1152/jappl.1997.82.6.1995

Mika, D., Bobin, P., Pomérance, M., Lechêne, P., Westenbroek, R. E., Catterall, W. A., et al. (2013). Differential regulation of cardiac excitation-contraction coupling by cAMP phosphodiesterase subtypes. *Cardiovasc. Res.* 100, 336–346. doi:10.1093/cvr/cvt193

Miki, K., Yoshimoto, M., and Tanimizu, M. (2003). Acute shifts of baroreflex control of renal sympathetic nerve activity induced by treadmill exercise in rats. *J. Physiology* 548, 313–322. doi:10.1113/jphysiol.2002.033050

Minisi, A. J., Dibner-Dunlap, M., and Thames, M. D. (1989). Vagal cardiopulmonary baroreflex activation during phenylephrine infusion. *Am. J. Physiology - Regul. Integr. Comp. Physiology* 257, R1147–R1153. doi:10.1152/ajpregu.1989.257.5.R1147

Min, S., Chang, R. B., Prescott, S. L., Beeler, B., Joshi, N. R., Strochlic, D. E., et al. (2019). Arterial baroreceptors sense blood pressure through decorated aortic claws. *Cell. Rep.* 29, 2192–2201.e3. doi:10.1016/j.celrep.2019.10.040

Missale, C., Nash, S. R., Robinson, S. W., Jaber, M., and Caron, M. G. (1998). Dopamine receptors: from structure to function. *Physiol. Rev.* 78, 189–225. doi:10.1152/physrev.1998.78.1.189

Miyamoto, Y., and Sancar, A. (1998). Vitamin B_2-based blue-light photoreceptors in the retinohypothalamic tract as the photoactive pigments for setting the circadian clock in mammals. *PNAS* 95, 6097–6102. doi:10.1073/pnas.95.11.6097

Miyazaki, H., Yoshida, M., Samura, K., Matsumoto, H., Ikemoto, F., and Tagawa, M. (2002). Ranges of diurnal variation and the pattern of body temperature, blood pressure and heart rate in laboratory Beagle dogs. *Exp. Anim.* 51, 95–98. doi:10.1538/expanim.51.95

Mizoguchi, H., Dzau, V. J., Siwek, L. G., and Vbarger, A. C. (1983). Effect of intrarenal administration of dopamine on renin release in conscious dogs. *Am. J. Physiology - Heart Circulatory Physiology* 13, H39–H45. doi:10.1152/ajpheart.1983.244.1.H39

Modlinger, R. S., Sharif-Zadeh, K., Ertel, N. H., and Gutkin, M. (1976). The circadian rhythm of renin. *J. Clin. Endocrinol. Metabolism* 43, 1276–1282. doi:10.1210/jcem-43-6-1276

Mortensen, L. H., and Fink, G. D. (1990). Hemodynamic effect of human and rat endothelin administration into conscious rats. *Am. J. Physiology* 158, H362–H368. doi:10.1152/ajpheart.1990.258.2.H362

Motiejunaite, J., Amar, L., and Vidal-Petiot, E. (2021). Adrenergic receptors and cardiovascular effects of catecholamines. *Ann. d'endocrinologie* 82, 193–197. doi:10.1016/j.ando.2020.03.012

Müller, D. N., Hilger, K. F., Bohlender, J., Lippoldt, A., Wagner, J., Fischli, W., et al. (1995). Effects of human renin in the vasculature of rats transgenic for human angiotensinogen. *Hypertension* 26, 272–278. doi:10.1161/01.hyp.26.2.272

Nakatsuka, N., and Andrews, A. M. (2017). Differentiating siblings: the case of dopamine and norepinephrine. *ACS Chem. Neurosci.* 8, 218–220. doi:10.1021/acschemneuro.7b00056

Navar, L. G. (2014). Physiology: hemodynamics, endothelial function, renin-angiotensin-aldosterone system, sympathetic nervous system. *J. Am. Soc. Hypertens.* 8, 519–524. doi:10.1016/j.jash.2014.05.014

Navar, L. G., and Rosivall, L. (1984). Contribution of the renin-angiotensin system to the control of intrarenal hemodynamics. *Kidney Int.* 25, 857–868. doi:10.1038/ki.1984.102

Neishi, Y., Mochizuki, S., Miyasaka, T., Kawamoto, T., Kume, T., Sukmawan, R., et al. (2005). Evaluation of bioavailability of nitric oxide in coronary circulation by direct measurement of plasma nitric oxide concentration. *PNAS* 102, 11456–11461. doi:10.1073/pnas.0501392102

Nishiyama, S. K., Zhao, J., Wray, D. W., and Richardson, R. S. (2017). Vascular function and endothelin-1: tipping the balance between vasodilation and vasoconstriction. *J. Appl. Physiology (1985)* 122, 354–360. doi:10.1152/japplphysiol.00772.2016

Nishiyama, A., and Kobori, H. (2018). Independent regulation of renin-angiotensin-aldosterone system in the kidney. *Clin. Exp. Nephrol.* 22, 1231–1239. doi:10.1007/s10157-018-1567-1

Nurminen, M.-L., and Vapaatalo, H. (1996). Effect of intracerebroventricular and intravenous administration of nitric oxide donors on blood pressure and heart rate in anaesthetized rats. *Br. J. Pharmacol.* 119, 1422–1426. doi:10.1111/j.1476-5381.1996.tb16054.x

Ohashi, N., Isobe, S., Ishigaki, S., and Yasuda, H. (2017). Circadian rhythm of blood pressure and the renin-angiotensin system in the kidney. *Hypertens. Res.* 40, 413–422. doi:10.1038/hr.2016.166

Ohke, H., Sato, T., Mito, K., Terumitsu, M., and Ishii, H. (2020). Effect of the parasympathetic vasodilation on temperature regulation via trigeminal afferents in the orofacial area. *J. Physiological Sci.* 71, 22–11. doi:10.1186/s12576-020-00749-y

Onuki, N., Takahashi, H., Suzuki, H., Saito, T., Maehara, K., and Maruyama, Y. (1999). Dissociation of chronotropic and inotropic responses in the rat heart during sympathetic stimulation. *Jpn. Circulation J.* 63, 710–717. doi:10.1253/jcj.63.710

Oosting, J., Struijker Boudier, H. A. J., and Janssen, B. J. A. (1997). Circadian rhythm and ultradian control of cardiac output in spontaneous hypertension in rats. *Am. J. Physiology - Heart Circulatory Physiology* 273, H66–H75. doi:10.1152/ajpheart.1997.273.1.H66

Perez-Olea, J., Quevedo, M., and Silva, R. (1981). Enhancement of blood pressure response to dopamine by angiotensin II. *Hypertension* 3, II-138–II-141. doi:10.1161/01.hyp.3.6_pt_2.ii-138

Pratt, O., Gwinnutt, C., and Bakewell, S. (2016). The autonomic nervous system - basic anatomy and physiology. *Update Anesth.* 24, 36–39. doi:10.1093/bjaed/mkw011

Rees, D. D., Palmer, R. M. J., and Moncada, S. (1989). Role of endothelium-derived nitric oxide in the regulation of blood pressure. *Proc. Natl. Acad. Sci. U. S. A.* 86, 3375–3378. doi:10.1073/pnas.86.9.3375

Reid, J. L. (1986). Alpha-adrenergic receptors and blood pressure control. *Am. J. Cardiol.* 57, 6E–12E. doi:10.1016/0002-9149(86)90716-2

Rengo, G. (2014). The adrenergic system in cardiovascular pathophysiology: a translational science point of view. *Front. Physiology* 5, 356. doi:10.3389/fphys.2014.00356

Rentero, N., Civindjian, A., Trevaks, D., Pequignot, J. M., Quintin, L., and Mcallen, R. M. (2002). Adrenomedullin influences magnocellular and parvocellular neurons of paraventricular nucleus via separate mechanisms. *Am. J. Physiology - Regul. Integr. Comp. Physiology* 283, R1293–R1302. doi:10.1152/ajpregu.00191.2002

Rodríguez-Colón, S. M., Li, X., Shaffer, M. L., He, F., Bixler, E. O., Vgontzas, A. N., et al. (2010). Insulin resistance and circadian rhythm of cardiac autonomic modulation. *Cardiovasc. Diabetol.* 9, 85. doi:10.1186/1475-2840-9-85

Roossien, A., Brunsting, J. R., Nijmeijer, A., Zaagsma, J., and Zijlstra, W. G. (1997). Effects of vasoactive intestinal polypeptide on heart rate in relation to vagal cardioacceleration in conscious dogs. *Cardiovasc. Res.* 33, 392–399. doi:10.1016/s0008-6363(96)00202-7

Ruffolo, R. R., and Hieble, J. P. (1994). Alpha-adrenoceptors. *Pharmacol. and Ther.* 61, 1–64. doi:10.1016/0163-7258(94)90058-2

Ruffolo, R. R., Stadel, J. M., and Hieble, J. P. (1994). Alpha-adrenoceptors: recent developments. *Med. Res. Rev.* 14, 229–270. doi:10.1002/med.2610140204

Salgado, H. C., Barale, A. R., Castania, J. A., Machado, B. H., Chapleau, M. W., and Fazan, R. (2007). Baroreflex responses to electrical stimulation of aortic depressor nerve in conscious SHR. *Am. J. Physiology - Heart Circulatory Physiology* 292, H593–H600. doi:10.1152/ajpheart.00181.2006

Salgado, H. C., and Krieger, E. M. (1978). Time course of baroreceptor resetting in short-term hypotension in the rat. *Am. J. Physiology* 234, H552–H556. doi:10.1152/ajpheart.1978.234.5.H552

Sanders, R. C., Zaritsky, A., and Mcniece-Redwine, K. (2011). "Chapter 73 - hypertension in the pediatric intensive care unit," in *Pediatric critical care*. Editors B. P. Furhrman and J. J. Zimmerman (Philadelphia, PA: Elsevier Saunders).

Schiffrin, E. (1995). Endothelin: potential role in hypertension and vascular hypertrophy. *Hypertrophy* 25, 1135–1143. doi:10.1161/01.hyp.25.6.1135

Schild, J. H., Clark, J. W., Hay, M., Mendelowitz, D., Andresen, M. C., and Kunze, D. L. (1994). A- and C-type rat nodose sensory neurons: model interpretations of dynamic discharge characteristics. *J. Neurophysiology* 71, 2338–2358. doi:10.1152/jn.1994.71.6.2338

Scott-Solomon, E., Boehm, E., and Kuruvilla, R. (2021). The sympathetic nervous system in development and disease. *Nat. Rev. Neurosci.* 22, 685–702. doi:10.1038/s41583-021-00523-y

Seagard, J. L., Van Brederode, J. F. M., Dean, C., Hopp, F. A., Gallenberg, L. A., and Kampine, J. P. (1990). Firing characteristics of single-fiber carotid sinus baroreceptors. *Circulation Res.* 66, 1499–1509. doi:10.1161/01.res.66.6.1499

Shaffer, F., and Ginsberg, J. P. (2017). An overview of heart rate variability metrics and norms. *Front. Public Health* 5, 258. doi:10.3389/fpubh.2017.00258

Shahoud, J. S., Sanvictores, T., and Aeddula, N. R. (2022). "Physiology, arterial pressure regulation," in *StatPearls* (Treasure Island (FL): StatPearls Publishing). Updated 2022 Aug 29.

Sharma, R., and Sharma, S. (2022). *Physiology, blood volume*. Trasure Island (Fl): StatPearls Publishing. Accessed 28th June 2022 2022.

Sleight, P. (1991). "Baroreceptors and hypertension," in *Baroreceptor reflexes*. Editors P. B. Persson and H. R. Kirchheim (Berlin, Heidelberg: Springer).

Smith, M. D., and Maani, C. V. (2023). "Norepinephrine," in *StatPearls* (Treasure Island (FL): StatPearls Publishing). Updated 2023 May 8.

Snelder, N., Ploeger, B. A., Luttringer, O., Rigel, D. F., Fu, F., Beil, M., et al. (2014). Drug effects on the CVS in conscious rats: separating cardiac output into heart rate and stroke volume using PKPD modelling. *Br. J. Pharmacol.* 171, 5076–5092. doi:10.1111/bph.12824

Snelder, N., Ploeger, B. A., Luttringer, O., Rigel, D. F., Webb, R. L., Feldman, D., et al. (2013). PKPD modelling of the interrelationship between mean arterial BP, cardiac output, and total peripheral resistance in conscious rats. *Br. J. Pharmacol.* 169, 1510–1524. doi:10.1111/bph.12190

Sonne, J., Goyal, A., and Lopez-Ojeda, W. (2023). "Dopamine," in *StatPearls* (Treasure Island (FL): StatPearls Publishing). Updated 2023 Jul 3.

Stauss, H. M. (2003). Heart rate variability. *Am. J. Physiology - Regul. Integr. Comp. Physiology* 285, R927–R931. doi:10.1152/ajpregu.00452.2003

Stauss, H. M., and Persson, P. B. (2000). Role of nitric oxide in buffering short-term blood pressure fluctuations. *News Physiological Sci.* 15, 229–233. doi:10.1152/physiologyonline.2000.15.5.229

Stegbauer, J., Vonend, O., Oberhauser, V., and Rump, L. C. (2003). Effects of angiotensin-(1-7) and other bioactive components of the renin-angiotensin system on vascular resistance and noradrenaline release in rat kidney. *J. Hypertens.* 21, 1391–1399. doi:10.1097/00004872-200307000-00030

Sunagawa, K., Kawada, T., and Nakahara, T. (1998). Dynamic nonlinear vago-sympathetic interaction in regulating heart rate. *Heart Vessels* 13, 157–174. doi:10.1007/BF01745040

Sundaram, K., Murugaian, J., Watson, M., and Sapru, H. (1989). M_2 muscarinic receptor agonists produce hypotension and bradycardia when injected into the nucleus tractus solitarii. *Brain Res.* 477, 358–362. doi:10.1016/0006-8993(89)91427-3

Švorc, P., Grešová, S., and Švorc, P. (2023). Heart rate variability in male rats. *Physiol. Rep.* 11, e15827. doi:10.14814/phy2.15827

Szentandrássy, N., Farkas, V., Bárándi, L., Hegyi, B., Ruzsnavsky, F., Horváth, B., et al. (2012). Role of action potential configuration and the contribution of C^{2+}a and K^{+} currents to isoprenaline-induced changes in canine ventricular cells. *Br. J. Pharmcology* 167, 599–611. doi:10.1111/j.1476-5381.2012.02015.x

Taher, M. F., Cecchini, A. B. P., Allen, M. A., Gobran, S. R., Gorman, R. C., Guthrie, B. L., et al. (1988). Baroreceptor responses derived from a fundamental concept. *Ann. Biomed. Eng.* 16, 429–443. doi:10.1007/BF02368008

Taneyama, C., Goto, H., Goto, K., Benson, K. T., Unruh, G. K., and Arakawa, K. (1990). Attenuation of arterial baroreceptor reflex response to acute hypovolemia during induced hypotension. *Anesthesiology* 73, 433–440. doi:10.1097/00000542-199009000-00011

Tangsucharit, P., Takatori, S., Zamami, Y., Goda, M., Pakdeechote, P., Kawasaki, H., et al. (2016). Muscarinic acetylcholine receptor M1 and M3 subtypes mediate acetylcholine-induced endothelium-independent vasodilatation in rat mesenteric arteries. *J. Pharmacol. Sci.* 130, 24–32. doi:10.1016/j.jphs.2015.12.005

Taylor, B. N., and Cassagnol, M. (2023). "Alpha-adrenergic receptors," in *StatPearls* (Treasure Island (FL): StatPearls Publishing). Updated 2023 Jul 10.

Teerlink, J. R., and Clozel, J.-P. (1993). Hemodynamic variability and circadian rhythm in rats with heart failure: role of locomotor activity. *Am. J. Physiology - Heart Circulatory Physiology* 264, H2111–H2118. doi:10.1152/ajpheart.1993.264.6.H2111

Thornton, S. N. (2010). Thirst and hydration: physiology and consequences of dysfunction. *Physiology and Behav.* 100, 15–21. doi:10.1016/j.physbeh.2010.02.026

Tindle, J., and Tadi, P. (2024). "Neuroanatomy, parasympathetic nervous system," in *StatPearls* (Treasure Island (FL): StatPearls Publishing).

Toda, N., and Okamura, T. (2015). Recent advances in research on nitrergic nerve-mediated vasodilatation. *Pflügers Archiv Eur. J. Physiology* 467, 1165–1178. doi:10.1007/s00424-014-1621-0

Tomankova, H., Valuskova, P., Varejkova, E., Rotkova, J., Benes, J., and Myslivecek, J. (2015). The M2 muscarinic receptors are essential for signaling in the heart left ventricle during restraint stress in mice. *Int. J. Biol. Stress* 18, 208–220. doi:10.3109/10253890.2015.1007345

Tomek, J., and Zaccolo, M. (2023). Compartmentalized cAMP signalling and control of cardiac rhythm. *Philosophical Trans. R. Soc. B. Biol. Sci.* 378, 20220172. doi:10.1098/rstb.2022.0172

Torretti, J. (1982). Sympathetic control of renin release. *Annu. Rev. Pharmacol. Toxicol.* 22, 167–192. doi:10.1146/annurev.pa.22.040182.001123

Uttamsingh, R. J., Leaning, M. S., Bushman, J. A., Carson, E. R., and Finkelstein, L. (1985). Mathematical model of the human renal system. *Med. and Biol. Eng. and Comput.* 23, 525–535. doi:10.1007/BF02455306

Velmurugan, B. K., Baskaran, R., and Huang, C.-Y. (2019). Detailed insight on β-adrenoceptors as therapeutic targets. *Biomed. and Pharmacother.* 117, 109039. doi:10.1016/j.biopha.2019.109039

Venkatasubramanian, R., Collins, T. A., Lesko, L. J., Mettetal, J. T., and Trame, M. N. (2020). Semi-mechanistic modelling platform to assess cardiac contractility and haemodynamics in preclinical cardiovascular safety profiling of new molecular entities. *Br. J. Pharmacol.* 177, 3568–3590. doi:10.1111/bph.15079

VIRTUAL PHYSIOLOGICAL RAT PROJECT (2023). *Virtual physiological rat project - project overview*. Accessed 21st April 2023 2023.

Volz, A.-K., Krause, A., Haefeli, W. E., Dingemanse, J., and Lehr, T. (2017). Target-mediated drug disposition pharmacokinetic-pharmacodynamic model of bosentan and endothelin-1. *Clin. Pharmacokinet.* 56, 1499–1511. doi:10.1007/s40262-017-0534-4

Von Borell, E., Langbein, J., Després, G., Hansen, S., Leterrier, C., Marchant, J., et al. (2007). Heart rate variability as a measure of autonomic regulation of cardiac activity for assessing stress and welfare in farm animals: a review. *Physiol. Behav.* 92, 293–316. doi:10.1016/j.physbeh.2007.01.007

Wallbach, M., and Koziolek, M. J. (2018). Baroreceptors in the carotid and hypertension - systematic review and meta-analysis of the effects of baroreflex activation therapy on blood pressure. *Nephrol. Dial. Transplant.* 33, 1485–1493. doi:10.1093/ndt/gfx279

Waxenbaum, J. A., Reddy, V., and Varacallo, M. (2023). "Anatomy, autonomic nervous system," in *StatPearls* (Treasure Island (FL): StatPearls Publishing). Updated 2023 Jul 24.

West, G. B., and Brown, J. H. (2005). The origin of allometric scaling laws in biology from genomes to ecosystems: towards a quantitative unifying theory of biological structure and organization. *Basal Metabolic Rate Cell. Energetics* 208, 1575–1592. doi:10.1242/jeb.01589

Wilson, C., Lee, M. D., and Mccarron, J. G. (2016). Acetylcholine released by endothelial cells facilitates flow-mediated dilatation. *J. Physiology* 594, 7267–7307. doi:10.1113/JP272927

Wright, P. T., Bhogal, N. K., Diakonov, I., Pannell, L. M. K., Perera, R. K., Bork, N. I., et al. (2018). Cardiomyocyte membrane structure and cAMP compartmentation produce anatomical variation in β_2AR-cAMP responsiveness in murine hearts. *Cell. Rep.* 23, 459–469. doi:10.1016/j.celrep.2018.03.053

Xiao, C., Shull, G. E., Miguel-Qin, E., and Zhuo, J. L. (2015). Role of the Na^+/H^+ exchanger 3 in angiotensin II-induced hypertension. *Physiol. Genomics* 47, 479–487. doi:10.1152/physiolgenomics.00056.2015

Zaccolo, M. (2009). cAMP signal transduction in the heart: understanding spatial control for the development of novel therapeutic strategies. *Br. J. Pharmacol.* 158, 50–60. doi:10.1111/j.1476-5381.2009.00185.x

Zajączkowski, S., Ziółkowski, W., Badtke, P., Zajączkowski, M. A., Flis, D. J., Figarski, A., et al. (2018). Promising effects of xanthine oxidase inhibition by allopurinol on autonomic heart regulation estimated by heart rate variability (HRV) analysis in rats exposed to hypoxia and hyperoxia. *PLOS ONE* 13, e0192781. doi:10.1371/journal.pone.0192781

Zeng, C., and Jose, P. A. (2011). Dopamine receptors: important antihypertensive counterbalance against hypertensive factors. *Hypertension* 57, 11–17. doi:10.1161/HYPERTENSIONAHA.110.157727

Zheng-Rong, W., Ling, W., Chao-Min, W., Cornelissen, G., Anand, I., and Halberg, F. (1999). Circadian rhythm of gene expression of myocardial contractile protein, left ventricular pressure and contractility. *Space Med. and Med. Eng.* 12, 391–396.

frontiers | Frontiers in Pharmacology

TYPE Original Research
PUBLISHED 11 November 2024
DOI 10.3389/fphar.2024.1453429

OPEN ACCESS

EDITED BY
Jiayu Liao,
University of California, Riverside, United States

REVIEWED BY
Joaquín Sáez Peñataro,
Hospital Clinic of Barcelona, Spain
Antonio Farina,
University of Florence, Italy

*CORRESPONDENCE
Yan Luo,
yanluo2018@cqu.edu.cn

RECEIVED 23 June 2024
ACCEPTED 29 October 2024
PUBLISHED 11 November 2024

CITATION
Yang Y, Li L, Tian J, Ma L, Wu Y, Luo Q and Luo Y (2024) Delayed immune-related adverse events profile associated with immune checkpoint inhibitors: a real-world analysis.
Front. Pharmacol. 15:1453429.
doi: 10.3389/fphar.2024.1453429

Delayed immune-related adverse events profile associated with immune checkpoint inhibitors: a real-world analysis

Yana Yang[1], Linman Li[2], Jing Tian[2], Linwen Ma[2], Yaoxin Wu[2], Qian Luo[3] and Yan Luo[3]*

[1]Nursing Department, The First Affiliated Hospital of Chongqing Medical University, Chongqing, China, [2]Health Management Center, The First Affiliated Hospital of Chongqing Medical University, Chongqing, China, [3]Radiation Oncology Center, Chongqing University Cancer Hospital, Chongqing, China

Background: Immune-related adverse events (irAEs) typically occur within 3 months of initiating immune-checkpoint inhibitors (ICIs), which has been extensively documented. But the clinical profiles of late-onset irAEs remain inadequately characterized. Therefore, this study aims to quantify the correlation between delayed irAEs and ICIs, and to delineate the profiles of delayed toxicities associated with ICIs using data from the Food and Drug Administration Adverse Event Reporting System (FAERS).

Methods: Data from the January 2011 to December 2023 in FAERS database were extracted. Four signal detection indices, reporting odds ratio (ROR), proportional reporting ratio (PRR), Bayesian confidence propagation neural network (BCPNN) and multi-item gamma Poisson shrinker (MGPS), were employed to evaluate the associations between ICIs and delayed irAEs.

Results: A total of 147,854 cases were included in this study, of which 3,738 cases related to delayed irAEs were identified. Generally, 8 signals at System Organ Class (SOC) level were found to be associated with ICIs. Males had a slightly higher reporting frequencies for respiratory disorders (ROR_{975} = 0.95) and blood and lymphatic system disorders (ROR_{025} = 1.22), but lower reporting frequencies for immune system disorders (ROR_{025} = 1.16). Three monotherapy (anti-PD-1, anti-PD-L1 and anti-CTLA-4) were all associated with significant increasing gastrointestinal disorders (ROR_{025} = 1.66, 1.16, 1.99) and metabolism disorders (ROR_{025} = 2.26, 1.74, 3.13). Anti-PD-1 therapy exhibited higher rates of respiratory toxicities (ROR_{025} = 1.46 versus 0.82) and skin toxicities (ROR_{025} = 1.27 versus 0.94) compared with anti-CTLA-4 therapy. At PT levels, pneumonitis (ROR_{025}: from 11.85 to 29.27) and colitis (ROR_{025}: from 2.11 to 24.84) were the most notable PT signals associated with all three ICI regimens. For outcomes of delayed irAEs, gastrointestinal disorders showed the highest proportion (51.06%) of death.

Conclusion: Our pharmacovigilance analysis indicates that a small percentage of patients receiving ICIs therapy experience delayed irAEs, which are challenging to manage and may result in severe consequences. Prompt identification and intervention of these delayed irAEs are crucial in clinical practice.

KEYWORDS

immune checkpoint inhibitors, delayed immune-related adverse events, FAERS, disproportionality analysis, outcomes

1 Introduction

Immune-checkpoint inhibitors (ICIs) have become a key component in the field of cancer therapy, allowing for the potential of long-term survival in patients with challenging malignant tumors, and offering new therapeutic options in (neo)adjuvant and maintenance settings (Johnson et al., 2022). The most widely used targets of ICIs include cytotoxic T lymphocyte-associated antigen-4 (CTLA-4), programmed cell death-1 (PD-1) and anti-programmed cell death ligand-1 (PD-L1) (Martins et al., 2019). Since the approval of the first ICI, ipilimumab, for metastatic melanoma by FDA in 2011, a total of more than 20 different malignancies worldwide have been treated with ICIs (Yin et al., 2023).

One distinguishing feature of ICIs, unlike conventional cancer therapeutic agents, is the potential for sustained responses, even in patients with metastatic solid tumors. However, by inhibiting CTLA4, PD-1 or PD-L1 checkpoints, ICIs can also lead to autoimmune effects known as immune-related adverse events (irAEs) (Singh et al., 2023). While most irAEs occur within the first 3 months of starting immunotherapy, they can also arise at any point during treatment or even months after treatment cessation (Weber et al., 2017). Early irAEs, occurring within 3 months, have been extensively studied (Tao et al., 2023; Zhang et al., 2023). However, the delayed irAEs, defined as those appearing more than 1 year after starting ICIs, have not yet been systematically investigated. Actually, real world data have demonstrated that delayed irAEs may be more frequent in long-term responsers to ICIs and can differ in severity and spectrum from early irAEs. Research by Owen et al. (2021) revealed that 118 melanoma patients treated with ICIs for over 12 months experienced a total of 140 delayed irAEs, with an estimated incidence of 5.3%. The most frequent delayed irAEs included colitis (22%), rash (18%) and pneumonitis (13%). These delayed irAEs are often more severe, distinct from early-onset irAEs, challenging to manage and can be fatal. However, the frequency of delayed irAEs after discontinuing ICIs treatment in a larger patient population, as well as the duration of increased risk for irAEs following immunotherapy cessation, remains unknown.

As the indications of ICIs expands in clinical practice, more patients will be exposed to immunotherapy, potentially leading to life-threatening delayed irAEs. Therefore, it is critical to gather accurate and comprehensive data on the incidence, clinical manifestations, and prognosis of the delayed irAEs from a large patient population. The Food and Drug Administration Adverse Event Reporting System (FAERS) is one of the largest pharmacovigilance databases providing valuable source of real-world data on adverse event, including reports from healthcare professionals, individual patients and drug manufacturers (Zhou et al., 2023). In this study, we aim to analyze the frequency, spectrum and outcomes of the delayed irAEs using FAERS data to enhance our understanding of the safety profiles of ICIs.

2 Materials and methods

2.1 Study design and data sources

We conducted a pharmacovigilance study on delayed irAEs based on data from the FAERS database spanning from the first quarter of 2011 to the fourth quarter of 2023. The FAERS database includes the following eight types of files: demographic information (DEMO), drug information (DRUG), indications for use (INDI), start and end dates for reported drugs (THER), adverse events (REAC), patient outcomes (OUTC), report sources (RPSR), and invalid reports (DELETED). Keywords used included immune checkpoint inhibitors such as anti-CTLA-4 agents (ipilimumab and tremelimumab), anti-PD-1 agents (nivolumab, pembrolizumab and cemiplimab), and anti-PD-L1 agents (atezolizumab, avelumab and durvalumab). AEs in the FAERS database were coded using preferred terms (PTs) according to the Medical Dictionary for Regulatory Activities (MedDRA) (version 26.1), which is logically structured to contain five levels. PTs are unique descriptors of a single medical concept, such as signs and symptoms and disease diagnosis. A specific PT can be assigned to several high-level terms (HLTs), high-level group terms (HLGTs), and system organ classes (SOCs), which are grouped by aetiology, site of presentation, or purpose. In this study, irAEs were identified using pre-specified list of PTs based on the Society for Immunotherapy of Cancer (SITC), (American Society of Clinical Oncology) ASCO, (European Society for Medical Oncology) ESMO and (National Comprehensive Cancer Network) NCCN guideline/consensus. The PTs of irAEs included in this study are provided in Supplementary Table S1. Cases were defined as a serious medical event if one or more of the following outcomes were reported: death, life-threatening event, hospitalization, disability, congenital anomaly, or other serious medical events.

2.2 Data processing procedure

Variables such as Case Identification (CASEID), age, sex, event date, drug names, and outcomes were extracted in each report. Data cleaning was performed prior to analysis with duplicate records removed based on FDA's recommended method selecting the latest FDA_DT if the CASEID was the same, and choosing the higher PRIMARYID if the CASEID and FDA_DT were the same. In cases

where a single patient had multiple reports, the most recent case was retained on the "latest FDA data received to date". Additionally, the time to onset of irAEs associated with ICIs was calculated as the interval between therapy start date (START_DT) and event onset date (EVENT_DT). Delayed irAEs in this study defined as those with onset >1 year after the initiation of ICIs. Reports were excluded when the START_DT was later than the EVENT_DT or when the report lacked a START_DT or EVENT_DT.

2.3 Statistical analysis

We conducted a comprehensive descriptive analysis of the clinical attributes of reports detailing delayed irAEs post-screening, encompassing variables such as gender, age, reporting year, reporting country, clinical outcomes, indication, treatment strategy, and additional clinical characteristics. Adisproportionality analysis was utilized to compare the proportion of specific AEs caused by the target drugs with the proportion of the same AEs in the full database (Zhou et al., 2023). In our study, all drugs in the database were selected as comparisons for the disproportionality approach. Based on the two-by-two contingency table, reporting odds ratio (ROR), proportional reporting ratio (PRR), Bayesian confidence propagation neural network (BCPNN) and multi-item gamma Poisson shrinker (MGPS) were employed to detect an association between various ICI regimens and adverse events in accordance with the disproportionality analysis. The criteria of a significant signal was identified by the 95% confidence interval lower end for ROR (ROR_{025}), PRR (PRR_{025}), IC (IC_{025}) and EBGM ($EBGM_{05}$) (Hauben et al., 2005; Noren et al., 2006; Guo et al., 2022; Jiang et al., 2022). A signal was considered significant if ROR_{025} was greater than 1 with at least 3 cases, PRR value was greater than 2 and Chi-Square was greater than 4, IC_{025} was greater than 0 and $EBGM_{05}$ was greater than 2. Shrinkage transformation was applied to reduce false-negative adverse signals. The equations for the above four algorithms are shown in Supplementary Tables S2, S3. The formula is as follows:

$$ROR = \frac{(a/c)}{(b/d)} = \frac{ad}{bc}$$

$$PRR = \frac{a/(a+b)}{c/(c=d)}$$

$$IC = \log_2 \frac{a(a+b+c+d)}{(a+b)(a+c)}$$

$$EBGM = \frac{a(a+b+c+d)}{(a+c)(a+b)}$$

Data were analyzed using SAS version 9.4 (SAS Institute Inc., Cary, NC, United States) and Microsoft Office Excel version 2023 (Microsoft Corp., Redmond, WA, United States).

3 Results

3.1 Descriptive analysis

In this study, a total of 17,854,647 cases were extracted from the FAERS database from 2011 to 2023 (Figure 1). After excluding duplicates, the number of cases was 15,245,964, among which 147,854 cases were associated with ICI-related AEs. Additionally, 3,738 cases were found to be associated with delayed irAEs, while 144,116 cases were related to early irAEs following exposure to ICIs.

The clinical characteristics of patients with irAEs were presented in Table 1, including gender, age, reporting year, indications, the distribution of various cancer types and combination therapy strategies. The data indicated that the majority of cases were reported after 2018, reflecting the increased use of ICIs in recent 5 years. Among all irAEs, males accounted for a larger proportion (N = 80,348, 54.34%) than females (N = 50,135, 33.91%). However, delayed irAEs only occurred in 2.31% (3,415/147,854) of all irAEs in the FAERS database. A total of 2,171 cases (63.57%) were reported in male patients, 1,164 cases (34.08%) in female patients, and gender information was not specified for 80 patients. Patients aged 65 years and older represented a larger proportion of delayed irAEs (N = 1947, 57.01%). Physician reported the most cases (N = 1,599, 46.82%), followed by pharmacist (N = 901, 26.38%). The United States reported the highest number of delayed irAEs (N = 776, 22.72%), followed by France (N = 491, 14.38%), Japan (N = 476, 13.94%), and Germany (N = 248, 7.26%). The most commonly reported indication was lung cancer (N = 1,014, 29.69%), followed by malignant melanoma (N = 720, 21.08%) and renal and ureteral cancer (N = 429, 12.56%). Hospitalization was the most frequently reported serious outcome (N = 2,159, 63.22%). Death or life-threatening events occurred in 921 cases (26.977%) of delayed irAEs, indicating the potentially life-threatening nature of delayed irAEs. Among the three categories of ICIs, anti-PD-1 agents were associated with more delayed irAEs (N = 2,304, 67.47%) compared to anti-PD-L1 (N = 865, 25.33%) and anti-CTLA4 (N = 246, 7.20%).

Among ICIs analyzed in this study, nivolumab had the highest number of cases (N = 1,697, 49.69%) of delayed irAEs, followed by atezolizumab (N = 676, 19.80%) and pembrolizumab (N = 560, 16.40%). In terms of combination therapy, the combination of nivolumab and ipilimumab was associated with the most frequently reported delayed irAEs (N = 317, 98.14%).

3.2 Signal of system organ class

Based on the original data, the signal strength of delayed irAEs at the System Organ Class (SOC) level was described in Supplementary Table S4. We identified delayed irAEs occurring in 27 different SOCs. The reporting cases and types of delayed irAEs at SOC level for various treatment strategies were visualized in Figure 2. Regarding different class-specific ICI regimens, anti-PD-1 drugs (nivolumab, pembrolizumab, and cemiplimab) accounted for the majority of reported delayed irAEs (N = 5,504, 73.42%). Cemiplimab and tremelimumab were approved by the FDA in September 2018 and October 2022, respectively, but were rarely used, leading to limited reporting of delayed irAEs. Among combination therapy, nivolumab + ipilimumab had the highest number of reported delayed irAEs at the SOC level (N = 667, 98.52%), as it was the most commonly used combination regimen in real-world settings.

We identified suspicious signals of ICIs using four pharmacovigilance algorithms (ROR, PRR, BCPNN, and MGPS) and presented the results in Table 2. The significant SOCs associated

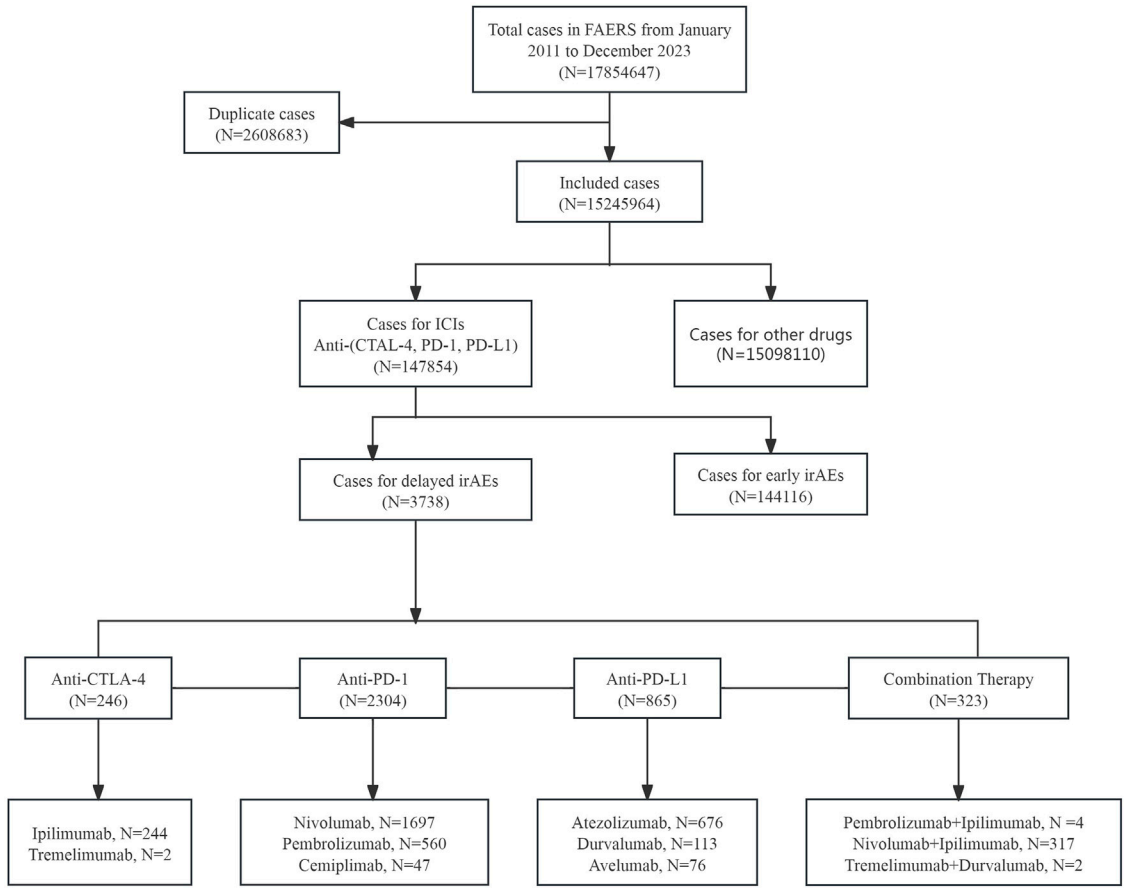

FIGURE 1
The process of data acquisition and data cleaning from FDA adverse event reporting database (FAERS).

with ICIs included gastrointestinal disorders (ROR_{025} = 1.30, SOC 10017947), respiratory, thoracic and mediastinal disorders (ROR_{025} = 1.41, SOC 10038738), metabolism and nutrition disorders (ROR_{025} = 2.27, SOC 10027433), skin and subcutaneous tissue disorders (ROR_{025} = 1.17, SOC 10040785), hepatobiliary disorders (ROR_{025} = 2.86, SOC 10019805), renal and urinary disorders (ROR_{025} = 1.42, SOC 10038359), blood and lymphatic system disorders (ROR_{025} = 1.81, SOC 10005329) and endocrine disorders (ROR_{025} = 10.50, SOC 10014698). Among these delayed irAEs, gastrointestinal disorders (N = 842, 11.23%), general disorders and administration site conditions (N = 838, 11.18%), infections and infestations (N = 657, 8.76%) and respiratory, thoracic and mediastinal disorders (N = 583, 7.78%) accounted for two-fifths of the reported adverse events. Notably, the strongest disproportionality association was for endocrine disorders (ROR_{025} = 10.50, χ^2 = 2074.69, IC_{025} = 3.23, $EBGM_{05}$ = 9.84). Moreover, sex-specific analyses of delayed irAEs at the SOC level were performed. Significant signals were detected in respiratory, thoracic and mediastinal disorders (ROR_{975} = 0.95), hematologic and lymphatic system disorders (ROR_{025} = 1.22), and immune system disorders (ROR_{025} = 1.16), as detailed in Supplementary Table S6.

The signal values and the association between class-specific ICIs and delayed irAEs are depicted in Figure 3. Among the different class-specific ICI regimens, anti-PD-1 drugs (nivolumab), anti-PD-L1 drugs (atezolizumab) and anti-CTLA-4 drugs (ipilimumab) demonstrated a significant association with gastrointestinal disorders and metabolism disorders. Respiratory system toxicities were significantly associated with anti-PD-1 drugs (pembrolizumab and nivolumab) and anti-PD-L1 drugs (atezolizumab, durvalumab and avelumab) drugs. Only anti-PD-1 drugs (pembrolizumab and nivolumab) exhibited significant signals in skin toxicities, while anti-CTLA-4 drugs did not show a significant association with skin toxicities and respiratory system toxicities. The combination regimen of anti-PD-1 drugs (nivolumab) and anti-CTLA-4 drugs (ipilimumab) did not result in any additional significant signals of delayed irAEs.

3.3 Signal of preferred terms

We assessed preferred terms (PT) levels in MedDRA for describing the delayed irAEs associated with different ICI regimens. The reported cases and types of delayed irAEs at PT level were visualized in Figure 4. A total of 1648 PT signals were identified from FAERS database, part of which are presented in Supplementary Table S5. Nivolumab exhibited the widest range of PTs among monotherapies, with a total of 1,145 PTs recorded.

10.3389/fphar.2024.1453429

TABLE 1 Clinical characteristics of patients with delayed irAEs.

Characteristics	Delayed irAEs (N = 3,415)	All irAEs (N = 147,854)
Gender		
Female	1,164 (34.08%)	50,135 (33.91%)
Male	2,171 (63.57%)	80,348 (54.34%)
Age		
<65	1,338 (42.99%)	44,696 (60.41%%)
≥65	1947 (57.01%)	58,542 (39.59%)
Reporting year		
~2017	401 (11.74%)	31,268 (21.15%)
2018	295 (8.64%)	15,709 (10.62%)
2019	436 (12.77%)	18,248 (12.34%)
2020	512 (14.99%)	17,787 (12.03%)
2021	563 (16.49%)	18,992 (12.85%)
2022	694 (20.32%)	21,689 (14.67%)
2023	514 (15.05%)	24,161 (16.34%)
Reporter Type		
Consumer	404 (11.83%)	38,728 (26.19%)
Health-professional	495 (14.49%)	18,886 (12.77%)
Pharmacist	901 (26.38%)	27,244 (18.43%)
Physician	1,599 (46.82%)	61,541 (41.62%)
Reporting Countries (top 5)		
USA	776 (22.72%)	57,792 (39.09%)
France	491 (14.38%)	10,736 (7.26%)
Japan	476 (13.94%)	30,954 (20.94%)
Germany	248 (7.26%)	5,823 (3.94%)
Italy	161 (4.71%)	3,184 (2.15%)
Indication (top 5)		
Lung Cancer	1,014 (29.69%)	42,543 (28.77%)
Malignant Melanoma	720 (21.08%)	24,071 (16.28%)
Renal and Ureteric Cancer	429 (12.56%)	12,416 (8.40%)
Hepatobiliary Malignancies	145 (4.25%)	6,629 (4.48%)
Head and Neck Carcinoma	108 (3.16%)	3,941 (2.67%)
Outcome		
Life-Threatening	258 (7.55%)	8,930 (6.04%)
Hospitalization	2,159 (63.22%)	59,077 (39.96%)
Death	663 (19.41%)	37,726 (25.52%)
Other Serious	2,109 (61.76%)	97,872 (66.20%)
Treatment strategy		
Anti-PD-1	2,304 (67.47%)	102,028 (69.01%)
Nivolumab	1,697 (49.69%)	60,636 (41.01%)
Pembrolizumab	560 (16.40%)	39,847 (26.95%)
Cemiplimab	47 (1.38%)	1,545 (1.04%)
Anti-PD-L1	865 (25.33%)	29,484 (19.94%)
Atezolizumab	676 (19.80%)	18,907 (12.79%)
Avelumab	76 (2.23%)	1853 (1.25%)
Durvalumab	113 (3.31%)	8,742 (5.90%)
Anti-CTLA4	246 (7.20%)	16,343 (11.05%)
Ipilimumab	244 (7.14%)	16,243 (10.99%)
Tremelimumab	2 (0.06%)	99 (0.07%)
Combination therapy	323 (9.46%)	14,838 (10.04%)
Pembrolizumab + Ipilimumab	4 (1.24%)	322 (2.17%)
Nivolumab + Ipilimumab	317 (98.14%)	14,449 (97.38)
Tremelimumab + Durvalumab	2 (0.62%)	67 (0.45%)

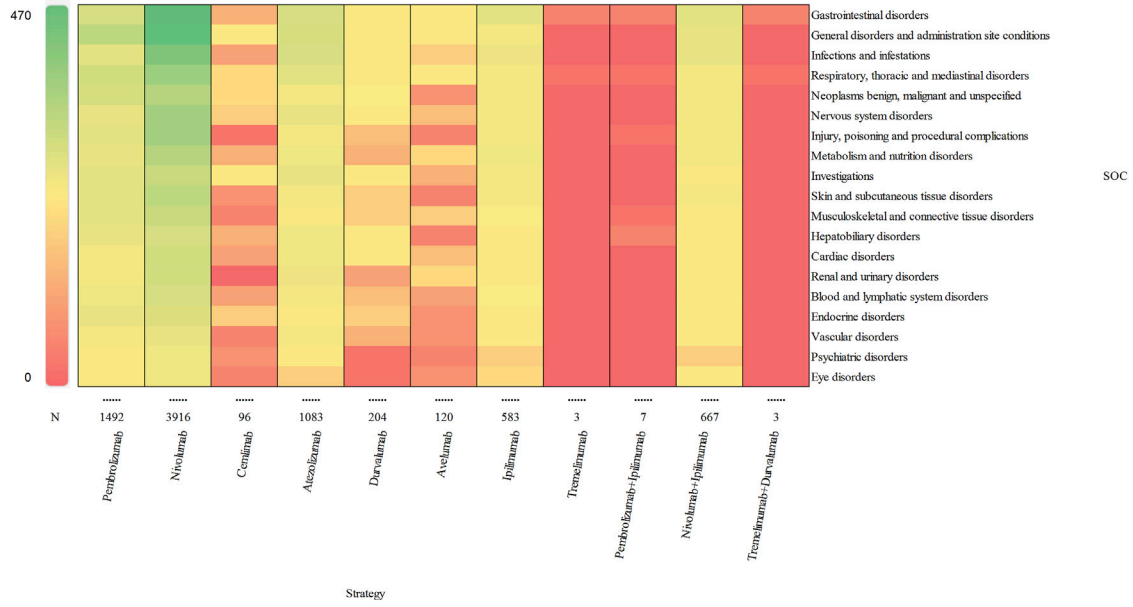

FIGURE 2
Visualization of reporting cases of delayed irAEs for different treatment strategies at SOC level.

Analysis of ICIs revealed significant delayed irAEs at the PT level, as shown in Table 3, including but not limited to following PTs: diarrhoea (ROR_{025} = 1.74, PT 10012735), pneumonia (ROR_{025} = 1.29, PT 10035664), colitis (ROR_{025} = 12.81 PT 10009887), pneumonitis (ROR_{025} = 26.45, PT 10035742), acute kidney injury (ROR_{025} = 2.15, PT 10069339), pemphigoid (ROR_{025} = 75.15, PT 10034277), adrenal insufficiency (ROR_{025} = 50.31, PT 10001367), anaemia (ROR_{025} = 1.22, PT 10002034), rash (ROR_{025} = 1.32, PT 10037844) and interstitial lung disease (ROR_{025} = 7.29, PT 10022611). Nivolumab, as one of the most widely used anti-PD-1 drug, exhibited 135 PTs as significant signals that were consistent across four algorithms, ranging from transaminases increased (ROR_{025} = 1.01) to fulminant type 1 diabetes mellitus (ROR_{025} = 320.93). Additionally, 29 PTs were significantly associated with combination treatment regimen of anti-PD-1 drugs (nivolumab) and anti-CTLA-4 drugs (ipilimumab), ranging from general physical health deterioration (ROR_{025} = 1.01) to autoimmune colitis (ROR_{025} = 196.05).

According to the report, an IC_{025} (the lower limit of 95% CI) value greater than 3.0 indicates a strong signal (Zou et al., 2023). In our study, we identified 10 strong signals at the PT level, including malignant neoplasm progression, colitis, pneumonitis, pemphigoid, adrenal insufficiency, type 1 diabetes mellitus, immune-mediated enterocolitis, hypophysitis, fulminant type 1 diabetes mellitus and encephalitis. Additionally, Figure 5 displays the top 10 most frequently reported PTs of delayed irAEs. Due to the lack of cases or only one case of delayed irAEs recorded for tremelimumab monotherpay, pembrolizumab + ipilimumab and tremelimumab + durvalumab combination therapy, they were excluded from the analysis. It is noteworthy that pneumonitis exhibited the most significant signals across different ICI regimens (ROR_{025}: from 11.85 to 29.27), followed by colitis (ROR_{025}: from 2.11 to 24.84). Further analysis revealed that nivolumab had most significant signal in pemphigoid (ROR_{025} = 104.75). Interestingly, ipilimumab combined nivolumab showed reduced associations with pneumonitis and colitis.

3.4 Outcomes

In order to improve the prognosis evaluation of delayed irAEs, we examined the proportions of death, life-threatening events, and hospitalization, as shown in Figure 6. Overall, the most severe outcomes of delayed irAEs at the SOC level were reported as death, with the highest proportions in gastrointestinal disorders (51.06%) and endocrine disorders (12.15%) respectively. Additionally, metabolism (12.12%) and respiratory disorders (11.19%) had a higher frequency of life-threatening events compared to other irAEs at SOC level. It is worth noting that the frequencies of hospitalization events were 81.21% for metabolism disorders and 80.29% for infections.

4 Discussion

With expanding application in oncology (Livingstone et al., 2022; Lorusso et al., 2024), ICIs have been associated with a higher incidence of irAEs than previously anticipated (Kato et al., 2017; Koyama et al., 2018; Johnson et al., 2022). Unfortunately, delayed irAEs has rarely been documented except for few studies (Owen et al., 2021; Couey et al., 2019). Additionally, details regarding delayed irAEs remain unclear. Therefore, we performed an analysis on delayed ICI-related adverse events using the FAERS database, presenting our findings as follows:

From the first quarter of 2011 to the fourth quarter of 2023, a total of 3,415 cases received ICI monotherapies and 323 cases

TABLE 2 Signal strength of delayed irAEs at the SOC level in FAERS database.

System organ class (SOC)	Reporting cases	ROR (ROR_{025}-ROR_{975})	PRR ($\chi 2$)	IC (IC_{025}-IC_{975})	EBGM ($EBGM_{05}$-$EBGM_{95}$)
Gastrointestinal disorders	842	1.39 (1.30–1.50)*	1.35 (82.14)*	0.43 (0.32–0.53)*	1.35 (1.25–1.45)
General disorders and administration site conditions	838	0.70 (0.65–0.75)	0.73 (96.64)	−0.45 (-0.55–0.34)	0.73 (0.68–0.79)
Infections and infestations	657	1.06 (0.98–1.15)	1.05 (2.04)	0.08 (-0.04–0.19)	1.05 (0.97–1.14)
Respiratory, thoracic and mediastinal disorders	583	1.53 (1.41–1.67)*	1.49 (99.08)*	0.57 (0.45–0.70)*	1.49 (1.37–1.62)
Neoplasms benign, malignant and unspecified	462	1.99 (1.81–2.19)*	1.93 (211.55)*	0.94 (0.80–1.08)*	1.92 (1.75–2.11)
Nervous system disorders	461	0.70 (0.64–0.77)	0.72 (53.57)	−0.47 (-0.61–0.33)	0.72 (0.66–0.79)
Injury, poisoning and procedural complications	419	0.63 (0.57–0.70)	0.65 (83.61)	−0.61 (-0.75–0.46)	0.65 (0.59–0.72)
Metabolism and nutrition disorders	407	2.51 (2.27–2.77)*	2.43 (346.30)*	1.27 (1.12–1.41)*	2.41 (2.18–2.67)*
Investigations	382	0.79 (0.72–0.88)	0.81 (19.13)	−0.31 (-0.46–0.16)	0.81 (0.73–0.89)
Skin and subcutaneous tissue disorders	356	1.30 (1.17–1.45)*	1.29 (23.85)*	0.36 (0.21–0.52)*	1.29 (1.16–1.43)
Musculoskeletal and connective tissue disorders	303	0.61 (1.54–1.68)	0.62 (72.75)	−0.68 (-0.84–0.51)	0.63 (0.56–0.70)
Hepatobiliary disorders	274	3.23 (2.86–3.65)*	3.15 (401.93)*	1.64 (1.45–1.81)*	3.12 (2.77–3.53)*
Cardiac disorders	263	1.08 (0.96–1.23)	1.08 (1.63)	0.11 (-0.07–0.29)	1.08 (0.95–1.22)
Renal and urinary disorders	260	1.61 (1.42–1.82)*	1.59 (57.27)*	0.66 (0.48–0.84)*	1.58 (1.40–1.79)
Blood and lymphatic system disorders	246	2.06 (1.81–2.34)*	2.03 (129.02)*	1.01 (0.82–1.19)*	2.02 (1.78–2.29)
Endocrine disorders	220	12.04 (10.50–13.80)*	11.71 (2074.69)*	3.50 (3.23–3.63)*	11.28 (9.84–12.94)*
Vascular disorders	167	0.98 (0.84–1.14)	0.98 (0.08)	−0.03 (-0.26–0.20)	0.98 (0.84–1.14)
Psychiatric disorders	98	0.27 (0.22–0.32)	0.28 (196.29)	−1.86 (-2.14–1.56)	0.28 (0.23–0.34)
Eye disorders	93	0.77 (0.63–0.95)	0.77 (6.17)	−0.37 (-0.66–0.06)	0.78 (0.63–0.95)

ROR, Reporting odds ratio; CI, Confidence interval; ROR_{025}, The lower limit of 95% CI of the ROR; ROR_{975}, The upper limit of 95% CI of the ROR; PRR, Proportional reporting ratio; χ, Chi-squared; IC, Information component; IC_{025}, The lower limit of 95% CI of the IC; IC_{975}, The upper limit of 95% CI of the IC; EBGM, Empirical Bayesian geometric mean; $EBGM_{05}$, The lower limit of 95% CI of EBGM; $EBGM_{95}$, The upper limit of 95% CI of EBGM. *Indicates statistically significant signals in algorithm.

received combination therapies reported delayed irAEs in our study, which we believe is the largest collection of cases of delayed irAEs to date. The reporting rate for delayed irAEs was approximately 2.31%, which is lower than 5.3% reported by Owen (Owen et al., 2021). This suggests that delayed irAEs are still uncommon. In our descriptive analysis, we observed that males accounted for a higher proportion of delayed irAEs compared to females. This difference may be partly due to the higher incidence of cancer in men, as lung cancer and melanoma were the most commonly reported indications for ICIs. Furthermore, Conforti's research demonstrated a higher propensity for males to undergo ICI therapy compared to females, attributed to the relatively lower participation rates of women in clinical trials (Conforti et al., 2018). Contrarily, our results contradicted Watson's analysis (Watson et al., 2019), which employed the World Health Organization (WHO) global database of individual case safety reports, revealing a heightened frequency of adverse drug reactions (ADRs) in females, especially during their reproductive years. Additionally, a separate investigation using the national pharmacovigilance center in the Netherlands found that medications such as thyroid hormones and antidepressants, which had the highest incidence of ADRs, were more frequently reported in women (de Vries et al., 2019).

Actually, to date, few studies have explored sex differences in irAEs, especially delayed irAEs. Extant literature delineates gender-specific disparities in immunological responses to both exogenous and endogenous antigens, highlighting distinct differences in both innate and adaptive immunity between males and females (Klein and Flanagan, 2016). Statistically, females exhibit more robust innate and adaptive immune responses compared to their male counterparts. On the other hand, females constitute approximately 80% of the global patient population suffering from systemic autoimmune diseases (Klein and Flanagan, 2016; Conforti et al., 2018). Consequently, the heightened predisposition of females to autoimmune pathologies could potentially render them more susceptible to irAEs (Menzies et al., 2017). To evaluate the impact of sex on the pharmacovigilance signal for delayed irAEs following ICIs initiation, we conducted further disproportionality analysis. Our results indicated that males had a slightly higher

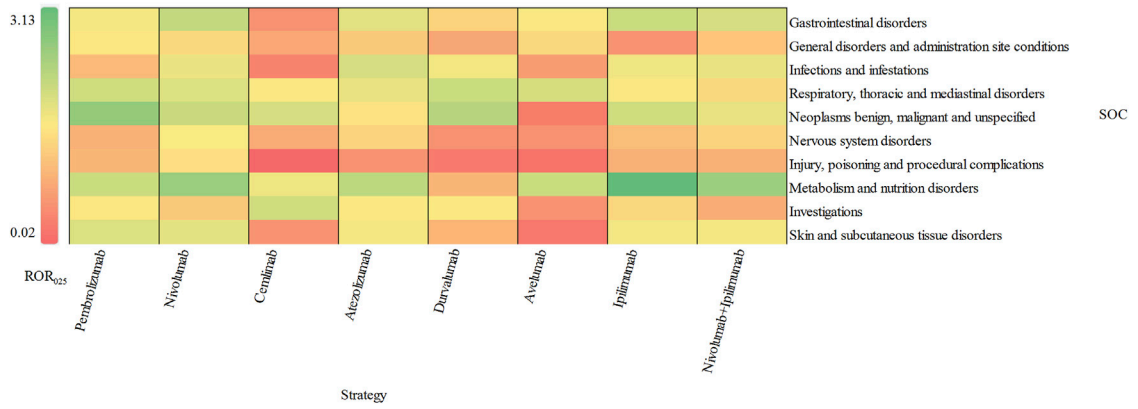

FIGURE 3
Visualization of delayed irAEs reporting rates for different treatment strategies at SOC level.

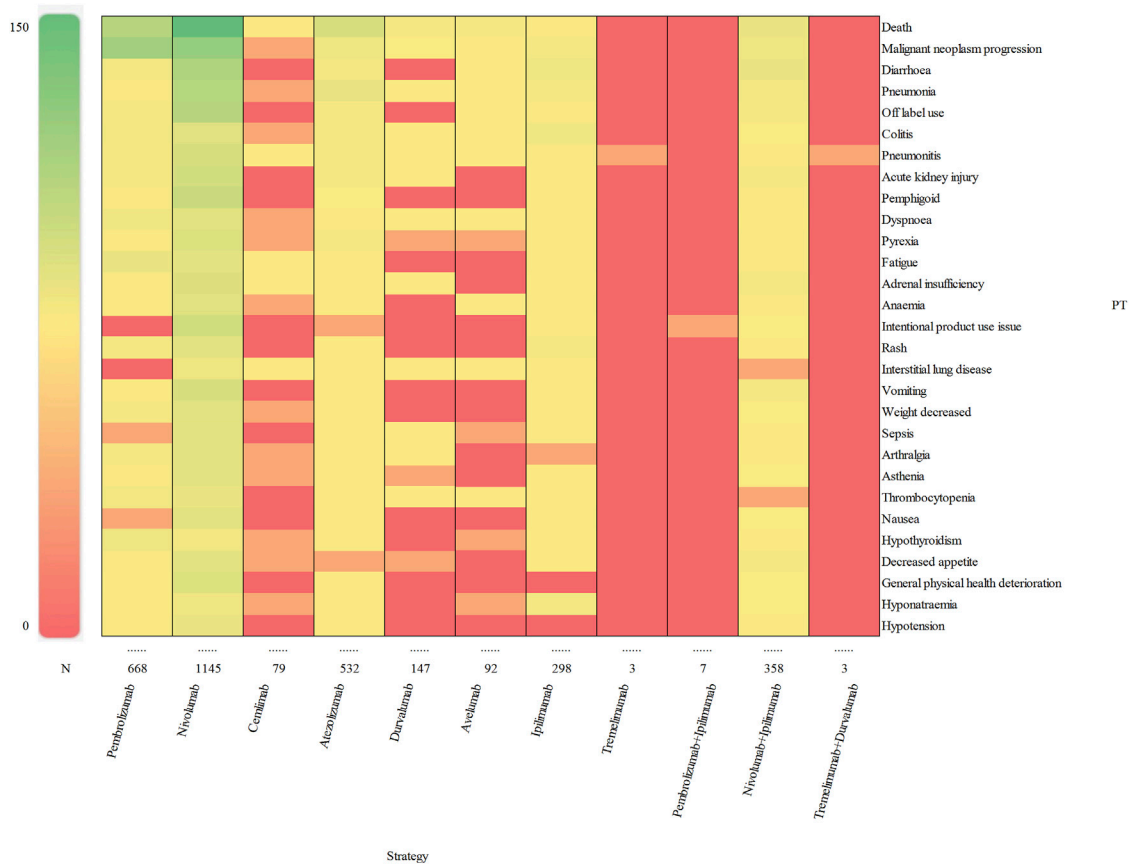

FIGURE 4
Visualization of reporting cases of delayed irAEs for different treatment strategies at PT level.

reporting frequencies of delayed irAEs in respiratory disorders (ROR_{975} = 0.95) and blood and lymphatic system disorders (ROR_{025} = 1.22), while females had significant higher reporting frequencies in immune system disorders (ROR_{025} = 1.16). These findings align with studies investigating respiratory toxicity linked to ICIs, which indicated that males exhibited a marginally higher incidence of respiratory system AEs compared to females (ROR = 1.74, 95% CI: 1.70~1.78) (Cui et al., 2022). This outcome may be partially attributed to greater exposure to cigarette smoke among men (Zhu et al., 2020; Suresh et al., 2018). Regarding hematologic and lymphatic system disorders, our result is different from Li's study (Li et al., 2023). The

TABLE 3 Signal strength of delayed irAEs at PT level.

System organ Class (SOC)	Preferred Terms (PTs)	Reporting Cases	ROR (ROR_{025}-ROR_{975})	PRR (χ^2)	IC (IC_{025}-IC_{975})	EBGM ($EBGM_{05}$-$EBGM_{95}$)
Gastrointestinal disorders	Diarrhoea	125	2.08 (1.74–2.48)*	2.06 (68.46)*	1.04 (0.77–1.29)*	2.05 (1.72–2.45)
	Colitis	79	16.09 (12.81–20.21)*	15.93 (1,047.06)*	3.92 (3.35–4.02)*	15.13 (12.05–19)*
	Vomiting	49	1.07 (0.81–1.42)	1.07 (0.25)	0.1 (-0.31–0.51)	1.07 (0.81–1.42)
	Nausea	42	0.70 (0.51–0.94)	0.7 (5.56)	−0.52 (-0.95–0.07)	0.7 (0.52–0.95)
	Abdominal pain	33	0.92 (0.65–1.29)	0.92 (0.25)	−0.12 (-0.62–0.38)	0.92 (0.65–1.29)
Infections and infestations	Pneumonia	116	1.55 (1.29–1.86)*	1.54 (22.16)*	0.62 (0.35–0.88)*	1.54 (1.28–1.85)
	Sepsis	46	2.42 (1.81–3.24)	2.41 (37.84)*	1.26 (0.8–1.64)*	2.4 (1.79–3.21)
	COVID-19	39	0.92 (0.67–1.26)	0.92 (0.26)	−0.12 (-0.57–0.34)	0.92 (0.67–1.26)
	Urinary tract infection	27	0.68 (0.46–0.99)	0.68 (4.12)	−0.56 (-1.09–0.01)	0.68 (0.47–0.99)
	Encephalitis	21	33.9 (21.54–53.33)*	33.81 (596.97)*	4.92 (3.05–4.35)*	30.29 (19.25–47.66)*
Respiratory, thoracic and mediastinal disorders	Pneumonitis	78	33.48 (26.45–42.38)*	33.14 (2,176.32)*	4.9 (4.1–4.79)*	29.76 (23.51–37.67)*
	Dyspnoea	62	0.85 (0.66–1.09)	0.85 (1.61)	−0.23 (-0.59–0.14)	0.85 (0.66–1.09)
	Interstitial lung disease	49	9.70 (7.29–12.90)*	9.64 (367.13)*	3.23 (2.59–3.42)*	9.35 (7.03–12.45)*
	Respiratory failure	29	2.46 (1.71–3.55)*	2.45 (24.83)*	1.29 (0.69–1.75)*	2.44 (1.69–3.52)
	Pulmonary embolism	28	1.38 (0.95–2.00)	1.37 (2.85)	0.46 (-0.1–0.98)	1.37 (0.95–1.99)
Nervous system disorders	Headache	25	0.41 (0.28–0.61)	0.41 (21.25)	−1.28 (-1.81–0.68)	0.41 (0.28–0.61)
	Dizziness	24	0.49 (0.33–0.74)	0.49 (12.51)	−1.02 (-1.56–0.41)	0.49 (0.33–0.74)
	Seizure	22	1.05 (0.69–1.6)	1.05 (0.06)	0.08 (-0.53–0.68)	1.05 (0.69–1.6)
	Cerebral infarction	16	3.39 (2.07–5.55)*	3.38 (26.57)*	1.75 (0.85–2.26)*	3.36 (2.05–5.5)*
	Syncope	15	0.80 (0.48–1.33)	0.8 (0.76)	−0.32 (-1.03–0.42)	0.8 (0.48–1.33)
Metabolism and nutrition disorders	Decreased appetite	41	2.01 (1.47–2.73)*	2 (20.42)*	1 (0.51–1.41)*	1.99 (1.46–2.71)
	Hyponatraemia	39	5.53 (4.03–7.6)*	5.51 (141.24)*	2.44 (1.82–2.75)*	5.42 (3.95–7.45)*
	Diabetic ketoacidosis	37	13.72 (9.86–19.1)*	13.66 (414.25)*	3.71 (2.83–3.79)*	13.08 (9.39–18.2)*
	Hyperglycaemia	32	7.79 (5.48–11.08)*	7.76 (183.64)*	2.92 (2.15–3.17)*	7.58 (5.33–10.78)*
	Dehydration	32	1.75 (1.23–2.47)*	1.74 (10.08)*	0.8 (0.26–1.27)*	1.74 (1.23–2.46)

(Continued on following page)

TABLE 3 (*Continued*) Signal strength of delayed irAEs at PT level.

System organ Class (SOC)	Preferred Terms (PTs)	Reporting Cases	ROR (ROR_{025}-ROR_{975})	PRR (χ^2)	IC (IC_{025}-IC_{975})	EBGM ($EBGM_{05}$-$EBGM_{95}$)
Skin and subcutaneous tissue disorders	Pemphigoid	68	99.13 (75.15–130.76)*	98.24 (4,853.32)*	6.19 (4.77–5.55)*	73.1 (55.41–96.42)*
	Rash	50	1.75 (1.32–2.31)*	1.74 (15.81)*	0.8 (0.37–1.18)*	1.74 (1.32–2.3)
	Pruritus	37	1.42 (1.02–1.96)*	1.41 (4.47)*	0.5 (0.01–0.95)*	1.41 (1.02–1.95)
	Vitiligo	11	57.47 (30.04–109.95)*	57.39 (506.32)*	5.58 (2.38–4.19)*	47.84 (25.01–91.53)*
	Erythema	9	0.62 (0.32–1.19)	0.62 (2.14)	−0.7 (-1.55–0.27)	0.62 (0.32–1.19)

ROR, Reporting odds ratio; CI, Confidence interval; ROR_{025}, The lower limit of 95% CI of the ROR; ROR_{975}, The upper limit of 95% CI of the ROR; PRR, Proportional reporting ratio; χ, Chi-squared; IC, Information component; IC_{025}, The lower limit of 95% CI of the IC; IC_{975}, The upper limit of 95% CI of the IC; EBGM, Empirical Bayesian geometric mean; $EBGM_{05}$, The lower limit of 95% CI of EBGM; $EBGM_{95}$, The upper limit of 95% CI of EBGM. *Indicates statistically significant signals in algorithm.

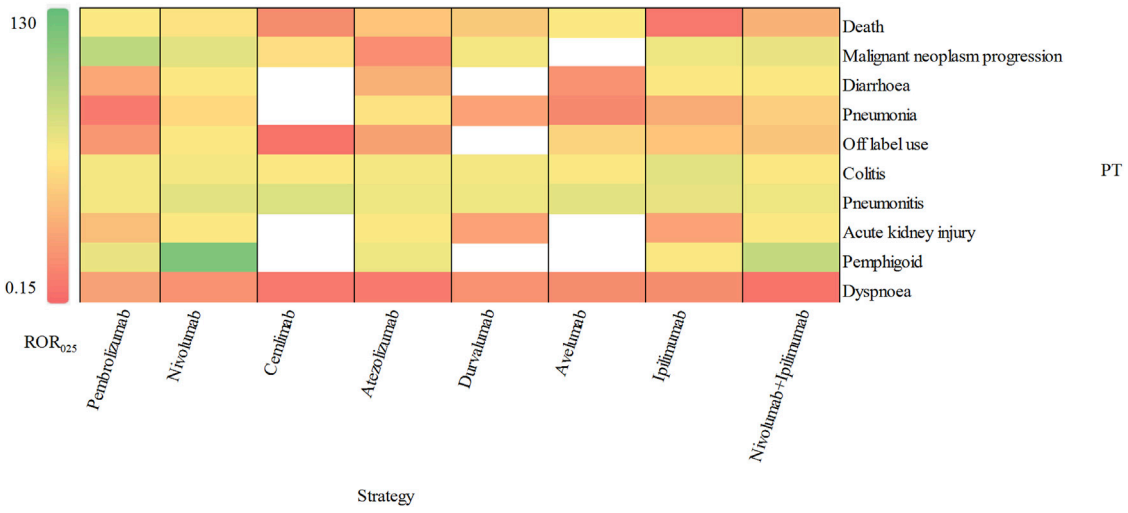

FIGURE 5
Visualization of delayed irAEs reporting rates for different treatment strategies at PT level.

specific determinants underlying sex-based disparities are not yet fully elucidated and necessitate additional investigation. No significant signals were detected between male and female patients for other delayed irAEs at the SOC level (Supplementary Table S3). Our findings suggest that sex difference may be an important biological variable for delayed irAEs, although the underlying factors are still unclear and require further investigation in the field of oncology. Furthermore, we observed that patients over 65 years old had a higher reporting frequency of delayed irAEs compared to those under 65 years old. Conversely for all irAEs, patients over 65 years old had much lower reporting rates. The impact of age difference on irAEs, particularly delayed irAEs is not well-established (Baldini et al., 2020; Paderi et al., 2021). and our analysis based on large-scale FAERS data may offer valuable evidence of the associations between age and delayed irAEs. Future studies should pay more attention to age differences in patients with delayed irAEs.

Importantly, we evaluated and compared the incidence of delayed irAEs across various immunotherapy regimens. Overall, there were more reports of delayed irAEs associated with anti-PD-1 inhibitors compared to anti-PD-L1 and anti-CTLA-4 inhibitors. Our analysis revealed that all ICIs demonstrated a higher reporting frequency of metabolism and nutrition disorders as compared to other delayed irAEs at SOC level (ROR_{025}: from 0.45 to 3.13), which was consistent with the findings from a previous study (Reese et al., 2020). Moreover, treatment with anti-PD-1 agents exhibited a higher reporting frequency of gastrointestinal disorders in comparison to other ICI regimens (ROR_{025} = 1.66). Conversely, metabolism and nutrition disorders were the most commonly reported delayed irAEs with anti-CTLA-4 medications as opposed to anti-PD-1/anti-PD-L1 medications (ROR_{025} = 3.13). Notably, significant signals for skin and subcutaneous disorders were observed with anti-PD-1 regimens (ROR_{025}: from 0.27 to 1.27), suggesting a higher likely-hood of skin toxicities with anti-PD-1 inhibitors. Interestingly, previous study have indicated that combination therapy is associated with increased rates of AEs involving multiple organ systems (Grimaldi et al., 2016). However, our study found that combination of anti-PD-1 and

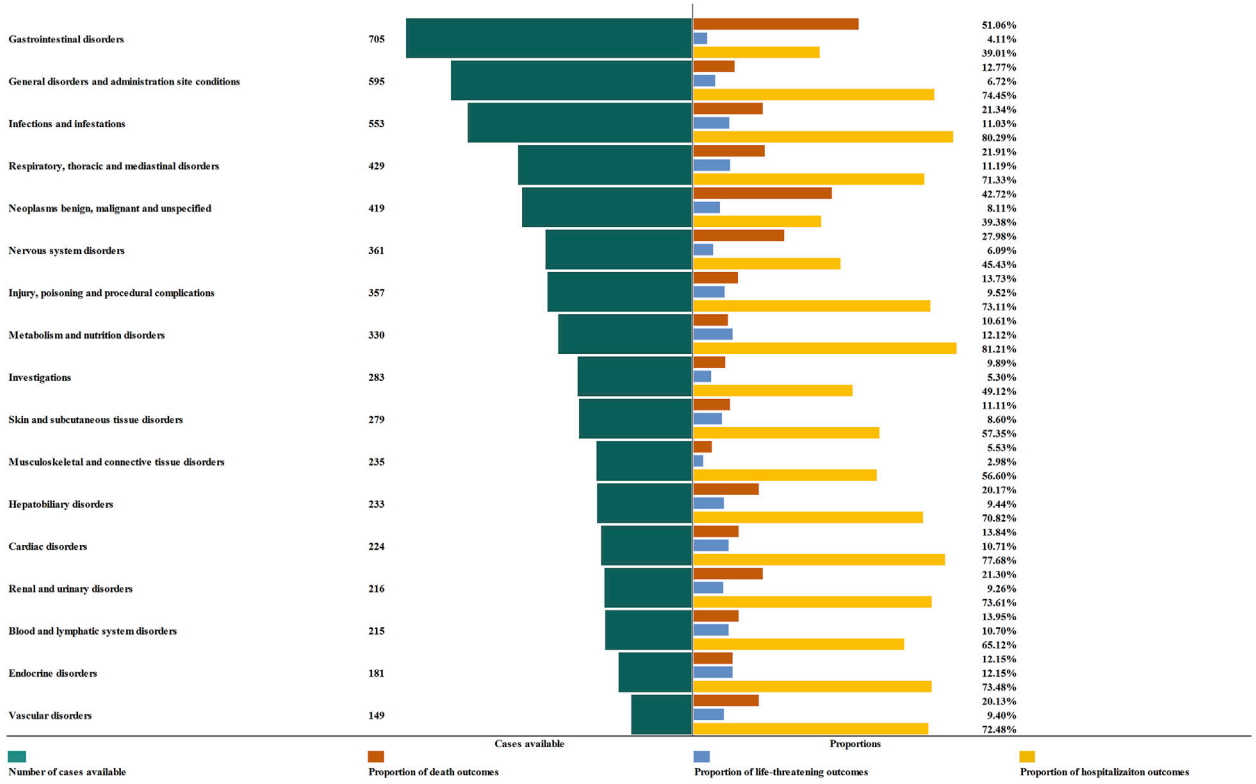

FIGURE 6
Cases and proportions of different outcomes of irAEs.

anti-CTLA-4 agents did not appear to further elevate the risk of delayed irAEs, in contrast to what has been reported for early irAEs.

Additionally, our study provides more precise data on the profile of delayed irAEs caused by different ICI regimens at the PT level. A total of 282 significant signals for potential toxicities were identified, including diarrhoea, pneumonia, colitis, pneumonitis, acute kidney injury and pemphigoid. Diarrhoea was more frequently recorded in patients receiving anti-PD-1 and anti-CTLA-4 therapy. Furthermore, we observed that ipilimumab alone or in combination with nivolumab had a higher risk of diarrhoea compared to other ICI regimens. It's worth noting that we identified two strong signals (IC_{025} > 3.0) for colitis and pneumonitis in all eight monotherapy regimens and one combination regimen. Owen reported that colitis was the most frequent delayed irAEs after adjuvant anti-PD-1 therapy in melanoma patients, which is consistent with our findings (Owen et al., 2021). The prognosis of delayed irAEs was thoroughly examined in our analysis. We observed that death accounted for 51.06% of the gastrointestinal disorders, indicating a significant impact of gastrointestinal complications on patient mortality. The study by Owen (Owen et al., 2021) demonstrated that the delayed gastrointestinal toxicities, such as colitis, increased the mortality rate of melanoma patients. Another severe outcome of delayed irAEs, life-threatening events, represented 12.15% of endocrine disorders. We noted a significant increase in endocrine-related delayed irAEs among female patients with various cancer types. The four of the most frequently recorded delayed irAEs at the PTs level were adrenal insufficiency, hypothyroidism, hypophysitis and hyperthyroidism, which aligns with previous study (Zhai et al., 2019). Given the high incidence of life-threatening events, it is crucial to closely monitor the signs and symptoms of endocrine-related delayed irAEs during ICI therapy.

Notably, delayed irAEs encompass both *de novo* toxicities and recurrences of previous events. Nevertheless, if the interval since the last dose exceeds 1 year, the probability of an alternative etiology increases (Naidoo et al., 2023). Essentially, attributing a re-emergent irAE is relatively straightforward if the patient is still receiving ICI treatment. However, the etiology of autoimmune toxicity emerging months or even years post-discontinuation of ICI treatment remains ambiguous. For example, viral infections may serve as alternative etiologies, potentially causing myocarditis (Rezkalla and Kloner, 2021) and chronic autoimmune conditions such as type 1 diabetes, rheumatoid arthritis and multiple sclerosis (Smatti et al., 2019). To date, clinical data and animal models on delayed or long-term irAEs are insufficient, and it is unclear whether there is a correlation between ICI treatment, intercurrent infections, and the onset of autoimmune disorders. Similar to recurrent irAEs, *de novo* autoimmune conditions should also be considered in differential diagnoses, particularly with the suspicion of an alternative etiology like viral infection. Naidoo et al. (2020) reported that myocarditis or pneumonitis were observed as manifestations that could confound attribution as re-emergent irAEs or *de novo* events arising from infectious etiology. Consequently, the diagnostic certainty of delayed irAEs can be variable, and the potential for misdiagnosis should be acknowledged. Commonly reported confounding factors include the diagnostic misattribution to the sequelae of concomitant

chemotherapy, radiotherapy, disease relapse, or septicemia (Couey et al., 2019). Conclusively, comprehensive and detailed data collection from real-world settings to improve the characterization and management of delayed irAEs is necessary.

As a matter of fact, there are several limitations that need to be addressed. Firstly, FAERS is a spontaneous reporting system with multiple sources of data, resulting in inherent constraints such as under reporting, incomplete patient demographic data, nonuniform data format and missing data. Availability of more detailed clinical data could potentially enhance a comprehensive evaluation of the patients' response rates associated with these irAEs and the durability of their responses.

Secondly, reports in the FAERS database do not require proof of a causal relationship with the drug. The information in the reports only reflects the observations and opinions of the reporters, which makes it impossible to determine whether the reported AEs were indeed caused by the drug. Thirdly, a case report in FAERS could involve several drugs, adverse events, and outcomes, leading to bias in pharmacovigilance analysis. Also, this study did not account for combination chemotherapy, which could have introduced bias into the results. Lastly, the calculation of fatality rates was not feasible due to the lack of comprehensive exposure data, in addition to the fact that mortality may also result from the underlying disease, concomitant irAEs, and other contributory factors. Notwithstanding, our investigation constitutes a comprehensive and meticulous quantification of the potential hazards associated with delayed irAEs in ICIs. These findings may offer critical evidence for subsequent research endeavors and clinical applications.

5 Conclusion

Our study systematically and scientifically evaluated the potential hazards using a large datasets from FAERS, outlining a profile of delayed irAEs. These findings provide valuable insights for future investigations and clinical applications in this specific field. In general, delayed irAEs occur in a small subset of cancer patients exposed to ICI regimens, which can be challenging to manage and may result in serious outcomes. Healthcare providers should be aware of the possibility of ICIs causing delayed irAEs, despite their low frequency. It is crucial to educate patients about these potential toxicities before initiating ICI therapy.

Data availability statement

The original contributions presented in the study are included in the article/Supplementary Material, further inquiries can be directed to the corresponding author.

Author contributions

YY: Data curation, Writing–original draft. LL: Resources, Writing–review and editing. JT: Resources, Writing–review and editing. LM: Data curation, Writing–review and editing. YW: Data curation, Writing–review and editing. QL: Data curation, Writing–review and editing. YL: Conceptualization, Funding acquisition, Supervision, Writing–original draft.

Funding

The author(s) declare that financial support was received for the research, authorship, and/or publication of this article. This work was supported by the National Natural Science Foundation of China (No. 82272755), Chongqing Science and Technology Commission (No. 2022NSCQ-MSX0706) and Fundamental Research Funds for the Central Universities (No. 2022CDJYGRH-007).

Acknowledgments

The authors would like to extend the sincere gratitude to all those who participated in this study.

Conflict of interest

The authors declare that the research was conducted in the absence of any commercial or financial relationships that could be construed as a potential conflict of interest.

Publisher's note

Supplementary material

The Supplementary Material for this article can be found online at: https://www.frontiersin.org/articles/10.3389/fphar.2024.1453429/full#supplementary-material

References

Baldini, C., Martin Romano, P., Voisin, A. L., Danlos, F. X., Champiat, S., Laghouati, S., et al. (2020). Impact of aging on immune-related adverse events generated by anti-programmed death (ligand)PD-(L)1 therapies. *Eur. J. Cancer* 129, 71–79. doi:10.1016/j.ejca.2020.01.013

Conforti, F., Pala, L., Bagnardi, V., De Pas, T., Martinetti, M., Viale, G., et al. (2018). Cancer immunotherapy efficacy and patients' sex: a systematic review and meta-analysis. *Lancet Oncol.* 19 (6), 737–746. doi:10.1016/S1470-2045(1830261-4)

Couey, M. A., Bell, R. B., Patel, A. A., Romba, M. C., Crittenden, M. R., Curti, B. D., et al. (2019). Delayed immune-related events (DIRE) after discontinuation of immunotherapy: diagnostic hazard of autoimmunity at a distance. *J. Immunother. Cancer* 7 (1), 165. doi:10.1186/s40425-019-0645-6

Cui, C., Deng, L., Wang, W., Ren, X., Wang, Y., and Cui, W. (2022). Respiratory system toxicity induced by immune checkpoint inhibitors: a real-world study based on the FDA adverse event reporting system database. *Front. Oncol.* 12, 941079. doi:10.3389/fonc.2022.941079

De Vries, S. T., Denig, P., Ekhart, C., Burgers, J. S., Kleefstra, N., Mol, P. G. M., et al. (2019). Sex differences in adverse drug reactions reported to the National Pharmacovigilance Centre in The Netherlands: an explorative observational study. *Br. J. Clin. Pharmacol.* 85 (7), 1507–1515. doi:10.1111/bcp.13923

Grimaldi, A. M., Marincola, F. M., and Ascierto, P. A. (2016). Single versus combination immunotherapy drug treatment in melanoma. *Expert Opin. Biol. Ther.* 16 (4), 433–441. doi:10.1517/14712598.2016.1128891

Guo, M., Shu, Y., Chen, G., Li, J., and Li, F. (2022). A real-world pharmacovigilance study of FDA adverse event reporting system (FAERS) events for niraparib. *Sci. Rep.* 12 (1), 20601. doi:10.1038/s41598-022-23726-4

Hauben, M., Madigan, D., Gerrits, C. M., Walsh, L., and Van Puijenbroek, E. P. (2005). The role of data mining in pharmacovigilance. *Expert Opin. Drug Saf.* 4 (5), 929–948. doi:10.1517/14740338.4.5.929

Jiang, J. J., Zhao, B., and Li, J. (2022). Does eltrombopag lead to thrombotic events? A pharmacovigilance study of the FDA adverse event reporting system. *J. Clin. Pharm. Ther.* 47 (10), 1556–1562. doi:10.1111/jcpt.13701

Johnson, D. B., Nebhan, C. A., Moslehi, J. J., and Balko, J. M. (2022). Immune-checkpoint inhibitors: long-term implications of toxicity. *Nat. Rev. Clin. Oncol.* 19 (4), 254–267. doi:10.1038/s41571-022-00600-w

Kato, T., Masuda, N., Nakanishi, Y., Takahashi, M., Hida, T., Sakai, H., et al. (2017). Nivolumab-induced interstitial lung disease analysis of two phase II studies patients with recurrent or advanced non-small-cell lung cancer. *Lung Cancer* 104, 111–118. doi:10.1016/j.lungcan.2016.12.016

Klein, S. L., and Flanagan, K. L. (2016). Sex differences in immune responses. *Nat. Rev. Immunol.* 16 (10), 626–638. doi:10.1038/nri.2016.90

Koyama, N., Iwase, O., Nakashima, E., Kishida, K., Kondo, T., Watanabe, Y., et al. (2018). High incidence and early onset of nivolumab-induced pneumonitis: four case reports and literature review. *BMC Pulm. Med.* 18 (1), 23. doi:10.1186/s12890-018-0592-x

Li, N., Feng, Y., Chen, X., Li, Y., Zhang, C., and Yin, Y. (2023). Hematologic and lymphatic system toxicities associated with immune checkpoint inhibitors: a real-world study. *Front. Pharmacol.* 14, 1213608. doi:10.3389/fphar.2023.1213608

Livingstone, E., Zimmer, L., Hassel, J. C., Fluck, M., Eigentler, T. K., Loquai, C., et al. (2022). Adjuvant nivolumab plus ipilimumab or nivolumab alone versus placebo in patients with resected stage IV melanoma with no evidence of disease (IMMUNED): final results of a randomised, double-blind, phase 2 trial. *Lancet* 400 (10358), 1117–1129. doi:10.1016/S0140-6736(22)01654-3

Lorusso, D., Xiang, Y., Hasegawa, K., Scambia, G., Leiva, M., Ramos-Elias, P., et al. (2024). Pembrolizumab or placebo with chemoradiotherapy followed by pembrolizumab or placebo for newly diagnosed, high-risk, locally advanced cervical cancer (ENGOT-cx11/GOG-3047/KEYNOTE-A18): a randomised, double-blind, phase 3 clinical trial. *Lancet* 403 (10434), 1341–1350. doi:10.1016/S0140-6736(24)00317-9

Martins, F., Sofiya, L., Sykiotis, G. P., Lamine, F., Maillard, M., Fraga, M., et al. (2019). Adverse effects of immune-checkpoint inhibitors: epidemiology, management and surveillance. *Nat. Rev. Clin. Oncol.* 16 (9), 563–580. doi:10.1038/s41571-019-0218-0

Menzies, A. M., Johnson, D. B., Ramanujam, S., Atkinson, V. G., Wong, A. N. M., Park, J. J., et al. (2017). Anti-PD-1 therapy in patients with advanced melanoma and preexisting autoimmune disorders or major toxicity with ipilimumab. *Ann. Oncol.* 28 (2), 368–376. doi:10.1093/annonc/mdw443

Naidoo, J., Murphy, C., Atkins, M. B., Brahmer, J. R., Champiat, S., Feltquate, D., et al. (2023). Society for Immunotherapy of Cancer (SITC) consensus definitions for immune checkpoint inhibitor-associated immune-related adverse events (irAEs) terminology. *J. Immunother. Cancer* 11 (3), e006398. doi:10.1136/jitc-2022-006398

Naidoo, J., Reuss, J. E., Suresh, K., Feller-Kopman, D., Forde, P. M., Mehta Steinke, S., et al. (2020). Immune-related (IR)-pneumonitis during the COVID-19 pandemic: multidisciplinary recommendations for diagnosis and management. *J. Immunother. Cancer* 8 (1), e000984. doi:10.1136/jitc-2020-000984

Noren, G. N., Bate, A., Orre, R., and Edwards, I. R. (2006). Extending the methods used to screen the WHO drug safety database towards analysis of complex associations and improved accuracy for rare events. *Stat. Med.* 25 (21), 3740–3757. doi:10.1002/sim.2473

Owen, C. N., Bai, X., Quah, T., Lo, S. N., Allayous, C., Callaghan, S., et al. (2021). Delayed immune-related adverse events with anti-PD-1-based immunotherapy in melanoma. *Ann. Oncol.* 32 (7), 917–925. doi:10.1016/j.annonc.2021.03.204

Paderi, A., Fancelli, S., Caliman, E., Pillozzi, S., Gambale, E., Mela, M. M., et al. (2021). Safety of immune checkpoint inhibitors in elderly patients: an observational study. *Curr. Oncol.* 28 (5), 3259–3267. doi:10.3390/curroncol28050283

Reese, S. W., Marchese, M., and Mcnabb-Baltar, J. (2020). Insights from pharmacovigilance: gastrointestinal-related immune checkpoint inhibitor adverse events. *Gastroenterology* 159 (4), 1195–1200. doi:10.1053/j.gastro.2020.06.093

Rezkalla, S. H., and Kloner, R. A. (2021). Viral myocarditis: 1917-2020: from the Influenza A to the COVID-19 pandemics. *Trends Cardiovasc Med.* 31 (3), 163–169. doi:10.1016/j.tcm.2020.12.007

Singh, N., Hocking, A. M., and Buckner, J. H. (2023). Immune-related adverse events after immune check point inhibitors: understanding the intersection with autoimmunity. *Immunol. Rev.* 318 (1), 81–88. doi:10.1111/imr.13247

Smatti, M. K., Cyprian, F. S., Nasrallah, G. K., Al Thani, A. A., Almishal, R. O., and Yassine, H. M. (2019). Viruses and autoimmunity: a review on the potential interaction and molecular mechanisms. *Viruses* 11 (8), 762. doi:10.3390/v11080762

Suresh, K., Naidoo, J., Lin, C. T., and Danoff, S. (2018). Immune checkpoint immunotherapy for non-small cell lung cancer: benefits and pulmonary toxicities. *Chest* 154 (6), 1416–1423. doi:10.1016/j.chest.2018.08.1048

Tao, Y., Li, X., Liu, B., Wang, J., Lv, C., Li, S., et al. (2023). Association of early immune-related adverse events with treatment efficacy of neoadjuvant Toripalimab in resectable advanced non-small cell lung cancer. *Front. Oncol.* 13, 1135140. doi:10.3389/fonc.2023.1135140

Watson, S., Caster, O., Rochon, P. A., and Den Ruijter, H. (2019). Reported adverse drug reactions in women and men: aggregated evidence from globally collected individual case reports during half a century. *EClinicalMedicine* 17, 100188. doi:10.1016/j.eclinm.2019.10.001

Weber, J. S., Hodi, F. S., Wolchok, J. D., Topalian, S. L., Schadendorf, D., Larkin, J., et al. (2017). Safety profile of nivolumab monotherapy: a pooled analysis of patients with advanced melanoma. *J. Clin. Oncol.* 35 (7), 785–792. doi:10.1200/JCO.2015.66.1389

Yin, Q., Wu, L., Han, L., Zheng, X., Tong, R., Li, L., et al. (2023). Immune-related adverse events of immune checkpoint inhibitors: a review. *Front. Immunol.* 14, 1167975. doi:10.3389/fimmu.2023.1167975

Zhai, Y., Ye, X., Hu, F., Xu, J., Guo, X., Zhuang, Y., et al. (2019). Endocrine toxicity of immune checkpoint inhibitors: a real-world study leveraging US Food and Drug Administration adverse events reporting system. *J. Immunother. Cancer* 7 (1), 286. doi:10.1186/s40425-019-0754-2

Zhang, Y. C., Zhu, T. C., Nie, R. C., Lu, L. H., Xiang, Z. C., Xie, D., et al. (2023). Association between early immune-related adverse events and survival in patients treated with PD-1/PD-L1 inhibitors. *J. Clin. Med.* 12 (3), 736. doi:10.3390/jcm12030736

Zhou, C., Peng, S., Lin, A., Jiang, A., Peng, Y., Gu, T., et al. (2023). Psychiatric disorders associated with immune checkpoint inhibitors: a pharmacovigilance analysis of the FDA Adverse Event Reporting System (FAERS) database. *EClinicalMedicine* 59, 101967. doi:10.1016/j.eclinm.2023.101967

Zhu, S., Fu, Y., Zhu, B., Zhang, B., and Wang, J. (2020). Pneumonitis induced by immune checkpoint inhibitors: from clinical data to translational investigation. *Front. Oncol.* 10, 1785. doi:10.3389/fonc.2020.01785

Zou, S. P., Yang, H. Y., Ouyang, M. L., Cheng, Q., Shi, X., and Sun, M. H. (2023). A disproportionality analysis of adverse events associated to pertuzumab in the FDA Adverse Event Reporting System (FAERS). *BMC Pharmacol. Toxicol.* 24 (1), 62. doi:10.1186/s40360-023-00702-w

frontiers | Frontiers in Pharmacology

TYPE Original Research
PUBLISHED 24 January 2025
DOI 10.3389/fphar.2024.1398370

OPEN ACCESS

EDITED BY
Ursula Gundert-Remy,
Charité University Medicine Berlin, Germany

REVIEWED BY
Sudin Bhattacharya,
Michigan State University, United States
Fei Chen,
Chinese Academy of Sciences and China National Center for Bioinformation, China

*CORRESPONDENCE
Sun Kim,
sunkim.bioinfo@snu.ac.kr

†PRESENT ADDRESS
Inyoung Sung,
BK21 FOUR Intelligence Computing, Seoul National University, Seoul, South Korea
Sangseon Lee,
Department of Artificial Intelligence, Inha University, Incheon, South Korea

‡These authors have contributed equally to this work

RECEIVED 09 March 2024
ACCEPTED 27 December 2024
PUBLISHED 24 January 2025

CITATION
Sung I, Lee S, Bang D, Yi J, Lee S and Kim S (2025) MDTR: a knowledge-guided interpretable representation for quantifying liver toxicity at transcriptomic level.
Front. Pharmacol. 15:1398370.
doi: 10.3389/fphar.2024.1398370

MDTR: a knowledge-guided interpretable representation for quantifying liver toxicity at transcriptomic level

Inyoung Sung[1†‡], Sangseon Lee[2†‡], Dongmin Bang[1,3], Jungseob Yi[4], Sunho Lee[3] and Sun Kim[1,5,4,3*]

[1]Interdisciplinary Program in Bioinformatics, Seoul National University, Seoul, Republic of Korea, [2]Institute of Computer Technology, Seoul National University, Seoul, Republic of Korea, [3]AIGENDRUG Co., Ltd., Seoul, Republic of Korea, [4]Interdisciplinary Program in Artificial Intelligence, Seoul National University, Seoul, Republic of Korea, [5]Department of Computer Science and Engineering, Seoul National University, Seoul, Republic of Korea

Introduction: Drug-induced liver injury (DILI) has been investigated at the patient level. Analysis of gene perturbation at the cellular level can help better characterize biological mechanisms of hepatotoxicity. Despite accumulating drug-induced transcriptome data such as LINCS, analyzing such transcriptome data upon drug treatment is a challenging task because the perturbation of expression is dose and time dependent. In addition, the mechanisms of drug toxicity are known only as literature information, not in a computable form.

Methods: To address these challenges, we propose a Multi-Dimensional Transcriptomic Ruler (MDTR) that quantifies the degree of DILI at the transcriptome level. To translate transcriptome data to toxicity-related mechanisms, MDTR incorporates KEGG pathways as representatives of mechanisms, mapping transcriptome data to biological pathways and subsequently aggregating them for each of the five hepatotoxicity mechanisms. Given that a single mechanism involves multiple pathways, MDTR measures pathway-level perturbation by constructing a radial basis kernel-based toxicity space and measuring the Mahalanobis distance in the transcriptomic kernel space. Representing each mechanism as a dimension, MDTR is visualized in a radar chart, enabling an effective visual presentation of hepatotoxicity at transcriptomic level.

Results and Discussion: In experiments with the LINCS dataset, we show that MDTR outperforms existing methods for measuring the distance of transcriptome data when describing for dose-dependent drug perturbations. In addition, MDTR shows interpretability at the level of DILI mechanisms in terms of the distance, i.e., in a metric space. Furthermore, we provided a user-friendly and freely accessible website (http://biohealth.snu.ac.kr/software/MDTR), enabling users to easily measure DILI in drug-induced transcriptome data.

KEYWORDS

drug-induced liver injury, one-class boundary, kernel distance, transcriptomic signature, degree of toxicity, liver toxicity

1 Introduction

Drug-induced hepatotoxicity (also known as drug-induced liver injury; DILI) is a serious issue for both drug development and patient safety (Kaplowitz, 2004; Wilke et al., 2007). Traditional studies of toxicity have used animal models. This approach is time-consuming and costly, and may not accurately predict human toxicity (Van Norman, 2019; Bracken, 2009). Meanwhile, *in vitro* bioassays offer a more direct insight into human biology, with lower costs and ethical concerns (Chapman et al., 2013; Van Norman, 2019). Because these bioassays enable high-throughput screening, there is a growing interest to use the bioassays for toxicity signature screening to analyze toxicity at the individual patient cases.

The increasing availability of large-scale chemical libraries and gene expression data has significantly advanced our ability to investigate drug-induced toxicities. Several public resources have been developed to facilitate high-throughput screening and toxicity profiling. Among these, Tox21, a collaborative US federal research program, focuses on developing *in vitro* assays to screen for potentially toxic chemicals. Tox21 has pioneered the use of medium-to high-throughput panel assays to test thousands of chemicals for potential toxicity (Andersen and Krewski, 2009; Krewski et al., 2010). ToxCast, another program led by the US Environmental Protection Agency, extends the capabilities of Tox21 by offering medium- and high-throughput screening data for a wide range of chemicals (Dix et al., 2007). However, high throughput panel assays cannot measure toxic effect of drug at the transcriptomic level, thus molecular level mechanism of action (MoA) of drug response cannot be analyzed. To overcome the limitation of the panel assays, other resources such as the Genomics of Drug Sensitivity in Cancer (GDSC, Garnett et al. (2012)) and the Cancer Cell Line Encyclopedia (CCLE, Barretina et al. (2012)) provide valuable gene expression data and drug response metrics, such as IC50 and AUC values, across various cancer cell lines. However, both GDSC and CCLE lack the gene expression data that reflect post-drug treatment states. To address these gaps, the Library of Integrated Network-Based Cellular Signatures (LINCS) serves as a comprehensive resource that provides *in vitro* gene expression data after drug treatment (Subramanian et al., 2017). LINCS allows for the analysis of drug-induced perturbations over time and across different doses in various cell lines.

1.1 Challenges

Understanding how a drug interacts and affects biological systems to induce hepatotoxicity with the drug-induced transcriptome data is a goal of this study. The perturbed biological mechanisms by dysregulated genes can be interpreted as a degree of hepatotoxicity at transcriptomic level. However, despite the abundance of drug response and gene expression data, measuring the degree of drug-induced hepatotoxicity faces three major challenges.

1. Data availability varies greatly depending on drug treatment conditions. For example, the LINCS dataset includes gene expression values for 12,328 genes across an average of 16 samples (with a standard deviation of 30) for varying dose and time point combinations (Supplementary Figure S1). It causes a high-dimensional low-sample issue and hinders accurate interpretation of the MoA of drugs.
2. Identifying toxic patterns or signatures among drug-treated expression data is challenging. In the current state of knowledge, hepatotoxic signatures at transcriptomic level are insufficient (Andrade et al., 2019), and these signatures are dose- and time-dependent, as exemplified by hormesis (Mattson, 2008). Furthermore, biological mechanisms related to hepatotoxicity are available only in the literature. If possible, we need computational method to translate drug-induced transcriptome data to known biological mechanisms related to hepatotoxicity.
3. Defining the boundaries of toxicity is complex. Cell survival is governed by maintaining homeostasis, which is influenced by various conditions such as temperature and oxygen levels (Chovatiya and Medzhitov, 2014). Any disruption beyond the homeostasis boundary can lead to cell death with cytotoxic effects. Consequently, the state of toxicity cannot be confined within a specific boundary between toxic and non-toxic labels.

1.2 Our approach

To address these challenges, we propose MDTR, a knowledge-guided Multi-Dimensional Transcriptomic Ruler for quantifying the degree of drug-induced hepatotoxicity at the transcriptomic level. We first compiled five biological mechanisms of hepatotoxicity from the recent literature (Andrade et al., 2019; Weaver et al., 2020; Han et al., 2020). To translate transcriptome data to the five hepatotoxicity mechanisms, MDTR incorporates KEGG pathways as representative of mechanisms, mapping transcriptome data to these pathways and subsequently aggregating them for each of the five hepatotoxicity mechanisms. This involves three steps: (1) Identifying the most-perturbed transcriptomic samples as outliers using Dual-SVDD. The rationale behind this assumption is that toxic signatures are distinct from all remaining transcriptomic samples. (2) Constructing a transcriptomic embedding space using the Radial Basis Function (RBF) kernel and defining a ruler in the kernel space. (3) Extending the ruler into a five-dimensional radar chart for interpreting hepatotoxicity based on the knowledge-guided biological mechanisms.

As a result, MDTR represents *the degree of DILI as the distances* that measure the perturbation of the biological mechanisms under the drug treated environment. MDTR distance outperforms existing methods, which measure distances between transcriptomic samples, in reflecting the dose-dependent effects of drug on liver injury. In addition to its quantitative capabilities, MDTR provides interpretive power for understanding the MoA. We also provide a website for calculating and visualizing the five-dimension radar chart using drug-treated transcriptomic data input by scientists.

2 Methods and materials

In this section, we introduce the details of MDTR, which aims to measure the degree of hepatotoxicity from drug-induced

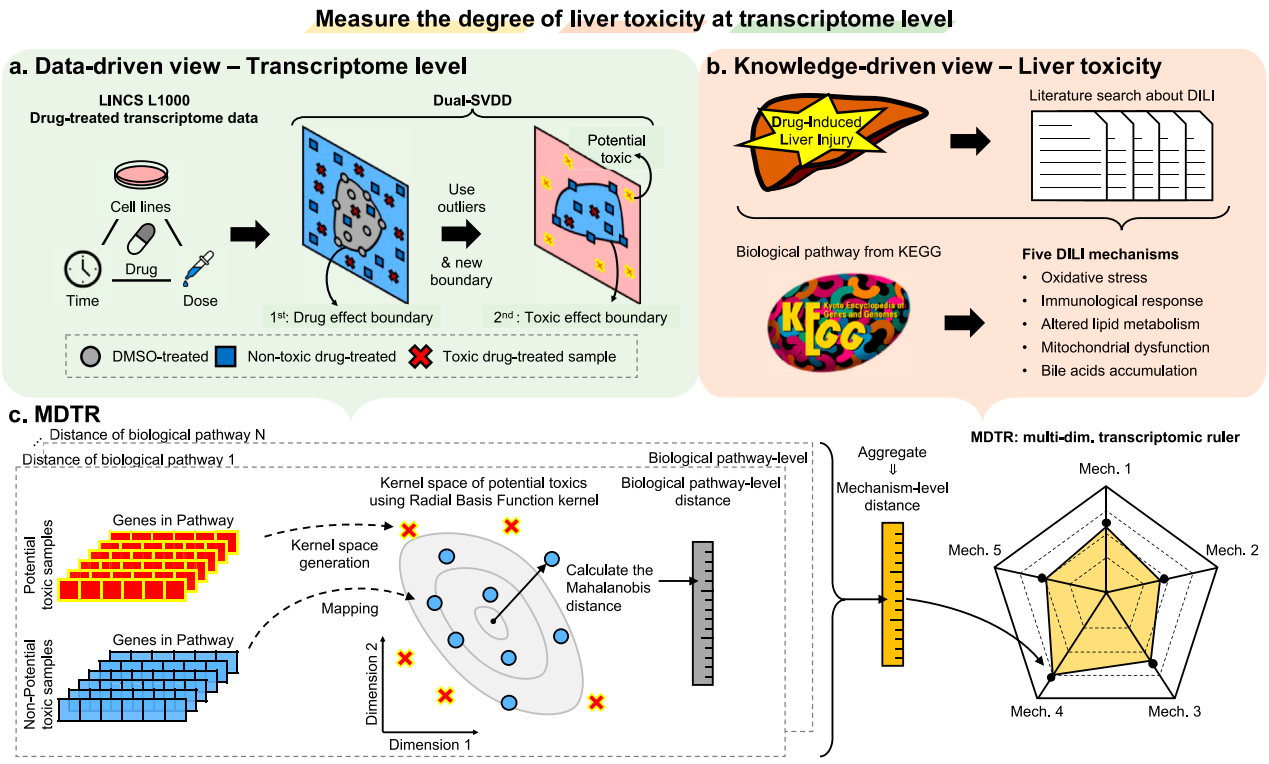

FIGURE 1
The overview of MDTR. To measure the degree of liver toxicity at the transcriptome level, hepatotoxic signatures were explored through both **(A)** data- and **(B)** knowledge-driven views, and **(C)** a knowledge-guided multi-dimensional ruler MDTR was proposed. **(A)** Dual-SVDD workflow. For drug-treated transcriptome data of LINCS, Dual-SVDD generates dual-boundaries to identify the most perturbed, i.e., potential toxic samples. **(B)** Literature search workflow. Five major DILI mechanisms were proposed through literature searches, and the corresponding biological pathways were collected from KEGG. **(C)** MDTR workflow. Each biological pathway within a mechanism calculates a pathway-level distance in the Radial Basis Function (RBF) kernel space. These pathway-level distances are then aggregated to form the mechanism-level distance, which serves as an axis in the multi-dimensional ruler.

transcriptome data. MDTR consists of two steps: (1) Exploration of hepatotoxic signatures through data- and knowledge-driven view. (2) Calculation of the degree of hepatotoxicity by a knowledge-guided multi-dimensional ruler. Figure 1 illustrates the overview of MDTR.

2.1 Exploration of hepatotoxic signatures at transcriptomic level

As mentioned in challenge #2, the signatures that can be utilized to measure drug-induced hepatotoxicity at the cellular level have not yet been clearly defined. To bridge the current gap in available data and knowledge, we explore hepatotoxic signatures through two approaches: (i) data-driven view: identification of potential toxic samples by Dual-SVDD. (ii) knowledge-driven view: literature mining of biological mechanisms related to drug-induced hepatotoxicity.

2.1.1 Data-driven view: identification of potential toxic samples by Dual-SVDD

Upon drug treatment, biological mechanisms are perturbed, leading to changes in gene expression levels. As mentioned in challenge #2, although the toxic signatures may not be clear, samples that are significantly influenced by the toxic drug, either by the treated time or dose, may show significant dysregulation in gene expression. Indeed, the perturbation signature of LINCS is known to be associated with cell viability linked to regulation of transcription factors such as apoptosis and proliferation (Szalai et al., 2019). In particular, toxic compounds can induce cell death signatures, suggesting the potential to predict MoA through drug-specific perturbation profiles (Niepel et al., 2017). Based on this understanding, we assumed that samples containing a toxic signature would show distinct perturbations among the toxic-treated transcriptome data, and we referred to these samples as "potentially toxic (PT)" samples. However, in the process of selecting PT samples, as mentioned in challenge #3, the processes of dysregulation due to toxicity are diverse, making it difficult to define them with a single, closed boundary. Therefore, we designed an approach of defining boundaries from relatively homogeneous effects and detecting PT samples as outliers compared to other drug-induced transcriptome samples.

To identify the PT samples, we propose a novel method called Dual-SVDD, which consists of two boundaries: the drug-effect boundary and the toxic-effect boundary. This method is based on the construction of a one-class boundary method, Support Vector Data Description (SVDD, Tax and Duin (2004)). Formally, given a set of samples $(\mathbf{x}_i, y_i)$ where $\mathbf{x}_i$ is a gene expression profile measured after treatment of drugs or dimethyl sulfoxide (DMSO), and y_i is 1 if

TABLE 1 The five hepatotoxicity mechanisms used in the MDTR. The table shows the mechanisms of hepatotoxicity categorized into five major groups based on literature search, serving as the axis of MDTR. For each mechanisms, it shows the action in the liver and the number of KEGG pathways belonging to the mechanism.

Mechanism	Hepatotoxicity process	Num. of pathways
Oxidative stress	Disruption of essential molecules through production of ROS	6
Immunological response	Immunological response including inflammation induced by drugs or metabolites	3
Altered lipid metabolism	Disruption of normal lipid metabolism and accumulation of lipids leading to tissue damage	13
Mitochondrial dysfunction	Impairment of MT function and subsequent disruption of cellular energy metabolism	2
Bile acids accumulation	Accumulation of bile acids and impaired bile flow in the liver can cause liver injury	2

*Num.: Number, ROS: Reactive oxygen species, MT: Mitochondria.

$\mathbf{x}_i$ is a DMSO-treated sample, and −1 otherwise (for toxic or non-toxic drug-treated samples), the drug-effect boundary is a hypersphere that encloses a majority of the DMSO-treated samples while minimizing distance between the center of the sphere and the closest DMSO-treated samples on the boundary. To address the non-linearity of gene interactions, we employed the RBF kernel in the optimization of the hypersphere using SVDD:

$$\min_{r,b,\alpha} \quad r^2 + \frac{1}{n}\sum_{i=1}^{n}\alpha_i \qquad \text{s.t.} \quad y_i\left(\sum_{j=1}^{n}\alpha_j k\left(\mathbf{x}_j,\mathbf{x}_i\right) + b - r^2\right) \le 1,$$
$$\alpha_i \ge 0, \quad \forall i \tag{1}$$

where r is the radius of the sphere, n is the number of samples, α_i is a Lagrange multiplier, b is a bias term, $k(\mathbf{x}_j,\mathbf{x}_i) = \exp(-\gamma|\mathbf{x}_i - \mathbf{x}_j|^2)$ is the RBF kernel function with width control parameter γ. In this study, γ is empirically set to $1/(d*\sigma)$ where d is the number of genes in $\{\mathbf{x}_i\}$ and σ is the variance of $\{\mathbf{x}_i\}$.

The samples with $\alpha_i > 0$ constitute the support vectors of the drug-effect boundary. Using the support vectors, for a new sample $\mathbf{x}$, the decision function $f^{DE}(\mathbf{x})$ is defined as below.

$$f^{DE}(\mathbf{x}) = \sum_{j=1}^{n}\alpha_j k\left(x_j, x\right) + b - r^2 \tag{2}$$

when $f^{DE}(\mathbf{x}) \le 0$, $\mathbf{x}$ is classified as a sample without drug-effect; otherwise, it is classified as a sample with drug-effect.

Then, we additionally designed a toxic-effect boundary. Instead of DMSO-treated samples, we utilized a target dataset X^{NT} consisting of non-toxic drug-treated samples where $f^{DE}(\mathbf{x}_i^{NT}) > 0$. A test dataset X^T was also constituted using toxic drug-treated samples where $f^{DE}(\mathbf{x}_i^T) > 0$.

Using the X^{NT} dataset and Equations 1, 2, we obtained the toxic-effect boundary and the decision function $f^{TE}(\mathbf{x})$. The dual-boundaries generated by Dual-SVDD are represented by $f^{DE}(\mathbf{x}) = 0$ and $f^{TE}(\mathbf{x}) = 0$, which are used to identify samples with potential drug effects and potential toxic signatures, respectively. We refer to samples in $X^{PT} = \{\mathbf{x}_1^{PT}, \ldots, \mathbf{x}_l^{PT}\}$ as 'potentially toxic (PT)' samples, where $\mathbf{x}_i^{PT} \in X^T$ and $f^{TE}(\mathbf{x}_i^{PT}) > 0$. These PT samples are considered to have a higher likelihood of possessing toxic signatures.

2.1.2 Knowledge-driven view: biological mechanisms related to drug-induced liver injury

Through a comprehensive literature review, we curated commonly discussed biological mechanisms related to hepatotoxicity in existing studies (Andrade et al., 2019; Weaver et al., 2020; Han et al., 2020), and summarized them into five biological mechanisms: *Oxidative stress*, *Immunological response*, *Altered lipid metabolism*, *Mitochondrial dysfunction*, and *Bile acids accumulation* (Table 1).

These biological mechanisms are conceptually associated with hepatotoxicity but their applicability in a computational approach is not known. To address this, we explored biological pathways associated with the mechanisms and utilized the gene sets within those pathways. To identify pathways relevant to these mechanisms, we used the KEGG Pathway Search function, which conducts a keyword search against the KEGG pathway database (Kanehisa, 2002). As the search function performs partial matches on text descriptions or legends for multiple keywords, there is a possibility of false positives in the search results. For example, when "oxidative stress" is searched, the term 'stress' may detect other stress-related pathways. Moreover, even if keywords are included in the description, there may be portions that are far from the main function of the pathway. Thus, we manually curated the search results to ensure their relevance to the mechanism. Further details of the selection process for each mechanism and the selected pathway list are provided in Supplementary Methods section and Supplementary Tables S1-S5.

2.2 Calculation of the degree of hepatotoxicity by a knowledge-guided multi-dimensional ruler

Through the exploration of hepatotoxic signatures from both data-driven and knowledge-driven perspectives, we identified PT samples with a high likelihood of harboring drug-induced hepatotoxic signatures, as well as biological mechanisms associated with hepatotoxicity and corresponding pathways. Leveraging this valuable information, we introduced MDTR, quantifies the degree of hepatotoxicity as dysfunctions of biological mechanisms. The MDTR is represented as a five-dimensional radar chart, with each dimension corresponding to a biological mechanism, calculated through *mechanism-level toxic distances*.

Formally, given a biological mechanism $M = \{p_1, \ldots, p_k\}$ of k pathways, the mechanism-level toxic distance $D_M(\mathbf{x})$ (Equation 3) is defined as a sum of multiple weighted *pathway-level distances* as below:

$$D_M(\mathbf{x}) = \sum_{p \in M} w(p, \mathbf{x}) d_p(\mathbf{x}) \tag{3}$$

where $w(p, \mathbf{x})$ (Equation 5) is a weight of pathway p with respect to $\mathbf{x}$ and $d_p(\mathbf{x})$ (Equation 4) is a pathway-level distance that measures the activity of how the pathway p is dysregulated on $\mathbf{x}$, which is calculated on the non-linear kernel space to learn complex interactions of genes.

Given a pathway $p = \{g_1, \ldots, g_{l_p}\}$ consisting of l_p genes and PT samples X_p^{PT}, the toxicity kernel space $H_p \in \mathbb{R}^d$ is derived from X_p^{PT} using KernelPCA with RBF kernel, implemented via the Python Scikit-learn package. The gamma parameter γ is set to $1/l$, while all other parameters remain at their default settings. To construct the toxicity kernel space H_p, the dimensionality d of H_p is determined by the first $\min(0.1 * l_p, 3)$ principal components. By considering the relationships between transcriptomic samples in the latent space represented by genes within pathways, we can alleviate the high dimensionality issue mentioned in challenge #1. After the construction of toxicity kernel space, PT samples X_p^{PT} and non-PT samples X_p^{non-PT} are mapped into the toxicity kernel space H_p with sample distribution $Q_p \in \mathbb{R}^d$. Then, a pathway-level distance $d_p(\mathbf{x})$ is calculated as the Mahalanobis distance in the toxicity kernel space of the mapped samples:

$$d_p(\mathbf{x}) = \sqrt{\left(\mathbf{z} - \boldsymbol{\mu}_p\right)^T S_p^{-1} \left(\mathbf{z} - \boldsymbol{\mu}_p\right)} \tag{4}$$

where $\mathbf{z}$ represents the latent embedding of the sample $\mathbf{x}$ mapped into the kernel space H_p. $\boldsymbol{\mu}_p$ and S_p are the mean vector and the positive-definite covariance matrix derived from Q_p, respectively. In other words, once the toxicity kernel space is constructed using PT samples, all samples, including both PT and non-PT samples, are mapped into this space. The Mahalanobis distance is then calculated for each sample in this toxicity kernel space. After calculating $d_p(\mathbf{x})$ for all samples, min-max normalization is performed to adjust the scale.

The weight $w(p, \mathbf{x})$ represents the significance of dysregulation of the pathway p in the sample x against the pathway-level distances of X_p^{non-PT}. Formally, as our observation, the distribution of $\{d_p(\mathbf{x}) | \mathbf{x} \in X_p^{non-PT}\}$ follows F-distribution. Then, the weight $w(p, \mathbf{x})$ is calculated as:

$$\begin{aligned} w(p, \mathbf{x}) &= -\log\left(F\left(d_p; d_1, d_2\right)\right) \\ &= -\log\left(I_{d_1 \cdot d_p / (d_1 \cdot d_p + d_2)}\left(\frac{d_1}{2}, \frac{d_2}{2}\right)\right) \end{aligned} \tag{5}$$

where d_p denotes $d_p(\mathbf{x})$. d_1 and d_2 are degrees of freedom that measured from $\{d_p(\mathbf{x}) | \mathbf{x} \in X_p^{non-PT}\}$. I is the regularized incomplete beta function.

2.3 Website for measuring the degree of toxicity through MDTR

The website (http://biohealth.snu.ac.kr/software/MDTR) is designed to measure the degree of liver toxicity of drugs by analyzing their gene expression data. The website uses MDTR to show the potential liver toxicity of drugs across the five mechanisms of hepatotoxicity.

Additionally, the website leverages the LINCS dataset to access gene expression data from 514 drugs across 70 different cell lines, specifically utilizing L1000 Level 5 data, which are generated by calculating z-scores relative to the controls. This provides a comprehensive assessment of potential hepatotoxicity at the transcriptomic level. The website is implemented using the Django 3.2 framework and Bootstrap 4.6 for the front-end. The interactive radar chart, representing the indicators of liver toxicity, is generated using Chart. js. Each axis of the radar chart represents an indicator of liver toxicity. The website is tested for compatibility and functionality on various web browsers, including Chrome, Microsoft Edge, Firefox, and Safari.

2.4 Preparation of drug hepatotoxicity information and drug-induced transcriptome data

Two databases, Drug Induced Liver Injury Rank (DILIrank, Chen et al. (2016)) and LiverTox (Hoofnagle, 2013), were used to gather information on drug-induced hepatotoxicity. DILIrank categorizes drugs into four classes based on their potential for causing hepatotoxicity, while LiverTox assigns likelihood scores indicating the extent of reported liver injury cases. For this study, drugs categorized as most-DILI concern in DILIrank, and A and B in LiverTox were considered hepatotoxic. Drugs categorized as no-DILI concern in DILIrank, and D and E in LiverTox were considered non-hepatotoxic. A total of 220 hepatotoxic drugs and 402 non-hepatotoxic drugs were used in the analysis.

Drug-treated samples from the LINCS database (accession number GSE92742) were obtained for investigating drug-induced hepatotoxicity at the transcriptomic level. For the gene expression matrix of these samples, we used Level 5 data, which are generated by calculating z-scores relative to the controls. Categorization of these samples into DMSO, non-toxic, and toxic groups was guided by annotations from DILIrank and LiverTox. A total of 20,529 drug-treated samples (6,405 toxic, 11,333 non-toxic and 2,791 DMSO-treated samples) were collected. From the LINCS dataset, among the 10,174 LINCS best inference genes, 4,693 genes related to drug-induced liver injury were selected based on the Comparative Toxicogenomics Database (CTD, Davis et al. (2021)) and enrichment analysis of Gene Ontology (GO) terms. Further description and discussion of drug hepatotoxicity information, transcriptome data collection, and the selection of gene sets are provided in the Supplementary Methods section.

3 Results and discussion

3.1 MDTR: a knowledge-guided representation for liver toxicity at transcriptomic level

Among the 1,896 drug-treated transcriptome samples, Dual-SVDD selected the most perturbed samples, the extreme point of MDTR. As a result, 64 potentially toxic (PT) samples were identified (Supplementary Table S6). We showed the utility of Dual-SVDD through its ability to distinguish toxic samples and the robustness of

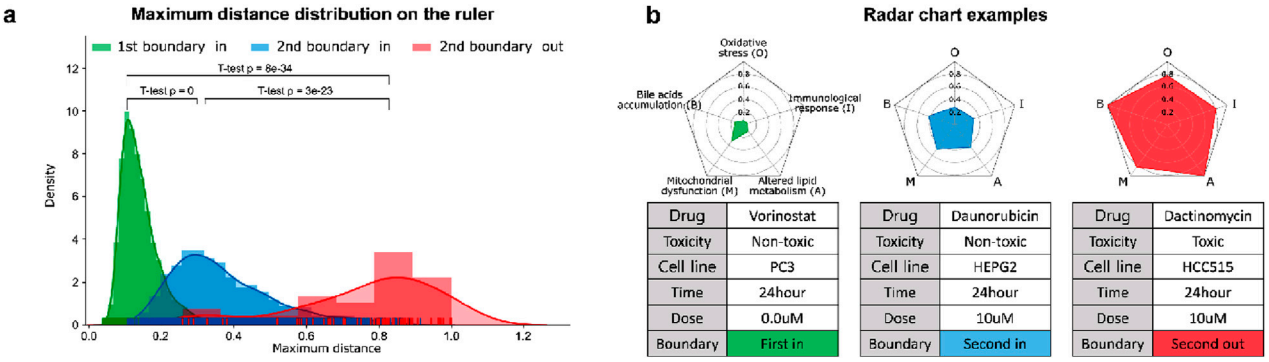

FIGURE 2
The results of MDTR. **(A)** Maximum distance distribution on the ruler. The density distribution shows the maximum values on the MDTR of the samples divided according to the Dual-SVDD boundary. **(B)** Examples of multi-dimensional rulers using radar charts for drug-treated transcriptome samples.

dual-boundaries (Supplementary Figure S2). In addition, to evaluate the reliability of the proposed measurement, we conducted self-validation by partitioning the total dataset and performing cross-check analyses (Supplementary Figure S3). As a result, our measurement method showed consistent distances regardless of the configuration of the data.

Based on the PT samples and the curated biological mechanisms, MDTR measures the degree of DILI. Figure 2A shows a distribution of maximum distances, representing the density distribution of maximum values on the MDTR of the samples. Notably, significant statistical differences were observed between the sample groups identified by Dual-SVDD. This indicates that the MDTR distance measured from PT samples meaningfully reflects the perturbation of gene expression affected by drug treatments. Among the drug-induced transcriptome data, Figure 2B illustrates examples of radar charts from MDTR. The red-colored radar chart (Figure 2B, right), representing the treated compound labels as structural toxicity as 'Toxic', shows greater distances in comparison to the other two examples. Interestingly, even when the chemical structural information is identical and labeled as 'Non-toxic', the MDTR results of the two drug-induced transcriptome samples (green vs. blue-colored) show obvious differences. This indicates the importance of analyzing drug hepatotoxicity at the transcriptome level.

We further investigated the capability of MDTR in identifying samples treated with hepatotoxic drugs. We screened top-rankded drugs for liver toxicity, labeled as 'Most-DILI' in DILIrank or assigned category 'A' in LiverTox, as well as drugs with an absence of reported toxicity, labeled as 'No-DILI' in DILIrank or category 'E' in LiverTox. Then, we used samples treated with the selected drugs in liver cell lines, including HEPG2, HUH7, and PHH. This resulted in the identification of 10 toxic and 43 non-toxic samples, respectively. When comparing the distances between the two sample groups, we observed larger distances for toxic samples across all mechanisms, with statistically significant differences found in all mechanisms except for Bile acids accumulation (Figure 3). Interestingly, similar results were observed when the experiment was conducted not only in liver cell lines but also in the entire cell lines belonging to the data used (Supplementary Figure S4). Therefore, we showed the effectiveness of the multi-dimensional ruler in stratifying toxic and non-toxic samples at the transcriptomic level.

3.2 Comparison of dose-dependent liver toxicity

Our research goal is not only to measure the five-dimensional toxic mechanisms in drug-treated transcriptomic samples, but also to facilitate the understanding of toxicity mechanisms using the multi-dimensional ruler in the form of the radar chart. We explored the drug treated environment, especially the sample distance according to the drug dose. For dose-dependence analysis, a total of 198 combinations of 33 drugs with five or more drug dose points in fixed cell line and time point were used. Under the assumption that toxicity increases with increasing drug dose (Schenker et al., 1999; Hoofnagle and Björnsson, 2019), the correlation between dose and distance was calculated, and then evaluated that higher correlation resulted in better results. We compared MDTR distance with three methods: (1) Mathematical distances (Cosine, Euclidean, and Mahalanobis) calculated from the expression values of all genes in LINCS, (2) Transcriptomic Signature Distance (TSD, Manatakis et al. (2020)), and (3) Pathway Activity Score Learning (PASL, Karagiannaki et al. (2023)) with mathematical distances similar to (1) (details in Supplementary Methods).

As shown in Table 2, MDTR outperformed the other distance methods, achieving 70% positive ratio. Additionally, MDTR consistently showed the highest positive correlation ratio even when the number of drug dose points was three or four (Supplementary Table S7). Notably, the Mahalanobis distance yielded better results than Cosine and Euclidean distances. In addition, distances calculated based on biological information (MDTR and PASL) exhibited better performances compared to using the entire genes without the prior knowledge.

The main advantages of MDTR are that it not only provides distances indicating the degree of toxicity depending on the drug-treated environment but also allows interpretation of the mechanisms of liver toxicity. Among drugs that show a positive correlation with MDTR and dose, we conducted case studies for the

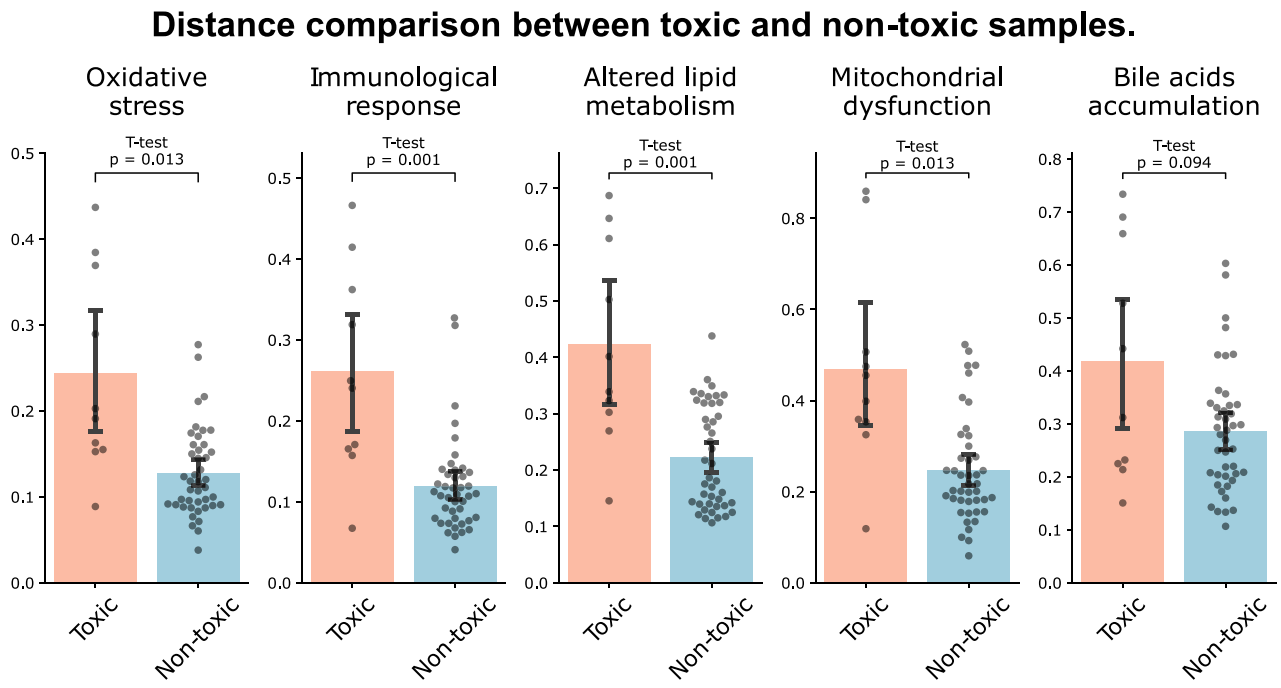

FIGURE 3
Distance comparison between toxic and non-toxic samples. The bar plot shows the distances between samples of toxic drugs (red) and samples of drugs with unknown toxicity (blue) in liver cell lines.

TABLE 2 Performance comparison for dose-distance relationship. The table shows the ratio (in numbers) of samples exhibiting a positive correlation between dose and distance among the 198 samples for MDTR and three comparison methods. Bold values indicate the best results.

Method	Positive ratio (Num. of positive samples)
MDTR	**0.70 (139)**
Raw + Cosine	0.62 (123)
Raw + Euclidean	0.62 (122)
Raw + Maha	0.64 (127)
TSD	0.64 (127)
PASL + Cosine	0.53 (105)
PASL + Euclidean	0.61 (121)
PASL + Maha	0.67 (133)

*Num.: Number, Maha.: Mahalanobis.

following three drugs: Doxorubicin, Mitoxantrone, and Rosiglitazone.

Case 1: We investigated Doxorubicin, a chemotherapy medication widely used for the cancer treatments, including breast and bladder cancer, while also known for its hepatotoxicity (Prasanna et al., 2020). In the MCF7 cell line and at the 6-h time point, Doxorubicin exhibited dose-dependent toxicity signature (Figure 4, $\rho = 0.93$, $p =$ 1.1e-6). These positive correlations were observed in 9 out of the 10 Doxorubicin-treated combinations (Supplementary Table S8). In particular, the radar chart revealed distinct changes across different dose points in two mechanisms: Mitochondrial dysfunction and Bile acids accumulation. These findings support the understanding of the potential association between bile acid metabolism and Doxorubicin sensitivity (Chen et al., 2017), as well as the preferential accumulation of Doxorubicin in the mitochondria and nucleus (Wallace et al., 2020).

Case 2: We investigated the potential toxicity of Mitoxantrone, a cytotoxic agent and anthracenedione analogue of Doxorubicin (Fox, 2004), which exhibits similar metabolic pathways (Paciucci and Sklarin, 1986; Llesuy and Arnaiz, 1990; Rossato et al., 2014a). Mitoxantrone, despite being classified with a likelihood score of D in the LiverTox database, showed a positive correlation between distance and dose across all combinations of MCF7, PC3, and A549 cell lines and 6 and 24 h time points, similar to Doxorubicin (Supplementary Table S9). For example, Figure 4B illustrates the dose-dependent changes in distance for Mitoxantrone in the PC3 cell line at the 24-hour time point ($\rho = 0.87$, $p = 0.012$).

In particular, the toxicity of the sample showed a non-monotonic tendency that decreased in the early stage of dose escalation (from 0.1 to 0.5μM) and then increased again after the 1uM dose (Tang et al., 2023). These results showed that MDTR is capable to capture the pattern of drugs showing such hormesis. Overall dose-distance relationship suggest that Mitoxantrone not only induces functional impairments observed with Doxorubicin, such as bile acids accumulation and mitochondrial dysfunction, but also affects lipid metabolism (Kharasch and Novak, 1985; Rossato et al., 2014b).

Furthermore, we performed the MDTR on an unseen drug, Rosiglitazone, a drug that has a lack of medical reports concerning

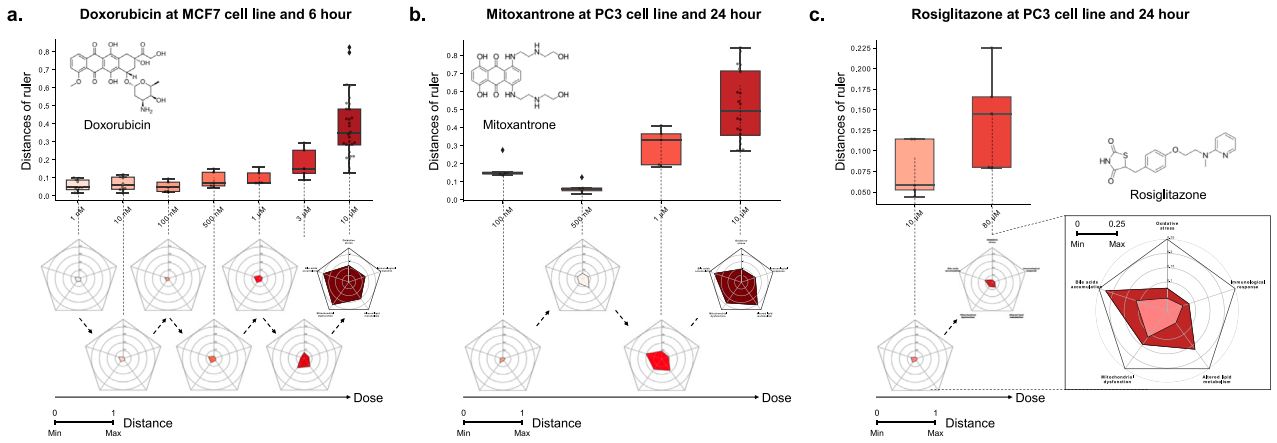

FIGURE 4
The relationship between the distance on the multi-dimensional ruler and the dose. The box plots and radar charts show the change in distance based on the dose of drug treatment under fixed cell line and time point. **(A)** Doxorubicin at MCF7 cell line and 6-hour, **(B)** Mitoxantrone at PC3 cell line and 24-hour, and **(C)** Rosiglitazone at PC3 cell line and 24-hour. Except the zoomed radar chart, all radar charts exhibit a scale ranging from a minimum of 0 to a maximum of 1.

liver toxicity and was not utilized in the generation of dual-boundaries or the calculation of the ruler.

Case 3: We investigated the liver toxicity of Rosiglitazone, a thiazolidinedione drug used for the treatment of type 2 diabetes treatment but discontinued in many countries due to cardiovascular risks (Nissen and Wolski, 2007). While its counterpart Troglitazone has been withdrawn from the market due to severe hepatotoxicity (Lloyd et al., 2002; Kaplowitz, 2005), limited research exists on the hepatotoxic effects of Rosiglitazone. To address this gap, we employed the multi-dimensional ruler to evaluate its toxicity. In the PC3 cell line at the 24-h time point, Figure 4C demonstrates an increase in toxic mechanisms corresponding to higher drug doses. Specifically, significant variations were observed in Bile acids accumulation and Lipid metabolism in response to varying doses. These findings align with known issues associated with Rosiglitazone, such as disturbances in fatty acid and triglyceride metabolism (Gershell, 2005; Tan et al., 2005; Watkins et al., 2002), as well as intrahepatic cholestasis (Zhang et al., 2020).

Through comparative and case study results, we show that MDTR is an interpretable method that can capture both known and potentially mechanisms of toxicity, while exhibiting a dose-dependent distance to hepatotoxicity.

3.3 MoA interpretation: Oxidative stress as a case study

Oxidative stress, one of the axis of MDTR, arises from an imbalance between oxygen-reactive species (ROS) generation and accumulation (Figure 5A, Jaeschke et al. (2002), Jaeschke et al. (2012)). The accumulation of ROS, triggered by factors such as AMP-activated protein kinase (AMPK) activation (Kang et al., 2016; Steinberg and Hardie, 2022) and an imbalance in glutathione (GSH) and glutathione disulfide (GSSG) levels (DeLeve and Kaplowitz, 1991; Yuan and Kaplowitz, 2009), promotes inflammation, disrupts cellular energy regulation, depletes antioxidants, impairs protein handling, and induces hepatocellular apoptosis, ultimately leading to liver damage.

To explore the biological implications of pathway-level distances within the mechanism, we focused on the Chemical carcinogenesis - ROS pathway (hsa05208, hereafter referred to as the ROS pathway), which is one of the six pathways chosen for the oxidative stress mechanism. We divided the samples evenly into four groups (Low, Middle1, Middle2, and High) based on each pathway distance. Then, we performed co-expression network analyses based on the expression values of samples within each group (Figure 5B). As a result, larger distances correspond to large co-expression network sizes, indicating that increased distance is associated with more interactions between genes and, simultaneously, a higher degree of gene dysregulation. For example, during the transition from the Low group to the Middle1 group, downregulation of MAPK8 (also known as JNK) may hinder the expression of the AP-1 transcription factor, potentially impacting the MAPK signaling pathway (Turner et al., 2014). Furthermore, as the network progressed from the Middle1 to Middle2 and High groups, upregulation of genes associated with PI3K signaling (e.g., PIK3CA or PIK3CD) and NADPH oxidase (e.g., NOX4) was observed, indicating ROS production (Koundouros and Poulogiannis, 2018). These findings validate the efficacy of the proposed pathway-level distance in capturing biological activity. Similar results were observed for the remaining pathways (Supplementary Figures S5-S9).

We next calculated the mechanism-level distance of oxidative stress as a weighted sum of the six related pathways, including the ROS pathway. To explore the association between oxidative stress signaling and the mechanism-level distance of samples, we performed GO enrichment analysis using commonly perturbed genes from the respective group. Figure 5C and Supplementary Figure S10 illustrate that as the distance increases, the GO terms related to oxidative stress, such as response to endoplasmic reticulum stress and cellular response to oxidative stress, exhibit

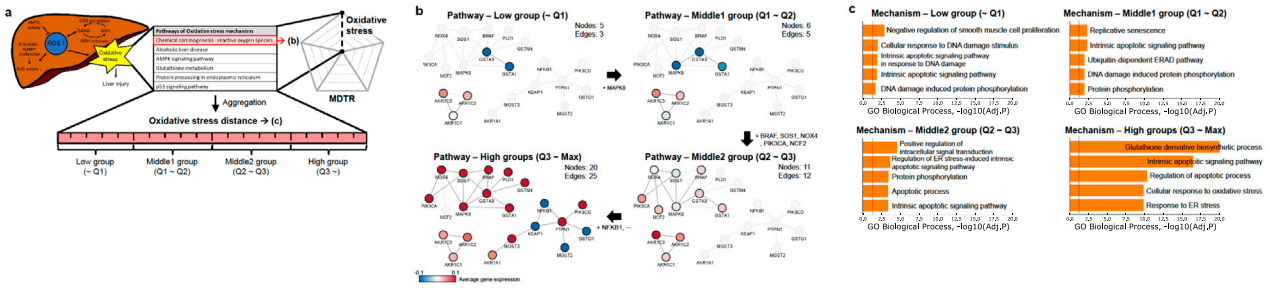

FIGURE 5
MoA of Oxidative stress **(A)** Conceptual illustration of liver injury caused by oxidative stress mechanism. **(B)** Co-expression network according to ROS pathway distance group. **(C)** GO biological process enrichment analysis according to oxidative stress mechanism distance group. The *x*-axis is represents -log (Adjusted *p*-value) and the dotted line represents -log (0.05).

more significant and abundant enrichment. These GO enrichment analysis results were consistently observed across all the mechanisms (Supplementary Figures S11-S14). Thus, our findings demonstrate that both pathway- and mechanism-level distance effectively reflect the activity level of the corresponding mechanism as the distance increases.

3.4 A web service for MDTR

Our model is implemented as a freely available website (http://biohealth.snu.ac.kr/software/MDTR). The website allows for our MDTR to be utilized from two perspectives (Supplementary Figure S15): (1) detection of hepatotoxicity from the user's drug-induced transcriptome data, (2) investigation of hepatotoxicity through drug-induced transcriptome data in the LINCS database by selecting any combinations of drugs, tissues, and cell lines.

4 Conclusion

In this study, we introduced MDTR that quantifies the degree of liver toxicity in terms of five hepatotoxicity mechanisms by analyzing transcriptome data. An important contribution of this study is that it sought to translate transcriptome data to toxicity-related mechanisms between transcriptome data and DILI mechanisms. To understand the DILI mechanisms at the transcriptomic level, MDTR integrated the KEGG pathways, mapped the transcriptome data to the pathway-specific kernel space to measure the distance, and aggregated the pathway-level distance to measure the mechanism-level distance. MDTR explores complex genetic relationships in a non-linear RBF kernel space constructed from biological pathways, while at the same time having the explanatory power of DILI through a five-dimensional radar chart where integrated pathways are represented on one axis.

We showed that MDTR represents dose-dependent liver toxicity compared to existing models that measure distance or similarity of transcriptome data. In addition, through the case studies, we showed the ability of MDTR to interpret dose-dependent DILI not only for drugs with known liver toxicity but also for drugs with no reported liver toxicity. Furthermore, MDTR measures distances for different drug-treated environments, especially for different treatment doses, thereby capturing not only monotonic drug responses but also non-monotonic phenomena such as hormesis. Lastly, we provided a user-friendly and freely accessible website, enabling users to easily measure DILI in drug-induced transcriptome data. Therefore, MDTR serves as both an interpretable and computational method, addressing the limitations of existing studies that relied only on experimental and literature information to measure potential drug toxicity across various treatment environments.

While we have expanded the gene set based on the functional analysis of genes curated from the CTD, future studies may further enhance this gene set by including genes with correlated expression levels within the dataset. Moreover, although the current study involved a manual curation process to identify liver toxicity mechanisms and their associated biological pathways from the literature, we plan to conduct a more comprehensive analysis of liver toxicity by utilizing additional external resources, such as Ingenuity Pathway Analysis (IPA).

Data availability statement

The original contributions presented in the study are included in the article/Supplementary Material, further inquiries can be directed to the corresponding author.

Author contributions

IS: Conceptualization, Data curation, Formal analysis, Investigation, Methodology, Software, Validation, Visualization, Writing–original draft, Writing–review and editing. SaL: Conceptualization, Formal analysis, Investigation, Methodology, Writing–original draft, Writing–review and editing. DB: Conceptualization, Formal analysis, Investigation, Writing–original draft, Writing–review and editing. JY: Investigation, Software, Visualization, Writing–original draft, Writing–review and editing. SuL: Conceptualization, Funding acquisition, Resources, Writing–original draft, Writing–review and editing. SK: Conceptualization, Funding acquisition, Resources, Supervision, Writing–original draft, Writing–review and editing.

Funding

The author(s) declare that financial support was received for the research, authorship, and/or publication of this article. This research was supported by a grant (No. DY0002259501) from Ministry of food and Drug Safety, the Bio and Medical Technology Development Program of the National Research Foundation (NRF) funded by the Ministry of Science and ICT (NRF-2022M3E5F3085677), the National Research Foundation of Korea (NRF) grant funded by the Korea government (MSIT) (RS-2022-NR067933 and No. NRF-2023R1A2C2006953), Institute of Information and communications Technology Planning and Evaluation (IITP) grant funded by the Korea government (MSIT) [NO. 2021-0-01343, Artificial Intelligence Graduate School Program (Seoul National University)], the ICT at Seoul National University, and AIGENDRUG Co. Ltd.

Conflict of interest

Authors DB, SuL, and SK were employed by AIGENDRUG Co., Ltd.

The remaining authors declare that the research was conducted in the absence of any commercial or financial relationships that could be construed as a potential conflict of interest.

Publisher's note

All claims expressed in this article are solely those of the authors and do not necessarily represent those of their affiliated organizations, or those of the publisher, the editors and the reviewers. Any product that may be evaluated in this article, or claim that may be made by its manufacturer, is not guaranteed or endorsed by the publisher.

Supplementary material

The Supplementary Material for this article can be found online at: https://www.frontiersin.org/articles/10.3389/fphar.2024.1398370/full#supplementary-material

References

Andersen, M. E., and Krewski, D. (2009). Toxicity testing in the 21st century: bringing the vision to life. *Toxicol. Sci.* 107, 324–330. doi:10.1093/toxsci/kfn255

Andrade, R. J., Chalasani, N., Björnsson, E. S., Suzuki, A., Kullak-Ublick, G. A., Watkins, P. B., et al. (2019). Drug-induced liver injury. *Nat. Rev. Dis. Prim.* 5, 58–22. doi:10.1038/s41572-019-0105-0

Barretina, J., Caponigro, G., Stransky, N., Venkatesan, K., Margolin, A. A., Kim, S., et al. (2012). The cancer cell line encyclopedia enables predictive modelling of anticancer drug sensitivity. *Nature* 483, 603–607. doi:10.1038/nature11003

Bracken, M. B. (2009). Why animal studies are often poor predictors of human reactions to exposure. *J. R. Soc. Med.* 102, 120–122. doi:10.1258/jrsm.2008.08k033

Chapman, K. L., Holzgrefe, H., Black, L. E., Brown, M., Chellman, G., Copeman, C., et al. (2013). Pharmaceutical toxicology: designing studies to reduce animal use, while maximizing human translation. *Regul. Toxicol. Pharmacol.* 66, 88–103. doi:10.1016/j.yrtph.2013.03.001

Chen, M., Suzuki, A., Thakkar, S., Yu, K., Hu, C., and Tong, W. (2016). Dilirank: the largest reference drug list ranked by the risk for developing drug-induced liver injury in humans. *Drug Discov. Today* 21, 648–653. doi:10.1016/j.drudis.2016.02.015

Chen, P., Li, D., Chen, Y., Sun, J., Fu, K., Guan, L., et al. (2017). p53-mediated regulation of bile acid disposition attenuates cholic acid-induced cholestasis in mice. *Br. J. Pharmacol.* 174, 4345–4361. doi:10.1111/bph.14035

Chovatiya, R., and Medzhitov, R. (2014). Stress, inflammation, and defense of homeostasis. *Mol. Cell* 54, 281–288. doi:10.1016/j.molcel.2014.03.030

Davis, A. P., Grondin, C. J., Johnson, R. J., Sciaky, D., Wiegers, J., Wiegers, T. C., et al. (2021). Comparative toxicogenomics database (ctd): update 2021. *Nucleic acids Res.* 49, D1138–D1143. doi:10.1093/nar/gkaa891

DeLeve, L. D., and Kaplowitz, N. (1991). Glutathione metabolism and its role in hepatotoxicity. *Pharmacol. and Ther.* 52, 287–305. doi:10.1016/0163-7258(91)90029-l

Dix, D. J., Houck, K. A., Martin, M. T., Richard, A. M., Setzer, R. W., and Kavlock, R. J. (2007). The toxcast program for prioritizing toxicity testing of environmental chemicals. *Toxicol. Sci.* 95, 5–12. doi:10.1093/toxsci/kfl103

Fox, E. J. (2004). Mechanism of action of mitoxantrone. *Neurology* 63, S15–S18. doi:10.1212/wnl.63.12_suppl_6.s15

Garnett, M. J., Edelman, E. J., Heidorn, S. J., Greenman, C. D., Dastur, A., Lau, K. W., et al. (2012). Systematic identification of genomic markers of drug sensitivity in cancer cells. *Nature* 483, 570–575. doi:10.1038/nature11005

Gershell, L. (2005). Type 2 diabetes market. *Nat. Rev. Drug Discov.* 4, 367–368. doi:10.1038/nrd1723

Han, H., Desert, R., Das, S., Song, Z., Athavale, D., Ge, X., et al. (2020). Danger signals in liver injury and restoration of homeostasis. *J. hepatology* 73, 933–951. doi:10.1016/j.jhep.2020.04.033

Hoofnagle, J. H. (2013). "Livertox: a website on drug-induced liver injury," in *Drug-induced liver disease* (Elsevier), 725–732.

Hoofnagle, J. H., and Björnsson, E. S. (2019). Drug-induced liver injury—types and phenotypes. *N. Engl. J. Med.* 381, 264–273. doi:10.1056/NEJMra1816149

Jaeschke, H., Gores, G. J., Cederbaum, A. I., Hinson, J. A., Pessayre, D., and Lemasters, J. J. (2002). Mechanisms of hepatotoxicity. *Toxicol. Sci.* 65, 166–176. doi:10.1093/toxsci/65.2.166

Jaeschke, H., McGill, M. R., and Ramachandran, A. (2012). Oxidant stress, mitochondria, and cell death mechanisms in drug-induced liver injury: lessons learned from acetaminophen hepatotoxicity. *Drug metab. Rev.* 44, 88–106. doi:10.3109/03602532.2011.602688

Kanehisa, M. (2002). "The kegg database," in *In Silico'Simulation of biological processes: novartis foundation symposium*. Editors G. R. Bock and J. A. Goode (Wiley Online Library), 91–103.

Kang, S. W. S., Haydar, G., Taniane, C., Farrell, G., Arias, I. M., Lippincott-Schwartz, J., et al. (2016). Ampk activation prevents and reverses drug-induced mitochondrial and hepatocyte injury by promoting mitochondrial fusion and function. *PloS one* 11, e0165638. doi:10.1371/journal.pone.0165638

Kaplowitz, N. (2004). Drug-induced liver injury. *Clin. Infect. Dis.* 38, S44–S48. doi:10.1086/381446

Kaplowitz, N. (2005). Idiosyncratic drug hepatotoxicity. *Nat. Rev. Drug Discov.* 4, 489–499. doi:10.1038/nrd1750

Karagiannaki, I., Gourlia, K., Lagani, V., Pantazis, Y., and Tsamardinos, I. (2023). Learning biologically-interpretable latent representations for gene expression data: pathway activity score learning algorithm. *Mach. Learn.* 112, 4257–4287. doi:10.1007/s10994-022-06158-z

Kharasch, E. D., and Novak, R. (1985). Mitoxantrone and ametantrone inhibit hydroperoxide-dependent initiation and propagation reactions in fatty acid peroxidation. *J. Biol. Chem.* 260, 10645–10652. doi:10.1016/s0021-9258(19)85133-5

Koundouros, N., and Poulogiannis, G. (2018). Phosphoinositide 3-kinase/akt signaling and redox metabolism in cancer. *Front. Oncol.* 8, 160. doi:10.3389/fonc.2018.00160

Krewski, D., Acosta, D., Jr, Andersen, M., Anderson, H., Bailar, J. C., III, Boekelheide, K., et al. (2010). Toxicity testing in the 21st century: a vision and a strategy. *J. Toxicol. Environ. Health, Part B* 13, 51–138. doi:10.1080/10937404.2010.483176

Llesuy, S. F., and Arnaiz, S. L. (1990). Hepatotoxicity of mitoxantrone and doxorubicin. *Toxicology* 63, 187–198. doi:10.1016/0300-483x(90)90042-f

Lloyd, S., Hayden, M. J., Sakai, Y., Fackett, A., Silber, P. M., Hewitt, N. J., et al. (2002). Differential *in vitro* hepatotoxicity of troglitazone and rosiglitazone among cryopreserved human hepatocytes from 37 donors. *Chemico-biological Interact.* 142, 57–71. doi:10.1016/s0009-2797(02)00054-6

Manatakis, D. V., VanDevender, A., and Manolakos, E. S. (2020). An information-theoretic approach for measuring the distance of organ tissue samples using their transcriptomic signatures. *Bioinformatics* 36, 5194–5204. doi:10.1093/bioinformatics/btaa654

Mattson, M. P. (2008). Hormesis defined. *Ageing Res. Rev.* 7, 1–7. doi:10.1016/j.arr.2007.08.007

Niepel, M., Hafner, M., Duan, Q., Wang, Z., Paull, E. O., Chung, M., et al. (2017). Common and cell-type specific responses to anti-cancer drugs revealed by high throughput transcript profiling. *Nat. Commun.* 8, 1186. doi:10.1038/s41467-017-01383-w

Nissen, S. E., and Wolski, K. (2007). Effect of rosiglitazone on the risk of myocardial infarction and death from cardiovascular causes. *N. Engl. J. Med.* 356, 2457–2471. doi:10.1056/NEJMoa072761

Paciucci, P. A., and Sklarin, N. T. (1986). Mitoxantrone and hepatic toxicity. *Ann. Intern. Med.* 105, 805–806. doi:10.7326/0003-4819-105-5-805_3

Prasanna, P. L., Renu, K., and Gopalakrishnan, A. V. (2020). New molecular and biochemical insights of doxorubicin-induced hepatotoxicity. *Life Sci.* 250, 117599. doi:10.1016/j.lfs.2020.117599

Rossato, L. G., Costa, V. M., Dallegrave, E., Arbo, M., Dinis-Oliveira, R. J., Santos-Silva, A., et al. (2014a). Cumulative mitoxantrone-induced haematological and hepatic adverse effects in a subchronic *in vivo* study. *Basic and Clin. Pharmacol. and Toxicol.* 114, 254–262. doi:10.1111/bcpt.12143

Rossato, L. G., Costa, V. M., Dallegrave, E., Arbo, M., Silva, R., Ferreira, R., et al. (2014b). Mitochondrial cumulative damage induced by mitoxantrone: late onset cardiac energetic impairment. *Cardiovasc. Toxicol.* 14, 30–40. doi:10.1007/s12012-013-9230-2

Schenker, S., Martin, R. R., and Hoyumpa, A. M. (1999). Antecedent liver disease and drug toxicity. *J. hepatology* 31, 1088–1097. doi:10.1016/S0168-8278(99)80325-0

Steinberg, G. R., and Hardie, D. G. (2022). New insights into activation and function of the ampk. *Nat. Rev. Mol. Cell Biol.* 24, 255–272. doi:10.1038/s41580-022-00547-x

Subramanian, A., Narayan, R., Corsello, S. M., Peck, D. D., Natoli, T. E., Lu, X., et al. (2017). A next generation connectivity map: L1000 platform and the first 1,000,000 profiles. *Cell* 171, 1437–1452. doi:10.1016/j.cell.2017.10.049

Szalai, B., Subramanian, V., Holland, C. H., Alföldi, R., Puskás, L. G., and Saez-Rodriguez, J. (2019). Signatures of cell death and proliferation in perturbation transcriptomics data—from confounding factor to effective prediction. *Nucleic Acids Res.* 47, 10010–10026. doi:10.1093/nar/gkz805

Tan, G., Fielding, B., Currie, J., Humphreys, S., Desage, M., Frayn, K., et al. (2005). The effects of rosiglitazone on fatty acid and triglyceride metabolism in type 2 diabetes. *Diabetologia* 48, 83–95. doi:10.1007/s00125-004-1619-9

Tang, S., Li, S., Tang, B., Wang, X., Xiao, Y., and Cheke, R. A. (2023). Hormetic and synergistic effects of cancer treatments revealed by modelling combinations of radio-or chemotherapy with immunotherapy. *BMC cancer* 23, 1040. doi:10.1186/s12885-023-11542-6

Tax, D. M., and Duin, R. P. (2004). Support vector data description. *Mach. Learn.* 54, 45–66. doi:10.1023/b:mach.0000008084.60811.49

Turner, M. D., Nedjai, B., Hurst, T., and Pennington, D. J. (2014). Cytokines and chemokines: at the crossroads of cell signalling and inflammatory disease. *Biochimica Biophysica Acta (BBA)-Molecular Cell Res.* 1843, 2563–2582. doi:10.1016/j.bbamcr.2014.05.014

Van Norman, G. A. (2019). Limitations of animal studies for predicting toxicity in clinical trials: is it time to rethink our current approach? *JACC Basic Transl. Sci.* 4, 845–854. doi:10.1016/j.jacbts.2019.10.008

Wallace, K. B., Sardão, V. A., and Oliveira, P. J. (2020). Mitochondrial determinants of doxorubicin-induced cardiomyopathy. *Circulation Res.* 126, 926–941. doi:10.1161/CIRCRESAHA.119.314681

Watkins, S. M., Reifsnyder, P. R., Pan, H. J., German, J. B., and Leiter, E. H. (2002). Lipid metabolome-wide effects of the PPARgamma agonist rosiglitazone. *J. lipid Res.* 43, 1809–1817. doi:10.1194/jlr.m200169-jlr200

Weaver, R. J., Blomme, E. A., Chadwick, A. E., Copple, I. M., Gerets, H. H., Goldring, C. E., et al. (2020). Managing the challenge of drug-induced liver injury: a roadmap for the development and deployment of preclinical predictive models. *Nat. Rev. Drug Discov.* 19, 131–148. doi:10.1038/s41573-019-0048-x

Wilke, R. A., Lin, D. W., Roden, D. M., Watkins, P. B., Flockhart, D., Zineh, I., et al. (2007). Identifying genetic risk factors for serious adverse drug reactions: current progress and challenges. *Nat. Rev. Drug Discov.* 6, 904–916. doi:10.1038/nrd2423

Yuan, L., and Kaplowitz, N. (2009). Glutathione in liver diseases and hepatotoxicity. *Mol. aspects Med.* 30, 29–41. doi:10.1016/j.mam.2008.08.003

Zhang, S., Yu, M., Guo, F., Yang, X., Chen, Y., Ma, C., et al. (2020). Rosiglitazone alleviates intrahepatic cholestasis induced by α-naphthylisothiocyanate in mice: the role of circulating 15-deoxy-Δ12, 14-pgj2 and nogo. *Br. J. Pharmacol.* 177, 1041–1060. doi:10.1111/bph.14886

frontiers | Frontiers in Pharmacology

TYPE Original Research
PUBLISHED 06 February 2025
DOI 10.3389/fphar.2025.1415701

OPEN ACCESS

EDITED BY
Huaqiang Zhai,
Beijing University of Chinese Medicine, China

REVIEWED BY
Simran D. S. Maggo,
Shenandoah University, United States
Bilgen Basgut,
Baskent University, Türkiye

*CORRESPONDENCE
Saiwei Wu,
20719022@zju.edu.cn

RECEIVED 11 April 2024
ACCEPTED 17 January 2025
PUBLISHED 06 February 2025

CITATION
Li Q, Shan W and Wu S (2025) Safety assessment of rosuvastatin-fenofibrate combination in the treatment of hyperlipidemia based on FDA's adverse event reporting system database. *Front. Pharmacol.* 16:1415701. doi: 10.3389/fphar.2025.1415701

Safety assessment of rosuvastatin-fenofibrate combination in the treatment of hyperlipidemia based on FDA's adverse event reporting system database

Qun Li[1], Wenya Shan[2] and Saiwei Wu[1]*

[1]Department of Pharmacy, The Fourth Affiliated Hospital of School of Medicine, International School of Medicine, International Institutes of Medicine, Zhejiang University, Yiwu, Zhejiang, China, [2]Department of Pharmacy, The First Affiliated Hospital of School of Medicine, Zhejiang University, Hangzhou, Zhejiang, China

Background: With the improvement of living standards, an increasing number of patients are presenting with mixed hyperlipidemia. In addition to cholesterol reduction, it is imperative to lower triglyceride levels. The combination of statin and fibrate for reducing lipid levels has commonly been applied in clinical therapy. However, the combination of drugs also increases the risk of adverse events (AEs). In this study, we analyzed the safety signals of rosuvastatin-fenofibrate combination by assessing the publicly available US Food and Drug Administration Adverse Event Reporting System (FAERS), so as to provide a reference for rational clinical use of rosuvastatin and fenofibrate, and reduce the occurrence of related AEs.

Methods: Reports to the FAERS from 1 January 2004 to 19 March 2020 were analyzed. The proportional report ratio (PRR), reporting odds ratio (ROR), and Bayesian Confidence Propagation Neural Network (BCPNN) analysis were used to extract data from FAERS for suspected signals referring to the combination of rosuvastatin and fenofibrate.

Results: A total of 68 safety signals were detected from the top 250 AEs in 3,587 reports, of which 28 signals were not included in the drug labels. All the detected AEs were associated with 12 System Organ Classes (SOC), such as gastrointestinal, musculoskeletal and connective tissue, general diseases, investigations and nervous system. The most frequent AEs were analyzed, and it was found that women generally have a higher susceptibility to experiencing AEs, including pain, nausea, fatigue, myalgia, diarrhea, dyspnea, headache, weakness, and dizziness.

Conclusion: Clinicians should pay more attention to the AEs of gastrointestinal and muscular system during combination therapy, and it is recommended to strengthen pharmaceutical care during clinical application.

KEYWORDS

FAERS, rosuvastatin, fenofibrate, adverse events, pharmacovigilance

Introduction

With the improvement of individuals' living standards, there has been a significant increase in the prevalence of dyslipidemia. Genetic defects and unhealthy lifestyle are two risk factors of hyperlipidemia (Lorenzatti and Toth, 2020), especially, the change in people's dietary structure towards high fat, high sugar and high calorific value, as well as ultra-processed foods, has led to a sharp increase in the prevalence of dyslipidemia (Arnett et al., 2019; Juul et al., 2021). Hypercholesterolemia stands as the primary contributor to cardiovascular diseases, which is one of the main reasons for adult death in the United States and causes huge economic losses every year (Dawber et al., 2015; Virani et al., 2020). Numerous guidelines advocate for statin usage to mitigate the morbidity and mortality associated with such conditions (Lloyd-Jones et al., 2017; Mach et al., 2020; Stone et al., 2014). Low density lipoprotein cholesterol (LDL-C) serves as a pivotal target for intervention in reducing atherosclerotic cardiovascular disease (ASCVD). Patients with hypertriglyceridemia exhibit elevated levels of residual lipoproteins that are likely to exert atherogenic effects. Consequently, non-high-density lipoprotein cholesterol (HDL-C) is also employed as an auxiliary intervention target. Although statins effectively lower LDL-C levels, the achievement of comprehensive lipid regulation necessitates the concomitant use of other lipid-modulating agents.

3- Hydroxy-3-methylglutaryl-coenzyme A (HMG-CoA) reductase inhibitors (statins) have been widely recommended to reduce the incidence rate and mortality of cardiovascular diseases (Heart Protection Study Collaborative Group, 2002; Lloyd-Jones et al., 2017; Mach et al., 2020; Pedersen et al., 2004; Stone et al., 2014). Statins primarily function by inhibiting HMG-CoA reductase, thereby impeding cholesterol synthesis within the body. Fibrates can augment lipoprotein lipase activity and diminish triglyceride levels. The 2019 ESC Lipid Guidelines suggest that a combination of statins and fibrates may be considered when a patient's TG > 2.3 mmol/L (Mach et al., 2020). According to the 2023 Chinese Lipid Management Guidelines, individuals with ASCVD or at high risk should receive moderate dose statin therapy if their TG > 2.3 mmol/L, and fibrates can be administered to further mitigate the risk of ASCVD (Joint Committee on the Chinese Guidelines for Lipid Management, 2023). Even so, the cardiovascular benefits of statins in combination with fibrates remain a subject of debate and controversy within the scientific community. The safety of combining statins and fibrates in the Chinese population is deemed acceptable; however, further verification is required to establish the long-term safety of this combination (Joint Committee on the Chinese Guidelines for Lipid Management, 2023). Nevertheless, due to the similar metabolic pathways of statins and fibrates, their combination has the potential to cause liver injury and increase the risk of myositis and myopathy (Joint committee for guideline, 2018), greatly increasing the occurrence rate of adverse events (AEs). It is well-established that the concurrent administration of statins and fibrates can give rise to significant adverse reactions. In 2001, cerivastatin, a promising statin, was introduced to the market; however, Bayer Pharmaceutical, its manufacturer, subsequently contraindicated the combination of cerivastatin and gemfibrozil due to frequent and severe reports of rhabdomyolysis-related deaths (Staffa et al., 2002). Consequently, Bayer withdrew cerivastatin from the international drug market that same year (Wooltorton, 2001). Overall, the drug labels of AEs after the combination therapy of these two drugs is still deficient, which is not conducive to actual clinical applications. The safety of combining statins and fibrates should be given significant attention.

The real-world data could provide post-marketing drug safety information, which is beneficial for clinicians to weigh risks and benefits. The US Food and Drug Adiministration (via the FDA Adverse Event Reporting System, FAERS), the World Health Organisation (via VigiBase) and the European Medicines Agency (via Eudra Vigilance) are the most widely used databases for reporting spontaneous adverse drug reactions abroad. FAERS Data files are provided in ASCII or SGML format to ensure consistency in compiling drug and adverse event data. Information transfer between databases is carried out directly using standardized data formats, as FDA only accepts electronic submissions of ICSRs in XML format. Herein, this study is aimed to analyze the AEs reports of FAERS, so as to provide references for rational clinical application through detecting safety signals and identifying potential drug risk signals.

Methods

Data source

In this study, we obtained data from the OpenFDA, a public data open project in the United States, and the original data of AEs were imported by FAERS (Joint committee for guideline, 2018). FAERS collects spontaneous safety reports and post-marketing clinical research reports related to drugs used in the United States and abroad. All AEs were coded using preferred terms (PT) from the Medical Dictionary for Regulatory Activities (MedDRA) (Ma et al., 2021).

We used Research AE as the analysis tool to extract AEs reports from the FAERS database which covered the period from 1 January 2004 to 19 March 2020. Research AE is a research AE analysis tool, which can directly extract AEs from the FAERS database through the interface of application programming (API). The generic names of rosuvastatin and fenofibrate were used as the keywords to perform searches, and the AEs reports were included when rosuvastatin and fenofibrate were the first suspect drugs. Reports pertaining to diseases, which related to drug indications, or concomitant disease were excluded from the analysis, other reports from the top 250 AE cases were left for signal detection in order to assess the association between drugs and AEs.

Signal detection method

Disproportionality analysis is a commonly used analytic method for AEs signal mining, which could be divided into two categories: frequentist and Bayesian methods. No "gold standard" is available, each of the above methods has its own shortages (van Puijenbroek et al., 2003). Both proportional reporting ratio (PRR) (Evans et al., 2001) and reporting odds ratio (ROR) (van Puijenbroek et al., 2002) are frequency methods. They are easy for calculation and can lead to

TABLE 1 Two-by-two frequency table.

Project	Adverse event of interest	All other adverse events	Total
Drug of interest	a	b	a + b
All other drugs	c	d	c + d
Total	a + c	b + d	a + b + c + d

a, the incidence of specific adverse events attributed to the drug. b, the incidence of non-specific adverse events associated with the drug. c, the incidence of specific adverse events reported for all drugs, excluding the drug in question. d, the incidence of non-specific adverse events reported for all drugs, excluding the drug under investigation.

TABLE 2 Demographic characteristics of patients and composition of serious adverse events.

Variables	Reports (n)	Percentage (%)
Gender		
Male	1954	54.47
Female	1,486	41.43
Unknown	147	4.10
Age, years		
<18	6	0.17
18–44	157	4.38
45–64	1,122	31.28
65–74	587	16.36
≥75	299	8.34
Unknown	1,416	39.48
Occupation		
Doctor	775	21.60
Pharmacist	218	6.08
Other medical staff	529	14.75
Lawyer	67	1.87
Consumer or non-medical Staff	1,386	38.64
Unknown	612	17.06
Serious adverse events		
Death	202	5.63
Hospitalization	1,110	30.95
Congenital anomalies	1	0.03
Disabling	121	3.37
Life threatening	123	3.43

a more sensitive output than bayesian approaches. The bayesian confidence propagation neural network (BCPNN) (Noguchi et al., 2019) is always applicable and large numbers of calculations can be made efficiently. Both approaches entailed inherent drawbacks, including: the limitation of frequentist statistical method mainly includes: i): false positive signals might be detected and ii): measured values are sensitive to small fluctuations. Correspondingly, the restriction of Bayesian Confidence Propagation Neural Network (BCPNN) mainly including: i): false-negative signals might be detected. ii): measured values are not specific and iii): signal value is difficult to be calculated (Bate et al., 2002; Noguchi et al., 2021). No one algorithm is universally better than others. In the present investigation, we used PRR, ROR, and BCPNN for safety signals detection. The two-by-two frequency table of disproportionality analysis is shown in Table 1.

Herein, the criteria of PRR and ROR were: a ≥ 3, the lower bound of 95% two-sided confidence interval (CI) > 1, and the criteria of BCPNN were: IC-2SD > 0 (Shen et al., 2019) and the algorithm was showed in Equation 1. The higher the scores of PRR, ROR, and BCPNN, the stronger the association between the drugs and AEs. In addition, to identify the impact of gender differences on AEs, we analyzed 10 AEs most frequently reported and performed ROR analysis (ROR > 1 means a higher likelihood of AEs occurring in females).

$$\alpha_1 = \beta_1 = 1;\ \alpha = \beta = 2;\ \gamma_{11} = 1;\ C = a + b + c + d;\ C_x = a + b;$$
$$C_y = a + c;\ C_{xy} = a;\ \gamma = \gamma_{11}\frac{(C+\alpha)(C+\beta)}{(C_x+\alpha_1)(C_y+\beta_1)};$$

$$E(IC) = log_2\frac{(C_{xy}+\gamma_{11})(C+\alpha)(C+\beta)}{(C+\gamma)(C_x+\alpha_1)(C_y+\beta_1)};$$

$$V(IC) = \frac{1}{(ln\,2)^2}\left\{\left(\frac{C-C_{xy}+\gamma-\gamma_{11}}{(C+\gamma_{11})(1+C+\gamma)}\right)+\left(\frac{C-C_x+\alpha-\alpha_1}{(C_x+\alpha_1)(1+C+\alpha)}\right)\right.$$
$$\left.+\left(\frac{C-C_y+\beta+\beta_1}{(C_y+\beta_1)(1+C+\beta)}\right)\right\};$$

$$IC-2SD = E(IC) - 2\sqrt{V(IC)} \quad (1)$$

Results

AEs reports and demographic characteristics of patients

In this study, a total of 3,587 AEs were reported with rosuvastatin and fenofibrate as the first suspect drugs. As shown in Table 2, doctors (21.60%), pharmacists (6.08%), and other medical staff (14.75%) were main reporters. The highest proportion of reports was by consumers and non-medical staff. In addition, there are more male patients (54.47%) than female patients (41.43%) and the patients aged 45~64 are counted the most percent (31.28%). Notably, the percentage of serious AEs was 43.41% after combined therapy, of which 1,110 (30.95%) reported cases were hospitalization or prolonged hospitalization.

Signal detection of AEs

As defined in MedDRA, the safety signals were classified according to System Organ Class (SOC). Herein, a total of 68 safety signals were detected from the top 250 AEs in 3,587 events. As shown in Tables 3 40 (58.82%) safety signals, involving 12 SOC, were listed in the drug labels, of which the top

TABLE 3 Significant disproportionality results displayed according to SOC and PT.

PT	Reports	Percentage (%)	PRR (95% CI)	ROR (95% CI)	IC (IC-2SD)	Listed in the drug labels
Blood and lymphatic system disorders						
Anemia	30	0.84%	1.57 (1.10, 2.24)	1.57 (1.10, 2.26)	0.62 (0.09)	No
Nephrogenic anemia	21	0.59%	48.35 (31.55, 74.10)	48.72 (31.64, 75.04)	3.93 (3.31)	No
Hemorrhagic anemia	7	0.20%	6.20 (2.96, 13.00)	6.21 (2.95, 13.04)	1.91 (0.88)	No
Gastrointestinal disorders						
Nausea	112	3.12%	1.52 (1.27, 1.82)	1.52 (1.26, 1.84)	0.57 (0.28)	Yes
Diarrhea	92	2.56%	1.70 (1.40, 2.08)	1.70 (1.38, 2.10)	0.73 (0.41)	Yes
Constipation	47	1.31%	2.60 (1.96, 3.44)	2.60 (1.94, 3.47)	1.31 (0.88)	Yes
Abdominal pain	34	0.95%	1.54 (1.10, 2.15)	1.54 (1.10, 2.16)	0.59 (0.09)	Yes
Gastrointestinal bleeding	34	0.95%	3.27 (2.35, 4.57)	3.28 (2.33, 4.60)	1.60 (1.11)	No
Epigastric pain	31	0.86%	1.64 (1.16, 2.33)	1.64 (1.15, 2.34)	0.68 (0.16)	Yes
Gastroesophageal reflux disease	25	0.70%	3.28 (2.22, 4.84)	3.28 (2.21, 4.87)	1.58 (1.01)	No
Abdominal discomfort	22	0.61%	1.60 (1.06, 2.42)	1.60 (1.05, 2.44)	0.63 (0.03)	Yes
Indigestion	21	0.59%	2.26 (1.48, 3.46)	2.26 (1.47, 3.48)	1.09 (0.47)	Yes
Pancreatitis	17	0.47%	3.00 (1.87, 4.82)	3.01 (1.86, 4.85)	1.43 (0.74)	Yes
Gastrointestinal disorder	14	0.39%	2.22 (1.31, 3.73)	2.22 (1.31, 3.75)	1.03 (0.28)	Yes
Upper gastrointestinal bleeding	10	0.28%	5.04 (2.71, 9.35)	5.04 (2.71, 9.39)	1.88 (1.00)	No
Acute pancreatitis	9	0.25%	3.76 (1.96, 7.21)	3.76 (1.95, 7.24)	1.55 (0.64)	Yes
General disorders and administration site conditions						
Fatigue	131	3.65%	2.01 (1.70, 2.37)	2.01 (1.68, 2.01)	0.94 (0.68)	Yes
Powerless	71	1.98%	2.00 (1.59, 2.52)	2.00 (1.58, 2.00)	0.95 (0.60)	Yes
Pain	69	1.92%	1.39 (1.10, 1.75)	1.39 (1.09, 1.77)	0.45 (0.09)	No
Edema	11	0.31%	2.06 (1.14, 3.71)	2.06 (1.14, 3.72)	0.91 (0.08)	Yes
Hearing loss	10	0.28%	3.29 (1.77, 6.10)	3.29 (1.77, 6.13)	1.44 (0.56)	No
Investigations						
Weight loss	55	1.53%	2.18 (1.68, 2.83)	2.18 (1.67, 2.85)	1.07 (0.68)	No
Increased blood glucose concentration	54	1.51%	2.69 (2.06, 3.49)	2.69 (2.05, 3.52)	1.36 (0.95)	Yes
Elevated serum creatinine phosphokinase	28	0.78%	7.87 (5.45, 11.36)	7.88 (5.42, 11.44)	2.65 (2.11)	Yes
Increased blood creatinine	27	0.75%	4.11 (2.83, 5.98)	4.11 (2.81, 6.02)	1.87 (1.32)	Yes
Decreased white blood cell count	19	0.53%	2.05 (1.31, 3.21)	2.05 (1.30, 3.22)	0.95 (0.30)	Yes
Abnormal liver function	17	0.47%	4.44 (2.77, 7.13)	4.45 (2.76, 7.17)	1.89 (1.20)	Yes
Increased glycosylated hemoglobin	16	0.45%	7.20 (4.42, 11.73)	7.21 (4.40, 11.79)	2.39 (1.69)	Yes
Increased aspartate aminotransferase	14	0.39%	2.43 (1.44, 4.09)	2.43 (1.44, 4.11)	1.14 (0.39)	Yes
Increased alanine aminotransferase	13	0.36%	1.99 (1.16, 3.42)	1.99 (1.15, 3.43)	0.89 (0.11)	Yes
Increased liver enzymes	12	0.33%	2.17 (1.23, 3.81)	2.17 (1.23, 3.82)	0.99 (0.18)	Yes
International standardization ratio rises	9	0.25%	2.20 (1.15, 4.23)	2.20 (1.14, 4.24)	0.97 (0.05)	No

(Continued on following page)

TABLE 3 (*Continued*) Significant disproportionality results displayed according to SOC and PT.

PT	Reports	Percentage (%)	PRR (95% CI)	ROR (95% CI)	IC (IC-2SD)	Listed in the drug labels
Elevated prostate specific antigen	8	0.22%	6.16 (3.08, 12.31)	6.17 (3.08, 12.35)	1.97 (1.00)	No
Metabolism and nutrition disorders						
Diabetes	41	1.14%	5.21 (3.85, 7.05)	5.21 (3.82, 7.10)	2.22 (1.76)	Yes
Poor appetite	30	0.84%	1.50 (1.05, 2.14)	1.50 (1.05, 2.15)	0.55 (0.03)	No
Dehydration	24	0.67%	1.74 (1.17, 2.59)	1.74 (1.16, 2.60)	0.75 (0.16)	No
Musculoskeletal and connective tissue disorders						
Myalgia	87	2.43%	5.23 (4.26, 6.42)	5.23 (4.22, 6.49)	2.26 (1.94)	Yes
Limb pain	55	1.53%	1.89 (1.46, 2.45)	1.89 (1.44, 2.47)	0.87 (0.48)	No
Joint pain	50	1.39%	1.47 (1.12, 1.93)	1.47 (1.11, 1.94)	0.53 (0.11)	Yes
Backache	40	1.12%	1.80 (1.32, 2.44)	1.80 (1.31, 2.46)	0.80 (0.34)	No
Muscle cramps	34	0.95%	1.85 (1.33, 2.59)	1.85 (1.32, 2.60)	0.84 (0.35)	Yes
Rhabdomyolysis	31	0.86%	7.24 (5.10, 10.26)	7.25 (5.08, 10.34)	2.58 (2.06)	Yes
Myasthenia	27	0.75%	2.38 (1.64, 3.46)	2.38 (1.63, 3.48)	1.17 (0.62)	Yes
Muscular atrophy	23	0.64%	18.09 (12.04, 27.16)	18.14 (12.01, 27.38)	3.39 (2.79)	No
Myopathy	17	0.47%	16.01 (9.97, 25.71)	16.04 (9.95, 25.88)	3.12 (2.43)	Yes
Muscle fatigue	14	0.39%	3.35 (1.99, 5.65)	3.35 (1.98, 5.67)	1.53 (0.78)	No
Intervertebral disc degeneration	11	0.31%	10.83 (6.01, 19.53)	10.85 (5.99, 19.63)	2.57 (1.73)	No
Osteoarthritis	11	0.31%	2.44 (1.35, 4.39)	2.44 (1.35,4.41)	1.12 (0.28)	No
Nervous system disorders						
Headache	87	2.43%	1.47 (1.20, 1.81)	1.47 (1.19, 1.83)	0.53 (0.21)	Yes
Dizzy	66	1.84%	1.37 (1.08, 1.73)	1.37 (1.07, 1.75)	0.43 (0.06)	Yes
Syncope	19	0.53%	1.87 (1.20, 2.93)	1.87 (1.19, 2.94)	0.83 (0.18)	No
Diabetic neuropathy	14	0.39%	20.68 (12.26, 34.88)	20.75 (12.25, 35.13)	3.16 (2.41)	No
Psychiatric disorders						
Insomnia	45	1.25%	1.66 (1.24, 2.22)	1.66 (1.24, 2.23)	0.70 (0.26)	Yes
Sleep disorders	24	0.67%	4.35 (2.92, 6.47)	4.35 (2.91, 6.51)	1.93 (1.34)	Yes
Irritability	13	0.36%	1.91 (1.11, 3.28)	1.91 (1.11, 3.30)	0.84 (0.06)	No
Abnormal dream	10	0.28%	2.89 (1.56, 5.36)	2.89 (1.55, 5.38)	1.30 (0.42)	Yes
Renal and urinary disorders						
Renal damage	28	0.78%	4.05 (2.81, 5.86)	4.06 (2.79, 5.89)	1.86 (1.32)	Yes
Renal calculus	20	0.56%	5.19 (3.36, 8.03)	5.19 (3.34, 8.07)	2.10 (1.47)	No
Hematuria	11	0.31%	2.97 (1.64, 4.96)	2.97 (1.64, 5.37)	1.34 (0.51)	Yes
Dysuria	10	0.28%	2.67 (1.44, 4.96)	2.67 (1.43, 4.97)	1.21 (0.33)	No
Respiratory, thoracic and mediastinal disorders						
Dyspnea	69	1.92%	1.31 (1.04, 1.65)	1.31 (1.03, 1.66)	0.37 (0.01)	Yes

(Continued on following page)

TABLE 3 (*Continued*) Significant disproportionality results displayed according to SOC and PT.

PT	Reports	Percentage (%)	PRR (95% CI)	ROR (95% CI)	IC (IC-2SD)	Listed in the drug labels
Chronic obstructive pulmonary disease	12	0.33%	2.27 (1.29, 4.00)	2.27 (1.29,4.01)	1.04 (0.24)	No
Skin and subcutaneous tissue disorders						
Itch	49	1.37%	1.70 (1.29, 2.24)	1.70 (1.28, 2.26)	0.73 (0.31)	Yes
Skin damage	9	0.25%	3.38 (1.76, 6.49)	3.39 (1.76, 6.52)	1.45 (0.53)	Yes
Eczema	8	0.22%	3.65 (1.82, 7.29)	3.65 (1.82, 7.31)	1.49 (0.52)	No
Vascular disorders						
Blush	42	1.17%	3.71 (2.75, 5.01)	3.71 (2.73, 5.04)	1.78 (1.33)	No
Hemorrhage	19	0.53%	1.91 (1.22, 2.99)	1.91 (1.22, 3.01)	0.87 (0.21)	No
Thromboembolism	14	0.39%	1.85 (1.10, 3.12)	1.85 (1.09, 3.13)	0.80 (0.05)	Yes

TABLE 4 Gender differences in adverse event reactions.

PT	Reports	ROR (95%CI)
Pain	252	1.21 (1.00, 1.45)
Nausea	115	1.62 (1.23, 2.15)
Fatigue	92	1.04 (0.78, 1.37)
Myalgia	91	1.43 (1.06, 1.94)
Diarrhea	83	1.48 (1.08, 2.04)
Dyspnea	80	1.68 (1.20, 2.35)
Headache	73	1.37 (0.98, 1.91)
Powerless	66	1.06 (0.76, 1.48)
Dizzy	61	1.12 (0.79, 1.58)
Weight loss	49	0.87 (0.60, 1.25)

ROR > 1 indicates females are more likely to have AEs, ROR < 1 indicates that males are more likely to have AEs.

5 AEs were gastrointestinal diseases (468 reports, 13.05%), musculoskeletal and connective tissue diseases (400 reports, 11.15%), general diseases (292 reports, 18.14%), investigations (272 reports, 7.58%) and nervous system diseases (186 reports, 5.19%), respectively. In addition, 28 (41.18%) signals were not included in the drug labels, which mainly including blushing, back pain, weight loss, poor appetite and so on.

Furthermore, according to the analysis of AEs in Table 4, we found that females exhibit a higher susceptibility to experiencing AEs, including pain, nausea, fatigue, myalgia, diarrhea, dyspnea, headache, weakness, and dizziness. Correspondingly, men are more likely to experience weight loss.

Discussion

According to the signal screening results, during the combined treatment of rosuvastatin and fenofibrate, the risks of gastrointestinal system disorders, musculoskeletal and connective tissue disorders, general disorders, medical tests as well as neurological disorders were increased when rosuvastatin and fenofibrate were applied in combination, which were consistent with previous researches (Ferdinand et al., 2012; Pepine et al., 2010; Roth et al., 2010). And the most commonly reported AEs were in the gastrointestinal system, mainly manifested as nausea, diarrhea and other discomfort, which would affect patients' appetite and sleep quality, thus further increasing their discomfort and even cause discontinuation of treatment in severe cases, greatly limits the therapeutic effect of patients. To improve patients' medication compliance, medication guide and health education could be strengthened, enabling them fully understand disease and drugs, reducing psychological burden and adjusting the diet as needed.

In addition, since both statins and fibrates have the potential to cause liver injury, myositis and myopathy, their combination is more likely to cause liver and kidney damage as well as muscle aches (Cranmer et al., 2021; Shen et al., 2019; van Puijenbroek et al., 2002). Therefore, it is recommended to closely monitor the indices of creatine kinase and liver enzymes, as well as reporting all unexplained muscle aches and pains. Besides, for special populations, such as the elderly and children, the overweight or

slim people and patients simultaneously using several drugs, the dose could be adjusted according to the patient's tolerance to avoid serious AEs (Alomar, 2014; Han et al., 2022; Zhang et al., 2023).

Furthermore, basing on the signal screening of FAERS database, we found that 28 signals were not included in the drug label, mainly including flushing, back pain, weight loss and loss of appetite, which suggests possible AEs outside instructions during the actual application of rosuvastatin and fenofibrate. Hence, our research is expected to provide data support beyond the instructions for rapid clinical evaluation of combined drugs.

However, this study still remains some deficiencies. On account of the detection of signal was based on the spontaneous reporting database, it was prone to have missed, duplicate, incomplete and irregular reports. While consumers or non-medical staff reports constituted the largest proportion, this subset of reports showed a greater tendency for incompleteness and irregularity, which consequently affected the accuracy of data analysis. In addition, the disproportionality analysis was focused on the number of reports, which failed to take the time-to-onset distribution into account (Noguchi et al., 2021). It also did not take into account patients' basic diseases and other combined medication issues as well as reports that one drug was regarded as a suspicious drug and another drug was regarded as an accompanying drug. Besides, because it is difficult to identify which patient was prescribed with these drugs and for what reason, many heterogeneous patients were also included in our analyzation. Additionally, since PT was fixed, we counted the AEs and checked them with the drug labels objectively, which might bias the judgment of whether the adverse event was expected or not. Moreover, the safety signals detected in the study only indicated a statistical correlation between drugs and AEs, specific methods to investigate drug-drug interaction are still need to be considered in further studies.

Conclusion

Based on the FDA adverse event database, this study identified a total of 68 positive signals. When rosuvastatin was combined with fenofibrate, the most prevalent AEs observed were related to gastrointestinal system diseases, musculoskeletal and connective tissue diseases, general diseases, investigations and nervous system diseases. Additionally, analysis of FAERS database data revealed 28 signals primarily associated with blushing, back pain, weight loss, poor appetite and so on, were not included in the drug labels. Therefore, more attention needs to be paid to the combined therapy of statin and fibrate. And we believe our real-world data analysis could be expected to provide helpful reference for rapid clinical assessment and further promote rational clinical medication.

Data availability statement

The datasets presented in this study can be found in online repositories. The names of the repository/repositories and accession number(s) can be found in the article/supplementary material.

Author contributions

QL: Data curation, Formal Analysis, Funding acquisition, Investigation, Writing–original draft. WS: Data curation, Formal Analysis, Investigation, Writing–original draft. SW: Conceptualization, Funding acquisition, Supervision, Writing–review and editing.

Funding

The author(s) declare that financial support was received for the research, authorship, and/or publication of this article. This work was supported by Administration of Traditional Chinese Medicine of Zhejiang Province, China (2018ZQ048), Foundation of Zhejiang Provincial Education Department (Y202148364) and Science and Technology program of Yiwu Science and Technology Bureau (Grant No. 18-3-29, 18-3-28).

Conflict of interest

The authors declare that the research was conducted in the absence of any commercial or financial relationships that could be construed as a potential conflict of interest.

Generative AI statement

The author(s) declare that no Generative AI was used in the creation of this manuscript.

Publisher's note

References

Alomar, M. J. (2014). Factors affecting the development of adverse drug reactions (Review article). *Saudi Pharm. J.* 22, 83–94. doi:10.1016/j.jsps.2013.02.003

Arnett, D. K., Blumenthal, R. S., Albert, M. A., Buroker, A. B., Goldberger, Z. D., Hahn, E. J., et al. (2019). 2019 ACC/AHA guideline on the primary prevention of cardiovascular disease: a report of the American college of cardiology/American heart association task force on clinical practice guidelines. *Circulation* 140, e596–e646. doi:10.1161/CIR.0000000000000678

Bate, A., Lindquist, M., Edwards, I. R., and Orre, R. (2002). A data mining approach for signal detection and analysis. *Drug Saf.* 25, 393–397. doi:10.2165/00002018-200225060-00002

Cranmer, M., Tamayo, D., Rein, H., Battaglia, P., Hadden, S., Armitage, P. J., et al. (2021). A Bayesian neural network predicts the dissolution of compact planetary systems. *Proc. Natl. Acad. Sci. U. S. A.* 118, e2026053118. doi:10.1073/pnas.2026053118

Dawber, T. R., Moore, F. E., and Mann, G. V. (2015). II. Coronary heart disease in the framingham study. *Int. J. Epidemiol.* 44, 1767–1780. doi:10.1093/ije/dyv346

Evans, S. J., Waller, P. C., and Davis, S. (2001). Use of proportional reporting ratios (PRRs) for signal generation from spontaneous adverse drug reaction reports. *Pharmacoepidemiol Drug Saf.* 10, 483–486. doi:10.1002/pds.677

Ferdinand, K. C., Davidson, M. H., Kelly, M. T., and Setze, C. M. (2012). One-year efficacy and safety of rosuvastatin + fenofibric acid combination therapy in patients with mixed dyslipidemia: evaluation of dose response. *Am. J. Cardiovasc Drugs* 12, 117–125. doi:10.2165/11597940-000000000-00000

Han, Y. Z., Guo, Y. M., Xiong, P., Ge, F. L., Jing, J., Niu, M., et al. (2022). Age-associated risk of liver-related adverse drug reactions. *Front. Med. (Lausanne)* 9, 832557. doi:10.3389/fmed.2022.832557

Heart Protection Study Collaborative Group (2002). MRC/BHF Heart Protection Study of cholesterol lowering with simvastatin in 20,536 high-risk individuals: a randomised placebo-controlled trial. *Lancet* 360, 7–22. doi:10.1016/S0140-6736(02)09327-3

Joint committee for guideline (2018). 2016 Chinese guidelines for the management of dyslipidemia in adults. *J. Geriatr. Cardiol.* 15, 1–29. doi:10.11909/j.issn.1671-5411.2018.01.011

Joint Committee on the Chinese Guidelines for Lipid Management (2023). Chinese guidelines for lipid management. *Chin. Circ. J.* 38, 237–271. doi:10.3760/cma.j.cn112148-20230119-00038

Juul, F., Vaidean, G., Lin, Y., Deierlein, A. L., and Parekh, N. (2021). Ultra-processed foods and incident cardiovascular disease in the framingham offspring study. *J. Am. Coll. Cardiol.* 77, 1520–1531. doi:10.1016/j.jacc.2021.01.047

Lloyd-Jones, D. M., Morris, P. B., Ballantyne, C. M., Birtcher, K. K., Daly, D. D., JR., Depalma, S. M., et al. (2017). 2017 focused update of the 2016 acc expert consensus decision pathway on the role of non-statin therapies for LDL-cholesterol lowering in the management of atherosclerotic cardiovascular disease risk: a report of the American college of cardiology task force on expert consensus decision pathways. *J. Am. Coll. Cardiol.* 70, 1785–1822. doi:10.1016/j.jacc.2017.07.745

Lorenzatti, A. J., and Toth, P. P. (2020). New perspectives on atherogenic dyslipidaemia and cardiovascular disease. *Eur. Cardiol.* 15, 1–9. doi:10.15420/ecr.2019.06

Mach, F., Baigent, C., Catapano, A. L., Koskinas, K. C., Casula, M., Badimon, L., et al. (2020). 2019 ESC/EAS Guidelines for the management of dyslipidaemias: lipid modification to reduce cardiovascular risk. *Eur. Heart J.* 41, 111–188. doi:10.1093/eurheartj/ehz455

Ma, R., Wang, Q., Meng, D., Li, K., and Zhang, Y. (2021). Immune checkpoint inhibitors-related myocarditis in patients with cancer: an analysis of international spontaneous reporting systems. *BMC Cancer* 21, 38. doi:10.1186/s12885-020-07741-0

Noguchi, Y., Nagasawa, H., Tachi, T., Tsuchiya, T., and Teramachi, H. (2019). Signal detection of oral drug-induced dementia in chronic kidney disease patients using association rule mining and Bayesian confidence propagation neural network. *Pharmazie* 74, 570–574. doi:10.1691/ph.2019.9426

Noguchi, Y., Tachi, T., and Teramachi, H. (2021). Detection algorithms and attentive points of safety signal using spontaneous reporting systems as a clinical data source. *Brief. Bioinform* 22, bbab347. doi:10.1093/bib/bbab347

Pedersen, T. R., Kjekshus, J., Berg, K., Haghfelt, T., Faergeman, O., Faergeman, G., et al. (2004). Randomised trial of cholesterol lowering in 4444 patients with coronary heart disease: the Scandinavian Simvastatin Survival Study (4S). *Atheroscler. Suppl.* 5, 81–87. doi:10.1016/j.atherosclerosissup.2004.08.027

Pepine, C. J., Jacobson, T. A., Carlson, D. M., Kelly, M. T., Setze, C. M., Gold, A., et al. (2010). Combination rosuvastatin plus fenofibric acid in a cohort of patients 65 years or older with mixed dyslipidemia: subanalysis of two randomized, controlled studies. *Clin. Cardiol.* 33, 609–619. doi:10.1002/clc.20830

Roth, E. M., Rosenson, R. S., Carlson, D. M., Fukumoto, S. M., Setze, C. M., Blasetto, J. W., et al. (2010). Efficacy and safety of rosuvastatin 5 mg in combination with fenofibric acid 135 mg in patients with mixed dyslipidemia - a phase 3 study. *Cardiovasc Drugs Ther.* 24, 421–428. doi:10.1007/s10557-010-6266-4

Shen, J., Yang, J., and Zhao, B. (2019). A survey of the FDA's adverse event reporting system database concerning urogenital tract infections and sodium glucose cotransporter-2 inhibitor use. *Diabetes Ther.* 10, 1043–1050. doi:10.1007/s13300-019-0611-9

Staffa, J. A., Chang, J., and Green, L. (2002). Cerivastatin and reports of fatal rhabdomyolysis. *N. Engl. J. Med.* 346, 539–540. doi:10.1056/NEJM200202143460721

Stone, N. J., Robinson, J. G., Lichtenstein, A. H., Bairey Merz, C. N., Blum, C. B., Eckel, R. H., et al. (2014). 2013 ACC/AHA guideline on the treatment of blood cholesterol to reduce atherosclerotic cardiovascular risk in adults: a report of the American College of Cardiology/American Heart Association Task Force on Practice Guidelines. *J. Am. Coll. Cardiol.* 63, 2889–2934. doi:10.1016/j.jacc.2013.11.002

VAN Puijenbroek, E. P., Bate, A., Leufkens, H. G., Lindquist, M., Orre, R., and Egberts, A. C. (2002). A comparison of measures of disproportionality for signal detection in spontaneous reporting systems for adverse drug reactions. *Pharmacoepidemiol Drug Saf.* 11, 3–10. doi:10.1002/pds.668

Van Puijenbroek, E., Diemont, W., and VAN Grootheest, K. (2003). Application of quantitative signal detection in the Dutch spontaneous reporting system for adverse drug reactions. *Drug Saf.* 26, 293–301. doi:10.2165/00002018-200326050-00001

Virani, S. S., Alonso, A., Benjamin, E. J., Bittencourt, M. S., Callaway, C. W., Carson, A. P., et al. (2020). Heart disease and stroke statistics-2020 update: a report from the American heart association. *Circulation* 141, e139–e596. doi:10.1161/CIR.0000000000000757

Wooltorton, E. (2001). Bayer pulls cerivastatin (Baycol) from market. *Cmaj* 165, 632.

Zhang, M., Lv, H., Yang, H., Zhang, H., Bai, X., and Qian, J. (2023). Elderly patients with moderate-to-severe ulcerative colitis are more likely to have treatment failure and adverse outcome. *Gerontology* 69, 119–129. doi:10.1159/000522569

frontiers | Frontiers in Pharmacology

TYPE Original Research
PUBLISHED 13 February 2025
DOI 10.3389/fphar.2025.1489210

OPEN ACCESS

EDITED BY
Huaqiang Zhai,
Beijing University of Chinese Medicine, China

REVIEWED BY
Yu Zhijian,
Shenzhen University, China
Luo Fang,
University of Chinese Academy of Sciences, China

*CORRESPONDENCE
Jifu Wei,
weijifu@njmu.edu.cn
Zhixian Liu,
liuzhixian@njmu.edu.cn

†These authors have contributed equally to this work

RECEIVED 31 August 2024
ACCEPTED 17 January 2025
PUBLISHED 13 February 2025

CITATION
Tang Q, Dong J, Zhang F, Zhao D, Yang Q, Wen J, Sun Y, Wei J and Liu Z (2025) Entrectinib can induce nerve cell damage by inhibiting PI3K-AKT and TGF-β signaling pathways. *Front. Pharmacol.* 16:1489210. doi: 10.3389/fphar.2025.1489210

Entrectinib can induce nerve cell damage by inhibiting PI3K-AKT and TGF-β signaling pathways

Qingshan Tang[1†], Jiachen Dong[1†], Feng Zhang[1], Dan Zhao[1], Qi Yang[1], Jiayu Wen[2], Yuhao Sun[2], Jifu Wei[2*†] and Zhixian Liu[2*†]

[1]Jiangsu Key Laboratory, Pharmacology and Safety Evaluation of Chinese Materia Medica, Nanjing University of Chinese Medicine, Nanjing, China, [2]Jiangsu Cancer Hospital, The Affiliated Cancer Hospital of Nanjing Medical University, Jiangsu Institute of Cancer Research, Nanjing, China

Background: The tyrosine receptor kinase inhibitor (TRKi) entrectinib is used to treat neurotrophic tyrosine receptor kinase (NTRK) fusion-positive solid tumors and ROS1-positive patients. Despite its impressive efficacy against cancer, the clinical application is still limited by the central nervous system (CNS)-related toxicities. However, the precise mechanism of such CNS-related toxicities remains elusive.

Methods: The effect of entrectinib-induced nerve cell damage was evaluated by the nerve cells (PC12, HT22 and SK-N-SH) based *in vitro* models. Various assays, including CCK-8, colony formation and EdU incorporation assays were utilized to estimate the cellular viability and proliferation ability. Cell apoptosis was measured by flow cytometry. Next, transcriptome sequencing technology was performed to identify differentially expressed genes (DEGs). Gene ontology (GO), kyoto encyclopedia of genes and genomes (KEGG) analysis and gene set enrichment analysis (GSEA) were applied to predict the potential functions of DEGs. Quantitative real time polymerase chain reaction (qRT-PCR) and Western blotting assays were performed to measure the expressions of thrombospondin-1 (THBS1), TGF-β1, PI3K, AKT and phosphorylated AKT (p-AKT) in the entrectinib-treated nerve cells. Additionally, we Preliminary observed and validated whether THBS1 overexpression could rescue nerve cell damage and the abnormalities in PI3K-AKT and TGF-β signaling pathways.

Results: Entrectinib significantly inhibited the nerve cells proliferation and colony formation, and induced nerve cells apoptosis. Transcriptome sequencing analysis and qRT-PCR revealed that THBS1 was downregulated within entrectinib treatment. KEGG and GSEA analysis also suggested that entrectinib directly caused the abnormalities in proliferation-related signaling pathway like PI3K-AKT pathway, and apoptosis-related signaling pathway including TGF-β pathway. We further demonstrated that THBS1, TGF-β1, PI3K, AKT and p-AKT were downregulated by entrectinib. Meanwhile, pretreatment with THBS1 overexpression plasmids significantly rescued nerve cells (PC12, HT22 and SK-N-SH) from cell death and the abnormalities in PI3K-AKT and TGF-β signaling pathways.

Conclusion: These results identified a critical role of entrectinib in promoting nerve cell damage by downregulating the expression of THBS1 while also inhibiting PI3K-AKT and TGF-β signaling pathways. Our findings will provide potential therapeutic targets for CNS-related toxicities.

KEYWORDS

entrectinib, nerve cell damage, THBS1, Pi3k-akt, TGF-β

1 Introduction

In recent years, cancer has become the leading cause of mortality worldwide. The increasing burden of cancer has become a challenging major public health problem (Tu et al., 2016; Jassim et al., 2023). Conventionally, there are three therapeutic modalities of cancer treatment such as surgical treatment, radiotherapy, and chemical drug therapy (Zheng et al., 2018; Yang et al., 2022). Nevertheless, the systemic toxicity associated with above therapies pose a significant challenge to patient tolerance and compliance (Mun et al., 2018). With the development and application of genetic testing in clinical treatment, molecular-targeting therapy has drawn widespread concern, bringing further options for clinical application (Bhamidipati and Subbiah, 2023; Li et al., 2023). Currently, targeted therapy has been an indispensable alternation to manage the disease for numerous cancers with oncogene addiction (Yuan et al., 2019; Benitez et al., 2021).

Entrectinib is an orally active small-molecule, which targets tyrosine kinase inhibitor of neurotrophic tyrosine receptor kinase (NTRK), ROS1 and anaplastic lymphoma kinase (ALK) genes. As the first-generation tyrosine receptor kinase inhibitor (TRKi), it is approved for the treatment of patients with NTRK fusion-positive solid tumors and adults with ROS1 fusion-positive non-small cell lung cancer (Frampton, 2021; Desai et al., 2022). Despite its impressive efficacy against cancer, the serious toxicities on the central nervous system (CNS) have also been popularly concerned by the public during the course of cancer therapy (Marcus et al., 2021). For example, the overall incidence of fatigue was 45%, taste disturbance was 42.3%, dysesthesia was 29.0%, cognitive impairment was 24.2% and peripheral sensory neuropathies was 18%. These symptoms not only significantly reduce the patient's quality of life but also pose substantial challenges in the management of treatment, and even result in treatment interruptions (Trendowski et al., 2019; Doebele et al., 2020; Frampton, 2021; Martineau et al., 2022). Nowadays, these clinical CNS-related toxicities were only addressed through dose modification and interruptions, even withdrawal of entrectinib (Marcus et al., 2021). Unfortunately, there has been no effective protocols available for relieving or treating these symptoms until now. Thus, it is crucial to illuminate the molecular mechanism underlying CNS-related toxicities.

Research indicated that the tropomyosin receptor kinases (TRK) protein, a member of the tyrosine kinase family, plays a critical role in modulating neuronal activity and axonal growth in both the central and peripheral nervous systems (Aydin-Abidin and Abidin, 2019; Jiang et al., 2021). Acting as a tyrosine receptor kinase inhibitor (TRKi), entrectinib can inhibit TRK, thus leading to on-target neurotoxicity (Giustini et al., 2022). Some chemotherapy drugs can lead to chemotherapy-induced peripheral neuropathy which is involved in nerve damage and axon loss (Fumagalli et al., 2020; Chen et al., 2024). Several factors, such as mitochondrial dysfunction, oxidative stress, microcirculation disturbance and neuroinflammation have been proposed as determinants of neurotoxicity (Staff et al., 2017; Wang et al., 2023; Chen et al., 2024). Evidence indicated that isoflurane could induce hippocampal cells apoptosis by inhibiting PI3K-AKT expression (Wang et al., 2016). However, due to the complexity of CNS-related toxicities, the mechanisms underlying entrectinib-induced neurotoxicity are not fully understood.

In this study, we aim to evaluate whether entrectinib could induce nerve cell damage *in vitro* model. The potential mechanism responsible for entrectinib-induced nerve cell damage will be investigated as well. Furthermore, this finding will offer important insights and potential therapeutic targets for the entrectinib-induced nerve cell damage.

2 Materials and methods

2.1 Cell line and cell culture

The rat adrenal pheochromocytoma cells PC12 (FH0415), mouse hippocampal neuron cells HT22 (FH1027) and human neuroblastoma cells SK-N-SH (FH0164) were purchased from Shanghai Fuheng Biotechnology Co., Ltd. (Shanghai, China). PC12 cells were cultured in RPMI-1640 medium (KGM31800, KeyGEN, Nanjing, China) supplemented with 10% fetal bovine serum (FBS, A6901FBS, Invigentech, United States) and 1% penicillin and streptomycin (C0222, Beyotime, Shanghai, China). HT22 and SK-N-SH cells were cultured in DMEM medium (KGM12800, KeyGEN, Nanjing, China) with 10% FBS and 1% penicillin and streptomycin. All cells were incubated in a 37°C with 5% CO_2 atmosphere.

2.2 Reagent and antibody

Entrectinib (HY-12678) was obtained from MedChemExpress (MCE, Shanghai, China) with the purity of 99.87%. THBS1 overexpression plasmids were synthesized by Corues Biotchnology (Nanjing, China). The relevant materials used in this study were provided as following: EnoGeneCell Counting Kit-8 (CCK-8, E1CK-000208, EnoGene, Nanjing, China), BeyoClick™ EdU-555 cell proliferation detection kit (C0075S, Beyotime, Shanghai, China), Annexin V-FITC/PI apoptosis detection kit (KGA107, KeyGEN, Nanjing, China), 4% paraformaldehyde (PFA, BL539A, Biosharp, Hefei, China), crystal violet (C0121, Beyotime, Shanghai, China), Trizol (R0016, Beyotime, Shanghai, China), Freezol reagent (R711-01, Vazyme, Nanjing, China), Evo M-MLV RT mix kit (AG11728,

Accurate, Changsha, China), AceQ Universal SYBR qPCR master mix (Q511-02, Vazyme, Nanjing, China), BCA protein assay kit (P0010, Beyotime, Shanghai, China), RIPA (P00138, Beyotime, Shanghai, China), ECL detection reagent (180-501, Tanon, Shanghai, China), lipofectamine 3000 transfection reagent (L3000015, Invitrogen, United States).

The antibodies used in Western blotting assay were obtained as following: THBS1 (1:1,000, 18304-1-AP, Proteintech, Wuhan, China), PI3K (1:600, 20584-1-AP, Proteintech, Wuhan, China), AKT (1:5,000, 60203-2-AP, Proteintech, Wuhan, China), p-AKT (1:2,000, 4060T, Cell signaling technology, United States), TGF-β (1:3,000, 21898-1-AP, Proteintech, Wuhan, China), GAPDH (1:60,000, 60004-1-Ig, Proteintech, Wuhan, China), HRP-conjugated affinipure goat anti-rabbit IgG (1:5,000, SA00001-2, Proteintech, Wuhan, China) and HRP-conjugated affinipure goat anti-mouse IgG (1:4,000, SA00001-1, Proteintech, Wuhan, China).

2.3 Cells model establishment and treatment

To establish entrectinib activated cells, nerve cells (PC12, HT22 and SK-N-SH) were treated with entrectinib for 48 h at the concentrations of 0, 0.5, 1, 2, 5, 10, and 20 μmol/L, respectively. To explore whether entrectinib influences the cellular proliferation ability and apoptosis, we employed entrectinib (2.3, 4.2 and 4.3 μmol/L, respectively) to the PC12, HT22 and SK-N-SH cells for 48 h. To observe the effect of THBS1 on entrectinib activated cells, nerve cells were divided into five groups: the normal control (NC), the overexpression (OE) group transfected with THBS1 overexpression plasmids, the entrectinib group exposed to entrectinib (2.3, 4.2 and 4.3 μmol/L, respectively), the NC + entrectinib group and the THBS1 overexpression group cultured in medium containing entrectinib (2.3, 4.2 and 4.3 μmol/L, respectively) for 48 h.

2.4 CCK-8 assay

PC12, HT22 and SK-N-SH cells were plated in 96-well plates at a density of 7×10^3 cells per well and incubated for 24 h. Subsequently, PC12, HT22 and SK-N-SH cells were treated with entrectinib and THBS1 overexpression plasmids for 48 h described above. After incubation, 10 μL CCK-8 solution was added into each well and incubated at 37°C for 2 h in the dark. Then, a microplate reader (Molecular Devices, Shanghai, China) was used to measure the absorbance at a wavelength of 450 nm.

2.5 EdU incorporation assay

PC12, HT22 and SK-N-SH cells were seeded into 24-well plates at a density of 3×10^4 cells per well and treated with entrectinib for 48 h. BeyoClick™ EdU-555 cell proliferation detection kit was used for the subsequent experiments. In brief, 20 μmol/L EdU was added into per well for 4 h. Hoechst 33342 was used to stain the nuclei for 10 min in the dark. Next, images were randomly captured by a fluorescence inverted microscope (Zeiss, Germany). Finally, ImageJ was utilized to count the total cell and proliferating cell numbers.

2.6 Colony formation assay

In six-well plates, PC12, HT22, SK-N-SH cells were cultured at a density of about 7×10^2 cells per well and then treated with entrectinib. The cultures were maintained for 14 days or until the number of single-cell clones exceeded 50. After rinsing with phosphate buffered saline (PBS), cells were fixed with 4% paraformaldehyde solution for 30 min. Next, 0.5% crystal violet solution was stained for 15 min. Finally, cells were washed several times with PBS and captured by a camera.

2.7 Flow cytometry analysis

PC12, HT22 and SK-N-SH cells were seeded into 6-well plates and treated with entrectinib and THBS1 overexpression plasmids for 48 h described above. Then, the treated cells were collected and stained with Annexin V-FITC and PI staining solution for 10 min. Following the recommendations of the manufacturer, the cells were analyzed by flow cytometry (BD Biosciences, United States) within 1 h. Data were analyzed by Flowjo software (v.10.8.1).

2.8 Gene differential expression analysis

PC12, HT22 and SK-N-SH cells were treated with entrectinib, respectively. After 48 h incubation, the total RNA was extracted by Trizol reagent and sequenced in Beijing Biomarker Technology Co., LTD. (Beijing, China). Briefly, according to the manufacturer's instructions, the sequencing library was generated by Hieff NGS ultima dual-mode mRNA library prep kit (Yeasen, Shanghai, China). The libraries were quantified preliminarily with Qubit 3.0 fluorescence quantitative analyzer and sequenced on an Illumina novaseq platform to generate 150 bp paired-end reads. Clean data were obtained by removing reads containing adapter, ploy-N and low-quality from raw data. The analysis of differentially expressed genes (DEGs) between PC12 and HT22 cells was performed by DESeq2 software (Love et al., 2014), while SK-N-SH cells were analyzed by edgeR software (Robinson et al., 2010). Genes with a statistical threshold of false discovery rate (FDR) < 0.05 and |fold change| > 2 were considered to be significantly differentially expressed. Volcano plots, a visualized plots to illustrate DEGs, were generated by bioinformatics software available at https://www.bioinformatics.com.cn/.

2.9 Gene ontology (GO) and kyoto encyclopedia of genes and genomes (KEGG) analysis

Functional enrichment analyses of GO (Ashburner et al., 2000) and KEGG (Kanehisa et al., 2014) in DEGs from PC12 and HT22 cells were performed by the R package

ClusterProfiler (v.4.6.2) (Yu et al., 2012). The R package ggplot2 (v.3.4.1) was utilized to visualize and screen biological functions and pathways associated with these DEGs. Enriched GO terms and KEGG pathways were presented to illustrate the analytical outcomes.

2.10 Gene set enrichment analysis (GSEA) analysis

GSEA software (v.4.3.2) (Subramanian et al., 2005) was performed to investigate functional enrichment pathways and landmark gene sets in gene expression datasets. Signature gene sets were extracted from the Molecular Signatures Database (MSigDB, available at https://www.gsea-msigdb.org). Enrichment results were considered significant if the normalized enrichment score (NES) > 1 and the nominal $P < 0.05$ in the entrectinib treatment.

2.11 RNA extraction and quantitative real time polymerase chain reaction (qRT-PCR)

According to the manufacturer's recommendations, total cellular RNA was extracted by Freezol reagent and reverse-transcribed into cDNA by the Evo M-MLV RT mix kit. The AceQ universal SYBR qPCR master mix kit was used for quantitative real-time PCR. The β-actin was served as the internal control. The expression of the target gene was calculated by the $2^{-\Delta\Delta CT}$ method. Primers used in this study were synthesized by Invitrogen Biotechnology Co., Ltd. (Invitrogen, United States), and their sequences were provided in Supplementary Table S1.

2.12 Western blotting assay

Total protein from cells was extracted through RIPA lysate with a mixture of phosphatase inhibitor and protease inhibitor. The concentration of extracted proteins was quantified through BCA protein assay kit. The protein samples were separated through 10% sodium dodecyl sulfate polyacrylamide gel electrophoresis (SDS-PAGE) and transferred to PVDF membranes. After blocking with 5% skim milk for 2 h, the PVDF membranes were incubated with the primary antibody overnight at 4°C. Subsequently, membranes were incubated with the corresponding secondary antibody and visualized by an enhanced chemiluminescence (ECL) reagent. Protein band intensities were analyzed by ImageJ software.

2.13 Statistical analysis

All experiments were conducted at least in triplicate to ensure reliability. Statistical analysis and graphical representation were carried out by GraphPad Prism (v.9.0). Differences in quantitative variables between two groups were assessed by the t-test, while differences among three or more groups were evaluated by one-way analysis of variance (ANOVA). $P < 0.05$ was considered as statistical significance.

3 Results

3.1 Entrectinib significantly inhibited the viability of nerve cells (PC12, HT22 and SK-N-SH)

Initially, the nerve cells (PC12, HT22 and SK-N-SH) were subjected to various concentrations of entrectinib (0, 0.5, 1, 2, 5, 10, and 20 μmol/L) for 48 h, and the impact of entrectinib on nerve cells viability was assessed by the CCK-8 assay. The results indicated that entrectinib significantly inhibited nerve cells viability compared with the control group, displaying a clear dose-dependent reduction trend (Figures 1A, C, E). Subsequently, the IC_{50} of entrectinib in PC12, HT22 and SK-N-SH cells was calculated as 2.3 μmol/L, 4.2 μmol/L, and 4.3 μmol/L, respectively (Figures 1B, D, F). Thus, the IC_{50} entrectinib incubation was selected for subsequent experiments. Collectively, these results preliminarily indicated that entrectinib showed an inhibitory effect on the nerve cells viability.

3.2 Entrectinib significantly inhibited nerve cells proliferation

To further investigate entrectinib's impact on nerve cell proliferation, we performed colony formation and EdU incorporation assays. As shown in Figures 2A–C, the relative colony number of nerve cells (PC12, HT22, SK-N-SH) was significantly decreased to 49.65%, 54.34%, and 50.21% after entrectinib treatment. In addition, EdU incorporation assay demonstrated that the red fluorescence had a notable reduction in the treatment of entrectinib, indicating that entrectinib could inhibit the replicative capacity of nerve cells (Figures 2D–F). These findings confirmed that entrectinib significantly inhibited the proliferation ability of nerve cells.

3.3 Entrectinib could induce nerve cells apoptosis

Moreover, Annexin V-FITC/PI apoptosis detection kit was employed to further explore the impact of entrectinib on nerve cells apoptosis. PC12, HT22 and SK-N-SH cells were treated with entrectinib of 2.3 μmol/L, 4.2 μmol/L and 4.3 μmol/L, respectively, and the apoptosis rate was significantly increased to 12.52%, 14.83% and 15.84% (Figures 3A–D). Taken together, these results indicated that entrectinib could significantly inhibit the viability and induce apoptosis within the nerve cells.

3.4 Identification of DEGs in PC12, HT22 and SK-N-SH cells

To further explore the impact of entrectinib on nerve cells transcription levels, we employed high-throughput sequencing technology on the entrectinib-treated nerve cells (PC12, HT22 and SK-N-SH) samples. Differential expression analysis revealed that 413, 338, and 481 DEGs were in PC12, HT22 and

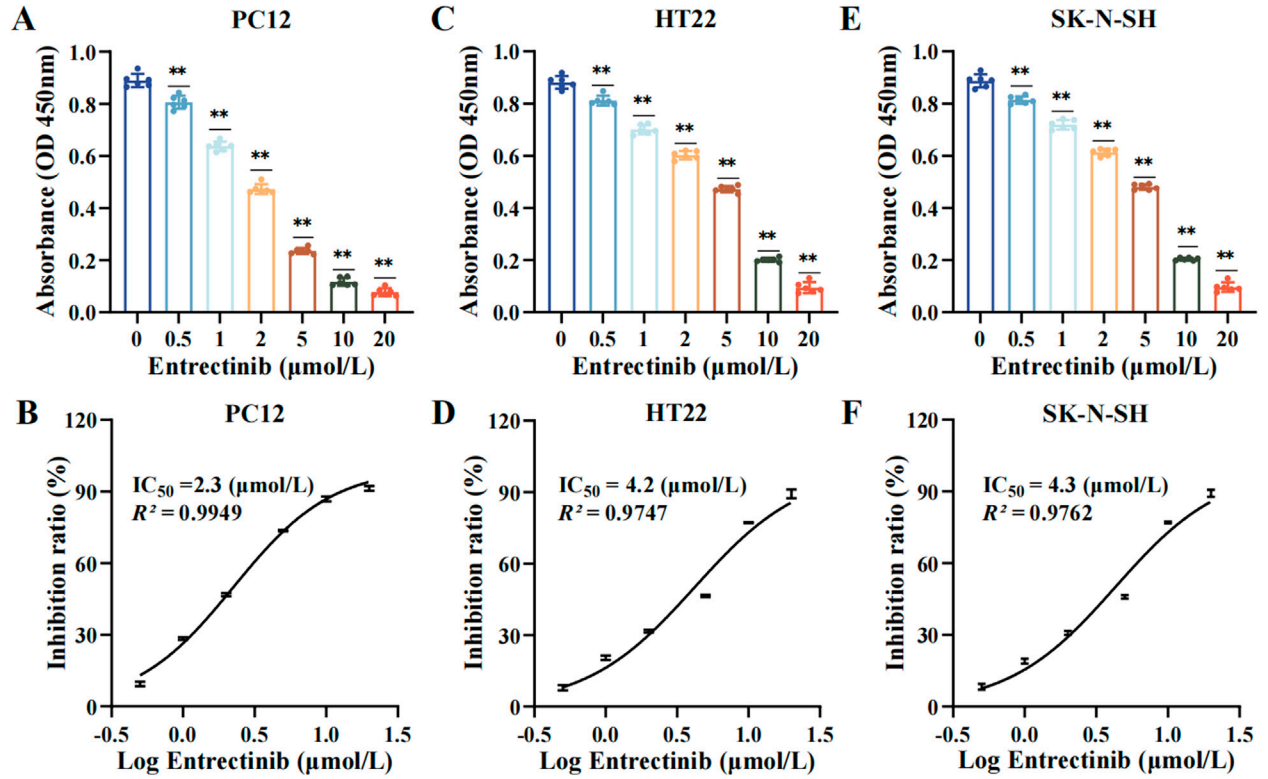

FIGURE 1
Entrectinib significantly inhibited nerve cells viability. **(A, C, E)** The absorbance of PC12, HT22 and SK-N-SH cells was subjected to the CCK-8 assay after treatment with entrectinib (0, 0.5, 1, 2, 5, 10, and 20 μmol/L). Data are shown as mean ± SD, $n = 6$ (**$P < 0.01$). **(B, D, F)** The IC_{50} value of PC12, HT22 and SK-N-SH cells was calculated by GraphPad Prism (v.9.0). Data are shown as mean ± SD, $n = 6$.

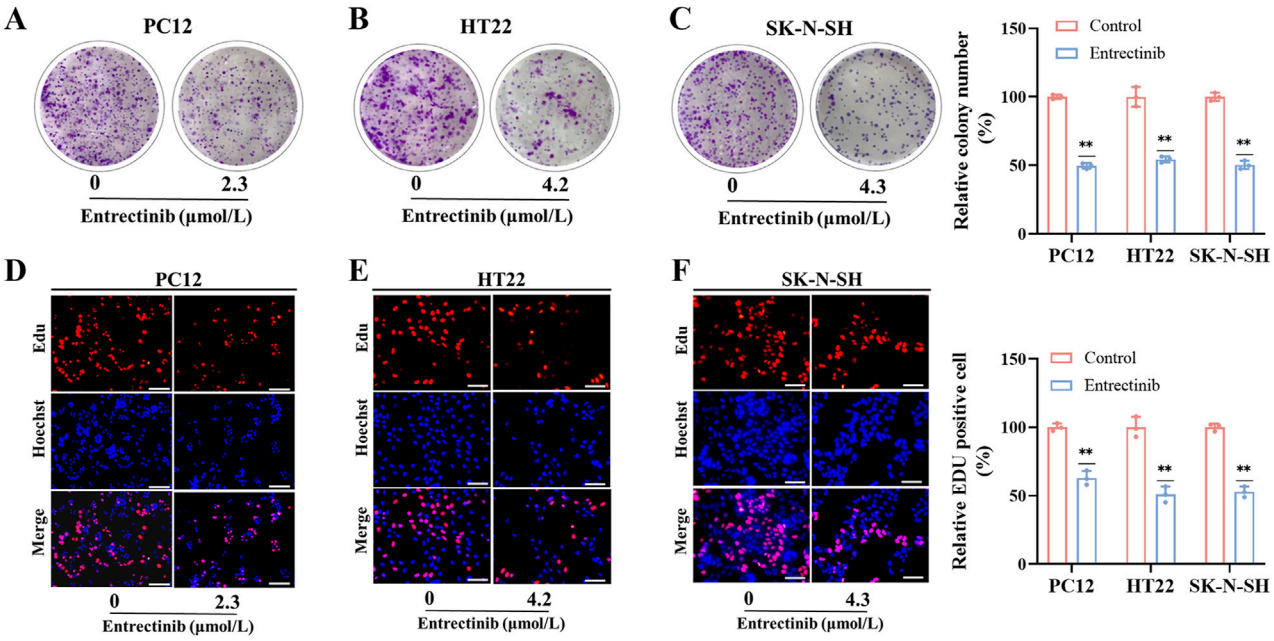

FIGURE 2
Entrectinib inhibited nerve cells proliferation. **(A–C)** PC12, HT22 and SK-N-SH cells treated with entrectinib (2.3, 4.2, and 4.3 μmol/L, respectively) were seeded into 6-plate wells, and the number of colonies was counted on the 14 days. The results are also shown in the bar chart. Data are shown as mean ± SD, $n = 3$ (**$P < 0.01$). **(D–F)** EdU incorporation assay was performed to determine the nerve cells proliferation ability of PC12, HT22 and SK-N-SH cells treated with entrectinib (2.3, 4.2, and 4.3 μmol/L, respectively), and the results are also shown in the bar chart. Scale bar = 40 μm. Data are shown as mean ± SD, $n = 3$ (**$P < 0.01$).

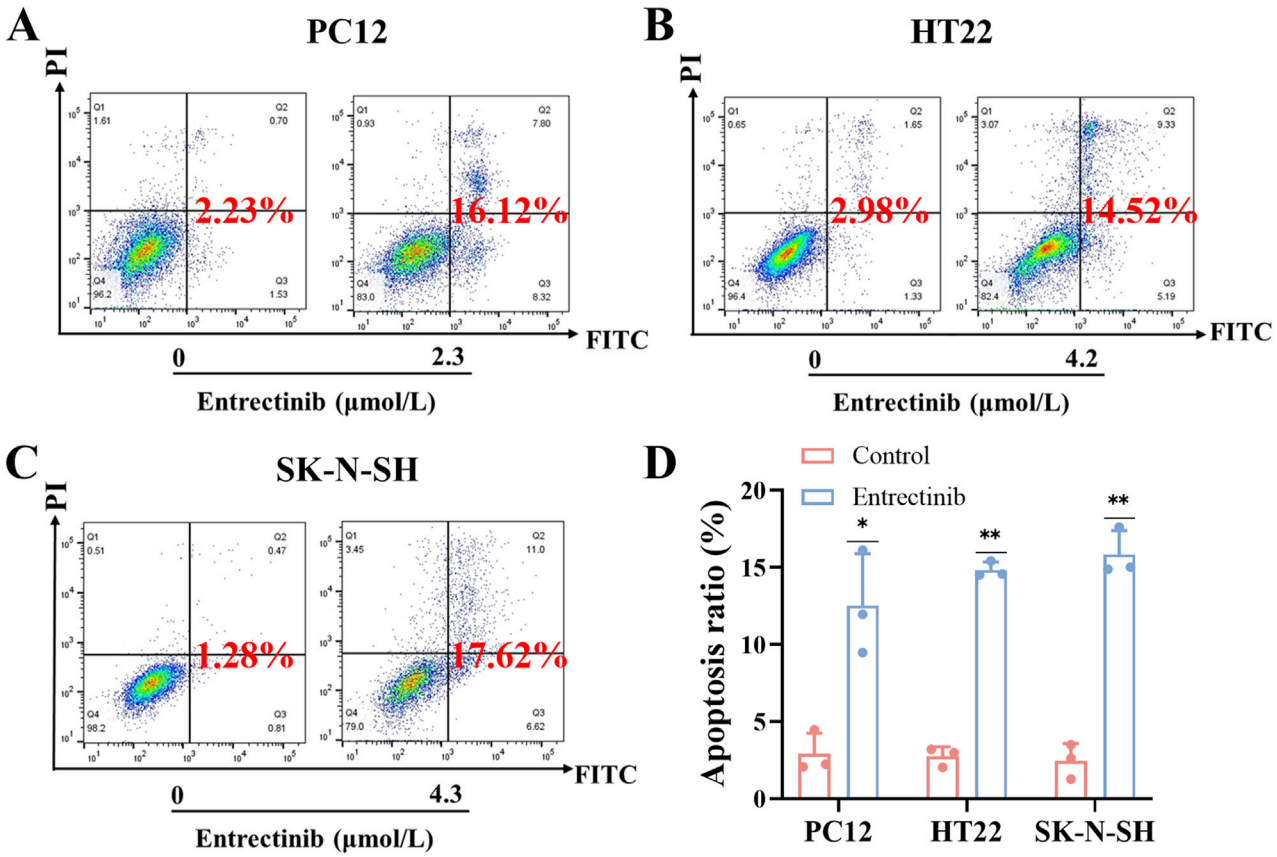

FIGURE 3
Entrectinib induced nerve cells apoptosis. **(A–C)** The effect of entrectinib on nerve cells (PC12, HT22 and SK-N-SH) apoptosis was measured by flow cytometry analysis. **(D)** Quantitative mean apoptosis ratio of **(A–C)**. Data are shown as mean ± SD, $n = 3$ (**$P < 0.01$).

SK-N-SH cells, respectively (Figures 4A–C; Supplementary Table S2). We then determined the intersection of DEGs present in the nerve cells, where 4 DEGs (FTL1, THBS1, FTL1-PS1, COL3A1) were intersected (Figure 4D). Notably, thrombospondin-1 (THBS1) was significantly downregulated in entrectinib treatment, implying that it might be involved in nerve cell damage (Figure 4E). These findings confirmed that entrectinib could induce extensive transcriptomic changes, and THBS1 was the most significant.

3.5 Exploration the functions and pathways of DEGs

Next, we conducted GO and KEGG pathway enrichment analyses to uncover the biological functions and pathways associated with DEGs. GO results revealed that DEGs were involved in biological processes including peptide cross-linking and epithelial cell proliferation regulation. Meanwhile, it also showed the relationship with cellular components and molecular functions, such as extracellular matrix, transcription repressor complex, growth factor activity and extracellular matrix binding (Figure 5A; Supplementary Table S3). Futhermore, KEGG analysis implicated that DEGs were enriched in pathways such as PI3K-AKT signaling pathway, TGF-β signaling pathway and p53 signaling pathway, et al. (Figure 5B; Supplementary Table S4). Similarly, GSEA was also performed across hallmark gene sets to identify potential signatures of response. The results showed that PI3K-AKT-mTOR signaling pathway, TGF-β signaling pathway and p53 signaling pathway (Figure 5C; Supplementary Table S5) were enriched in entrectinib treatment. The above results suggested that the entrectinib-induced nerve cell damage may be related to the PI3K-AKT-mTOR signaling pathway, p53 signaling pathway and TGF-β signaling pathway.

3.6 Entrectinib could downregulate THBS1 expression while also inhibiting PI3K-AKT and TGF-β signaling pathways

To validate the transcriptome sequencing analysis results, we further performed qRT-PCR and Western blotting assays. Compared with the control group, the expression of THBS1 was significantly decreased after entrectinib treatment within the nerve cells (Figures 6A, B), which was in parallel with sequencing results. Additionally, the levels of relative proteins involved in PI3K-AKT and TGF-β signaling pathways were examined as well. Obviously, entrectinib could downregulate the expressions of PI3K, AKT,

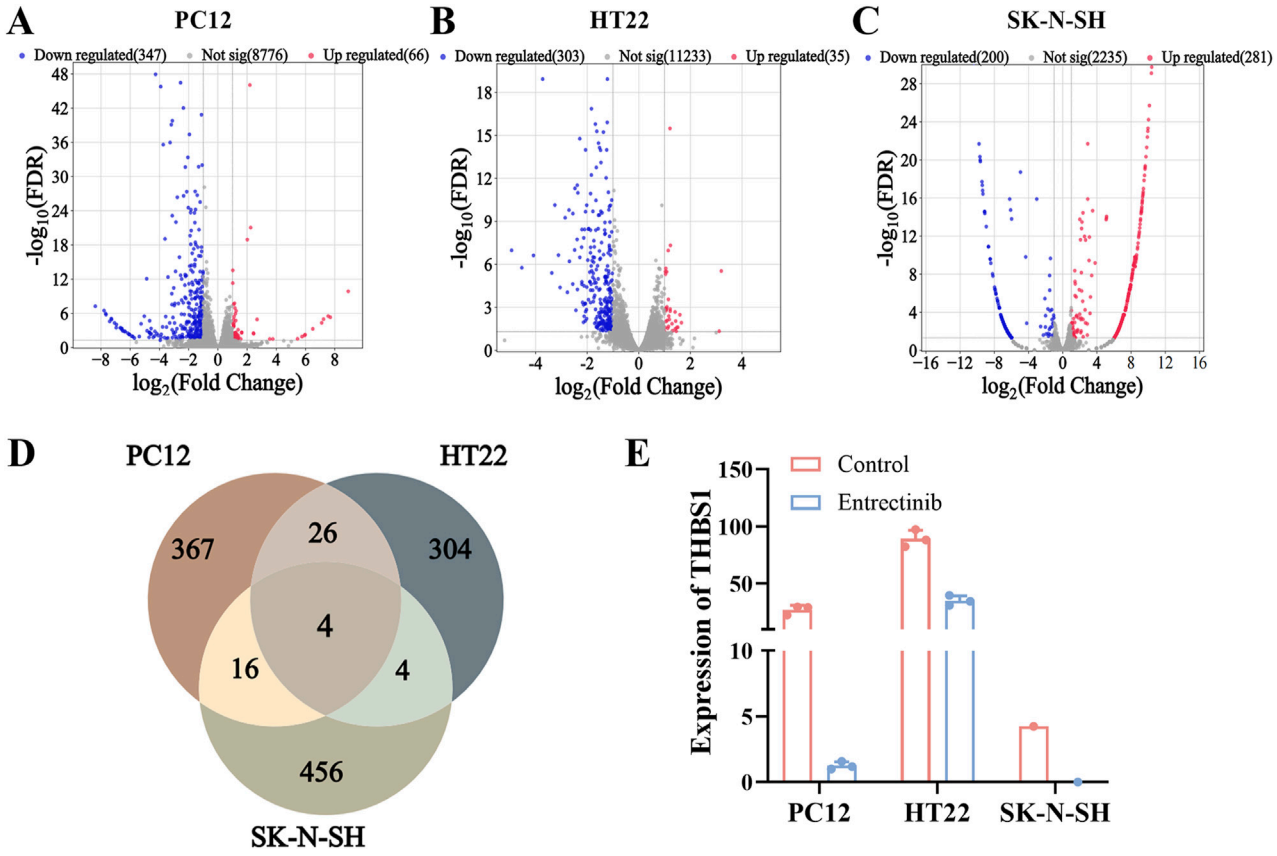

FIGURE 4
Transcriptome sequencing analyses identified THBS1 target involved in nerve cell damage. **(A–C)** The DEGs of PC12, HT22 and SK-N-SH cells were presented in the form of volcano plot, where red represents upregulated genes, blue represents downregulated genes, and gray represents genes with insignificant differences (Set threshold FDR < 0.05 and |fold change| > 2). **(D)** Venn diagram was performed to illustrate overlap between DEGs by PC12, HT22 and SK-N-SH cells. **(E)** The expression of THBS1 was identified by transcriptome sequencing analyses.

phosphorylated AKT (p-AKT) and TGF-β1 proteins within the nerve cells (PC12, HT22 and SK-N-SH) (Figures 6B–C). Therefore, these results demonstrated that entrectinib could downregulate THBS1 expression while also inhibiting PI3K-AKT and TGF-β signaling pathways.

3.7 THBS1 overexpression could rescue nerve cell damage induced by entrectinib and activate PI3K-AKT and TGF-β signaling pathways

To preliminary observe and validate whether THBS1 overexpression could rescue nerve cell damage and the abnormalities in PI3K-AKT and TGF-β signaling pathways, nerve cells were transfected with THBS1 overexpression plasmids. As shown in Figures 7A–E, THBS1 overexpression can rescue nerve cell damage induced by entrectinib. Additionally, the expressions of PI3K, AKT, phosphorylated AKT (p-AKT) and TGF-β1 proteins were also upregulated by THBS1 overexpression in the entrectinib-treated cells (Figures 7F–H). These above results suggested that THBS1 plays an important functional role in rescuing nerve cell damage and the abnormalities in the PI3K-AKT and TGF-β signaling pathways induced by entrectinib.

4 Discussions

Entrectinib, a novel multi-target TRKi, has demonstrated considerable therapeutic efficacy in tumors harboring NTRK, ROS1 or ALK gene fusions (Desai et al., 2022). It can penetrate the blood-brain barrier and exhibit CNS activity, underscoring its potential in treating brain tumors (Liu et al., 2018; Desai et al., 2022; Jiang et al., 2022). However, bulk evidences suggest that entrectinib can cause serious neurotoxicity following prolonged application, such as sensory neuropathy and peripheral neuropathy (Delgado et al., 2021; Giustini et al., 2022). However, the underlying mechanism of entrectinib-induced neurotoxicity remains elusive.

In this study, we investigated the effects of entrectinib on PC12, HT22 and SK-N-SH cells *in vitro*, focusing on its impact on the proliferation and apoptosis of nerve cells. Initially, a CCK-8 assay was carried out to determine cellular viability, we demonstrated that entrectinib inhibited the cell viability in a dose-dependent trend. Furthermore, EdU incorporation and colony formation assays were used to analyze the nerve cells proliferation. We also observed a

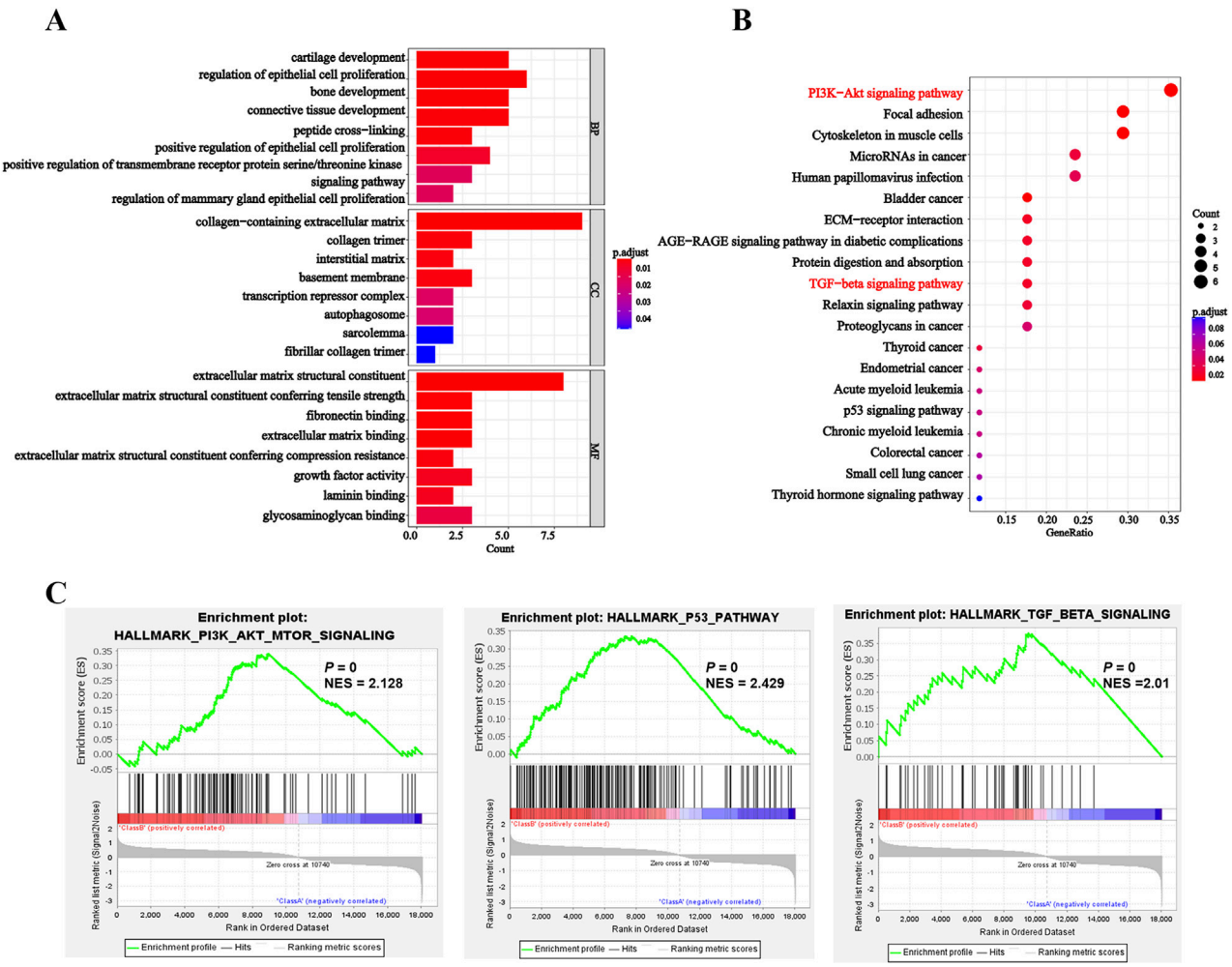

FIGURE 5
Entrectinib induced the nerve cell damage by affecting the PI3K-AKT-mTOR signaling pathway, p53 signaling pathway and TGF-β signaling pathway. **(A, B)** The R package ClusterProfiler (v.4.6.2) was used for clustering analysis of potential targets and pathways of entrectinib-induced nerve cell damage. Histogram and bubble plots showed the results of GO and KEGG enrichment analysis. **(C)** GSEA of hallmark gene sets between control groups and entrectinib-treated groups.

significant inhibition of cell proliferation and clonogenic potential after entrectinib administration, confirming its anti-proliferative effects *in vitro*. Flow cytometry analysis further demonstrated that entrectinib effectively increased the apoptosis ratio of nerve cells. Taken together, these results indicated that entrectinib could significantly inhibit proliferation ability and induce apoptosis within the nerve cells.

Subsequently, transcriptome sequencing was performed to explore the gene expression changes of entrectinib-treated nerve cells. The transcriptome sequencing analysis identified THBS1 was intersected by PC12, HT22 and SK-N-SH cells, and it showed a downregulated trend. THBS1 belongs to adhesion glycoprotein, which plays a pivotal role in mediating cell-cell and cell-matrix interactions (Huang et al., 2017; Yao et al., 2023). THBS1, first discovered in platelets, but now many studies indicate that it plays a crucial role in the development of diseases (Firlej et al., 2011). Moreover, THBS1 is also involved in the physiological and pathological processes of the nervous system and indispensable for axon regeneration (Bray et al., 2019; Yao et al., 2023). Therefore, we further examined the expression of THBS1 within entrectinib treatment. The results revealed that the expression of THBS1 was significantly decreased by entrectinib, which was in parallel with sequencing results. In addition, THBS1 overexpression rescued entrectinib-induced nerve cell damage. Collectively, these results indicated that entrectinib-induced nerve cell damage may be related to the downregulation of THBS1.

KEGG and GSEA analysis results revealed that the PI3K-AKT and TGF-β signaling pathways were significantly enriched in entrectinib treatment. The PI3K-AKT signaling pathway plays an important role in intracellular signal transduction and regulates diverse cellular processes including cell cycle, adhesion, migration, inflammation, metabolism and survival (Jafari et al., 2019; Xiao et al., 2022). In addition, the PI3K-AKT signaling pathway also exerts profound influence on nervous system physiology, governing processes such as myelin formation (Gaesser and Fyffe-Maricich, 2016), axon regeneration (Huang et al., 2019), nerve cell regeneration (Luo et al., 2019) and apoptosis (Wang et al., 2022; Kilic et al., 2017; Lu et al., 2022). It was reported that PI3K-AKT

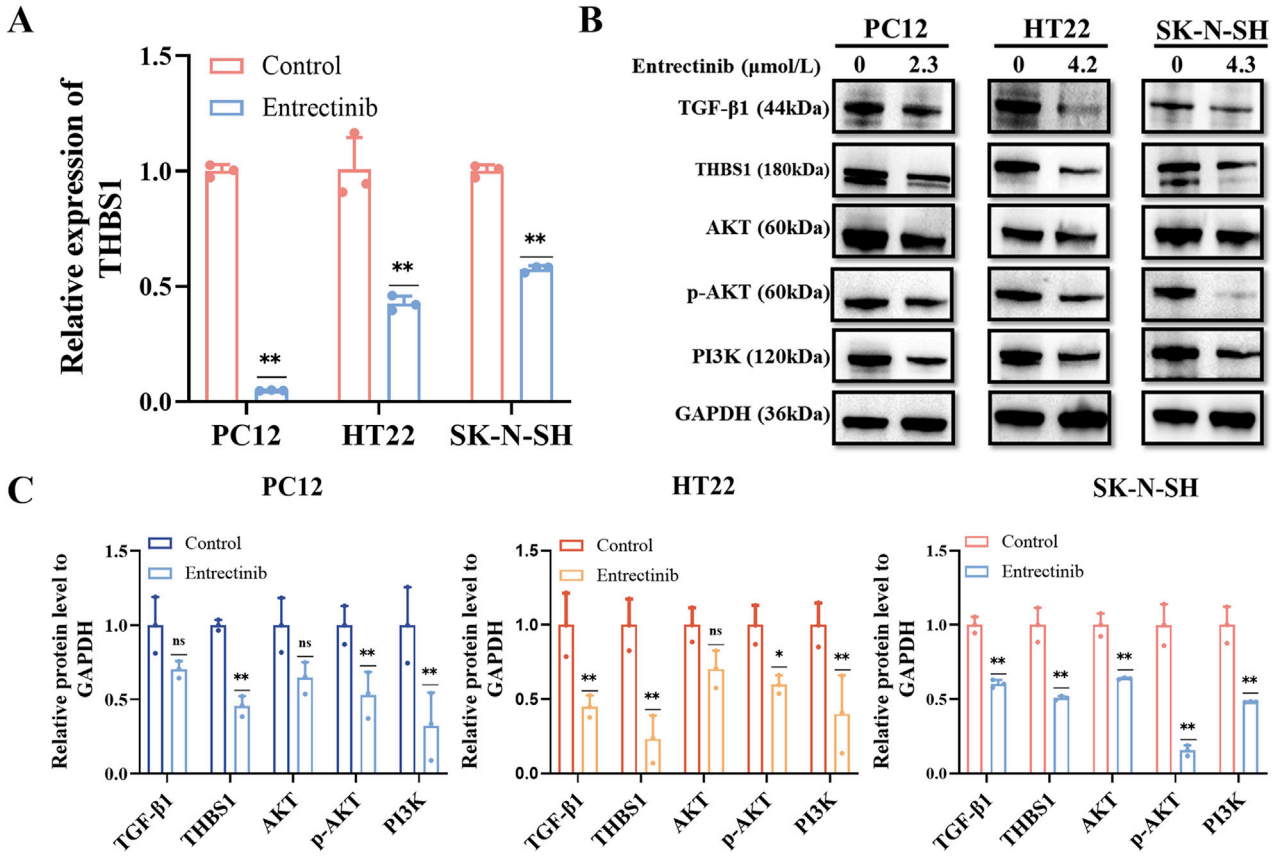

FIGURE 6
Entrectinib downregulated THBS1 expression while also inhibiting PI3K-AKT and TGF-β signaling pathways. **(A)** The expression of THBS1 in PC12, HT22 and SK-N-SH cells treated with entrectinib was detected by qRT-PCR. Data are shown as mean ± SD, $n = 3$ (**$P < 0.01$). **(B)** The expressions of PI3K, AKT, p-AKT, TGF-β and THBS1 proteins in PC12, HT22, SK-N-SH cells treated with entrectinib were detected by Western blotting assay. **(C)** The quantitative analyses of TGF-β1, THBS1, AKT, p-AKT and PI3K proteins in **(B)** are shown. Data are shown as mean ± SD, $n = 3$ (*$P < 0.05$, **$P < 0.01$).

signaling pathway could regulate neurotoxicity and mediate the survival of neurons (Goyal et al., 2023). Receptor tyrosine kinase (RTK), serving as principal upstream regulator of the PI3K-AKT pathway, modulated AKT activity through activating PI3K (Haddadi et al., 2018; Rai et al., 2019). It is worth noting that PI3K, as a crucial anti-apoptotic regulator, triggers the activation of its downstream target AKT upon its activation. Phosphorylation of transmembrane receptors such as RTK can lead to the activation of PI3K and p-AKT, thus activating neuroprotective effects (Griffin et al., 2005; Wang et al., 2022). Therefore, Western blotting assay was performed to examine the protein levels of PI3K, AKT and p-AKT within entrectinib treatment, we found that entrectinib could downregulate the levels of these proteins. Moreover, THBS1 overexpression can rescue the levels of relative proteins involved in PI3K-AKT signaling pathways in the entrectinib-treated nerve cells (PC12, HT22 and SK-N-SH). Thus, the reduction of the PI3K-AKT signaling pathway caused by THBS1 inhibition may be related to the entrectinib-induced nerve cell damage.

As we all known, THBS1 is a potential upstream target with TGF-β signaling pathway (Sun et al., 2022). TGF-β is a multifunctional peptide that governs the diverse cellular processes like cell proliferation, differentiation, death and migration (Jakowlew, 2006; Hata and Chen, 2016; Deng et al., 2024; Giarratana et al., 2024). TGF-β signaling pathway is also involved in neurotrophic signaling transmission and is closely related to the normal development and function of nerves (Meyers and Kessler, 2017; Ding et al., 2024). Brionne et al. (2003) research showed that the downregulation of TGF-β1 in primary neurons resulted in a strong reduction of survival. In addition, TGF-β1 heterozygous knockout mice displayed heightened sensitivity to toxic insults. THBS1 serves as a key activator of TGF-β, significantly activates TGF-β1 factor and TGF-β signaling pathway (Atanasova et al., 2019; Bedolla et al., 2024). Additionally, previous publications have reported that TGF-β signaling pathway induced renal injury may be related to the regulation of THBS1 (Sun et al., 2022). Taken together, we conducted qPCR and Western blotting assays to examine the expressions of THBS1 and TGF-β1 within entrectinib treatment. We found that entrectinib significantly downregulated the expressions of THBS1 and TGF-β1. Additionally, THBS1 overexpression can rescue TGF-β1 expression in the entrectinib-treated nerve cells, implicating that the reduction of the TGF-β signaling pathway caused by THBS1 inhibition may be a potential mechanism for the entrectinib-induced nerve cell damage.

10.3389/fphar.2025.1489210

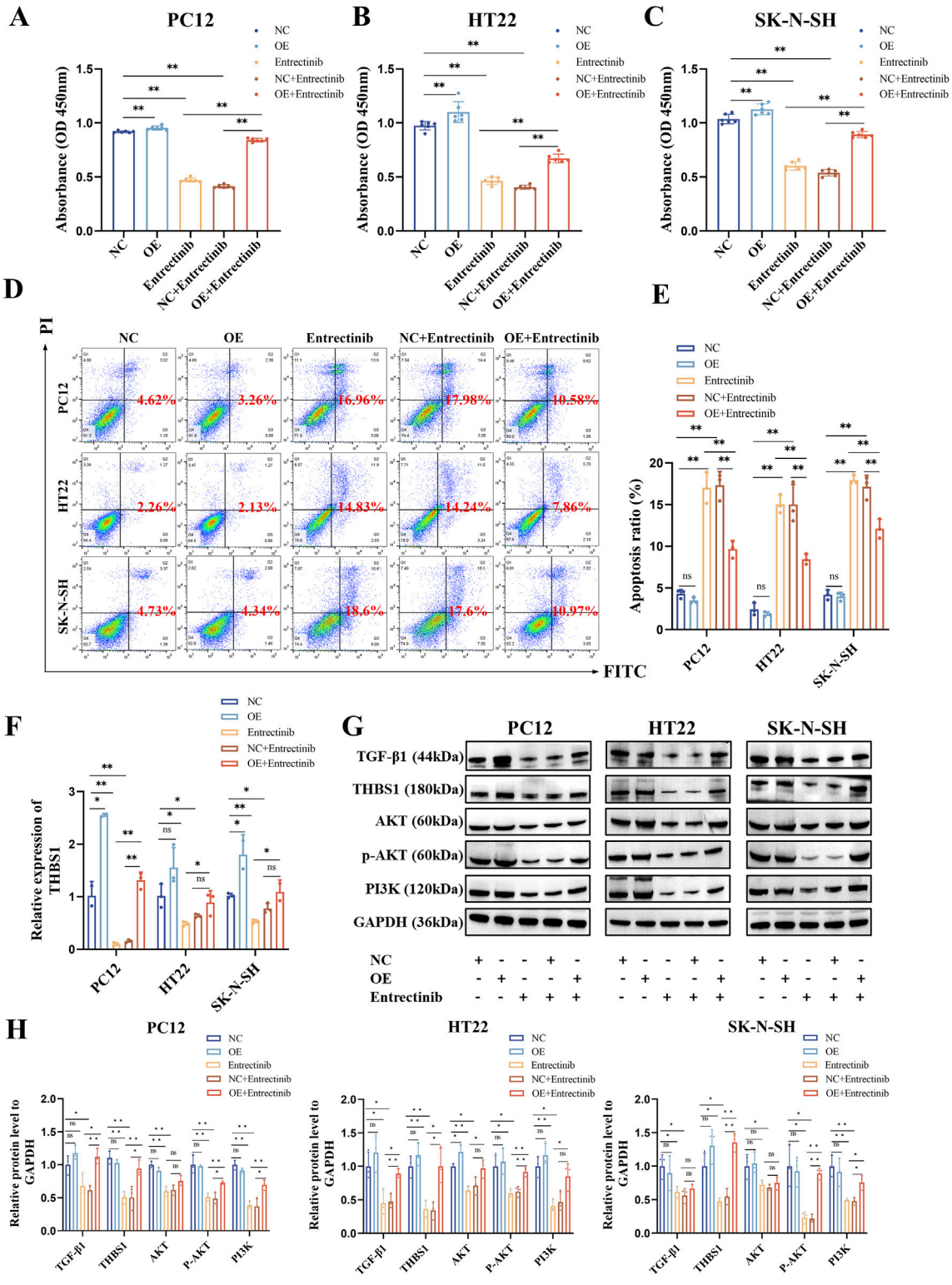

FIGURE 7
THBS1 overexpression rescue nerve cell damage and the abnormalities in the PI3K-AKT and TGF-β signaling pathways induced by entrectinib. **(A–C)** Overexpression of THBS1 in entrectinib-treated cells rescued cell viability. Data are shown as mean ± SD, $n = 6$ (**$P < 0.01$). **(D, E)** Overexpression of THBS1 in entrectinib-treated cells rescued cell apoptosis. Data are shown as mean ± SD, $n = 3$ (**$P < 0.01$). **(F)** qRT-PCR measured the efficiency of THBS1 overexpression. Data are shown as mean ± SD, $n = 3$ (*$P < 0.05$, **$P < 0.01$). **(G)** Western blotting assay examined the levels of PI3K, AKT, p-AKT, TGF-β and THBS1 proteins in PC12, HT22, SK-N-SH cells after treatement with entrectinib or THBS1 overexpression plasmids or the combination for 48 h. **(H)** Representative quantification were shown. Data are shown as mean ± SD, $n = 3$ (*$P < 0.05$, **$P < 0.01$).

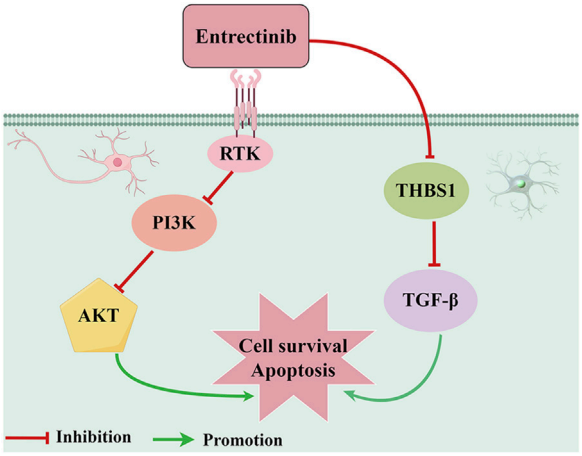

FIGURE 8
Proposed action pathway of entrectinib in inducing nerve cell damage. Entrectinib induced nerve cell damage by downregulating THBS1 expression while also inhibiting PI3K-AKT and TGF-β signaling pathways. The figure was drawn by Figdraw.

5 Conclusion

In conclusion, our findings proposed a putative mechanism whereby entrectinib-induced nerve cell damage may downregulate THBS1 expression while also inhibiting PI3K-AKT and TGF-β signaling pathways (Figure 8). Although our current study offers valuable insights, there still exists some limitations. Due to the limited availability of appropriate animal models, we were unable to investigate the effects of entrectinib on the proteins and gene expression levels within the nerve cells *in vivo*. Thus, future studies should aim to comprehensively illustrate the intricate mechanism based on *in vivo* experiments. In a word, our study contributed important insights into the molecular mechanism underlying entrectinib's neurotoxic effects and proposes potential therapeutic targets.

Data availability statement

The raw data presented in the study are deposited in the Sequence Read Archive (SRA) repository, accession number is PRJNA1219491.

Author contributions

QT: Data curation, Investigation, Writing–original draft. JD: Conceptualization, Writing–original draft. FZ: Writing–original draft, Supervision. DZ: Formal Analysis, Writing–original draft. QY: Methodology, Writing–original draft. JYW: Visualization, Writing–original draft. YS: Software, Writing–original draft. JFW: Funding acquisition, Supervision, Writing–review and editing. ZL: Funding acquisition, Supervision, Writing–review and editing.

Funding

The author(s) declare that financial support was received for the research, authorship, and/or publication of this article. This study was funded by China International Medical Foundation (Z-2021-46-2101-2023 to ZL) and Yishan Research Project of Jiangsu Cancer Hospital (No. YSZD202406 to JW).

Acknowledgments

We acknowledge all authors participating in this study.

Conflict of interest

The authors declare that the research was conducted in the absence of any commercial or financial relationships that could be construed as a potential conflict of interest.

Publisher's note

Supplementary material

The Supplementary Material for this article can be found online at: https://www.frontiersin.org/articles/10.3389/fphar.2025.1489210/full#supplementary-material

SUPPLEMENTARY TABLE S1
The qPCR primers used in this study.

SUPPLEMENTARY TABLE S2
The differentially expressed genes between control groups and entrectinib-treated groups in this study.

SUPPLEMENTARY TABLE S3
The results of GO analysis in this study.

SUPPLEMENTARY TABLE S4
The results of KEGG analysis in this study.

SUPPLEMENTARY TABLE S5
The results of GSEA analysis in this study.

SUPPLEMENTARY TABLE S6
The raw data of transcriptome sequencing in this study.

References

Ashburner, M., Ball, C. A., Blake, J. A., Botstein, D., Butler, H., Cherry, J. M., et al. (2000). Gene ontology: tool for the unification of biology. The Gene Ontology Consortium. *Nat. Genet.* 25 (1), 25–29. doi:10.1038/75556

Atanasova, V. S., Russell, R. J., Webster, T. G., Cao, Q., Agarwal, P., Lim, Y. Z., et al. (2019). Thrombospondin-1 is a major activator of TGF-β signaling in recessive dystrophic epidermolysis bullosa fibroblasts. *J. Invest. Dermatol.* 139 (7), 1497–1505.e5. doi:10.1016/j.jid.2019.01.011

Aydin-Abidin, S., and Abidin, I. (2019). 7,8-Dihydroxyflavone potentiates ongoing epileptiform activity in mice brain slices. *Neurosci. Lett.* 703, 25–31. doi:10.1016/j.neulet.2019.03.013

Bedolla, A., Wegman, E., Weed, M., Stevens, M. K., Ware, K., Paranjpe, A., et al. (2024). Adult microglial TGFβ1 is required for microglia homeostasis via an autocrine mechanism to maintain cognitive function in mice. *Nat. Commun.* 15 (1), 5306. doi:10.1038/s41467-024-49596-0

Benitez, J. C., Geraud, A., Texier, M., Massard, C., Paci, A., Soria, J. C., et al. (2021). Late phase 1 studies: concepts and outcomes. *Lancet Oncol.* 22 (10), e446–e455. doi:10.1016/S1470-2045(21)00467-8

Bhamidipati, D., and Subbiah, V. (2023). Impact of tissue-agnostic approvals for patients with gastrointestinal malignancies. *Trends Cancer* 9 (3), 237–249. doi:10.1016/j.trecan.2022.11.003

Bray, E. R., Yungher, B. J., Levay, K., Ribeiro, M., Dvoryanchikov, G., Ayupe, A. C., et al. (2019). Thrombospondin-1 mediates axon regeneration in retinal ganglion cells. *Neuron* 103 (4), 642–657.e7. doi:10.1016/j.neuron.2019.05.044

Brionne, T. C., Tesseur, I., Masliah, E., and Wyss-Coray, T. (2003). Loss of TGF-beta 1 leads to increased neuronal cell death and microgliosis in mouse brain. *Neuron* 40 (6), 1133–1145. doi:10.1016/s0896-6273(03)00766-9

Chen, X., Gan, Y., Au, N. P. B., and Ma, C. H. E. (2024). Current understanding of the molecular mechanisms of chemotherapy-induced peripheral neuropathy. *Front. Molec. Neurosci.* 17, 1345811. doi:10.3389/fnmol.2024.1345811

Delgado, J., Pean, E., Melchiorri, D., Migali, C., Josephson, F., Enzmann, H., et al. (2021). The European Medicines Agency review of entrectinib for the treatment of adult or paediatric patients with solid tumours who have a neurotrophic tyrosine receptor kinase gene fusions and adult patients with non-small-cell lung cancer harbouring ROS1 rearrangements. *ESMO Open* 6 (2), 100087. doi:10.1016/j.esmoop.2021.100087

Deng, Z., Fan, T., Xiao, C., Tian, H., Zheng, Y., Li, C., et al. (2024). TGF-β signaling in health, disease, and therapeutics. *Signal Transduct. Target. Ther.* 9 (1), 61. doi:10.1038/s41392-024-01764-w

Desai, A. V., Robinson, G. W., Gauvain, K., Basu, E. M., Macy, M. E., Maese, L., et al. (2022). Entrectinib in children and young adults with solid or primary CNS tumors harboring NTRK, ROS1, or ALK aberrations (STARTRK-NG). *Neuro-Oncology* 24 (10), 1776–1789. doi:10.1093/neuonc/noac087

Ding, Z., Jiang, M., Qian, J., Gu, D., Bai, H., Cai, M., et al. (2024). Role of transforming growth factor-β in peripheral nerve regeneration. *Neural Regen. Res.* 19 (2), 380–386. doi:10.4103/1673-5374.377588

Doebele, R. C., Drilon, A., Paz-Ares, L., Siena, S., Shaw, A. T., Farago, A. F., et al. (2020). Entrectinib in patients with advanced or metastatic NTRK fusion-positive solid tumours: integrated analysis of three phase 1-2 trials. *Lancet Oncol.* 21 (2), 271–282. doi:10.1016/S1470-2045(19)30691-6

Firlej, V., Mathieu, J. R., Gilbert, C., Lemonnier, L., Nakhle, J., Gallou-Kabani, C., et al. (2011). Thrombospondin-1 triggers cell migration and development of advanced prostate tumors. *Cancer Res.* 71 (24), 7649–7658. doi:10.1158/0008-5472.CAN-11-0833

Frampton, J. E. (2021). Entrectinib: a review in NTRK+ solid tumours and ROS1+ nsclc. *Drugs* 81 (6), 697–708. doi:10.1007/s40265-021-01503-3

Fumagalli, G., Monza, L., Cavaletti, G., Rigolio, R., and Meregalli, C. (2020). Neuroinflammatory process involved in different preclinical models of chemotherapy-induced peripheral neuropathy. *Front. Immunol.* 11, 626687. doi:10.3389/fimmu.2020.626687

Gaesser, J. M., and Fyffe-Maricich, S. L. (2016). Intracellular signaling pathway regulation of myelination and remyelination in the CNS. *Exp. Neurol.* 283 (Pt B), 501–511. doi:10.1016/j.expneurol.2016.03.008

Giarratana, A. O., Prendergast, C. M., Salvatore, M. M., and Capaccione, K. M. (2024). TGF-β signaling: critical nexus of fibrogenesis and cancer. *J. Transl. Med.* 22 (1), 594. doi:10.1186/s12967-024-05411-4

Giustini, N. P., Oh, H., and Eaton, K. D. (2022). Development of neuropathic arthropathy with entrectinib: case report. *JTO Clin. Res. Rep.* 3 (11), 100419. doi:10.1016/j.jtocrr.2022.100419

Goyal, A., Agrawal, A., Verma, A., and Dubey, N. (2023). The PI3K-AKT pathway: a plausible therapeutic target in Parkinson's disease. *Exp. Mol. Pathol.* 129, 104846. doi:10.1016/j.yexmp.2022.104846

Griffin, R. J., Moloney, A., Kelliher, M., Johnston, J. A., Ravid, R., Dockery, P., et al. (2005). Activation of Akt/PKB, increased phosphorylation of Akt substrates and loss and altered distribution of Akt and PTEN are features of Alzheimer's disease pathology. *J. Neurochem.* 93 (1), 105–117. doi:10.1111/j.1471-4159.2004.02949.x

Haddadi, N., Lin, Y., Travis, G., Simpson, A. M., Nassif, N. T., and McGowan, E. M. (2018). PTEN/PTENP1: 'Regulating the regulator of RTK-dependent PI3K/Akt signalling', new targets for cancer therapy. *Mol. Cancer* 17 (1), 37. doi:10.1186/s12943-018-0803-3

Hata, A., and Chen, Y. G. (2016). TGF-B signaling from receptors to smads. *Cold Spring Harb. Perspect. Biol.* 8 (9), a022061. doi:10.1101/cshperspect.a022061

Huang, H., Kaur, S., and Hu, Y. (2019). Lab review: molecular dissection of the signal transduction pathways associated with PTEN deletion-induced optic nerve regeneration. *Restor. Neurol. Neurosci.* 37 (6), 545–552. doi:10.3233/RNN-190949

Huang, T., Wang, L., Liu, D., Li, P., Xiong, H., Zhuang, L., et al. (2017). FGF7/FGFR2 signal promotes invasion and migration in human gastric cancer through upregulation of thrombospondin-1. *Int. J. Oncol.* 50 (5), 1501–1512. doi:10.3892/ijo.2017.3927

Jafari, M., Ghadami, E., Dadkhah, T., and Akhavan-Niaki, H. (2019). PI3k/AKT signaling pathway: erythropoiesis and beyond. *J. Cell. Physiol.* 234 (3), 2373–2385. doi:10.1002/jcp.27262

Jakowlew, S. B. (2006). Transforming growth factor-beta in cancer and metastasis. *Cancer Metastasis Rev.* 25 (3), 435–457. doi:10.1007/s10555-006-9006-2

Jassim, A., Rahrmann, E. P., Simons, B. D., and Gilbertson, R. J. (2023). Cancers make their own luck: theories of cancer origins. *Nat. Rev. Cancer* 23 (10), 710–724. doi:10.1038/s41568-023-00602-5

Jiang, Q., Li, M., Li, H., and Chen, L. (2022). Entrectinib, a new multi-target inhibitor for cancer therapy. *Biomed. Pharmacother.* 150, 112974. doi:10.1016/j.biopha.2022.112974

Jiang, T., Wang, G., Liu, Y., Feng, L., Wang, M., Liu, J., et al. (2021). Development of small-molecule tropomyosin receptor kinase (TRK) inhibitors for NTRK fusion cancers. *Acta Pharm. Sin. B* 11 (2), 355–372. doi:10.1016/j.apsb.2020.05.004

Kanehisa, M., Goto, S., Sato, Y., Kawashima, M., Furumichi, M., and Tanabe, M. (2014). Data, information, knowledge and principle: back to metabolism in KEGG. *Nucleic Acids Res.* 42 (Database issue), D199–D205. doi:10.1093/nar/gkt1076

Kilic, U., Caglayan, A. B., Beker, M. C., Gunal, M. Y., Caglayan, B., Yalcin, E., et al. (2017). Particular phosphorylation of PI3K/Akt on Thr308 via PDK-1 and PTEN mediates melatonin's neuroprotective activity after focal cerebral ischemia in mice. *Redox Biol.* 12, 657–665. doi:10.1016/j.redox.2017.04.006

Li, Z., Zou, J., and Chen, X. (2023). In response to precision medicine: current subcellular targeting strategies for cancer therapy. *Adv. Mater.* 35 (21), e2209529. doi:10.1002/adma.202209529

Liu, D., Offin, M., Harnicar, S., Li, B. T., and Drilon, A. (2018). Entrectinib: an orally available, selective tyrosine kinase inhibitor for the treatment of NTRK, ROS1, and ALK fusion-positive solid tumors. *Ther. Clin. Risk Manag.* 14, 1247–1252. doi:10.2147/TCRM.S147381

Love, M. I., Huber, W., and Anders, S. (2014). Moderated estimation of fold change and dispersion for RNA-seq data with DESeq2. *Genome Biol.* 15 (12), 550. doi:10.1186/s13059-014-0550-8

Lu, T., Li, H., Zhou, Y., Wei, W., Ding, L., Zhan, Z., et al. (2022). Neuroprotective effects of alisol A 24-acetate on cerebral ischaemia-reperfusion injury are mediated by regulating the PI3K/AKT pathway. *J. Neuroinflamm.* 19 (1), 37. doi:10.1186/s12974-022-02392-3

Luo, S., Li, H., Mo, Z., Lei, J., Zhu, L., Huang, Y., et al. (2019). Connectivity map identifies luteolin as a treatment option of ischemic stroke by inhibiting MMP9 and activation of the PI3K/Akt signaling pathway. *Exp. Mol. Med.* 51 (3), 1–11. doi:10.1038/s12276-019-0229-z

Marcus, L., Donoghue, M., Aungst, S., Myers, C. E., Helms, W. S., Shen, G., et al. (2021). FDA approval summary: entrectinib for the treatment of NTRK gene fusion solid tumors. *Clin. Cancer Res.* 27 (4), 928–932. doi:10.1158/1078-0432.CCR-20-2771

Martineau, C., Turcotte, M. K., Otis, N., Provost, F., Themens, L., Guay, M. P., et al. (2022). Management of adverse events related to first-generation tyrosine receptor kinase inhibitors in adults: a narrative review. *Support. Care Cancer* 30 (12), 10471–10482. doi:10.1007/s00520-022-07401-y

Meyers, E. A., and Kessler, J. A. (2017). TGF-B family signaling in neural and neuronal differentiation, development, and function. *Cold Spring Harb. Perspect. Biol.* 9 (8), a022244. doi:10.1101/cshperspect.a022244

Mun, E. J., Babiker, H. M., Weinberg, U., Kirson, E. D., and Von Hoff, D. D. (2018). Tumor-treating fields: a fourth modality in cancer treatment. *Clin. Cancer Res.* 24 (2), 266–275. doi:10.1158/1078-0432.CCR-17-1117

Rai, S. N., Dilnashin, H., Birla, H., Singh, S. S., Zahra, W., Rathore, A. S., et al. (2019). The role of PI3K/akt and ERK in neurodegenerative disorders. *Neurotox. Res.* 35 (3), 775–795. doi:10.1007/s12640-019-0003-y

Robinson, M. D., McCarthy, D. J., and Smyth, G. K. (2010). edgeR: a Bioconductor package for differential expression analysis of digital gene expression data. *Bioinformatics* 26 (1), 139–140. doi:10.1093/bioinformatics/btp616

Staff, N. P., Grisold, A., Grisold, W., and Windebank, A. J. (2017). Chemotherapy-induced peripheral neuropathy: a current review. *Ann. Neurol.* 81 (6), 772–781. doi:10.1002/ana.24951

Subramanian, A., Tamayo, P., Mootha, V. K., Mukherjee, S., Ebert, B. L., Gillette, M. A., et al. (2005). Gene set enrichment analysis: a knowledge-based approach for interpreting genome-wide expression profiles. *Proc. Natl. Acad. Sci. U. S. A.* 102 (43), 15545–15550. doi:10.1073/pnas.0506580102

Sun, J., Ge, X., Wang, Y., Niu, L., Tang, L., and Pan, S. (2022). USF2 knockdown downregulates THBS1 to inhibit the TGF-β signaling pathway and reduce pyroptosis in sepsis-induced acute kidney injury. *Pharmacol. Res.* 176, 105962. doi:10.1016/j.phrs.2021.105962

Trendowski, M. R., El Charif, O., Dinh, P. C., Jr., Travis, L. B., and Dolan, M. E. (2019). Genetic and modifiable risk factors contributing to cisplatin-induced toxicities. *Clin. Cancer Res.* 25 (4), 1147–1155. doi:10.1158/1078-0432.CCR-18-2244

Tu, Z., Xiao, R., Xiong, J., Tembo, K. M., Deng, X., Xiong, M., et al. (2016). CCR9 in cancer: oncogenic role and therapeutic targeting. *J. Hematol. Oncol.* 9, 10. doi:10.1186/s13045-016-0236-7

Wang, C. M., Cai, X. L., and Wen, Q. P. (2016). Astaxanthin reduces isoflurane-induced neuroapoptosis via the PI3K/Akt pathway. *Mol. Med. Rep.* 13 (5), 4073–4078. doi:10.3892/mmr.2016.5035

Wang, C. Y., Lin, T. T., Hu, L., Xu, C. J., Hu, F., Wan, L., et al. (2023). Neutrophil extracellular traps as a unique target in the treatment of chemotherapy-induced peripheral neuropathy. *EBioMedicine* 90, 104499. doi:10.1016/j.ebiom.2023.104499

Wang, Q., Shen, Z. N., Zhang, S. J., Sun, Y., Zheng, F. J., and Li, Y. H. (2022). Protective effects and mechanism of puerarin targeting PI3K/Akt signal pathway on neurological diseases. *Front. Pharmacol.* 13, 1022053. doi:10.3389/fphar.2022.1022053

Xiao, C. L., Yin, W. C., Zhong, Y. C., Luo, J. Q., Liu, L. L., Liu, W. Y., et al. (2022). The role of PI3K/Akt signalling pathway in spinal cord injury. *Biomed. Pharmacother.* 156, 113881. doi:10.1016/j.biopha.2022.113881

Yang, J., Zhao, Y., Zhou, Y., Wei, X., Wang, H., Si, N., et al. (2022). Advanced nanomedicines for the regulation of cancer metabolism. *Biomaterials* 286, 121565. doi:10.1016/j.biomaterials.2022.121565

Yao, L., Lu, F., Koc, S., Zheng, Z., Wang, B., Zhang, S., et al. (2023). LRRK2 Gly2019Ser mutation promotes ER stress via interacting with THBS1/TGF-β1 in Parkinson's disease. *Adv. Sci. (Weinh)* 10 (30), e2303711. doi:10.1002/advs.202303711

Yu, G., Wang, L. G., Han, Y., and He, Q. Y. (2012). clusterProfiler: an R package for comparing biological themes among gene clusters. *OMICS* 16 (5), 284–287. doi:10.1089/omi.2011.0118

Yuan, M., Huang, L. L., Chen, J. H., Wu, J., and Xu, Q. (2019). The emerging treatment landscape of targeted therapy in non-small-cell lung cancer. *Signal Transduct. Target. Ther.* 4, 61. doi:10.1038/s41392-019-0099-9

Zheng, P. P., Li, J., and Kros, J. M. (2018). Breakthroughs in modern cancer therapy and elusive cardiotoxicity: critical research-practice gaps, challenges, and insights. *Med. Res. Rev.* 38 (1), 325–376. doi:10.1002/med.21463

frontiers | Frontiers in Pharmacology

TYPE Original Research
PUBLISHED 11 July 2025
DOI 10.3389/fphar.2025.1522937

OPEN ACCESS

EDITED BY
Jiayu Liao,
University of California, Riverside, United States

REVIEWED BY
Chao Ji,
Indiana University, United States
Akhilesh Kumar Kuril,
Bhagwant University, India

*CORRESPONDENCE
Xiaohong Huang,
ysrred@gmail.com
Yingze Zhang,
dryzzhang@hotmail.com

RECEIVED 05 November 2024
ACCEPTED 30 June 2025
PUBLISHED 11 July 2025

CITATION
Huang X, Feng Z, Li X, Zhu D and Zhang Y (2025) Osteoporosis diagnosis and ingredients of prescription medications: a population-based study.
Front. Pharmacol. 16:1522937.
doi: 10.3389/fphar.2025.1522937

Osteoporosis diagnosis and ingredients of prescription medications: a population-based study

Xiaohong Huang[1]*, Zhendong Feng[2], Xiaohua Li[3], Dongxu Zhu[4,5] and Yingze Zhang[1,4,5,6]*

[1]Shandong Institute of Traumatic Orthopedics, Medical Research Center, The Affiliated Hospital of Qingdao University, Qingdao, China, [2]National Institute on Drug Dependence and Beijing Key Laboratory of Drug Dependence, Peking University, Beijing, China, [3]Department of Pathology, Weifang People's Hospital, Weifang, China, [4]School of Medicine, Nankai University, Tianjin, China, [5]Department of Orthopedics, The Affiliated Hospital of Qingdao University, Qingdao, China, [6]Department of Orthopedics, The Third Hospital of Hebei Medical University, Shijiazhuang, China

Background: Osteoporosis (OP) is common in the elderly, who typically have multiple comorbidities. Current guidelines for managing drug-induced OP are limited due to the complexity of multi-agent medications and the lack of sufficient clinical data.

Methods: Information of demographics, health status, prescription medication use, OP diagnoses, and bone fracture history in US adults aged ≥50 years was from NHANES. Administration of individual medication ingredients was extracted and association between medication component use and OP diagnosis was determined. National trends in OP diagnosis, prescription medication use, and medication ingredient administrations were examined.

Results: OP diagnosis prevalence rose from 9.00% to 13.23% during 1999–March 2020 (p-trend = 0.00). Increased medication prescription was noted in OP patients ($p\text{-trend}_{\text{No. prescription medications=4–7}} < 0.0001$, $p\text{-trend}_{\text{No. prescription medications}\geq 8} < 0.0001$, and $p\text{-trend}_{\text{Days taking medications}\geq 500} < 0.0001$). Thirty-four medication ingredients were correlated with OP diagnosis, including three OP-specific medications, three avoided in OP patients in current practice, seven contribute to OP but commonly prescribed, four relieved OP when treating diseases causing secondary OP, two bone health-friendly agents, and 15 lack of prior statistical records to support their clinical use in OP. Amongst 10 ingredients associated with OP diagnosis may be underlying their roles in regulating bone remodeling, sympathetic activity, and gastric acidity, whereas the remaining five were not clear.

Conclusion: The findings of this study contribute to updating and improving the existing guidelines. Efforts are recommended to examine how the use of medications contribute to OP and to identify alternative treatments for comorbidities.

KEYWORDS

osteoporosis diagnosis, fragility fractures, active pharmaceutical ingredients, rational drug use, disease management

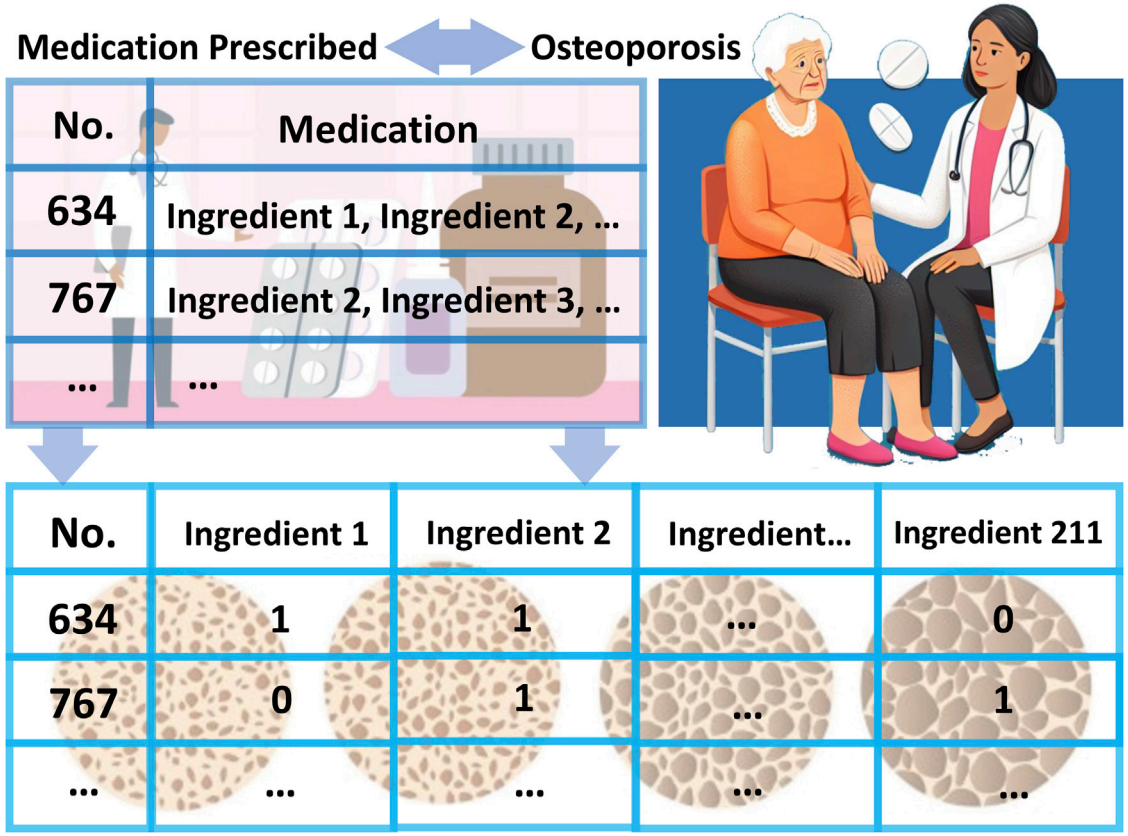

GRAPHICAL ABSTRACT

Introduction

As the global population ages, the number of fractures is expected to increase—by 310% from 1990 to 2050 (Gullberg et al., 1997)—leading to heightened morbidity and mortality. Annual fractures and costs are expected to increase by almost 50% by 2025 (Burge et al., 2007). Osteoporosis (OP), characterized by reduced bone mass and compromised bone structure, is the leading cause of fractures in the elderly. Moreover, Centers for Disease Control and Prevention (CDC) reported that 76.9% of Medicare and Medicaid recipients aged 65 and older have multiple chronic conditions (Peter et al., 2020). And prescription medications used to treat diseases can further elevate the risk of OP via bone–organ axes (Deng et al., 2024; Foessl et al., 2023). Particularly, most medicines contain multiple active substances to increase their effectiveness, to target different aspects of the disease, and or to simultaneously relieve several symptoms, which make it complex and difficult to manage drug-induced OP. However, drug holiday or switching to bone health-friendly medications is recommended but not always feasible, attributing to the limited clinical data and unclear mechanisms.

Dealing with the modifiable factors, such as avoiding specific OP risk associated ingredients or carefully including them in combined pharmacotherapy, is crucial for effective OP prevention and treatment. The aim of this study is to determine the association between the active pharmaceutical ingredient use and OP diagnosis, and the finding of this study will contribute to develop rational drug use strategies for OP management. Specifically, this study 1) examined the national trend in OP diagnoses; 2) analyzed the variety and duration of medication prescribed in the OP diagnosed population; 3) determined the association between drug ingredient use and OP diagnosis and tracked national trend in the related ingredient use.

Abbreviations: ACEI, angiotensin-converting enzyme inhibitor; AR, 5-alpha reductase; BMD, bone mineral density; BMI, body mass index; CDC, Centers for Disease Control and Prevention; CI, confidence interval; DEXA, dual-energy X-ray absorptiometry; NHANES, National Health and Nutrition Examination Survey; NSAID, non-steroidal anti-inflammatory drug; OP, osteoporosis; OR, odds ratio; PIR, family income to poverty ratio; SNS, sympathetic nervous system; STROBE, Strengthening the Reporting of Observational Studies in Epidemiology.

Materials and methods

Database and study population

Participants in National Health and Nutrition Examination Survey (NHANES), a nationally representative survey conducted in 2-year

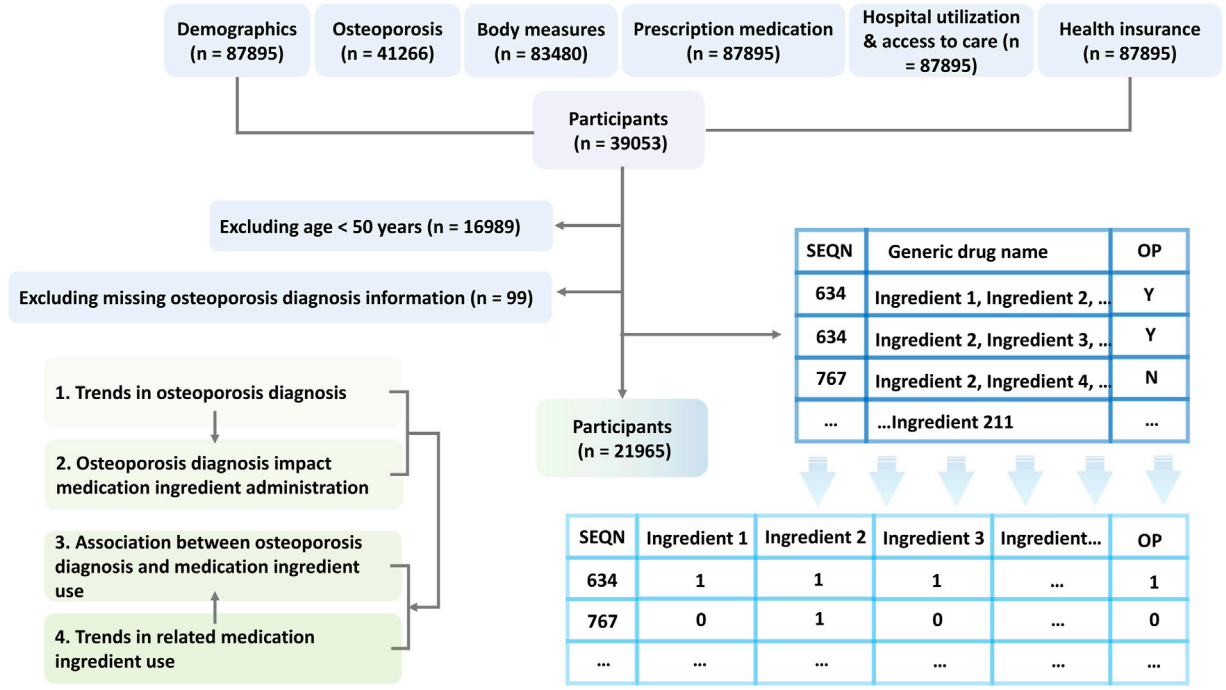

FIGURE 1
Participants, study design, and prescription medication ingredient identification.

cycles from 1999 to March 2020, provided written informed consent, and the National Center for Health Statistics Research Ethics Review Board approved the study protocols. This study followed the Strengthening the Reporting of Observational Studies in Epidemiology (STROBE).

Our analysis focused on cycles with complete records in demographics, osteoporosis, body measures, prescription medication, hospital utilization and access to care, and health insurance, as shown in Figure 1. Thus, eight cycles (1999–2000, 2001–2002, 2003–2004, 2005–2006, 2007–2008, 2009–2010, 2013–2014, 2017–March 2020) were included in this study. The study sample was limited to adults aged 50 and older with a definite answer regrading OP diagnosis (yes/no).

Prescription medication and individual medication ingredient administration

Data on prescription medication use, including generic drug name, No. prescription medications, and days taking medications, were obtained from "prescription medication" questionnaires. The individual ingredients of these drugs were extracted from the records under "generic drug name", as shown in Figure 1. These ingredients were then categorized into therapeutic classes based on the Multum Lexicon Plus drug database (Centers for Disease Control and Prevention CDC, 2007).

Osteoporosis diagnosis and bone fracture history

Based on the responses to the question "Ever told had osteoporosis/brittle bones (yes/no)", individuals diagnosed with OP were classified into the OP group, while those who explicitly stated they had not been diagnosed with OP were categorized into the non-OP group. In addition, bone fracture history was determined by aggregating reported cases of hip, wrist, and vertebral fractures.

Clinical, demographic and socioeconomic characteristics

Clinical and demographic information, including age, sex, body mass index (BMI), race/ethnicity, and self-reported health status, were collected from standardized questionnaires and physical examinations. BMI categories were defined as follows: underweight (<18.5), normal weight (18.5–24.9), overweight (25–29.9), and obese (≥30). Because postmenopausal women with low BMI exhibit osteopenia with predisposition for OP, and fat mass assumes a determining role in predicting the bone mineral density (BMD) of the lumbar vertebrae and femoral neck of postmenopausal women (Wu and Du, 2016). Race/ethnicity analyzed included non-Hispanic white, non-Hispanic black, Hispanic, and Other (including multiple races). This assessment was conducted because of the recognized racial and ethnic disparities in the risk and incidence of OP (Thomas, 2007). Individuals with a confirmed diagnosis may report a lower self-assessment of their health, whereas those who view their health more positively may be underdiagnosed. Therefore, the current health status of the participants was analyzed, self-reported as "excellent or very good", "good", or "fair or poor".

Socioeconomic information, including education level, family income to poverty ratio (PIR), and insurance status, which reflects the medication adherence and accessibility within the population,

was collected using standardized questionnaires. The education level of the household head was categorized as less than a high school degree, a high school degree, or higher than a high school degree. PIR was calculated as the ratio of family income to the poverty threshold and categorized as <1, 1–1.9, 2–2.9, 3–3.9, or ≤4. Insurance status was self-reported as either insured (including public and private sources) or uninsured. These characteristics were evaluated to assess the socioeconomic status of households in relation to medication use (Venkatesh et al., 2019; McCabe et al., 2023).

Statistical analysis

Prevalence rates and 95% confidence intervals (CIs) were reported for categorical variables. The chi-square ($\chi 2$) test was used to evaluate the consistency of distributions of categorical covariates between OP and non-OP groups, including the clinical, demographic and socioeconomic characteristics.

Trends of OP diagnosis across the survey cycles and OP prevalence by bone fracture history, No. prescription medications, and days taking prescription medications were calculated using a linear regression model. The combined survey cycle was considered as a continuous variable.

To determine medication strategy influenced by OP diagnosis, logistic regression was used to analyze the association between OP diagnosis and medication ingredient administration. The threshold for statistical significance was set at $p < 0.05$. Odds ratios (ORs) with 95% CIs were derived from a multivariable logistic regression model to assess the altered medication administration by OP diagnosis. National trends in the prescription of specific medication ingredients associated with OP diagnosis were then outlined using linear regression, adjusting for education level, RIP, and insurance status.

To assess the robustness of the association results, sensitivity analyses were performed by 1) assessing the change in use of each ingredient by OP diagnosis, 2) excluding adults aged ≥80 years or with a BMI ≥30 kg/m^2 who were more prone to multiple comorbidities.

Data analysis for this study applied rigorous methods tailored to structured survey data, including stratification, clustering, and weighting to ensure nationally representative estimates. SAS software (version 9.4) was used, with statistical significance set at $p < 0.05$. Python (version 9.3) was used to generate diagrams.

Results

Characteristics of study population

This study identified a final sample size of 21,965 individuals, representing 669,561,146 noninstitutionalized US adults aged 50 and older (Supplementary Table S1). Among them, 2,408 individuals were diagnosed with OP, constituting 11.06% [95% CI, 10.38%–11.75%] of the participants (Table 1). Among OP patients, 24.11% [95% CI, 22.10%–26.11%] had a history of bone fractures, 19.43% (17.70–21.16) were aged 80–89 years, and 30.26% [95% CI, 27.95%–32.58%] were of obesity. OP patients reported similar distributions across health status categories: excellent or very good (33.00% [95% CI, 30.10%–35.90%]), good (34.68% [95% CI, 32.10%–37.26%]), and fair or poor (32.32% [95% CI, 29.46%–35.18%]). OP patients had a higher prevalence of using ≥8 prescription medications compared to non-OP individuals (36.86% [95% CI, 33.96%–39.76%] vs. 23.22% [95% CI, 22.12%–24.32%]), as well as a longer duration of taking prescription medications (64.04% [95% CI, 61.07%–67.00%] vs. 51.76% [95% CI, 50.48%–53.03%]). And the vast majority were insured, with a rate of 96.18% [95% CI, 95.02%–97.34%] in OP group (Supplementary Table S2).

Trends in osteoporosis diagnosis and prescription medication use

The prevalence of OP diagnosis increased from 9.00% [95% CI, 7.83%–10.17%] in the 1999–2002 cycle to 11.78% [95% CI, 10.31%–13.25%] in the 2003–2006 cycle, decreased to 10.75% [95% CI, 9.44%–12.06%] in the 2007–2010 cycle, plateaued until the 2013–2014 cycle and then increased again to 13.23% [95% CI, 11.57%–14.89%] in the 2017–March 2020 cycle (Figure 2; Supplementary Table S3). The prevalence of OP patients with a history of sustained bone fractures increased from 1.87% [95% CI, 1.43%–2.32%] to 3.84% [95% CI, 3.00%–4.68%].

The prevalence of prescription medication use in the OP diagnosed population was increased, indicated by an rising trend in OP patients using ≥8 medications, rising from 2.48% [95% CI, 1.94%–3.01%] in the 1999–2002 cycle to 5.02% [95% CI, 3.95%–6.90%] in the 2017–March 2020 cycle (p-trend = 0.00), and the increase in the proportion of elderly adults who taking prescription medications for more than 500 days (p-trend <0.0001), from 4.72% [95% CI, 3.86%–5.57%] to 9.86% [95% CI, 8.29%–11.43%].

Osteoporosis diagnosis and medication ingredient administration

Significant correlations were found between OP diagnosis and 34 medication ingredients, among the 211 ingredients extracted from the "generic drug name" field, categorized into 22 subcategories across 10 agents (Table 2). And the national trends of these ingredients were explored further (Figure 3; Supplementary Table S4). Of these, 7 ingredients were used sparingly in osteoporotic patients, including an anticonvulsant topiramate (OR 0.18 [95% CI, 0.09–0.37], $p < 0.0001$), an angiotensin-converting enzyme inhibitor (ACEI) quinapril (OR 0.59 [95% CI, 0.38–0.92], $p = 0.02$), a nasal decongestant pseudoephedrine (OR 0.26 [95% CI, 0.10–0.69]), $p = 0.01$), two alpha-blockers tamsulosin (OR 0.37 [95% CI, 0.21–0.67], $p = 0.00$) and terazosin (OR 0.40 [95% CI, 0.22–0.72], $p = 0.00$), a 5-alpha reductase (AR) inhibitor finasteride (OR 0.51 [95% CI, 0.27–0.95]), $p = 0.04$), a non-steroidal anti-inflammatory drug (NSAID) indomethacin (OR 0.15 [95% CI, 0.05–0.47], $p = 0.00$); and, the remaining 27 ingredients were commonly used in OP cases. Among them, 13 ingredients showed increasing trends, including cyclobenzaprine (p-trend = 0.01), gabapentin (p-trend <0.0001), oxycodone (p-trend = 0.00), losartan (p-trend <0.0001), famotidine

TABLE 1 Clinical and demographic characteristics by osteoporosis diagnosis among US adults aged 50 and older, 1999–March 2020[a].

Characteristic	% (95% CI)		p–value[b]
	OP	Non-OP	
Unweight sample, No.	2408	19557	NA
Weighted sample, No.[c]	74082254	595478892	NA
Bone fracture history			
Yes	24.11 (22.10–26.11)	13.52 (12.74–14.30)	<0.0001
No	75.89 (73.89–77.90)	86.48 (85.70–87.26)	
Age, y			
50–59	21.59 (18.99–24.19)	44.94 (43.73–46.15)	<0.0001
60–69	29.51 (27.04–31.97)	29.54 (28.50–30.58)	
70–79	29.47 (27.43–31.52)	17.18 (16.51–17.85)	
≥80	19.43 (17.70–21.16)	8.35 (7.80–8.89)	
Sex			
Male	11.61 (10.10–13.13)	50.97 (50.28–51.65)	<0.0001
Female	88.39 (86.87–89.90)	49.04 (48.35–49.72)	
Race/ethnicity			
Non-Hispanic white	82.25 (79.55–84.95)	75.57 (73.05–78.09)	<0.0001
Non-Hispanic black	5.53 (4.45–6.61)	10.26 (8.84–11.67)	
Hispanic	7.11 (5.45–8.77)	8.62 (7.16–10.08)	
Other	5.11 (3.83–6.39)	5.56 (4.78–6.33)	
BMI, kg/m^2			
Underweight <18.5	5.51 (4.35–6.67)	3.10 (2.71–3.48)	<0.0001
Normal weight 18.5–24.9	33.92 (31.61–36.22)	23.66 (22.68–24.63)	
Overweight 25–29.9	30.31 (27.99–32.62)	35.77 (34.81–36.74)	
Obese ≥30	30.26 (27.95–32.58)	37.47 (36.20–38.75)	
Self-reported health status			
Excellent or very good	33.00 (30.10–35.90)	44.97 (43.56–46.37)	<0.0001
Good	34.68 (32.10–37.26)	33.50 (32.52–34.48)	
Fair or poor	32.32 (29.46–35.18)	21.53 (20.47–22.59)	
No. prescription medications			
1–3	24.02 (21.41–26.62)	38.99 (37.66–40.32)	<0.0001
4–7	39.12 (36.48–41.76)	37.79 (36.71–38.87)	
≥8	36.86 (33.96–39.76)	23.22 (22.12–24.32)	
Days taking medications			
0/refused/missing	8.77 (7.33–10.20)	24.80 (23.86–25.74)	<0.0001
<500	27.19 (24.36–30.03)	23.45 (22.48–24.41)	
≥500	64.04 (61.07–67.00	51.76 (50.48–53.03)	

[a]Data from NHANES., data are present as prevalence, % (95% CI) unless indicated otherwise.
[b]Calculated with $\chi 2$ test to determine the consistency of categorical distribution of variables between OP and non-OP groups.
[c]Data are weighted to be nationally representative.

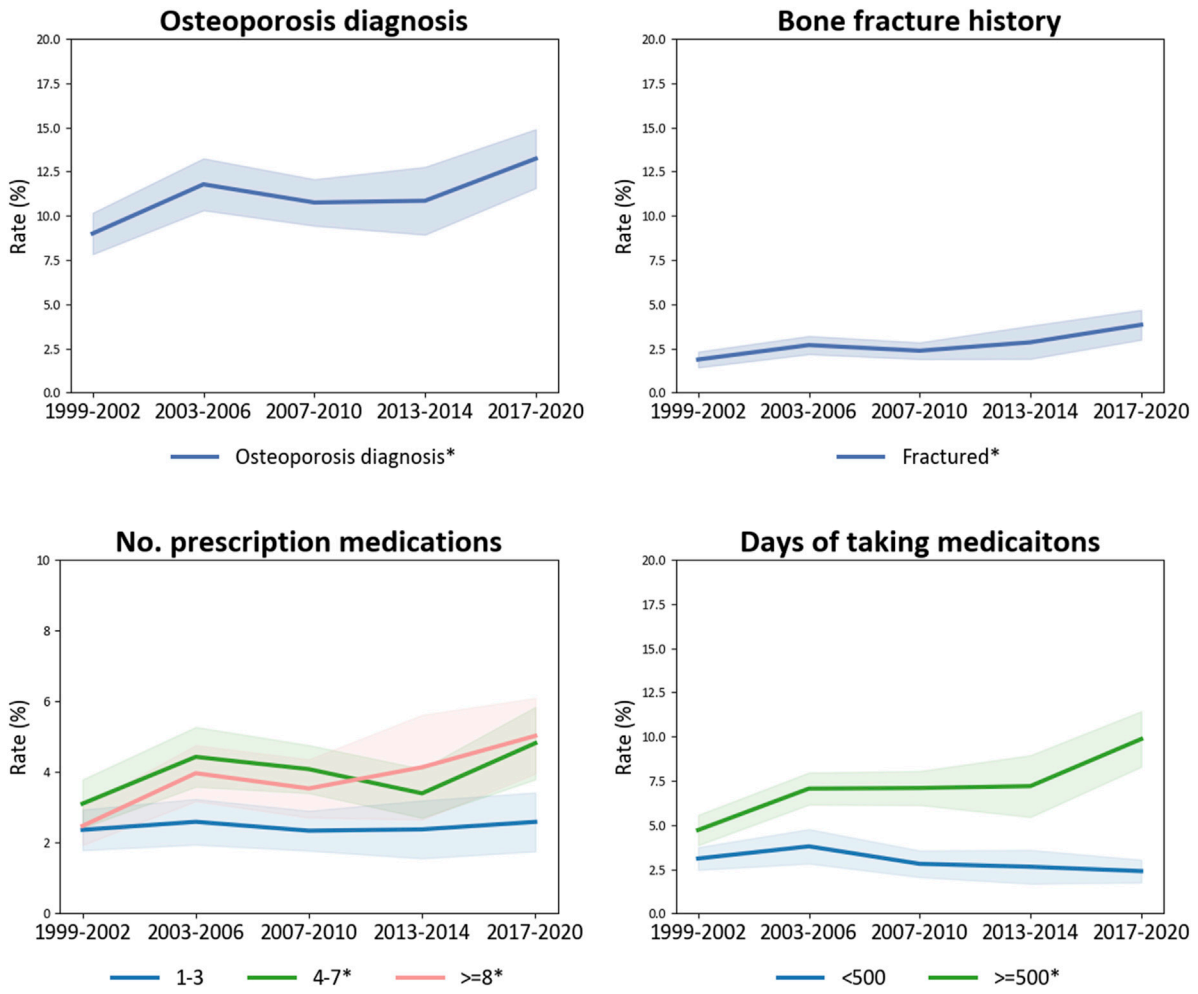

FIGURE 2
Trends in osteoporosis diagnosis among US adults aged 50 years and older, 1999–March 2020 and trends of bone fractures, No. prescription medications used, and days taking medications in the elderly diagnosed with osteoporosis. Abbreviations: BMI, body mass index. *The prevalence is significantly altered.

(p-trend = 0.01), pantoprazole (p-trend <0.0001), omeprazole (p-trend <0.0001), oxybutynin (p-trend = 0.05), (p-trend <0.0001), tamsulosin (p-trend <0.0001), finasteride (p-trend <0.0001), thyroid desiccated (p-trend <0.0001), levothyroxine (p-trend = 0.00), and meloxicam (p-trend = <0.0001); six showed decreasing trends, including quinapril (p-trend = <0.0001), pseudoephedrine (p-trend = <0.0001), brompheniramine (p-trend = 0.05), terazosin (p-trend = 0.00), raloxifene (p-trend = <0.0001), rofecoxib (p-trend = <0.0001); the prevalence of six ingredients initially increased and decreased in recent years, including carisoprodol (p-trend = 0.00), pregabalin (p-trend <0.0001), topiramate (p-trend <0.0001), lovastatin (p-trend <0.0001), alendronate (p-trend <0.0001), risedronate (p-trend <0.0001); and, the consumption of remind nine ingredients remained stable (p-trend >0.05). Through the 2017–March 2020 cycle, levothyroxine (12.33% [95% CI, 10.54%–14.12%]) in the hormones/hormone modifiers, omeprazole (10.62% [95% CI, 8.86%–12.38%]) in the gastrointestinal agents, and losartan (10.58% [95% CI, 9.05%–12.11%]) in the cardiovascular agents were among the most common OP-related ingredients administrated to 10% of US adults aged 50 and older.

Sensitivity analysis

The associations between OP diagnosis and administration of individual drug ingredients remained robust, as the direction and magnitude of most changes in the medication ingredient administration remained in the crude weighted logistic regression model adjusted for a single ingredient (Table 2) and in the multivariable model in a population excluding elderly aged ≥80 years (Supplementary Table S5) or obese individuals (Supplementary Table S6).

Discussion

This study updates the national trend in OP diagnosis and highlights the rising trends in fragility fractures and medications

10.3389/fphar.2025.1522937

TABLE 2 Association between osteoporosis diagnosis and prescription medication ingredient administration among US adults aged 50 and older, 1999–March 2020[a,b].

Prescription medication[c]	Univariate[d]	Multivariate[e]	
	OR (95% CI)	OR (95% CI)	p-value
CNS agents			
Skeletal muscle relaxants			
Carisoprodol	3.72 (1.68–8.23)	2.66 (1.14–6.22)	0.02
Cyclobenzaprine	3.45 (2.31–5.17)	2.44 (1.56–3.83)	0.00
Anticonvulsants[f]			
Pregabalin	2.50 (1.41–4.44)	2.04 (1.07–3.91)	0.03
Topiramate	0.53 (0.24–1.15)	0.18 (0.09–0.37)	<0.0001
Gabapentin	2.76 (2.15–3.55)	1.90 (1.41–2.55)	<0.0001
Narcotic analgesics			
Oxycodone	2.58 (1.77–3.75)	2.07 (1.30–3.32)	0.00
Gastrointestinal agents			
H2-blockers			
Famotidine	2.12 (1.35–3.33)	2.23 (1.36–3.66)	0.00
Prokinetics			
Metoclopramide	2.82 (1.58–5.03)	2.15 (1.15–4.01)	0.02
PPIs[f]			
Pantoprazole	1.96 (1.47–2.60)	1.56 (1.12–2.17)	0.01
Omeprazole	1.74 (1.49–2.02)	1.28 (1.00–1.63)	0.05
Anticholinergics			
Dicyclomine	3.52 (1.80–6.91)	2.25 (1.21–4.16)	0.01
Oxybutynin	3.25 (2.01–5.24)	2.28 (1.40–3.71)	0.00
Cardiovascular agents			
ARBs			
Losartan	1.69 (1.35–2.11)	1.55 (1.21–1.99)	0.00
ACEIs			
Quinapril	0.79 (0.46–1.36)	0.59 (0.38–0.92)	0.02
Genitourinary tract agents			
Alpha blockers			
Tamsulosin	0.49 (0.29–0.80)	0.37 (0.21–0.67)	0.00
Terazosin	0.45 (0.25–0.79)	0.40 (0.22–0.72)	0.00
Respiratory agents			
Nasal decongestants			
Pseudoephedrine	0.89 (0.45–1.79)	0.26 (0.10–0.69)	0.01
Bronchodilators			
Albuterol	2.13 (1.72–2.64)	1.41 (1.05–1.90)	0.02

(Continued on following page)

10.3389/fphar.2025.1522937

TABLE 2 (*Continued*) Association between osteoporosis diagnosis and prescription medication ingredient administration among US adults aged 50 and older, 1999–March 2020[a,b].

Prescription medication[c]	Univariate[d]	Multivariate[e]	
	OR (95% CI)	OR (95% CI)	p-value
Antihistamines			
Promethazine	4.95 (2.09–11.74)	4.88 (1.32–18.03)	0.02
Brompheniramine	3.05 (0.72–13.01)	7.90 (1.64–38.08)	0.01
Hormones/hormone modifiers			
AR inhibitors			
Finasteride	0.37 (0.18–0.80)	0.51 (0.27–0.95)	0.04
Furosemide	1.95 (1.62–2.33)	1.39 (1.08–1.79)	0.01
Thyroid hormones[f]			
Thyroid desiccated	2.24 (1.01–4.97)	2.85 (1.06–7.67)	0.04
Levothyroxine	2.31 (2.02–2.64)	1.82 (1.54–2.15)	<0.0001
Mineralocorticoid receptor antagonists			
Spironolactone	2.25 (1.53–3.33)	1.69 (1.04–2.75)	0.04
SERMs			
Raloxifene	7.06 (4.78–10.42)	6.69 (4.30–10.40)	<0.0001
Metabolic agents			
Statins[g]			
Lovastatin	1.80 (1.29–2.51)	1.69 (1.15–2.49)	0.01
Bone resorption inhibitors			
Alendronate	28.44 (21.87–36.97)	33.73 (24.79–45.89)	<0.0001
Risedronate	18.78 (12.02–29.34)	22.02 (13.42–36.15)	<0.0001
Antineoplastics[f]			
Antimetabolites			
Methotrexate[f]	4.16 (2.49–6.95)	2.09 (1.02–4.28)	0.04
Topical agents			
NSAIDs			
Indomethacin	0.23 (0.07–0.76)	0.15 (0.05–0.47)	0.00
Meloxicam	2.60 (1.81–3.74)	1.80 (1.18–2.73)	0.01
Rofecoxib	2.66 (1.75–4.06)	2.48 (1.54–3.98)	0.00
Anti-infectives			
Beta-lactamase inhibitors			
Clavulanate	2.32 (0.74–7.29)	5.30 (1.27–22.14)	0.02

[a]Data from NHANES.
[b]Name of the medication ingredients is based on the NHANES records.
[c]The medication ingredients are categorized into therapeutic classes based on the Multum Lexicon Plus drug database.
[d]Univariable logistic regression is used to control for correlation between individual drug and OP.
[e]Multivariable logistic regression is used to control for correlations among various risk factors. Data are present as OR (95% CI), and p-value is interpreted as a measure of statistical evidence. Medication ingredients with statistical significance obtained from multivariable logistic regression were presented; note that, uncertainty in the distribution of the outcome has been excluded despite a p-value <0.05 from multivariate regression.
[f]Listed as a risk factor in OP guideline (LeBoff et al., 2022).
[g]Stains are also known as HMG-CoA reductase inhibitors.

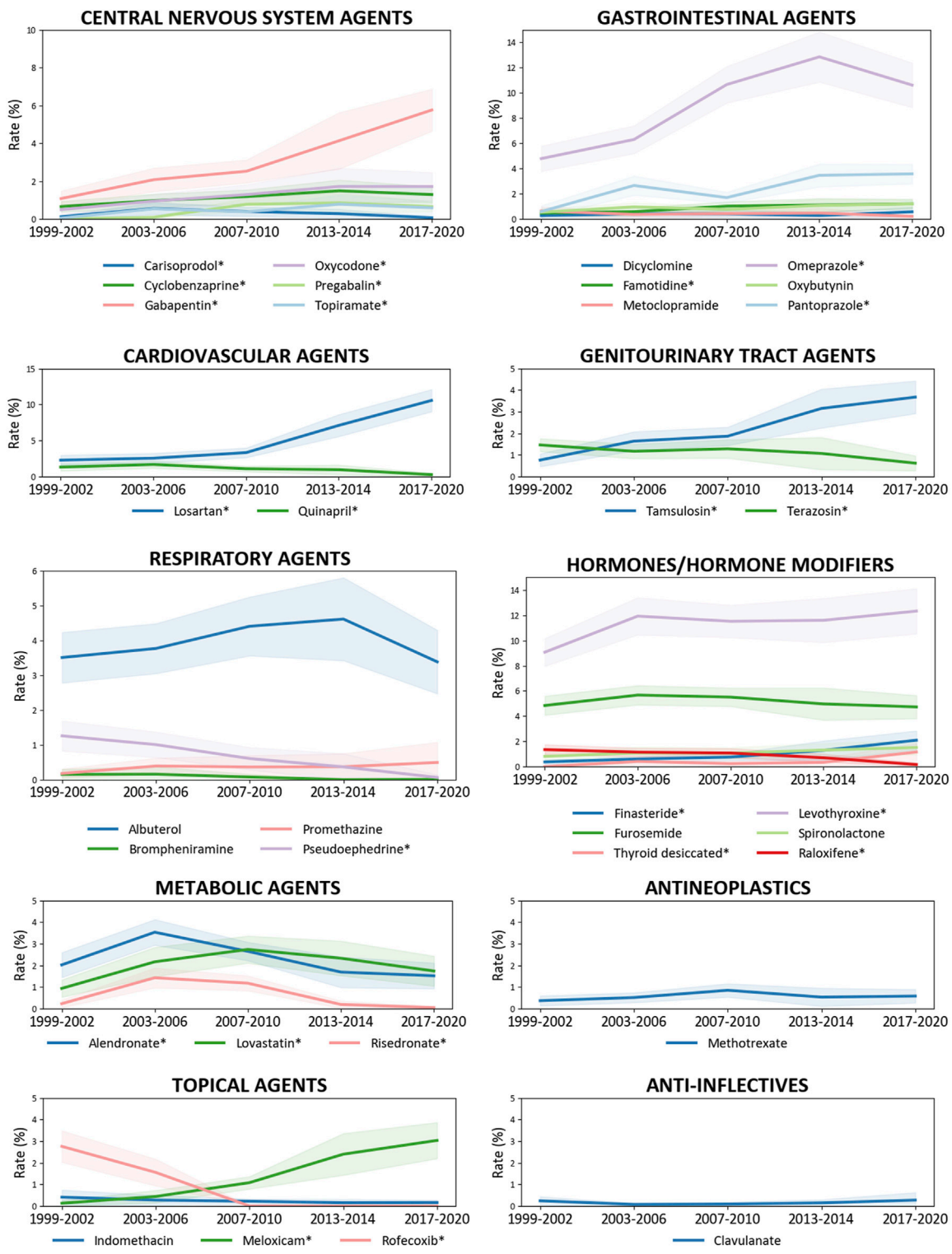

FIGURE 3
Trends in the administration of prescription medication ingredients related to osteoporosis diagnosis among US adults aged 50 years and older, 1999–March 2020. The prescription medications are categorized into therapeutic classes using the Multum Lexicon Plus drug database. National trends in the prevalence of corresponding medication ingredients in Table 2 are determined by linear regression in Supplementary Table S4. *The prevalence is significantly altered.

prescribed for OP patients, underscoring the need for vigilance in preventing drug-induced OP. And the prevalent medication ingredients in this study emphasize the involvement of the bone–thyroid, bone–gastrointestinal, and bone–cardiovascular axes in OP development, hinting the importance of comorbidities management and rational drug administration in the elderly.

Based on clinical reports

Though the OP diagnosis was increased, the use of bisphosphonates (alendronate, risedronate) and raloxifene, the FDA-approved OP drugs (LeBoff et al., 2022), was decreased. This may be due to the emergency of anabolic and catabolic treatments such as denosumab (Prolia, 2010), abaloparatide (Tymlos, 2017), and romosozumab (Evenity, 2019) (Kuril et al., 2024). Except for the OP drugs, the ingredients identified in this study can be classified as follows, based on the clinical reports bonding medical application and OP as well as the national trends in medication prescribed:

- Avoided in OP patients due to their adverse effects on bone formation or bone fracture healing, including topiramate, indomethacin, and rofecoxib (Zheng et al., 2020; Heo et al., 2011).
- Increased OP or fracture risk but are commonly used, including methotrexate, thyroid desiccated, levothyroxine, furosemide, gabapentin, pregabalin, and omeprazole (Ricciardi et al., 2013; Sakr, 2024; Jørgensen et al., 2023; Roux et al., 2009).
- Relieve OP symptoms, treat diseases that induced secondary OP, and or treat OP complications, including oxycodone used in osteoporotic pain management (Ali et al., 2024), losartan and quinapril used to treat hypertension and diabetic nephropathy (Huang and Ye, 2024; Liu et al., 2020; Barkhordarian et al., 2023), and clavulanate used in anti-infection.
- Bone health-friendly agents, including spironolactone and famotidine (Song et al., 2024; Haddadi et al., 2024).
- Lack of clinical supports, including carisoprodol, brompheniramine, promethazine, dicyclomine, oxybutynin, albuterol, pseudoephedrine, pantoprazole, metoclopramide, tamsulosin, terazosin, finasteride, meloxicam, lovastatin, and cyclobenzaprine.

Based on bench data

Experimental studies investigating the role of medication ingredients in regulating bone hemostasis have been emerged. And the association found between OP diagnosis and compounds without prior clinical evidence may underlie their effects on bone remodeling, sympathetic regulation, and gastric acidity.

- Bone remodeling The balance between osteoclastogenesis and osteoblast expressing receptor activator of nuclear factor-kappa B ligand (RANKL) and osteoprotegerin (OPG) is regulated by systemic hormones, such as parathyroid hormone and local signaling molecules (Celebi Torabfam and Porsuk, 2024). Carisoprodol, a skeletal muscle relaxant, is associated with increased OP risk by inhibiting osteoblast differentiation and reducing bone density through inhibiting Wnt/beta-catenin signaling pathway (YRKM, 2022). Similarly, histamine promotes bone resorption by inducing osteoclast formation and increasing RANKL expression in osteoblasts and bone marrow cells (Ng et al., 2022; Biosse-Duplan et al., 2009). And histamine receptor H_1 antagonists (brompheniramine and promethazine) and histamine receptor H_2 antagonist (famotidine) contribute to protect against this (Abra et al., 2013). And the alpha-blocker, tamsulosin, exerts significant anti-osteoporotic effects by inhibiting the activity of transmembrane protein 16A (TMEM16A), which reduces the differentiation and function of osteoclasts, thereby decreasing bone resorption (Li et al., 2025).
- Sympathetic regulation The neurotransmitters norepinephrine (NE) and acetylcholine (Ach) released from the terminals of sympathetic and parasympathetic nerve fibers, respectively, in bone tissue can promote and inhibit neuropeptide Y (NPY) produced by osteocytes, thereby affecting the osteogenic differentiation of bone marrow stem cells (BMSCs) and OP development (Zhang et al., 2021). Thereby, bone loss in chronic heart failure underlies the adverse impact of the increased sympathetic tone on bone health (Guan et al., 2023). Herein, dicyclomine, oxybutynin, albuterol, and pseudoephedrine increase sympathetic nervous system (SNS) activity. Specifically, anticholinergics block Ach (Ogawa et al., 2021; Lerche, 2024), while albuterol and pseudoephedrine activate NE receptors, with albuterol binding to beta-adrenoceptors (Cardet et al., 2019) and pseudoephedrine stimulating alpha-1 adrenergic receptors (Perrin et al., 2015). In contract, the cardiovascular agents (losartan and quinapril) reduce SNS activity (Houglum et al., 2024).
- Gastric acidity A variety of enteroendocrine cells (EECs) distributed in the gastrointestinal tract, sensing external stimuli and regulating metabolism and behaviors by secreting various neuroendocrine peptides, and gut microbiota has been considered as a virtual endocrine organ (Huang et al., 2022). Thus, changes in the acidity of digestive system affects endocrine and body's ability to absorb bone-boosting calcium (Chanpaisaeng et al., 2021). Therefore, the acid blockers, including H_2 blocker (famotidine) and PPIs (pantoprazole and omeprazole), are commonly used in OP patients. Long-term use of PPIs has been reported to be associated with lower femoral neck BMD and a higher risk of OP (Fattahi et al., 2019).

Note that, OP increases infection risk and antibiotic use. For example, combination drug amoxicillin/clavulanate is often prescribed (Khan, 2023). Hence, a significant correlation of OP with only one specific anti-infective agent, clavulanate, was observed, which is due to the frequent prescription of amoxicillin in common conditions.

Implications for practice and researchers

This study emphasizes the importance of a multidisciplinary approach for healthcare professionals in managing OP, particularly among the elderly with multiple health issues. Traditional anticonvulsants contribute to OP (LeBoff et al., 2022), while it has been reported in 2016 that the effect of new antiepileptic

drugs such as gabapentin and topiramate on bone metabolism and bone density are scanty and controversial (Arora et al., 2016). The finding of this study revealed that pregabalin and gabapentin were still commonly prescribed in elder patients with OP diagnosis while topiramate was avoided. Moreover, the risk of OP varies with lovastatin dosage, i.e., lower doses (up to 10 mg daily) lows OP risk while higher doses increase the risk (Leutner et al., 2019), suggesting need the for examining cumulative drug exposure. This study underscores the urgent need for researchers to explore the mechanisms of action of medications in their intended conditions and OP development which lack of clinical and experimental supports and significantly associated with OP diagnosis, including terazosin, meloxicam, finasteride, metoclopramide, and cyclobenzaprine.

Limitations

This study has several limitations. 1) Data of 2011–2012 and 2015–2016 OP questionnaires are not collected, limiting the continuity in national trend analysis from 1999 to March 2020. 2) The cross-sectional design limits the ability to establish causality of disease occurrence and medication intake with OP. It also restricts the evaluation of cumulative drug exposure on OP risk, given that OP is a chronic condition (Foessl et al., 2023). 3) There was a potential bias due to the exclusion of participants with missing data. 4) Though the survey staffs aimed to capture all prescription medication use, underreporting is possible, and data on most over-the-counter medications were not collected. 5) Lack of data on medication adherence, which may affect the interpretation of medication use. 6) Reliance on self-reported data for key variables introduces a risk in the recall and social desirability. 7) Limited fracture history data, focusing on self-reported hip, wrist, and vertebral fractures. 8) Residual confounding may arise from unmeasured variables, including smoking, physical activity, diet, and comorbid conditions.

Conclusion

This study illustrates the association between OP clinical diagnosis and medication prescribed, pointing out aspects that need attention in clinical practice to prevent drug-induced OP in treat elderly with multi-comorbidities. Medication containing ingredients that pose risks for OP should be closely monitored in populations susceptible to the condition. Moreover, it has been found in this study that 15 medication ingredients significantly associated with OP diagnosis were lack of clinical support, amongst five with unclear mechanisms of actin in regulating bone homeostasis. And collaborative efforts between clinicians and researchers are vital for developing evidence-based guidelines to navigate the complexities of treating OP, especially in the context of polypharmacy.

Data availability statement

The original contributions presented in the study are included in the article/Supplementary Material, further inquiries can be directed to the corresponding authors.

Ethics statement

The studies involving humans were approved by Participants in NHANES provided written informed consent and study protocols were approved by the National Center for Health Statistics Research Ethics Review Board. The studies were conducted in accordance with the local legislation and institutional requirements. Written informed consent for participation in this study was provided by the participants' legal guardians/next of kin.

Author contributions

XH: Conceptualization, Data curation, Investigation, Visualization, Writing – original draft, Writing – review and editing. ZF: Data curation, Formal Analysis, Writing – review and editing. XL: Data curation, Writing – original draft. DZ: Data curation, Writing – original draft. YZ: Conceptualization, Writing – original draft, Writing – review and editing.

Funding

The author(s) declare that no financial support was received for the research and/or publication of this article.

Conflict of interest

The authors declare that the research was conducted in the absence of any commercial or financial relationships that could be construed as a potential conflict of interest.

Generative AI statement

The author(s) declare that no Generative AI was used in the creation of this manuscript.

Publisher's note

Supplementary material

The Supplementary Material for this article can be found online at: https://www.frontiersin.org/articles/10.3389/fphar.2025.1522937/full#supplementary-material

References

Abrahamsen, B., and Vestergaard, P. (2013). Proton pump inhibitor use and fracture risk—effect modification by histamine H1 receptor blockade. Observational case–control study using national prescription data. *Bone* 57, 269–271. doi:10.1016/j.bone.2013.08.013

Ali, K., Blake, N., and Ahmed, N. (2024). Assessing the relationship between opioid therapy and osteoporosis. *Int. J. Pain* 15, 55–69. doi:10.56718/ijp.24-015

Arora, E., Singh, H., and Gupta, Y. K. (2016). Impact of antiepileptic drugs on bone health: need for monitoring, treatment, and prevention strategies. *J. Fam. Med. Prim. Care* 5, 248–253. doi:10.4103/2249-4863.192338

Barkhordarian, M., Lawrence, J. A., Ulusan, S., Erbay, M. I., Aronow, W. S., and Gupta, R. (2023). Benefit and risk evaluation of quinapril hydrochloride. *Expert Opin. Drug Saf.* 22, 271–277. doi:10.1080/14740338.2023.2203481

Biosse-Duplan, M., Baroukh, B., Dy, M., de Vernejoul, M.-C., and Saffar, J.-L. (2009). Histamine promotes osteoclastogenesis through the differential expression of histamine receptors on osteoclasts and osteoblasts. *Am. J. Pathology* 174, 1426–1434. doi:10.2353/ajpath.2009.080871

Burge, R., Dawson-Hughes, B., Solomon, D. H., Wong, J. B., King, A., and Tosteson, A. (2007). Incidence and economic burden of osteoporosis-related fractures in the United States, 2005–2025. *J. bone mineral Res.* 22, 465–475. doi:10.1359/jbmr.061113

Cardet, J. C., Jiang, X., Lu, Q., Gerard, N., McIntire, K., Boushey, H. A., et al. (2019). Loss of bronchoprotection with ICS plus LABA treatment, β-receptor dynamics, and the effect of alendronate. *J. Allergy Clin. Immunol.* 144, 416–425.e7. doi:10.1016/j.jaci.2019.01.049

Celebi Torabfam, G., and Porsuk, M. H. (2024). The role of the receptor activator of nuclear factor Kappa-B ligand/osteoprotegerin ratio in vascular diseases: a therapeutic approach. *Angiology* 76, 309–322. doi:10.1177/00033197231226275

Centers for Disease Control and Prevention (CDC) (2007). NHANES 1988-2014 data documentation: Prescription medications—drug information. Available online at: https://wwwn.cdc.gov/Nchs/Nhanes/1999-2000/RXQ_DRUG.htm.

Chanpaisaeng, K., Teerapornpuntakit, J., Wongdee, K., and Charoenphandhu, N. (2021). Emerging roles of calcium-sensing receptor in the local regulation of intestinal transport of ions and calcium. *Am. J. Physiology-Cell Physiology* 320, C270–C278. doi:10.1152/ajpcell.00485.2020

Deng, A., Wang, F., Wang, S., Zhang, Y., Bai, L., and Su, J. (2024). Bone-organ axes: bidirectional crosstalk. *Mil. Med. Res.* 11, 37. doi:10.1186/s40779-024-00540-9

Fattahi, M. R., Niknam, R., Shams, M., Anushiravani, A., Taghavi, S. A., Omrani, G. R., et al. (2019). The association between prolonged proton pump inhibitors use and bone mineral density. *Risk Manag. Healthc. Policy* 12, 349–355. doi:10.2147/RMHP.S223118

Foessl, I., Dimai, H. P., and Obermayer-Pietsch, B. (2023). Long-term and sequential treatment for osteoporosis. *Nat. Rev. Endocrinol.* 19, 520–533. doi:10.1038/s41574-023-00866-9

Guan, Z., Yuan, W., Jia, J., Zhang, C., Zhu, J., Huang, J., et al. (2023). Bone mass loss in chronic heart failure is associated with sympathetic nerve activation. *Bone* 166, 116596. doi:10.1016/j.bone.2022.116596

Gullberg, B., Johnell, O., and Kanis, J. A. (1997). World-wide projections for hip fracture. *Osteoporos. Int.* 7, 407–413. doi:10.1007/pl00004148

Haddadi, K., Tahmasbi, N., Alaee, A., Alipour, A., and Ehteshami, S. (2024). Comparison of vicious effect of oral pantoprazole and famotidine on new bone formation in patients with lumbar spine fusion surgery: a randomized control trial. *Iran. J. Neurosurg.* 10, 0. doi:10.32598/irjns.10.1

Heo, K., Rhee, Y., Lee, H. W., Lee, S. A., Shin, D. J., Kim, W. J., et al. (2011). The effect of topiramate monotherapy on bone mineral density and markers of bone and mineral metabolism in premenopausal women with epilepsy. *Epilepsia* 52, 1884–1889. doi:10.1111/j.1528-1167.2011.03131.x

Houglum, J. E., Harrelson, G. L., and Seefeldt, T. M. (2024). "Drugs for treating hypertension and heart disease," in *Principles of pharmacology for athletic trainers* (New York: Routledge), 210–235.

Huang, X., Hu, J., Peng, H., and Cheng, H.-W. (2022). Embryonic exposure to tryptophan yields bullying victimization via reprogramming the microbiota-gut-brain axis in a chicken model. *Nutrients* 14, 661. doi:10.3390/nu14030661

Huang, Y., and Ye, J. (2024). Association between hypertension and osteoporosis: a population-based cross-sectional study. *BMC Musculoskelet. Disord.* 25, 434. doi:10.1186/s12891-024-07553-4

Jørgensen, E. B., Overgaard, L. K., Folkestad, L., Damkier, P., Hallas, J., and Henriksen, D. P. (2023). The risk of fragility fractures following initiation of gabapentin and pregabalin—A Danish, nationwide, high-dimensional propensity score-matched cohort study. *Basic Clin. Pharmacol. Toxicol.* 132, 384–391. doi:10.1111/bcpt.13825

Khan, S. (2023). Amoxicillin/clavulanate. Available online at: https://www.medicinenet.com/amoxicillin_clavulanate/article.htm (Accessed January 23, 2023).

Kuril, A. K., Manchuri, K. M., and Anand, S. P. (2024). Emerging protein and peptide therapeutics for osteoporosis: advances in anabolic and catabolic treatments. *J. Pharm. Res. Int.* 36, 85–102. doi:10.9734/jpri/2024/v36i117603

LeBoff, M. S., Greenspan, S. L., Insogna, K. L., Lewiecki, E. M., Saag, K. G., Singer, A. J., et al. (2022). The clinician's guide to prevention and treatment of osteoporosis. *Osteoporos. Int.* 33, 2049–2102. doi:10.1007/s00198-021-05900-y

Lerche, P. (2024). *Anticholinergics. Veterinary anesthesia and analgesia: the sixth edition of lumb and jones*, 314–318.

Leutner, M., Matzhold, C., Bellach, L., Deischinger, C., Harreiter, J., Thurner, S., et al. (2019). Diagnosis of osteoporosis in statin-treated patients is dose-dependent. *Ann. Rheumatic Dis.* 78, 1706–1711. doi:10.1136/annrheumdis-2019-215714

Li, S., Sun, W., Li, S., Zhu, L., Guo, S., He, J., et al. (2025). Tamsulosin ameliorates bone loss by inhibiting the release of Cl− through wedging into an allosteric site of TMEM16A. *Proc. Natl. Acad. Sci.* 122, e2407493121. doi:10.1073/pnas.2407493121

Liu, M. M., Dong, R., Hua, Z., Lv, N. N., Ma, Y., Huang, G. C., et al. (2020). Therapeutic potential of liuwei dihuang pill against KDM7A and Wnt/β-catenin signaling pathway in diabetic nephropathy-related osteoporosis. *Biosci. Rep.* 40, BSR20201778. doi:10.1042/BSR20201778

McCabe, S. E., Schulenberg, J. E., Wilens, T. E., Schepis, T. S., McCabe, V. V., and Veliz, P. T. (2023). Prescription stimulant medical and nonmedical use among US secondary school students, 2005 to 2020. *JAMA Netw. Open* 6, e238707. doi:10.1001/jamanetworkopen.2023.8707

Ng, C. W., Chan, B. C. L., Ko, C. H., Tam, I. Y. S., Sam, S. W., Lau, C. B. S., et al. (2022). Human mast cells induce osteoclastogenesis through cell surface RANKL. *Inflamm. Res.* 71, 1261–1270. doi:10.1007/s00011-022-01608-9

Ogawa, Y., Hirai, T., and Mihara, K. (2021). A meta-analysis of observational studies on anticholinergic burden and fracture risk: evaluation of conventional burden scales. *J. Pharm. Health Care Sci.* 7, 30–12. doi:10.1186/s40780-021-00213-y

Perrin, S., Montani, D., O'Connell, C., Günther, S., Girerd, B., Savale, L., et al. (2015). Nasal decongestant exposure in patients with pulmonary arterial hypertension: a pilot study. *Eur. Respir. J.* 46, 1211–1214. doi:10.1183/13993003.00051-2015

Peter, B., Lindsey, I. B., and Brian, W. W. (2020). Prevalence of multiple chronic conditions among US adults, 2018. *Prev. chronic Dis.* 17, E106. doi:10.5888/pcd17.200130

Ricciardi, B., Paul, J., Kim, A., Russell, L., and Lane, J. (2013). Osteoporosis drug therapy strategies in the setting of disease-modifying agents for autoimmune disease. *Osteoporos. Int.* 24, 423–432. doi:10.1007/s00198-012-2113-8

Roux, C., Briot, K., Gossec, L., Kolta, S., Blenk, T., Felsenberg, D., et al. (2009). Increase in vertebral fracture risk in postmenopausal women using omeprazole. *Calcif. Tissue Int.* 84, 13–19. doi:10.1007/s00223-008-9188-4

Sakr, M. (2024). *Thyroid and parathyroid endocrine emergencies. Head and neck and endocrine surgery: from clinical presentation to treatment success*. Springer, 453–491.

Song, S., Cai, X., Hu, J., Zhu, Q., Shen, D., Ma, H., et al. (2024). Effectiveness of spironolactone in reducing osteoporosis and future fracture risk in middle-aged and elderly hypertensive patients. *Drug Des. Dev. Ther.* 18, 2215–2225. doi:10.2147/DDDT.S466904

Thomas, P. A. (2007). Racial and ethnic differences in osteoporosis. *JAAOS-Journal Am. Acad. Orthop. Surg.* 15, S26–S30. doi:10.5435/00124635-200700001-00008

Venkatesh, A. K., Chou, S.-C., Li, S.-X., Choi, J., Ross, J. S., D'onofrio, G., et al. (2019). Association between insurance status and access to hospital care in emergency department disposition. *JAMA Intern. Med.* 179, 686–693. doi:10.1001/jamainternmed.2019.0037

Wu, S.-F., and Du, X.-J. (2016). Body mass index may positively correlate with bone mineral density of lumbar vertebra and femoral neck in postmenopausal females. *Med. Sci. Monit.* 22, 145–151. doi:10.12659/msm.895512

Yrkm, S. (2022). The effects of carisoprodol on endochondral ossification: a review of the literature and implications for bone health. *Ann. Musculoskelet. Med.* 6, 001–004. doi:10.17352/amm.000029

Zhang, Y., Chen, C. Y., Liu, Y. W., Rao, S. S., Tan, Y. J., Qian, Y. X., et al. (2021). Neuronal induction of bone-fat imbalance through osteocyte neuropeptide Y. *Adv. Sci.* 8, 2100808. doi:10.1002/advs.202100808

Zheng, Z., Johansson, H., Harvey, N. C., Lorentzon, M., Vandenput, L., Liu, E., et al. (2020). Potential adverse effect of nonsteroidal anti-inflammatory drugs (NSAIDs) on bisphosphonate efficacy: an exploratory post hoc analysis from a randomized controlled trial of clodronate. *J. Bone Mineral Res.* 37, 1117–1124. doi:10.1002/jbmr.4548

Frontiers in Pharmacology

Explores the interactions between chemicals and living beings

The most cited journal in its field, which advances access to pharmacological discoveries to prevent and treat human disease.

Discover the latest Research Topics

See more →

Frontiers

Avenue du Tribunal-Fédéral 34
1005 Lausanne, Switzerland
frontiersin.org

Contact us

+41 (0)21 510 17 00
frontiersin.org/about/contact